Kopmann, Rebekka; Folke, Frederik (Hg.)

Proceedings of the XXIXth TELEMAC Users Conference 12-13 October 2023

Vorgeschlagene Zitierweise / Suggested citation:

Kopmann, Rebekka; Folke, Frederik (Hg.) (2023): Proceedings of the XXIXth TELEMAC Users Conference 12-13 October 2023. Karlsruhe: Bundesanstalt für Wasserbau.

BAW
Federal Waterways Engineering
and Research Institute

openTELEMAC

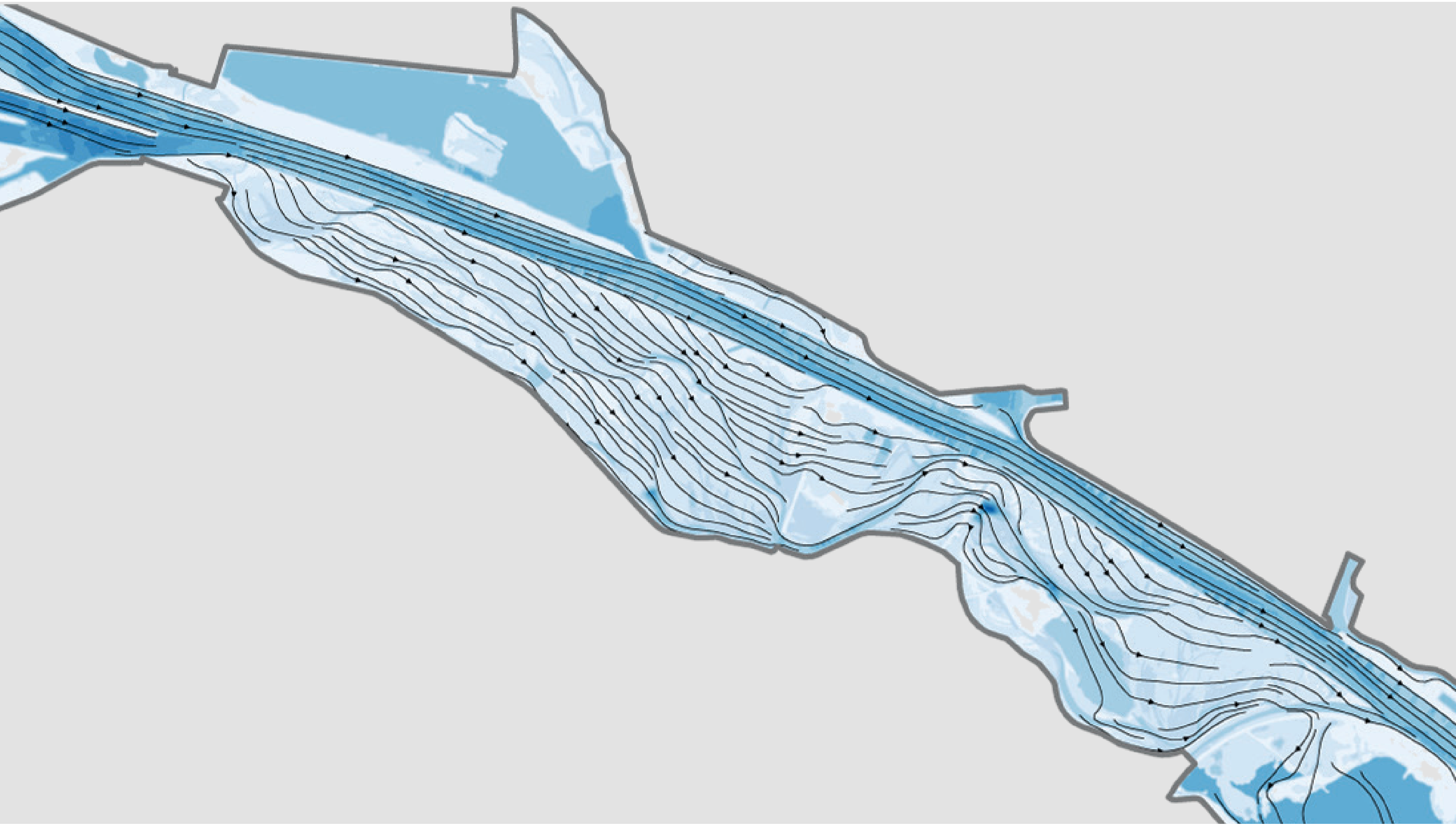

Proceedings of the
29th TELEMAC-MASCARET Users Conference 2023

12-13 October 2023, Karlsruhe

Proceedings of the XXIXth TELEMAC Users Conference
12-13 October 2023

Organised by
Bundesanstalt für Wasserbau
Kussmaulstr. 17
76187 Karlsruhe
Germany
www.baw.de

Edited by
Rebekka Kopmann
Frederik Folke

Published by:
Bundesanstalt für Wasserbau (BAW)
Federal Waterways Engineering and Research Institute
Kussmaulstrasse 17, 76187 Karlsruhe | P.O. Box 21 02 53, 76152 Karlsruhe
E-Mail: info@baw.de
www.baw.de

BAWProceedings
ISBN 978-3-939230-86-1 (online)
ISSN 2700-8444 (online)

Local Organizing Committee

Rebekka Kopmann
Frederik Folke
Thomas Brudy-Zippelius
Simone Knobloch
Claudia Zeman-Zachar

International Reviewer

Lars Backhaus (BAW)
Thomas Benson (HRW)
Birgit Bleyel (BAW)
Alexander Breugem (IMDC)
Thomas Brudy-Zippelius (BAW)
Antonia Dallmeier (TUM)
Clemens Dorfmann (flussbüro)
Noémie Durand (France Energies Marines)
Frederik Folke (BAW)
Sebastian Gegenleithner (Universität Graz)
Matthieu Gonzales de Linares (Artelia)
Robert Hagen (BAW)
Michiel Knaapen (HRW)
Rebekka Kopmann (BAW)
Elisabeth Rudolph (BAW)
Najibullah Sadid (BAW)
Peter Servouse (BAW)
Leopold Stadler (BAW)
Pablo Tassi (EDF)
Martin Utz (BAW)

Members of the TELEMAC Consortium

ARTELIA
www.arteliagroup.com

Federal Waterways Engineering and Research Institute
www.baw.com

Centre d'études et d'expertise sur les risques, l'environnement, la mobilité et l'aménagement
www.cerema.fr

Centre Européen de Recherche et de Formation Avancée en Calcul Scientifique
www.cerfacs.fr

Science and Technology Facilities Council Daresbury Laboratory
www.stfc.ac.uk

Électricité de France, Recherche & Développement, Laboratoire National d'Hydraulique et Environnement
www.edf.com

École des Ponts, ParisTech
www.ecoledesponts.fr

HR Wallingford
www.hrwallingford.com

International Marine and Dredging Consultants
www.imdc.be

Foreword of the XXIXth TELEMAC Users Conference

Dear TELEMAC Users,

We are delighted to welcome all participants to the 29th TELEMAC Users Conference (TUC) at the Federal Waterways Engineering and Research Institute (BAW) in Karlsruhe. As Germany's scientific competence centre for waterways engineering, numerical modelling is an indispensable method for the BAW to provide scientific and technological services in the field of hydraulic engineering. BAW's first contact with TELEMAC took place almost 30 years ago and was intensified by joining the TELEMAC-MASCARET consortium in 2010. We are very pleased to share a fruitful cooperation with a vibrant community of enthusiastic TELEMAC developers worldwide.

Exactly a decade has passed since the last TUC in Karlsruhe and we are excited to be hosting it again. In these ten years, TELEMAC has made significant progress. The sediment transport module GAIA has replaced SISYPHE, new modules such as NESTOR for dredging or Khione for ice modelling have emerged, Python has been integrated and used for API and pre- and post-processing, to name just a few examples. The conference format has also changed: driven by the pandemic, online and now hybrid conferences have been adopted. This year, we will have participants from 12 countries and 4 continents due to the hybrid format. For the first time, we have decided to include a poster session and a meeting for young scientists. In collective intelligence sessions, research topics around TELEMAC will be discussed in order to find new ideas, motivation and a better network between the (young) researchers. With the Young Scientists Meeting we want to initiate, refresh and deepen the interaction and collaboration between senior and young scientists, thus fostering an even stronger network within the TELEMAC community.

It is amazing to see the wide range of applications – from coast to estuaries to rivers – and further numerical developments covered by this year's contributions. The main topics are waves, sediments, floods, data assimilation, and water quality. All these topics are well aligned with the BAW's mission and we are eager to learn from other researchers, discover exciting projects, and exchange knowledge.

We look forward to engaging discussions around TELEMAC and all topics related to hydro- and morphodynamics. We are confident that the TUC will once again provide an invaluable platform for networking, collaboration, and knowledge sharing to the benefit of all participants. On behalf of the BAW and the TELEMAC-MASCARET consortium, we extend our gratitude to all authors and participants and wish you a productive and enjoyable conference experience in Karlsruhe.

Rebekka Kopmann and Frederik Folke

Chairs of the local organizing committee

Content

Session 1: Water Quality

Session 2: Data Assimilation

Session 3: Flooding

Session 4: Coastal Applications

Session 5: Waves and Sediments

Poster Session

Session 6: Sediments, Rivers and Estuaries

Session 7: Modelling and Methods

Modelling bathing water quality in the Marne River with TELEMAC-2D/WAQTEL

Lan Anh Van[1], Francesco Piccioni[1], Guido Petrucci[1], Aurélie Janne[2], Claire Beyeler[3]
[1]: PROLOG INGENIERIE, 69-71 Rue du Chevaleret, 75013 Paris
[2]: Syndicat Mixte Marne Vive, Avenue Charles de Gaulle, 94100 Saint-Maur-des-Fossés
[3]: Mairie de Saint-Maur-des-Fossés, Avenue Charles de Gaulle, 94100 Saint-Maur-des-Fossés

Abstract **– Swimming in the Marne River has been forbidden since 1970. This was motivated by the very poor water quality at that time and by safety conditions that were sometimes difficult to manage. Since 2015, the measurements of bacteriological quality along the river have shown a real improvement in the water quality, even if numerous contaminant sources persist and the quality remains heterogeneous. With the Paris Olympic Games starting next summer, the reopening of bathing sites in the Marne River is a major objective of the Syndicat Marne Vive (SMV). In addition to the measurements required by the Bathing Water Directive, numerical modelling can be considered as a powerful tool to evaluate the water quality and identify the main sources of contamination. Given the heterogeneity of the water quality along the river and the numerous potential sources of pollution, a two-dimensional model has been developed by coupling the TELEMAC-2D hydrodynamic model with its water quality module WAQTEL. The model was validated against in situ measurements of Escherichia Coli (*E. coli*) – the main faecal contamination indicator - in dry and wet weathers. Results show that the model can simulate not only the longitudinal evolution but also the transversal dispersion of bacteriological pollutants. The developed model was then used to classify the various sources of pollution in the study area and anticipate the impact of management measures on the future bacteriological state of the Marne River.**

Keywords: bathing waters directive; water quality; Escherichia Coli; numerical modelling.

I. INTRODUCTION

Bathing and aquatic sports are popular recreational activities, particularly during summer. In large metropolitan areas, having access to bathing sites can largely improve the life quality of inhabitants. However, due to the strong anthropic pressure, bathing in rivers and lakes located in large urban areas is often prohibited. When considering the establishment of a bathing site, it is paramount to ensure that the water quality allows swimming without any risk [1].

Nowadays, the demand for bathing sites in urban areas is ever increasing. Faced with this demand, bathing sites have opened in various European metropolises such as Amsterdam, Rotterdam, Dublin, or Berlin and Copenhagen [2]. However, the water quality of the bathing sites remains a central concern for the visitors. In most cases, the bathing sites are located in densely inhabited areas and therefore are particularly exposed to bacteriological contamination, which can arise from permanent or accidental wastewater overflows, and/or urban storm water discharges. The monitoring of the water quality is therefore crucial in such a context. The European Bathing Waters Directive 2006/7/EC identifies two microbiological parameters, *Escherichia coli* (*E. coli*) and *intestinal enterococci* (*IE*), as faecal indicator bacteria (FIBs) and suggests the use of their measurement for the management of bathing waters [3].

In Paris, with the preparation of the Paris-2024 Olympic and Paralympic Games, multiple potential bathing sites along the Seine and Marne rivers have been identified and put forward within the framework of an expression of interest [4]. In this context, this study focuses on the accurate determination of the microbiological quality of the Marne River, which is of particular interest as the Marne is the main tributary of the Seine upstream of Paris.

Recent measurements carried out in the Marne River in the Parisian Region show that the concentrations of *E. coli* et IE vary considerably not only along the longitudinal axis of the river, but also transversally to its flow, even in sections that are not influenced by external sources of contaminants [5]. Indeed, the transfer dynamics of micropollutants in a riverine environment are particularly complex as multiple factors are at interplay (bacterial mortality rate, sediment resuspension, water turbidity, local pollution inputs, turbulence, and mixing dynamics etc.). All these factors are site dependent and might vary over space and time.

In such a complex environment as the Marne River, the simple monitoring of FIBs is not sufficient to fully understand the transfer dynamics of micropollutants and predict the water quality at a specific bathing site. A 2D model is therefore needed.

In this study, the 2D hydrodynamic model TELEMAC-2D was coupled with the water quality model WAQTEL with the objective of reproducing (i) the average dry weather water quality profile over roughly 40 km of the Marne River as well as (ii) the impact of a rain event on the water quality of potential bathing sites. For this purpose, data from the local authorities of the sewage system were used to estimate the contamination sources under dry weather and 1D sewage system models were integrated in the modelling chain to simulate the contamination sources under wet conditions.

II. MATERIALS AND METHODS

A. Study area

1) The Marne River

The Marne is a 514 km long navigable river located in France. It is one of the main tributaries of the Seine River. Their confluence is located 2 km upstream of Paris. The Marne River presents a complex geomorphology with pronounced meandering and islands of different shapes and sizes around which the turbulence plays an important role and influences the mixing dynamics. Its discharge is regulated by a series of navigation dams. At the Gournay-sur-Marne gauging station (about 30 km upstream of the confluence with the Seine), its daily average discharge during the bathing season (i.e., from June to September) between 2017 and 2022 is of 52.2 m³/s, with a maximum of 252 m³/s (July 2021).

2) Bathing legislation and monitoring

Bathing is prohibited in the most downstream portion of the Marne River since 1970 due to safety and sanitary reasons. In the European Union, bathing waters are regulated by the "Bathing Waters Directive" of 2006 (2006/7/EC). The directive exploits two main parameters to designate waters with sufficient or insufficient quality for bathing: *Escherichia coli* (*E. coli*) and *intestinal enterococci*. The thresholds defined in the directive for these two parameters are, 900 MPN/100mL and 330 MPN/100mL respectively based upon a 90-percentile evaluation of the data from four consecutive monitoring seasons. More details on this matter can be found in the 2006/7/EC directive [3].

The water quality of the Marne River in the last 30 km of its course has been monitoring during the bathing season by the Syndicat Marne Vive (SMV) since 2015 (except 2016). Water samples are taken at multiple sites and subsequently analysed. Numerous parameters are measured, among which *E. coli* and *IE*. Preliminary analysis of the available dataset in terms of *E. coli* and *IE* showed that, in the study area, the most critical parameter regarding the bathing legislation thresholds is the *E. coli*. Indeed, it is observed that the median of *IE* concentrations is in general lower than the threshold fixed by the Bathing Waters Directive. Moreover, the two parameters show a strong correlation (linear regression coefficient (R^2) of 0.65 over the ensemble of available data). For these reasons, the modelling effort was focused on the *E. coli*. In this paper, only the results of *E. coli* will be presented and analysed. The map in Figure *1* shows all measuring sites in the SMV monitoring protocol. Dark green dots represent sites characterised by three samplings a week; light green dots represent sites with one sampling a week. The site "SMV0" is located 32 km upstream of the confluence with the Seine River; the site "SMV15" is located around 100 m upstream of the confluence. Since the objective of these measurements is for monitoring the bathing waters at the future bathing sites, all samples are taken close to the riverbank (left or right depending on the site).

Previous studies conducted by SMV showed that five measuring sites present characteristics particularly favourable to the opening of a bathing site (due to sanitary and/or morphological reasons) [6,7]. The five potential bathing sites (red dots in Figure *1*) are located, from upstream to downstream, in the municipalities of Chelles, Nogent-sur-Marne, Champigny-sur-Marne, Saint-Maur-des-Fossés and Saint-Maurice.

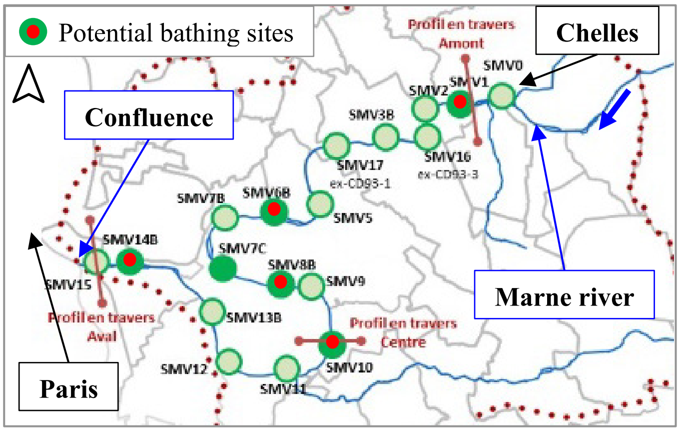

Figure 1. SMV measuring sites on the Marne River (source: SMV).

3) Definition of the model domain

The model domain extends from the inlet of Ru du Bouillon (a small tributary of the Marne River) until the confluence with the Seine River over 40 km approximately. The upstream boundary is located 9 km upstream of the first potential bathing site (Chelles – SMV1), corresponds to a transfer time of around 10 hours. The extent of the 2D model is shown in Figure *2*, along with a detail of the triangular mesh. The final mesh has 131 876 nodes and 244 007 elements with an average density of 5 m.

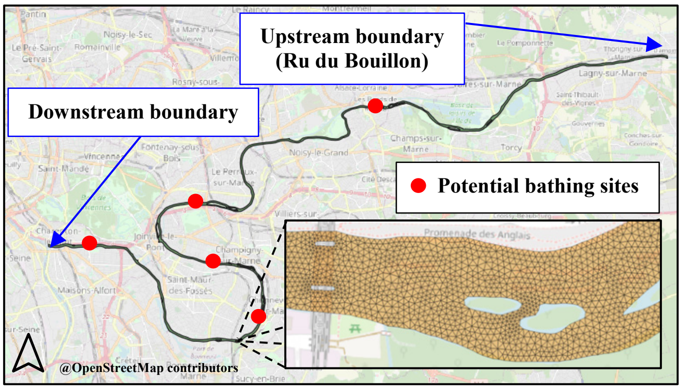

Figure 2. Model domain and a zoom of the unstructured mesh.

B. Model development

For the present study, a 2D model has been proposed by the direct coupling of TELEMAC-2D [8] and WAQTEL [9] modules. For each step of calculation time, the coupling is done in the following way:

- TELEMAC-2D calculates the difference in level of the free-surface level, and the velocity field.
- WAQTEL calculates the transport of suspended sediments, and the transport of bacteria.

In the water quality module WAQTEL [9], the sub-module MICROPOL was selected. This module is dedicated to model the evolution of micropollutants in rivers. It introduces 5 tracers:

- Suspended sediment (SS)

- Bed sediments (SF)
- Dissolved micro-pollutants (C)
- Micro-pollutants absorbed by SS (C_{SS})
- Micro-pollutants absorbed by BS (C_{SF})

The evolution of suspended (SS) and bed sediments (SF) involved in this module is represented by the classical deposition and resuspension laws for cohesive sediments of Krones and Partheniades. The sediment parameters include the settling velocity, the erosion rate (or Partheniades coefficient), the critical shear stress for erosion and for re-suspension. In this study, the main calibrated parameter is the settling velocity. According to tests carried out on different mud [10], the settling velocity generally ranges from 0.1 to 1.0 mm/s with increasing sediment concentration. A value of 0.1 mm/s was selected after the calibration step. The other parameters were selected from the literature ([11], [12]).

The model assumes that the transfer of micropollutants between the dissolved and particulate phases correspond to either adsorption or ionic exchanges modelled by a reversible reaction of 1st kinetic order. For the sake of simplicity, we considered that these two fractions evolved independently, without any interaction between them. The ratio of free bacteria to total bacteria was estimated equal to 50% according to the observations made in [13].

The model also includes an exponential decay law of micropollutant concentrations in each compartment of the modelled ecosystem, through a constant *L*.

$$X_\tau = X_0\ \varepsilon^{-\Lambda\tau} \qquad (1)$$

where:

C_0: concentration of micropollutant at time 0

C_t: concentration of micropollutant at time t,

L: decay rate.

In this study, the decay rate was considered as the mortality rate of the modelled bacteria (*E. coli*). It was calibrated using the data collected on the Marne River by Mouchel et al. in [5]. A value of $0.072\ h^{-1}$ was assigned to both the dissolved and particulate phases of the bacteria pool.

The internal sources of each of these tracers correspond to the phenomena of deposition/re-suspension and exponential decay, represented in Figure 3.

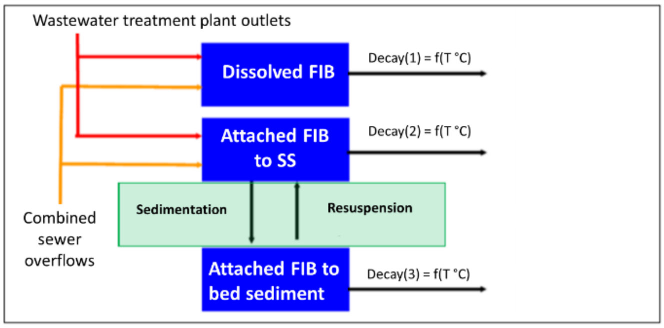

Figure 3. Sketch of the different processes included in the coupled model for the tracers (adapted from [13]).

C. *Estimation of the pollution sources*

Along the study zone, the land use in the watershed of the Marne River changes drastically from mostly agricultural (department 77, upstream of the measuring site SMV2 in Figure *1*) to extremely urbanised as its course passes through the Paris region (departments 93 and 94). In such a context, the wastewater and rainwater drainage systems represent an important source of pollution. Indeed, the study area includes a high number of outlets from the rainwater drainage system. Under dry conditions, poor connections can constitute a direct and chronic source of contamination. Under wet conditions, rainfall runoff and overflows constitute short-term sources of contamination.

Furthermore, within the study area, two wastewater treatment plants (WWTP) for a total of more than 500 000 in population equivalent (PE) discharge their waters in the Marne River. Their outlets are located in Saint-Thibault-des-Vignes (STV, left bank, 7.5 km upstream of the potential bathing site Chelles) and in Champigny-sur-Marne (MAV, left bank, 1.9 km upstream of the potential bathing site Saint-Maur-des-Fossés).

The data analysis collected within this study allowed to identify, in the model's perimeter, a total of 75 pollution sources under wet conditions and 44 under dry conditions (34 well-documented and 10 additional pollution sources estimated based on the PE method).

In this study, all dry weather pollution sources were modelled by constant discharge and *E. coli* concentration. The discharges were estimated based on the collected data. The associated *E. coli* concentrations were obtained either from measurements, when available, or from characteristic values based on the nature of the source (Table *1*).

Table 1 Characteristic *E. coli* concentrations based on the nature of the outlet (according to [14]).

	Nature of the contribution		
	Wastewater	***Rainwater***	***Mixed waters***
E. coli **concentration (MPN/100mL)**	10^7	10^4	10^6

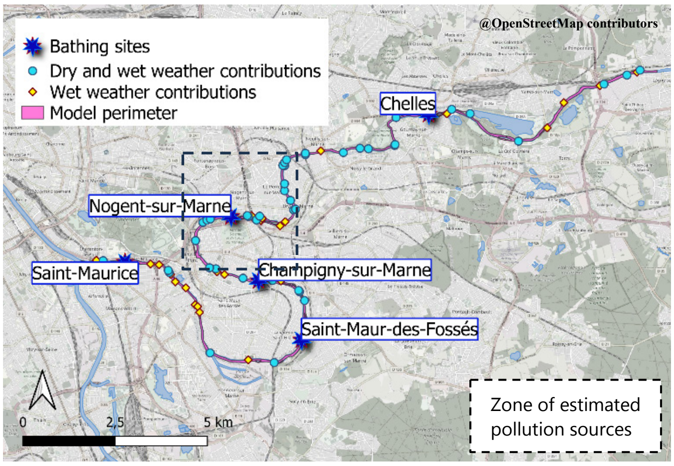

Figure 4: Modelled dry (blue dots) and wet weather pollution sources (yellow dots) in the study area.

Under wet weather, the discharge of the pollution sources varies over time depending on the rainfall intensity. When available, 1D drainage network models were used to estimate the variable discharge over time. This is the case for 50 of the 75 modelled contributions. *E. coli* concentration was calculated from the values given in Table *1*. For the remaining sources, whose contribution under wet weather remains unknown, their dry weather discharge and concentration were then used.

For the two wastewater treatment plants, data were available to define a daily discharge and *E. coli* concentration.

D. Data analysis

The complete dataset in terms of *E. coli* (collected by SMV over six bathing seasons from 2017 to 2022) is shown in Figure *5*. In the boxplot, all *E. coli* data available from all measuring sites on the Marne River are gathered and presented per year.

The data in Figure *5* show a strong variability of *E. coli* concentration within a single bathing season, as well as an intense interannual variability. The former can be associated with local rainfall and discharge conditions which impact the microbiological condition of the river leading to strong occasional peaks in the FIB concentration. The latter can be explained by specific external conditions that characterise a whole bathing season. Data from 2017, 2019, 2020 and 2022 are comparable in terms of overall microbiological pollution, with the average *E. coli* concentrations under 2 000 MPN/100mL. The bathing seasons of 2018 and 2021 show remarkably higher *E. coli* concentrations. The 2018 season was characterised by the prolonged (several weeks) bursting of a wastewater pipe in Chelles (upstream of the first bathing site) discharging its wastewaters directly in the Marne River. In 2021, the Marne River was characterised by particularly high discharges that might influence the resuspension and/or the mortality rate of the bacteria. For these reasons, data of 2018 and 2021 were discarded from all further analysis.

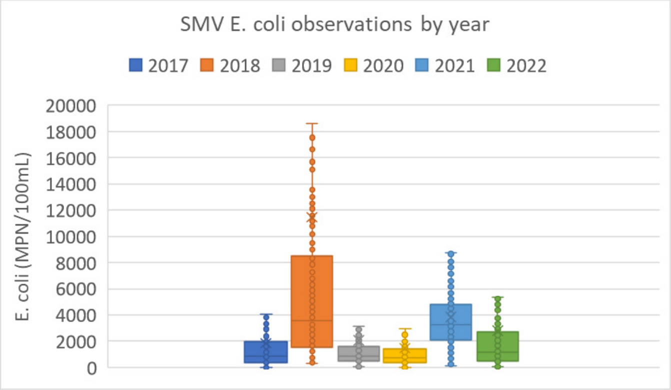

Figure 5. Boxplot of measured *E. coli* concentrations in the Marne River during summers from 2017 to 2022.

E. Model calibration

1) Hydrodynamics

The hydrodynamic model was first calibrated using the data of water velocity measured by an Acoustic Doppler Current Profile (ADCP) at three potential bathing sites along the river during the summer of 2022 (Chelles, Saint-Maur-des-Fossés and Saint-Maurice). At each site, different ADCP profiles were measured. Since the model is in two dimensions, the simulated values are the average velocities over the water column. The available measurements were therefore aggregated to calculate the average measured velocities over the water column. The results show good agreement between the measurement and the model, as seen in the Figure 6. A Strickler of 40 $m^{1/3}/s$ was selected.

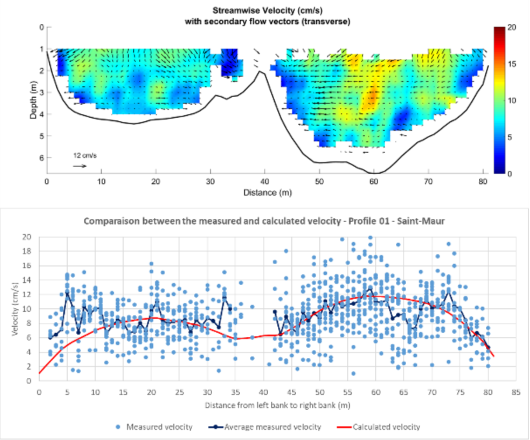

Figure 6: Measured ADCP velocity data at profile 1 of Saint-Maur (upper) and comparison between the measured and calculated average velocity (lowers) at different profiles.

2) *Water quality under dry weather*

The water quality model was calibrated in terms of *E. coli* under dry weather conditions, by comparing the longitudinal profile of *E. coli* between the model results and the “average” dry weather data in the Marne River. To do so, the *E. coli* data collected under dry weather during bathing season were first filtered to keep only data corresponding to a representative discharge of the bathing season in the Marne (from 30 to 40 m3/s). Then, the median of the filtered data was calculated at each measuring site. The data of 2018 and 2021 were excluded from the dataset because of exceptional environmental conditions and non-representative of the average dry weather profile (see section II.D).

A simulation with a constant discharge of 37 m^3/s was carried out. Model results were then extracted (under stationary condition) at each measuring station and were compared to the calculated medians.

The main model parameters involved in the calibration were the mortality rate, the settling velocity, the critical shear stress for re-suspension (see in II.B). Contamination sources were also included in the calibration process. Indeed, preliminary tests showed that the 34 documented dry weather sources were not sufficient to correctly reproduce the longitudinal profile of *E. coli* concentration observed in the river under dry weather. In particular, the average *E. coli* concentration observed under dry weather between the measuring sites SMV5 and SMV9 was underestimated by the model. Therefore, additional sources were estimated from the non-conformity rate of the local watershed and the population data. This allowed to estimate a population equivalent of around 18 000 discharging wastewaters in the Marne River. Such contribution was therefore distributed to 10 contamination inputs located between the measuring sites SMV5 and SMV9.

F. *Model validation under wet weather*

The model was then validated under wet weather conditions by simulating two consecutive rain events on the 14^{th} and 16^{th} of August 2022. The two events started respectively at 15:25 on the 14^{th} and at 18:49 on the 16^{th}. They were characterised by a total rainfall depth of 9.6 mm and 14.8 mm respectively over a span of roughly five hours for the first event and 30 minutes for the second one. These events were selected because of (i) the amount of *E. coli* measurements in the days following the events, which allowed a comparison with the model results and (ii) the difference in their intensity.

A six-day simulation was run from the 14^{th} until the 19^{th}. The contributions of the 75 modelled sources (discharge and *E. coli* concentration) were estimated as described in section II.C. A 15-minute time interval hydrograph measured at the Gournay-sur-Marne station was applied at the upstream boundary of the model. Model results in terms of simulated *E. coli* concentration were compared to the measurements at the five potential bathing sites.

III. RESULTS AND DISCUSSION

A. *Dry weather model results*

Results of the calibrated model at each measuring site from upstream to downstream the Marne River are shown in Figure 7. They are compared to the median of the SMV data collected under dry weather conditions over the bathing seasons 2017, 2019, 2020 and 2022.

Regarding the measurements, the graph shows the typical microbiological profile of the Marne River under dry weather conditions: a decrease in the *E. coli* concentration between SMV0 and SMV16 followed by a strong increase in the concentration at SMV3B. Between SMV17 and SMV9 is a sector in which the *E. coli* concentration remains at high values. Downstream of SMV10, absence of major pollution sources leads to the decrease in *E. coli* concentrations. The dry weather medians of the different bathing seasons show a similar pattern, comparable in terms of order of magnitude.

The coupled TELEMAC-2D/ WAQTEL model reproduces very well the dry weather microbiological profile of the Marne River, as represented by the green line in Figure 7. The interplay between the mortality rate derived from [5] and the contamination sources is well balanced and allows the model to reproduce all macroscopic variations in *E. coli* concentration. Nevertheless, the model tends to approach the maximum values within the measured years, i.e., 2022. As discussed previously, strong annual variability can be observed from the measurements. For instance, the concentration values in 2020 are particularly low and, for some sites, considerably lower than the other years. In order to avoid any underestimation of the pollution in the study area, it was then decided to calibrate the model with the higher range of concentrations of *E. coli*.

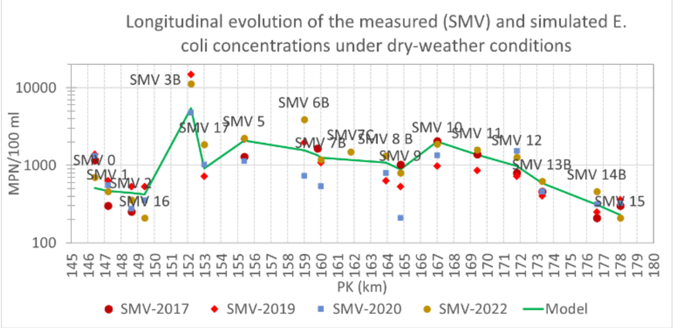

Figure 7: Model results under dry weather: longitudinal evolution of the measured (SMV) and simulated *E. coli* concentrations.

B. *Wet weather model results*

Model results at the five potential bathing sites are shown in terms of *E. coli* concentration in Figure 8, together with the results of three consecutive SMV measuring campaigns carried out on the 16th, 18th and 19th of August 2022. At the Saint-Maur-des-Fossés bathing site, data from an additional transversal profile are also available on the 17th of August.

The coupled TELEMAC-2D/WAQTEL model results are very satisfactory at five potential bathing sites. At each site, three observations are available to evaluate the model performance (four at the Saint-Maur-des-Fossés site).

The first SMV campaign is conducted on the 16th of August, about 40 hours after the first rain event but before the start of the second one. The observations are well reproduced at the sites Chelles and Champigny-sur-Marne. Differences between model results and observations can be seen at the sites of Nogent-sur-Marne. It must be noted that a measurement problem was identified in 2022 at this site. Downstream of the study area, a possible time lag is observed at Saint-Maur-des-Fossés and Saint-Maurice.

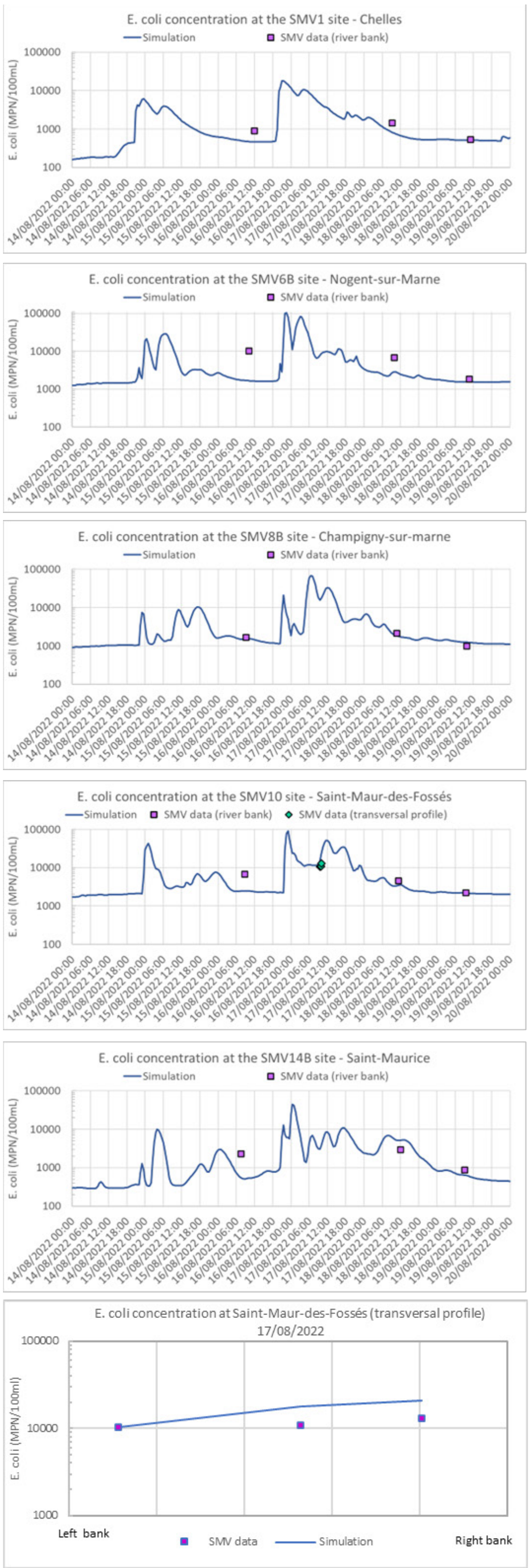

Figure 8: Model results and measurements of *E. coli* concentration during the validation simulation at the five potential bathing sites.

Measurements taken on the 18th of August are very well reproduced by the model, except at the Nogent-sur-Marne site. These measurements were taken 40 hours after the second rain event.

The latter campaign (19th of August) was taken when the impact of the second rain event was over, i.e., under dry weather conditions. The *E. coli* concentrations are correctly reproduced by the model at all sites. This confirms that the average dry weather conditions are correctly simulated by the model. Eventually, data from the transversal profile taken on the 17th of August at Saint-Maur-des-Fossés (around 15 hours after the second rain) are also extremely well reproduced by the model.

In general, the good agreement between simulated and observed concentrations shows that the model is capable to correctly reproduce the impact of a rain event on the bacteriological dynamic in the Marne River. This is of particular importance in the management of a bathing site.

An extract of the 2D model results in terms of *E. coli* concentration under wet weather conditions is show as an example in Figure 9. The figure represents the simulated *E. coli* concentration at 21:30 of the 16th of August, around two hours and a half after the second rain event. The main pollution sources are marked with black arrows. The figure stresses out the importance of the development of a 2D model by showing how, at multiple locations, the presence of morphological features such as islands or bends which influence the transversal mixing dynamics, resulting in local differences in the *E. coli* concentration on the two banks of the river. As seen from Figure 9:, the Nogent-sur-Marne bathing site is mainly impacted by the pollution source located upstream of the three following islands: Île d'Amour, Île du Moulin and Île des Loups. Due to the presence of these islands, the *E. coli* concentrations are less diffused but concentrated on the left channel. Hence, the impact of this source to the site Nogent-sur-Marne, which is located on the right bank is less. On the other hand, without the presence of any morphological features, the diffusion of the pollution sources located upstream of Champigny-sur-Marne and Saint-Maurice looks quite homogeneous over the river cross section after a certain distance.

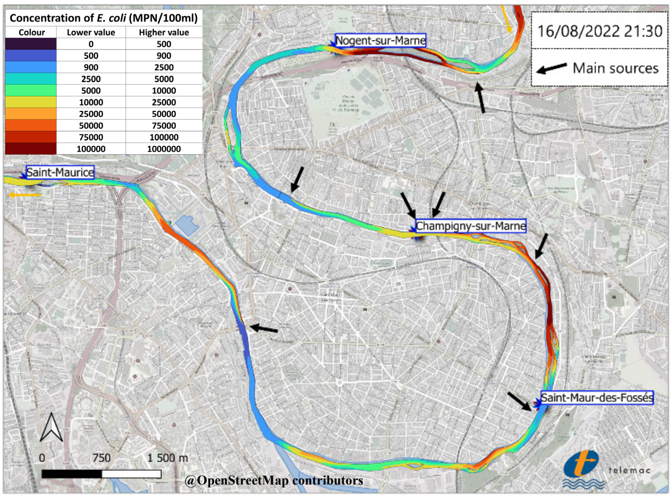

Figure 9: Extract of the 2D model in terms of *E. coli* concentration under wet weather conditions.

C. Discussion

The results presented in the previous sections show that the coupled TELEMAC-2D and WAQTEL model can be used for the modelling of the microbiological dynamics in a complex riverine system such as the Marne River. It can model not only the "average" dry weather stationary conditions, but also the time-dependent and event-dependent wet weather conditions. In fact, modelling the microbiological dynamics in a riverine environment under wet conditions entails a higher grade of complexity compared to the stationary dry weather simulation. Under wet weather, the multiple factors are complicated by the addition of a time-varying component. Indeed, the estimation of pollution inputs after a rain event is not an easy task.

The developed modelling chain involves different stages: from rainfall-runoff modelling at the scale of the watershed to 1D hydrodynamic transfer via sewage system simulation to 2D coupled hydrodynamic and microbiological modelling. It is necessary to note that in the development of such modelling chain, multiple hypothesis have been taken. Overall, the developed modelling tool can be considered reliable and robust, and the methodology used for its development can be extended and applied to different study sites.

However, it has to be highlighted that a high level of detailed information (multiple data sources, extensive knowledge of the watershed and of the sewage system, availability of drainage system models and so on) is needed for the development of the present modelling chain. Moreover, the availability of an extensive dataset of *E. coli* concentration, covering six bathing seasons and at 18 measuring sites over around 30 km of river was paramount for the development (calibration and validation) of the model.

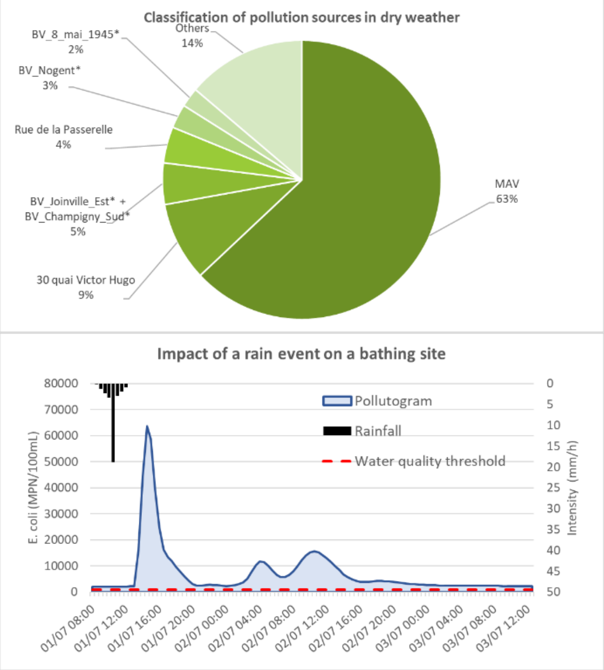

Figure 10: Example of model results: classification of pollution sources in dry weather (upper) and simulation of the impact of a rain event (lower) at the bathing site of Saint-Maur-des-Fossés.

The resulting model is a powerful tool that can be exploited for the management of water quality at bathing sites. The model can be used to classify the pollution sources and to carry out future scenarios, both under dry and wet weather. This allows to identify the main sources and to plan adequate actions for the improvement of water quality on the study area (Figure *10*).

The results of this work show that the coupled TELEMAC-2D and WAQTEL model can be successfully used to reproduce a complex dynamic such as that of the *E. coli* in a riverine ecosystem. However, through the different tests performed, it was observed that the coupled model struggles when the river discharge increases strongly. This work was carried out in the framework of a recreational use of future bathing sites. For this reason, the model was set up under quite low river discharge conditions (less than 50 m^3/s). Preliminary data analysis showed that with higher discharges (e.g., greater than 100 m^3/s), measurements of *E. coli* also increased consistently. The reason behind this behaviour is still uncertain and could be related to an ensemble of factors: (i) higher discharge causing an increase in turbidity and a decrease in the overall mortality rate of the bacteria, (ii) higher velocity causing bacteria to impact a greater area during their survival time, or (iii) re-suspension processes introducing in the river an additional stock of pollutants trapped in the sediments. The model is not able to capture these phenomena and tends to underestimate microbial concentrations under higher discharge conditions. Such limitations should be further addressed in order to achieve a more robust and adaptable model configuration.

Finally, the execution of a long-term simulation covering a whole bathing season (four months) within the framework of this study could also have provided additional information. For instance, it would allow to directly calculate the 90th percentile value from the simulated *E. coli* concentrations, an important indicator for the classification of bathing water quality [3].

IV. CONCLUSIONS AND PERSPECTIVES

In this paper, a coupled TELEMAC-2D and WAQTEL model has been developed to model the transfer of *E. coli* bacteria from different point sources to five bathing sites on the Marne River. The results show that developed model is a robust and powerful tool for the management of water quality of bathing sites.

The approach used in this work is close to that of digital twin: it entails the use of multiple models in a chain capable of taking into account the physical processes of rainfall, runoff production, transport through the watershed (potentially, through a drainage system) and impact on the receiving environment.

The development of such an approach can lead to an integrated and quasi real-time management of the drainage system and of the bathing sites located in the receiving environment.

ACKNOWLEDGEMENT

The authors would like to thank the SMV for having funded the study, as well as all the local authorities of the sewage system for providing a substantial amount of data and resources to carry out the study.

REFERENCES

[1] T. Kistemann, A. Schmidt, and H.-C. Flemming, "Post-Industrial River Water Quality—Fit for Bathing Again?" International Journal of Hygiene and Environmental Health 219, no. 7, Part B (2016): 629–42. https://doi.org/10.1016/j.ijheh.2016.07.007.

[2] J. Meyerhoff, Alexandra Dehnhardt, and H. Volkmar, "Take Your Swimsuit along: The Value of Improving Urban Bathing Sites in the Metropolitan Area of Berlin." Journal of Environmental Planning and Management 53, no. 1 (January 1, 2010): 107–24. https://doi.org/10.1080/09640560903399863.

[3] European Union (EU), "Directive 2006/7/EC of the European Parliament and of the Council of 15 February 2006 Concerning the Management of Bathing Water Quality and Repealing Directive 76/160/EEC.," n.d.

[4] J.-M. Mouchel, F. Lucas, L. Moulin, S. Wurtzer, A. Euzen, J.-P. Haghe, V. Rocher, S. Azimi, and P. Servais, "Bathing Activities and Microbiological River Water Quality in the Paris Area: A Long-Term Perspective." In The Seine River Basin, edited by Nicolas Flipo, Pierre Labadie, and Laurence Lestel, 323–53. Cham: Springer International Publishing, 2021. https://doi.org/10.1007/698_2019_397.

[5] J.-M. Mouchel, I. Colina-Moreno, and N. Kasmi, "Evaluation of faecal indicator bacteria levels in the Seine in the Paris metropolitan area in dry weather - Evaluation des teneurs en bactéries indicatrices fécales en Seine dans l'agglomération parisienne par temps sec." PIREN-Seine. Paris, France, 2018

[6] SMV, PROLOG INGENIERIE, « Identification de sites potentiels de baignade en Mmarne, au regard de la qualité bactériologique et des travaux d'assainissement à réaliser », 2018.

[7] SMV, F. S. Lucas, P. Servais, « Étude de la qualité bactériologique de la zone aval de la Marne », 2016.

[8] "TELEMAC-2D User Manual - Version V8p2." EDF R&D, December 1, 2020.

[9] "WAQTEL Technical Manual - Version V8p2." EDF R&D, December 1, 2020.

[10] J. C., Winterwerp, On the dynamics of high-concentrated mud suspensions., 1999.

[11] L.-A. Van , "Numerical modelling of sand-mud mixtures settling and transport processes : application to morphodynamic of the Gironde estuary (France)". PhD thesis. Université Paris-Est, 2012. English.

[12] B. Mengual, P.L. Hir, F. Cayocca, T. Garlan, "Modelling Fine Sediment Dynamics: Towards a Common Erosion Law for Fine Sand, Mud and Mixtures." Water 2017, 9, 564. https://doi.org/10.3390/w9080564

[13] M. Poulin, S. Pierre , J.-M. Mouchel, C. Therial, L. Lesage, V. Rocher, A. Goncalves, S. Masnada, F. Lucas, and N. Flipo, « Modelling faecal contamination in the Seine – Impact of contamination sources in wet weather. PIREN-Seine program : Report on modelling Faecal contanimation during wet weather - Modélisation de La Contamination Fécale En Seine : Impact Des Rejets de Temps de Pluie. Programme PIREN-Seine Rapport Modélisation de La Contamination Fécale Par Temps de Pluie." Programme PIREN-Seine, 2013.

[14] R. Mailler, S. Pichon, J. Bernier, S. Guérin, S. Azimi, V. Rocher, Etat des lieux de la contamination bactériologique de la Seine en agglomération parisienne, 2016.

[15] L.-A. Van, K.-D. Nguyen, F. Le Marrec, A. Jairy, "Development of a Tool for Modeling the Fecal Contamination in Rivers with Turbulent Flows - Application to the Seine et Marne Rivers (Parisian Region, France)". Water 2022, 14, 1191. https://doi.org/10.3390/w14081191.

Modelling of dissolved oxygen dynamics in the highly turbid Loire estuary

Anne Levasseur[1], Régis Walther[1], Guillaume Isserty[1], Olivier Bertrand[1]
anne.levasseur@arteliagroup.com
[1]: ARTELIA, 6 rue de Lorraine, 38130 Echirolles, France

***Abstract* –A three-dimensional water quality model coupled to a sediment transport model is constructed to simulate the spatial and temporal variations of dissolved oxygen concentrations in the Loire estuary. It includes the major biogeochemical processes influencing oxygen consumption and production in the water column: algal growth and mortality, organic matter degradation, exchange with the atmosphere, and the influence of nitrogen load. Biogeochemical fluxes are based on the submodule EUTRO from the module WAQTEL, with new developments to includes the specific features of the interactions between the organic fraction of SPM and the water quality variables for applications in turbid estuaries. The organic matter is represented as a fraction of the total suspended matter concentration. The model is calibrated using an extensive set of observations collected in Summer 2019 within the estuary: high-frequency observations of dissolved oxygen concentrations at 5 monitoring stations, and biweekly measurements of chlorophyll *a* and ammonium concentrations at 6 locations. The error between modelled and observed dissolved oxygen concentration is estimated by means of the Willmott Skill Score (WSS). A WSS above 0.7 on a scale of 0 to 1 is obtained for all stations, demonstrating the ability of the model to represent the variability of oxygen concentration within the estuary under the influence of tides, river inputs and SPM distribution.**

Keywords: dissolved oxygen, Loire estuary, estuarine turbidity maximum

I. INTRODUCTION

The Loire estuary is a highly turbid and macrotidal estuary located in France in the Bay of Biscay. It is the outlet of the Loire River drainage basin, covering a surface of about 117 000 km^2. The Loire River has a mean annual flow of 842 m^3/s over the period 1971-2021 at Montjean-sur-Loire [1], the most downstream hydrometric station not influenced by the tides.

Dissolved oxygen in estuaries is of primary importance for benthic and pelagic fauna. More specifically, fish responses to a depleted oxygen level include altered capacity for migration and reduced growth of salmonids at level below 5 mg/l (threshold for hypoxia), increased juvenile mortality, reduced growth and productivity, increased mortality of salmonids at level below 3 mg/l (critical threshold), mortality for most species at level below 2 mg/l, and for all species below 1 mg/l (lethal threshold) [2].

In the Loire estuary, the main process of oxygen depletion is the degradation of organic matter associated with sediment aggregates. Depleted levels of oxygen are caused by [2]:

- High water temperature in Summer which accelerates organic matter degradation and the associated oxygen consumption
- Low river inflow conditions which limit the water renewal and increase the residence time of particulate organic matter
- High tidal range which tends to resuspend estuarine mud deposited on the bed

As a result, observations show recurrent events of oxygen depletion in Summer during low river flow and increased water temperature. The most intense are observed during spring tides in the Estuarine Turbidity Maximum Zone (ETMZ).

The objective of this work is to develop a three-dimensional model of dissolved oxygen (DO), coupled to the hydrosedimentary model of the Loire estuary. At first, datasets available for the calibration are presented in II, then a brief overview of the hydrosedimentary model is given in III. The procedure for the inclusion of water temperature and light attenuation are described in section IV and section V. The processes of the oxygen model and its coupling with the hydrosedimentary model is described in section VI . Comparison of modelled results against observations is presented and discussed in section VII.

II. DATASETS AVAILABLE

A. *High frequency monitoring*

DO concentrations measurements at 10 to 60 minutes interval are made available at 6 stations (Donges, Paimboeuf, Cordemais, Le Pellerin, Trentemoult, Bellevue) along the Loire estuary for the years 2007-2019. It is part of the measurements recorded by the network of hight frequency monitoring stations called SYVEL, installed and maintained by the Groupement d'Intérêt Public Loire Estuaire (GIP Loire Estuaire), a public/private sector partnership organisation dedicated to the Loire estuary, with contributions from other stakeholders [3]. This network also records water temperature and turbidity measurements. In addition to SYVEL, a sensor at Montjean-sur-Loire provides high-frequency measurements of water temperature.

B. *Monthly and bi-monthly survey*

Regular measurements of water quality parameters are made as part of the monitoring programs for the Loire estuary organised by the French Water Agency, the departmental directorate of territories (direction départementale des territoires et de la mer - DDTM), and the French Research Institute for

Exploitation of the Sea (Institut français de recherche pour l'exploitation de la mer - IFREMER). It is based on the collection of in situ water samples near the surface at fixed monitoring stations. All data are available through the NAIADES portal [4], starting from year 2005. The frequency is monthly or bimonthly. For this work, the water quality parameters dissolved oxygen (O_2), the biochemical oxygen demand (BOD), ammonium (NH_4^+), and Chlorophyll *a* (Chl *a*) as a proxy of phytoplankton biomass are extracted from 2010 onwards. Chl *a* measurements are generally available only during the productive period, from March to October. Figure 1 shows the locations of the stations used for calibration.

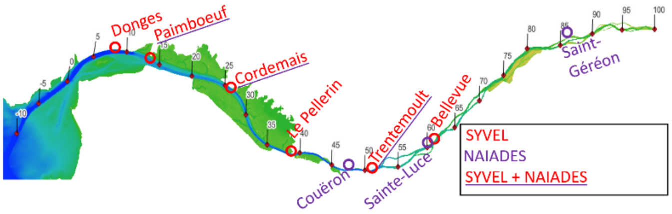

Figure 1. Locations of the stations used for calibration with specification on the type of data : high-frequency sensors (SYVEL) or in situ sampling survey (NAIADES)

III. THREE-DIMENSIONAL MODELLING OF ESTUARINE CIRCULATION AND SUSPENDED SEDIMENT TRANSPORT

A. Model domain

The model domain encompasses the whole estuary, from the mouth of the estuary up to the kilometre point 99, identified as the limit for the influence of the tides (Figure 2). It extends 100 km offshore in the Bay of Biscay. The model grid is composed of approximately 55000 nodes for each horizontal plane and there are 12 layers from top to bottom.

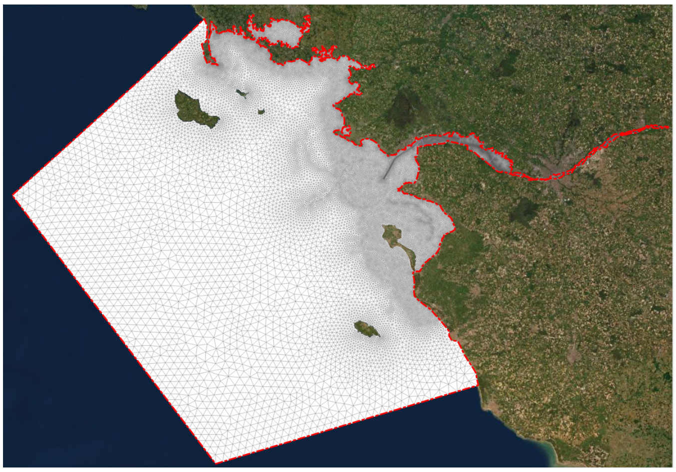

Figure 2. Model grid

B. Modelling hydrodynamic and sediment transport

An overview of the development of the three-dimensional numerical model is given in the companion paper, published in the TELEMAC User Conference 2022 [5]. It gives an extensive description of the configuration, calibration and results of the hydrodynamic model coupled to a sediment transport model. Most importantly, the numerical model represents the specific features of the ETMZ and the estuarine circulation under the influence of tides, inputs of freshwater from upstream and density gradients.

IV. WATER TEMPERATURE

A. Methods

For this application, it is assumed that vertical variations of temperature are negligible in the internal estuary and do not significatively influence the density gradient, controlled by salinity and Suspended Particulate Matter (SPM). The variations of mean daily water temperature as a function of the time t and the longitudinal distance x T(x,t) are calculated using the following sinusoidal equation established in a report of the port of Le Havre and Saint-Nazaire, and documented in [6]and [7]:

$$T(x,t)=Ta(x)+Tb(x) \sin(2 p (t-T\_phase)/365.25) \quad (1)$$

With t the time, x the distance, and the following parameters Ta and Tb :

$$Ta (x) = (Tmax(x)+Tmin(x))/2 \quad (2)$$

$$Tb (x) = (Tmax(x)-Tmin(x))/2 \quad (3)$$

Tmin is the annual water temperature and Tmax is the annual maximal water temperature. T_phase is the phase of the annual curve which determines the position of the maximum over the course of the year.

B. Fitting procedure

High frequency datasets of the water temperature are used to calculate the best parameters Tmin and Tmax and represent the seasonal variation. At each date, the longitudinal profile of the temperature is obtained by linearly interpolating the temperature between stations. The fitting procedure is based on the calculation of the least-square residual. Daily means were already available for the station of Mauves-sur-Loire. High-frequency datasets are processed by the following method for each station:

- Datasets starting from 1st January 2007 are used
- A daily mean of the water temperature is calculated. If the number of recorded values for the day is below 48 for a record at 15-minute intervals, or below 12 for hourly measurements, the daily mean is considered as not representative and discarded.
- At the final stage, the interannual daily temperature is calculated for the years to obtain a representative seasonal cycle of the daily temperature.

Tmin ranges from 5.90 to 7.35 degrees, while Tmax ranges from 23.00 to 21.23 degree Celsius depending on the stations (Table I). The number of years represent the average number of years available for the calculation of the interannual daily mean. It is in the order of 10 years, apart from stations Cordemais and Donges, where the time-series is only 6 or 7 years.

From upstream to downstream, Tmin is increased while Tmax is reduced (Table I and Figure 3). It illustrates the reduced amplitude of the annual temperature near the mouth of the estuary, as representative of ocean water. The degree of correlation between the fitted curve and the interannual seasonal cycle of the temperature is above 0.99 for all stations, indicating that the fitted curve is representative of the observations.

Table I Results of the fitting procedure

Station	*Tmin*	*Tmax*	*Tphase*	*Number of years*	*Correlation coefficient*
-	°C	°C	days	-	-
Montjean-sur-Loire	5.90	23.29	110.69	9.71	0.9944
Mauves-sur-Loire	5.79	23.68	111.27	10.60	0.9960
Bellevue	5.44	23.26	111.11	11.24	0.9961
Trentemoult	6.19	23.00	111.12	11.59	0.9951
Le Pellerin	6.22	23.06	111.69	11.20	0.9950
Cordemais	6.19	22.58	114.67	6.13	0.9946
Paimboeuf	6.90	21.65	115.88	9.45	0.9950
Donges	7.35	21.23	119.49	7.33	0.9943

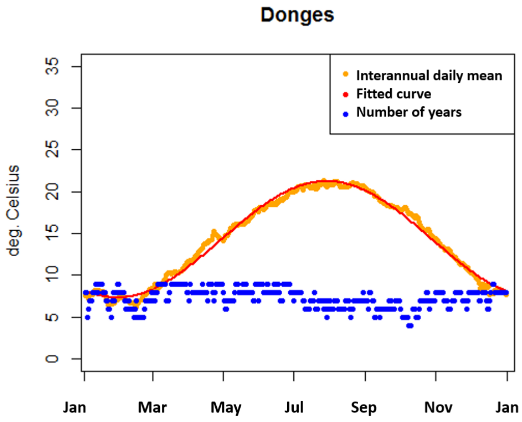

Figure 3. Interannual daily surface temperature, fitted curve and number of value used to calculate the interannual value at the downstrean station (Donges).

V. LIGHT ATTENUATION

A. *Solar radiation*

The numerical model reads the solar radiation variable in time and space. The datasets used are the hourly mean surface downward short-wave radiation flux provided by ERA5. The grid horizontal resolution is 0.25 degrees. A correction factor of 0.45 is applied to extract only the visible fraction of the radiation, used by aquatic phytoplankton during photosynthesis. The diurnal variation for available solar radiation is taken into account.

B. *Light attenuation in the water column*

Light attenuation in the water column varies according to the Beer-Lambert law :

$$Iz2=Iz1 \exp(-Kd\,(z2-z1)) \qquad (4)$$

With Iz2 the light at depth z2, Iz1 the light at depth z1, Kd the light attenuation coefficient in m^{-1} between z1 and z2, z1 and z2 the water depth. The attenuation coefficient is variable in time and space, and calculated as a function of SPM concentration, using the formulation defined specifically for the Loire estuary using observations [8]:

$$Kd=4.59 \text{ Log } (SPM-3.57) \qquad (5)$$

With SPM in mg/l. This function is valid for SPM concentration ranging from 10 to 500 mg/l. Il is considered for the calculation a minimal SPM concentration of 7 mg/l, which gives a minimal Kd of 0.31 m^{-1}.

VI. THREE-DIMENSIONAL MODELLING OF DISSOLVED OXYGEN CONCENTRATION

A. *General description*

The choice of the state variables takes advantages of the existing literature on water quality models of the Loire estuary [6][7] and Gironde estuary [10]. The following phenomena are identified as the key processes:

- Oxygen consumption by particulate organic matter of terrestrial, urban and detrital origin.
- The oxygen consumption by nitrification of the detritus in ammonium NH_4^+
- The exchanges of oxygen with the atmosphere.

The state variables of the water quality model are dissolved oxygen (O_2), ammonium (NH_4^+), the particulate organic detritus (NOR), the phytoplankton PHY expressed as chlorophyll a, and the biochemical demand (BOD5). Temperature is a diagnostic variable, which influences biogeochemical fluxes. The state variables are tracers in the model, subject to advection, and dispersion. In addition, source and sink terms representing the biogeochemical fluxes between the state variables are considered (Figure 4). For this purpose, the WAQTEL module is activated and coupled with TELEMAC-3D, GAIA and TOMAWAC.

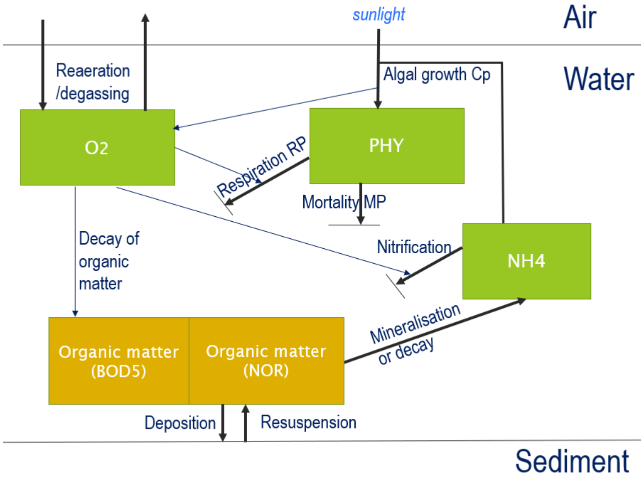

Figure 4. State variables (O2, PHY, NH4, BOD5, NOR) and biogeochemical fluxes

The source and sink terms or biogeochemical fluxes activated for the state variables of the oxygen model are summarized below:

$$F(\mathbf{PHY})=\text{algal net production} \quad (6)$$

$$F(\mathbf{NH4}) = \text{-algal net prod.} + \text{NOR decay} - \text{nitrification} \quad (7)$$

$$F(\mathbf{O2}) = \text{algal net prod.} - \text{nitrification} - \text{BOD decay} - \text{reaeration/degassing} \quad (8)$$

The state variables PHY, NH4 and NOR are advected. The variables **NOR** and **BOD5** are expressed as forcing variables, proportional to the other prognostic variables SPM and PHY. The formulations of the biogeochemical fluxes are detailed in the following sections.

B. Organic Matter

1) NOR

The particulate organic matter NOR is assumed as a fraction of SPM. In this way, particulate organic matter is represented as a particle subject to deposition, resuspension, without explicitly resolving organic matter as a cohesive sediment.

$$\mathbf{NOR}=\delta N \times MSO \times \mathbf{SPM} \quad (9)$$

With NOR the particulate organic matter (mg/l), the SPM concentration simulated by the hydrosedimentary module, MSO the ratio of organic matter in SPM, δN the stoichiometric ratio.

MSO is established using existing survey and publications. Measurements of organic matter in SPM in the estuary done in 1986 and 1990 during winter and summer indicates [6]: A quasi-constant ratio of 0.7% for SPM concentration above 100mg/l, and a variable percentage of 2 to 6% upstream and 12 to 22% downstream for SPM below 100 mg/l. Measurements from a benthic survey done in June and October 2008 in the mudflat of the Loire estuary gives a value of 6% for MSO [9]. More recent measurements. at the station Montjean-sur-Loire provides a ratio of 18%, stable throughout the year and the season. This ratio agrees with measurements presented by [6].

Consequently, the ratio of organic matter MSO is then established as a function of SPM concentration. It is a calibration parameter of the model. The formulae used provides a variation of MSO of 2% in the ETMZ and 5% in areas of low turbidity (external estuary):

- If SPM<10mg/l, MSO=5%
- If 10mg/l<SPM<100mg/l: MSO=-0.33333 x MES+0.05333
- If SPM> 100mg/l: MSO=2%

2) BOD

Measurements of the biochemical oxygen demand (BOD5) show a strong correlation with Chl *a* (Table II). The ratio between both parameters is almost constant throughout the estuary. This relationship is established using datasets at Sainte-Luce, Paimboeuf, Cordemais, Couëron, Trentemoult, Saint-Géréon for several years.

Table II Correlation between BOD5 and chlorophyll *a*

Parameter	**Ratio of BOD5 to Chl a**	**Coefficient of determination**	**Years**
Saint-Géréon	0.0560	0.7806	2007-2018
Sainte-Luce	0.0689	0.799	2007-2018
Trentemoult	0.0553	0.8152	2013-2020
Couëron	0.0554	0.7943	2013-2020
Cordemais	0.0677	0.8098	2007-2018
Paimboeuf	0.0648	0.6233	2013-2020
All stations	0.0611	0.7789	2007-2020

BOD5 is representative for the fresh organic matter of phytoplanktonic origin. The following ratio is used in the model:

$$\mathbf{BOD5}=f\_BOD \times \mathbf{PHY} \quad (10)$$

With f_BOD equal to 0.06. As a remark, there is no correlation between BOD5 and SPM concentration.

C. Definitions of the biogeochemical processes

1) Algal net production.

The algal growth Cp varies with light, nutrient availability, and temperature using the formulae:

$$CP=Cmax\ g1\ EFF\ LNUT \quad (11)$$

$$Eff=I/Is \exp(1-I/Is) \quad (12)$$

$$LNUT=NH4/(KN+NH4) \quad (13)$$

With the maximum algal growth rate Cmax, the factor of temperature influence g1. EFF is the light limitation factor, varying from 0 to 1 and calculated as the Steele function which includes photoinhibition [11]. LNUT is the nutrient limiting factor expressed by a Michaelis-Menten formulation.

Phytoplankton mortality rate (DP) is calculated as:

$$DP=(RP+MP)\ g2 \quad (14)$$

$$MP=M1+M2\ PHY \quad (15)$$

With the algal biomass respiration rate RP, the effect of temperature g2, the cellular mortality coefficient M1, and the population mortality due to predation or overpopulation M2.

2) Mineralisation of the nitrogen fraction of the particulate organic material.

The mineralisation of detritus into nitrogen nutrient is the following:

$$MINE=K620\ g2\ NOR\ (O2-O2\_crit)/(O2\_opt-O2\_crit) \quad (16)$$

$$g2 = (1.050)^{(temp-20)} \quad (17)$$

with K620 the transformation rate of non-degradable nitrogen NOR modulated by temperature through the influence factor g2 and the level of oxygenation. More specifically, mineralisation is inhibited for oxygen level below O2_crit, fixed at 0.5 mg/l, and is augmented at oxygen concentration above the optimal oxygen concentration O2_opt of 5.5 mg/l.

3) Nitrification

Nitrification is a sink term of oxygen and ammonium. It is implemented as :

$$\mathrm{NITR}=-\mathrm{K520}\ \mathrm{g2}\ \mathrm{NH4}/(\mathrm{k\_NH4}+\mathrm{NH4}) \tag{18}$$

With the kinetics of nitrification K520 and g2 the temperature factor. This zero-order kinetics is modulated by the concentration of ammonium and the half-saturation constant k_NH4 set at 0.3 mg/l through a Michaelis-Menten law. At high ammonium concentration, nitrification is increased which compensated the high production of ammonium by decomposition of organic matter in the ETMZ. It represents the self-cleaning character of the ETMZ for nutrients.

4) Oxygen concentration related to degradation of BOD5

The degradation law of the biogenic organic matter is expressed as :

$$\mathrm{DEG\_BOD}=-\mathrm{K120}\ \mathrm{g3}\ \mathrm{BOD5} \tag{19}$$

$$\mathrm{g3} = (1.047)^{(\mathrm{temp}-20)} \tag{20}$$

With the kinetics of degradation K120 and g2 the temperature factor. This zero-order kinetics is modulated by the concentration of ammonium and the half

5) Exchange of oxygen with the atmosphere.

The exchange of oxygen from air to water is described by:

$$\mathrm{EXCH}= \mathrm{k2}\ \mathrm{g4}\ (\mathrm{Cs}-[\mathrm{O2}]) \tag{21}$$

$$\mathrm{g4} = (1.025)^{(\mathrm{temp}-20)} \tag{22}$$

with Cs the oxygen saturation constant, calculated as a function of temperature and salinity. The gas transfer k2 is a constant.

6) Synthesis and biogeochemical parameters

The source and sink terms for the state variables of the oxygen model are described below:

$$\mathrm{F}(\mathbf{PHY})=(\mathrm{Cp}-\mathrm{Dp})\ \mathbf{PHY} \tag{23}$$

$$\mathrm{F}(\mathbf{NH4}) = \mathrm{fn}\ (\mathrm{dtn\ DP} - \mathrm{CP})\ \mathbf{PHY} + \mathrm{k620\ g2}\ \mathbf{NOR} \times (\mathbf{O2}-\mathrm{O2\_crit})/(\mathrm{O2\_opt}-\mathrm{O2\_crit}) - \mathrm{k520} \times \mathbf{NH4} / (\mathrm{k\_NH4} + \mathbf{NH4})\ \mathrm{g2}\ \mathbf{NH4} \tag{24}$$

$$\mathrm{F}(\mathbf{O2}) = \mathrm{f}(\mathrm{Cp}-\mathrm{Rp})\ \mathrm{g1}\ \mathbf{PHY} - \mathrm{n\ k520} \times \mathbf{NH4} / (\mathrm{k\_NH4}+\mathbf{NH4})\ \mathrm{g2}\ (\mathbf{NH4}) - \mathrm{k120\ g3}\ \mathbf{BOD5} + \mathrm{k2\ g4}\ (\mathrm{Cs}-\mathbf{O2}) \tag{25}$$

The variables **NOR** and **BOD5** are expressed as forcing variables, proportional to other prognostic variables SPM and PHY (equation 9 and 10).

The calibration and the set-up of the dissolved oxygen model has led to a set of specific values for the parameters (Table III).

Table III Parameters of the biogeochemical fluxes

Parameter	**Symbol**	**Unit**	**Value**
Kinetic degradation constant for the organic load at 20°C	K120	d^{-1}	0.18
Convertion coefficient of BOD5	f_BOD	-	0.06
Stoichiometric equivalent between organic matter and phosphorus	δN	-	0.08
Percentage of organic matter	MSO	%	Variable 5% to 2%
Transformation rate of NOR into NO3 through heterotrophic and autotrophic bacterial mineralisation	K620	d^{-1}	0.008
Reaeration coefficient	K2	d^{-1}	0.45
Kinetics of nitrification at 20°C	K520	d^{-1}	2.9
Half-saturation constant for nitrification	K_NH4	mg/l	0.3
Quantity of oxygen consumed by nitrification	n	mg O_2 / mg NH_4	5.2
Oxygen produced by photosynthesis	f	mg O_2 / mg Chl *a*	0.15
Algal biomass respiration rate at 20°C	RP	d^{-1}	0.05
Algal mortality coefficient at 20°C	M1	d^{-1}	0.1
Algal mortality coefficient at 20°C	M2	d^{-1}	0.03
Average proportion of directly assimilable nitrogen in living phytoplankton	fn	mg N / mg Chl *a*	0.0035
Proportion of directly assimilable nitrogen in dead phytoplankton	dtn	%	0.5
Algal growth maximum rate at 20°C	Cmax	d^{-1}	1.7
Nitrate half-saturation constant	KN	mg N / l	0.03
Optimal irradiance for photosynthesis	Is	$W.m^{-2}$	86
O2 optimal concentration for mineralisation	O2_opt	mg/l	5.5
O2 critical concentration for mineralisaton	O2_crit	mg/l	0.5

D. Initial conditions

At the starting date of the simulation, the water quality variables are constant, except for NOR and SPM concentrations. SPM concentration is initialised with a previous computation file extracted from a simulation with the hydrosedimentary model run over a whole year. This ensures that the SPM spatial distribution at the initial time is representative, with the accurate position of the ETMZ. Dissolved oxygen concentration is 8 mg/l, Chl *a* concentration is 10µg/l, and ammonium concentration is 0.05mg/l. NOR and BOD are calculated as a fraction of SPM concentration and Chl *a*, as specified by equation (9) and (10), respectively.

E. Boundary conditions

The offshore boundary conditions are established using results from a regional model covering the Bay of Biscay called

IBI and available through the Copernicus marine data store [12]. IBI provides daily mean concentration of Chl *a*, ammonium, and dissolved oxygen. A comparison of IBI modelled results against observations at the buoy MOLIT located offshore near the boundary has demonstrated that IBI represents accurately the seasonal trend in the observations, but not their detailed daily fluctuations. Therefore, only a mean value for summer 2019 has been extracted and prescribed. The results are in Table IV.

Table IV : Value of the state variables at the offshore boundary

State variables	**units**	**Offshore boundary**	**source**
PHY	µg/l	10	Regional model IBI, mean value in summer 2019
NH4	mg/l	0.05	Regional model IBI, mean value in summer 2019
O2	mg/l	8	Regional model IBI, mean value in summer 2019
NOR	mg/l	equation (9)	NOR is a fraction of SPM
BOD5	mg/l	equation (10)	BOD5 is a fraction of PHY

At the upstream boundary, measurements from NAIADES are used to prescribe the concentration of the state variables PHY and NH4 (Table V). For dissolved oxygen, the saturation constant is calculated using high frequency temperature measurements and then the final dissolved oxygen concentration is derived from the saturation constant using a percentage saturation of 93%, representative of the degree of saturation during summer 2019 and calculated using datasets from NAIADES.

Table V : Value of the state variables at the upstream boundary

State variables	**units**	**Upstream boundary**	**source**
PHY	µg/l	5	Measurements at Montjean-sur-Loire in Summer 2019
NH4	mg/l	0.05	Measurements at Montjean-sur-Loire in Summer 2019
O2	mg/l	Cs*0.93	Cs is calculated using temperature measurements at Montjean-sur-Loire. Percentage of saturation set at 93% using bimonthly measurements
NOR	mg/l	equation (9)	NOR is a fraction of SPM
BOD5	mg/l	equation (10)	BOD5 is a fraction of PHY

F. *WWTP outfalls in the estuary*

The outfalls from the five major Wastewater Treatment Plant (WWTP) are included in the model domain. The discharge rate and the concentration of the effluent in SPM, NH_4 and O_2 are available through the environmental monitoring conducted to meet the national regulations (Table VI). Dissolved oxygen, which is not measured, is estimated using the water quality class defined by the concentration in BOD5, using the French water quality standards. It is assumed that the Chl *a* concentration is zero in treated wastewater effluent.

Table VI : WWTP discharge rate and effluent concentration

Name of the WWTP	**Discharge rate**	**SPM**	**NH_4^+**	**O_2^***	**Chl *a* ***
	m^3/s	**mg /l**	**mg (NH4)/l**	**mg (O2)/l**	**µg/l**
Saint-Nazaire Ouest	0.139	5.5	2.6	7	0
Saint-Nazaire Est	0.123	2.8	0.9	7	0
Nantes 1 Tougas	1.211	8.3	6.5	7	0
Nantes 2 Petite Californie	0.353	10.4	6.4	4	0
Ancenis la Bigoterrie	0.073	3.5	1.6	7	0

*. Estimation

VII. COMPARISON OF MODEL RESULTS AGAINST OBSERVATIONS

A. *Dissolved oxygen : comparison with high frequency measurements*

Figure 5 demonstrates that the model realistically reproduces the seasonal variation under the influence of the upstream river discharge, the spring-neap tidal cycle and the semi-diurnal cycle (variations between high tide and low tides) of the observed dissolved oxygen concentration at all stations (see locations on Figure 1). The range of modelled oxygen levels is 4 to 9 mg/l at Bellevue, and 2 to 8 mg/l at Trentemoult, in agreement with observations. Cordemais and Le Pellerin are representative of depleted oxygen conditions coinciding with the ETMZ during the low flow conditions, with a range of 2 to 6 mg/l. Observations indicates depleted level up to 1 mg/l during high tide in the ETMZ. At Donges, representative of the estuarine mouth, modelled and observed dissolved oxygen vary from 4 to 7 mg/l.

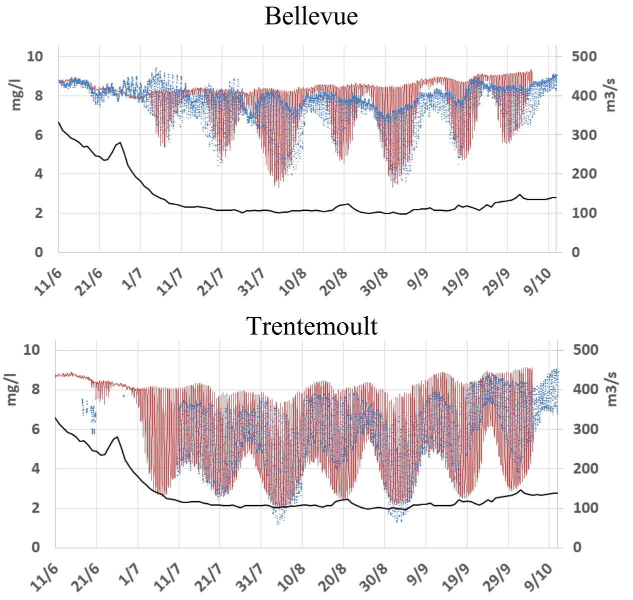

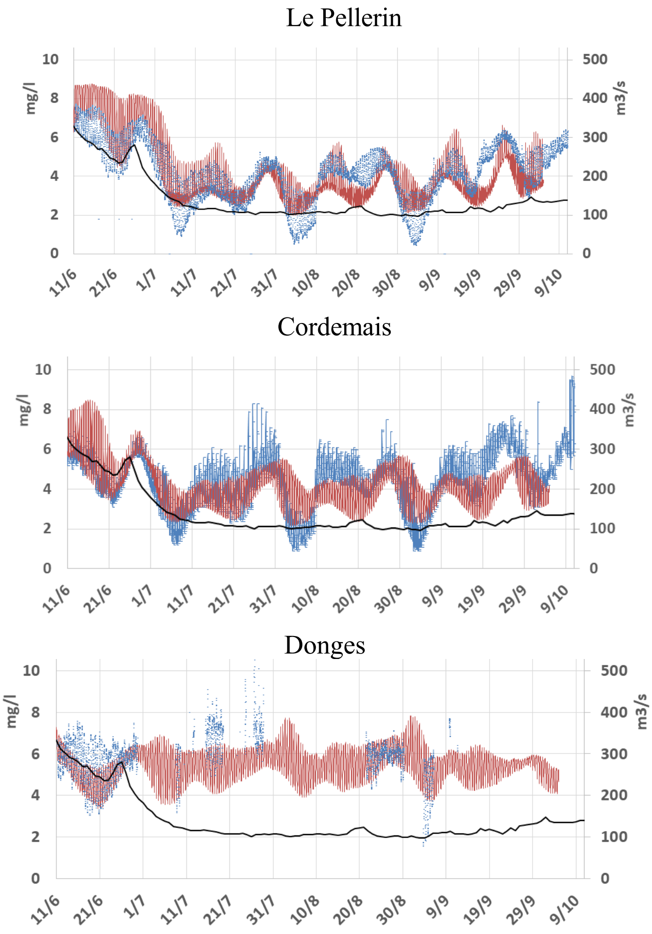
Le Pellerin

Cordemais

Donges

Figure 5. Surface DO : Comparison of model results (red lines) against observations (blue dots) at 5 stations in 2019. River flow is the black line

The error between observations and model for dissolved oxygen is estimated using the Willmott Skill Score (WSS) [13], for each station SYVEL from 11/06/2016 to 05/10/2019. The time step is 1 hour, which corresponds to the lowest temporal frequency of dataset. WSS is defined by:

$$\mathrm{WSS} = 1 - \frac{\sum(\mathrm{Ymod}-\mathrm{Yobs})^2}{\sum(|\mathrm{Ymod}-\overline{\mathrm{Yobs}}|+|\mathrm{Yobs}-\overline{\mathrm{Yobs}}|)^2} \quad (26)$$

With the modelled concentration Ymod, the observed concentration Yobs and $\overline{\mathrm{Yobs}}$ the mean observed concentration. It is considered that a model accurately reproduces dissolved oxygen when WSS is above 0.7 [10]. A WWS ranging from 0.731 to 0.886 is obtained (Table VII). This result indicates that the model accurately reproduces dissolved oxygen fluctuations in Summer 2019.

Table VII : Estimation of WSS for dissolved oxygen

Station:	Number of measurements	**WSS**
Donges	928	0.731
Paimboeuf	0	-
Cordemais	2805	0.761
Le Pellerin	2787	0.859
Trentemoult	2082	0.886
Bellevue	2713	0.874

B. Ammonium : Comparison with in situ measurements

Observed ammonia concentrations available are bimonthly or monthly surface measurements. They are representative of seasonal variations. Results are plotted over the whole year to show the seasonal trend in the observations. The comparison of modelled concentration against observations shows that modelled concentrations are in the range of value at Saint-Géréon, Donges and Cordemais (Figure 6). At Sainte-Luce, Trentemoult, and Couëron, the model tends to overestimate concentration, with values ranging from 0.1 to 0.4 mg/l instead of 0.1mg/l in the observations. which means that the filtering effect of the ETMZ is slightly underestimated by the oxygen model.

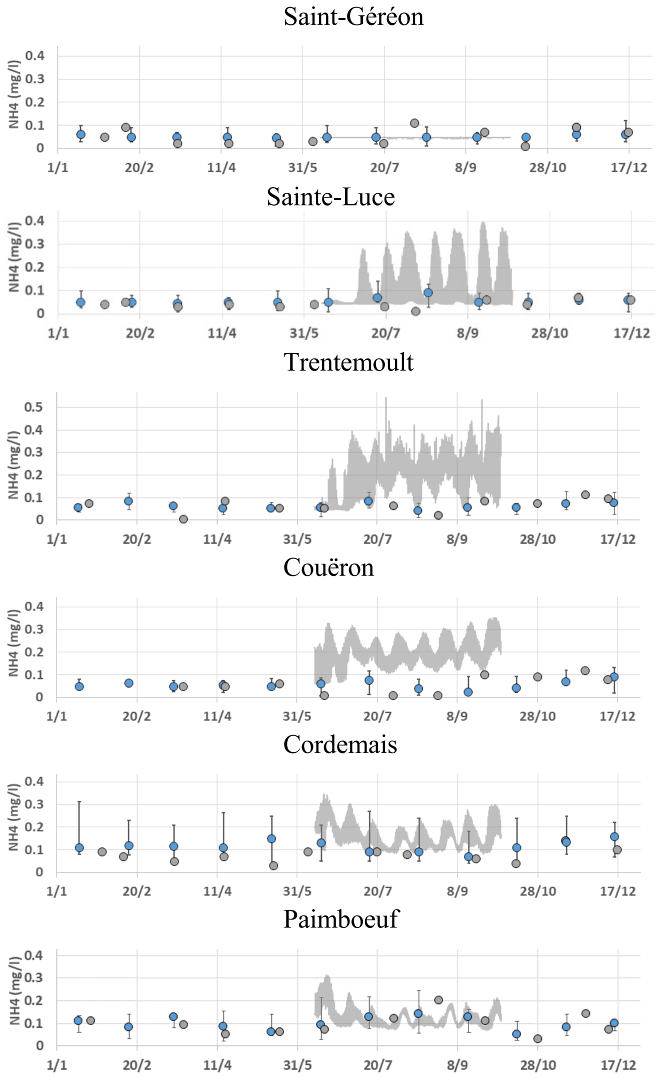
Saint-Géréon

Sainte-Luce

Trentemoult

Couëron

Cordemais

Paimboeuf

Figure 6. Surface ammonium : Comparison of model results (grey line) against observations (grey dot: in situ measurements, blue dots with error bar: percentile 10%, median, percentile 90% for the past 10 years and per month)

C. Chl a : Comparison with in situ measurements

Modelled Chl *a* concentration is approximately 5 mg/l at all stations during the whole simulation period in Summer 2019 (Figure 7). Observations in 2019 are scarce, however some samples are up to 20 mg/l in August, which suggest that ephemeral peaks and/or heterogeneities occurs in phytoplankton distribution which are not represented by the model. The interannual monthly median value, the 10% percentile and the 90% percentile over the past ten years is also plotted to assess the seasonal variability of Chl *a* measurements. It shows that samples collected in year 2019 are representative of a low productive year.

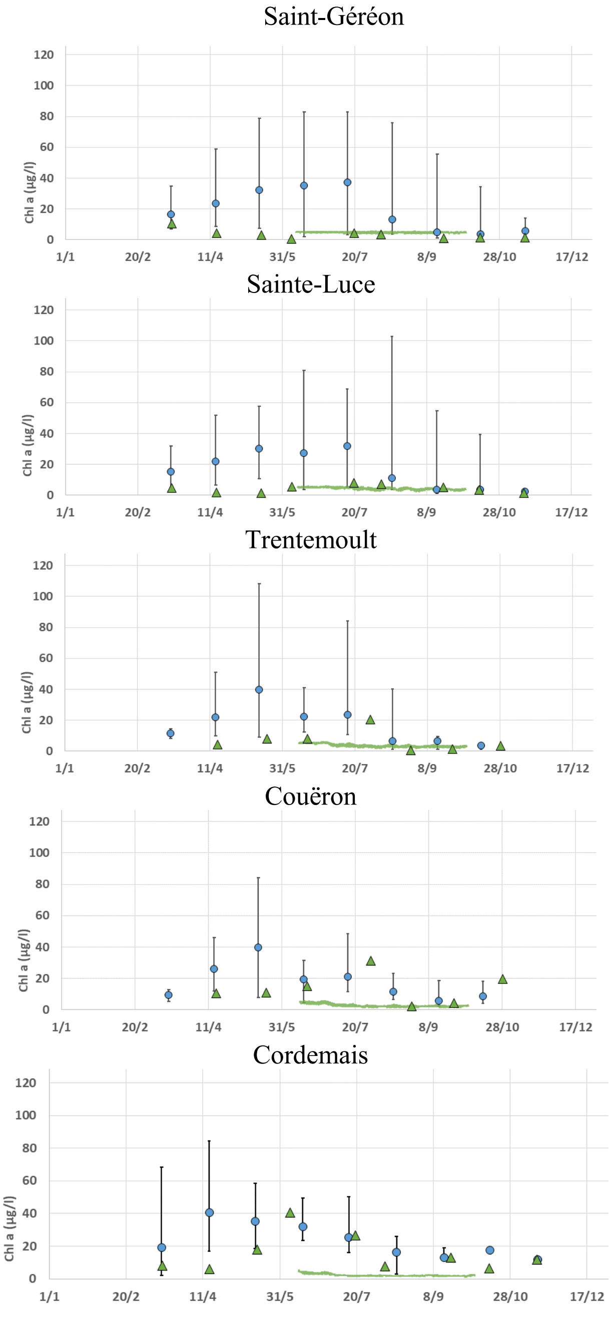

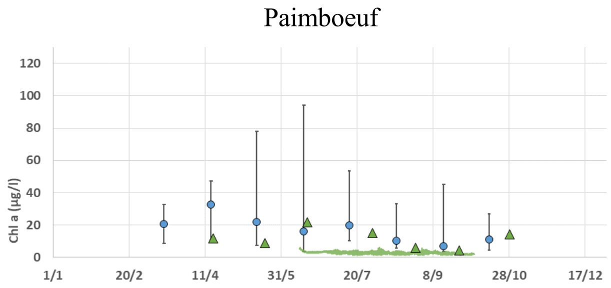

Figure 7. Surface Chl *a* : Comparison of model results (green line) against observations (green triangle: in situ measurements, blue dots with error bar: percentile 10%, median, percentile 90% for the past 10 years and per month)

VIII. CONCLUSION

The model developed in this work is based on a simple biogeochemical model coupled to a hydrosedimentary model. Comparison with observations demonstrates its ability to reproduce the seasonal trends and the variation in DO concentration under the influence of the tidal cycles and the subsequent SPM distribution, more specifically intensity and location of the ETMZ. It provides a useful tool for investigating the response of the system to anthropogenic activities and variations in hydrologic and meteorological conditions.

ACKNOWLEDGEMENT

Authors acknowledge GIP Loire Estuaire, for funding the project and providing datasets used in the modelling work.

REFERENCES

[1] https://www.hydro.eaufrance.fr/, statistics analysis of discharge data freely available online and accessed on 24/07/2023

[2] L'oxygène de l'eau, edited in june 2020, technical factsheet L2 A1 from GIP Loire estuary (in French).

[3] Fallou H., 2018. Le réseau de mesures SYVEL : un outil performant et indispensable à la compréhension et au suivi du fonctionnement de l'estuaire de la Loire. La houille Blanche, N°1, p97-99

[4] https://naiades.eaufrance.fr,accessed on 24/07/2023

[5] Isserty G., Walther R., Bertrand O., 3D hydrosedimentary models of the Loire Estuary using TELEMAC-3D-TOMAWAC and GAIA. In : Bourban, Sébastien E.; Pham, Chi Tuân; Tassi, Pablo; Argaud, Jean-Philippe; Fouquet, Thierry; El Kadi Abderrezzak, Kamal; Gonzales de Linares, Matthieu; Kopmann, Rebekka; Vidal Hurtado, Javier. Proceedings of the XXVIIIth TELEMAC User Conference 18-19 October 2022. Paris-Saclay: EDF Direction Recherche et Développement. p. 153-161.

[6] Thouvenin B, Romana L.-A., 1992. Modélisation mathématique de l'oxygène dissous dans l'estuaire de la Loire. Première phase. Technical report from IFREMER.

[7] Thouvenin B., Le Hir P. Maurice L., Romana L-A., 1995. Synthèse des études relatives à la modélisation de l'oxygène dissous dans l'estuaire de la Loire. Techanical report IFREMER

[8] Meybeck M. ,1983. Quantification du déséquilibre en nutriments (C,P,N) dans l'estuaire de la Loire. Technical Report of the GRECO-Ica « Capacité d'acception du milieu marin et chimie marine « .

[9] Bio-littoral. Etude des invertébrés benthiques de l'estuaire de la Loire. Campagne DCE octobre 2008. Rapport final 2009

[10] Lajaunie-Salla K. 2016. Modélisation de la dynamique de l'oxygène dissous dans l'estuaire de la Gironde. Phd thesis from the University of Bordeaux.

[11] Steele J. H. 1962. Environmental control of photosynthesis in the Sea. *Limnology and Oceanography,* vol 7 p137-150.

[12] https://data.marine.copernicus.eu/products, last accessed on 24/07/2022

[13] Willmot C. J. 1982. Some comments on the evaluation of model performance. Bulletin of American meteorological Society, 1309-1313

Improving predictions within Thames estuary for a UK emergency oil spill model

David Haverson[1], Claire Beraud[1], John Alridge[1], Lenka Fronkova[1]
david.haverson@cefas.gov.uk
[1]: Centre for Environment, Fisheries & Aquaculture Science, Pakefield Road, Lowestoft, NR33 0HT, UK

Abstract – **To help with the assessment of oil spills in the Thames Estuary, a new validated TELEMAC2D model was created, extending an existing shelf model 58.5 km up the full tidal extent of the estuary. Using a harmonic decomposition, the results of the model were converted into their individual harmonic components to force an operational emergency response oil spill model. Testing of a hypothetical oil spill near Tilbury Port showed a distinctly different spatial extent of an oil spill, with the plume travelling further upstream of the release site, compared to with the old hydrodynamic forcing, whilst the downstream plume extent remained similar. The new improved model forcing will allow an improved ability to assess the risk of oil spills within the Thames Estuary that could not be achieved using the previous model.**

Keywords TELEMAC2D, weirs, oil spills.

I. INTRODUCTION

Cefas (Centre for Environment, Fisheries & Aquaculture Science) has a dedicated Emergency Response team providing advice about the environmental impact significance of oil and chemical spill incidents in UK waters. Advice and assessments are provided to the UK's Marine Management Organisation (MMO) and the Department for Environment, Food and Rural Affairs (DEFRA) for each pollution report received, over 200 a year. The vast majority are very minor fuel spills that require no substantial action. However, some incidents require more in-depth advice which involves providing information on the likely marine and coastal resources at risk, using modelling to understand the fate of the spill or advising the MMO on the need for oil dispersant, containment booms or fisheries/shellfisheries closures. Examples include the clean-up of a diesel spill in 2021, after a train derailment, into the Loughor Estuary, Wales, and an oil slick 12 nautical miles off the coast near Deal, England in 2022, that raised concerns about the potential harm to local seal populations.

To support the assessment of oil spills, Cefas provide an operational emergency response oil spill model, using the Oil Spill Contingency and Response component of the Marine Environmental Modelling Workbench (MEMW-OSCAR) [1]. OSCAR is a deterministic model that uses hydrodynamic and wind forcing to drive oil dispersion and accounts for weathering, physical, biological and chemical processes affecting oil at sea. The primary source of tidal current forcing is the Copernicus data portal which provides output with a resolution of approximately 1.5 km [2]. Where high-resolution in the nearshore region is required, or inclusion of riverine flow necessary, a secondary option can be used based on a stored database of tidal and residual currents derived from a TELEMAC2D hydrodynamic model of the UK shelf (developed at Cefas) with resolution down to 500 m in some estuarine locations [3]. However, it is desirable to further improve the resolution of tidal currents at locations prone to spill incidents, associated with large ports and/or high densities of shipping traffic. The Thames Estuary was identified as one such location.

II. MODEL DESCRIPTION

A. Model Domain

The existing TELEMAC2D model output provides tidal currents up to 3.5 km upstream of the Queen Elizabeth II Bridge at Dartford, with a resolution of approximately 50 m. To improve the representation of the Thames estuary, a new high-resolution TELEMAC2D model (v8p2r1) of the entire Thames estuary was created, representing the whole length of the Thames River up to the extent of the tidal reach. This added a further 58.5 km up the River Thames to the Teddington Weir.

The new model domain was created using an unstructured finite element grid comprising 187,250 nodes (353,431 elements). The model resolution is approximately 5 m at its finest, along the narrowest parts of the River Thames, extending to 50 m along the open coastal boundary. Figure 1 provides an overview of the model domain extent and the bathymetric depths. The model domain extends as far east as Herne Bay on the Kentish coast and extends west all the way to the end of the tidal extent up the River Thames to the Teddington Lock and Weir. Initially, the coastal open boundary was set at the mouth of the River Thames near Canvey Island. However, initial tests showed that the tidal elevations were underestimated. As such, the domain was extended to its current size to encompass a larger coastal region, providing more boundary points to force the boundary conditions. This greatly improved the tidal elevations along the River Thames. The larger domain also includes the Medway Estuary. The domain extends to the end of the tidal reach up the River Medway to the Allington Lock and Weir.

Bathymetry for the model was provided from two sources: the DEFRA Marine Digital Elevation Model (DEM) – 1 arc second [4] and the Environment Agency's SurfZone Digital Elevation Model 2019 [5]. The SurfZone DEM combines lidar and bathymetric surveys and provides good details on the large intertidal regions, such as in the Medway Estuary, but was limited to shallow regions near the coastline. As such, the remaining areas were filled in with the DEFRA Marine DEM.

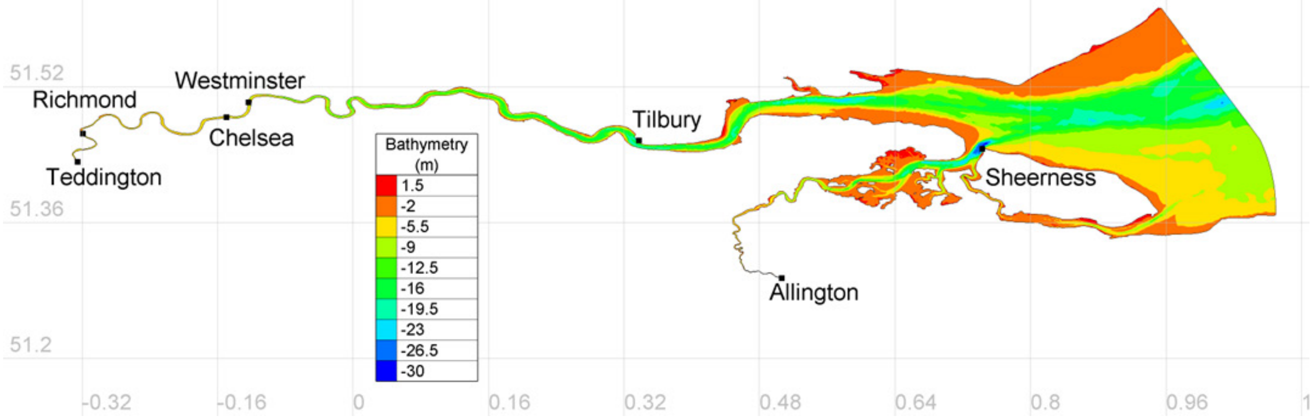

Figure 1. Extent of the new TELEMAC2D model domain and notable locations.

The SurfZone DEM has a vertical reference of Ordnance Datum Newlyn (ODN) which is referenced to Mean Sea Level, whereas the Marine DEM is referenced to Chart Datum. Therefore, the Marine DEM was converted from Chart Datum to Mean Sea Level using the Vertical Offshore Reference Frames (VORF) dataset [6], so that the whole model domain used a common vertical datum of ODN.

Water depths vary along the River Thames, with typical depths of approximately 20 m at the mouth near Canvey Island to approximately 4 m at upper reaches just before the Teddington Weir.

B. *Boundary forcing*

The hydrodynamics are forced along the open maritime boundary using 11 tidal constituents (M2, S2, N2, K2, K1, O1, P1, Q1, M4, MS4 and MN4) from the OSU TPXO European Shelf 1/12° regional model [7]. The TPXO harmonics are used to drive the prescribed elevations and velocities at the open boundaries. However, a limit was set whereby conditions are driven only on parts of the open boundary that are deeper than 5 m to avoid unrealistic and excessive tidal velocities on the intertidal flats near the edges of the open boundary.

C. *River discharges*

The model domain includes three weir structures: the Richmond Weir and Teddington Weir on the River Thames and the Allington Weir on the River Medway. For simplification, Richmond Weir is set in the model with a fixed height. However, in reality the weir is open for two hours either side of high tide. In addition to the maritime open boundary, the model is forced with the two main riverine sources at the end of the River Thames, just upstream at the Teddington Weir, and the end of the River Medway, just upstream at the Allington Weir. Within the TELEMAC model, a flow rate coefficient of 0.4 is used for the formulation of river flow over the weirs.

Daily mean river flows were provided by the National River Flow Archive [8]. The Thames at Kingston has an annual mean flow of 65.5 m^3/s. The Medway at Teston has an annual mean flow of 11.2 m^3/s.

III. MODEL VALIDATION

A. *Tidal elevations*

To validate the model, tidal elevations were sourced from the UK tide gauge network. One tide gauge from the network is within the model domain, at Sheerness. To supplement the tide gauge record, water levels were also taken from the Environment Agency's flood warning service. However, data availability is limited to observations over the last 5 days. As such, at the time of this project, 14 days' worth of observations at nine locations along the River Thames in addition to Sheerness, between the 31^{st} December 2022 and 14th January 2023, were taken from the flood warning portal. The only exception to this is at Tilbury, where tidal observations were missing from the data portal after 10:45 am 8th January 2023.

The model was run for a 'spin up' period of 30 days starting on the 1^{st} November 2022, before running for another 30-day-period over December 2022 to provide sufficient time for tidal elevations along the River Thames to reach equilibrium and ensure there is no lag from the initial flat starting position. Locations of the validation points are shown in Figure 3.

Figure 2 shows the comparison of the modelled tidal elevations compared to the observations for three of the nine EA tidal records at the upper reaches of the Thames Estuary between the 31^{st} December 2022 and 14th January 2023. Whilst the results show a deviation in the tidal ranges, these are to be expected. The observations include both the meteorological effects (such as pressure and storm surges) as well as the astronomical effects. Whereas the TELEMAC model is purely tidal and does not include the meteorology. Pressure records indicate a period of strong low pressure over the observation period and the National Tidal and Sea Level Facility indicate large positive storm surges occurred (however, data are not yet available to include in the boundary conditions to force the model), explaining the model under predicting the low and high water levels compared to observations. Despite this, the model is shown to perform well in replicating the timing on high and low water along the entire length of the Thames.

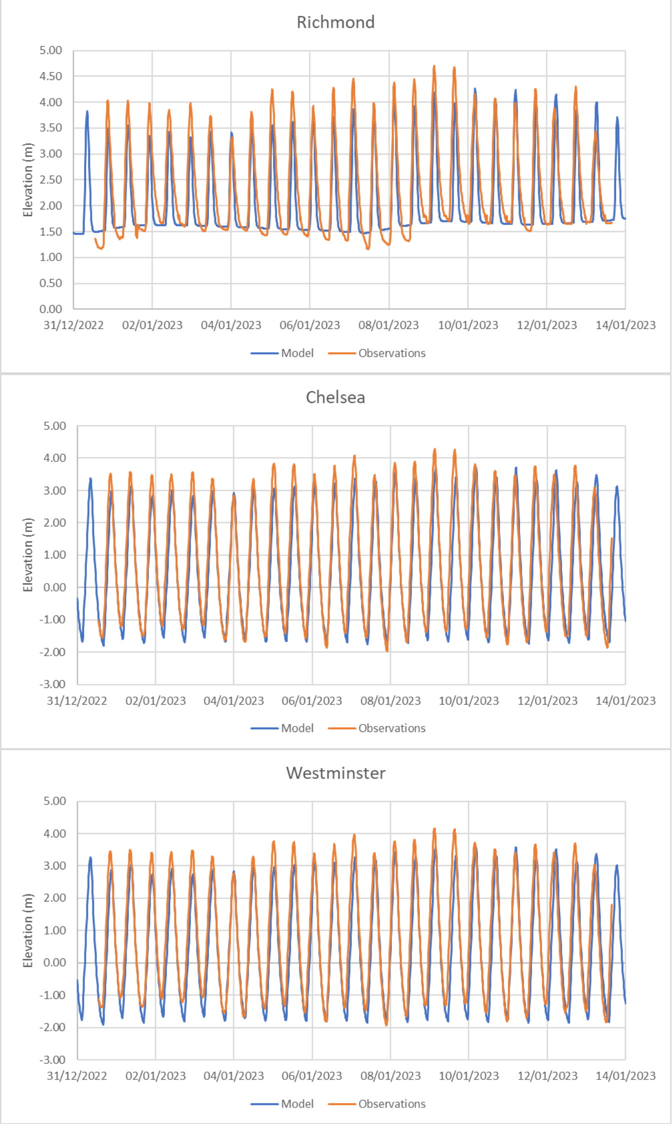

Figure 2. Time series comparison of the modelled (blue) and observed (orange) tidal elevations at Richmond, Chelsea and Westminster.

To validate tidal ranges in the model, observed tidal ranges at port locations along the Thames and within the Medway published on UK Admiralty charts were compared against the model results. Table 1 summarises the port locations, their tidal ranges and the model results. Results show that, at most locations, the predicted tidal ranges are within ±5% which is very good. The two locations that have the largest deviation are at Kew Bridge and Allington Lock, which are at the upper reaches of both the River Thames and the River Medway, respectively, and represent areas where the bathymetry is at its poorest quality, due to the resolution of the bathymetry whereby the width of the river of the river is represented by a couple of cells. Whilst this means some of the finer scale features may not be captured, results show that the high water values are well replicated and the over prediction occurs at the low water, which is heavily influenced by the model bathymetry. The over prediction in tidal range is likely to over predict the downstream dispersion of a plume if released near the river boundary. However, this is likely to be restricted to the last few kilometres of the estuary where the risk of large-scale oil spills is minimal due to the lack of ports. Despite these two locations near the edge of the model domain, the tidal elevations are shown to be well represented across the whole domain and are considered to be well validated for their intended purposes.

B. *Tidal currents*

Unlike tidal elevations, the availability of tidal current observations for validation is much more limited. The only available data found was tidal diamond data from Admiralty charts. Whilst it not the most reliable data source, it can provide a useful insight into the tidal characteristics. As such, it will be used as a guide rather than rigid data points. A total of twelve tidal diamonds across the model domain were used, three of which (A-C) were within the eastern half of the Thames. Table 2 shows the results of comparison between the model and the tidal diamond data.

For most of the tidal diamond locations (Figure 3), tidal currents are within ±0.2 m/s and all replicate the ebb flow bias, with tidal currents being faster on the ebb flow (after high water) than the flood tide (before high water). The largest discrepancy is at tidal diamond G and H (see Table 2) which are located at the mouth of the Medway Estuary, where tidal currents are underestimated between 0.5 and 0.8 m/s, despite tidal elevations being well replicated in the Medway. There are a number of possible reasons to explain this. One reason may be a difference in the bathymetric levels on the date of the observations compared to those used in the model grid or that a local 3D effect is not well replicated in 2D flows. Another reason may be that tidal diamonds are typically surface samples of tidal currents and may well be heavily influenced by the freshwater river flow out of the Medway on the ebb tide (not modelled here), water running off the intertidal mudflats and potentially meteorological effects (not modelled here). Given this, the peak spring currents on the flood tide may represent a better reflection of the performance of the tidal currents in this location, as the effect of the freshwater influence will be negated by the incoming tide and the tidal currents will be flooding onto the mudflats instead of off. The difference in the modelled tidal currents and the tidal diamonds reduces to -0.1 and 0.3 m/s. Given this underprediction is spatially limited to inshore of the mouth of the Medway and the rest of the model domain performs well, the modelled tidal currents are considered to be suitably validated for their intended purposes.

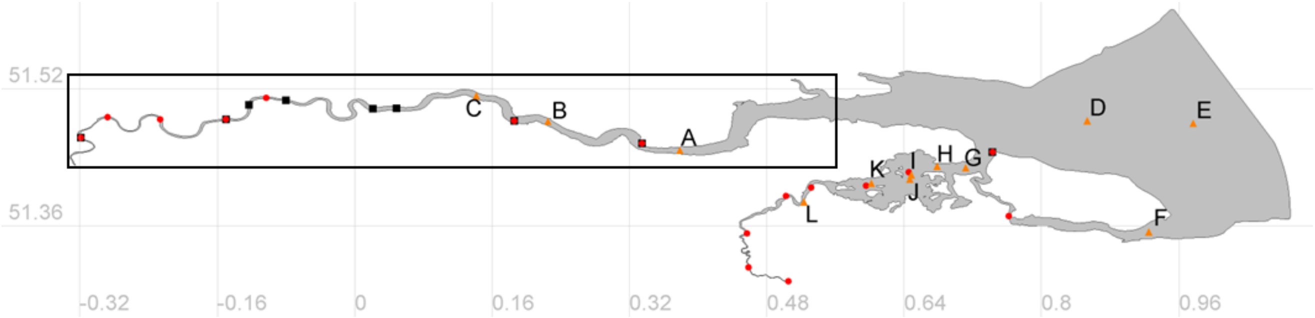

Figure 3. Location of validation points: tide gauges (black squares), admiralty tidal ranges (red circles) and admiralty tidal diamonds (orange triangles). The black box denotes the extent of the OSCAR domain.

Table 1. Comparison of observed and model tidal ranges at port locations.

Location	Tidal Range (m)	Model Predicted Range (m)	Percentage Difference (%)
Sheerness	5.20	5.35	2.9
Tilbury	5.90	6.28	6.4
Erith	6.00	6.16	2.7
London Bridge	6.60	6.52	-1.2
Chelsea Bridge	6.40	6.03	-5.8
Hammersmith Bridge	5.70	6.02	5.6
Kew Bridge	5.30	6.04	14.0
Grovehurst Jetty	5.30	5.41	2.1
Bee Ness	5.40	5.48	1.5
Darnet Ness	5.50	5.53	0.5
Chatham	5.70	5.65	-0.9
Strood Pier	5.70	5.76	1.1
Wouldham	5.30	5.13	-3.2
New Hythe	3.90	3.87	-0.8
Allington Lock	3.50	3.90	11.4

Table 2. Comparison of modelled peak spring tidal currents and Admiralty tidal diamonds.

Tidal Diamond	Peak Spring Current (m/s)	Modelled Peak Spring Current (m/s)	Percentage Difference (%)
A	1.39	1.50	7.9
B	1.44	1.23	-14.6
C	1.54	1.27	-17.5
D	0.93	1.08	16.1
E	1.23	1.07	-13.0
F	0.77	0.90	16.9
G	1.80	1.01	-43.9
H	1.49	0.94	-36.9
I	0.87	0.76	-12.6
J	0.87	0.76	-12.6
K	0.72	0.78	8.3
L	0.57	0.75	31.6

IV. OIL SPILL MODELLING WITH OSCAR

A. Transformation of Telemac outputs into tidal constituents

The TELEMAC2D model provides instantaneous tidal currents and elevations over the unstructured domain. However, for the oil spill model, tidal currents are generated for a specific time and date based on tidal harmonic constituents. Therefore, using a harmonic decomposition written in Python, the results of the validated TELEMAC2D model over the entire domain (Figure 1) can be converted into their individual harmonic components: Z0, M2, S2, N2, K1, O1, M4 and M6 tidal constituents together with bathymetry information at the mesh nodes.

Furthermore, OSCAR requires two separate files of the residual currents of both the tides and the rivers as the rivers are handled separately from the tidal constituents. Therefore, the model was rerun twice, one with only the tides and again with only the rivers. This then gives OSCAR the ability to conducting sensitivity testing for different riverine flows, such as summer or winter mean flows.

B. Conversion into regular grid readable for OSCAR

Unlike TELEMAC, which uses an unstructured triangular grid, OSCAR can only deal with gridded data. Therefore, the output of the validated tidal constituents from the Thames model was interpolated onto a regular grid. Due to computational memory limits, a regular grid, with a spatial resolution of 0.0005 by 0.0004 degrees longitude and latitude (approximately 35 x 50 m) was defined covering the River Thames (see Figure 3), rather than the full domain. Whilst this downscaling reduces the very upper reaches of the Thames estuary to a single grid point, flow still reaches the entire length of the estuary and the larger intertidal areas found in the lower reaches of the estuary and are still well covered.

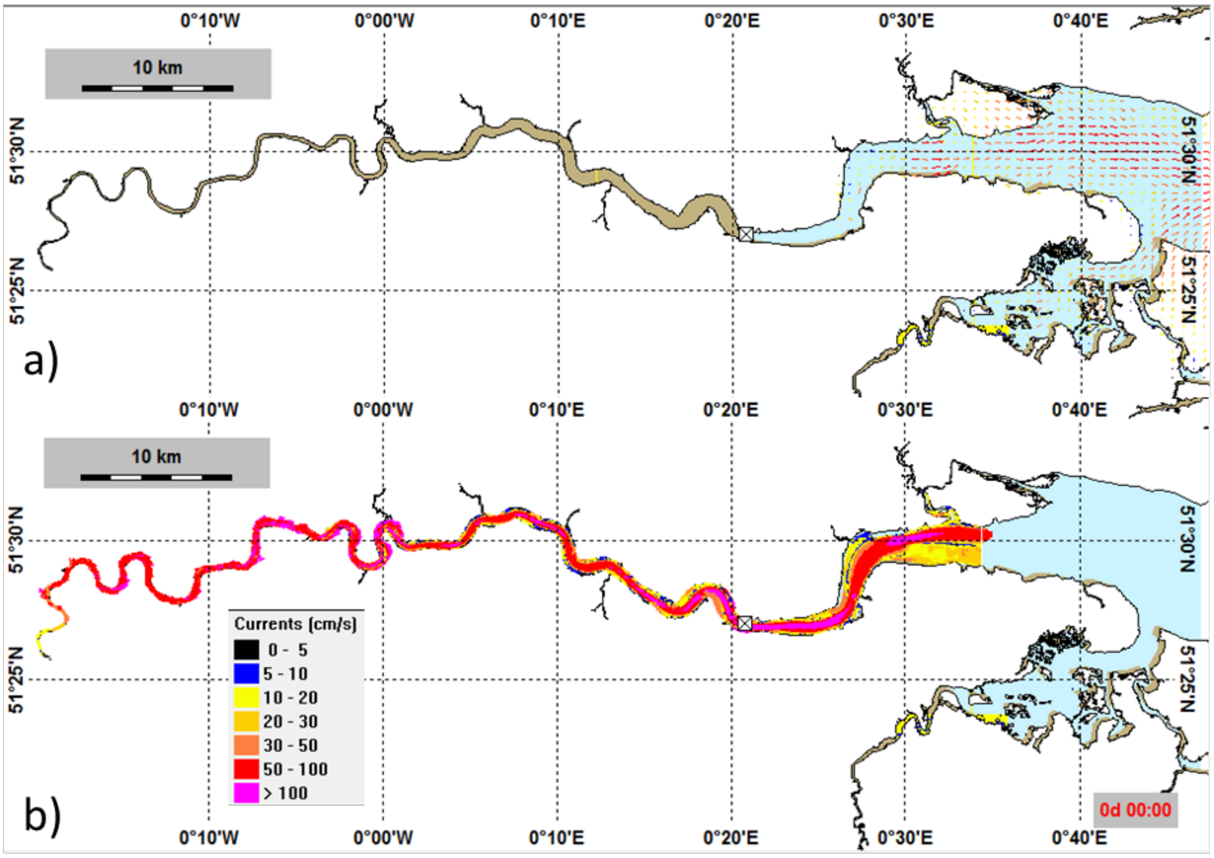

Figure 4. Comparison of OSCAR velocity field over the Thames estuary from the upstream tidal limit down to the estuary mouth in the original shelf model (a) and the new high resolution model (b).

The high resolution regular grid was set such that it overlaps the extent of the original shelf model by approximately 15 km. Therefore, when a spill is located within the overlap of the original shelf model domain and the new high resolution domain, the user is given the choice of utilising results from either the high-resolution model or the shelf model. Figure 4 shows a comparison of OSCAR velocity field over the Thames estuary from the upstream tidal limit down to the estuary mouth with the high resolution TELEMAC2D model and the standard Copernicus forcing. In addition to the tidal constituents, the high-resolution bathymetry was also converted into a regular mesh to be uploaded into OSCAR bathymetry dataset.

C. Running OSCAR

A hypothetical scenario was simulated whereby an oil tanker leaving the Tilbury harbour collides with another ship near the entrance of the harbour (location: 51.45, 0.41), leading to a spillage of 500 m^3 of IF-380 Heavy Fuel Oil. To demonstrate the improvement in the OSCAR spill model capability with the new hydrodynamic forcing, two OSCAR simulations were run for three days to predict where the spill is likely to hit the estuary banks. The first simulation used the standard bathymetry database from OSCAR and its currents field from the Copernicus database; with the second simulation using the improved bathymetry and the current field from the TELEMAC2D high resolution model.

Figure 5 shows the output plots from OSCAR showing the instantaneous surface oil plume and concentration of the beached oil released from Tilbury Port on the flood tide, using the standard Copernicus forcing (upper panel) and the new high resolution TELEMAC2D forcing (lower panel). The background of both plots shows the standard OSCAR low resolution bathymetry and land mask, whilst the black line represents the high resolution extent of the Thames Estuary, provided by DEFRA, that was used to generate the boundary of the TELEMAC2D model domain.

The largest difference between the new and old model occurred on the flood tide (see Figure 5), whereby the plume extent reached a further 8 km upstream of the release site when using the TELEMAC2D forcing leading to shoreline impacts not accounted for by the previous modelling. This is due to the improved resolution and extent of the new model domain. Under both scenarios the plume travelled approximately 13 km downstream, although, the density of the oil was higher when OSCAR was forced with the high resolution TELEMAC2D model. The extent of shore hits (where oil has beached on the shoreline) downstream of Tilbury harbour was similar when using either the old Copernicus forcing or the new high resolution model.

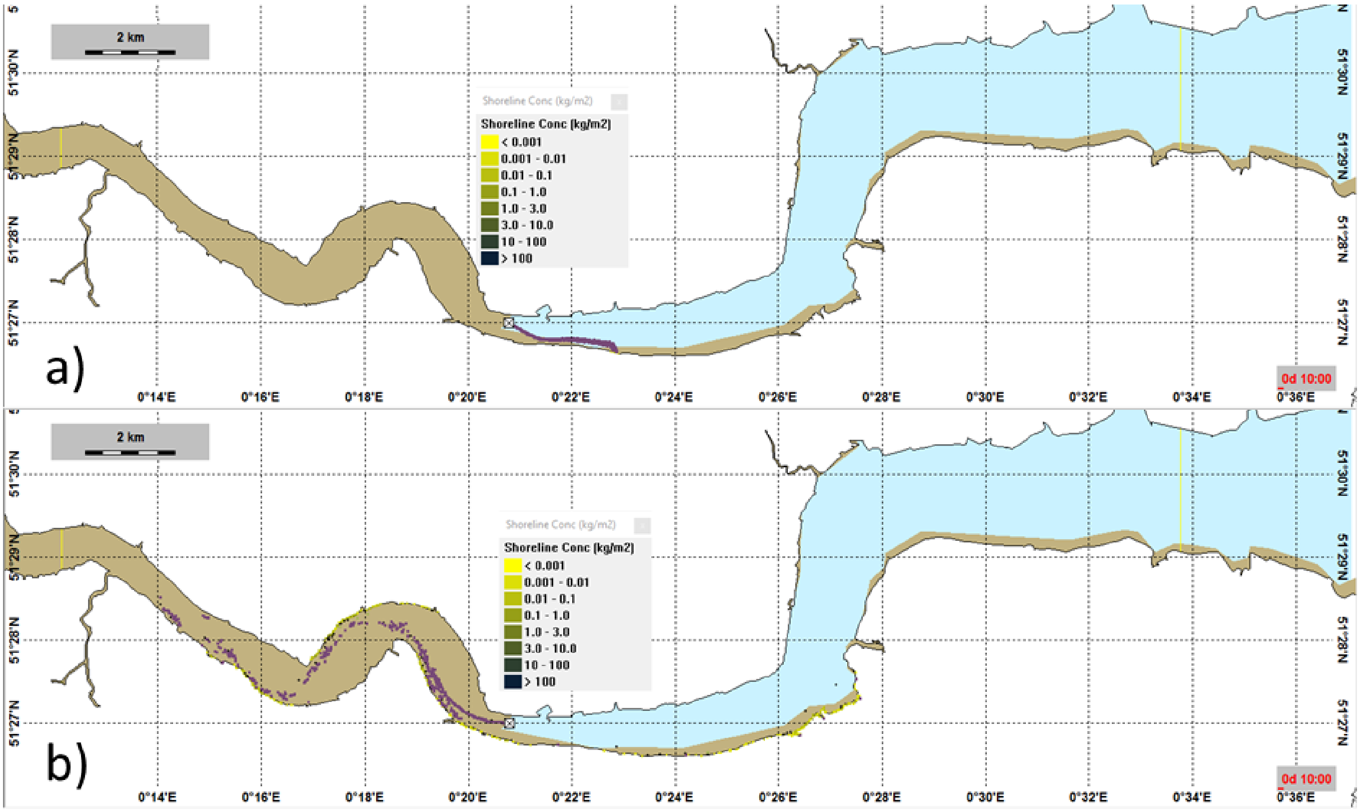

Figure 5. Outputs from OSCAR showing the instantaneous surface oil plume and concentration of the beached oil released from Tilbury Port on the flood tide, using (a) the standard Copernicus forcing and (b) the new high resolution TELEMAC2D forcing. The background shows the land mask used by the Copernicus model with the black line representing the new high resolution coastline.

The upper panel of Figure 5 shows the release of oil travelling downstream using the Copernicus forcing, but upstream in the lower panel with the TELEMAC2D forcing. Due to the lack of the tidal prism, by not including the full Thames Estuary, in the Copernicus model, the tidal velocities are near zero and close to the boundary, the flow is dominated by the riverine flow. Whereas, due to the full reach of the Thames estuary, and subsequent larger tidal prism, being available in the TELEMAC2D model, the currents on the flood tide last much longer, allowing the plume to travel its full potential upstream of the release site on the flood cycle.

As such, the improved hydrodynamic forcing provided by the TELEMAC2D model, will allow for more accurate assessments within the Thames Estuary that could not be achieved using the previous model that used Copernicus hydrodynamics. The improved resolution will also enhance the modelling of dispersion of oil travelling downstream and into the southern North Sea due to the improvements in the tidal currents and the timing of the full tidal cycle.

V. SUMMARY

The tidal database available for the oil spill model used by Cefas extends over the UK shelf and has good resolution in the coastal zone. Nevertheless, there is scope to improve the representation of the tidal currents in the smaller coastal estuaries. Therefore, a validated high resolution TELEMAC2D hydrodynamic model was developed for the Thames estuary to improve the predictions of oil spills. Instantaneous velocity fields were analysed and converted into tidal harmonic constituents for use with the MEMW-OSCAR oil spill model. The new high resolution model of the Thames supplements the results from the existing UK shelf model, extending tidal predictions a further 58.5 km upstream to the extent of the tidal reach at Teddington Weir. Testing of a hypothetical oil spill near Tilbury showed the new improved model forcing will allow an improved ability to assess the risk of oil spills within the Thames Estuary compared to the previous model.

ACKNOWLEDGEMENT

This work was funded by the DEFRA Marine Emergency Response Research 2 fund. The modelling presented in this paper was carried out on the High Performance Computing Cluster supported by the Research and Specialist Computing Support service at the University of East Anglia.

REFERENCES

[1] OSCAR – Oil Spill Contingency and Response modelling software, https://www.sintef.no/en/software/oscar/, Date Accessed 25th July 2023.

[2] Copernicus Marine Service: Atlantic- European North West Shelf-Ocean Physics Reanalysis, https://doi.org/10.48670/moi-00059, Date Accessed 25th July 2023.

[3] Aldridge, J., Beraud, C. and Rees, J. (2018) Marine Emergency Response Research (MERR) Resilience in modelling large scale

incidents. Centre for Environment, Fisheries and Aquaculure Science.

[4] Defra's Marine Digital Elevation Model (DEM) - 1 arc second (south), https://www.data.gov.uk/dataset/e05d3f72-8e67-4cc0-aa2e-abb79e14243c/defra-s-marine-digital-elevation-model-dem-1-arc-second-south, Date Accessed 25th July 2023.

[5] Environment Agency’s SurfZone Digital Elevation Model 2019, https://www.data.gov.uk/dataset/fe455db0-5ce5-4d63-8b38-d74612eb43d5/surfzone-digital-elevation-model-2019, Date Accessed 25th July 2023.

[6] Turner J.F., J.C. Iliffe, M.K. Ziebart, C. Wilson and K.J. Horsburgh. 2010. Interpolation of Tidal Levels in the Coastal Zone for the Creation of a Hydrographic Datum. Journal of Atmospheric and Oceanic Technology, 27(3), pp. 605-613.

[7] Egbert, Gary D., and Svetlana Y. Erofeeva. "Efficient inverse modelling of barotropic ocean tides." Journal of Atmospheric and Oceanic Technology 19.2 (2002): 183-204.

[8] National River Flow Archive, https://nrfa.ceh.ac.uk/, Date Accessed: 5th January 2023.

Data assimilation in TELEMAC using optimal interpolation with application to the North Sea

Kai Chu[1], W. Alexander Breugem[1]
kai.chu@imdc.be, Antwerp, Belgium
[1]: IMDC NV

Abstract – **Ensemble Kalman Filtering is a powerful technique for performing data assimilation. However, the disadvantage of this technique is that it is computationally expensive, thus making the application in TELEMAC-2D and especially TELEMAC-3D difficult. Therefore, in the present paper, an alternative methodology was applied, namely Optimal Interpolation. In this technique, the Kalman Gain, used for data assimilation using a Kalman filter is parametrized and precomputed, rather than computed during an Ensemble Kalman Filtering simulation. Therefore, only a single computation needs to be performed, meaning that the computational cost of a simulation with data assimilation is comparable to the computational cost of a simulation without data assimilation. This method was implemented in TELEMAC and applied in the test cases in TELEMAC-2D. Here, measured water level data are assimilated into IMDC's continental shelf model of the North Sea (iCSM), where it is shown that in a reanalysis, the root mean square error (RMSE) in the water levels decreases by a factor of two with data assimilation.**

Keywords: TELEMAC-2D, TELEMAC-3D, Data-assimilation, Kalman Filter, optimal interpolation, reanalysis, continental shelf model.

I. INTRODUCTION

In order to increase the predictive power of operational models, data assimilation is often used. Further, data assimilation is often applied to perform a reanalysis, in which a combination of observed data and model simulation is adopted to generate an accurate high resolution dataset, which can be for example used to obtain boundary condition data for nesting smaller scale models.

Ensemble Kalman Filtering [1] [2] is a powerful technique for performing data assimilation. However, this technique is computationally expensive, thus making the application in models like TELEMAC-2D and especially TELEMAC-3D difficult. Therefore, in the present paper, an alternative methodology was applied, namely Optimal Interpolation [3] [4]. In this technique, the Kalman Gain, used for data assimilation with Kalman filter is parametrized and precomputed. Therefore, only a single computation needs to be performed, meaning that the computational cost of a simulation with data assimilation is comparable to the computational cost of a simulation without data assimilation.

The objective of this paper is to implement data assimilation using Optimal Interpolation in TELEMAC by means of a generic module, which can then be used in any of the TELEMAC modules. Further it is the objective to test the data assimilation for hindcast simulations in TELEMAC-2D using IMDC's Continental Shelf Model of the North Sea (iCSM), in which measured water level data are assimilated into the model.

The structure of the paper is as follows. First the data assimilation methodology is explained, including details on the implementation in TELEMAC. The iCSM model is presented next, and it is described how data assimilation is applied in this model. The results of the validation calculation are shown in a subsequent section. An outlook on future activities with respect to data assimilation is given thereafter. The paper is ended with some conclusions.

II. DATA ASSIMILATION

A. Optimal interpolation methodology

Data assimilation using optimal interpolation is performed using the following equation to update a model variable x_{mod}, using measurement data x_{meas}:

$$\vec{x}_{update} = \vec{x}_{mod} + K(\vec{x}_{meas} - H^T\vec{x}_{mod})$$

Here, x_{mod}, x_{meas} and x_{update} are vectors. The x_{mod} and x_{update} have the same size, which in TELEMAC-2D equal to the number of nodes in the mesh (NPOIN × 1). X_{meas} has a different size, namely the number of observation points that are used for data assimilation (NOBS × 1). H is an operator that maps the modelled data to the location of the observations. In case linear interpolation is used, H can be written as a matrix of size NOBS × NPOIN. Finally K is the Kalman Gain (a matrix of size NPOIN × NOBS), which determines how the difference between model and observations (at the location of the observations) is used to update the model prediction.

The Kalman Gain K is determined from:

$$K = P_f H^T \left(H P_f H^T - R\right)^{-1}$$

Here $P_f H^T$ is the covariance between the model data (size NPOIN × NOBS) at the location of the observation and the model data anywhere in the model. R is the correlation matrix (size NOBS × NOBS), which prescribes the uncertainty of the measurements. When using Ensemble Kalman Filtering, multiple simulations are performed using perturbed model data and/or observations as a kind of Monte-Carlo simulations, to determine $P_f H^T$ using statistical calculations.

In Optimal Interpolation, K is not determined during the simulation, but precomputed. There are often two approaches to do so:

- Perform a prior calculation using Ensemble Kalman filtering, and store the calculated values of K, for using in later simulations. Typically, in such calculations, K is averaged in time [5].
- Parametrize $P_f H^T$.

In the present study, experiments were initially performed with the first method, in which ADAO (Data Assimilation and Optimization) [6] was used to determine K. However, these experiments were unsatisfactory. The main reason was that in ADAO it is needed to prescribe the full matrix P_f (size NPOIN × NPOIN) to have perturbations to the model data that vary smoothly in space, which is too large to be practically possible. Therefore, method two was used. The following parametrization was used, which used the correlation function with the distance between the location of the observations $\vec{x}_{obs}$ and the model location of each node in the model $\vec{x}$ [7]:

$$P_f H^T = \sigma_{mod}^2 e^{\left(\frac{-|\vec{x}-\vec{x}_{obs}|}{L}\right)}$$

Here σ_{mod} is the standard deviation of the model data (i.e a measure of the uncertainty in the model), and L is the correlation length scale over which the model data is correlated.

The matrix R is parametrized as:

$$R = \begin{pmatrix} \sigma_{meas}^2 & 0 \\ 0 & \sigma_{meas}^2 \end{pmatrix}$$

Here σ_{meas} is the standard deviation in the observations (i.e. a measure of the uncertainty in the observations, assumed to be 0.1 m throughout the study).

B. Implementation in TELEMAC

In order to assimilate the optimal interpolation in TELEMAC, a new module named OPTIMAC was programmed. This module was written in FORTRAN to be easily integrated in the rest of the codes in TELEMAC, such that it can be used in any kind of calculations (with or without TelApy, serial and in parallel). In this module, a precomputed Kalman Gain (which is stored in a SELAFIN file) is used in combination with an ASCII input file containing the data to be assimilated. This file contains x, and y coordinates of the location of the observations (and the z coordinate in case of data assimilation in TELEMAC-3D), as well as time series of the observed data. The module consists of three functional parts:

- **Initialization**. Here, data is allocated for the necessary arrays. The precomputed Kalman Gain, is read from a SELAFIN file. Then, the location of the measurements are read from the ASCII file. The coefficients of the matrix H (interpolation matrix) are determined using linear interpolation, for use in all future interpolation steps.
- **Application**. For every time step during the simulation, it is checked whether observation data is available. In case new data are available, a model variable is updated. A no data value (-999) is used to handle gaps in the time series. A threshold for the water depth is used, to prevent the use of data assimilation in areas with very shallow water depths, in order to prevent instabilities due to the combination of wetting and drying and data assimilation. Note that no validation of the observation data is performed inside the calculation. It is assumed that data validation has been performed previously (before the start of the TELEMAC simulation). This validation is very important, because the algorithm readily assimilates wrong data in the model, leading to an incorrect result of the simulation.
- **Finalization**: The allocated arrays are cleaned and internal variables are reset for the use in a new calculation.

It should be noted that this methodology was developed particularly for the case, where the number of observations is rather low, which occurs for example when a couple of point measurements are used in the data assimilation. It is not very suited for cases where large fields of data need to be assimilated, such as happens for example when using data assimilation on satellite data.

C. Determination of the distance

The parametrized equation for the Kalman gain depends on the distance between the location of the observations and the nodes in the mesh. However, this distance should take into account the presence of the coastlines in the model. Therefore, the distance was defined as the shortest distance between two nodes following the edges of the model. This distance was calculated in MATLAB using Dijkstra's algorithm [8], by converting the mesh to a graph. For the location of the observation, the closest node in the mesh is used (Figure 1). Note that using this method, the distance is expected to be somewhat larger than in reality. However, because the parameter L is used as a tuning parameter in this study, this assumption shall not lead to any problems.

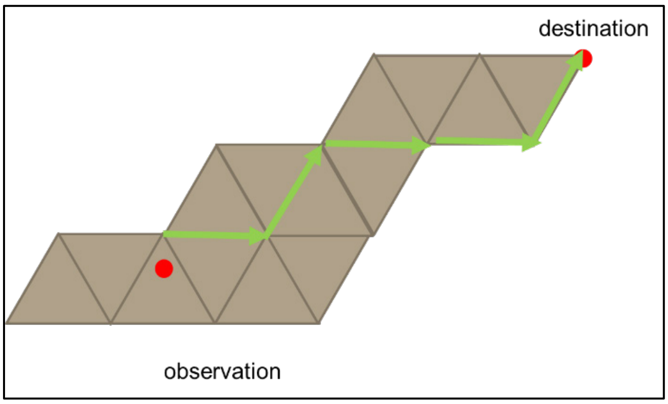

Figure 1. Determination of distance between the observation point and all nodes in the mesh using Dijkstra's algorithm.

III. MODEL SETUP OF THE CONTINENTAL SHEL MODEL OF THE NORTH SEA

A. *Model setup for iCSM*

The IMDC Continental Shelf Model (iCSM) is a 2D barotropic tidal surge model developed in-house in TELEMAC-2D [9] [10], focusing on the continental shelf of the North Sea (Figure 2). The model is built in a spherical Mercator projection with Coriolis effect included. The computational mesh consists of approximately 150,000 nodes and 292,000 elements. The unstructured mesh is refined near the coastal zones, e.g. with a minimal resolution of 500 m at Belgian coast. Mesh refinement is also applied along the coastlines of the UK, France and The Netherlands as well as in the Wadden Sea and the English Channel.

The bathymetry in iCSM is derived from the European Marine Observation and Data Network (EMODnet) which is referenced to Mean Sea Level (version 2020). The model includes the most dominant physical processes in the North Sea, such as inverse barometer correction, which accounts for an isostatic response of the oceans to atmospheric pressure. The self-attraction and loading [11] due to three effects is also taken into account: the deformation of the seafloor under the weight of the water column; the redistribution of Earth mass and its corresponding changes in the gravitational field; the gravitational attraction induced by the water body on itself. It has a well-acknowledged impact on the tidal phases and therefore is included in the iCSM using a beta (β) approximation approach. The internal tidal dissipation considers the dissipation of tidal energy through generation of internal tides which is the dominant mechanism when tides propagate over steep topography in deep stratified waters. This is important in the Bay of Biscay and is also included in iCSM.

To account for the effect of bottom friction, a spatially-varying roughness field of Nikuradse value was automatically calibrated [12] on bottom friction using ADAO with three-dimensional variational assimilation (3D-Var). This automated optimization tool allows to find the best possible parameter set for the model.

In its present form, the model reproduces the hydrodynamics in the European Continental Shelf accurately. For instance, the Root-Mean-Squared-Error (RMSE) of water levels along the Belgian coast is in the order of 10 cm. The RMSE of stationary velocity magnitude in the Belgian Coastal Zone is of the order 0.1 m/s, which is considered as top-of-range numerical model accuracy.

The details of the model setup and its performance are referred to [12], thus will not be elaborated here.

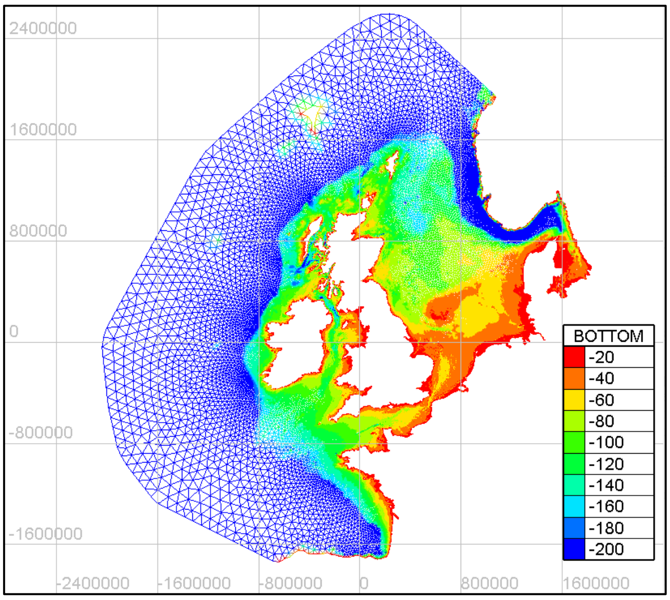

Figure 2. iCSM model mesh and bathymetry (horizontal system: Spherical Mercator projection. Vertical datum: MSL).

B. *Model setup for assimilation of measured water levels*

Measurement of water level data at 29 stations in the North Sea are used in this study (Figure 3). Table 1 presents the model simulations carried out in this study.

Run01 is the base run without data assimilation, which is used to compare to all the experiments using data assimilation. Run02 assimilates measured water level at all the 29 stations as shown in Figure 3, the purpose of this run is to test the module developed for this study (§II). Run03 is a validation run which investigates whether data assimilation could improve water level predictions at stations where no data assimilation is applied directly. The validation stations are selected in a way to have at least one station per coastal zone/country (Figure 5). More sensitivity runs using different validation stations will be considered in future studies. Run04 to Run07 are sensitivity runs with different values of standard deviation of the model data (σ_{mod}) and the length scale over which the model data is correlated (L). Note that an attempt was made to determine L directly from the results of a separate model simulation without data assimilation by determining the autocorrelation of the modelled water levels around the different measurement stations. These data suggested that the shape of $P_f H^T$ might look more like a Gaussian function than an exponential function, but give correlation length in the order of 100 km, used in this study. This is something that will be studied further in future.

Table 1: Summary of model simulations carried out in this study.

Run ID	σ_{mod}	L	Description
Run01	-	-	Base run without data assimilation, same as [12].
Run02	0.1m	100 km	Full data assimilation using measured water level at all 29 stations.
Run03	0.1 m	100 km	Idem Run02, but with 7 validation stations and 22 assimilation stations.
Run04	0.25 m	100 km	Idem Run03
Run05	0.05 m	100 km	Idem Run03
Run06	0.1 m	50 km	Idem Run03
Run07	0.25 m	150 km	Idem Run03

Figure 3: Top: Observation stations of water level used for data assimilation in the North Sea. Bottom: Close up of the Belgian and Dutch coast.

The Kalman Gain is firstly computed for Run02 using $\sigma_{meas} = 0.1$ m; $\sigma_{mod} = 0.1$ m; L = 100 km. Note that the Kalman gain has a size of NPOIN × NOBS (hence 29 maps). The 29 maps of the Kalman Gains are assembled into one graph (Figure 4) for readability, by presenting the maximum value of Kalman Gain at each computational node.

The Kalman Gain is recomputed for Run03 using 22 measurement stations, see the map in Figure 5.

Figure 6 shows the comparison of computed Kalman Gain with different values of σ_{mod} of 0.1 m (Run03), 0.25 m (Run04) and 0.05 m (Run05). It clearly shows the trend that higher σ_{mod} leads to higher values of the Kalman Gain. It essentially means that the updated water level will be based more on measurement data than on the model.

Figure 7 shows the comparison of the computed Kalman Gain with different values of L of 100 km (Run03), 50 km (Run06) and 150 km (Run07). It clearly shows the trend that larger L leads to higher values of Kalman Gain. It essentially means that the updated water level will be based more on the measurement data than on the model results since the Kalman Gain has a larger area of influence.

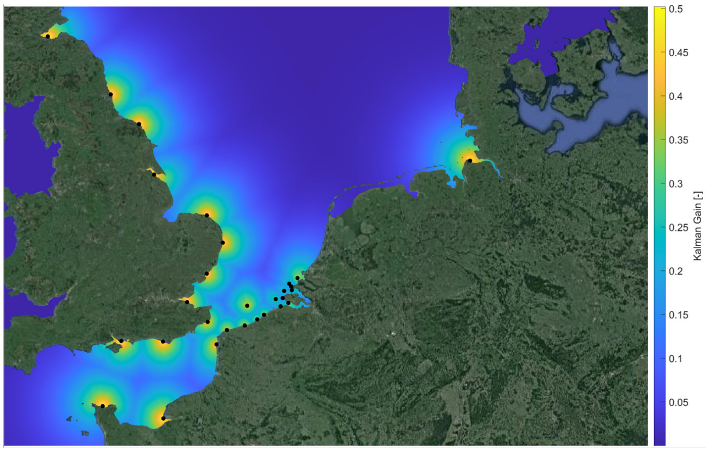

Figure 4: Kalman Gain with 29 measurement stations (Run02).

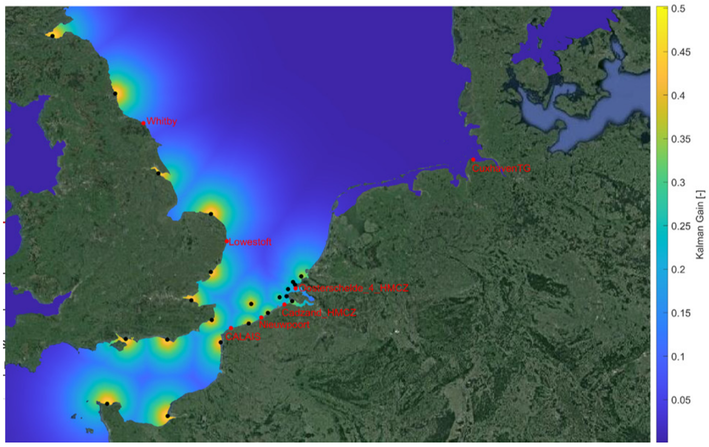

Figure 5: Kalman Gain with 22 measurement stations and 7 stations (marked in red) for validation (Run03).

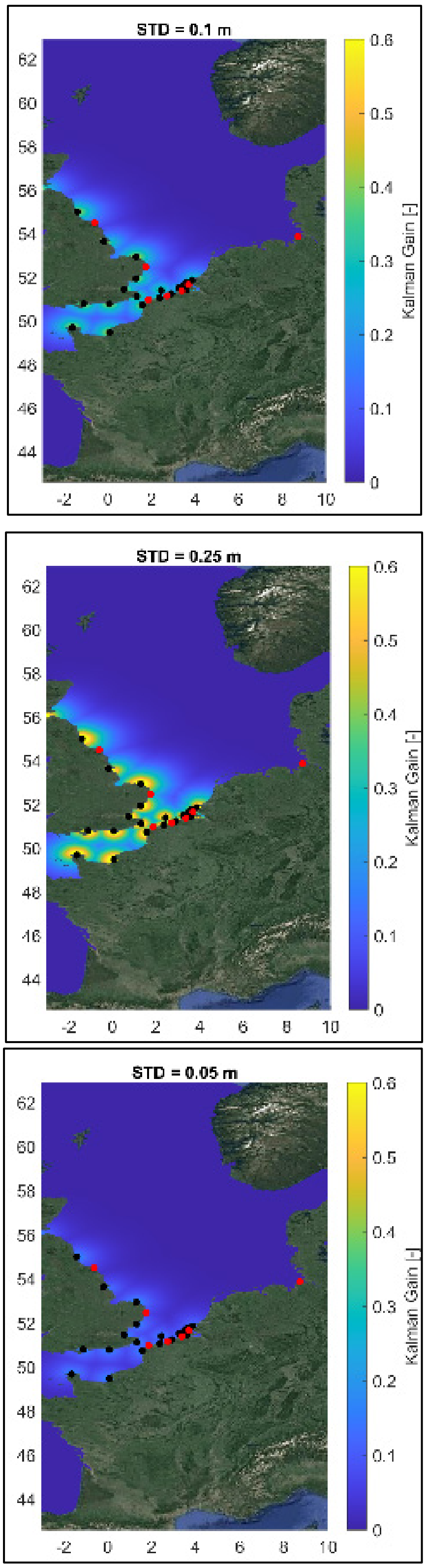

Figure 6: Comparison of Kalman Gain with 22 measurement stations and 7 stations (marked in red) for validation with different values of σ_{mod} (Top:Run03; Middle: Run04; Bottom: Run05).

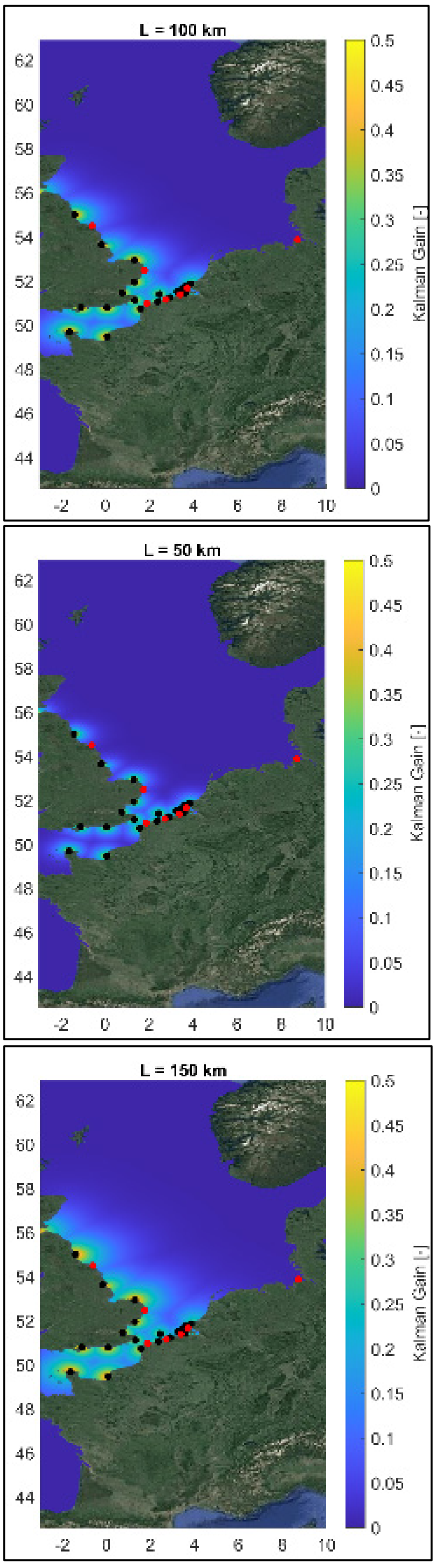

Figure 7: Comparison of Kalman Gain with 22 measurement stations and 7 stations (marked in red) for validation with different values of L (Top:Run03; Middle: Run06; Bottom: Run07).

IV. MODEL RESULTS

Figure 8 shows the comparison of the RMSE of the water levels at the coastal stations from Run01, 02 and 03. The RMSE is lowered by 50% on average using data assimilation. The RMSE at the validation stations (Run03) is slightly higher than the RMSE with direct data assimilation at those stations (Run02), but it is still lower than the RMSE without data assimilation (Run01). It should be noted that if data assimilation is not applied at Cuxhaven in the German Bight, the RMSE becomes substantially larger than when data assimilation is applied locally. This is reasonable since the data assimilation at the remaining stations are too far away to have a substantial impact on the water level at Cuxhaven.

Figure 9 compares the RMSE of water level from Runs 01, 03, 04, and 05. In general, different values of σ_{mod} lead to comparable RMSE values, which are always lower than those obtained without using data assimilation. Lower value of σ_{mod} (0.05 m) result in slightly higher values of the RMSE, implying that the updated water level is dependent more on model predictions than the measurements when assuming the model error is lower (0.05 m). However, this is less justified along the British coast where the original model (Run01, no data assimilation) already produces higher RMSE values.

Figure 10 compares the RMSE of the water level from Runs 01, 03, 06, and 07. In general, different values of L lead to comparable RMSE values, which are always lower than those obtained without using data assimilation. It is noted that the lower value of L = 50 km results in slightly higher values of the RMSE at Leith, North Shields and Whitby in UK, implying that the updated water level is dependent more on the model predictions than on the measurement data with smaller Kalman Gain (Figure 7). Again, this is less justified along the British coast, where the original model (Run01, no data assimilation) already produces higher RMSE values. Interestingly, the RMSE at Immingham and Sheerness are less sensitive to L even when the original model (Run01, no data assimilation) produces a RMSE up to 25 cm. This probably suggests that a station dependent L could be investigated for future studies.

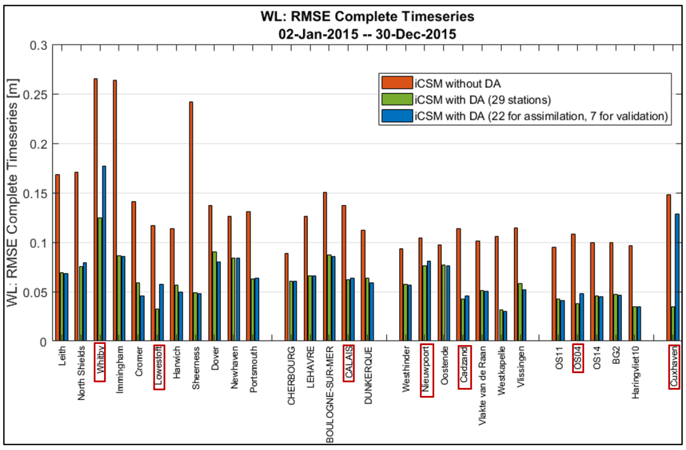

Figure 8: RMSE of water levels from Run01, Run02 and Run03. The stations with red outbox are the seven validation stations.

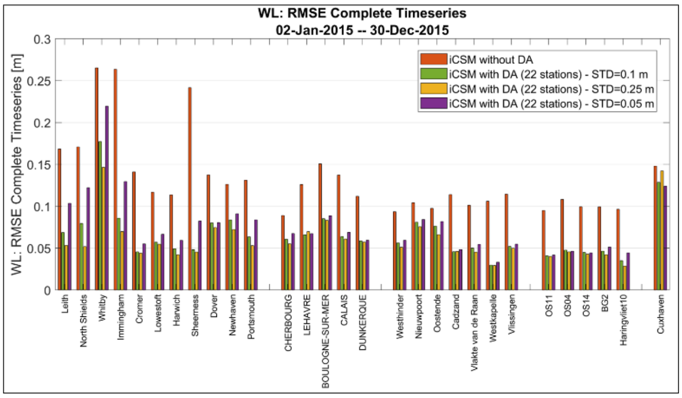

Figure 9: RMSE of water levels using different values of σ_{mod} from Run03, Run04 and Run05.

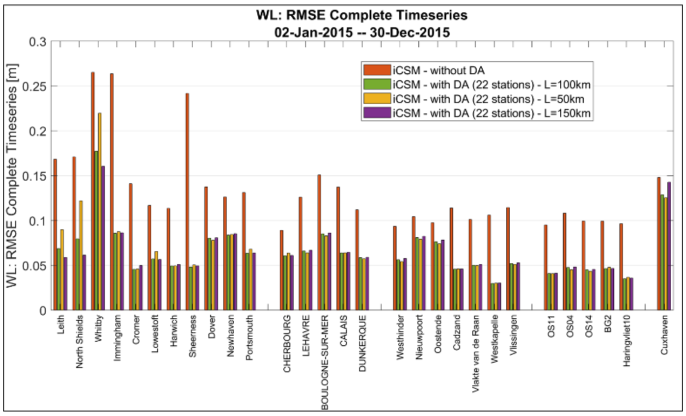

Figure 10: RMSE of water levels using different values of L from Run03, Run06 and Run07.

V. OUTLOOK

The application of data assimilation in iCSM shows a decrease of the RMSE of a factor two, meaning that more accurate boundary conditions for the IMDC's Scheldt model are obtained. Tests of using these updated boundary conditions for the nested Scheldt model will be investigated in the future.

The data assimilation module was implemented in a generic way, meaning that it can easily be applied within other TELEMAC modules. Tests, in which the methodology is applied to assimilate salinity data in IMDC's TELEMAC-3D Scheldt model has already been started and show promising results. Note hereby that in this case, the data assimilation is applied to a three dimensional field rather than a two dimensional one. Due to the generic way the module is setup, this was possible without any changes to the data assimilation code.

It is the intention to apply the presented data assimilation module OPTIMAC to IMDC's North Sea wave model in TOMAWAC [13], in order to improve the predicted wave conditions in the Belgian Coastal Zone. The challenge for this is that in TOMAWAC, wave energy density spectra are the principle variable, which at each location in time depend on the direction and frequency of the wave components. This means that the data assimilation needs to be performed on a four-dimensional variable. The preferred data assimilation methodology depends on the availability of the data. In case measured wave spectra are available, it is preferred to assimilate these directly. However, often only integrated parameters (significant wave height, peak period) or simplified (1D) spectra are available. In this case, it is needed to develop some extra code that parametrizes the effect of these simplified variables on the full two-dimensional wave spectrum. To perform well, it is likely that the Kalman Gain needs to be different for each frequency and especially for each direction in the spectrum.

VI. SUMMARY AND CONCLUSIONS

In this paper, OPTIMAC, a generic module that performs data assimilation in TELEMAC using Optimal Interpolation, was presented. The module was tested by performing data assimilation in IMDC's continental shelf model of the North Sea. In this model, observed water level data were assimilated in a one year hindcast simulation. The RMSE of water level in the North Sea is significantly reduced by 50% with data assimilation. Sensitivity analysis on standard deviation of the model data (σ_{mod}) and the correlation length scale (L) used in Optimal Interpolation have been carried out. In general, different values of σ_{mod} and L lead to relatively comparable RMSE values, which are always lower than those obtained without using data assimilation.

The computational time with and without data assimilation is rather similar, meaning that the Optimal Interpolation algorithm developed for TELEMAC in this study is computational efficient.

ACKNOWLEDGEMENT

The authors want to acknowledge the internal research and innovation program of IMDC for its financial support.

REFERENCES

[1] M. Katzfuss, J. R. Stroud and C. K. Wikle, Understanding the Ensemble Kalman Filter, The American Statistician, 70:4, 2016, pp. 350-357, DOI: 10.1080/00031305.2016.1141709.

[2] G. Evensen, Data Assimilation: The Ensemble Kalman Filter. Germany: Springer Berlin Heidelberg, 2009.

[3] J.L. Hoyer and J. She, Optimal interpolation of sea surface temperature for the North Sea and baltic sea. J Mar Syst. 65, 2007, pp. 176–189.

[4] P.R. Oke, G.B. Brassington, D.A. Griffin and A. Schiller, "Ocean data assimilation: a case for ensemble optimal interpolation". Aust. Meteorol. Oceanogr. J., 59, 2009, pp. 67-76.

[5] F. Zijl, J. Sumihar and M. Verlaan, "Application of data assimilation for improved operational water level forecasting on the northwest European shelf and North Sea". Ocean Dynamics 65, 2015, pp. 1699–1716. DOI: https://doi.org/10.1007/s10236-015-0898-7.

[6] J.P. Argaud, User documentation, in the SALOME 9.3 platform, of the ADAO module for "Data Assimilation and Optimization", Technical report 6125-1106-2019-01935-EN, EDF / R&D, 2019.

[7] C.D. Rodgers, Inverse methods for atmospheric sounding: theory and practice. Series on Atmospheric, Oceanic and Planetary Physics, V2.World Scientific, Singapore, 2000.

[8] T.H. Cormen, H.Thomas, C.E. Rivest, L. Ronald and C. Stein, "Section 24.3: Dijkstra's algorithm". Introduction to Algorithms (Second ed.). MIT Press and McGraw–Hill, 2001, pp. 595–601. ISBN 0-262-03293-7.

[9] W.A. Breugem, T. Verbrugghe and B. Decrop, "A continental shelf model in TELEMAC 2D". TELEMAC User Conference, Proceedings. Presented at the TELEMAC User Conference, 2014.

[10] K. Chu, W.A. Breugem and B. Decrop, "Improvement of a Continental Shelf Model of the North Sea". Telemac user conference 2020, Antwerp, Belgium, 2020.

[11] M. I. Apecechea, M. Verlaan, F. Zijl, C.L. Coz and H. Kernkamp, "Effects of self-attraction and loading at a regional scale: a test case for the Northwest European Shelf". Ocean Dynamics, 67, 2017, pp. 729–749.

[12] K. Chu, W.A. Breugem, L. Wang, and B. Decrop, "Automatic calibration of a continental shelf model of the North Sea using data assimilation algorithm". Proc. 39th IAHR World Congr. Int. Assoc. Hydro-Environ. Eng. Res., Granada, Spain, 2022.

[13] Q.H. Zhang, S. Doorme, J. Figard, W.A. Breugem and K. Bakhtiari, "Application of TOMAWAC for wave propagation and wave energy assessment: a reliable 20-year database for North Sea metocean condition, with a focus near the Belgian coast". *Submitted to*: Telemac user conference, Karlsruhe, Germany, 2023.

Front type implementation for flood extent and flood modelling image assimilation

Quentin Bonassies[1], Sophie Ricci[1], Thanh Huy Nguyen[1], Andrea Piacentini[1], Malak Sadki[1], Christophe Fatras[2], Alice Andral[2], Santiago Pena Luque[3], Raquel Rodriguez Suquet[3]
quentin.bonassies@cerfacs.fr
[1] CECI, CERFACS/CNRS UMR 5318, Toulouse, 31057, France
[2] Collecte Localisation Satellites (CLS), 31520, Ramonville Saint-Agne, France
[3] Centre National d'Etudes Spatiales (CNES), Toulouse, 31401, France

Abstract **– Flood forecasting with 2D hydrodynamic model is a powerful tool for risk assessment and decision makers as they provide water elevation maps over a computational domain. However, those models have uncertainties inherent to them due to the data used to construct them. Data assimilation (DA) is an efficient way to reduce these uncertainties. The assimilation of flood extent maps, derived from synthetic aperture radar (SAR) observations or, in the near future, 2D water surface elevation (WSE) observed from the Surface Water and Ocean Topography (SWOT) satellite is a hot topic as these data provide information in the floodplain. In this work, we propose an innovative framework to directly assimilate the location and the shape of the flood extent, by treating these data as interfaces (front-type) information. This approach allows to overcome the limitations of classical amplitude error correction, therefore allowing for the correction of flood edge position and/or deformation errors. To deal with complex front topology, an object-oriented approach based on the Chan-Vese (CV) contour fitting functional typically used in image processing was proposed. This study demonstrates the capability of the CV measure in a context of 2D flood forecasting to formulate the discrepancy between observed and simulated flood extents, used for DA analysis based on an ETKF algorithm for sequential parameter estimation. An OSSE experiment on a small toy model is presented to show the merit of the CV distance implemented in an ETKF algorithm.**

Keywords: Chan-Vese, Front Data, Data Assimilation, Remote Sensing, TELEMAC-2D, OSSE

I. INTRODUCTION

Between 1995 and 2015, floods accounted for 43% of the global natural hazards making it one of the most devastating and frequent weather-related disasters worldwide. Estimating and reducing the risk of flooding has become essential and attracted significant attention in the hydrometeorological and remote sensing (RS) communities, as well as the public and private sectors [1]. Flood studies aim at mitigating the impacts of flooding on population, as they allow flood management services to better identify flood-prone areas and reduce socio-economic losses with timely and reliable alerts. Moreover, the world population reached 8 billion in 2022 and is still in constant growth. Associated urbanisation growing is often located in floodplains and inundation-prone areas. Thus, increasing vulnerability to flood events and putting pressure on operational flood forecasting services [2]. Several international initiatives have joined efforts in forecasting and monitoring river hydrodynamics, in order to provide Decision Support Systems with accurate flood forecasting capability. Risk assessment relies on Earth Observations (EO) and river hydrodynamic software. The latter solves Shallow Water (SW) equations that are used to predict water surface elevations (WSE) and discharge in the riverbed or floodplains, further used to assess flood risks.

Hydrodynamic models are powerful tools for flood forecasting systems as they provided a fine resolution description of the flow in time and space. However, various sources of uncertainties in the model and in the inputs, for instance, hydrological forcing, initial conditions, model parameters and structures, translate into uncertainties in the model outputs. Data assimilation (DA) reduces these uncertainties by combining the model forecasts with various types of observations, such as in-situ gauge and satellite EO data. In the present work, we use the TELEMAC-2D (T2D) software (www.opentelemac.org), implemented for a simplified test channel case characterized by a narrow parabolic-shaped bathymetry, a slightly inclined topography, and an artificial hill located at mid-length of the channel. An ensemble-based DA filtering algorithm, namely the Ensemble Transformed Kalman Filter (ETKF) is used to sequentially combine observed flood extents, as wet/dry interface position, with T2D WSE simulated maps to improve flood forecasts. The ETKF is here favoured with respect to the Ensemble Kalman Filter (EnKF). Indeed, the computation of the covariance matrices is formulated in the ensemble subspace instead of in the state or observation subspace. A localisation feature is added to the ETKF using a geolocalized polygon that includes the ensemble of front lines. This DA algorithm is carried out within the context of an Observing System Simulation Experiment (OSSE). Synthetical flood extents, which mimic the flood extent maps derived from synthetic aperture radar (SAR) images, are assimilated to account for the error in the upstream inflow. The *a priori* water inflows differ from the true inflow, and the ETKF analysis aims at bringing the *a priori* value closer to the true and consequently bring the simulated fronts closer to the synthetical fronts.

Over the past decades, the literature on DA for hydrodynamic models mainly focused on the assimilation of in-situ or RS-derived WSE observation (*e.g.* [3], [4]). This stems from the fact that WSE is a state variable in any hydraulic model, thereby rendering the DA more straightforward. WSE maps can be derived from SAR images, by combining RS-derived flood extent maps and topography data, yet such methods still require further research (*e.g.* [5]). Alternatively, fully automated methods for mapping flood extents from satellite images are described in the literature (*e.g.* [6], [7]). Machine learning algorithms, for instance integrated in FloodML, allow to retrieve flood extents from SAR images ([12]). Recent research works have developed methods to directly assimilate RS-derived flood extents, water masks or probabilistic flood maps, in hydraulic models and flood forecasting chains (*e.g.* [8], [9] & [10]), thereby paving the way for operational applications. Cooper *et al.* [11] proposed an observation operator that directly considers the SAR backscatter values as observations in order to bypass the flood edge identification or flood probability estimation processes. Another approach stands in the computation and the assimilation of wet surface ratio (WSR) in floodplain areas from SAR-derived flood extents [13]. Satellite SAR imagery data provides flood extent information with a large coverage from the observed backscatter (BS) values. Satellite SAR systems are capable of monitoring flood events with day-and-night imaging ability, regardless of weather conditions. In addition, the recently launched wide-swath radar interferometry SWOT satellite is able to compute water surface elevation (WSE) maps from its interferometric observations. In this paper, we propose a framework for the direct assimilation of flood extent location and shape (derived from Sentinel-1 SAR images), considering the wet-dry interface as an innovative information. Such front-type information aims to overcome the limitations of classical amplitude error correction and allows for the correction of flood edge position and/or deformation errors.

In several research fields, such as wildfire modelling ([15], [16] & [17]), tumour growth monitoring ([18], [19]) and oil spill detection and surveillance ([20]), DA algorithms have been developed to treat images as front-type information. Such approach was developed by Rochoux *et al.* ([16]) for data-driven surface wildfire propagation at a regional scale, based on a fire front mapping and shape recognition. In this work, the position of markers, *i.e.* the finite set of points positioned along the observed and the simulated fire front, are matched and compared. The resulting discrepancies were used in an ETKF algorithm to reduce the errors in the propagation model parameters and state. This prototype was evaluated with a synthetic and controlled grassland fire experiment. However, it was shown that this marker-based method was suboptimal for complex front geometry due to the computation of Euclidean distances between markers. Indeed, to deal with complex front topology, an object-oriented approach derived from the Chan-Vese (CV) contour fitting function used in image processing ([14]) was proposed in [15]. This front shape similarity measure was implemented and evaluated for a field-scale experiment in [17]. A similar idea is here applied for the assimilation of SAR-derived flood extent in the context of flood modelling. However, it should be noted that the comparison of non-hydrometric observations, *e.g.* flood edge locations, or flood probability measures, with the model outputs is not straightforward and requires the development of appropriate observation operators. In the present study, the ETKF algorithm is implemented for an OSSE experiment using a 2D hydrodynamic model as forward model. RS-derived front-type data are assessed with respect to simulated flood extent using the CV metrics.

II. MATERIALS AND METHODS

A. *TELEMAC-2D solver*

Free-surface hydraulic modelling is principally governed by the Shallow Water equations (SWE, also known as Saint-Venant equations derived from Navier-Stokes Equations), which express mass and momentum conservation averaged in the vertical dimension. In this work, the hydrodynamic numerical model TELEMAC-2D is used to simulate and predict the water level (denoted by H [m]) and velocity (with horizontal components denoted by u and v [m/s]) from which flood risks can be assessed. It solves the SWE with an explicit first-order time integration scheme, a finite-element scheme and an iterative conjugate gradient method. A complete description of the underlying theoretical approach is provided in [21]. At each point within the mesh representing the model topography and bathymetry (for mesh nodes in the river channel), the results of the simulation are water height and velocity averaged over the vertical axis.

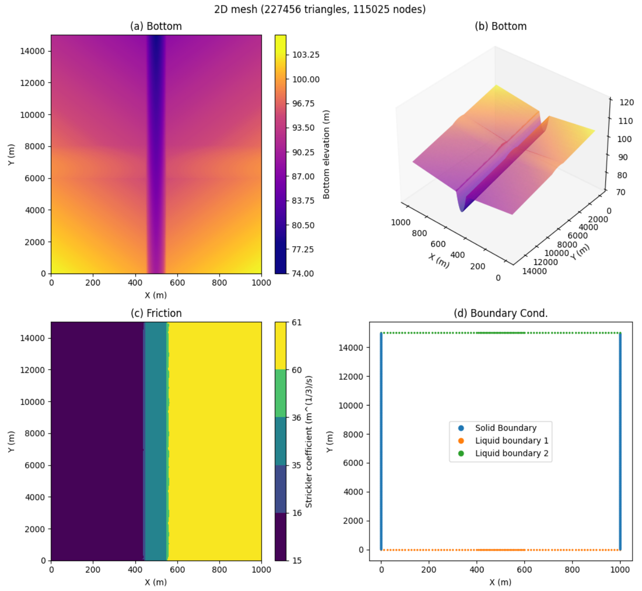

Figure 1. Topography and bathymetry of the mesh (a and b), Friction coefficients (c) and boundary condition (d). For illustration purposes, the x-axis and y-axis are not proportionally scaled.

B. *TELEMAC-2D test case*

A 15km-long parabolic-shape channel with a uniform slope and simplified floodplain test case was set for our work (Figure 1). The riverbed is characterized by a parabolic geometry (10m maximum depth). The catchment has a constant slope of 0.8% from upstream to downstream (x-axis). The floodplain has a uniform slope of 8% in the perpendicular direction to the river centerline (y-axis). Two topographic extrusions at around y = 7000 m are added in the floodplains. The extrusion is generated with the following equations:

$$T = 10 - [(x - 500)^2 + (y - 7000)^2] * 1.10^5$$

with x ∈ [0; 450] ∪ [550; 1000] and y ∈ [6000; 8000]

$$Z = T + \min(|T|)$$

The topography and bathymetry of the model are displayed in Figure 1 (a) and (b).

The upstream and downstream boundary condition, respectively represented in orange and green in Figure 1 (d) are prescribed with a constant inflow and a rating curve. The Strickler coefficient is prescribed to 15 $m^{1/3}/s$ in the left floodplain, to 60 $m^{1/3}/s$ in the right floodplain and to 35 $m^{1/3}/s$ in the channel (Figure 1 - (c)). The triangular mesh contains around 115,000 nodes, and the global mean mesh edge length is 12.5 m. Within the riverbed, the triangles are oriented with a mean edge horizontal length of 6.25 m and a mean edge vertical length of 12.5m. Floodplains are described on an unstructured mesh with a mean edge length of 12.5 m.

Preliminary analyses on the impact of the mesh density, the computational time steps and the friction coefficients were carried out. It was shown that an efficient computation with reasonable CPU resource cost (around 2 min per run on 6 nodes of Intel Xeon Gold 6140 core) was achieved with a time step of 10 s for this 115,000-node mesh. In addition, such analyses showed that the dynamics of the flow is mostly driven by the inflow, and that the impact of a variation in friction coefficients is of lesser importance. This motivates the choice of the DA control vector as a corrective term to the inflow in this preliminary work.

A spin-up simulation with a constant inflow of 5,000 m^3/s is integrated over 48 h to provide the initial condition for all ensemble members of the DA strategy. These members are characterized by an inflow value prescribed between 4000 m^3/s and 6000 m^3/s.

OSSE Framework

For the DA ensemble test case, two OSSE experiments are set. The OSSE framework is based on a deterministic reference simulation (denoted as *the truth*) with a chosen set of parameters, in our case, a prescribed corrective term to the inflow named β. β is supposed to be a random variable with a gaussian distribution characterised by a zero-mean and a standard deviation (std) here chosen to 700 m^3/s. This factor is added to a constant *a priori* water flow rate prescribed as the inflow boundary condition for each ensemble member. Two different ensembles of 60 members with *a priori* settings are generated for our following tests: (i) 4,500 and (ii) 5,500 m^3/s, respectively experiment A and B (noted exp.A and exp.B).

Synthetical observations are generated from the truth simulation water level (WL) maps, thresholded to express a water mask and to mimic SAR derived flood extent maps.

C. *Wet-dry pixels interface and level set variable*

Level-set (LS) map and LS functions are closely related to shape optimization and topology analysis. It is used in several research domains to compare and analyse the evolution of an object in images as it allows a straightforward treatment of topology changes (see [22]). In hydrodynamic study, it can be used to take into account the changes and deformations of the wet/dry interfaces of a flood map. The wet/dry interfaces are extracted from the WL map, thus defining the LS function noted Φ. It is here defined as follows:

$$\Phi(x, y) = WL(x, y) - WL_{fr}$$

where (x, y) denotes the (lon,lat) coordinates of a grid cell and WL_{fr} is the threshold between wet and dry areas (WL_{fr} = 5 cm in our case). The LS value is null at the interface between wet and dry areas. An example of a level-set map for exp.B is shown in Figure 2 (a).

In the framework of OSSE, this simulated interface position is compared to synthetical water mask derived from the truth simulation, also thresholded to WL_{fr} and represented as a water mask as shown in Figure 2 (b).

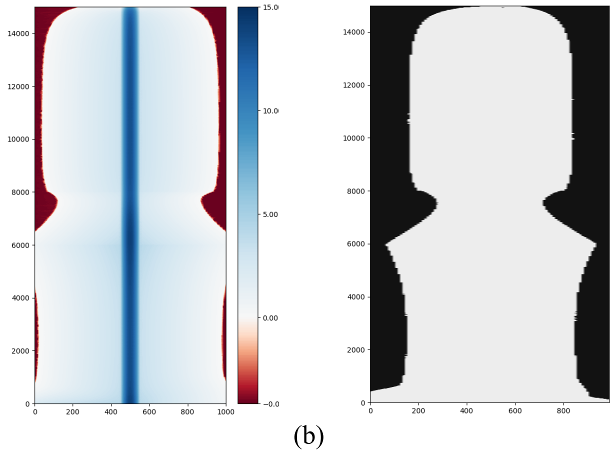

(a) (b)

Figure 2. (a) Simulated level-set function computed from T2D water level (from exp.B) (b) Observed binary flood extent map from a synthetical SAR image (from the truth WL map)

D. *The Chan-Vese contour fitting functional*

CV distances derived from the CV functional are based on two scalars, noted as C0 and C1, which rely on the formulation of the contingency map (Figure 3) between the observed and the simulated images. In the contingency map, each pixel is identified as one of the four following outcomes:

- False Negative (FN - in yellow in Figure 3) if the pixel is flooded in the observation but dry in the simulation,
- True Negative (TN - in blue in Figure 3) if the pixel is non flooded in the observation and dry in the simulation,
- False Positive (FP - in green in Figure 3) if the pixel is non flooded in the observation and wet in the simulation,
- True Positive (TP - in orange in Figure 3) if the pixel is flooded in the observation and wet in the simulation.

C0 quantifies the mismatch between the observed and the simulated flooded area. It is the ratio between the number of flooded pixels that the simulation misses (FN) and the total of the non-flooded pixels in the simulation (TN + FN).

C1 quantifies the match between the observed and the simulated flooded area. It is the ratio between the number of flooded pixels that the simulation hits (TP) and the total of flooded pixels in the simulation (TP + FP).

C1 and C0 are then defined as follow:

$$C_0 \approx \frac{FN}{TN+FN} \; and \; C_1 \approx \frac{TP}{TP+FP}$$

In the following, a buffer around the fronts is determined to reduce the computational cost of the CV metric and the subsequent algebra in the DA algorithm. The contingency map (Figure 3) is only computed in this buffer zone near the fronts (*i.e.* white pixels outside the buffer are not taken into account). The buffer localisation is described in subsection II-F. The observed image is considered as the reference binary map and the LS simulation as the experiment to be assessed with respect to this reference.

Figure 3 displays the contingency map for two typical scenarios. In Figure 3 (a), the simulated flooded area is totally included within the observed flooded area, hence FP = 0 and TP+FP = TP, so that 0 < C0 < 1 (TN ≠ 0, FN ≠ 0) and C1=1. In Figure 3 (b) the simulated flooded area fully contains the observed flooded area, thus FN = 0, therefore C0 = 0 and 0 < C1 < 1 (TP ≠ 0, FP ≠ 0).

Two other scenarios are also possible in general: (i) the perfect agreement scenario, when the simulated flooded surface perfectly matches the observed flooded surface, *i.e.* FN = 0 and FP = 0, so that C0=0 and C1=1 (TN ≠ 0, TP ≠ 0); and (ii) the total disagreement scenario, where the simulated flooded surface and the observed flooded area do not overlap nor intersect, thus TP = 0 and FN ≠ TN+FN, so that 0 < C0 < 1 and C1 = 0 (TN ≠ 0, FP ≠ 0). This last scenario is not possible in our case since the riverbed is wet in both simulation and observation. An intermediate state, more common in practice, is the partial agreement, when the simulated flooded surface partially overlaps the observed flooded area, leading to TP ≠ 0, FN ≠ 0, so that 0 < C0 < 1 and 0 < C1 < 1.

The CV functional can be seen as a discrepancy functional between two LS. We decompose the CV functional in two functionals of the following form:

$$\mathcal{J} = \mathcal{J}^+ + \mathcal{J}^- \qquad (1)$$

where:

$$\mathcal{J}^+ = \int_\Omega Hv(\Phi)\left(\Phi^{obs} - Cmax\left(\Phi^{obs},\Phi\right)\right)^2 dxdy$$

$$\mathcal{J}^- = \int_\Omega \left(1 - Hv(\Phi)\right)\left(\Phi^{obs} - Cmin\left(\Phi^{obs},\Phi\right)\right)^2 dxdy$$

where Ω is the buffer area. ϕ^{obs} is the binary observed map and ϕ the simulated LS function. Hv the Heaviside function, it is equal to 1 if ϕ is non-negative and to 0 otherwise. Cmax and Cmin are respectively the max and min between C0 and C1. $\mathcal{J}$ will be used as an analytical metric for results assessment in Section III.

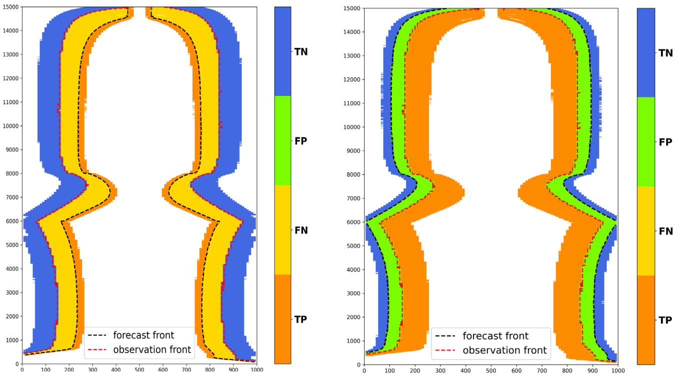

(a) exp.A (b) exp.B

Figure 3. Examples of contingency maps
blue = TN; green = FP; yellow = FN; orange = TP
dashed black line=forecast front; dashed red line=observed front

From $\mathcal{J}^+$ and $\mathcal{J}^-$, which are squared functionals, we define Chan-Vese distances that are compatible with the ETKF algorithm:

$$D\left(\Phi^{obs},\Phi\right) = D^+\left(\Phi^{obs},\Phi\right) + D^-\left(\Phi^{obs},\Phi\right) \qquad (2)$$

D^+ and D^- are defined as follow:

$$D^+\left(\Phi^{obs},\Phi\right) = Hv(\Phi)\left(\Phi^{obs} - Cmax\left(\Phi^{obs},\Phi\right)\right) \; and$$

$$D^-\left(\Phi^{obs},\Phi\right) = \left(1 - Hv(\Phi)\right)\left(\Phi^{obs} - Cmin\left(\Phi^{obs},\Phi\right)\right).$$

E. Buffer localisation

The observation operator in the ETKF is formulated in the observation space, here described as the number of pixels. This dimension is reduced when a buffer zone is prescribed.

The buffer selects only the points that are the most informative near the ensemble of fronts (from observation image and the simulated runs). It consists in three steps (illustrated by 0): (i) extract all the fronts in the ensemble LS maps and the binary flood extend; (ii) compute for each front line a polygon around it with a buffer chosen as twice the size of the pixel; (iii) merge all the buffer polygons in order to build a unique buffer polygon that is their union altogether.

F. Ensemble-based data assimilation algorithm (ETKF)

1) Description of the control vector

The control vector, denoted by **x** composed of a single parameter noted β, that is an additive factor to the water flow rate Qup at the upstream boundary condition. **x** is of size (1x Ne) where Ne is the ensemble size. In the following, **x** is noted $\mathbf{x^f}$ or $\mathbf{x^a}$ for forecast and analysis respectively. It is indexed with i that represents the i-th member between [1, Ne].

The implemented DA algorithm consists of a cycled deterministic ETKF where each cycle involves one or several binary flood extent observations. Each assimilation cycle c covers a time window T = [t_{start}, t_{end}] of 3h-duration where $n_{obs,c}$ are assimilated. In our case, $n_{obs,c}$ is the number of pixels

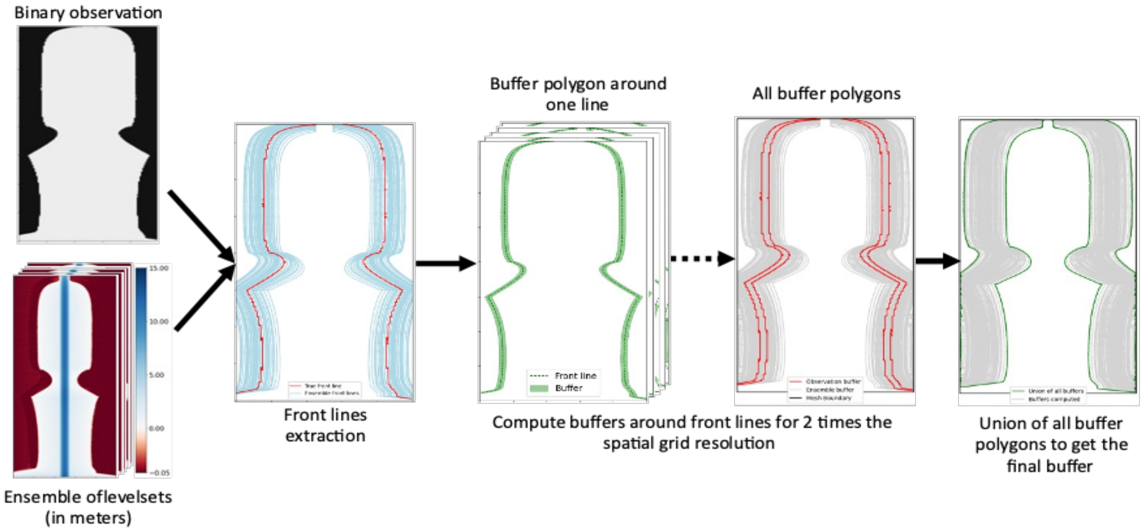

Figure 4. Framework for the buffer selection

to be assimilated from all the observed images over the cycle c. Over a DA cycle and for each member of the ensemble, the *a priori* Qup is used to run the *a priori* simulation with the hydrodynamic deterministic model with Qup = 4,500 (exp.A) or 5,500 m3/s (exp. B). This is the forecast step; it defines the background or *a priori* hydraulic state. The simulated WL map is expressed as a water mask that is the model equivalent to the observed flood extent at the observation time. The CV discrepancy between observed and simulated flood extent for each member is used to determine the misfits and the covariance matrices, leading to the estimation of the analysis of β. This is the analysis step, it describes the a posteriori, or analysed hydraulic state. These steps are further detailed in the following. For each member, the updated control vector is used to perform the analysed trajectory with the hydrodynamic model. For each DA cycle, the analysed trajectory starts with a spin-up of 2h at t_{start} - 2h in order to reduce the impact of the initial condition on the analysis. There is 1h of overlap between the 3h-assimilation window and the 2h-spin-up window. It provides a final analysed state at t_{start} + 2h which correspond to the end of the assimilation window for cycle c.

2) *ETKF forecast step*

An ETKF is used in our DA experiment. The ETKF performs the linear algebra of the analysis mostly in the ensemble subspace, which is of a smaller dimension than that of the observation space. For cycle c, the forecast step consists of the propagation in time, over T, of the background control and model state vectors.

The control vector x^i is then of size one, the observation space is of space n_{obs} and the hydraulic state subspace of size m. We consider a time t included in the assimilation cycle c. $\mathcal{M}_c: R \rightarrow R^n$ denote the hydraulic model at the cycle c, of size n.

The background hydraulic state, $s_c^{f,i}$, associated with the ensemble i-th member of the control background vector is equal to:

$$s_c^{f,i} = \mathcal{M}_c\left(s_{c-1}^{a,i}, x_c^{f,i}\right) \tag{3}$$

where $x_c^{f,i}$ is the forecasted control vector resulting from the previous analysis cycle. $s_{c-1}^{a,i}$ is the analysed state from the previous cycle that is used as the initial condition for the current cycle. For the first cycle, it is provided by a restart file. Along DA cycles, x_c^f is generated using $x_{c-1}^{a,\ i}$ and a random perturbation in order to avoid the ensemble collapse.

The equivalent of control vector in the observation space for each member, denoted by $y_t^{f,i}$, stems from:

$$y_c^{f,i} = \mathcal{H}_c\left(s_c^{f,i}\right) \tag{4}$$

where $\mathcal{H}_c: R^m \rightarrow R^{nobs}$ is the observation operator in cycle c, from the model state space to the observation space, that selects, extracts and eventually interpolates model outputs at times and locations of the observation vector $\mathbf{y}^o$.

3) *ETKF analysis step*

Details on the ETKF can be found in [23], [24] and [25].

The EnKF methods, including the ETKF variant, are based on the Kalman filter equations:

$$\boldsymbol{x}^a = \boldsymbol{x}^f + \mathbf{K}\,\mathrm{D}(\boldsymbol{y}^o; \boldsymbol{y}^f) \tag{5}$$

$$\mathbf{P}^a = (\mathbf{I} - \mathbf{KH})\mathbf{P}^f \tag{6}$$

$$\mathbf{K} = \mathbf{P}^f\mathbf{H}^T(\mathbf{HP}^f\mathbf{H}^T + \mathbf{R})^{-1} \tag{7}$$

with $\mathbf{x^a}$ the analysed control vector of the ensemble (of size (1 x Ne)), **K** the Kalman gain (of size (Ne x n_{obs})), $\mathbf{P^a}$ the analysis error covariance matrix (of size (n x n)), $\mathbf{P^f}$ the forecast error covariance matrix (of size (n x n)) and **R** the observation error covariance matrix (of size (n_{obs} x n_{obs})) which is taken diagonal in this study. D($\mathbf{y^o}$; $\mathbf{y^f}$) is the innovation vector between the observation $\mathbf{y^o}$ and the model equivalent related to the forecast ensemble states. In this work, D is the CV distance defined in subsection II-E.

The principle of the EnKF methods is to stochastically the covariances matrices **P** within the ensemble.

$$\bar{\mathrm{x}} = \frac{1}{\mathrm{Ne}}\sum_{\mathrm{i}=0}^{\mathrm{Ne}} \mathrm{x_i} \qquad (8)$$

is the control ensemble mean and **P** reads:

$$\mathbf{P} = \frac{1}{\mathrm{Ne}-1}\sum_{i=0}^{Ne}(x_i-\bar{x})(x_i-\bar{x})^T = \frac{1}{\mathrm{Ne}-1}\mathbf{X}\mathbf{X}^{\mathrm{T}} \qquad (9)$$

with $[X]_i = (x_i - \bar{x})$ the matrix of the ensemble anomalies. We note $\mathbf{X_a}$ the analysed anomaly vector and $\mathbf{X_f}$ the forecasted anomaly vector.

For each member of the ensemble, the *a priori* is updated during the analysis step:

$$x^{a,i} = x^{f,i} + \mathbf{K}\,\mathrm{D}(y^o; y^{f,i}). \qquad (10)$$

In the EnKF, in order to avoid ensemble collapse, an ensemble of perturbed observations is used in place of the deterministic observation vector. This way, (6) is validated in a statistical way.

In contrast to the EnKF, the ETKF updates in an explicit way the ensemble means and anomalies inside the ensemble subspace instead of working the algebra in the observation space (as in (3)). The ensemble mean is updated using the analysis (1) and the anomalies are updated with an explicit transformation represented by the ensemble transform matrix **T**:

$$\mathbf{X}_a = \mathbf{X}_f\mathbf{T} \qquad (11)$$

The analysed anomalies are defined such that the analysed covariance matrix respect (6), given (9) and (11):

$$\mathbf{P}^a = (\mathrm{I}-\mathbf{KH})\mathbf{P}^f = (\mathrm{I}-\mathbf{KH})\mathbf{X}_f\mathbf{X}_f^{\mathrm{T}} \qquad (12)$$

$$\mathbf{P}^a = \mathbf{X}_a\mathbf{X}_a^{\mathrm{T}} = \mathbf{X}_f\mathbf{T}\mathbf{T}^{\mathrm{T}}\mathbf{X}_f^{\mathrm{T}} \qquad (13)$$

If we develop (12) according to (7) and (9) we can choose $\mathbf{TT^T}$ as:

$$\mathbf{TT}^{\mathrm{T}} = \left(\mathrm{I} - \frac{1}{Ne-1}\mathbf{Y}_f^T\left(\frac{1}{Ne-1}\mathbf{Y}_f\mathbf{Y}_f^T + \mathbf{R}\right)^{-1}\right) \qquad (14)$$

$$and\ \mathbf{Y}_f = \mathbf{HX}_f \qquad (15)$$

(14) is equivalent, according to the Sherman-Morrison-Woodbury formula [23], to:

$$\mathbf{TT}^{\mathrm{T}} = \left(I*(Ne-1) + \mathbf{Y}_f^T\mathbf{R}^{-1}\mathbf{Y}_f\right)^{-1}. \qquad (16)$$

In the present work, $\mathbf{Y}_{\mathrm{f,i}}$ is computed as the CV distance between the mean ensemble background and each member of the ensemble:

$$[\mathbf{Y}_f]_i = \mathbf{H}[\mathbf{X}_f]_i = \frac{D(Hv(\bar{y}^f); y^{f,i})}{\sqrt{Ne-1}} \text{ and } \bar{y} = \frac{1}{Ne}\sum_{i=1}^{Ne} y^{f,i}$$

[26] propose to decompose **T** in eigenvectors such that the ensemble mean is preserved. **T** is a positive symmetric matrix. The orthogonal matrix **U** (generally chosen as the identity matrix) is introduced so that **T** decomposes as:

$$\mathbf{T} = \sqrt{Ne-1}\,C\Gamma^{-\frac{1}{2}}C^T\mathbf{U} \qquad (17)$$

where *C* are the eigenvectors (because **T** is symmetric) and **Γ** the eigenvalues matrix of **T**. The analysed thus reads:

$$\mathbf{X}_a = \mathbf{X}_f\mathbf{T} = \sqrt{Ne-1}\,\mathbf{X}_f C\Gamma^{-\frac{1}{2}}C^T\mathbf{U} \qquad (18)$$

and the ensemble mean can is updated:

$$\bar{x}^a = \bar{x}^f + \mathbf{X}_f\mathbf{w_a} \qquad (19)$$

$$with\ \mathbf{w}_a = (C\Gamma^{-1}C^T)\mathbf{Y}_f^T\mathbf{R}^{-1}\mathrm{D}(y^o; \bar{y}^f) \qquad (20)$$

with $\mathrm{D}(y^o; \bar{y}^f)$ the CV distance between the observation and the ensemble mean.

For each member, the analysed control vector is updated as:

$$x^{a,i} = \bar{x}^a + \mathbf{X}_a^i \qquad (21)$$

where $\mathbf{X}_a^{\mathrm{i}}$ is the i-th column of the matrix $\mathbf{X_a}$.

We can now compute the new analysed state for the next cycle with the hydrodynamic model and the analysed control vector with:

$$s_c^{a,i} = \mathcal{M}_c\left(s_{c-1}^{a,i}, x_c^{a,i}\right) \qquad (22)$$

III. EXPERIMENTAL SETTING AND RESULTS

The result of the DA for the corrective term on the upstream forcing using the CV metric to compute the discrepancy between observed and simulated front is assessed in this section. In the following, these results are displayed with two types of figures with similar layout for exp.A ($Q_{\text{up, }a\ priori}$ = 4,500 m3/s) and exp.B ($Q_{\text{up, }a\ priori}$ = 5,500 m3/s). Four DA cycles are carried out.

Figure 5 and Figure 7, represent the ensemble fronts for the forecast (subplot a) and the analysis (subplot b) for the last time of the last DA cycle, at physical time t = 124,000 s with a start at t0 = 86,400 s. Members of the ensemble (forecast or analysed) are plotted in thin grey lines, the ensemble mean (forecast or analysis) is plotted in green, and the observed front is plotted in red.

In Figure 6 and Figure 8, subplots (a) represents the evolution of the ensemble means (upper panels) and the standard deviations (bottom panels) over the DA cycles for the forecast control vector (in blue) and the analysis control vector (in red). Subplots (b) show the evolution of the mean CV functional (eq. (1)) computed between the ensemble members' levelset and the observed binary images used for results analysis. The smaller the CV functional the better; it reaches zero if the two images used for the comparison are perfectly equal.

A. Results for experiment A

In exp.A, the *a priori* is lower than the truth. Since the true value for Qup is $5000 m^3/s$, β is expected to be positive and to be close to 500 m3/s (because of the observation error) allowing for an inflow forecasted and analysed close to the truth.

For a given DA cycle, the buffer limits the observation space so that the number of pixels is about 50,000 for one image instead of 150,000 for the whole domain. In the present case where three images are assimilated over T for cycle c, n_{obs} = 150,000.

The forecasted and analysed front lines for the last DA cycle are shown in Figure 5 (a) and (b) respectively. The analysis is brought closer to the truth so that the members, mean and observations seem to overlap.

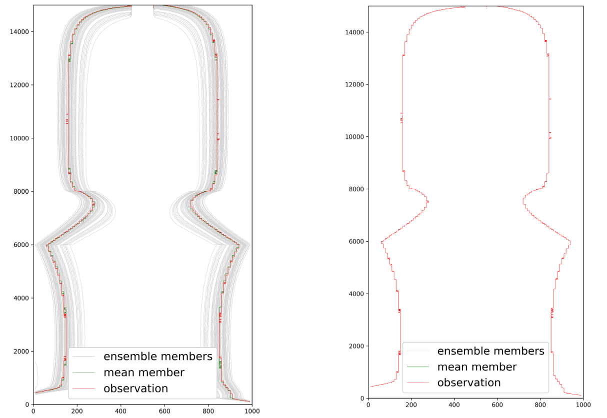

(a) forecast front lines (b) analysis front lines

Figure 5. Exp.A - Front lines of the ensemble members (in light grey), the observation (in red) and the ensemble mean (in green) for the last time of the last cycle of DA.

This illustrates how the DA algorithm is capable of correctly increasing the inflow to almost reach the truth inflow value.

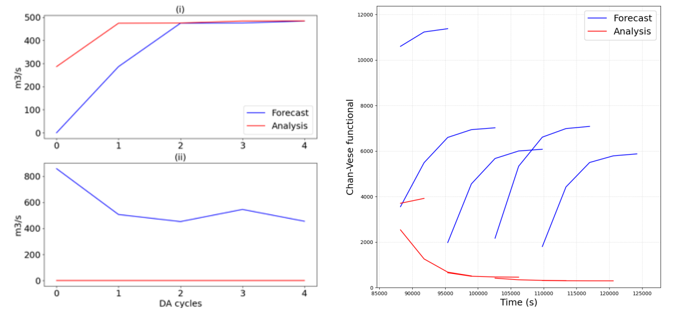

(a) Summary of the analysis phases. (i) ensemble mean; (ii) ensemble std

(b) Chan-Vese functional evolution in time.

Figure 6. Analysis metric for Exp.A.
In blue the forecast, in red the analysis

The upper panel in subplot a in Figure 6 shows the evolution of the ensemble mean for β along the DA cycles. It should be noted that, as expected, the analysis as well as the forecast is reaches almost 500 m^3/s which give the truth value when added to the *a priori* value of 4,500 m^3/s. Since the truth is prescribed as a constant value, the analysis converges to this value along the DA cycles and the std of the ensemble decreases to zero. This shows that the ETKF DA efficiently brings the *a priori* close to the truth, with a high certainty in spite of the limited number of members in the ensemble. Indeed, before the analysis, the forecast std values are found between 400 and 800 m^3/s. The values are greatly reduced with the DA algorithm. Figure 6 (b) displays the Chan-Vese functional over time from eq. (1). This clearly shows the improvement brought by the DA analysis with the cost function metrics. As expected, the forecast and analysis cost functions decrease over the DA cycles, with a smaller $\mathcal{J}$ value for the analysis. The CV functional for the analysis runs decreases almost exponentially. Even though it does not reach zero (perfect state) for the ensemble, it converges quite well towards it. Indeed, we put a strong trust on observations so that we expect that the analysis phase brings the control vector near the truth.

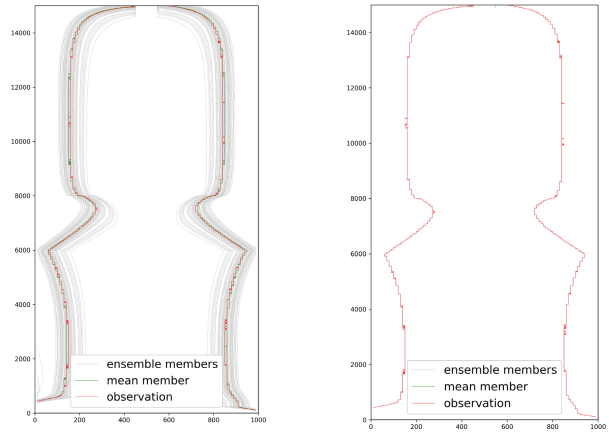

(a) forecast front lines (b) analysis front lines

Figure 7. Exp.B - Front lines of the ensemble members (in light grey), the observation (in red) and the ensemble mean (in green) for the last last time of the last cycle of DA.

B. *Results for experiment B*

In exp.B, a second *a priori* setting was tested when the inflow ensemble mean is greater than the truth, *i.e.* 5,500 m^3/s compared to the true value 5,000 m^3/s. As opposed to exp.A, here the beta factor is expected to be negative and approach - 500 m^3/s, which allows for decreased inflow closer to the truth.

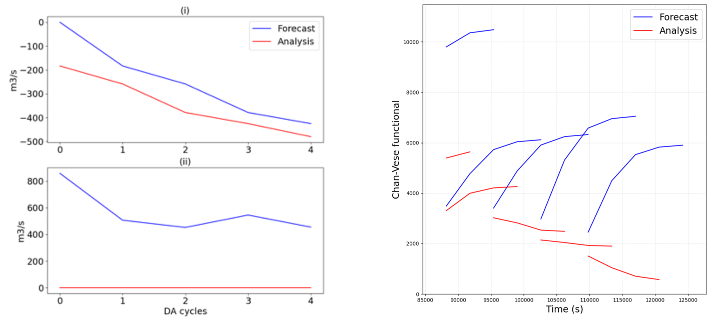

(a) Summary of the analysis phases. (i) ensemble mean; (ii) ensemble std

(b) Chan-Vese functional evolution in time.

Figure 8. Analysis metric for Exp.B.
In blue the forecast, in red the analysis

Similarly to Section III A, Figure 7 (a) and (b) show the forecasted and analysed front lines for the last DA cycle. For the analysis all members, mean and observations seem to overlap.

Figure 8 (a) (upper panel) shows the evolution of the mean ensemble beta factor evolution. The analysis as well as the forecast reaches - 500 m^3/s which give the truth value when added to the *a priori* value of 5,500 m^3/s.

It seems that the convergence over the DA cycles is slower than in expA. This suggests that the non-linearity between the inflow and the flood extent is stronger when removing water from the system, which may relate to the incapacity of the model to wash out water from the floodplain as evapotranspiration processes are not accounted for. This question is currently being investigated. The ensemble inflow std value of the analysis is almost zero (Figure 8 (a) bottom panel) meaning that the ETKF DA is most certain. Similarly, to expA, the CV cost function significantly decreases over the DA cycles with reduced values for the analysis with respect to the forecast as shown in Figure 8 (b), with a lesser efficiency than for exp.A.

IV. DISCUSSION AND CONCLUSION

In conclusion, the implementation of the ETKF with the CV metric for front distance estimation shows promising results. The OSSE framework allows for a sanity validation of the algorithm here applied to a simplified test case. The construction of a buffer zone to reduce the size of the observations space allows to reduce the computational cost of the ETKF DA algorithms. For now, the buffer selection phase is done for each cycle in the algorithm. This phase could be adapted to be more efficient.

Further work will focus on more advanced test cases where the simulated and observed fronts intersect. This could result from uncertainties in topography and Strickler coefficient.

The perspective for this work is to apply the CV-ETKF strategy to real test cases, in unsteady conditions, for instance for the Garonne Marmandaise model, and extend the observations to other satellite-derived flood extents, for instance from SWOT.

ACKNOWLEDGEMENT

The authors acknowledge the primary works of E. Combes during his internship on the Chan-Vese functional for hydrodynamics T2D models.

REFERENCES

[1] United Nations Office for Disaster Risk Reduction, 2018, The human Cost of Weather-related Disasters, Available from: https://www.unisdr.org/files/46796_cop21weatherdisastersreport2015.pdf

[2] F. Dottori, L. Mentaschi, A. Bianchi, L. Alfieri, and L. Feyen. Adapting to rising river flood risk in the EU under climate change. Joint Research Centre (JRC), 2020.

[3] R. Hostache, X. Lai, J. Monnier, and C. Puech. Assimilation of spatially distributed water levels into a shallow-water flood model. Part II: Use of a remote sensing image of Mosel River. J Hydrol, 390(3-4):257–268, 2010.

[4] H. Oubanas, I. Gejadze, P.-O. Malaterre, et al. Discharge estimation in ungauged basins through variational data assimilation: The potential of the swot mission. Water Resour. Res., 54(3):2405–2423, 2018.

[5] F. Cian, M. Marconcini, P. Ceccato, and C. Giupponi. Flood depth estimation by means of high-resolution SAR images and lidar data. Nat. Hazards Earth Syst. Sci., 18(11):3063–3084, 2018.

[6] M. Chini, R. Hostache, L. Giustarini, and P. Matgen. A hierarchical split-based approach for parametric thresholding of SAR images: Flood inundation as a test case. IEEE Trans. Geosci. Remote Sens., 55(12):6975–6988, 2017.

[7] Sandro Martinis, Jens Kersten, and André Twele. A fully automated TerraSAR-X based flood service. ISPRS J. Photogramm. Remote Sens., 104:203–212, 2015.

[8] B. Revilla-Romero, N. Wanders, P. Burek, P. Salamon, and A. de Roo. Integrating remotely sensed surface water extent into continental scale hydrology. J. Hydrol., 543:659–670, 2016.

[9] A. Dasgupta, R. Hostache, R. Ramsankaran, et al. A mutual information-based likelihood function for particle filter flood extent assimilation. Water Resour. Res., 57(2):e2020WR027859, 2021.

[10] C. Di Mauro, R. Hostache, P. Matgen, et al. Assimilation of probabilistic flood maps from SAR data into a coupled hydrologic/hydraulic forecasting model: a proof of concept. Hydrol. Earth Syst. Sci., 25:4081–4097, 2021.

[11] E.S. Cooper, S.L. Dance, J. García-Pintado, N.K. Nichols, and P.J. Smith. Observation operators for assimilation of satellite observations in fluvial inundation forecasting. Hydrol. Earth Syst. Sci., 23(6):2541–2559, 2019.

[12] S. Peña-Luque, S. Ferrant, M.C.R. Cordeiro, et al. Sentinel-1 & 2 multitemporal water surface detection accuracies, evaluated at regional and reservoirs level. Remote Sens., 13(16), 2021.

[13] Nguyen, T. H., Ricci, S., Piacentini, A., Fatras, C., Kettig, P., Blanchet, G., et al. (2022). Dual state-parameter assimilation of SAR-derived wet surface ratio for improving fluvial flood reanalysis. Water Resources Research, 58, e2022WR033155. https://doi.org/10.1029/2022WR033155

[14] T. F. Chan and L. A. Vese, "Active contours without edges," in IEEE Transactions on Image Processing, vol. 10, no. 2, pp. 266-277, Feb. 2001, doi: 10.1109/83.902291.

[15] Rochoux, M. C., Collin, A., Zhang, C., Trouvé, A., Lucor, D., and Moireau, P. (2018). Front shape similarity measure for shape-oriented sensitivity analysis and data assimilation for eikonal equation. ESAIM: Proceedings and Surveys, 63:258-279

[16] Rochoux, M. C., Emery, C., Ricci, S., Cuenot, B., Trouvé, A. (2014). Towards predictive data-driven simulations of wildfire spread – Part II: Ensemble Kalman Filter for the state estimation of a front-tracking simulator of wildfire spread, Natural Hazards and Earth System Sciences, doi:0.5194/nhess-15-1721-2015

[17] Zhang, C., Collin, A., Moireau, P., Trouvé, A., Rochoux, M. C. (2018). Front shape similarity measure for data-driven simulations of wildland fire spread based on state estimation: Application to the RxCADRE field-scale experiment. Proceedings of the Combustion Institute

[18] Martins, M., Ferreira Jr, S., and Vilela, M. (2007). Multiscale models for the growth of avascular tumors. Physics of Life Reviews, 4(2):128-156.

[19] Collin, A., Chapelle, D., and Moireau, P. (2015). A Luenberger observer for reaction-diffusion models with front position data. J Comput Phys, 300(C):288-307.

[20] Li, L., Le Dimet, F.-X., Ma, J., Vidard, A. (2017). A level-set based image assimilation method: Potential applications for predicting the movement of oil spills. IEEE Transactions on Geoscience and Remote Sensing, Institute of Electrical and Electronics Engineers. doi:10.1109/TGRS.2017.2726013

[21] M. Hervouet, Hydrodynamics of free surface flows: modelling with the finite element method. Wiley Online Library, 2007, vol. 360.

[22] van Dijk, N.P., Maute, K., Langelaar, M. et al. Level-set methods for structural topology optimization: a review. Struct Multidisc Optim 48, 437–472 (2013). https://doi.org/10.1007/s00158-013-0912-y

[23] M. Asch, M. Bocquet, and M. Nodet, Data assimilation: methods, algorithms, and applications. SIAM, 2016.

[24] P. Sakov et P. R. Oke (2008a). A deterministic formulation of the Ensemble Kalman Filter : an alternative to ensemble square root filters. Tellus A, 60(2):361–371.

[25] B. R. Hunt, E. J. Kostelich et I. Szunyogh (2007). Efficient data assimilation for spatiotemporal chaos : A local ensemble transform Kalman filter. Physica D, 230:112 – 126.

[26] E. Ott, B. R. Hunt, I. Szunyogh, A. V. Zimin, E. J. Kostelich, M. Corazza, E. Kalnay, D. Patil et J. A. Yorke (2004). A local Ensemble Kalman filter for atmospheric data assimilation. Tellus A, 56:415–428.

Flood forecast with chained hydrologic-hydraulic modelling and data assimilation

Thanh Huy Nguyen[1,2], Andrea Piacentini[1], Simon Munier[3], Sophie Ricci[1,2], Raquel Rodriguez Suquet[4], Sophie Le Gac[4], Francois Boy[4], Christophe Fatras[5], Quentin Bonassies[1,2], Malak Sadki[1,2], Santiago Pena Luque[4]
[1] CERFACS, Toulouse, 31057, France
[2] CECI, CERFACS/CNRS UMR 5318, Toulouse, 31057, France
[3] Centre National de Recherches Météorologiques (CNRM), Toulouse, 31057, France
[4] Centre National d'Etudes Spatiales (CNES), Toulouse, 31401, France
[5] Collecte Localisation Satellites (CLS), 31520, Ramonville Saint-Agne, France
thnguyen@cerfacs.fr

Abstract – **Early warning and prediction of flood events have become all the more essential as the occurrence and intensity of flooding have increased in recent decades. In this work, the upstream boundary condition for a local-scale hydrodynamic TELEMAC-2D (T2D) model is provided by the outputs of a large-scale hydrologic model ISBA-CTRIP. The studied test case is the Garonne Marmandaise catchment (southwest of France), that is prone to flooding, with a focus on a medium-sized flood event that occurred in January-March 2022. To account for the uncertainties related to the inflow provided by ISBA-CTRIP as well as the friction coefficients and hydraulic state, we focus on the assimilation of remote-sensing flood observations, namely longitudinal river water surface elevation (WSE) profiles provided by Sentinel-6MF altimetry data, and 2D flood extent observations derived from Sentinel-1 SAR images acquired during overflowing events. An Ensemble Kalman Filter (EnKF) with a dual state-parameter data assimilation (DA) approach is implemented on top of the T2D model. The observation operator associated with the longitudinal river WSE profiles and the water surface ratio (WSR) observations, as well as the dual state-parameter sequential correction, were implemented and validated. This work paves the way toward a cost-effective and reliable methodology for flood forecasting and flood risk assessment that allows moving towards a perspective working with poorly-gauged or ungauged catchments.**

Keywords: Flooding, data assimilation, ensemble Kalman Filter, remote sensing, Garonne.

I. INTRODUCTION

Flooding is one of the most common and costliest natural disasters worldwide in recent decades. In the context of operational flood forecasting, the challenges lie in producing reliable forecasts given constrained computational resources and within processing time that is compatible with real-time forecasting. Flood hydrodynamic models typically depend on observed data from gauge networks, e.g., water level and/or discharge that describe the forcing time-series at the upstream and lateral boundary conditions (BCs) of the model. However, this information is not always available, due to a lack of in-situ gauge data—which is declining worldwide [1]—or because the stream gauge measurements acquired during high-overflowing periods are unreliable. Additionally, in order to reach longer forecast lead times, a forecasted inflow discharge should be described, e.g., discharge simulated by large-scale hydrologic models [2].

While hydrologic and hydraulic numerical models play an essential role in flood forecasting, their capabilities remain limited due to uncertainties in their input data such as rainfall, inflow, geometry and topography of the catchment and the river (e.g., topographic and bathymetric errors from Digital Elevation Models (DEMs)), as well as hydraulic parameters (calibration of friction coefficients). As a result, data assimilation (DA) prevails as an efficient tool to reduce these uncertainties, by combining numerical model outputs with various Earth Observations from space or from in-situ stream gauge measurements. In this regard, the volume of data from space missions have been increasing considerably in recent years. They provide heterogeneous and relevant data such as altimetry (Sentinel-6, SWOT), optical (Sentinel-2, Pléiades) and radar (Sentinel-1, TerraSAR-X). In particular, Synthetic Aperture Radar (SAR) is capable of all-weather global imagery of continental waters, which are depicted by low backscatter pixels resulting from the specular reflection of the radar pulses upon their incidence against the water surfaces. Based on such information, our previous studies [3, 4, 5] have focused on the assimilation of wet surface ratio (WSR) derived from Sentinel-1 (S1) SAR images, in addition to in-situ water level data. As such, an ensemble DA approach has been developed to accommodate these 2D WSR observations alongside in-situ water level time-series within an Ensemble Kalman Filter (EnKF) framework has been implemented on the TELEMAC-2D (T2D) hydrodynamic model set up over the Garonne Marmandaise catchment.

In this work, we focus on the usage of remote sensing data and the improvement of flood forecasting relying on only this data, compared to the conventional method that uses only in-situ data. The merits of such DA methods (both the one using only in-situ and only RS data) are demonstrated in the high uncertainty conditions. Indeed, the upstream BC of the T2D model is provided by the large-scale hydrologic ISBA-CTRIP model [6], with the purpose of extending forecast lead time beyond the hydraulic network transfer time. As such, this work aims at near real-time flood forecasting by making the most out of the large volume of heterogeneous data from space.

II. STUDY AREA AND MODELS

Free-surface hydraulic modelling is mainly governed by the Shallow Water equations (SWE), also known as Saint Venant equations derived from Navier-Stokes Equations. They express mass and momentum conservation averaged in the vertical dimension. In this work, the hydrodynamic numerical model TELEMAC-2D is used to simulate and predict the water level (denoted by H [m]) and velocity (with horizontal components denoted by u and v [m.s^{-1}]) from which flood risks can be assessed effectively. It solves the SWE with an explicit first-order time integration scheme, a finite-element scheme and an iterative conjugate gradient method. A complete description of the underlying theoretical approach is provided in [7].

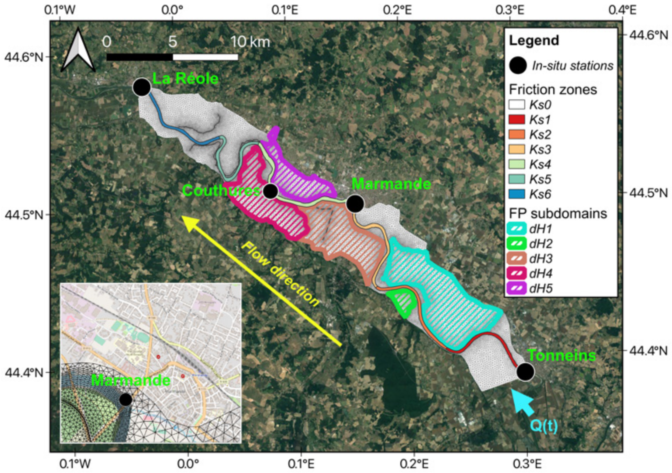

Figure 1. TELEMAC-2D Garonne Marmandaise model and control vector [3]. Inset figure magnifies the impacted urban area around Marmande.

The study area is the Garonne Marmandaise catchment (southwest France) which extends over a 50-km reach of the Garonne River between Tonneins and La Réole (Figure 1). This catchment has been equipped with hydraulic infrastructures, and a progressively constructed system of dykes and weirs to protect the floodplains from flooding events such as the historic flood of 1875 and to manage submersion and flood retention areas. Over this catchment, observing in-situ stations operated by the VigiCrue network (https://www.vigicrues.gouv.fr/) can be found at Tonneins, Marmande, and La Réole (black solid circles). In 2021, an additional station was installed by Vortex.io (https://www.vortex-io.fr/) at Couthures-sur-Garonne, henceforth called Couthures for short, to provide additional observations following the January-February 2021 major flood event occurred on this catchment. In this work, we focus on the flood event that occurred in December 2021 - January 2022. In-situ WL measured every 15 minutes during this flood event at Tonneins (blue line), Marmande (orange line), and La Réole (green line), and at Couthures (cyan line), are shown in Figure 2. Vertical lines stand for the overpass time of the Sentinel-1 (in grey/yellow dash-dotted lines for S1A and S1B, respectively) and Sentinel-6 (cyan dotted lines).

The large-scale hydrologic model ISBA-CTRIP [8] consists in the coupling between the ISBA land surface model (LSM) [9] and the CNRM-modified version of the TRIP river routing model (RRM) [10]. While ISBA simulates the exchanges of heat and water balance at the soil-atmosphere-vegetation and hydrology (i.e., surface and deep run-off) interfaces, CTRIP deals with the lateral transfer of freshwater towards the continent-ocean interface. Regarding the spatial resolution, the ISBA model is defined at global scale on a 0.5°×0.5° regular grid. On such a grid, the energy and water budget over continental surfaces are established, considering a three-layer soil. ISBA provides a diagnostic of the surface runoff and the gravitational drainage (i.e., water percolating to the deep layers of the soil), later used as forcing inputs for the RRM. On the other hand, the CTRIP model is defined on a regular latitude-longitude grid at an improved 1/12° resolution and it follows a river network to transfer water laterally from one cell to another, down to the interface with the ocean. This present work takes advantage of the recent CTRIP version from [8, 11] with a gridded map of discharge. The uncertainties in these simulated discharges mainly stem from uncertainties in the LSM inputs (i.e., precipitation), RRM parameters and catchment description.

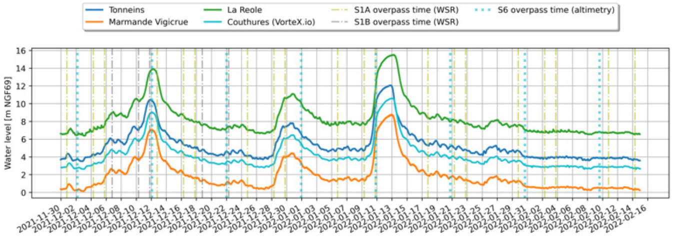

Figure 2. Water level time series at VigiCrue and Vortex.io observing stations, as well as S1 and S6 overpass times.

The TELEMAC-2D model over the Garonne Marmandaise catchment was developed and calibrated by EDF R&D [12]. It was built on a mesh of 41,000 nodes based on existing bathymetric cross-sectional profiles and topographic data [12]. A local rating curve at Tonneins is used to translate the observed WLs into a discharge time-series that is applied over the whole upstream interface (cyan arrow in Figure 1), including both river bed and floodplain boundary cells. Such a modelling strategy was implemented in order to cold start the T2D model with any inflow value. However, it prompts an artificial over-flooding over the upstream first meander, which would remain for a small period of time until the water returns to the river bed. On the other hand, the downstream BC at La Réole is described with a local rating curve built from gauge measurements. Over the simulation domain, the friction Strickler coefficient [13] is defined over seven zones, Ks_1 to Ks_6 for different segments of the river bed and Ks_0 for the entire floodplain. They are illustrated in Figure 1 by solid-coloured segments of the river bed and white region for the floodplain. It is worth noting that the description of friction coefficients is highly prone to uncertainties related to the zoning assumption, the calibration procedure, and the set of calibration events. In the absence of in-situ data in every river segment, their a priori values are set based on the calibration process from the original setting by EDF [12].

In addition, in order to account for the evapotranspiration, ground infiltration and rainfall processes that are lacking in the TELEMAC-2D Garonne model, a state correction in the floodplain has been implemented. Five subdomains delineated in the floodplain, represented by hatched coloured regions in

Figure 1 which involve a uniform WL correction over each subdomain, are added to the control vector. These state corrections are considered as zero-mean gaussian random vectors. These zones were determined based on the description of the storage areas [12] and the dyke system of the catchment. It is worth-noting that the first storage area of the model, at the first meander near Tonneins, is excluded in this study because of the aforementioned artificial over-flooding effect. In addition, several storage areas within the downstream region are not considered either, because they are not fully observed by S1, and some spurious dynamics may be caused by the errors in topography near La Réole [12]. Over each of the five zones, the ratio between the area of wet surfaces (observed by S1 images) and the total area of the subdomain is computed to provide observations in the floodplain.

In addition to the S1-derived flood extend observations, we also leverage data from a recent altimetry satellite, namely Sentinel-6-Michael Freilich (S6) [14]. These data were processed with Fully-focused SAR [15] allowing, for every S6 overpass, a profile of water surface elevation every 10 m along the river centreline. For this studied catchment, the S6 observations cover a similar area to that of the Ks_2 and Ks_3 friction coefficient of the riverbed. These relevant observations are taken advantage of in order to improve the performance of flood forecasting when relying on only remote-sensing data, compared to the conventional method that uses only in-situ data.

III. METHOD

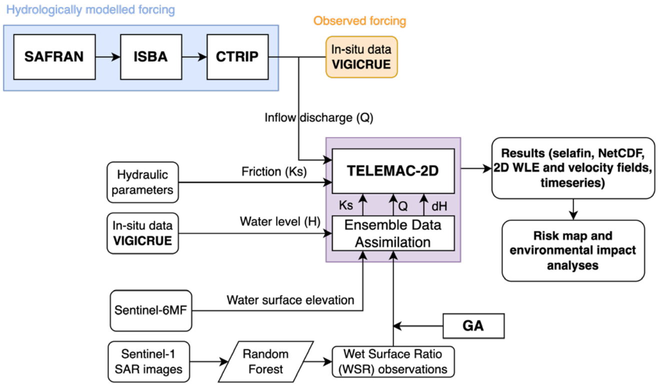

Figure 3. Overview workflow.

The general workflow for this study is illustrated in Figure 3. As aforementioned, the chained multi-physics and multi-scales modelling approach involves a direct supply of discharge forcing data for the T2D hydraulic model by a hydrologic model (blue block in Figure 3), instead of an observed streamflow from an in-situ gauging station (orange block in Figure 3). A similar approach was carried out between T2D and the large-scale RAPID hydrologic model within a twin experiment setup [2]. Here, the differences between two discharge time-series, respectively in blue and orange lines, are depicted by Figure 4, which shows the underestimated discharges with shortened duration over several peaks of the studied flood event. There are also a few days with low regimes where ISBA-CTRIP discharge is a little higher than the observed discharge, e.g., before the third peak of the flood event.

A. Data assimilation

Figure 2 depicted all the data used in this work. The WL time-series at the three VigiCrue stations (Tonneins, Marmande and La Réole) as well as the S6 river WSE profiles and the S1-derived WSR computed over the five floodplain zones, are assimilated with the EnKF algorithm implemented on the TELEMAC-2D Garonne model (purple box in Figure 3). This allows for a sequential correction of the friction, the inflow discharge, and water level averaged over selected subdomains of the floodplain. The WL time-series observed at Couthures is used for validation only. Moreover, the WSR observations derived from S1 flood extent maps, being a ratio and non-gaussian, require a special treatment called Gaussian anamorphosis (GA) to be rendered into gaussian variables that are more compatible and optimal for the EnKF. The full description of the performed cycled EnKF algorithm and the applied GA can be found in [3, 5, 16, 17].

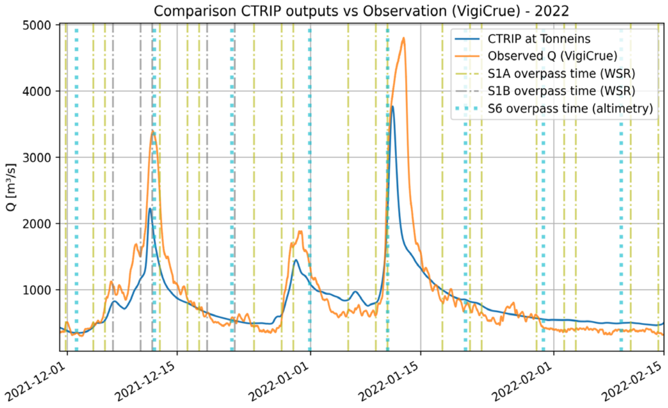

Figure 4. ISBA-CTRIP discharge (blue line) and observed discharge (orange line) time-series at Tonneins over the 2021-2022 flood event.

The observation error, for the computation of the corresponding covariance matrix R, is set proportional to the value of the in-situ WL observations (i.e., 10%) and to that of the WSE observations along the river centreline (i.e., 15%), whereas it is prescribed as a scalar fixed value for the WSR observations. The standard deviation of the S1-derived WSR observations is fixed to 0.1 (and up to 0.2 depending on how early the observation time within each assimilation window). These values stem from the assessment of the flood mapping algorithm that provides the wet/dry classification results (validated on five test sites all over the world) with an overall accuracy of 86.86% [16]. In addition, as opposed to [16], here no model-observation bias was taken into account for the in-situ WL data. All DA experiments were carried out using 75 members.

B. Control vector

Table I summarises the variables included in the control vector of the performed EnKF. The friction coefficients are considered as random variables with a gaussian Probability Density Function (PDF) with mean and standard deviation estimated from the calibration process. The uncertainty in the upstream BC is also taken into account in order to address the underestimated discharge provided by the hydrologic ISBA-CTRIP model. Therefore, a multiplicative factor μ applied on the time-dependent discharge time-series is considered as a random variable with a gaussian PDF centred at 1. In addition, the WL corrections applied uniformly on each of the five selected subdomains are denoted $\delta H_{1\text{-}5}$. They are considered as zero-mean gaussian random vectors.

Table I Gaussian PDF of uncertain input variables.

Variables	**Unit**	**Calibrated/ default value x_0**	**Standard deviation σ_0**	**95% confidence interval**
Ks_0	$m^{1/3}s^{-1}$	17	0.85	17 ± 1.67
Ks_1	$m^{1/3}s^{-1}$	45	2.25	45 ± 4.41
Ks_2, Ks_3	$m^{1/3}s^{-1}$	38	1.9	38 ± 3.72
Ks_4, Ks_5, Ks_6	$m^{1/3}s^{-1}$	40	2.0	40 ± 3.92
μ	-	1	0.06	1 ± 0.0136
$\delta H_{1..5}$	m	0	0.25	0 ± 0.0566

C. *Experimental setup*

Three experiments were carried out, one in open-loop (OL) mode and two in DA mode. The first DA experiment involves only in-situ data assimilation (hence named IDA) as in conventional research works, whereas the second DA assimilates only RS observations (so-called RSDA). The three experiments are fed with the upstream BC provided by the ISBA-CTRIP discharge (blue line in Figure 4). In this work, the observed discharge was not used as forcing data for the experiments, it only serves as a reference for the ISBA-CTRIP discharge. The IDA experiment focuses on the sequential correction of friction coefficients and inflow discharge. Additionally, the RSDA experiment treats the hydraulic state variable in five floodplain subdomains, representing evapotranspiration and ground infiltration processes that are unavailable in the T2D Garonne model. The DA experiments were implemented with a cycled EnKF with an 18-hour assimilation window sliding with 6-hour overlapping. The simulation results were comprehensively assessed with 1D and 2D metrics with respect to the observations.

Table II Summary of the Free Run and DA experiment settings.

Exp.	**DA?**	**Assimilated observations**	**Nb of members**	**Control variables**
OL	No	-	1	-
IDA	Yes	In-situ WSE	75	$Ks_{0..6}$, μ
RSDA	Yes	S1 WSR + S6 WSE	75	$Ks_{0..6}$, μ, $\delta H_{1..5}$

IV. EXPERIMENTAL RESULTS

In this section, quantitative performance assessments are carried out in the control and in the observation spaces by:

(i) comparing the parameters yielded by the different DA analyses (subsection IV-A);

(ii) comparing the different analysed WL time-series with observations at in-situ observing stations, or along the river centreline at S6 dates (subsection IV-B and IV-C);

(iii) comparing the different analysed WSR with S1-derived WSR observations in the floodplain (subsection IV-D);

A. *Results in the control space*

The analysed parameters from the two DA experiments are shown in Figure 5. The horizontal dashed lines stand for the default values (Table 1) which were used for the OL experiment, whereas the orange curves show the parameters of IDA (assimilating only in-situ data), and those of RSDA (assimilating only RS data) are represented by the green curves. Vertical lines represent the observation time of the S1 (grey/yellow dash-dotted lines) and S6 (cyan dotted lines), providing WSR observations over the floodplain and WSE at river centreline, respectively, that are altogether assimilated in the RSDA experiment.

Panels from the left column of Figure 5 show the friction coefficient in the floodplain Ks_0 and in the riverbed $Ks_{1\text{-}6}$. Since RSDA only assimilated remote-sensing data, its parameters have been corrected fewer times over the flood event compared to IDA. This is because the friction and inflow parameters stay constant within a DA cycle and if no observation was available during a cycle, they would remain the same from the previous cycle. On the other hand, the assimilation of in-situ data leads to many parameters to change significantly from the default/calibrated values and with a large variance between 20 and 70 $m^{1/3}s^{-1}$.

The first panel on the right column (Figure 5) presents the multiplicative factor μ obtained from the analyses. The resulting μ from IDA fluctuates considerably due to a potential equifinality when μ is combined with the friction coefficients in the control vector. On the other hand, RSDA-analysed parameter μ remains mostly more than one, showing the need to have more water into the catchment to account for the low ISBA-CTRIP discharge. Second to sixth panel from the right column of Figure 5 reveals the hydraulic state corrections $\delta H_{1\text{-}5}$. They are strictly negative in all five floodplain subdomains. This is because the flood event is not a major one with relatively mild overflowing, thus the observed flood extent maps are not prevailing, with most days showing little to no water detected in the floodplain. It leads to the δH trying to empty the floodplain.

Last panel shows the reconstructed upstream inflow discharge, i.e., the ISBA-CTRIP output multiplied by the analysed factor μ from the two DA experiments (orange: IDA, green: RSDA), in comparison to the observed discharge (black-dashed line). With the information from either in-situ data (IDA) and S6-derived WSE along the river centreline (RSDA) the flood peak discharge has been improved to match the same height as the observed discharge, however the phase delay remains unresolved. The evaluation of the DA experiments, in the control space for a real event, does not involve quantitatively assessing the performance of DA strategies, as the true values of the controlled parameters are unknown. Nevertheless, based on this diagnosis, it should be noted that there are potential equifinality issues here when only one type of observation was assimilated.

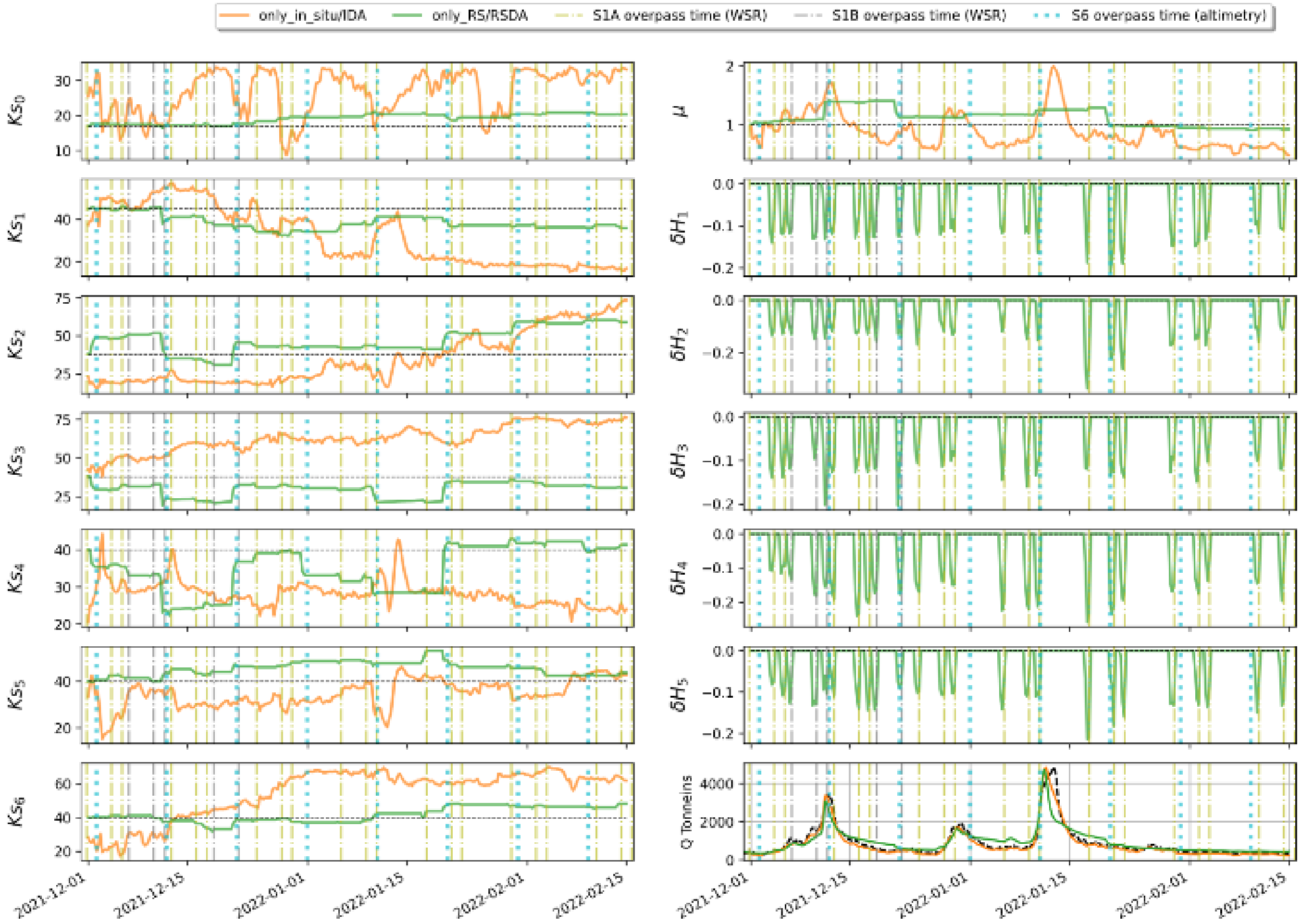

Figure 5. Evolution of controlled parameters for roughness, multiplicative correction to the inflow, and state correction in the floodplain.

B. Results in the observation space: WLs at observing stations

Table III Water level RMSE w.r.t. in-situ WL at VigiCrue observing stations. Lowest RMSE values are underlined.

Exp.	**RMSE [m]**			
	Tonneins	**Marmande**	**La Réole**	**Couthures**
OL	1.162	0.940	0.940	0.787
IDA	0.189	0.137	0.140	0.280
RSDA	0.810	0.990	0.886	0.647

The root-mean-square errors (RMSE) computed over time for the 2021-2022 flood event using the WLs simulated by the experiments OL, IDA and RSDA, with respect to the observed WLs at observing stations are summarised in Table III. Figure 6 displays the WLs simulated by the different experiments, at Tonneins (red lines), Marmande (blue lunes), Couthures (cyan lines) and La Réole (green lines), in comparison to the corresponding observed WLs (black-dashed lines). It can be noted that the simulated WLs at different observing stations (either those used for assimilation, or that of Couthures used for validation only) are improved significantly in IDA (Figure 6b) compared to the OL experiment (Figure 6a) throughout the flood event; even though there is still a minor underestimation at Tonneins (red line) and La Réole (green line) by IDA compared to the observations near the third flood peak.

For RSDA (Figure 6c), with the contribution of RS data, only the WLs at the peaks are improved. This is due to a number of reasons. First, the S1-derived flood extent maps offer limited knowledge on the flow dynamics in the floodplain to correct the involved uncertainties. Second, during the period following a S6 pass at high flows (of which the respective S6 data was assimilated), the simulated WLs in the river still remain much higher than the observations, and hence causes higher misfits compared to the OL experiment. This stays until the next S6 pass (typically when it is of low flow) where the WLs are reduced and become similar to the observed WLs. The fact that the WLs are not consistently improved by the RSDA (compared to OL) can be underwhelming in general, regarding the merits of assimilating RS data without in-situ data. However, the improved peak WLs and the immediate correction of the WL overestimation at the next assimilation represent what RS data can offer in terms of uncertainty reduction at S6 assimilation times. This current limitation also advocates for the need of more frequent observations from space in order to improve the 10-day revisit frequency of the S6 satellite. It can be expected that for a more significant flood event, the S1 observations shall satisfy such a need for a denser observing network, as shown in [3, 5].

C. Results in the observation space: WSE profiles along the river centreline

Figure 7 shows the WSE profiles along the river centreline, from which the S6 data were measured. There are eight panels associated with eight S6 overpasses. The black-dashed lines represent the WSE profiles observed by the S6 satellite, whereas the WSE profiles simulated by the OL, IDA, and RSDA experiments are represented by the blue, orange and green lines, respectively. The curvilinear abscissa of the plots follows the flow direction, i.e., smaller abscissa is upstream of a greater abscissa. Three particular dates are noted "high flow" (with panel title in boldface), as they correspond to the three high-flow dates, namely 2021-12-12 (first peak of the event), 2021-12-31 (slightly after the second peak) and 2022-01-10 (before the third peak of the event).

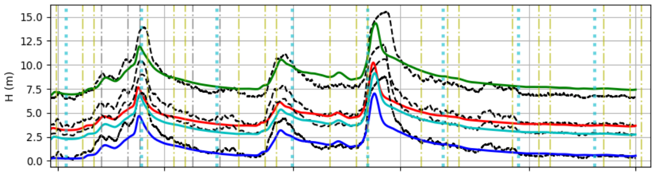

(a) OL (RMSE: 1.162, 0.940, 0.940, 0.787)

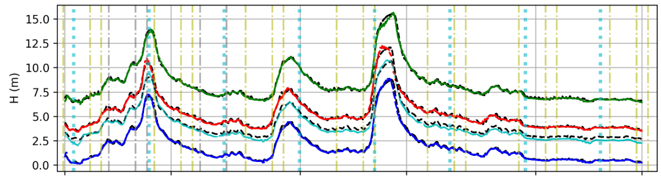

(b) IDA (RMSE: 0.189, 0.137, 0.140, 0.2

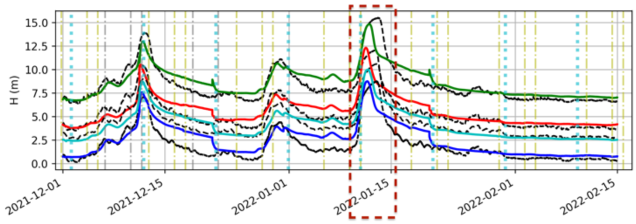

(c) RSDA (RMSE: 0.810, 0.990, 0.886, 0.647)

Figure 6. Simulated WL compared to observations by (a) OL, (b) IDA and (c) RSDA.

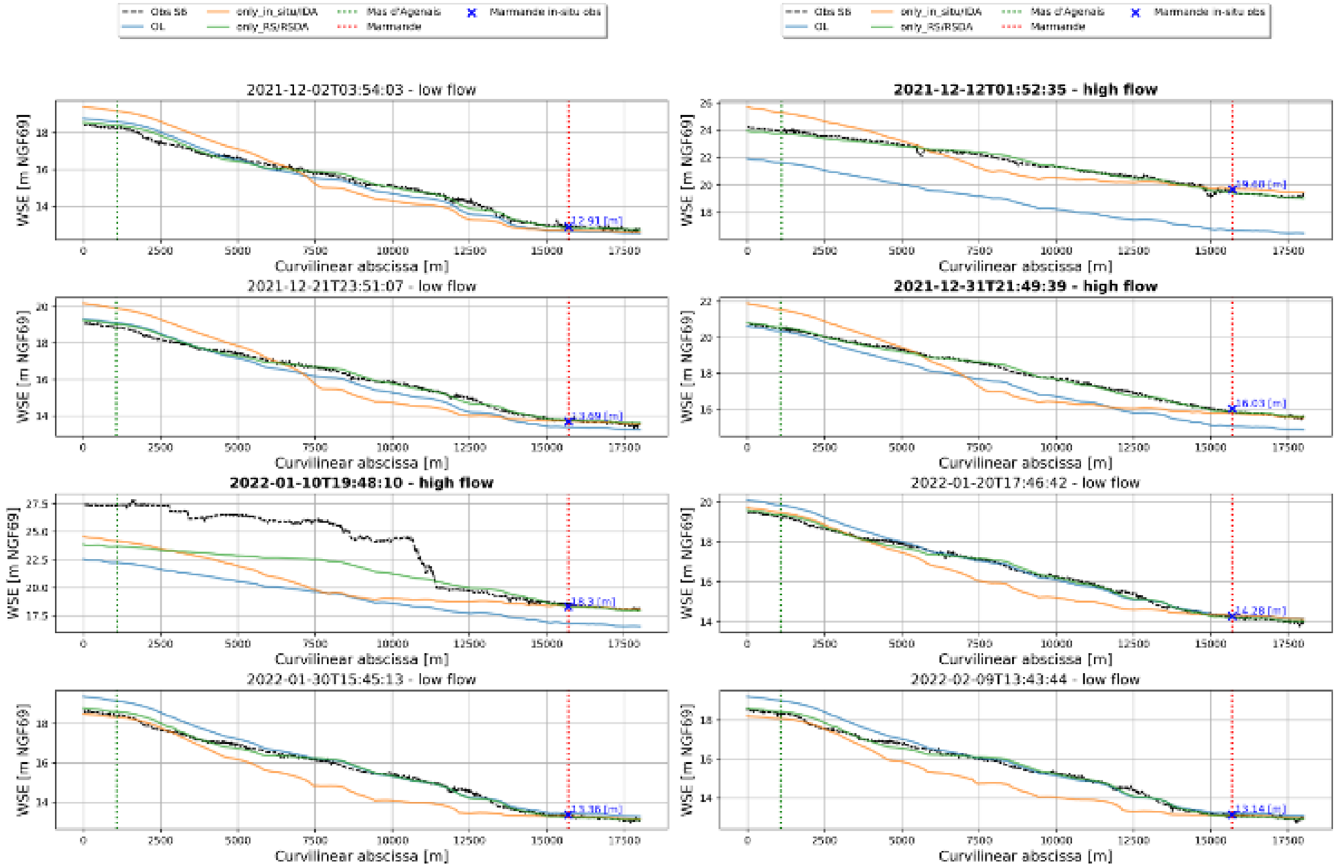

Figure 7. Simulated WSE at river centreline compared to S6-derived WSE observations.

The S6 measurements allow to validate experiments in high spatial density (up to 10 m in this work) that is not possible when using in-situ WL data. It reveals different outcomes yielded by one experiment to reveal at different segments of the river. For instance, OL experiment (blue lines) shows an underestimation of WSEs in one part of the profile and an overestimation in another on all eight overpasses. The underestimation became global and especially problematic on high-flow days, as shown by the gaps between the blue lines and black-dashed lines on these panels. It results in a gap of more than two metres at the first flood peak on 2021-12-12. In addition, after the third peak of the event, the WSEs yielded by OL show a slight overestimation over the left part of the profile (between the curvilinear abscissa 0 and 6,000 m). The area of observation by the S6 satellite over the studied catchment, despite covering only a part of it, is also interesting as it stretches to the Marmande in-situ station, where the local residents have been regularly impacted by flooding.

On most days, the WSEs along the river simulated by the IDA (orange lines) are coherent with the S6 observations over the right part of the profile (between the curvilinear abscissa 15,000 and 17,500 m). This is due to the fact that there is an observing station at Marmande, whose location along the curvilinear abscissa is represented by the vertical red-dotted line in Figure 7, around the curvilinear abscissa at 16,800 m. The in-situ WSEs measured at this station are shown by the blue crosses in each panel. Indeed, thanks to this assimilation, the resulting WSEs by IDA, in the vicinity of the in-situ station, stay very close to the observations. However, at positions along the river further away from the Marmande station, the WSEs simulated by IDA differ significantly from the observed WSEs. Underestimated WSEs at the middle part of the profiles by IDA are also a common problem, as shown throughout the flood event with the orange lines far below (more than one metre) the black-dashed lines.

Considering the RSDA experiment (green lines), as one can expect, the simulated WSEs along the river are quite consistent throughout the event, with slightly underperformances at high-flow dates. Moreover, the S6 measurements on 2022-01-10 present a part of the observation (i.e., between the abscissa 0 and 10,000 m) being erroneous due to a false initiation problem with the Fully-focused SAR processing. This error can be easily diagnosed when analysing the OL/IDA WSEs on this day. In this work, a process of quality control has been applied on RSDA to reject those erroneous S6 observations from the assimilation. This results in RSDA (green line) taking into account only partially the observations on 2022-01-10. This rejection of misfits demonstrates the flexibility of the performed DA strategy regarding errors with large magnitudes. However, this contributes to the simulated peak WLs at observing stations different from each other. As such, back in Figure 6, the peak WLs following this S6 overpass (shown by the red rectangle) from RSDA shows a similar height for Tonneins (red line) and Marmande (blue line) compared to their respective observed peak, but it exhibits smaller peaks for Couthures (cyan line) and La Réole (green line), hence creates larger misfits for these two downstream stations. This is because the part of the S6 observations near Marmande that are not rejected in the DA.

It should be reemphasized that, as mentioned in the previous subsection, the fact that there is only one S6 overpass every 10 days imposed the controlled parameters to remain the same even for several days after the assimilation. This was the reason why the WLs within the river or at the observing stations have the tendency to stay much higher than the observed WLs. This situation is even more severe when only a part of the observations (i.e., the 2022-01-10 incident) is taken into account for the DA.

D. Results in the observation space: WSR in the floodplain

Figure 8 displays the S1-derived WSR (black lines) at S1 overpass times and the WSR computed for OL (blue lines), IDA (orange lines) and RSDA (green lines) experiments over the five subdomains of the floodplain. As aforementioned, the observed flood extent maps derived from S1 SAR image present little water surfaces in the floodplain. This is due to the fact that the S1 images were acquired during relatively low flow dates, and right before the third peak of the flood event occurred, one of the two S1 satellites (Sentinel-1B, shown by yellow dash-dotted vertical line in Figure 4) became defected. This reduced the S1 observation capacity by a half after mid-December 2021. In Figure 8, the black lines show the observed WSRs that are almost zeros throughout the event. These lines are overlapped by the blue lines that represent the OL experiment, which shows underestimation of the flood extent due to the low forcing discharge simulated by the ISBA-CTRIP hydrologic model. Therefore, its resulting WSRs are similar to the observed ones. When only in-situ data was assimilated (in IDA), the WSRs over the different floodplain subdomain are much higher than the observed WSRs. Such an overestimation starts around the third peak for the first three subdomains ($\delta H_{1,2,3}$), whereas this was the case since the beginning of the flood for the downstream subdomains (δH_4 and δH_5).

Figure 8. Simulated and observed WSR values in the five floodplain zones.

The assimilation of RS data by RSDA (S1 for the WSRs in the floodplain and S6 for the WSEs along the river) yields WSRs more coherent to the observations derived from S1 images, especially in the subdomain 3 and 5. The δH_2 subdomain (which is significantly smaller compared to the other subdomains), however, has been overestimated at the third flood peak. This could stem from the rejection and non-assimilation of the erroneous S6 measurements on 2022-01-10 (between the abscissa 0 and 10,000 m as mentioned above) which led to the RSDA experiment keeping the same friction coefficient at the corresponding river segment, i.e., Ks_2 at the fourth and fifth S6 overpasses (vertical cyan lines). On the other hand, the WSR associated with the δH4 subdomain still is overestimated even though the state correction in this zone is active the whole event.

V. Conclusions and Perspectives

This study presents the merits of assimilating 2D flood extent observations derived from remote sensing Sentinel-1 SAR images and Sentinel-6-Michael Freilich altimetry data with an Ensemble Kalman Filter implemented on a hydrodynamic TELEMAC-2D model. The flood extent information from S1 SAR images is expressed in terms of Wet Surface Ratio or WSR computed over defined sensitive subdomains of the floodplain, whereas the altimetry data from S6 are obtained as WSEs over the river centreline every 10 days. The S6 observations cover nearly half of the studied catchment. The S1-derived WSRs are assimilated jointly with the S6 altimetry data, and its results were compared against the case when only in-situ water level observations were assimilated. The study was carried out over the Garonne Marmandaise catchment, focusing on the flooding event in December 2021-January 2022 when both types of satellite observation were available. Three experiments were realised; one in open-loop mode and two others in DA mode. The control vector gathers friction and forcing correction, and is augmented with correction of the hydraulic state in subdomains of the floodplain. All of the DA experiments were implemented by a cycled EnKF with an 18-hour assimilation window sliding with 6-hour overlapping. The simulation results were comprehensively assessed with 1D and 2D metrics with respect to assimilated data.

The first DA experiment IDA involves only in-situ observations whereas the other one RSDA assimilates both WSR observations derived from S1 2D flood extent maps and WSE observations from the S6 altimetry data. While both DA experiments focus on the sequential correction of friction coefficients and inflow discharge, RSDA additionally handles a dual state-parameter estimation within the EnKF, by treating inflow discharge and friction coefficients as well as the hydraulic state variable in five particular floodplain subdomains, representing evapotranspiration and/or ground infiltration processes that are unavailable in the TELEMAC-2D model. This difference was due to the availability of S1-derived observations (i.e., WSR) of the floodplain that involves only RSDA.

It has been shown that the assimilation of in-situ data in IDA significantly improves the simulation in the river bed, especially when there is a significant amount of uncertainty involving the upstream discharge provided by ISBA-CTRIP. The water levels at observing stations simulated by RSDA suggest that without in-situ data it is nearly impossible to compensate for such an underestimated discharge, even though the WSEs along the rivers have been improved significantly at times. Nevertheless, IDA overestimates the flow dynamics in the floodplain as shown by the WSRs in the five floodplain subdomains. Indeed, the in-situ observations located in the river bed, do not provide information on the dynamics in the floodplain. Previous works [3, 4, 18] have shown that the assimilation of RS data is beneficial when an observed discharge was used as forcing data, but in order to account for hydrologically-modelled forcing discharge, in-situ data is essential.

On the other hand, S6 data assimilation allows to substantially improve the WLs (both at observing stations and along the observed river segment) whenever there are observations available for assimilation, with a fine spatial resolution of the WSE in the river. The added value from S6 altimetry data regarding the dense WSE profile along the river allows to diagnose in fine detail the behaviour of the simulated WSEs, varying between the part near an observing station and those far away from it. This beneficial feature will be even more advantageous for a large-swath altimetry satellite like the recently launched SWOT that provides WSEs from the river as well as from the floodplain. This study validated the assertion that a densification, in time and space, of the observing network, especially in the floodplain with remote sensing data and advanced DA strategy, allows to improve the representation of the dynamics of the flow in the floodplains. In addition, the necessity of in-situ data has been reemphasized, especially when there are high amounts of uncertainties to be dealt with, e.g., underestimated discharge provided by a large-scale hydrologic model. Lastly, this work advocates for the multi-source data assimilation strategy implemented on top of a chained hydrologic-hydraulic model, making the most out of Earth Observation heterogeneous data. Such a diverse combination between models and observations, aiming at new observing strategies, heralds towards a Digital Twin framework in hydrology.

Acknowledgement

This work was supported by CNES, CERFACS and SCO-France. The authors gratefully thank the EDF R&D for providing the Telemac-2D model for the Garonne River, and the SCHAPI, SPC Garonne-Tarn-Lot and SPC Gironde-Adour-Dordogne for providing the in-situ data.

References

[1] Fekete, B. M., Looser, U., Pietroniro, A., & Robarts, R. D. (2012). Rationale for monitoring discharge on the ground. Journal of Hydrometeorology, 13(6), 1977-1986.

[2] Nguyen, T. H., Ricci, S., Piacentini, A., Bonassies, Q., Suquet, R. R., Luque, S. P., ... & David, C. (2023). Reducing Uncertainties of a Chained Hydrologic-hydraulic Model to Improve Flood Forecasting Using Multi-source Earth Observation Data. arXiv preprint arXiv:2306.10059.

[3] Nguyen, T. H., Ricci, S., Piacentini, A., Fatras, C., Kettig, P., Blanchet, G., ... & Baillarin, S. (2022). Dual State-Parameter Assimilation of SAR-derived Wet Surface Ratio for Improving Fluvial Flood Reanalysis. Water Resources Research, vol. 58, no. 11, p. e2022WR033155, 2022. e2022WR033155 2022WR033155.

[4] Nguyen, T. H., Ricci, S., Piacentini, A., Suquet, R. R., Blanchet, G., Luque, S. P., & Kettig, P. (2022). Enhancing Flood Forecasting with Dual State-Parameter Estimation and Ensemble-based SAR Data Assimilation. TELEMAC-MASCARET User Conference 2022, Paris-Saclay, 297-305.

[5] Nguyen, T. H., Ricci, S., Piacentini, A., Simon, E., Suquet, R. R., & Luque, S. P. (2023). Dealing With Non-Gaussianity of SAR-derived Wet

Surface Ratio for Flood Extent Representation Improvement. arXiv preprint arXiv:2306.08466.

[6] Munier, S., & Decharme, B. (2022). River network and hydro-geomorphological parameters at 1/12° resolution for global hydrological and climate studies. Earth System Science Data, 14(5), 2239-2258.

[7] Hervouet, J. M. (2007). Hydrodynamics of Free Surface Flows: Modelling with the Finite Element Method. John Wiley & Sons.

[8] Decharme, B., Delire, C., Minvielle, M., Colin, J., Vergnes, J. P., Alias, A., ... & Voldoire, A. (2019). Recent changes in the ISBA-CTRIP land surface system for use in the CNRM-CM6 climate model and in global off-line hydrological applications. Journal of Advances in Modeling Earth Systems, 11(5), 1207-1252.

[9] Noilhan, J., & Planton, S. (1989). A simple parameterization of land surface processes for meteorological models. Monthly Weather Review, 117(3), 536-549.

[10] Oki, T., & Sud, Y. C. (1998). Design of Total Runoff Integrating Pathways (TRIP)—A global river channel network. Earth Interactions, 2(1), 1-37.

[11] Decharme, B., Alkama, R., Papa, F., Faroux, S., Douville, H., & Prigent, C. (2012). Global off-line evaluation of the ISBA-TRIP flood model. Climate Dynamics, 38(7), 1389-1412.

[12] Besnard, A., & Goutal, N. (2011). Comparison between 1D and 2D Models for Hydraulic Modeling of a Floodplain: Case of Garonne River. La Houille Blanche-Revue Internationale De L'Eau, (3), 42-47.

[13] Gauckler, P. (1867). Etudes Théoriques et Pratiques sur l'Ecoulement et le Mouvement des Eaux. Gauthier-Villars.

[14] Dinardo, S., Maraldi, C., Cadier, E., Rieu, P., Aublanc, J., Guerou, A., ... & Scharroo, R. (2023). Sentinel-6 MF Poseidon-4 Radar Altimeter: Main Scientific Results from S6PP LRM and UF-SAR Chains in the First Year of the Mission. Advances in Space Research.

[15] Egido, A., & Smith, W. H. (2016). Fully Focused SAR Altimetry: Theory and Applications. IEEE Transactions on Geoscience and Remote Sensing, 55(1), 392-406.

[16] Nguyen, T. H., Ricci, S., Fatras, C., Piacentini, A., Delmotte, A., Lavergne, E., & Kettig, P. (2022). Improvement of Flood Extent Representation with Remote Sensing Data and Data Assimilation. IEEE Transactions on Geoscience and Remote Sensing, 60, 1-22.

[17] Nguyen, T. H., Ricci, S., Piacentini, A., Simon, E., Rodriguez Suquet, R., & Pena Luque, S. (2023). Gaussian Anamorphosis for Ensemble Kalman Filter Analysis of SAR-derived Wet Surface Ratio Observations. arXiv preprint arXiv:2304.01058.

[18] Ricci, S., Nguyen, T. H., Le Gac, S., Boy, F., Piacentini, A., Rodriquez-Suquet, R., Pena Luque, S., et al. (2023). Comparisons and Water Level Analyses using Sentinel-6MF Satellite Altimetry Data with 1D Mascaret and 2D Telemac Models. EGU General Assembly 2023, no. EGU23-6513.

Comparing data assimilation algorithms for parameter estimation on TELEMAC-2D

Jean-Paul Travert[1,2], Cédric Goeury[1,2], Vito Bacchi[1], Fabrice Zaoui[1], Sébastien Boyaval[2,3]
jean-paul.travert@edf.fr, Chatou, France
[1]: National Laboratory for Hydraulics and Environment, EDF R&D, Chatou, France
[2]: LHSV, Ecole des Ponts, EDF R&D, Chatou, France
[3]: MATHERIALS, Inria, Paris, France

Abstract – **Numerical models play an essential role in fluvial hydraulics for modelling flood dynamics. These models are often used as prediction tools to design effective mitigation measures or estimate possible damages due to overflowing for future events in specific areas. Before using these models, they need to be calibrated against observations to assess their accuracy for past and future events. In this study, we implement and compare in a realistic scenario different data assimilation algorithms for parameter estimation to evaluate which is most suitable for calibrating hydraulic models. In this work, the goal is to retrieve the friction, a distributed parameter in two-dimensional flood models. Water depth measurements at different places among the channel and floodplains are used as observations in Data Assimilation algorithms. The methodology is conducted on a twin experiment. Different levels of observation errors and various configurations of observations are tested, both temporally and spatially. The 3DVAR algorithm was more efficient for most configurations for identifying the parameters.**

Keywords: **Data Assimilation, Parameter Estimation, Roughness.**

I. INTRODUCTION

During flood events, it is essential to predict water depths accurately. For floods, a common choice is to perform a numerical simulation with 2D Shallow Water Equations (SWE) models. However, uncertainties arise when constructing a numerical model with these equations for real cases. The primary sources of uncertainties in flood modelling are the model inputs (boundary conditions, initial conditions, topography and bathymetric data) and the physical processes modelled by the friction [1].

To reduce uncertainties and accurately predict floods, models are calibrated. Calibration aims at adjusting uncertain physically based parameters (e.g., friction values) to fit measurements. For a long time, measurements were only water levels from stage gauging stations, gauge leashes or aerial photographs. Still, satellite imagery can now get more distributed data on the floodplains. These measurements can be water depths, flood contour, and velocities, but we will focus in this work on water depths. Using distributed water depths for calibrating models may lead to significant improvements compared to using water depths only in the channel.

The water depths and flood extent are usually very sensitive to the inlet discharge [2]. A stage gauging station at the inlet of the domain standardly allows one to reduce the uncertainty on the boundary and initial conditions strongly. Topography can now be known with a high degree of precision using modern numerical terrain models. Bathymetric data can be similarly known at the price of costly terrain measurements: we assume they are certain. So, the friction coefficients account for most of the remaining uncertainties which could be reduced by e.g., new data such as satellite images [2].

Data Assimilation (DA) aims to find the best compromise between observations and numerical models. This subfield of inverse problems, first applied to numerical weather prediction, is widely used in geosciences and hydraulics [3].

This paper uses DA for inverse parameters estimation from observations and the outputs of a numerical model (e.g., water depths).

This paper aims to compare and implement different algorithms of DA with parallelisation capabilities working with the TELEMAC-MASCARET software suite (www.opentelemac.org) and especially TELEMAC-2D. Most DA algorithms are designed for real-time updating of the states, but here we seek to evaluate parameters (distributed friction) fixed at the start of a simulation.

Section II mathematically sets the parameter estimation problem. Sections III, IV and V present various DA algorithms to tackle the issue. Section VI presents numerical results to compare the various algorithms in a schematic test case for a flood event under different configurations. Finally, in Section VII, the conclusions and perspectives of this work are presented.

II. PROBLEM SETTING

Two significant components define the inverse problem. On the one hand, uncertain measurements (e.g., water depths), and on the other hand, the numerical model simulating hydraulic states. Our goal is to estimate the distributed friction parameters of the model through a comparison between water depth measurements and the outputs generated by the numerical model.

A. Setting of the parameter estimation problem

The evaluation of the model parameters uncertainties relies on limited information from the initial estimation of the parameters (including physical laws, previous simulations, expert opinions, etc) and imperfect measurements.

Let $\mathcal{M}$ be the non-linear numerical model depending on some control parameters $\boldsymbol{\theta}$. Let $\boldsymbol{x_k} \in \mathbb{R}^{N_x}$ be the state vector i.e. the hydrodynamic variables at a time k (the water depths and velocities computed in the numerical model). The state vector $\boldsymbol{x_k}$ satisfies (1):

$$\boldsymbol{x_k} = \mathcal{M}_{k:k-1}(\boldsymbol{x_{k-1}}, \boldsymbol{\theta}) + \boldsymbol{\eta_k}\,, \tag{1}$$

where $\boldsymbol{\theta} \in \mathbb{R}^{N_p}$ are the model parameters (distributed friction in our case), $\mathcal{M}_{k:k-1}\colon \mathbb{R}^{N_x \times N_p} \to \mathbb{R}^{N_x}$ is the model from time $k-1$ to k, and $\boldsymbol{\eta_k} \in \mathbb{R}^{N_x}$ are the model errors.

Our objective is to estimate the parameters vector $\boldsymbol{\theta}$ knowing the observations $\boldsymbol{y_k}$. We consider that these observations are noisy and are available at discrete times k. Considering that the errors are additive, the observation model is given in (2).

$$\boldsymbol{y_k} = \mathcal{H}(\boldsymbol{x_k}) + \boldsymbol{\epsilon_k}\,, \tag{2}$$

where $\boldsymbol{y_k} \in \mathbb{R}^{N_y}$ are the observations, $\mathcal{H}\colon \mathbb{R}^{N_x} \to \mathbb{R}^{N_y}$ is an observation operator mapping (selection, linear, etc) from model to observational space and $\boldsymbol{\epsilon_k} \in \mathbb{R}^{N_y}$ are the errors of observation. In most DA algorithms, we consider independent and identically distributed errors $\boldsymbol{\epsilon_k} \sim \mathcal{N}(\boldsymbol{0}, \boldsymbol{R_k})$ and $\boldsymbol{\eta_k} \sim \mathcal{N}(\boldsymbol{0}, \boldsymbol{Q_k})$. In this work, it is assumed that the model errors are null with $\boldsymbol{Q_k} = \boldsymbol{O_{N_x,N_x}}$.

From these two equations, the estimation problem is defined. In the parameter estimation problem, the goal is to improve the characterisation of parameters $\boldsymbol{\theta}$. The problem can be written in a probabilistic framework from the random nature of uncertainties. Applying the Bayes' theorem, it comes in (3):

$$p(\boldsymbol{\theta}|\boldsymbol{y}) = \frac{p(\boldsymbol{y}|\boldsymbol{\theta})p(\boldsymbol{\theta})}{p(\boldsymbol{y})}, \tag{3}$$

Equation (3) is at the core of the parameters estimation problem as it enables to estimate the distributions of the unknows $\boldsymbol{\theta}$ based on the observations **y**. It relies on the prior belief on the parameters $p(\boldsymbol{\theta})$, the likelihood of the observations to occur for different values of the unknows $p(\boldsymbol{y}|\boldsymbol{\theta})$ and the probability of the observations $p(\boldsymbol{y})$ independently from $\boldsymbol{\theta}$.

B. Shallow Water Equations with friction parameter

All the simulations throughout this paper are conducted using the hydrodynamic module TELEMAC-2D solving the 2D SWE [4-5]. This model represents the $\mathcal{M}$ model from paragraph A.

The conservative form of the equations write as follows in (4), where the system unknows are the velocities $\boldsymbol{u} = (u, v)^T$ along the x and y Cartesian coordinates, and the water depths $h = \eta - z_b$ with η the free surface elevation and z_b the bottom elevation,

$$\begin{cases} \dfrac{\partial h}{\partial t} + \nabla \cdot (h\boldsymbol{u}) = 0 \\ \dfrac{\partial (h\boldsymbol{u})}{\partial t} + \nabla \cdot (h\boldsymbol{u} \otimes \boldsymbol{u}) = -g\nabla\boldsymbol{\eta} + \dfrac{h\boldsymbol{F}}{\rho} + \nabla \cdot (h\nu_e \nabla \boldsymbol{u}) - \dfrac{\tau_b}{\rho} \end{cases}, \tag{4}$$

where $\boldsymbol{F}$ are external forces (e.g., Coriolis, centrifugal, surface tension …), ν_e is the effective viscosity resulting from kinematic, turbulent and dispersive viscosity, and $\boldsymbol{\tau_b}$ is the bottom shear stress. The water density ρ and the gravitational acceleration g are considered constant. No external forces and viscosity effects are considered in this work except the bottom shear stress $\boldsymbol{\tau_b}$.

In the Shallow Water Equations, the equations need closure for the bed shear stress component $\boldsymbol{\tau_b}$ that is not analytically described as a function of h and $\boldsymbol{u}$. Different formulas are available in the literature, but the bed shear stress is often denoted as in (5),

$$\boldsymbol{\tau_b} = \frac{1}{2} \cdot \rho \cdot C_f \cdot |\boldsymbol{u}| \cdot \boldsymbol{u}\,, \tag{5}$$

where C_f is a dimensionless friction coefficient. The friction coefficient is based on empirical or semi-empirical formulas [6]. In these equations, different parameters are defined depending on the soil surface, the land use and other physical properties.

The most widely used empirical formula is the Strickler formula [7] defined as in (6),

$$V = K_s \cdot R_h^{\frac{2}{3}} \cdot \sqrt{S_0}\,, \tag{6}$$

where K_s is the Strickler coefficient (defined from tables, calibration …), R_h the hydraulic radius, V the mean velocity of the cross section and S_0 the bottom slope. There is an equivalent formula called the Manning formula mainly used by the Anglo-Saxon community with $K_s = \frac{1}{n}$ instead, n being the Manning coefficient.

This term in the equation induces energy dissipation due to the friction representing the water flow resistance caused by underlying surfaces. The energy losses directly impact the hydrodynamic variables. The friction parameter accounts for physical considerations such as surface roughness (irregularities of the bottom of the flow), channel irregularities or seasonal changes with growing vegetation, and phenomena such as turbulence or local errors in the topography. Thus, it remains difficult to estimate this parameter on a physical basis, and it should be adjusted with a calibration process by comparing water elevation and/or flood extent.

In TELEMAC-2D the friction term is considered in the momentum equation from the SWE and is implicitly treated [4]. The two components of the bottom friction calculated in x and y directions are given in (7),

$$\begin{cases} \tau_{bx} = -\frac{u}{2h} C_f(h, K_s)\sqrt{u^2 + v^2} \\ \tau_{by} = -\frac{v}{2h} C_f(h, K_s)\sqrt{u^2 + v^2} \end{cases}, \qquad (7)$$

where $C_f = \frac{2g}{h^{1/3} K_s^2}$ for the Strickler formula.

In the parameter estimation problem, the unknown parameters $\boldsymbol{\theta}$ that we aim to evaluate are the distributed frictions K_s from (6). The hydraulic states $\boldsymbol{x_k}$ at time k are represented in the equations by the water depths compared at the position of water depth observations. For evaluating, the parameters based on the measurements, different DA algorithms are presented in the next sections.

III. VARIATIONAL APPROACH: 3DVAR

The first option for estimating the parameters from uncertain measurements and numerical models is to use a variational approach. The goal is to evaluate the unknowns by minimising a cost function quantifying the misfit between model predictions and measurements.

Most DA methods assume that errors are approximated with Gaussian assumption. For parameter estimation, the most used function for this minimisation problem is defined in (8),

$$\begin{cases} J(\boldsymbol{\theta}) = J_b(\boldsymbol{\theta}) + J_o(\boldsymbol{\theta}) \\ J_b(\boldsymbol{\theta}) = \frac{1}{2}\left(\boldsymbol{\theta} - \boldsymbol{\theta^b}\right)^T \boldsymbol{B}^{-1}\left(\boldsymbol{\theta} - \boldsymbol{\theta^b}\right) \\ J_o(\boldsymbol{\theta}) = \frac{1}{2}\left(\boldsymbol{y} - \mathcal{H}\left(\mathcal{M}(\boldsymbol{\theta})\right)\right)^T \boldsymbol{R}^{-1}\left(\boldsymbol{y} - \mathcal{H}\left(\mathcal{M}(\boldsymbol{\theta})\right)\right) \end{cases}, \qquad (8)$$

where $\boldsymbol{\theta^b}$ is a background knowledge (a first guess on the set of unknown parameters), and $\boldsymbol{B}$, $\boldsymbol{R}$ are the background and observation error covariance matrices respectively. The proposed parameter estimation method is an extension for non-linear models of the computation of the Maximum A Posteriori (MAP) of (3) without model errors. In the linear and Gaussian assumptions case, equation (3) can be derived as $p(\boldsymbol{\theta}|\boldsymbol{y}) \propto e^{-J(\boldsymbol{\theta})}$. Indeed, considering a Gaussian approximation, the prior distribution can be written as

$$p(\boldsymbol{\theta}) = \frac{1}{\sqrt{(2\pi)^{N_p}\det(\boldsymbol{B})}} \mathrm{e}^{\left(-\frac{1}{2}\left(\boldsymbol{\theta} - \boldsymbol{\theta^b}\right)^T \boldsymbol{B}^{-1}\left(\boldsymbol{\theta} - \boldsymbol{\theta^b}\right)\right)}. \qquad (9)$$

As for the likelihood, using Gaussian assumption with (1) and (2), it can be written as

$$p(\boldsymbol{y}|\boldsymbol{\theta}) = \frac{1}{\sqrt{(2\pi)^{N_y}\det(\boldsymbol{R})}} \mathrm{e}^{\left(-\frac{1}{2}\left(\boldsymbol{y} - \mathcal{H}\left(\mathcal{M}(\boldsymbol{\theta})\right)\right)^T \boldsymbol{R}^{-1}\left(\boldsymbol{y} - \mathcal{H}\left(\mathcal{M}(\boldsymbol{\theta})\right)\right)\right)}. \qquad (10)$$

Finally, by combining (3), (9) and (10), we get (11) where the cost function appears:

$$p(\boldsymbol{\theta}|\boldsymbol{y}) \propto \mathrm{e}^{\left(-\left(J_b(\boldsymbol{\theta}) + J_o(\boldsymbol{\theta})\right)\right)}. \qquad (11)$$

Equation (8) is the traditional data assimilation cost function called 3DVAR [8-9]. The 3DVAR algorithm is programmed without dynamic evolution, considering only one assimilation window. The method is exact in the case of a linear model $\mathcal{M}$.

The cost function $J(\boldsymbol{\theta})$ from equation (8) should be minimised using an optimisation method. A gradient descent method is used which is available in the ADAO data assimilation library. From all the optimisation methods, we resort to the Broyden-Fletcher-Goldbarb-Shanno (BFGS) algorithm. The algorithm is based on the application of the Newton method to the gradient of $J(\boldsymbol{\theta})$. The algorithm is purely iterative as it explores a direction with a set of parameters and then updates the parameters before launching a new simulation.

IV. FILTERING APPROACHES: ENSEMBLE-BASED APPROACHES

Kalman filters are sequential DA techniques, and the uncertainty in the state/parameters evolves from one observation to another, unlike the 3DVAR approach.

The Kalman Filter (KF) gives an exact solution of the Bayes problem in (3) for Gaussian errors and linear model assumptions ($\mathcal{M} \cong \boldsymbol{M}$ and $\mathcal{H} \cong \boldsymbol{H}$ with $\boldsymbol{M}$ and $\boldsymbol{H}$ being the tangent linear models). There are two different steps in the algorithm. First, the system's future states and uncertainties are computed based on the current states and dynamic model. Secondly, an analysis step is carried out to refine the state estimate by combining the forecast and the observation with a linear combination of the available information. The solution is given in (12) and (13). More details on the derivation of the solution can be found in [10]. In the parameter estimation problem, we only update the parameters, not the states. The f and a superscript respectively denote for forecast and analysis.

Forecasting step:

During the forecast step, the goal is to propagate the system state using the dynamics of the system and evaluate the error covariance matrix of the forecast in (12).

$$\begin{cases} \boldsymbol{x_k^f} = \boldsymbol{M_{k:k-1} x_{k-1}^a} \\ \boldsymbol{P_k^f} = \boldsymbol{M_{k:k-1} P_{k-1}^a M_{k:k-1}^T} + \boldsymbol{Q_k} \end{cases}. \qquad (12)$$

Analysis step:

For the analysis, the goal is to find $\boldsymbol{L_k}$ and $\boldsymbol{K_k}$ (the Kalman gain) as $\boldsymbol{x_k^a} = \boldsymbol{L_k x_k^f} + \boldsymbol{K_k y_k}$. We describe hereafter in (13) the analysis step for the optimal linear combination between the prior and the observations. In this case, it is the exact solution of (3) with $\boldsymbol{x_k^a}$ having minimum variance and being unbiased.

$$\begin{cases} \boldsymbol{\theta_k^a} = \boldsymbol{\theta_k^f} + \boldsymbol{K_k}(\boldsymbol{y_k} - \boldsymbol{H_k x_k^f}) \\ \boldsymbol{K_k} = \boldsymbol{P_k^f H_k^T}\left(\boldsymbol{R_k} + \boldsymbol{H_k P_k^f H_k^T}\right)^{-1} \\ \boldsymbol{P_k^a} = (\boldsymbol{I} - \boldsymbol{K_k H_k})\boldsymbol{P_k^f} \end{cases}. \qquad (13)$$

However, the KF does not handle well non-linear models and is computationally expensive for covariance matrix estimations. The Ensemble Kalman Filter (EnKF) is a possible extension in the linear case with a reduced computation cost. Instead of having a single estimate of states/parameters, the EnKF uses an ensemble of possible states (called members) capturing the uncertainty in the estimation. The states are forwarded in time with the model (forecast) and then updated with the perturbed observations (analysis). The implementation is based on [11] (open source access) and summarised in Figure 1.

Forecasting step:

Each member $i \in [1, N_e]$ is forecasted from t_k to t_{k+1} with Equation (1) without model error, and then the covariance matrix P_{k+1} and mean ensemble for the parameters are computed in (14).

$$\begin{cases} P_{k+1}(\boldsymbol{\theta}_{\boldsymbol{k+1}}) = \frac{1}{N_e-1}\sum_{i=1}^{N_e}\left(\boldsymbol{\theta}_{\boldsymbol{k+1}}^{\boldsymbol{i}} - \overline{\boldsymbol{\theta}_{\boldsymbol{k+1}}}\right)\left(\boldsymbol{\theta}_{\boldsymbol{k+1}}^{\boldsymbol{i}} - \overline{\boldsymbol{\theta}_{\boldsymbol{k+1}}}\right)^T \\ \overline{\boldsymbol{\theta}_{\boldsymbol{k+1}}} = \frac{1}{N_e}\sum_{i=1}^{N_e}\boldsymbol{\theta}_{\boldsymbol{k+1}}^{\boldsymbol{i}} \end{cases} .(14)$$

Analysis step:

To be in a comparable set-up as 3DVAR, the updating step is carried out only at the end of an observation window. The observation window is set to the simulation time, so the parameters (distributed friction) are not updated during a run.

First the Kalman gain $\boldsymbol{K}$ is computed below,

$$\boldsymbol{K}_{\boldsymbol{k+1}} = \boldsymbol{P}_{\boldsymbol{k+1}}\boldsymbol{H}^T(\boldsymbol{H}\boldsymbol{P}_{\boldsymbol{k+1}}\boldsymbol{H}^T + \boldsymbol{R})^{-1} . \qquad (15)$$

Then the parameters are updated accordingly to:

$$\boldsymbol{\theta}_{\boldsymbol{k+1}}^{\boldsymbol{i,a}} = \boldsymbol{\theta}_{\boldsymbol{k+1}}^{\boldsymbol{i}} + \boldsymbol{K}_{\boldsymbol{k+1}}(\boldsymbol{y}_{\boldsymbol{k+1}} + \boldsymbol{\epsilon}_{\boldsymbol{k}}^{\boldsymbol{i}} - \boldsymbol{H}\boldsymbol{x}_{\boldsymbol{k+1}}^{\boldsymbol{i}}). \qquad (16)$$

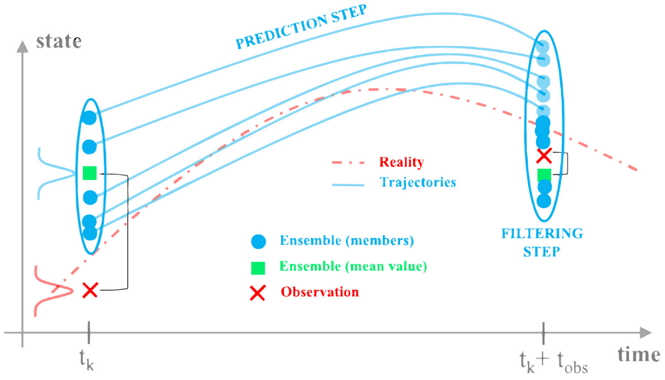

Figure 1. Sketch illustrating EnKF extracted from [11].

V. PARTICLE FILER WITH RESAMPLING

Particle Filter (PF) solves Bayes' equation (3) based on a sequential Monte Carlo method without linear model or Gaussian error assumptions. The goal is to use a set of random samples (called particles) to get a direct solution of (3). The simplest version is the bootstrap Particle Filter introduced in [12]. From this basic version, we added resampling with Kernel Density Estimation (KDE) for creating an iterative calculation chain.

The methodology is declined step by step. Each simulation can be parallelised, and all the particles can interact with each other at the observation time step.

1) Initialisation: Sampling procedure for the prior distribution

The first step is to sample $N \in \mathbb{R}$ particles $[\boldsymbol{\theta}^{\boldsymbol{1}}, .., \boldsymbol{\theta}^{\boldsymbol{N}}]$. The parameter vector $(\boldsymbol{\theta}^{\boldsymbol{i}})_{1\le i\le N} \in \mathbb{R}^{N_p}$ is a realisation of the prior distribution (the first guess) based on expert opinions, physical laws or previous simulations. The particles are drawn from $\mathcal{N}(\boldsymbol{\theta}^{\boldsymbol{b}}, \boldsymbol{B})$. The probability density function of the parameter at time k is represented in (17):

$$p_k(\boldsymbol{\theta}) \cong \sum_{i=1}^{N} w_k^i \delta(\boldsymbol{\theta} - \boldsymbol{\theta}_{\boldsymbol{k}}^{\boldsymbol{i}}) , \qquad (17)$$

where $w_k^i \in \mathbb{R}^{N_p}$ is the weight of particle i (or likelihood of the particle) at time k and δ is a Dirac function ($\delta(0) = 1$). At initialisation, usually a uniform weight is considered with $w_0 = [w_0^0, \dots, w_0^N] = [\frac{1}{N}, \dots, \frac{1}{N}]$.

2) Forecasting the particles

During the forecast step, each particle is forwarded with the numerical model until the next observation as in (18),

$$p_{k+1}(\boldsymbol{\theta}) \cong \sum_{i=1}^{N} \boldsymbol{w}_{\boldsymbol{k}}^{\boldsymbol{i}} \delta(\boldsymbol{\theta} - \boldsymbol{\theta}_{\boldsymbol{k+1}}^{\boldsymbol{i}}) , \qquad (18)$$

where $\boldsymbol{\theta}_{\boldsymbol{k+1}}^{\boldsymbol{i}} = \mathcal{M}_{k+1:k}(\boldsymbol{x}_{\boldsymbol{k}}, \boldsymbol{\theta}_{\boldsymbol{k}}) = \boldsymbol{\theta}_{\boldsymbol{k}}^{\boldsymbol{i}}$. In the case of the model parameters and friction coefficients, the parameters are not updated during a simulation. For the parallel implementation, each particle is forwarded until the next observation using *Runsize* processors. All the particles are run simultaneously when using *Runsize* × N_e processors otherwise the maximum of particles is launched and when the next time step of observation is reached the processors are used for other particles waiting in the queue, so that every particle reaches the observation step for the analysis step and before forwarding the model to the next observation.

3) Analysis step

During this step, the weights of the particles are updated according to (19),

$$w_{k+1}^{a,i} \cong w_{k+1}^{f,i} p(\boldsymbol{y}_{\boldsymbol{k+1}} | \boldsymbol{x}_{\boldsymbol{k+1}}^{\boldsymbol{i}}, \boldsymbol{\theta}_{\boldsymbol{k+1}}^{\boldsymbol{i}}) , \qquad (19)$$

where in this case $w_{k+1}^{f,i} = w_k^{a,i}$, because the forward model does not change the weights. The choice of the likelihood $p(\boldsymbol{y}_{\boldsymbol{k+1}} | \boldsymbol{x}_{\boldsymbol{k+1}}^{\boldsymbol{i}}, \boldsymbol{\theta}_{\boldsymbol{k+1}}^{\boldsymbol{i}})$ is an open question. We choose a Gaussian likelihood (with assumption of independence between the observations, uncorrelated in time and in space) defined in (20), so that it can be compared with the other DA algorithms based on Gaussian errors:

$$p(\boldsymbol{y}_{\boldsymbol{k+1}} | \boldsymbol{x}_{\boldsymbol{k+1}}^{\boldsymbol{i}}, \boldsymbol{\theta}_{\boldsymbol{k+1}}^{\boldsymbol{i}}) = \prod_{l=1}^{N_{obs}} \frac{1}{\sigma^l\sqrt{2\pi}} e^{-\frac{1}{2}\left(\frac{x_{k+1}^{i,l} - y_{k+1}^{l}}{\sigma^l}\right)} ,(20)$$

where N_{obs} is the number of spatial observations, σ^l is the standard deviation of observation $l \in [1; N_{obs}]$ considered constant for all spatial observations in the following.

Each particle weight is updated by comparing the water depths of the control vector of the numerical model and the observations. After that, all the processors communicate to normalise the weights so that $\sum_{i=1}^{N} w_k^{a,i} = 1$.

4) Resampling after each simulation

A well-known problem of PF is the curse of dimensionality, with one or few particles weights' largely dominating the others after some observations leading to poor distributions characterisation. At each new observation, and iteration, the parameters $\boldsymbol{\theta^i}$ are resampled using KDE and the weights are reset to 1/N. Then, after resampling we get back to step 2. The whole process can be visualised in Figure 2.

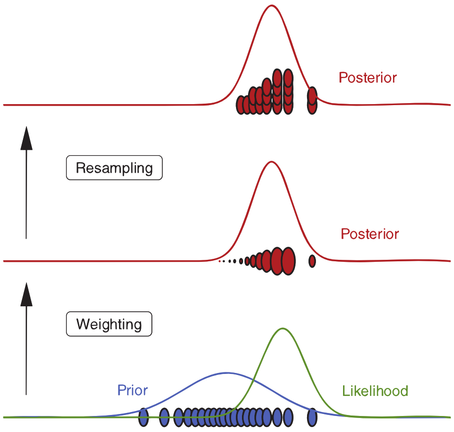

Figure 2. Schematic of PF with resampling extracted from [10].

VI. NUMERICAL STUDIES

In this section, the three DA algorithms are compared on a simple test case of flood under different configurations. The experiment is based on a numerically generated synthetic experiment, where the parameters' true values and the hydraulic variables' states are known. We resort to a synthetic experiment to have control over the test case and to focus on the numerical comparison and implementation of the algorithms.

A. Definition of the test case

1) Geometry

The test case is based on a 100 m wide and more than 10.25 km long channel with floodplains on both sides. On the floodplains, a constant slope along the y Cartesian coordinates is set to $S_{fp} = 0.002\, m/m$. Along the channel in the x direction, the slope is fixed to $S_{channel} = 0.001\, m/m$. The crest of the channel delineation with the floodplain has a slope $S_{b1} = 0.0012\, m/m$ until halfway of the reach and then $S_{b2} = 0.0008\, m/m$. Under these considerations, the channel depth is lower at $x = 5000\, m$, so it overflows in the middle without having much sensitivity to the boundary conditions. The channel section is trapezoidal, transitioning from the bank to the channel elevation on 10 m. Figure 3 describes the geometric configuration at three cross-sections along the numerical domain.

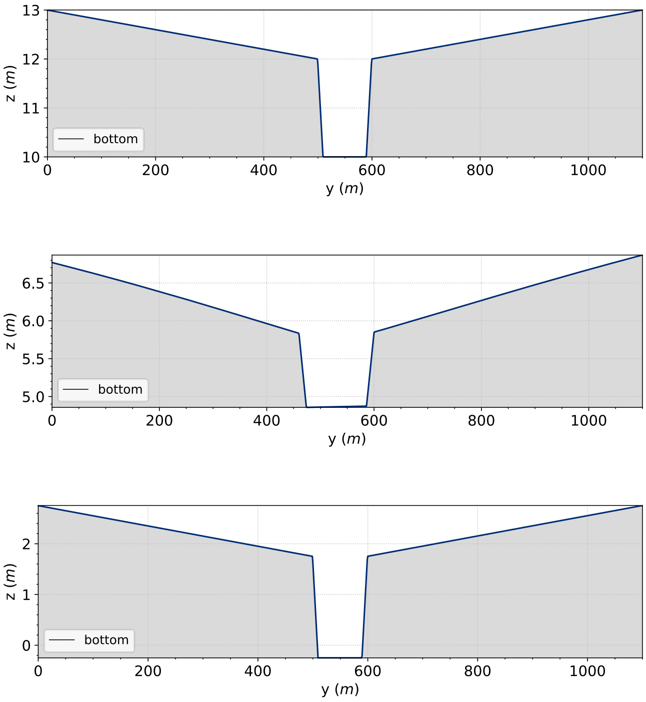

Figure 3. Elevation along a cross-section at $x = 0\, m$ (top), $x = 5000\, m$ (middle) and $x = 10\,000\, m$ (bottom).

The mesh is composed of 477 371 unstructured triangular elements. The number of elements may appear high for a test case, but the goal was to use a similar number of elements as in industrial application cases. The mesh is refined with different resolutions (prior mesh convergence has been carried out making sure the mesh is fine enough for our test case) from 2 m in the transition zone between the channel and the floodplains up to 15 m at the floodplain. As for the channel, the mesh resolution is of 5 m.

2) Initial conditions, inputs, and numerical considerations

For the upstream boundary condition of the model, we use a linear flow rate from 30 $m^3 \cdot s^{-1}$ to 620 $m^3 \cdot s^{-1}$ for the first five minutes. Then the discharge is constant at 620 $m^3 \cdot s^{-1}$. For the downstream condition, the depth is imposed with a linear rating curve with water depths between 0.5 m and 3.3 m for the respective discharges. The total simulation time is of 2 hours 30 (steady state is not reached). An overflow is modelled with changing water height during the simulation over the floodplain (by starting from a low discharge steady state).

3) Friction zoning and generated observations

In this case, three friction zones are considered with one friction for the channel and one friction zone on each side of the river channel. In the sloped regions between the channel and the floodplains, the friction is the same as the channel. The water depth observations are generated from the simulations with an initial guess of Strickler coefficients (in $m^{1/3} \cdot s^{-1}$)

equal to $[K_1^b;\ K_2{}^b;\ K_3^b] = [30; 20; 10]$ with the zoning defined in Figure 4.

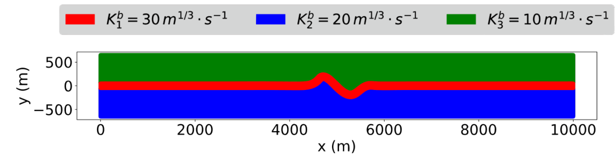

Figure 4. Roughness zones for the synthetic experiment.

From the reference simulation with the three friction zones, water depths are extracted at each mesh node at different times.

We consider two observation networks. A first approach OBS9 considers only 9 observation points (3 in the channel, 3 in the right floodplain, and 3 in the left floodplain). For the second configuration, two other points are added to the observation network (one in each floodplain) called OBS11 in the following. In Figure 5 the observation networks with 9 (OBS9) and 11 (OBS11) points are visualised.

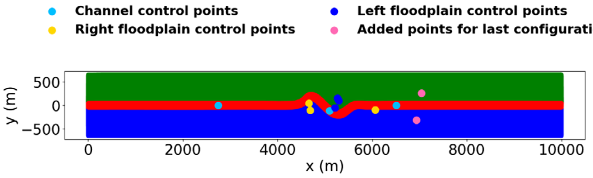

Figure 5. Observation network for the different DA experiments.

The water depths extracted from the synthetic experiment with the reference Strickler values are disturbed by considering different noise levels (adding a Gaussian noise to every observation). The water depths without noise at the different control points of OBS9 and OBS11 are visualised in Figure 6 for the reference simulation.

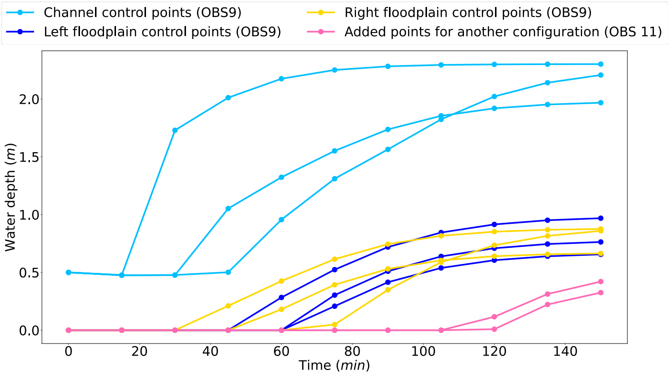

Figure 6. Water depths every 15 minutes at the OBS9 and OBS11 control points.

B. Software tools

Parameter identification under a probabilistic framework combined with optimisation and free-surface flows computation requires the call to different modules. Thus, external or internal libraries to TELEMAC-MASCARET are available to gain real-time interaction capabilities with the TELEMAC-2D simulations, enabling on-the-fly adjustments and optimisations. In this work, the TELEMAC-2D solver (version V8P4) is coupled with TelApy, a module of the TELEMAC-MASCARET system, and ADAO, a Python data assimilation library (https://pypi.org/project/adao/).

1) The TelApy component of the TELEMAC system

One of the strengths of the TELEMAC-MASCARET software is the possibility to interact with the code during the simulations through Application Programming Interfaces (APIs) implemented for each module. The TelApy component is a Python source code wrapping the Fortran APIs [13-14]. The APIs provide the user with flexibility by allowing the control of the simulations while they are running. At any time during the simulation, the user can stop the simulation and retrieve or change the variables of the simulations through a list of variables declared as pointers. Thanks to that component, it is easier to implement a complete and efficient chain of calculations for parameter estimation under uncertainties. This component has been widely used to implement data assimilation strategies for parameter estimation or conjointly with the data assimilation library presented hereafter. In this work, TelApy is used for the three presented algorithms.

2) The Data Assimilation library (ADAO)

The variational approach described previously has been used through the Data Assimilation library called ADAO [8]. The ADAO module aims to simplify and provide different data assimilation and optimisation methodologies while being able to interact with other modules or codes in Python or SALOME (a scientific computing environment developed by EDF and CEA for industrial applications from mesh to post-treatment). It is used for various applications in the engineering field and provides a ready-to-use interface for users with an adapted implementation for industrial cases.

C. Results

1) DA variational algorithm: 3DVAR

The initial state of the friction parameters is set to $\boldsymbol{\theta^b} = [K_1^b;\ K_2^b;\ K_3^b] = [35; 12; 18]$ with $\boldsymbol{B} = 100 \cdot \boldsymbol{I_3}$ as background covariance errors. The parameters are constrained between $5\, m^{1/3} \cdot s^{-1}$ and $90\, m^{\frac{1}{3}} \cdot s^{-1}$ and the differential increment is imposed arbitrarily to 10^{-2} for computing the observation operator approximated derivatives.

The results are not sensitive to the initial state, and the approach on the test case was robust for any initial state with a similar number of iterations for convergence.

The 3DVAR algorithm is studied with different observation configurations (OBS9 and OBS11), different noising of the observations ($\sigma^l = 0.05 / 0.1 / 0.2\ m$) and different numbers of observation times (2, 10).

The roughness at the floodplains has low sensitivity to the water depth observations. Therefore, the water depths are noised with a small standard deviation of $\sigma^l = 0.05\ m$ with $\boldsymbol{R} = (\sigma^l)^2 \cdot \boldsymbol{I_{Nobs}}$. Two observation times ($\#T_{obs} = 2$) are considered with T = [1h15, 2h30]. We compare configuration

OBS9 (9 points) and configuration OBS11 (11 points) in Figure 7.

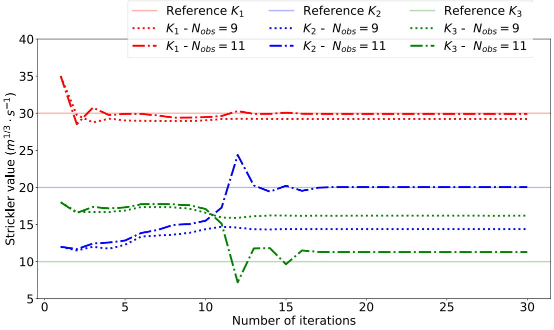

Figure 7. Comparison of parameter estimation for the three friction zones with two different observation networks OBS9 and OBS11 and $\sigma^l = 0.05\ m$.

In Figure 7, after a few iterations the channel roughness value is identified. For the floodplain coefficients it needs more iteration because of the lower sensitivity on the water depths. For OBS9, the floodplain parameters could not be identified correctly. Adding two more observation points in the floodplains improved the identification especially for K_2. It is essential to choose the observation points carefully to identify the parameters of the floodplains. K_3 is more rough leading to lower velocities and slower changes. This coefficient is more difficult to identify because of lower sensitivity (for information, switching the roughness values for K_2 and K_3 leads to similar results with a better identification of the rougher zone). For further investigations OBS11 is used.

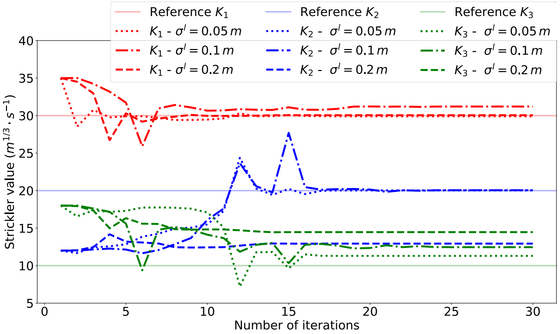

Figure 8. Comparison of parameter estimation for the three friction zones with OBS11 with $\sigma^l = 0.05\ m$, $\sigma^l = 0.1\ m$ and $\sigma^l = 0.2\ m$.

In Figure 8 parameter estimation is compared for different noising values of the observed water depths. Up to $\sigma^l = 0.1\ m$ the parameters are identified, but the floodplain parameters are far from the reference for higher values. With higher standard deviation on the measurement errors, we get almost no information from the measurement as a change in the roughness leads to low water changes compared to measurement errors.

Another test was to add times of observations. Instead of T = [1h15, 2h30], observed water depths are acquired every 15 minutes (10 observations). In Figure 9, the identification of the parameters is slightly comparable by adding more temporal observations. The channel is closer to the reference as well as K_3. For K_2 the identification is a bit worse. For that test case, adding temporal observations does not change much the identification of the parameters. Considering the Gaussian uncertainties on the measurements, the differences between the two experiments are insignificant.

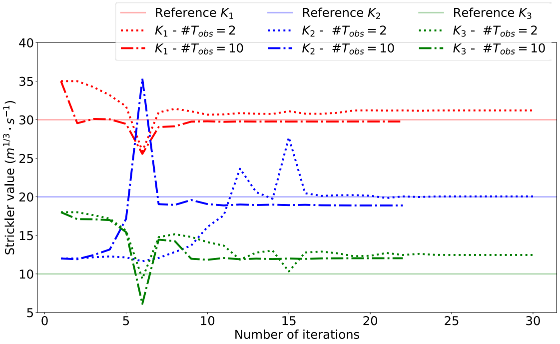

Figure 9. Comparison of parameter estimation for the three zones with configuration 2, $\sigma^l = 0.1\ m$ and different number of temporal observations.

With only two temporal observations, it is possible to evaluate the roughness values because the water depths at these time steps are sensible to all the roughness zones. The floodplain values are not identified for other sets of two temporal observations as T = [1h00, 2h00] instead of T = [1h15, 2h30]. It is probably because at these time steps the water depths for the added points for OBS 11 configuration are zero (no sensitivity yet from the roughness), as shown in Figure 6.

In every case, the cost function no longer reduces after 20 iterations (one iteration corresponds to four simulations for exploring the three parameters). When adding temporal observations, the convergence is faster with more information available. For this case, twenty iterations represent 2h40 of computing time on 96 processors (Intel(R) Xeon(R) Platinum 8260 CPU @ 2.40GHz) on the CRONOS Cluster from EDF.

2) *Ensemble Kalman Filter (EnKF)*

For EnKF the error is propagated on the parameters (distributed friction), and they are updated at the end of an assimilating window (smoothing processing). The assimilation window is set to the simulation time to be comparable with 3DVAR. According to the 3DVAR investigations the OBS11 observation network with a noise value of $\sigma^l \leq 10\ cm$ for the observations are chosen for the comparison. EnKF relies on the number of members chosen to represent the possible states and the number of temporal observations. The initial state members are drawn from a multivariate Gaussian $\mathcal{N}(\boldsymbol{\theta^b}, \boldsymbol{B})$ and the parameters are bounded as in 3DVAR. We explore the role of the number of temporal observations and the ensemble size.

The algorithm is inefficient at evaluating the parameters for only two temporal observations. This can be explained by the fact that it is a sequential DA algorithm. With only two observations, there are not enough steps to converge towards the reference parameters. Therefore, 10 observations every 15 minutes are used instead. Figure 10 describes the evolution of the mean Strickler values for 25 and 100 ensemble sizes and configuration OBS11 with observation noise of $\sigma^l = 0.1\,m$ and 10 temporal observations.

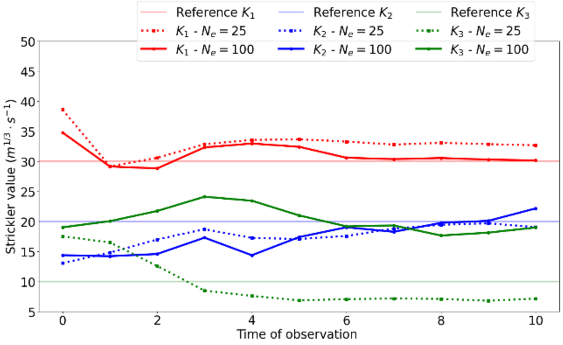

Figure 10. Evolution of the mean parameters' values for the three zones with configuration OBS11, $\sigma^l = 0.1\,m$ for different ensemble sizes (25 and 100) of EnKF.

For EnKF with several temporal observations, it is possible to identify the coefficients on the floodplains. As for 3DVAR the channel and the right floodplain are well identified at the end of the simulations for $N_e = 100$. For a smaller ensemble size N_e, the identification of the channel value is not as good, and it impacts the floodplain identification. Indeed, as the Strickler value is higher for the channel, the floodplain parameter values are lower to compensate. Having enough members is essential to sample correctly the search space. If not, the algorithm may diverge to another solution that is considered equally good, considering the uncertainties.

The algorithm works better for steady state as described in [11]. However, by doing an analysis step only at the end of the assimilation window, it can work for non-steady-state simulations if the parameters are not updated during the simulation.

Attempts to add more temporal observations did not lead to a better identification of the parameters. As for the comparison with 3DVAR, the identified coefficients for K_1 and K_2 are similar and the same identification problem for the third zone is encountered. The disadvantage of EnKF compared to 3DVAR is the need for more observations to get similar results, at least in this test case.

3) *Particle Filter*

Again, the OBS11 observation network with a noise value of $\sigma^l \leq 10\,cm$ for the observations and 2 observation times are chosen. The particles are drawn from a multivariate Gaussian $\mathcal{N}(\boldsymbol{\theta^b}, \boldsymbol{B})$ and the parameters are bounded as in 3DVAR.

Without resampling we identify only the channel roughness as the water depth is very sensitive on the chosen control points to channel roughness and not floodplains (see Figure 11). The weight of a particle is unique, so it privileges the identification of the channel parameter. Furthermore, in most cases, the weight of one particle dominates the other, so the posterior distribution is not very well described.

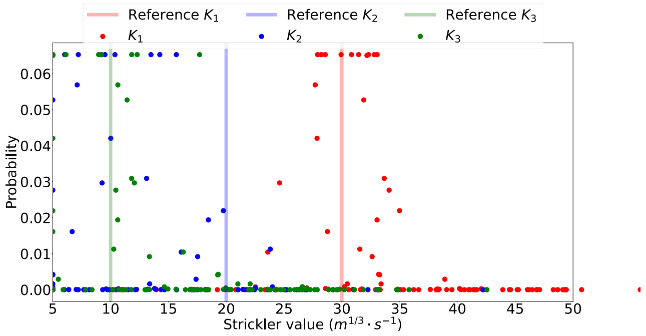

Figure 11. After first iteration of the Particle Filter with 100 particles.

Thus, we apply the Particle Filter iteratively by using the new posterior distribution for each parameter and use it as prior for a new iteration after resampling. After first iteration, the variance of the Strickler parameters is low compared to the floodplains, so it is better identified. Then, at the next iteration, with resampling, the search space is drastically reduced for the channel parameter value compared to floodplains. The identification of the floodplains values is easier. Therefore, for the channel which was greatly identified the variance is low and at the next iterations the prior distribution is more centered on the predicted channel value, and thus it can focus on the identification of the coefficients from the floodplains by having high-density sampling around channel reference value with low variance. In Figure 12 the channel parameter is well identified with a distribution around it (underestimating slightly the parameter), and the floodplains posterior distributions for the roughness are not centered on the reference but are near the value of the references.

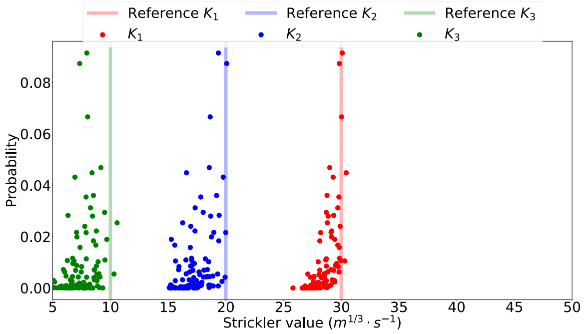

Figure 12. After five iterations of the Particle Filter with 100 particles.

The number of particles at the initialisation also plays a role in exploring the set of parameters. When using more particles at the start, more sets of parameters are explored, so that the resampling might be more efficient.

However, with the iterative process and resampling if the set of samples grasp the suitable parameters at first, it can converge quickly and give similar results. In Figure 13, it can be seen with the same number of iterations and only 25 particles instead of 100 showing the importance of the initial sampling. For other initial samples, 25 particles may not be enough to converge to the reference values.

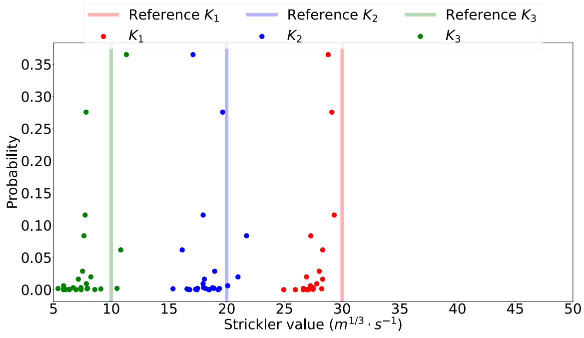

Figure 13. After five iterations of the Particle Filter with 25 particles.

When having more temporal measurements, floodplain values are difficult to find in this inverse problem because for most observations time step, only the channel roughness influences the water depths at the control points. Furthermore, looking more closely at the water depths, the tricky point is that different parametrisations of the roughness may lead to the same output when comparing observations and models; it is called equifinality [15].

VII. CONCLUSION

In this paper different methodologies for parameter estimation were carried out on a simplified but real-world dimensioned test case. It shows the potential of using observations combined with numerical models to improve the characterisation of friction parameters for flood studies. The TELEMAC-MASCARET software linked with ADAO and TelApy can lead to a faster learning curve for the user for Data Assimilation. It is possible to implement other DA algorithms, as it was the case with the implementation of the Particle Filter with resampling and parallelisation capabilities.

The 3DVAR algorithm was more adapted for parameter estimation under uncertainties on the test case. It was shown that identifying the three parameters was possible up to a specific error of observations. When the number of temporal measurements increases, the performance decreases, so it might be interesting to compare it with a 4DVAR approach to consider the dynamic evolution of the model. Another finding is the importance of the observation network. Indeed, adding 2 observation points on the floodplains where the water height was more sensitive to the friction floodplains at specific time steps led to a most straightforward estimation.

As for the EnKF, it proves to be adapted when enough temporal observations are available. It should be used with a smoothing procedure by updating the parameters at the end of an assimilation window and not at each observation (to compare it with the other algorithms).

The Particle Filter reaches better results than the prior distribution and enables the practitioner to know the uncertainties through a posterior distribution of the parameters given the uncertainties. However, using a Particle Filter with resampling in an iterative process requires much computation. The resampling procedure must be improved, so that the algorithm keeps exploring a wider set of samples, as it tends to explore a very restrained range of values when converging. The hyperparameter in the resampling method may be adapted to reach better performance.

For the number of calls to the TELEMAC-2D code, between the Particle Filter, EnKF, and 3DVAR, the latter is more efficient in general. For similar results 3DVAR needed around 80 calls to the code, while PF needed 500 calls for five iterations with 100 particles and 125 with 25 particles (5 iterations of the PF). It is difficult to compare the number of calls to the code between the two methods as it depends on the number of chosen particles for the PF and the initial sampling. For the EnKF around 100 calls to the code were necessary to identify the parameters, but it was working only with ten temporal observations instead of two for the 3DVAR. The advantage of the PF and EnKF is that we can launch the particles in parallel.

In perspective, the methodologies should be conducted on real-world applications to evaluate different DA algorithms with a complete review of the available parameters to evaluate their performance. In the PF there is a need to work on the resampling procedure and the definition of the likelihood between the observations and the model predictions.

ACKNOWLEDGEMENT

The authors gratefully acknowledge the French National Association of Research and Technology (ANRT) for funding and the open-source community, especially that of the TELEMAC-MASCARET (hydrodynamics) and ADAO (data assimilation).

REFERENCES

[1] P. Bates, D. Pappenberger, and R. J. Romanowicz, “Uncertainty in flood inundation modelling”, Applied uncertainty analysis for flood risk management, 2014, pp. 232-269.

[2] F. Pappenberger,K. J. Beven, M. Ratto and P.Martgen, “Multi-method global sensitivity analysis of flood inundation models." Advances in water resources, 2008, pp. 1-14.

[3] M. Asch, M. Bocquet, and M. Nodet, “Data assimilation: methods, algorithms, and applications”, Society for Industrial and Applied Mathematics, 2016.

[4] J.-M. Hervouet, “Hydrodynamics of Free Surface Flows: Modeling with the Finite Element Method”, John Wiley & Sons, Ltd: Hoboken, NJ, USA, 2007.

[5] A. B. de Saint Venant, « Théorie du mouvement non permanent des eaux, avec application aux crues des rivières et à l’introduction des marées dans leur lit », Rapport technique, Académie des sciences, 1871.

[6] H. Morvan, D. Knight, N. Wright, X. Tang and A. Crossley. “The concept of roughness in fluvial hydraulics and its formulation in 1d, 2d and 3d numerical simulation models”, Journal of Hydraulic Research, 2008, vol. 46, pp. 191-208.

[7] R. Manning, J. P. Griffith, T. Pigot, and L. F. Vernon-Harcourt, “On the flow of water in open channels and pipes”, 1890.

[8] J.-P. Argaud, “User Documentation, in the SALOME 7.5 platform, of the ADAO module for Data Assimilation and Optimization”, EDF R&D report, 2016.

[9] O. Talagrand, “Assimilation of observations, an introduction (gtspecial issueltdata assimilation in meteology and oceanography: Theory and practice)”, Journal of the Meteorological Society of Japan. Ser. II, 75(1B), 1997, pp.191-209.

[10] A. Carrassi, M. Bocquet, L. Bertino, G. Evensen, “Data assimilation in the geosciences: An overview of methods, issues, and perspectives”, Wiley Interdisciplinary Reviews: Climate Change, 2018.

[11] F. Zaoui, C. Goeury, Y. Audouin, “Ensemble Integrations of Telemac-Mascaret for the optimal model calibration." In XXVth Telemac & Mascaret User Club, 2018.

[12] N. Gordon, D. J. Gordon, A. F. Smith, “Novel approach to nonlinear/non-Gaussian Bayesian state estimation”, IEE proceedings F (radar and signal processing), vol.140, No.2, 1993, pp. 107-113.

[13] C. Goeury, Y.Audouin, F. Zaoui, “User documentation v7p3 of TelApy module”, 2017

[14] C. Goeury, Y. Audouin, and F. Zaoui, “Interoperability and computational framework for simulating open channel hydraulics: Application to sensitivity analysis and calibration” of Gironde estuary model. Environmental Modelling & Software”, 2022.

[15] K. Beven, “A manifesto for the equifinality thesis”, 2006, pp. 18-36.

Modelling of the Seine and Marne in Paris with MASCARET for VNF

Patrick Chassé[1], Fabrice Daly[1], Olivier Monfort[2], Alexandre Hequet[2]
Patrick.chasse@cerema.fr, 60280 Margny lès Compiègne, France
[1]: Cerema Risques Eau Mer – REL Dept
[2]: Voies Navigables de France, SGVE Dept

Abstract **– In 2020, the VNF establishment (Voies Navigables de France) commissioned a study on the Paris Reach of river Seine from Cerema (DTec REM). Modelling the Paris Reach with the Qgis MASCARET plugin is one part of it.**

Keywords: Flood, MASCARET, 1D hydraulic modelling, Navigation dams, Calibration, Validation.

I. INTRODUCTION

Firstly, we present the construction of the hydrodynamic model, the input data and the assumptions made, then we show the results of calculations for the various simulated floods.

II. CONSTRUCTION OF THE HYDRAULIC MODEL

The Cerema model was produced with the Qgis MASCARET plugin, which is part of the TELEMAC-MASCARET calculation chain developed by a consortium of several French and European organizations (EDF-LNHE, Cerema, Cerfacs, BAW, HR-Walingford, Daresbury Laboratory), but more particularly by Artélia with the assistance of Cerema for MASCARET

A. Model extent

The Cerema model has an influence that extends from the Ablon reach upstream to the Courbevois's bridge downstream on the Seine. On the Marne it extends from the Créteil dam upstream to the confluence with the Seine downstream. Figure 1 shows the extent of the model.

The MASCARET model represents a length of 53.9 km on the Seine including the Marne and is made up of 96 cross sections. The mesh step is 50 m along flow direction and the vertical step for calculating the hydraulic parameters is 0.20 m.

B. Data and the assumptions made

There are three water level stations and five navigation dams (Ablon, Port à l'Anglais and Suresnes (1 and 2) on the Seine and Saint Maurice on the Marne). The topographic and bathymetric data used are as follows:

- the RGE Alti 5 m (a digital terrain model) from IGN (Institut Géographique National) for the main channel bed
- the bathy points of VNF for the floodplains

The boundary conditions imposed on the model are:

- the flow at the Saint-Fargeau station upstream of the Seine
- A rating curve at the Courbevois's bridge
- the flow at the Créteil station upstream on the Marne

III. MODEL CALIBRATION ON THE 2021'S FLOOD

We have used the 2021 flood to calibrate the Strickler roughness coefficients of the model: a Strickler value of 60 $m/s^{1/3}$ was found for the main channel bed of the Paris reach and 8 $m/s^{1/3}$ for the urbanized floodplains. The Strickler values of the Ablon and Créteil reaches were set to 40 $m/s^{1/3}$ for the main channel and 12 $m/s^{1/3}$ for the floodplains. We have also added head loss coefficients of 1.5 upstream of the Paris bridges. Figure 2 presents the longitudinal profile of the simulated water levels (blue line) of the 2021 flood compared to the observations (red marks). The Nash–Sutcliffe model efficiency coefficient (NASH) is used to assess the predictive skill of hydrological models. It is defined with the differences between the observed (X_{obs}) and the simulated (X_{sim}) values compared to the differences between the observed values and their mean value ($X_{obsmean}$):

$$NASH = 1 - \frac{\Sigma(X_{obs} - X_{sim})}{\Sigma(X_{obs} - X_{obsmean})} \tag{1}$$

The NASH's number calculated on these results is 0.98, which is very good.

Figures 3 to 6 show the comparison between the simulated and observed water levels and discharges for the 2021 flood at Austerlitz station and Alfortville station. The simulated and observed water levels for the 2021 flood for the Marne at Saint Maurice presented in Figures 7. In Figures 8 and 9 the water levels upstream and downstream of the Suresnes dam are visualised.

IV. DATA AT THE NAVIGATION DAMS

Data at the navigation dams allows us to compare observed and simulated water levels, as well as observed and simulated movements of the weir.

Figure 10 and 11 show the weir movements of the Ablon dam and the Port à l'Anglais dam on the Seine during the 2021 flood.

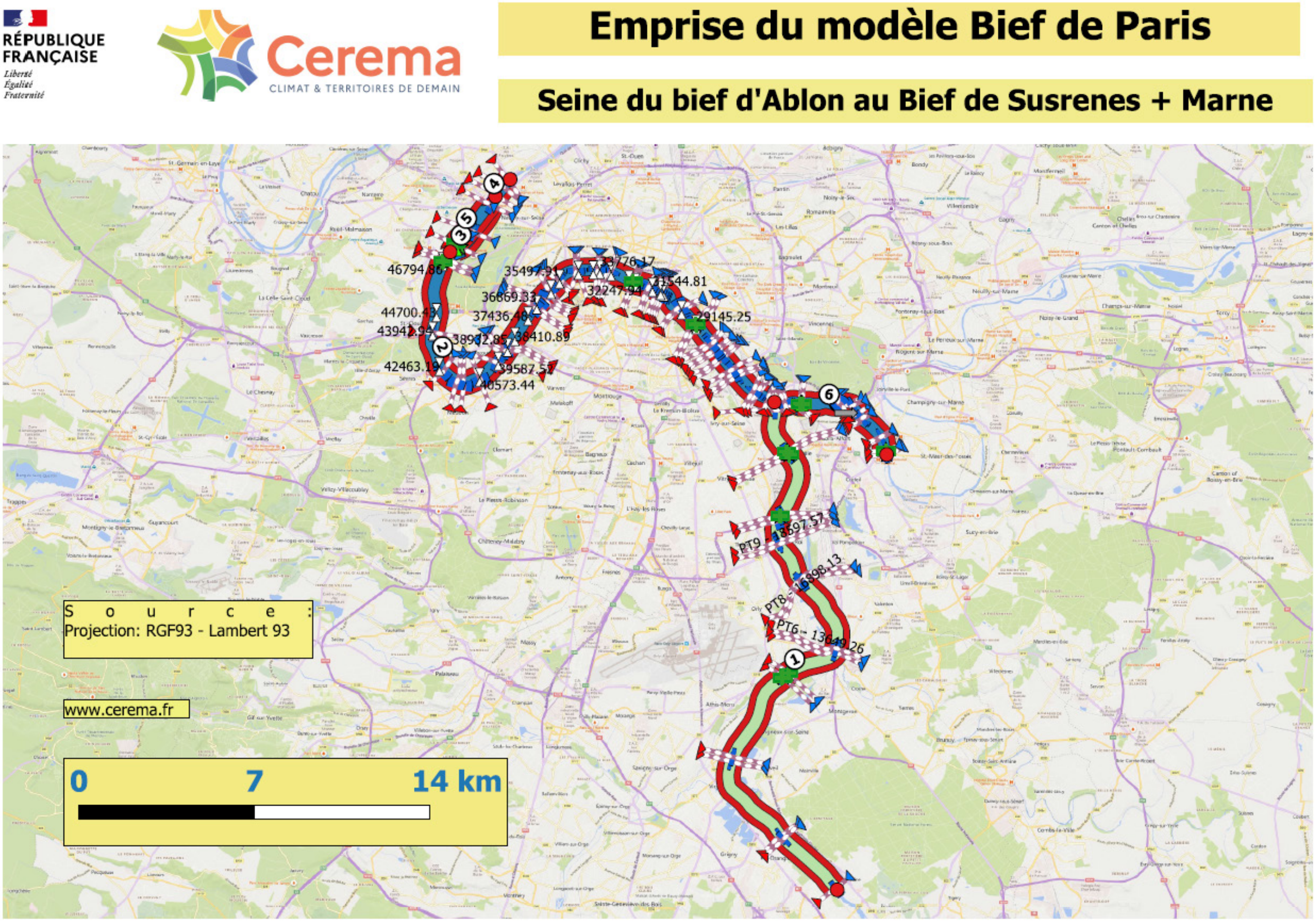

Figure 1. Model extension.

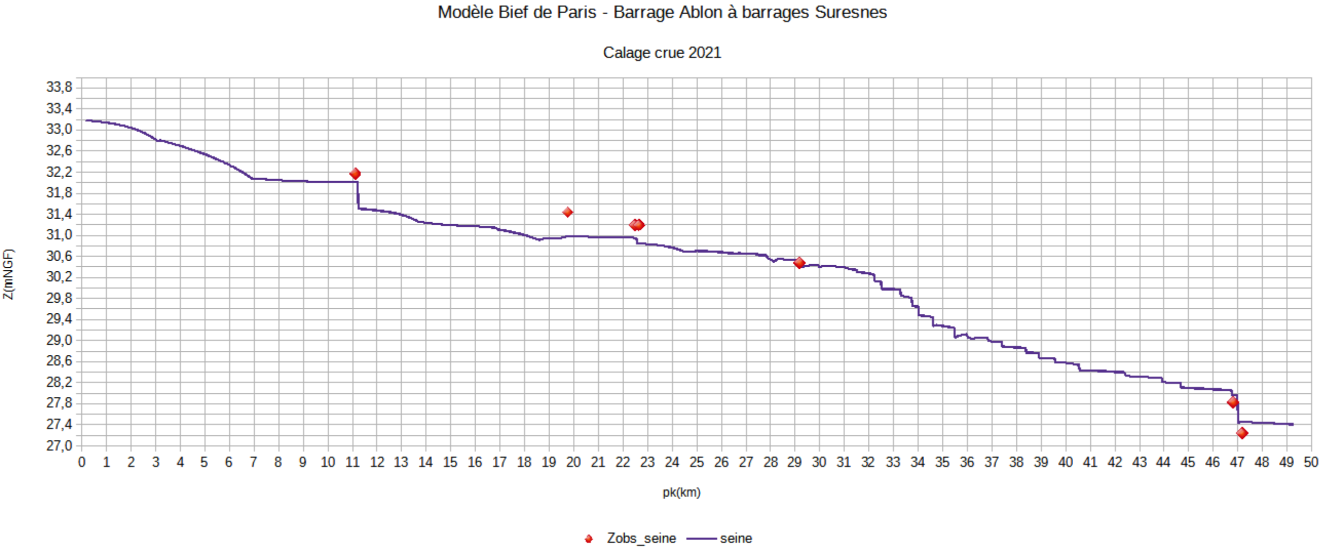

Figure 2. Results of calibration for the 2021 flood. Red marks water level observations, blue line: simulated water levels.

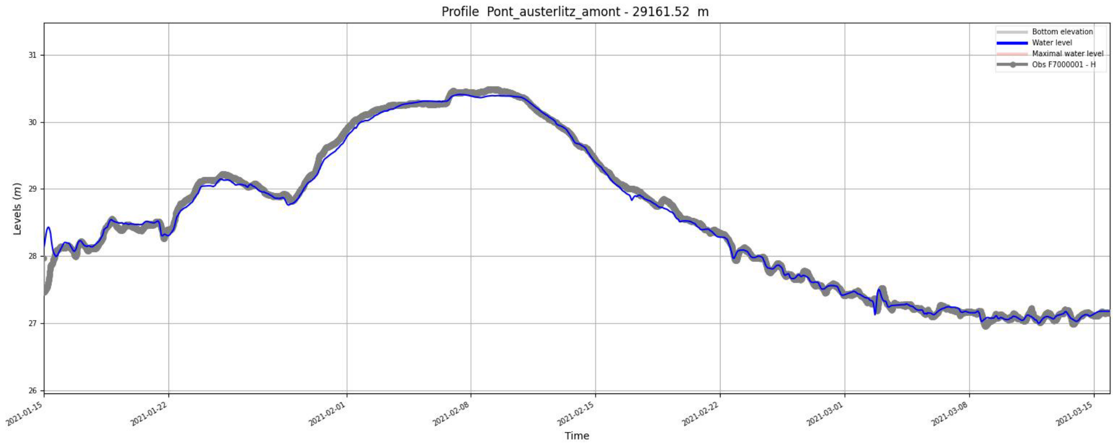

Figure 3. Comparison of simulated (blue line) and observed (grey line) water levels at Austerlitz's bridge for 2021 flood.

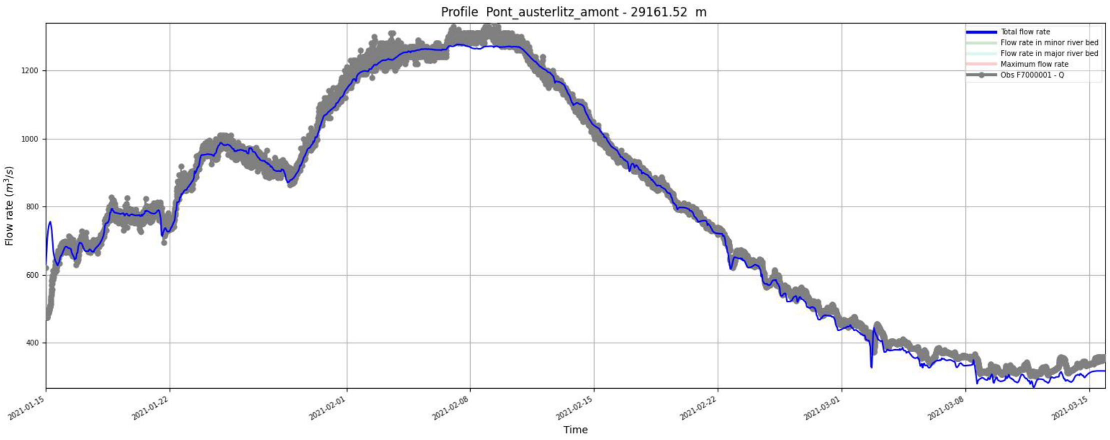

Figure 4. Comparison of simulated (blue line) and observed (grey line) discharges at Austerlitz's bridge for 2021 flood.

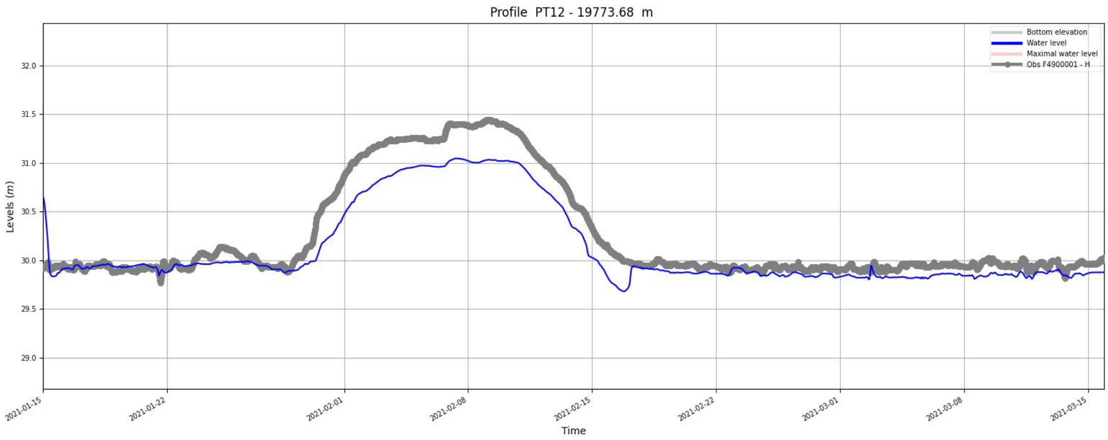

Figure 5. Comparison of simulated (blue line) and observed (grey line) water levels at Alfortville station for 2021 flood.

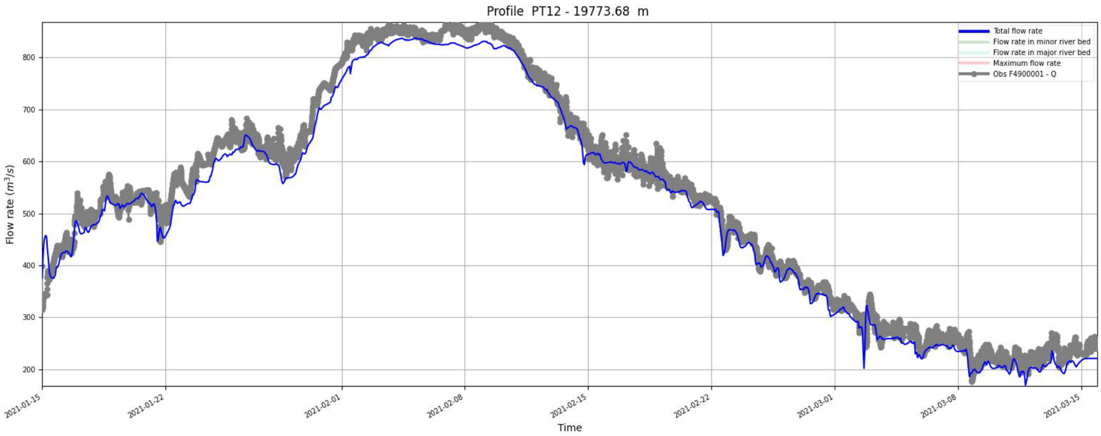

Figure 6. Comparison of simulated (blue line) and observed (grey line) discharges at Alfortville station for 2021 flood.

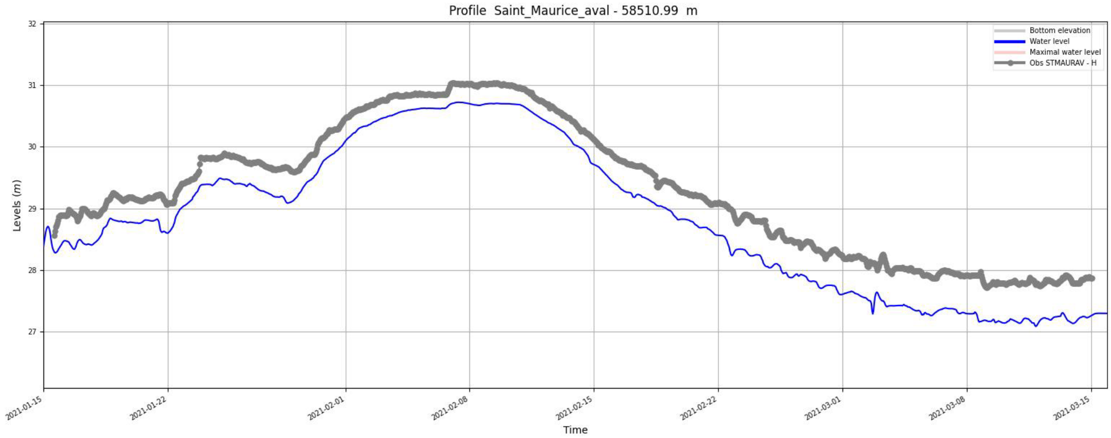

Figure 7. Comparison of simulated (blue line) and observed (grey line) water levels at the Saint Maurice dam (Marne) for 2021 flood.

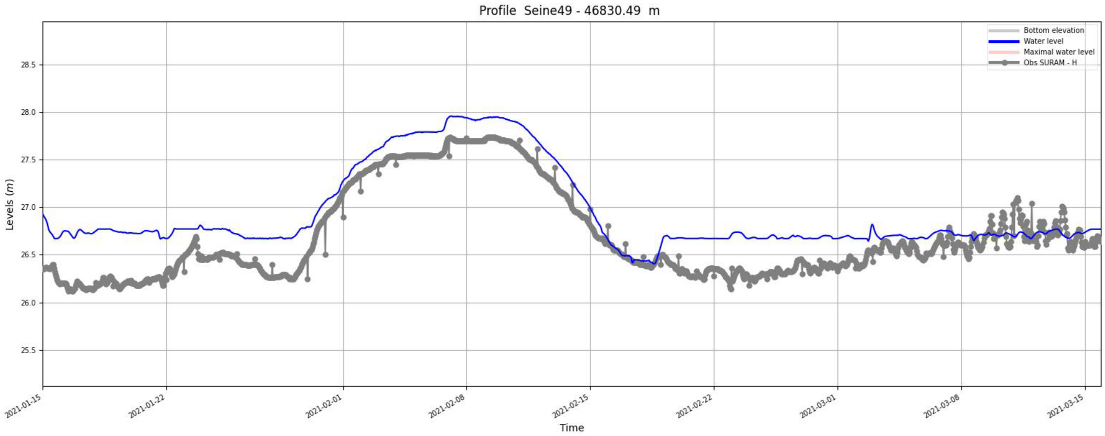

Figure 8. Comparison of simulated (blue line) and observed (grey line) water levels at the upstream Suresnes dam for 2021 flood.

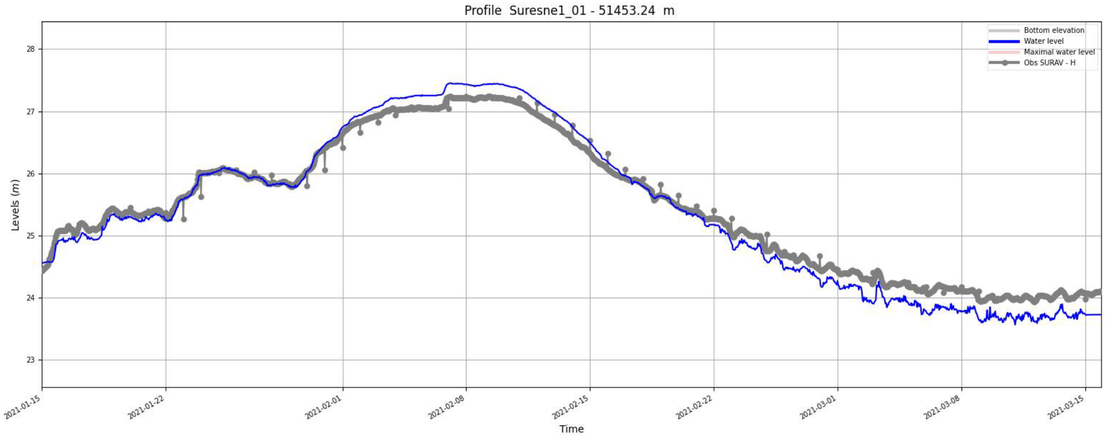

Figure 9. Comparison of simulated (blue line) and observed (grey line) water levels at the downstream Suresnes dam for 2021 flood.

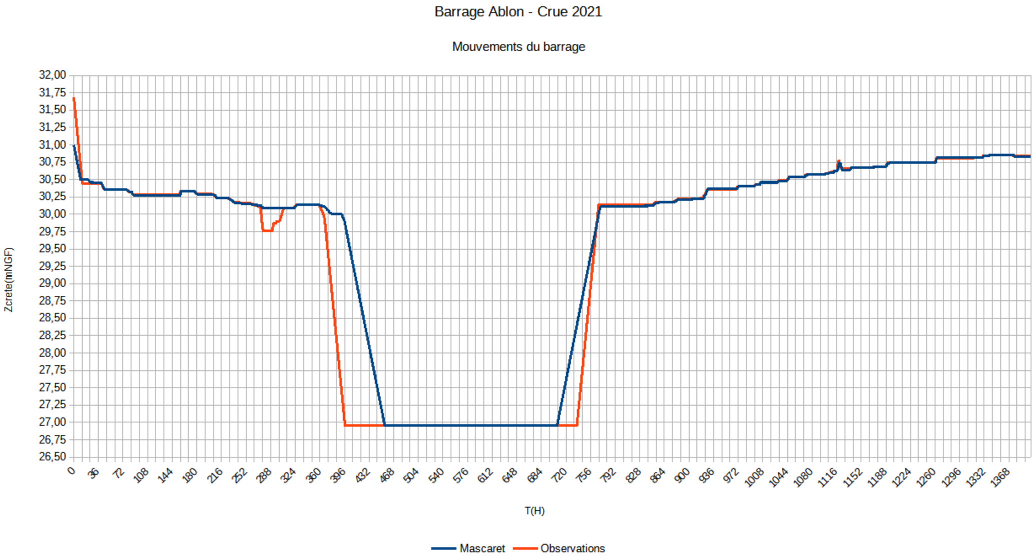

Figure 10. Comparison of observed and simulated weir movements of Ablon dam for the 2021 flood.

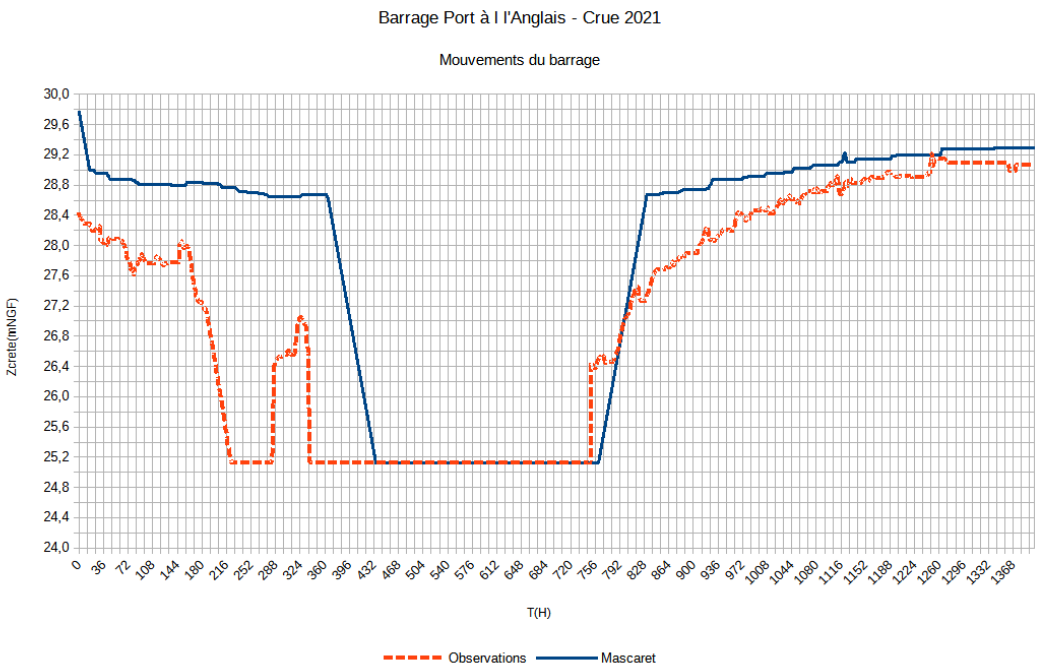

Figure 11. Comparison of observed and simulated weir movements of Port à l'Anglais dam movements for the 2021 flood.

V. VALIDATION ON THE 2020'S FLOOD

After the calibration of the model with Strickler values and singular head loss at the bridges, we use the 2020 flood as a validation flood.

Figure 12 presents the longitudinal profile of the simulated water levels (blue line) of the 2020 flood compared to the observations (red marks). The number of NASH calculated from the observations is 0.78, which is satisfying for this 2020 validation flood.

Figure 13 to 16 show the comparison of simulated and observed water levels and discharges for the 2020 flood, at Austerlitz station and Alfortville station. The agreement between measurements and simulations is not so close than for the calibrated 2021 floods but still satisfying.

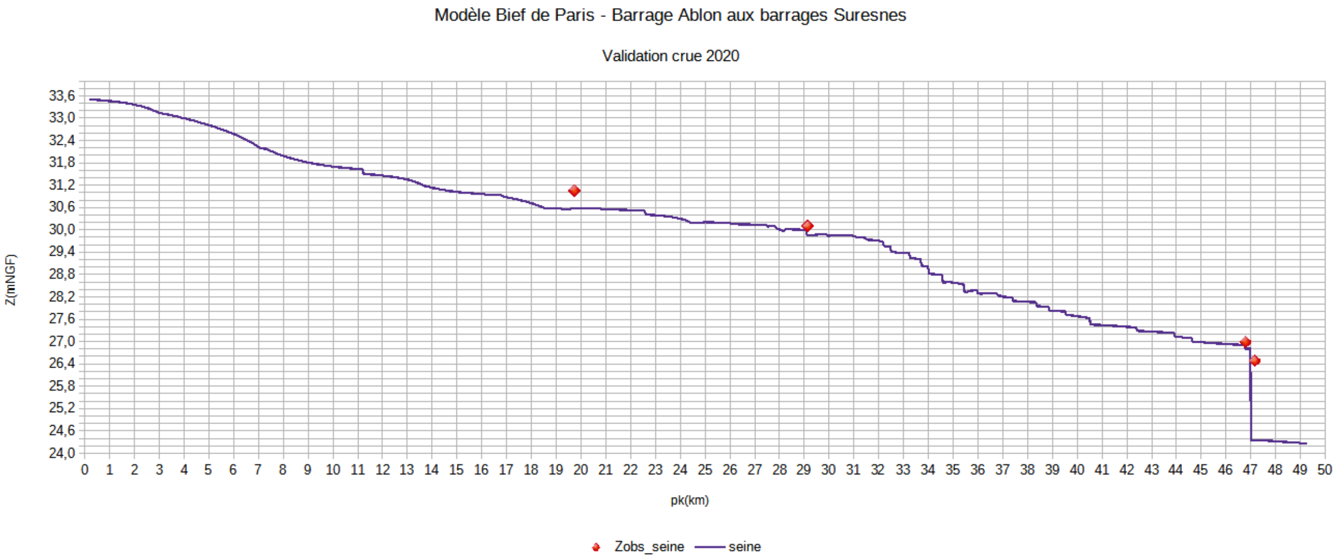

Figure 12. Results of validation for the 2020 flood. Red marks water level observations, blue line: simulated water levels.

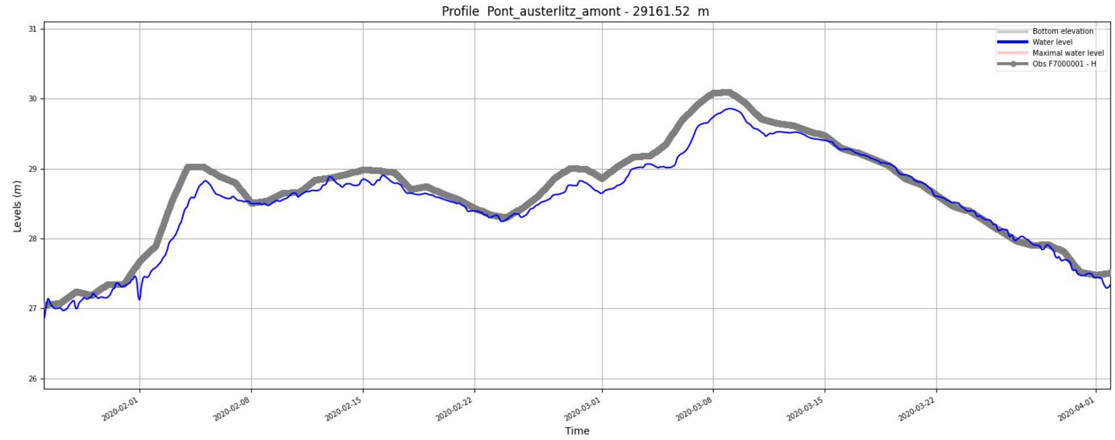

Figure 13. Comparison of simulated (blue line) and observed (grey line) water levels at Austerlitz's bridge for 2020 flood.

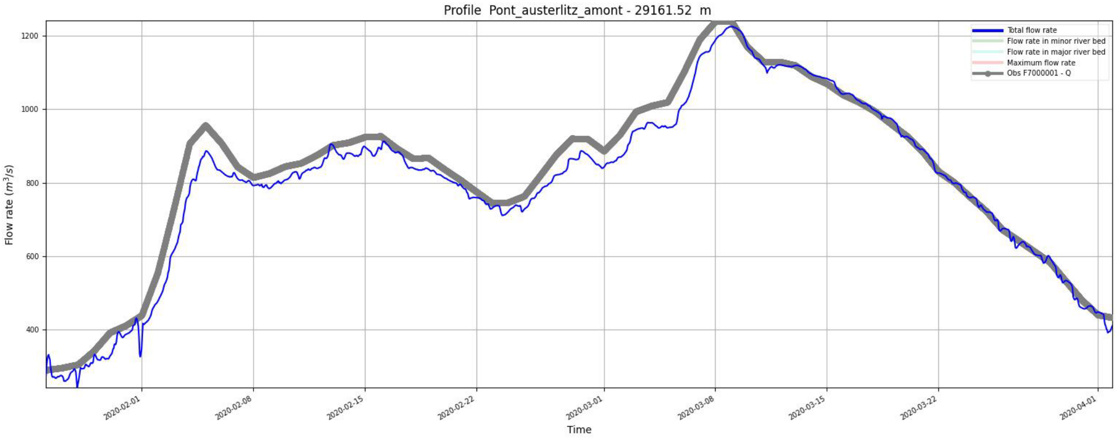

Figure 14. Comparison of simulated (blue line) and observed (grey line) discharges at Austerlitz's bridge for 2020 flood.

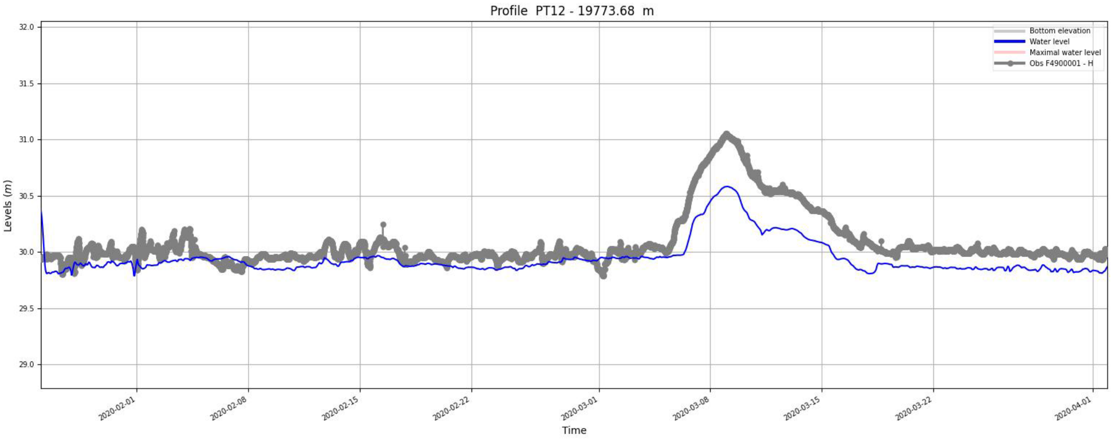

Figure 15. Comparison of simulated (blue line) and observed (grey line) water levels at Alfortville station for 2020 flood.

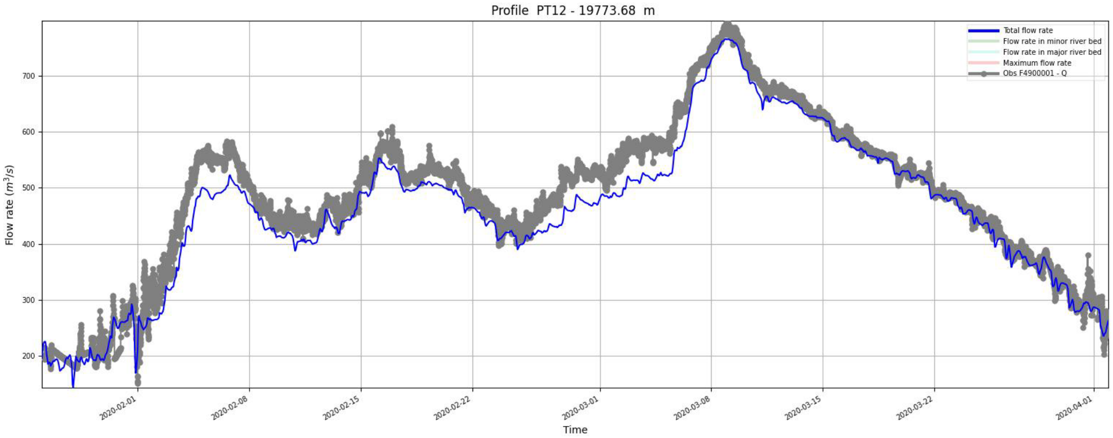

Figure 16. Comparison of simulated (blue line) and observed (grey line) discharges at Alfortville station for 2020 flood.

VI. CONCLUSION AND PERSPECTIVES

The results of the model are rather satisfaying for the two simulated floods, in particular following the last adjustment which consisted of adding singular head losses upstream of the Paris bridges.

The NASH numbers are very good for the 2021 and satisfying for the 2020 flood. Following the study, VNF agents were trained in the model.

ACKNOWLEDGEMENT

Cerema thanks VNF for financing this project.

REFERENCES

[1] Gestion de la ligne d'eau du Bief de Paris – Proposition du Cerema - 2020

[2] Bief de Paris – Analyse du comportement – Version définitive - 01/11/2022

Two-dimensional modelling of floods due to levee breaching: Application to Enza River, Italy

Zied Amama[1,2], Sébastien E. Bourban[1,2], Jean-Robert Courivaud[3], Mark Morris[4], Kamal El Kadi Abderrazzak[1,2]
zied.amama@edf.fr
[1]: National Laboratory for Hydraulics and Environment, EDF R&D, Chatou, France
[2]: Saint Venant Laboratory for Hydraulics, Chatou, France
[3]: EDF CIH, La Motte Servolex, France
[4]: HR Wallingford, Wallingford, UK

***Abstract* – As overflow and overtopping erosion pose significant threats to embankment dams and levees, predicting flow propagation in protected areas is vital for effective flood risk management. In this paper, simplified breach growth laws were integrated with the two-dimensional (2D) shallow water equations solver TELEMAC-2D. We applied this model for simulating the levee breaching and associated inundation that occurred on the Enza River, Italy, in December 2017. We compared the computed and observed flood maps. The study evaluated various empirical breach growth models for levees, finding that models allowing specification of breach time and width performed better than those based on physical characteristics for this test case, though the latter models faced data availability challenges and were affected by the presence of multiple breaches.**

Keywords: Breach, Levees, Overtopping, 2D model.

1) INTRODUCTION

Failure of levees induced by overtopping flows can lead to widespread inundations. Accurately representing these events is critical for generating flood risk maps and for planning management strategies. Current 2D computational models, based on shallow water equations, are recognized tools for simulating flood extent, but the initiation and expansion of breaches remains a challenge. In the context of numerical modeling of levee breaching caused by overflows (i.e. surface erosion), there are three distinct approaches [1,2]:

1. Parametric models: these models utilize simple regression equations, generally in dimensional form, to estimate breach peak discharge, ultimate breach width and duration, based on a limited number of parameters (e.g. embankment height, upstream water level, reservoir water volume) [3]. Because these equations were derived mainly from statistical analysis of historical failure of dams, their application to levees is questionable.
2. Simplified physically-based models: the flow is calculated using simple fluid dynamic equations (e.g. Bernoulli equation, 1-D quasi-steady flow in the breach channel). The temporal variation of the breach geometry is simulated using parametric equations, considering some physical processes (i.e. erosion, deposition, head cut migration) and properties of the dike materials. These models contain empirical formulas (e.g. erosion rate formula, broad-crested/weir equation for computing the breach outflow discharge), and require input parameters (e.g. final breach width and depth, side-slope, critical shear stress or velocity for initiation of erosion).
3. Detailed physically-based models: these models discretize and solve the flow and sediment transport governing equations using a computational mesh of the whole domain (main channel, dike, and floodplain). The governing equations are generally 1D or 2D shallow water equations for hydrodynamic, convection diffusion equation for suspended load and Exner equation for bed changes, completed with empirical formulations for deposition, erosion and bedload transport and, in some models, including a side slope failure operator. Some detailed physically-based models are only hydrodynamic, solving the shallow water equations in the main channel and floodplain, whereas the dike breaching (e.g. initiation conditions, formation time, breach shape, breach width and depth growth) is simulated according to parametric formulations or user input data [4].

The aim of this study is to simulate the flood event of the Enza River in Italy that occurred in December 2017 with the TELEMAC-2D solver (*www.opentelemac.org*) using hydrodynamic detailed physically-based model and parametric formulations for dike breaching. In recent updates, various laws for simulating the breach expansion were implemented within the code. The present study discusses the capabilities and limitations of the 2D model, and evaluates the performance of each breaching law in accurately estimating the flood extent.

2) APPLICATION

A. *Enza river flood event*

In December 2017, in northern Italy, the right levee of the Enza River collapsed between Sorbolo and Lentigione villages [5]. Due to extreme hydroclimatic conditions, the water level exceeded the levee crest along 250m, initiating surface erosion of multiple breaches that accounted for a 160m final breach width. The silt loam-made levee was 5m high, 3m wide crest with inner and outer side slopes of 1:2 and 2:3 (V:H), respectively. The breaching duration was estimated at 4 h (with an error of 0.5 to 1 h, personal communication by S. Dazzi), generating an overflow volume into the floodplain of 20Mm^3 [6]. The flooded surface was around 6.38km². Figure 1 shows the digital terrain model based on 1m resolution LIDAR data and the surveyed flood extent. The measured upstream discharge hydrograph and the downstream water level limnigram recorded on Po River are shown in Figure 2. Figure 3 shows the flood event from an aerial view with the three simultaneous breaches.

B. Numerical model

The 2D shallow water equations solver TELEMAC-2D was used in combination with its BREACH module. Seven empirical laws described herein were applied to model the breach expansion, six of them gradually lowering and widening the breach topography. Except for Froehlich's [16] formula, the breach shape is assumed rectangular.

1) *Instantaneous widening:* the breach width is set at the final width B_f instantaneously once the breaching initiation time is exceeded. This approximation is sometimes made when no information about the breach growth is available [7,8].

2) *Linear equation:* recent advances in the study of overtopping-induced levee failures indicate that the breaching process unfolds gradually, rather than instantaneously [9,10]. Consequently, a simple approach for breach widenning would be the use of a time-dependent linear formula defined as:

$$B(t) = E_w(t - T_i) + B_0 \quad \text{if} \quad T_i \le t \le T_i + T_f \qquad (1)$$

where t is time in h, B the breach width in m, E_w the widening rate in m/h, T_i the breach initiation time in h, T_f the breaching duration in h, and B_0 the initial breach width in m.

3) *USBR [11] fomula:* a time-linear increase in breach width, derived from twenty-one dam failure cases, with a widening rate of 91m/h (Eq.2). No distinctions were made concerning the embankment material.

$$B(t) = 91(t - T_i) + B_0 \quad \text{if} \quad T_i \le t \le T_i + T_f \qquad (2)$$

4) *Von Thun and Gillette [12] formulas:* derived from historical events. For resistant dikes (i.e., cohesive material), the formula is:

$$B(t) = 4h_w(t - T_i) + B_0 \quad \text{if} \quad T_i \le t \le T_i + T_f \qquad (3)$$

where h_w is the water depth above the breach invert in m at the time of failure and notch location. In this case, we consider the time of failure as the time when overtopping is starting. The value of h_w is then considered as the difference between the crest height and the minimal bottom elevation of the breach (erodible depth). Since h_w is constant, this law is equivalent to a linear time-dependent formula with a breach widening rate of $4h_w$.

5) *Verheij [13] formulas:* developed for sandy and clay levees from field and laboratory data sets [14]. For cohesive clay dikes the formula is:

$$B(t) = 13.4\sqrt{t - T_i} + B_0 \quad \text{if} \quad T_i \le t \le T_i + T_f \qquad (4)$$

6) *Verheij and Van der Knaap [15] formula:* the equation is an improvement of the previous ones using similar data. It takes into account the difference of water levels between upstream and downstream sides of the dike ΔH:

$$B(t) = \frac{f_1 g^{0.5} \Delta H^{1.5}}{u_c} log\left[1 + f_2 \frac{g}{u_c}(t - T_i)\right] + B_0 \qquad (5)$$

where u_c is the critical flow velocity for initiation of erosion in m/s, f_1 and f_2 empirical coefficients, g the gravitational acceleration in m/s², ΔH in m assimilated in TELEMAC-2D to the head loss between upstream (i.e. main channel) and downstream (i.e. floodplain) sides of the dike. It is determined by calculating the maximum value of the differences between hydraulic head upstream and downstream. This choice was made to accounts for localized high-velocity flow zones that could pose a higher risk of erosion at a specific point along the dike. In this model, the widening stops when ΔH becomes void.

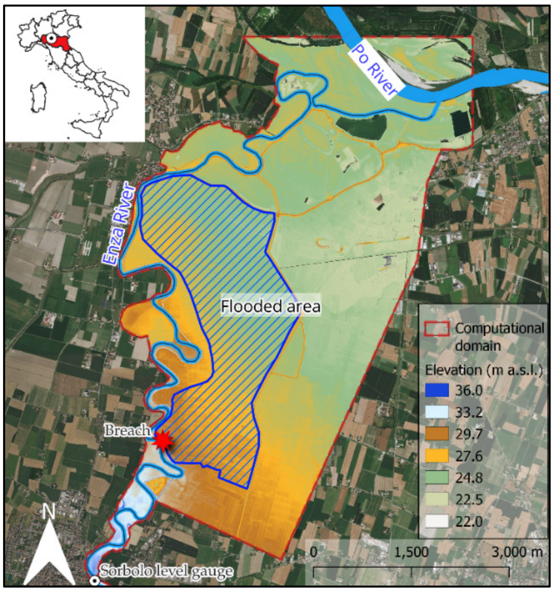

Figure 1. Study area with digital elevation model and flooded area during December 2017 event

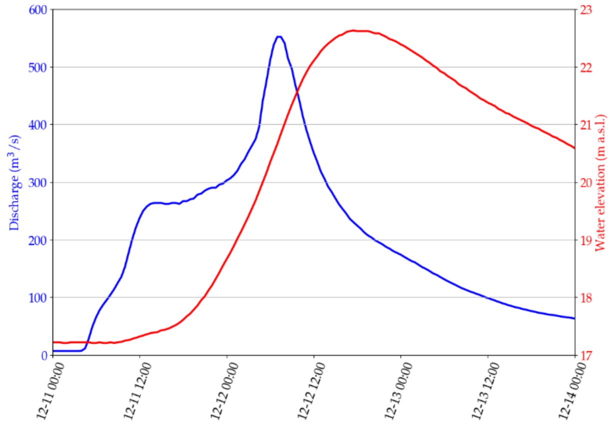

Figure 2. Upstream flow discharge hydrograph and downstream water level limnigram. Horizontal axis is in MM-dd HH:mm

Figure 3. Three simultaneous breaches during the flood event (Reggio Emilia)

7) Breach deepening law: breach deepening is faster relatively to lateral expansion [10]. For the previous empirical laws, the breach deepening is modelled as a linear-time law:

$$z_b(t) = z_{b0} - (z_{b0} - z_{bmin})\frac{t-T_i}{T_d} \quad \text{if} \quad T_i \le t \le T_i + T_d \qquad (6)$$

where z_{bmin} the breach minimum elevation in m, z_{b0} the breach initial elevation in m, and T_d the duration to reach z_{bmin} in h. The default value of T_d is T_f/10.

8) Froehlich [16] formula: using field data, three models for earthen dam breaching based on sine-curve time breach expansion were poposed to better reproduce the three phases of breach growth than linear models: a slow start; an acceleration phase then another slow phase. The difference between the three models lies in the breach shape progression that can start with triangular, rectangular or trapezoidal shape, ultimately ending trapezoidal. The fully trapezoidal breach shape-type model was adjusted in TELEMAC-2D with the following laws for the top breach width and bottom elevation:

$$B(t) = \frac{1}{2}\left\{1 + sin\left[\pi\left(\frac{t-T_i}{T_f} - \frac{1}{2}\right)\right]\right\}(B_f - B_0) + B_0$$

$$\text{if} \quad T_i \le t \le T_i + T_f \qquad (7)$$

$$z_b(t) = z_{b0} - \frac{1}{2}\left\{1 + sin\left[\pi\left(\frac{t-T_i}{T_d} - \frac{1}{2}\right)\right]\right\}(z_{b0} - z_{b,min})$$

$$\text{if} \quad T_i \le t \le T_i + T_d \qquad (8)$$

C. Numerical domain and breach parameters

A 1m resolution digital terrain model was mapped on a triangular mesh with size ranging from 3m to 85m. The total number of elements is around 220 000. The time step was 1s. The upstream measured inflow discharge was imposed at the first liquid boundary. Recorded downstream water level limnigram at Po River was imposed at boundaries 2 and 3 (Figure 4). The Strickler coefficient was set to 20m$^{1/3}$s^{-1}, as suggested by Dazzi et al. [17]. The three observed breaches were combined in one breach to simplify parametrization and modelling approach, which differs from the three observed.

For each empirical law, the breach initiation time T_i was set at December 12th 5:30 am, when overtopping started in field. The final breach width B_f = 160m was selected as a stopping criterion to match observations, except for Verheij and Van der Knaap [15] equation where the difference in hydraulic head stops the breach widening. According to observation, the final breach width was reached in around 4h, thus an erosion rate of 40m/h was chosen when using the linear time widening equation (Eq. 2). However, because of uncertainties on total breaching duration, two additional erosion rates were tested, namely E_w = 30m/h and 60m/h. Duration of 23h was taken for Verheij (2002) [13] and Verheij and Van der Knaap [15] formulas. This duration corresponds to the time when the embankment toe is dry using the model with no breach. Using the Verheij and Van der Knaap [15] formula, we used u_c = 0.5m/s, f_1 =1.3 and f_2 = 0.04 (default values by Verheij and Van der Knaap [13]). A total breach expansion duration of 4h was taken for Froehlich's [16] equation to match observation. A default initial breach width of 1.5m was used in all simulations.

An additional linear model was used to represent the three simultaneous breaches. Using a widening rate of 12.5m/h for each breach, the total summed breach width of 150m was reached in 4h. The remaining 10m accounts for the gaps between breaches. Table I presents the different parameters used for each simulation.

Table I Parameters selected for different empirical models

Model	E_w	B_f	T_d	B_0	T_f	z_{bmin}	other
Instantaneous	∞	160	0	X	X	30	X
Linear 30 m/h	30	160	0.40	1.5	X	30	X
Linear 40 m/h	40	160	0.40	1.5	X	30	X
Linear 60 m/h	60	160	0.40	1.5	X	30	X
Three breaches - Linear 12.5 m/h	12.5	150	0.40	1.5	X	30	X
USBR [11]	91	160	0.40	1.5	X	30	X
Von Thun and Gillette [12]	$4h_w$	160	0.40	1.5	X	30	X
Verheij [13]	X	X	0.40	1.5	23	30	X
Verheij and Van der Knaap [15]	X	X	0.40	1.5	23	30	f_1:1.3 f_2:0.04 u_c:0.5
Froehlich [16]	X	160	0.40	1.5	4	30	X

Figure 4. Representation of the computational domain mesh and liquid boundaries

3) RESULTS AND DISCUSSION

The first numerical test was performed without the use of the breach module, which allowed us to verify that TELEMAC-2D model was able to reproduce the location of the initial overtopping occurring in the observed breached area (Figure 5). Here below we present and discuss the numerical results with the levee breaching. It can be observed that the water surface elevation overtops the levee crest at a location comparable to the observed case.

A. Breach expansion

Breach width evolution is displayed for each model in Figure 6. Of particular interest, Verheij [13] and Verheij and Van der Knaap [15] equations yield different results, compared to other laws. The widening is slow and the observed final breach of around 160m is not reached. The Froehlich [16] law provides similar trend as linear laws. The Von Thun and Gillette [12] equation reached the maximum breach width in around 9h with a linear trend. This suggest that the water depth above the minimal bottom elevation of the breach h_w was around 4.5m during the breaching initiation. For each model, the final breach width is of 162m. The imposed value of 160m is exceeded in some cases because of the polyline interpolation on the computational mesh.

B. Breach discharge

Figure 7 illustrates the computed breach discharge hydrographs, which are characterized by distinct patterns (one or two peak or gradual rise) depending on the empirical model. Table II presents the estimated total overflow volumes and maximum discharges.

All linear laws exhibit a similar increasing growth shape with one discernible peak occurring around 8:00 am. The instantaneous breaching provides an extremely sharp and instantaneous peak discharge (360m³/s), followed by a second peak around 8:00 am. The first peak is explained by the release of volumes contained by the dike before the breach. The second peak is matching the flood wave imposed by the upstream hydrograph. The linear widening rate of 60 m/h stands out with a higher peak discharge of 260m³/s, surpassing the counterparts with breaching rates of 40 m/h and 30 m/h (i.e. 245 and 224m³/s, respectively), whereas the USBR [11] linear law yields an earlier peak at 7:00 am, yet with a discharge lower than 257m³/s. The results by Froehlich's [16] model are comparable to the linear model with a rate of 60m/h. Using three breaches combined with a linear widening law displayed a similar peak as that given by the 60m/h linear model. Using the Von Thun and Gillette [17] model, the breach discharge exhibits a sharper and delayed increase, culminating in a peak discharge at 8:00 am. However, the peak discharge, 200m³/s, was lower than that of the linear and Froehlich [16] equations. The Verheij [13] and Verheij and Van der Knaap [15] equations yielded a delayed and gradual rise in breach discharge compared to the other models. Despite having a higher widening rate in the latter phase than the Verheij and Van der Knaap [15] model (Figure 6), the breach discharge evolution was similar with Verheij's [13] equation.

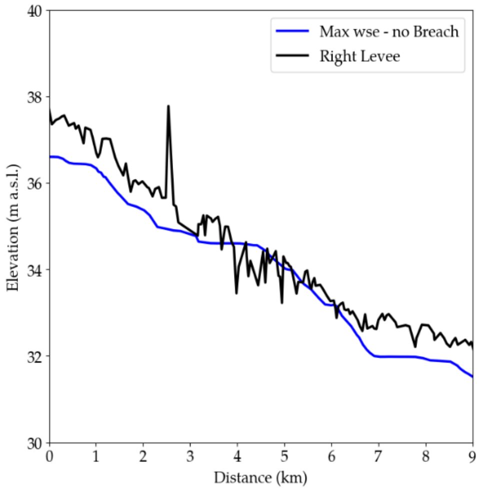

Figure 5. Longitudinal profile of right levee crest elevation and maximum free water surface elevation (wse) shown without considering levee breaching. Origine of distance is at Sorbolo gauge station

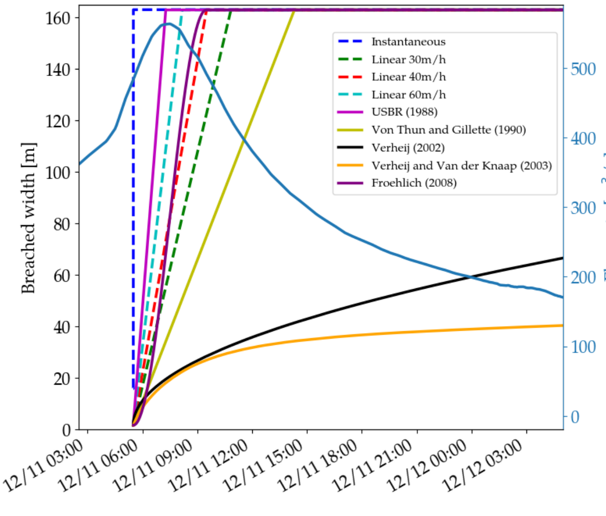

Figure 6. Computed breach widenning. Imposed flood discharge is also shown

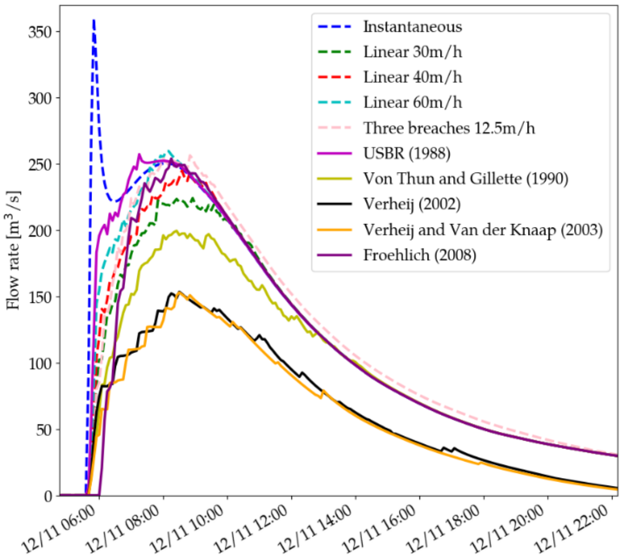

Figure 7. Breach discharge time evolution

Table II Estimated total overflow volumes and maximum discharges for different empirical models

Model	**Peak discharge [m^3/s]**	**Total overflow volume [Mm^3]**
Instantaneous	360	8.0
Linear 30 m/h	224	7.1
Linear 40 m/h	245	7.4
Linear 60 m/h	260	7.6
Three breaches - Linear 12.5 m/h	256	7.8
USBR [11]	257	7.8
Von Thun and Gillette [12]	200	6.6
Verheij [13]	154	4.1
Verheij and Van der Knaap [15]	153	3.9
Froehlich [16]	254	7.2

C. *Floodmaps*

The observed flood extent is depicted in Figure 8, compared with computed maximum water depths reached on December 12th at 7:00 am. Instantaneous model, linear models (with one or three breaches), and the USBR [11] formula demonstrated similar trends in flood extents. For sake of brevity, only instantaneous and 60 m/h linear model are presented here. These models and the Froehlich model successfully reproduce the flood extent, although there were instances of flood extent being broader than observed in the southern and northwestern region and slightly narrower downstream. This suggests that these models captured the main inundated areas but may require refinement in accounting for localized variations. On the contrary, the Verheij [13] model and Verheij and Van der Knaap [15] model exhibit a different pattern. Flood areas were not generated in regions where observations indicated no inundation, demonstrating their capacity to avoid false positives. Nevertheless, some underestimation of the flooded surface was observed both upstream and downstream from the breach location.

Regarding the overflow volume, results indicate that all laws fail in reproducing the observed volume (20Mm^3). Again, Verheij [13] and Verheij and Van der Knaap [15] formulas rank as the worst ones. Those results can be explained by the uncertainties on multiple breach modelling parameters, such as breach minimum elevation, width of levee considered as erodible and physical breach model parameters. In a previous study considering a wider erodible area and lower minimum breaching elevation, the simulated volume could reach the value of 15Mm^3 with linear breach expansion model [18].

4) CONCLUSION

The integration of simplified breach growth laws with the TELEMAC-2D solver was employed to simulate and analyse the severe flood breach that occurred along the Enza River in Italy in December 2017. Although most of laws are simple, different results were obtained. The present study underscored the complexity of accurately modelling flood events caused by levee breaching, where a delicate balance between breach initiation, expansion, and discharge dynamics needs to be captured.

REFERENCES

[1] M. West, M. Morris, and M. Hassan, “A guide to breach prediction,” HRPP770, HR Wallingford, 2018.

[2] ASCE/EWRI Task Committee on Dam/Levee Breaching, “Earthen embankment breaching,” Journal of Hydraulic Engineering, 2011.

[3] J.R. Courivaud, “Rupture des barrages en remblai par surverse. Synthèse de l’état de l’art sur la compréhension des processus physiques et sur la modélisation,” Rapport EDF, HP-76/2002/002/B.t, 2003.

[4] I. Rifai, “Overtopping induced fluvial dike failure,” PhD thesis, Paris-Est University, 2018.

[5] M. Antonelli, and G. Della Vecchia, “Civil and environmental engineering for the sustainable development goals emerging issues,” SpringerBriefs in Applied Sciences and Technology, 2022.

[6] S. Dazzi, F. Aureli, R. Vacondio, and P. Mignosa, “Simulation of the December 2017 flood on the Enza River using a 2D SWE code coupled with a levee breach erosion model,” Proceedings of the 5th IAHR Europe Congress - New Challenges in Hydraulic Research and Engineering, 2018.

[7] G. Di Baldassarre, A. Castellarin, and A. Brath, “Probability weighted hazard maps for comparing different flood risk management strategies: a case study,” Natural Hazards, Special Issue on Modeling and simulation of dangerous phenomena, and innovative techniques for hazard mapping and mitigation, 50(3), 479–496, 2009.

[8] G. Di Baldassarre, A. Castellarin, and A. Brath, “Analysis of the effects of levee heightening on flood propagation: example of the River Po, Italy,” Hydrological Sciences Journal, 2009.

[9] M. Morris, M. Hassan, A. Kortenhaus, and P. Visser, “Breaching processes: A state of the art review,” FLOOD site Project Report, T06-06-03, HR Wallingford, U. K., 2009.

[10] I. Rifai, S. Erpicum, P. Archambeau, D. Violeau, M. Pirotton, K. El Kadi Abderrezzak, and B. Dewals, “Overtopping induced failure of noncohesive, homogeneous fluvial dikes,” Water Resources Research, pages 3373–3386, 2017.

[11] USBR (United States Bureau of Reclamation), “Downstream hazard classification guidelines,” ACER Technical Memorandum No. 11, United States Department of the Interior, 1988.

[12] J.L. Von Thun, and D.R. Gillette, “Guidance on breach parameters,” Internal Technical Memorandum, United States Bureau of Reclamation, Denver, Colorado, 1990.

[13] H. Verheij, “Time dependent breach development in cohesive material,” Internal Research Summary Report, Delft Hydraulics Laboratory, 2002.

[14] J. Danka, and L. Zhang, “Evaluation of empirical methods for estimating breaching parameters of dikes,” in Geotechnical Safety and Risk V, IOS Press, 2015.

[15] H. Verheij, and F. Van der Knaap, “Modification breach growth model in HIS-OM,” Technical report, WL | Delft Hydraulics, Delft, The Netherlands, 2003.

[16] D.C. Froehlich, “Embankment dam breach parameters and their uncertainties,” Journal of Hydraulic Engineering, 2008.

[17] S. Dazzi, R. Vacondio, and P. Mignosa, “Integration of a levee breach erosion model in a GPU-Accelerated 2D shallow water equations code,” Water Resources Research, 55(1), 682–702, 2019.

[18] Z. Amama, S.E. Bourban, J.R. Courivaud, M. Morris and K. El Kadi Abderrezzak, “Numerical modelling of flood due to levee breaching using TELEMAC2D: application to Enza River, Italy,” 4th Meeting of European Working Group on Overflow and Overtopping Erosion, Lyon, 2023.

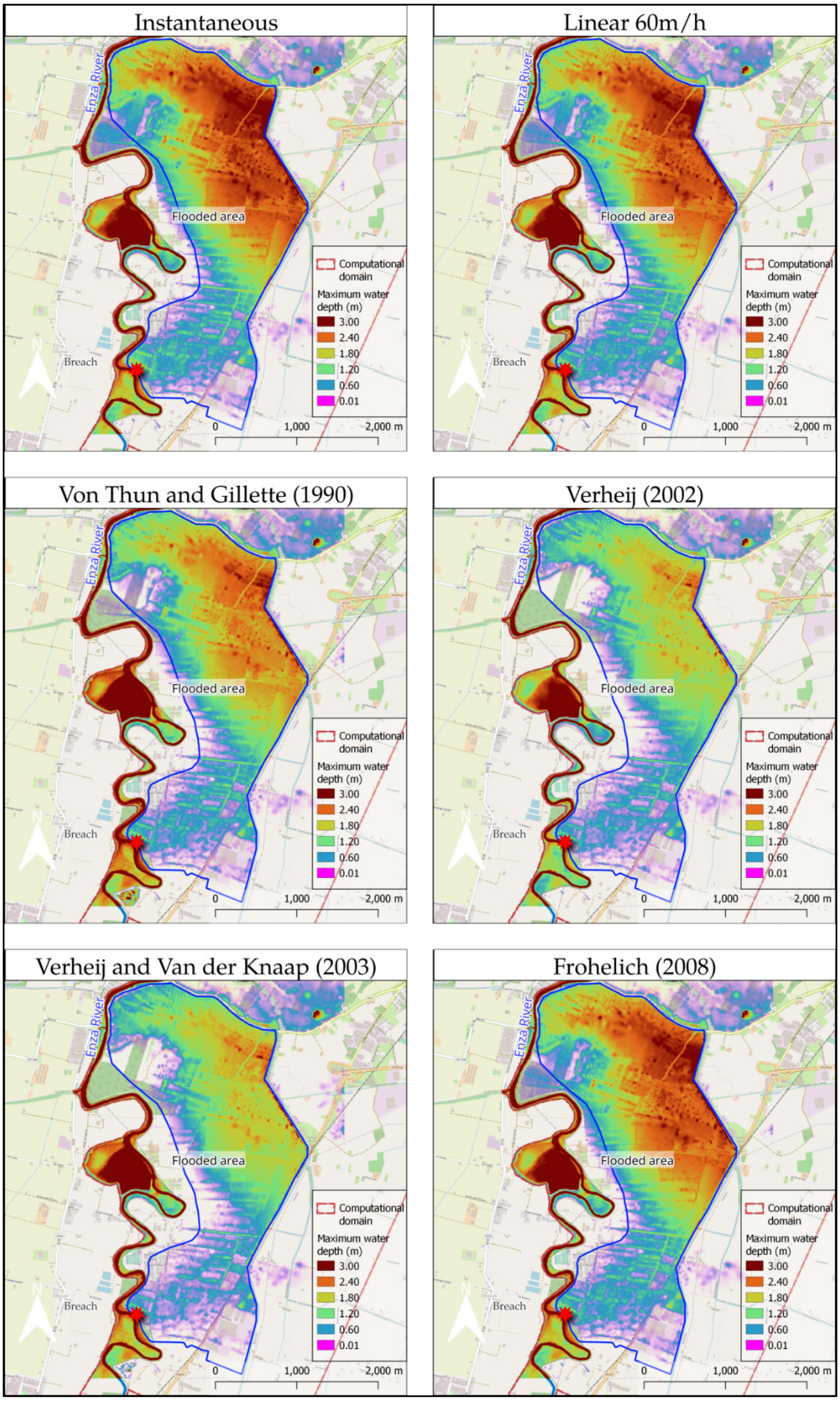

Figure 8. Simulated maximum water depths and observed flood extent (blue line)

Forensic study of the Tula flooding in 2021

Coral García-Govea[1], Victor Rosales-Sierra[2]
coralgg@hotmail.com, Mexico city
[1]: Universidad Autónoma Metropolitana
[2]: Instituto Mexicano del Petróleo

***Abstract* – In September 2021 the city of Tula was flooded by the renewed drainage system of Mexico City. After the event, it was not clear how much water was discharged from the drainage system of Mexico City and how much water was discharged by the runoff of the surrounding sub-basins. A numerical model based on TELEMAC-2D will be used to compute different scenarios of runoff and drainage discharge. The results will be compared to the water depth levels found at the site. This work will define the amount of each discharge and show the potential risk of the renewed drainage system of Mexico City.**

Keywords: Drainage, Mexico City, Flooding, Tula, Valle del Mezquital, Telemac-2D, TEO, Hydrorivers, Inverse Distance Weighting Method, Culverts, Curve Number.

I. INTRODUCTION

Mexico City has been built on the soil of a system of drained lakes. The ancient city, named “Tenochtitlan”, was in harmony with the lakes before the Spanish conquest. The Mexica empire flourished thanks to a sophisticated agricultural system named “Chinampas”. That system consisted of islands build of wood and mud in the water. The result was an increase of production of corn and vegetables that strengthened the “Mexica” empire. There was a problem with salt contamination coming from the northeastern side of the Texcoco lake into the western side where the centre of the city was built. Emperors “Moctezuma” and “Axayacatl” solved the problem with a long dike that is considered a masterpiece of Mesoamerican hydraulic engineering. The extension of the system of lakes is shown in Figure 1.

After the Spanish conquest, the city of “Tenochtitlan” took the name of “Nueva España”. Being one of the most important cities of the Spanish empire, it started to grow. The lake became an obstacle. The solution was to drain the lake. Between 1600 to 1800, a tunnel and a channel named “Tajo de Nochistongo” were built to conduct the water out of the endoreic basin. In the beginning of the XX century, a new channel named “Gran Canal de Desagüe” connected to the “Valle del Mezquital” basin though “Tequisquiac” was built to improve drainage. At that time a new agricultural paradise appeared at the “Valle del Mezquital” basin. Hundreds of acres of land were fed with highly nutritious but untreated wastewater from Mexico City. More on this subject is found in [1].

Around 1970 the “Gran Canal de Desagüe” channel collapsed because of the sinking of Mexico City. The flow was reduced from 80 m^3/s to 15 m^3/s. The problem arose because most of the water for consumption for the growing population came from the aquifer. The channels that conducted the water to the “Valle del Mezquital” basin changed to uphill slope.

Figure 1. Map of Mexico Tenochtitlan in 1529. The white star represents the location of the center of today´s Mexico City (ancient “Tenochtitlan”) in the west side of the big lake “Texcoco”. The black line represents the dike that divided the salty waters coming from the northwestern lakes and the fresh waters of the southern lakes. Source: https://commons.wikimedia.org/w/index.php?curid=9263087

The new solution was a deep drainage system that was finished in 1975. It efficiently conducted the water to the outside of Mexico City. The system consisted of two tunnels. One tunnel named “Tunel Emisor Poniente” (TEP) that conducted an approximate flow of 30 m3/s of the water from the western sub-basins to the “Tajo de Nochistongo” channel which was connected to the Tula River. The second Tunnel named “Tunel Emisor Central” (TEC) conducted the main drainage of about 200 m3/s to the Tula River. From that time on, the newly desiccated land got urbanized not only in Mexico City but in neighboring places. That caused an increase in population and an increase in urbanized areas. At the end of the XX century, the deep drainage system started to decrease in its efficiency and some improvements in the drainage system were applied, but it was insufficient. In 2014 the total capacity of discharge from Mexico City was around 195 m3/s but the required discharge was 345 m3/s according to [2]. At that time, the lowlands in the east of the city were being frequently flooded. At the end of 2020 a new complementary drainage tunnel named "Tunel Emisor Oriente" (TEO) started to operate increasing the capacity of the drainage to 345 m3/s. Most of that water is offloaded to the Tula River in the "Valle del Mezquital" basin.

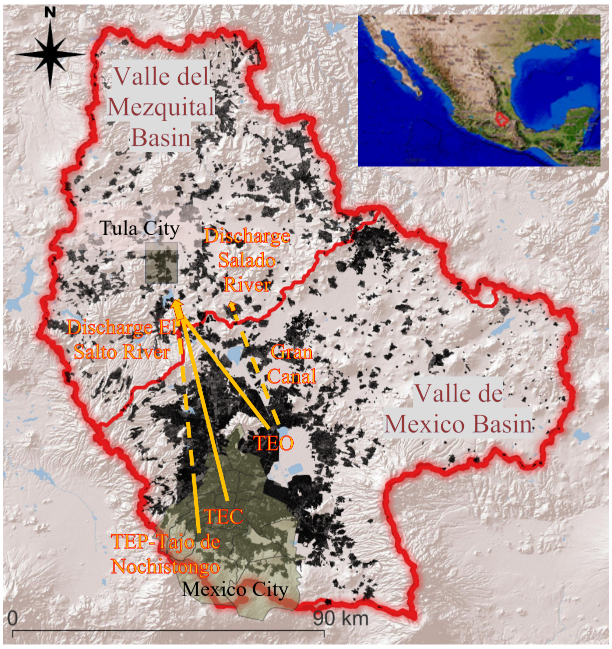

Figure 2. Map of the "Valle de Mexico" and the "Valle del Mezquital" basins. The thick red line represents the contour of both basins and the thin red line the division of the basins. The black spots represent urban areas. The continuous yellow lines represent the tunnel drainage system: "Tunel Emisor Poniente", "Tunel Emisor Central", "Tunel Emisor Oriente". The dashed yellow lines represent open channels: "Tajo de Nochistongo" and "Gran Canal de Desagüe". The yellow arrows show the approximate points of discharge.

The area of the study is located inside the geographical coordinates -99.69,19.04 and -98.18,20.27 (longitude and latitude). It consists of two of the higher basins of the Panuco River that discharge into the Gulf of Mexico. The "Valle de Mexico" is a natural endoreic basin. The "Valle del Mezquital" is an exoreic basin. An artificial connection is achieved by a drainage system of three main deep subterranean tunnels and two main channels: "Tunel Emisor Poniente", "Tunel Emisor Central", "Tunel Emisor Oriente", the "Tajo de Nochistongo" channel that is the continuation of TEP and the "Gran Canal de Desagüe" channel. Most of the discharge points are located close together at the "El Salto" River upstream from Tula River. The "Gran Canal de desagüe" channel discharges into another river; "Salado", that joins the Tula River far downstream in the north of the basin. See Figure 2.

In September 2021, the renewed drainage system of Mexico City was tested by a period of heavy rain. The system proved to be efficient in avoiding flooding in Mexico City, but the volume of water which was sent to the "Valle del Mezquital" basin generated a new problem of flooding in the city of Tula, downstream from the Mexico City deep drainage exit. There is no official information about the amount of discharge, there are only newspaper reports mentioning that the water authority determined that the flooding was caused by a flow of around 178 m^3/s from the Mexico City drainage system plus a local flow of 322 m^3/s. The local discharges seem to be very high compared to Mexico City discharge. The "Valle del Mezquital" basin is a very dry zone; therefore, its runoff is much inferior to that of the "Valle de Mexico" basin.

The computation of the runoff is complex. One way to have a realistic computation is by using a robust model that considers both rain and runoff in a detailed and deterministic manner. Simulating the drainage from the "Valle de Mexico" basin to the "Valle del Mezquital" basin in a realistic way is another challenge. To obtain a precipitation model is difficult because rain distribution is not even throughout the large areas studied. These complexities are addressed in this work.

II. METHODOLOGY

The methodology consists of three main parts. First, the creation of the Model with complex river Networks is solved using sub-meshes instead of channel meshes. Second, the problems of the rain distribution and the runoff simulation are solved using the Inverted Distance Method for the rain distribution and the Curve Number method for the runoff. Third, the simulation of the drainage system of Mexico City is solved by using the method of "tubes and culverts" available in the code Telemac2D. The methods available in Telemac-2D are described in the technical documents [3] and [11].

A. Mesh setup with complex river networks

The model was created using the elevation data from the Shuttle Radar Topography Mission (SRTM) of NASA, the details of the data are found in [4], plus a method used to incorporate the riverbeds. This method is necessary in order to solve the problem of flow continuity in the riverbeds of the model.

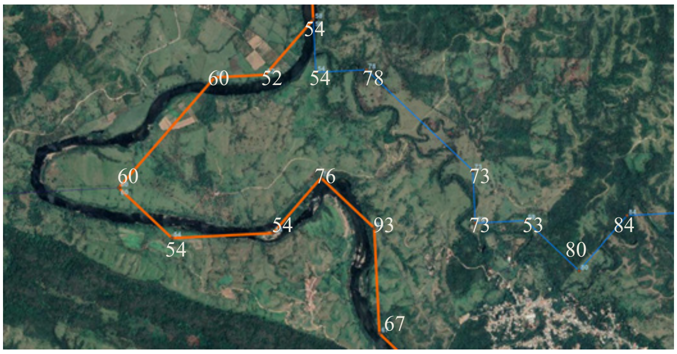

Figure 3. Problem of flow continuity on riverbeds. The orange line represents a riverbed and the numbers represent the elevation on each vertex. The rivers flow from south to north. The problem is that the elevations, taken from the raster image, are not always descendent to guarantee a downstream flow.

The problem of continuity arises from the procedures of "river network extraction" and "catchment delimitation" methods. The methods create river networks in the form of lines that are limited by the resolution of the topographic raster images used for the extraction as shown in Figure 3.

The best way to create riverbeds on the model is with the Channel Mesher method available with the Blue Kenue software. The details of the method are available in [5]. Each channel must be created one by one, and the topography must be corrected in order to maintain flow continuity. Another way is to create a refined sub-mesh around the full river network with the topography corrected for continuity. This method is useful when the river network has many branches.

The delimited basins and river network were obtained from the Hydrorivers database. The method used by Hydrorivers is described in [4]. Hydrorivers delimits the basins at 12 levels of different sizes and creates a river network for each basin in the world.

There are three networks in the domain. The “Xochimilco” Network is located in the south of the “Valle de Mexico” basin. At its lowest point, there is a permanent lake and a channel system named “Xochimilco”. The “Texcoco” Network is located in the north of the “Valle de Mexico” basin. The western part of the network flows over Mexico City. The eastern part of this network flows to the north of Mexico City and then turns southward to its lowest point. At that point, near the old airport of Mexico City, there is a permanent lake named “Nabor Carrillo”. The Tula Network flows from south to north; its exit point is at the artificial lake created by the “Zimapan” dam and then its flow goes to the Panuco River. The domain description is shown in Figure 4.

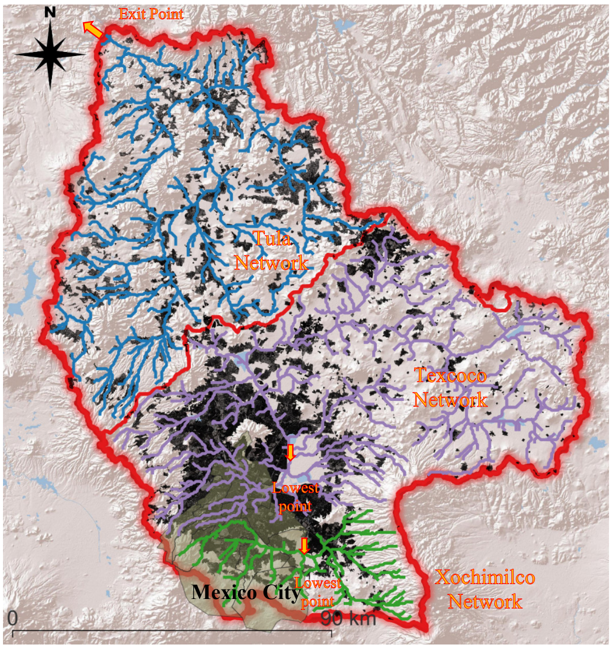

Figure 4. River Networks in the “Valle de Mexico” and the “Valle del Mezquital” basins. The green line represents the “Xochimilco” Network with its lowest point in “Xochimilco” lake. The purple line represents the “Texcoco” Network with its lowest point in “Nabor Carillo” Lake near the old airport. The blue line represents the “Tula” Network with its exit point to the Panuco River.

Building a model with three river networks using the “Channel Mesher” method is cumbersome. The solution is to convert each river network from lines to a unique polygon. The software QGIS was used for this purpose. QGIS methods and software are described in [6]. The polygon is imported to the “Blue Kenue” software and is used as an “outline” to delimit the domain by containing only the river network. This is meshed as a grid of finite elements. Each grid of the three river networks is used as a sub mesh in a full domain model of the two basins. The element size of the sub meshes is around 100m and the size of the elements of the full domain model is 500m. The meshing arrangement is shown in Figure 5.

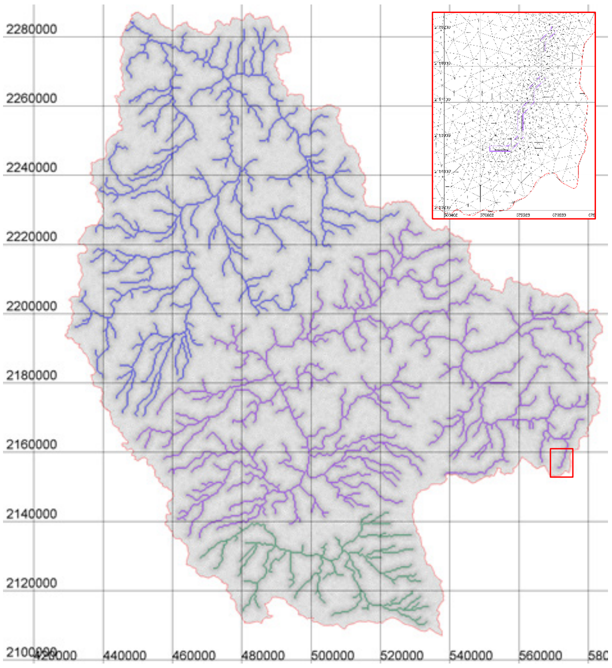

Figure 5. Finite elements model mesh. The size of the elements is between 100 m to 500 m. The small elements are located inside the river networks. The continuous coloured lines are superposed on the grey mesh to visualize the river networks. A detail of the mesh is shown in the red rectangle.

B. Rain distribution and runoff setup

The rain in the model needs to be distributed in space to get a more realistic flow around the domain. The rain distribution model setup is achieved by programming the Inverse Distance Method. This method computes the rain in each node of the grid by interpolating the known rain values of specific stations. On the other hand, the rain data was obtained from ERA5 database [7]. The resolution of the ERA5 grid accounts for approximately 10 stations inside the Telemac2d domain. For the interpolation, the programmed subroutine takes 10 points as local stations. The data from ERA5 is shown in Figure 6.

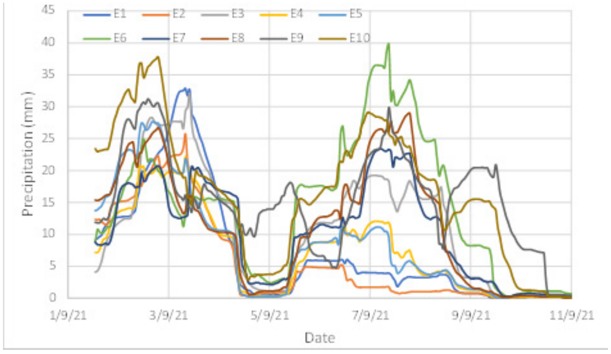

Figure 6. Rain variation the first 10 days of September 2021. The colours represent different rain points obtained from ERA5 precipitation data.

The method of interpolation computes the inverse distance, d_i, of each point of the grid to each rain station to estimate a weighting factor w_i. The interpolated precipitation of the point is obtained by the addition of the product of the precipitation of each station, P_i, by its weighting factor, w_i, at each time step. The formulas (1) and (2) were programmed into subroutine "runoff_scs_cn.f" of Telemac2d using a matrix of 10 stations. A similar method was validated by [8] for Taiwan.

$$w_i = \frac{(\frac{1}{d_i})}{\sum_{i=1}^{N}(\frac{1}{d_i})} \tag{1}$$

$$P = \sum_{i=1}^{N} w_i P_i \tag{2}$$

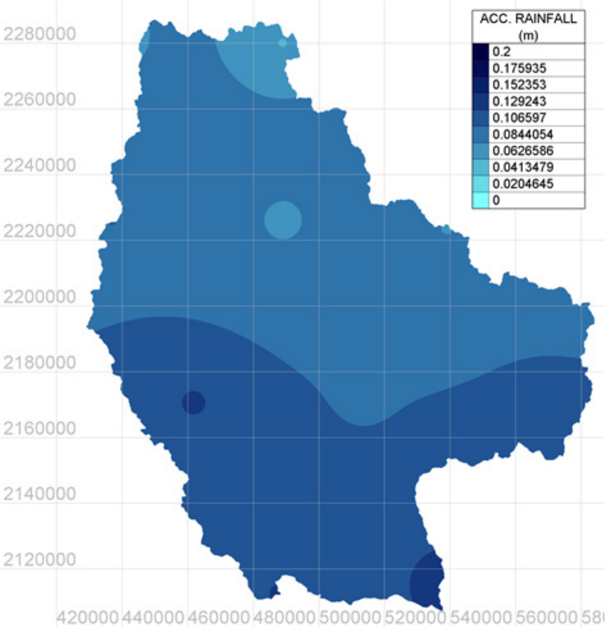

Figure 7. Interpolated rain accumulation after 9 days.

The resulting distributed rain is shown in Figure 7 for a simulation after 9 days of precipitation with ERA5 data.

The model is set up using the subroutines of the code for the Runoff Curve Number method proposed by the Service of Soils Conservation in the United States. This method has been developed in high latitudes corresponding to US territories. When used in tropical territories with lower latitudes, the method can present inconsistencies. To solve this problem Hernández-Jimenez [9] generated the Curve Numbers in Mexican territories using the method TR-55 of the USGS. The Curve Number was created by the adaptation of local Mexican soil, vegetation, and land use characteristics.

The Curve Number in the domain has a range of 50 to 99 as showed in Figure 8. The lower numbers correspond to the higher altitudes with strong vegetation in the south and west of the domain. The numbers above 80 correspond to urban and semiurban zones in the domain. The higher numbers are around water bodies.

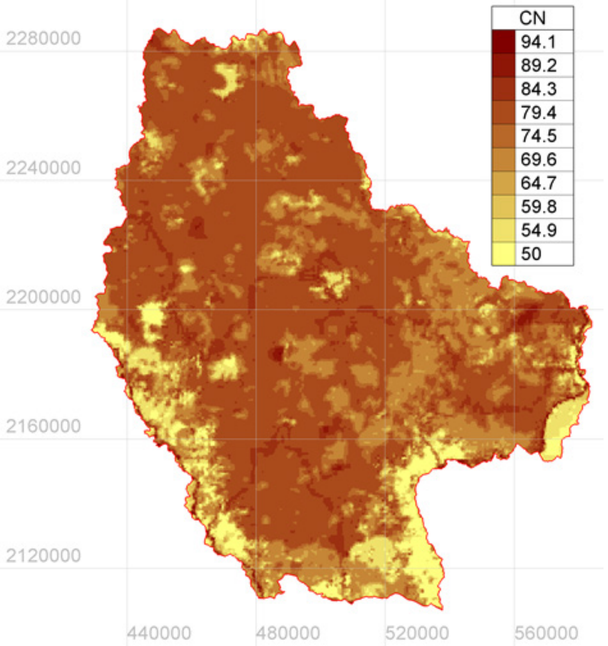

Figure 8. Distribution of the Curve Number in the domain. Source Hernández Juarez, 2014.

C. *Drainage setup*

The drainage system of Mexico City is one of the most complex in the world. Rain and wastewaters are mixed and discharged with little treatment to the "Valle del Mezquital" basin.

The setup of the model is simplified using 6 tubes for runoff and two points for discharge of wastewater. The runoff goes into the inlets of the tubes in rain events. The wastewater is a constant discharge product of human use considered as source points in the model. One part of the water for human consumption is imported from outside of the basin at about 20 m^3/s and the other part is pumped out from the aquifer at about 70 m^3/s. After use, the wastewater is sent to the outside. As the water for consumption is imported and pumped, it can be separated from the runoff. Then in the model this amount of water is injected directly into two discharge points: one for the discharge of the "Gran canal de desagüe" channel with 30 m^3/s into the Salado River and another as part of the drainage tunnel system with 60 m^3/s into the Tula River.

The arrangement of the simplified drainage system is shown in Figure 9. The red lines join the inlets and outlets of the tubes. The list of points and its corresponding elements of the drainage system are presented in Table I.

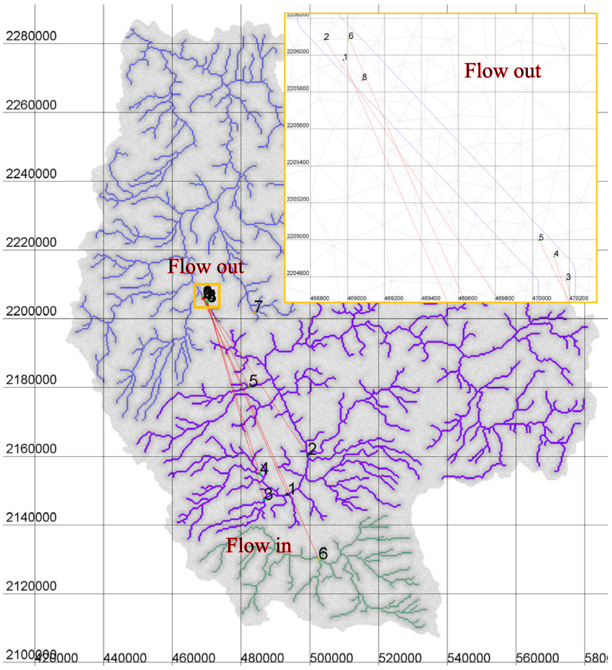

Figure 9. Location of the drainage points from Mexico City to the “Valle del Mezquital” basin. Six red lines represent the simplified tubes of drainage with input in the south and output in the north. Two more points, 7 and 8, represent point sources of wastewater.

Table I Elements of the Drainage system of Mexico City

N	*Name*	*Drainage element*
1	Tunel Emisor Central TEC1	Tube (in – out)
2	Tunel Emisor Oriente TEO	Tube (in – out)
3	Tunel Emisor Poniente TEP1	Tube (in – out)
4	Tunel Emisor Poniente TEP2	Tube (in – out)
5	Tunel Emisor Poniente TEP3	Tube (in – out)
6	Tunel Emisor Central TEC2	Tube (in – out)
7	Discharge of Wastewater 30m^3/s	Source (out)
8	Discharge of Wastewater 60m^3/s	Source (out)

The runoff is treated by the Curve Number subroutine in Telemac2D. Part of the rain is evaporated or filtrated, and the rest is converted into runoff. This amount of water flows to the river networks and then to its lowest points. To simulate the drainage of Mexico City, 6 points representing the tube inlets are inside the “Valle de Mexico” basin, the location is adapted from [10] in a simplified manner. All the tubes have an outlet in the “Valle del Mezquital” basin around the site of the main discharge known as “El Portal” on the Tula River.

Table II Main parameters of the method of culverts and tubes in Telemac2D

N	*LRG*	*HAUT1*	*LBUS*	*Z1*	*Z2*	*LENGTH*
1	5.50	5.50	180.56	2229.18	2122.04	62067.22
2	6.00	6.00	146.49	2228.20	2118.27	54932.82
3	2.25	2.25	425.41	2236.00	2172.74	59823.89
4	2.25	2.25	372.33	2240.00	2170.22	52358.29
5	2.25	2.25	196.38	2251.00	2166.87	27615.48
6	2.25	2.25	591.13	2229.00	2122.29	83128.06

The method of culverts and tubes in Telemac2D manual [11] was verified by the results of a hydraulic analysis made by [2]. The main parameter to adapt the method of culverts into tubes was the Loss Friction parameter for long tubes represented in Telemac2D by the variable *LBUS*. Table II presents the main parameters used in the model.

$$Q = S_{12}\left(\frac{2g(Z1-Z2)}{CS_2+CE_1+LBUS}\right) \tag{3}$$

$$LBUS = \lambda\frac{LENGTH}{HAUT1} \tag{4}$$

The discharge, Q, is obtained according to [11] by using formula (3). The gravitational acceleration constant is represented by g. Some of the parameters for the tubes were obtained from the physical elevations of the terrain, $Z1$, $Z2$, and the distance from the inlet and outlet, $LENGTH$. The parameter of the crossing area, S_{12}, was obtained from the physical diameter of the tunnel $HAUT1$. The other parameters are empirical representations of the combined friction losses CE_1, CS_2, $LBUS$. The friction coefficients in the inlet and outlet of the tube, CE_1 and CS_2, can take values from 0 to 1 and for long tubes these coefficients are negligible compared to $LBUS$. The Loss Friction parameter $LBUS$, formula (4), was derived from the geometrical characteristics of the tunnel and the friction along the walls represented by the Manning Friction coefficient $\lambda = 0.016$ reported by [2].

III. STUDY CASES

The main case of study is to compute in a more realistic manner, the flow during September 2021 that caused the flooding in Tula City. The idea is to estimate with more certitude the discharges from Mexico City and the local runoff. A second case is the analysis of the role of the new element of the drainage system TEO. A third case is a simulation without the drainage system. This last case serves to visualize the increase of the flow in Tula caused by the runoff from Mexico City conducted by the drainage system versus the local runoff. Table III shows the drainage elements of the system operating in each study case.

Table III Simulation Cases for Analisys

Drainage element	*Case 1*	*Case 2*	*Case 3*
1	X	X	
2	X		
3	X	X	
4	X	X	
5	X	X	
6	X	X	
7	X	X	X
8	X	X	X

RESULTS

The results of the simulation show the computed runoff by applying the method of the SCS Curve Number. The results serve to compare the discharges in the Tula City with different cases of Mexico City drainage elements in operation. These results also distinguish the volume of water from the drainage system coming from Mexico City versus the local runoff. Last of all, a result from a monitoring point in Tula shows the increase of the water depth that caused the flooding.

The computed accumulated runoff of the domain after 9 days of simulation is presented in Figure 10. The runoff is greater in places around Mexico City where the urban areas are denser. The result is compatible with the local Mexican data of the runoff coefficient published by INEGI [12]. This coefficient has values of +0.3 for dense urban areas, around +0.2 for rural semi urbanized areas and around +0.10 for vegetated areas.

A comparison of the resulting flooding area of the three cases of study is shown in Figure 11. The red areas represent the case without drainage runoff system (tubes), all the runoff goes to the lower zones of the Valley around the Mexico City's old airport. The yellow areas show the case without the TEO tunnel operating (this kind of flooding would be expected before 2020) there is an important area of buildings surrounding the airport that would be flooded. The blue areas represent the areas of flooding with the full system of drainage operating. The area is reduced to maintain Mexico City free of flooding. This is the actual case.

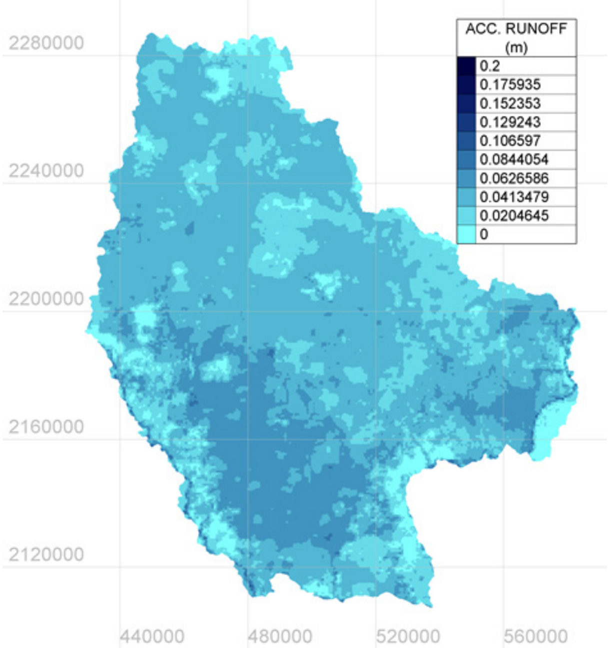

Figure 10. Resulting runoff after 9 days of simulation.

The resulting discharge in Tula is presented in Figure 12. The three lines represent the different cases of discharge including local runoff in Tula and the operation of different drainage elements from Mexico City. The continuous line represents the full operating system, the dashed line, the system before 2020 without TEO tunnel, and the dotted dashed line, only represents the discharge of the wastewater without runoff from Mexico City. The wastewater corresponds to the first 60m^3/s in the graph. From the dotted dashed line, we see that the local runoff peak discharge added 140 m^3/s to reach 200 m^3/s. The dashed line represents the runoff from Mexico City without TEO. The result is a peak of approximately 320 m^3/s. The continuous line represents the real event with the drainage system in full operation and a peak of nearly 400 m^3/s.

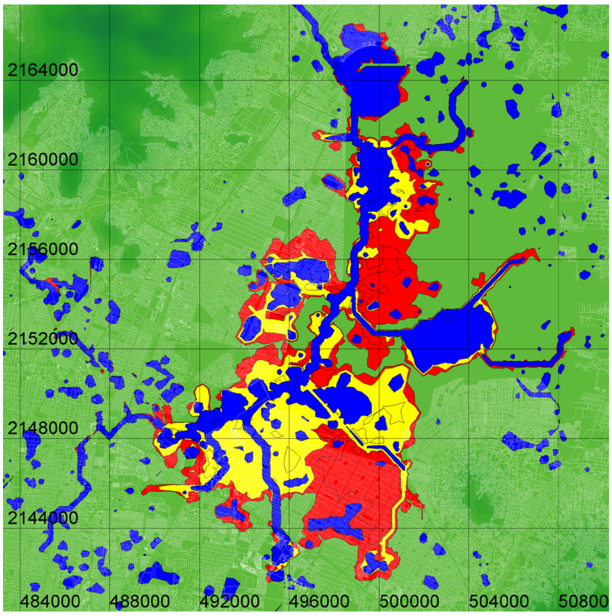

Figure 11. Resulting flooding in Mexico City after 9 days of simulation. The red colour represents the case without the drainage system, the yellow colour represents the case without the TEO tunnel and the blue colour represents the case with the full drainage system operating.

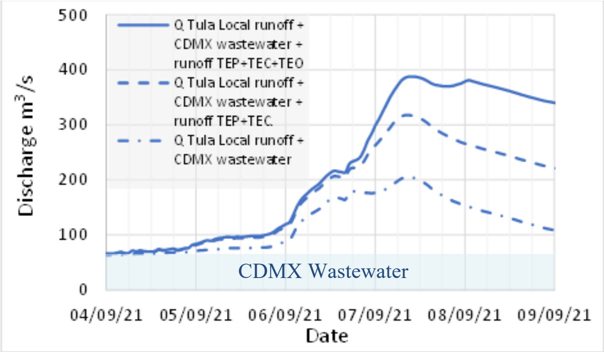

Figure 12. Discharge at Tula. The continuous line represents the real approximation considering the full drainage from Mexico City (CDMX), the dashed line represents an approximation without the TEO Tunnel which opened at the end of 2020, and the dashed dotted line represents an approximation without the tunnels TEP, TEC TEO where only the CDMX wastewater is considered.

The separated flows from each element of the fully operational drainage system of the Mexico City are shown in Figure 13. The continuous lines in red, yellow, and green represent the elements of the drainage system. The dashed line is the accumulated discharge of the three elements; and the blue continuous line represents the total discharge, including 60m^3/s of wastewater added to the runoff. As we can see, the amount of discharge in the event of September 2021 was around 280m^3/s. The total capacity of the system is 345m^3/s. The TEO tunnel discharged most of the water, an amount equivalent to 110 m^3/s.

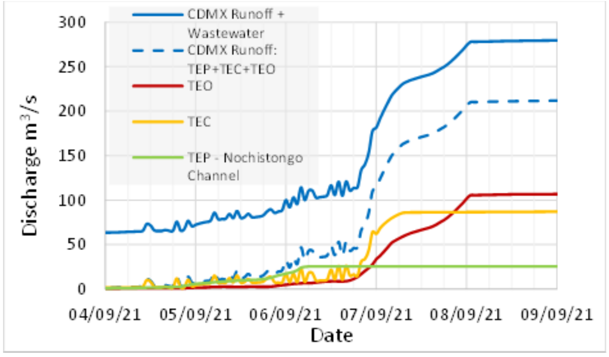

Figure 13. Discharge from CDMX into the Tula River. The green, yellow and red lines represent the runoff discharged from each drainage element coming from Mexico City. The dashed blue line represents the sum of these three elements. The continuous blue line represents the sum of the runoff plus the wastewater discharged from Mexico City, CDMX.

A comparison of the resulting flow from Mexico City with its drainage system fully operating versus the three local river runoffs is presented in Figure 14. The red line represents the full discharge from Mexico City including wastewater and the other continuous lines represent the local river discharges in the "Valle del Mezquital" basin. The blue dashed line represents the total discharge in Tula City. The addition of the discharges of the three local rivers is approximately 140 m^3/s, we can see that the peak of the local rivers is during the night of September 6th, but the peak of the Mexico City discharge is on the 8th of September.

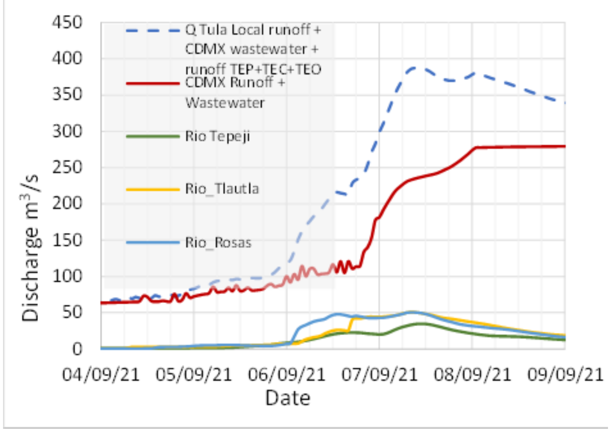

Figure 14. Comparison of discharges from CDMX and local rivers. The blue dashed line represents the total discharge at the Tula River from CDMX and the rivers from the "Valle del Mezquital" basin. The red line represents the discharge from CDMX. The continuous blue, yellow, and green lines represent the discharge of each of the three local rivers around Tula City.

The result of the water depth in the Tula City during the event of September 2021 is shown in Figure 15. The monitoring point has a water depth of around 1 m before the peak of the discharge and rises to almost 2 m after the peak. The difference from 1m to 2m caused an overtopping of the local fences of the river and flooded the city.

The result is consistent with the local inspection made on the 20th of September 2021 where water marks on the walls of the buildings showed depths of 1.4m to 2.0m in the places that were flooded.

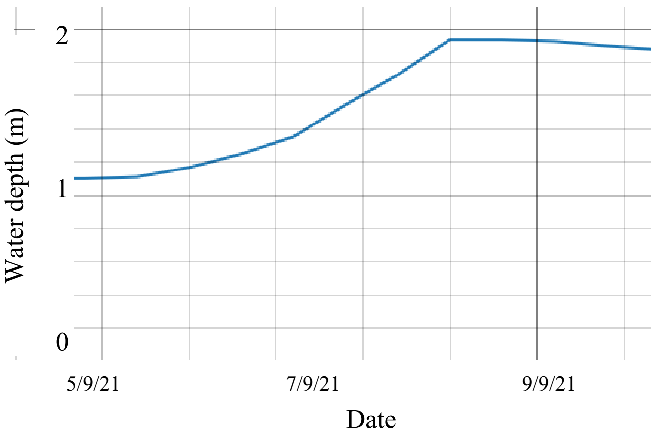

Figure 15. Water depth in Tula City. The blue line represents the variation of the water depth within the Tula River. Its value was approximately 1m up until the night of September 6th. After that time, water depth increased to 2m causing the city to flood.

IV. DISCUSSION

The mean annual rainfall in 24 hrs is defined with a value of between 40 mm to 65 mm according to [13]. Figure 6 shows the rainfall values accumulated in 24 hrs in each of the 10 stations from ERA5 during the event of September 2021. During this event, the total amount of rain in 24 hrs is barely 40mm; this means that the event in September 2021 is not exceptional and that more severe rain events can be expected in the future. Tula City is greatly at risk for more flooding.

The results show that the TEO tunnel, on its own, manages a runoff of around 110m^3/s. This is 30% of the total discharge at Tula. The operation of the TEO has an important impact on the increase of the risk of flooding in Tula City.

On the other hand, we can observe that the peaks of the local river discharges are lagged with respect to the peak of the Mexico City discharge. The peak of the flooding can grow depending on the lag of the peaks in future events. This parameter depends on rain distribution.

It is important to mention that the model has been simplified, then the results can have errors due to these simplifications. If the model was improved with a better definition of the drainage system and with measurements of a monitor system, the results could be more accurate.

Some parts of the model can be coarsely defined because the river network was created by an automatic process. This issue may influence the velocity of the flow producing errors in the peak time. For the future improvement of the model, it is important to increase detail in the river networks and have a more detailed drainage system.

Mexico City has one of the most complex drainage systems of the world. The city continues to grow, expanding the urban areas and increasing the pressure on water availability for consumption therefore increasing discharge to the Tula River. Tula City is expanding as well, reducing the course of the Tula River.

We consider that a new paradigm of development is needed to reduce the risk of flooding in Tula City. Planning for water retention in extreme scenarios is needed to better control the peaks of the discharges. This model shows a promising tool for studies of water control to reduce water discharge from Mexico City to Tula in the future. Some researchers are now discussing new ways of water management [14] to reduce the discharge from Mexico City as opposed to formal plans to increase the capacity of the flow of the Tula River [15].

ACKNOWLEDGEMENT

This work had no financial funding. Open software and open data were fundamental for this work.

Coral Garcia-Govea and Victor Rosales-Sierra thank the developers of open-source software: Open Telemac, Qgis, Blue Kenue. We also thank open data from Hydrorivers, Era5, INEGI, CONAGUA, NOAA. We appreciate the students and colleagues from our institutions who participated in the discussions and who showed interest in the topic of this article. Finally, we wish to thank the technical review given by Mr Thomas Brudy-Zepelius of the TUC conference and to Ms. Margo Fernandez Rogers for the proofreading of this article.

REFERENCES

[1] J. Legorreta, El agua y la Ciudad de México, De Tenochtitlán a la Megalópolis del siglo XXI, Universidad Autónima Metropilitana-Azcapotzalco, 2006.

[2] Hernandez-Rivas Edgar, Efectos hidráulicos causados por la rehablitación del Sistema de drebaje Profundo de la Cuidad de México, Facultad de Estudios superiores Unidad Aragón UNAM, Tesis 14 nov 2013.

[3] J-M. Hervouet. Hydrodynamics of free surface flows. Modelling with the finite element method. John Wiley & Sons, Ltd, Paris, 2007.

[4] Lehner, B., Verdin, K., Jarvis, A. New global hydrography derived from spaceborne elevation data. Eos, Transactions, AGU, 89(10): 93-94, 2008.

[5] CHC, Blue Kenue Reference Manual, Canadian Hydraulics Centre, September 2011.

[6] QGIS Development Team. QGIS Geographic Information System. Open Source Geospatial Foundation Project. http://qgis.osgeo.org". 2023

[7] Muñoz Sabater, J., ERA5-Land hourly data from 1950 to present. Copernicus Climate Change Service (C3S) Climate Data Store (CDS), 2019. (Accessed on 2-Jun-2023).

[8] Feng-Wen Chen and Chen-Wuing liu, “Estimation of the spatial rainfall distribution using inverse distance weighting (IDW) in the middle of Taiwan,” Paddy Water Environ, ISSN 1611-2490, Volume 10, Number 3, 2012.

[9] Hernández-Jimenez Félix, Obtención del Número de Cirva (NC) para la República Mexicana mediante el uso de Sistemas de Información Geográfica aplicando la metodología del TR-55, Facultad de ingeniería UNAM, Tesis 14 jan 2014.

[10] Abedrop L. S., Espinoza V., Collado J., Morales J. M., Hernández J., El gran reto del agua en la Cuidad de México, Sistema de guas de la Ciudad de México, 2012.

[11] Telemac-2D, Telemac-2D User Manual, Version v8p3 October 28, 2022

[12] Instituto Nacional de Estadística, Geografía e Informática, “Conjunto de datos vectoriales de la carta de Aguas superficiales. Escala 1:250 000. Serie I. Ciudad de México,” 1983. https://www.inegi.org.mx/temas/hidrologia/. (Accessed on 3-May-2023)

[13] Mora-Dominguez R., Arganis. M. L., Carrizosa E. Tormentas de diseño para cuencas del Valle de México, H2O Gestión del agua, SACMEX, Núm. 14 / April - June 2017

[14] Escobar-Niera C., Courty L., Laurent Courty, Centeno-Álvarez J. C., Pedrozo-Acuña A. “Las inundaciones en el Valle del Mezquital: un síntoma de los límiytes de la ingeniería convencional,” PERSPECTIVAS IMTA Nº. 36, 2021

[15] Comisión Nacional del Agua, Programa Hídrico Regional 2021-2024 Región Hidrológico-Administrativa XIII Aguas del Valle de México. 2021.

TELEMAC-2D upgrades: Rainfall spatialization and control sections

Nabil Hocini, Frédéric Pons
nabil.hocini@cerema.fr, Aix-en-Provence, FRANCE
CEREMA Méditerranée, Natural Hazards Department

Abstract – **Over the past 30 years, the frequency of natural disasters related to intense rainfall events has increased due to climate change. In this context, hydrodynamic rainfall-runoff modelling is of paramount importance to understand and predict the consequences of climate change. It is therefore essential to make advances in this field, particularly by improving runoff modelling through numerical solution of river hydrodynamics equations, as done by the TELEMAC-2D model. In this paper, we present a method for integrating spatialized rainfall into the calculation of net rainfall, using the SCS-CN model integrated in TELEMAC-2D. We have added a module that allows us to consider spatialized rainfall from radar rainfall products, such as the Antilope products from Météo France, satellite data or even rain gauge data if we have a dense network of rain gauges in the area to be modelled. This module assigns to each node of the TELEMAC-2D mesh the value of the nearest rain pixel. We have applied this method for rainfall-runoff hydrodynamic model of the Real Collobrier catchment in the Var, with a surface area of about 92 km². New variables are also added to the control section module of TELEMAC-2D.**

Keywords: Rainfall-runoff, spatial rainfall, hydrodynamics.

I. INTRODUCTION

Rainfall spatial variability effect on rainfall-runoff modelling has been studied in different climatic contexts, scales and for small and large catchments. Conclusions are contrasted on depend on a large range of parameters: basin hydrologic regime, topography, rainfall data resolution (rain gauge density or radar data resolution) [1]–[4]. A study made in France, shows a gain in hydrograph generation for study cases eastern France, but it shows no added value for western France study cases compared to basin averaged rainfall [5].

More recently, a multitude of studies using 2D hydrodynamic models for rainfall-runoff transfer, using different production functions (SCS CN, SCS CN modified, HORTON, GA…) [6]–[10]. Those studies show that it is possible to use hydrodynamic models as rainfall runoff models by adding production function to compute effective rainfall, but the main part of those studies use basin averaged rainfall with or without spatially distributed infiltration/runoff parameters. Notably, studies involving the TELEMAC-2D rainfall runoff module, and spatial rainfall have been introduced in recent studies [6], [11], [12].

This article proposes another approach to input spatial rainfall to TELEMAC-2D, with a simple file format, and a nearest neighbour interpolation. This new approach is usable for all production functions available in TELEMAC-2D. A new file format for control sections was developed and is presented in this paper, where height variables are added, which allows us to compare TELEMAC-2D output heights with height observed data (water depth sensors, higher water marks…).

These developments are tested, and the results are shown in the following sections of this article.

II. SPATIAL RAIONFALL MODULE PRESENTATION AND TEST CASE

A. *Rain fall spatial distribution in TELEMAC-2D*

The primary objective of this work is to introduce rainfall spatial distribution for the three production functions already supported in TELEMAC-2D : SCS-CN [13], HORTON [14] and Green & Ampt [15] .

Currently, TELEMAC-2D's calculation code uniformly integrates rainfall over the entire calculation area. However, due to the spatial heterogeneity of rainfall, even within small catchment areas, there is a need to incorporate spatially distributed rainfall data, especially from radar rainfall data (in Raster format). The main issue is to create a TELEMAC-2D format text file, that will allow us to assign rainfall values corresponding to spatial rainfall data to each mesh node in the computation domain at every time step. The proposed approach involves assigning a rainfall value, corresponding to the centroid of the nearest radar rainfall pixel.

As an initial step, we tested this approach for the SCS-CN method, which has been implemented in the subroutine "runoff_scs_cn.f". Currently, this subroutine includes an option "RAINDEF=3" for integrating a homogeneous rainfall hyetograph within a given calculation domain. To spatialize rainfall in TELEMAC-2D, we have introduced a fourth option with the keyword "RAINDEF=4". This new option builds upon the module used in "RAINDEF=3", but with the additional capability of injecting spatialized rainfall data into all mesh nodes.

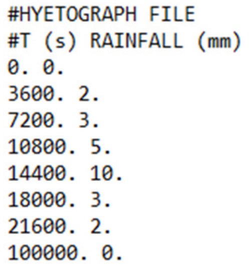

```
#HYETOGRAPH FILE
#T (s) RAINFALL (mm)
0. 0.
3600. 2.
7200. 3.
10800. 5.
14400. 10.
18000. 3.
21600. 2.
100000. 0.
```

Figure 1. Example of a homogeneous hyetograph in TELEMAC-2D

The current format for the rainfall data is based on a text file with two columns: one for time and the other for the cumulative rainfall between consecutive time steps (Figure 1).

The introduction of the "RAINDEF=4" option for spatial rainfall imply to create a new TELEMAC-2D format text file. This file contains x, y coordinates of rain pixels centroids, and the corresponding rain values, in a vector format for each rainfall time (Figure 2). This format offers the advantage of eliminating the need to reproject rainfall raster data into the mesh projection, as such reprojection often leads to anomalies. Instead, we simply convert the raster to a point-based representation and project these points onto the mesh projection (Figure 3). By using this approach, we can effectively integrate spatialized rainfall data into TELEMAC-2D, ensuring accurate representation and avoiding potential projection-related issues.

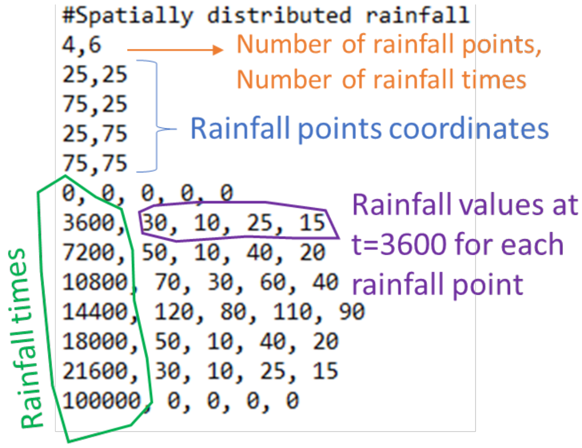

```
#Spatially distributed rainfall
4,6
25,25
75,25
25,75
75,75
0, 0, 0, 0, 0
3600, 30, 10, 25, 15
7200, 50, 10, 40, 20
10800, 70, 30, 60, 40
14400, 120, 80, 110, 90
18000, 50, 10, 40, 20
21600, 30, 10, 25, 15
100000, 0, 0, 0, 0
```

Figure 2. New proposed format for spatial rainfall integration in TELEMAC-2D rainfall-runoff module

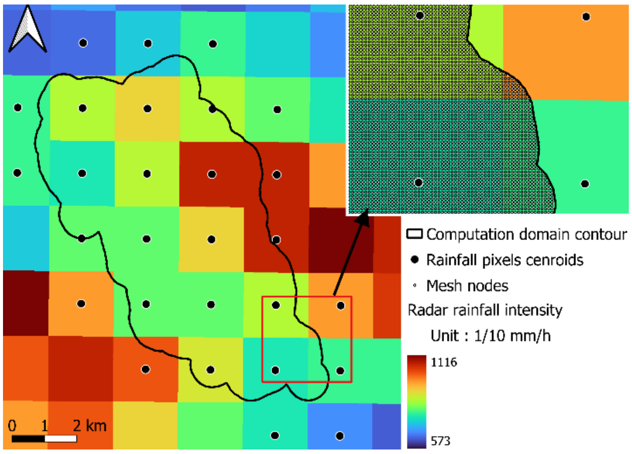

Figure 3. Explanatation of matching process between mesh nodes and rainfall centroids

The newly developed "RAINDEF=4" option can be used for the rain gauge data instead of radar rainfall data (particularly applicable when rain gauge density is high).

To facilitate the reading of the new file format, a dedicated subroutine called "rain_interpol.f" has been created, which consists of two main parts. In the first part, during the initial time step, the identifier of the rainfall point closest to each mesh node is calculated. This process results in the creation of a NPOIN vector size (representing the number of nodes), effectively assigning each node to the corresponding rainfall point identifier. In the second part of the subroutine, the rainfall data from the file is read, starting with the first-rainfall time (time 0 is not considered). The rain values at each node are then determined using the previously calculated vector of identifiers. This approach ensures that each node receives the appropriate rain value based on its associated rain point. To progress to the next rainfall time, the "rain_interpol" function is invoked whenever the rainfall time changes. This allows the function to read the appropriate rainfall line corresponding to the new time step. It's very important to note that the reading process is based on the rainfall time and not the calculation time step. To ensure accuracy, it is essential to have computation time steps smaller than the rain time steps, which is typically the case.

In summary, the "rain_interpol" function plays a crucial role in synchronizing the rainfall data with the calculation time steps. By calling this function whenever there is a change in the rainfall time, TELEMAC-2D can effectively use the corresponding rainfall values for accurate simulations.

B. Test cases

To verify the accuracy of the new routine, two discharge comparison tests are conducted between homogeneous and spatial rainfall inputs. These tests are conducted on the computational domain shown in Figure 3, with a geometry represented with a regular triangular mesh with 34771 nodes and a resolution of 10 meters. These tests involve the following scenarios:

- The same rainfall value is applied uniformly for both homogeneous rainfall and all spatial rainfall points. In this case, the curve number is set to 100, meaning no infiltration, and a Strickler friction coefficient of 15 $m^{1/3}/s$ is used.

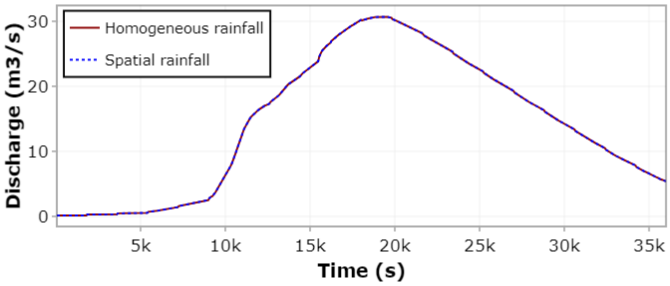

Figure 4. Discharge over time of spatial rainfall and homogeneous rainfall: same rainfall volume, same rainfall values for all mesh nodes, infiltration (CN=100)

- Different rainfall values are assigned to spatial rainfall pixels, ensuring that the total rainfall volume matches the value used in the homogeneous rainfall test. The curve number is again set to 100, and the Strickler friction coefficient remains 15 $m^{1/3}/s$.

Both tests are performed on a regular triangular mesh with a 10 m resolution. The mesh is automatically generated using Cartino2D [16], a tool developed at CEREMA for the automated creation of both regular and irregular meshes for TELEMAC-2D.

The primary objective of the first test is to validate that the flow discharges at the output remain identical between the two options as shown in Figure 4. For the second test, the aim is to verify that different results are obtained for the same volume of cumulative rainfall between homogeneous and spatial rain inputs (as shown in Figure 5). This comparison helps validate the correctness of the newly introduced "RAINDEF=4" option for spatial rainfall integration, confirming its ability to handle spatially and temporally varying rainfall values.

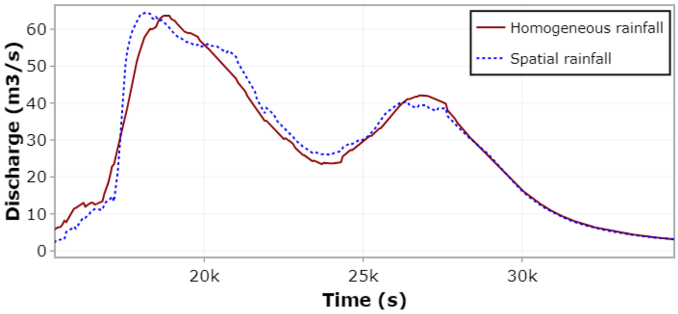

Figure 5. Discharge over time of spatial rainfall and homogeneous rainfall : same rainfall volume but different values in nodes for spatial rainfall part, no infiltration (CN=100)

In this specific example, the computation times for both the homogeneous and spatialized rainfall versions are equivalent. However, it's important to note that on larger computational domains, where certain areas may have zero rain pixels.

C. Actual case study : Réal Collobrier catchment

After successfully verifying the accuracy of the new routine, our next crucial step is to apply it in a real case study, specifically focusing on the rainfall event that occurred from June 15th to June 16th , 2010, in the Réal Collobrier catchment (Var, France). During this event, the catchment experienced an intense rainfall period, with a cumulative rainfall reaching up to 350 mm over 48 hours in the upstream. (Figure 6).

The Réal Collobrier research catchment is situated in south-eastern France, specifically at the western edge of the Maures Mountain range along the Mediterranean coast. Encompassing an area of 70 km2, it stretches up to a maximum length of 16 km and a maximum width of 9.6 km. The elevation within the catchment area ranges from 70 meters at the outlet on the western side to 780 meters in the north-eastern region. On average, the elevation is approximately 335 meters [17].

For this case study, radar rainfall data from Meteo France are available at two different temporal resolutions: 1 hour and 15 minutes, and a spatial resolution of 1000m*1000m. For this study, the 15-minute radar rainfall data is used.

In addition to the radar rainfall data, we are fortunate to have observed hourly discharge data from two gauging stations: Malière and Pont de Fer (as shown in Figure 6). These observed discharge measurements are valuable in our study as they allow us to directly compare and validate the simulated discharges obtained from both the spatial and homogeneous rainfall inputs.

The computation domain mesh is a triangular unstructured mesh with variable resolution, with 3.5 million nodes, with finer elements in flood-prone areas. The element resolution ranges from 25m to 3m, and this mesh is generated automatically using the Cartino2D tool.

In this simulation, the following parameters are used for both the homogeneous and spatial rainfall input computations without any calibration attempt:

- Homogeneous Curve Number: 65
- Antecedent moisture condition: 1 (dry condition)
- Strickler Coefficient: 15 $m^{1/3}/s$

By applying these parameters to both rainfall input options, we can perform a comparative analysis of the hydrological response using the traditional homogeneous rainfall approach and the newly introduced option for spatial rainfall.

This study allowed us to gain insights into the differences in flood forecasting, runoff patterns, and overall hydrodynamics resulting from the use of spatially distributed rainfall data. By using the high-resolution radar rainfall data and the refined mesh, we can capture localized variations and simulate the catchment's response with greater accuracy.

The graphics shown in Figure 7 and Figure 8 show the discharges comparison respectively at Malière's and Pont de Fer's gauging stations.

In Figure 7, we observe an overall overestimation of discharge in both simulations, whether using spatial or homogeneous rainfall inputs, when compared to the observed discharges. However, despite the overestimation, the general patterns and the timing of peak discharges are largely consistent with the observed data. This suggests that the simulations capture the essential characteristics of the hydrological response during the rainfall event. One noticeable difference is the rate of increase in discharge. In both simulations, the discharge rises rapidly, while the observed discharge shows a more gradual increase. This disparity may be attributed to several factors, including the spatial distribution of rainfall and the hydrological processes represented in the model. It is essential to thoroughly analyse these aspects to better understand the reasons for the differences in the rate of discharge increase.

In Figure 8, we notice the same rapid increase of the simulated discharge in the hydrographs beginning. We observe also that the patterns are respected in the two simulations compared to observation.

In both figures, we observe a discharge peak for the spatial rainfall simulations, which is not represented in the homogeneous rainfall simulations different rainfall values, which can be very high, the result is that we have net rainfall more quickly with spatial rainfall.

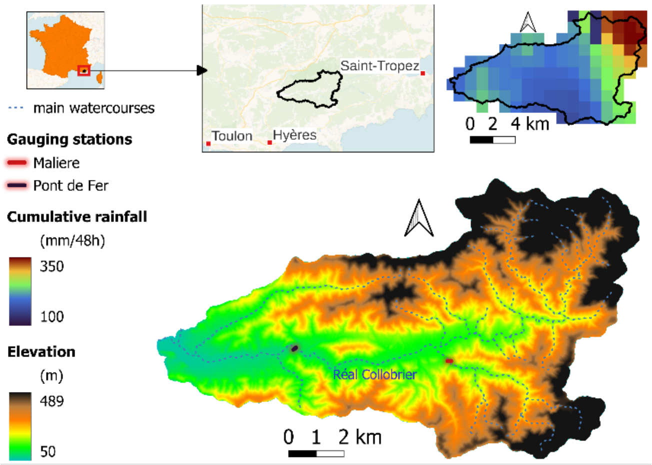

Figure 6. Réal Collobrier geographic, topographic and cumulative rainfall for june 2010 rainfall event. (basemap: CartoDB)

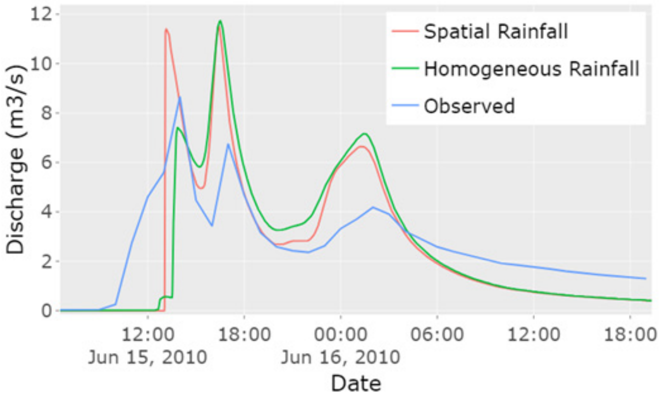

Figure 7. Simulated and observed hydrographs for june 2010 rainfall event in Réal Collobrier at Malière's gauging station

In Figure 7 and Figure 8 a notable systematic difference is observed at the beginning of the simulation. Specifically, in the computation with spatialized rainfall, there is an initial flow peak, contrasting with the simulation based on homogeneous rainfall. This discrepancy arises due to the faster crossing of the initial abstraction on the nodes where the rainfall exceeds the average rainfall across the basin (mean domain rainfall at one timestep).

The spatialized rainfall data provides a more localized representation of rainfall distribution, and in areas with higher rainfall intensities, the initial abstraction is exceeded more rapidly, and effective rainfall is produced before other nodes. This results in an earlier response and an earlier flow peak in the simulations that use spatial rainfall data.

On the other hand, in the simulation with homogeneous rainfall, the rainfall is uniformly distributed over the entire catchment, and the exceeding of the initial abstraction progresses at a more consistent pace across all nodes (homogeneous curve number case only). Consequently, the initial flow peak is less pronounced or may occur later in the simulation compared to the spatialized rainfall case.

This difference in the initial response is an essential aspect to consider when interpreting the simulation results and understanding the impact of spatial rainfall integration on the hydrological modelling outcomes.

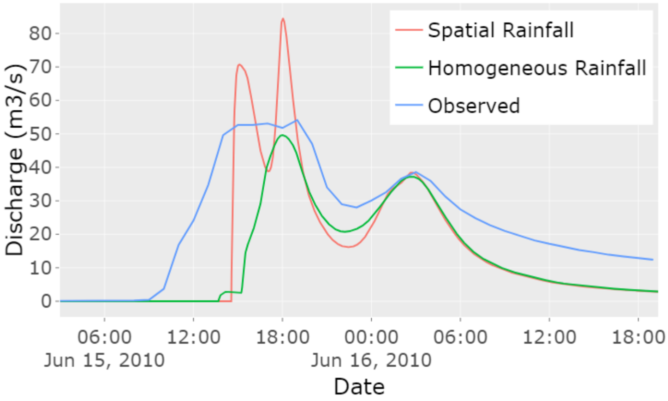

Figure 8. Simulated and observed hydrographs for june 2010 rainfall event in Réal Collobrier at Pont de Fer's gauging station

III. DEVELOPMENTS FOR CONTROL SECTIONS

Another significant development made in this study involves the addition of variables to the control sections subroutine "fluxpr_telemac2d.f" along with the proposal of a new output file format.

Adding of new variables and new format for output file

In order to enhance the capabilities of the "fluxpr_telemac2d.f" subroutine, five additional variables have been incorporated: mean waterline elevation, maximum waterline elevation, minimum waterline elevation, maximum water depth, and the hydraulic head.

To achieve this, modifications have been made to the "fluxpr_telemac.f" subroutine, that work both in sequential and parallel mode. In this subroutine, the control section is divided into segments based on the elements crossed by the control section. For each segment, the new variables are calculated, including mean, maximum, and minimum values. To calculate the hydraulic head, the mean velocity is calculated over the control section,then the velocity head is calculated and added to the mean water elevation.

As a result of these improvements, the control section output file now presents a more comprehensive dataset, as illustrated in Figure 9. This dataset includes the newly added variables, offering valuable insights into the flow characteristics and water levels along the control section.

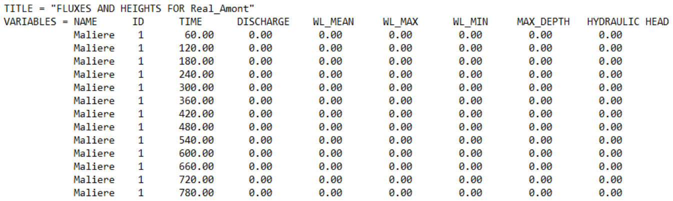

```
TITLE = "FLUXES AND HEIGHTS FOR Real_Amont"
VARIABLES = NAME      ID      TIME      DISCHARGE     WL_MEAN     WL_MAX      WL_MIN      MAX_DEPTH   HYDRAULIC HEAD
            Maliere   1        60.00     0.00          0.00        0.00        0.00        0.00        0.00
            Maliere   1       120.00     0.00          0.00        0.00        0.00        0.00        0.00
            Maliere   1       180.00     0.00          0.00        0.00        0.00        0.00        0.00
            Maliere   1       240.00     0.00          0.00        0.00        0.00        0.00        0.00
            Maliere   1       300.00     0.00          0.00        0.00        0.00        0.00        0.00
            Maliere   1       360.00     0.00          0.00        0.00        0.00        0.00        0.00
            Maliere   1       420.00     0.00          0.00        0.00        0.00        0.00        0.00
            Maliere   1       480.00     0.00          0.00        0.00        0.00        0.00        0.00
            Maliere   1       540.00     0.00          0.00        0.00        0.00        0.00        0.00
            Maliere   1       600.00     0.00          0.00        0.00        0.00        0.00        0.00
            Maliere   1       660.00     0.00          0.00        0.00        0.00        0.00        0.00
            Maliere   1       720.00     0.00          0.00        0.00        0.00        0.00        0.00
            Maliere   1       780.00     0.00          0.00        0.00        0.00        0.00        0.00
```

Figure 9. Example of new control section output file with new variables

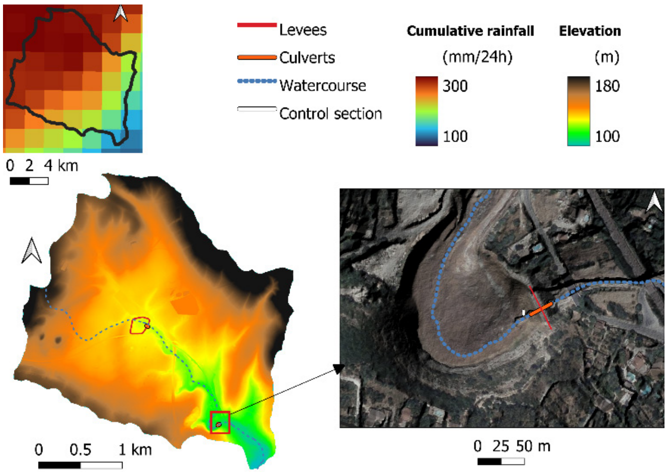

Figure 10. Case study with a 7 km² catchment in Nîmes southern France.(basemap : IGN)

For the demonstration of the new control section subroutine, we have selected an actual case study in a small catchment area of approximately 7 km², situated in the city of Nîmes, southern France. The elevation of the basin varies from approximately 100m downstream to 200m upstream, as shown in Figure 10.

To conduct this case study, we have access to radar rainfall data with a temporal resolution of 5 minutes and a spatial resolution of 500m. The data covers the rainfall event that occurred between October 10th and 11th, 2014, during which a cumulative rainfall of up to 300 mm was observed over a 24-hour period (Figure 10).

A unique feature of this case study is the presence of two retention ponds, one located upstream and another downstream within the catchment area (Figure 10). Additionally, a water depth sensor was installed in the downstream retention pond, enabling the direct comparison of the simulated water elevations to the observed water levels.

The computation triangular unstructured mesh is automatically created using Cartino2D tool, it has 1.5 million elements, with a resolution ranging from 25 m to 3 m. Ponds levees, output culverts and a control section at the water depth sensor are integrated to the model. Two computations are conducted with homogeneous and spatial rainfall.

In the simulations, the following parameters are used for both the homogeneous and spatial rainfall input computations:

- Homogeneous Curve Number: 65
- Antecedent moisture condition: 2 (normal condition)
- Strickler Coefficient: 15 $m^{1/3}/s$

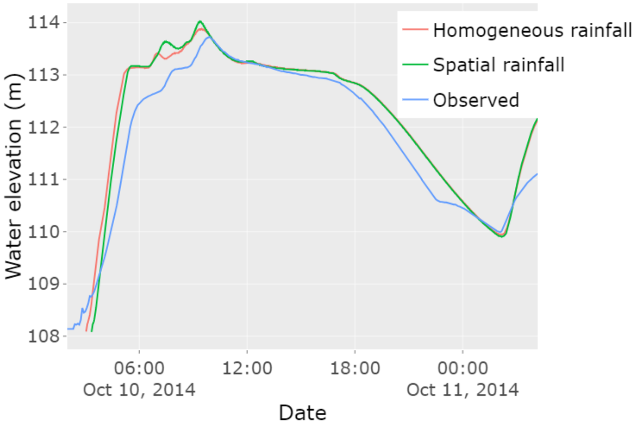

Figure 11. water elevation comparison at pond at water level sensor

Figure 11 represents the water elevation comparison between simulations in the cross section computed with the new subroutine, and observation data. It shows an interesting match between simulations and observation, and not a notable difference between homogeneous and spatial rainfall simulations for water level variable.

IV. CONCLUSION AND PERSPECTIVES

The principal objective of the work presented in this paper is to introduce a new methodology for integrating spatial rainfall data into the TELEMAC-2D rainfall-runoff modelling framework. Furthermore, developments are made in order to enhance the control section subroutine through the introduction of new height-related variables, accompanied by a proposal for an output file format update.

These developments have been tested — both in a synthetic way and within a real case study without any calibration attempt. The tests illustrated that rainfall spatial distribution is successfully added to TELEMAC-2D for the three production functions available (SCS-CN, HORTON and GREEN&AMPT). However, in this article only the tests using the SCS-CN production function are shown. The first test case is conducted without infiltration (CN=100) showing that there is a difference between flood hydrographs, but no difference in water volume. The second actual case study in Réal Collobrier catchment with infiltration (CN=65) shows a difference between the time of exceeding the initial abstraction according to the rainfall node value, and the result is the presence of effective rain over a few nodes, which creates runoff and therefore a flow rate.

Finally, the other development showed is the adding of height variables to the control section TELEMAC-2D module, and its new proposed output file format. These variables can be used to calibrate or verify the results of a TELEMAC-2D computation by comparing the computed heights to observed ones, or to create a synthetic rating curve for a river section.

AKNOWLDGEMENT

This study is financed thanks to ANR (French National Research Agency), in MUFFINS research project. We thank Météo France for the ANTILOPE rainfall dataset, INRAE for the observed discharges in Réal Collobrier catchment, Nimes Métropole for water depth observations and IGN for the DTMs.

REFERENCES

[1] R. Adams, A. W. Western, and A. W. Seed, 'An analysis of the impact of spatial variability in rainfall on runoff and sediment predictions from a distributed model', *Hydrological Processes*, vol. 26, no. 21, pp. 3263–3280, 2012, doi: 10.1002/hyp.8435.

[2] L. Nicótina, E. Alessi Celegon, A. Rinaldo, and M. Marani, 'On the impact of rainfall patterns on the hydrologic response', *Water Resources Research*, vol. 44, no. 12, 2008, doi: 10.1029/2007WR006654.

[3] D. Zoccatelli, M. Borga, A. Viglione, G. B. Chirico, and G. Blöschl, 'Spatial moments of catchment rainfall: rainfall spatial organisation, basin morphology, and flood response', *Hydrology and Earth System Sciences*, vol. 15, no. 12, pp. 3767–3783, Dec. 2011, doi: 10.5194/hess-15-3767-2011.

[4] M. Sangati, M. Borga, D. Rabuffetti, and R. Bechini, 'Influence of rainfall and soil properties spatial aggregation on extreme flash flood response modelling: An evaluation based on the Sesia river basin, North Western Italy', *Advances in Water Resources*, vol. 32, no. 7, pp. 1090–1106, Jul. 2009, doi: 10.1016/j.advwatres.2008.12.007.

[5] F. Lobligeois, V. Andréassian, C. Perrin, P. Tabary, and C. Loumagne, 'When does higher spatial resolution rainfall information improve streamflow simulation? An evaluation using 3620 flood events', *Hydrology and Earth System Sciences*, vol. 18, no. 2, pp. 575–594, Feb. 2014, doi: 10.5194/hess-18-575-2014.

[6] R. Yassine *et al.*, 'Simulation of the Alex Storm Flash-Flood in the Vésubie Catchment (South Eastern France) Using Telemac-2D Hydraulic Code', in *Advances in Hydroinformatics*, P. Gourbesville and G. Caignaert, Eds., in Springer Water. Singapore: Springer Nature, 2022, pp. 847–863. doi: 10.1007/978-981-19-1600-7_52.

[7] P. Brigode, F. Bourgin, R. Yassine, O. Delestre, and P.-Y. Lagrée, 'Are Hydrologic-Hydraulic Coupling Approaches Able to Reproduce Alex Flash-Flood Dynamics and Impacts on Southeastern French Headwaters?', in *Advances in Hydroinformatics*, P. Gourbesville and G. Caignaert, Eds., in Springer Water. Singapore: Springer Nature, 2022, pp. 419–436. doi: 10.1007/978-981-19-1600-7_27.

[8] F. Taccone, G. Antoine, O. Delestre, and N. Goutal, 'A new criterion for the evaluation of the velocity field for rainfall-runoff modelling using a shallow-water model', *Advances in Water Resources*, vol. 140, p. 103581, Jun. 2020, doi: 10.1016/j.advwatres.2020.103581.

[9] P. Costabile, C. Costanzo, D. Ferraro, F. Macchione, and G. Petaccia, 'Performances of the New HEC-RAS Version 5 for 2-D Hydrodynamic-Based Rainfall-Runoff Simulations at Basin Scale: Comparison with a State-of-the Art Model', *Water*, vol. 12, no. 9, p. 2326, Aug. 2020, doi: 10.3390/w12092326.

[10] G. Barbero, P. Costabile, C. Costanzo, D. Ferraro, and G. Petaccia, '2D hydrodynamic approach supporting evaluations of hydrological response in small watersheds: Implications for lag time estimation', *Journal of Hydrology*, vol. 610, p. 127870, Jul. 2022, doi: 10.1016/j.jhydrol.2022.127870.

[11] K. Broich, T. Pflugbeil, M. Disse, and H. Nguyen, 'Using TELEMAC-2D for Hydrodynamic Modeling of Rainfall-Runoff', Jan. 2020, doi: 10.5281/ZENODO.3611524.

[12] J.-P. Travert, F. Taccone, and V. Bacchi, 'Modelling runoff for extreme rainfall events on large catchments using TELEMAC-2D', 2022.

[13] S. USDA, 'Soil Conservation Service National Engineering Handbook', *Section 4: Hydrology, Chapters 4–10*. USDA Washington, DC, USA, pp. 15–7, 1972.

[14] R. E. Horton, 'The role of infiltration in the hydrologic cycle', *Eos, Transactions American Geophysical Union*, vol. 14, no. 1, pp. 446–460, 1933.

[15] W. H. Green and G. A. Ampt, 'Studies on Soil Phyics.', *The Journal of Agricultural Science*, vol. 4, no. 1, pp. 1–24, May 1911, doi: 10.1017/S0021859600001441.

[16] F. Pons, M. Alquier, E. Paya, C. Moulin, N. Panier, and A.-E. Chollet, 'Premiers tests de la méthode Cartino2D sur le territoire de Toulon Provence Méditerranée', *LHB*, vol. 107, no. 1, pp. 1–13, Jan. 2021, doi: 10.1080/00186368.2021.1912968.

[17] N. Folton, E. Martin, P. Arnaud, P. L'Hermite, and M. Tolsa, 'A 50-year analysis of hydrological trends and processes in a Mediterranean catchment', *Hydrology and Earth System Sciences*, vol. 23, no. 6, pp. 2699–2714, Jun. 2019, doi: 10.5194/hess-23-2699-2019.

Multi-site study of the efficiency of coastal protection measures in the Comoros Islands

Juliette Nozières[1], Camille Lequette[1], Jean-Baptiste Saulnier[1], Tristan Plouvier[1], Julien Fornasari[1], Mathieu Gervais[1],
Tanguy Paquereau-Gaboreau[1], Esteban Escobar-Valencia[1], Christophe Brière[1]
juliette.nozieres@egis-group.com
[1]: EGIS Water & Maritime, Guyancourt, France

***Abstract* – As part of the development of a coastal risk management action plan for the Comorian coasts, an in-depth study of coastal flooding hazard was carried out for 4 priority sites in the Union of the Comoros in order to define proper protection scenarios and assess their efficiency. The 4 sites have specific morphological characteristics requiring a dedicated approach for each regarding protection design and model implementation. For each site, a coupled wave-current dynamic flood model was set up for the present state using TELEMAC-2D/TOMAWAC. The models were run in extreme conditions, including cyclonic ones (based on the cyclone Kenneth, 2019), considering a potential increase of storm surge and cyclonic wave conditions due to climate changes. Several protection scenarios of hybrid risk mitigation measures were then implemented and simulated using the models set up, in order to compare them and feed a Cost-Benefice Analysis.**

Keywords: Comoros archipelago, Coastal flooding and hazard, Cyclones, climate change, TELEMAC-2D, TOMAWAC.

I. INTRODUCTION

The Union of the Comoros, made up of 3 islands located at the northern end of the Mozambique Channel, is particularly vulnerable to natural disasters such as tropical storms, flooding and sea level rise. In April 2019, the intense tropical Cyclone Kenneth passed across the islands, hitting the northern Ngazidja Island (Grande Comore) and reportedly causing three deaths, at least 20 injuries and extensive damage to houses across the archipelago, due to strong winds and torrential rains. Several cities were exposed to coastal flooding and erosion, which caused serious damage to homes and infrastructures. A Post-Kenneth Recovery and Resilience Project was therefore implemented by the Ministry of Land Management, Urban Planning, Land Affairs and Transport – funded by the World Bank.

The mission of EGIS is part of this project. It aims at drawing up a coastal risk management action plan over the next ten years on the Comorian coasts with respect to coastal flooding and erosion risk assessment, and identifying 4 priority sites (Foumbouni, Djioezi, Nioumachoua and Ouani, see Figure 1) for which various coastal protection measures are studied at Preliminary and Detailed project design stages.

An in-depth study of coastal flooding hazard was carried out for the 4 selected sites in order to define protection scenarios and assess their efficiency. The 4 sites have specific morphological characteristics requiring a dedicated approach for each regarding protection, design, and model implementation.

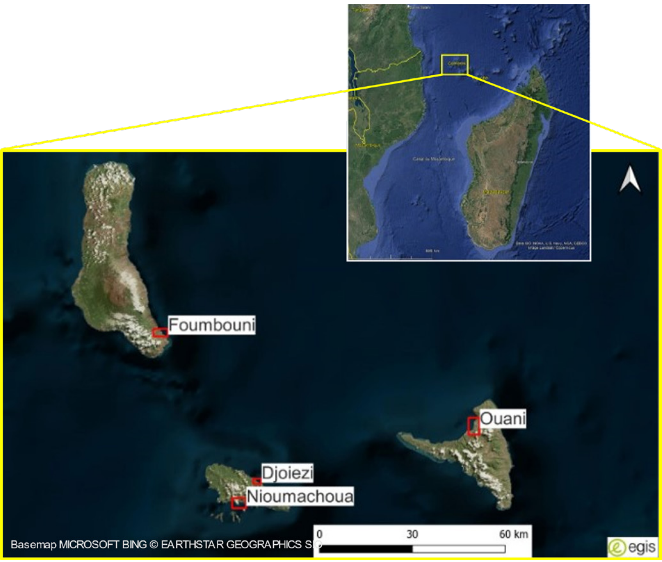

Figure 1. Location of the 4 priority sites in the Comoros archipelago

For each site, a coupled wave-current TELEMAC-2D/TOMAWAC dynamic flood model was set up for the present state and run in extreme conditions including cyclonic conditions (based on the cyclone Kenneth). Potential increase of storm surge and cyclonic wave conditions due to climate changes have also been considered. The results highlighted the strong exposure of the study sites to coastal flooding hazard, and the need for the development of a relocation strategy for the most exposed stakes in the short to mid-term. Several scenarios of hybrid risk mitigation measures (hard/soft) were also adapted to the specific nature and dynamics of each site and simulated using the coupled models in order to assess their efficiency and feed a Cost-Benefit Analysis.

II. STUDY AREA AND CONTEXT

A. *Sites selection*

The first phase of the project aimed to qualify coastal risks at the overall scale of the 3 islands and to identify the most vulnerable locations. Among these locations, 4 sites were identified as priority sites and selected for the next phase of the study, using a multi-criteria analysis:

- Foumbouni, on Grande Comore; rocky urban area with high human stakes, particularly since the passage of Kenneth;

- Djoièzi, on Mohéli; urban sandy area, with high human stakes and a strategic road, exposed chronically;

- Nioumachoua, on Mohéli; mixed sandy area (urban/rural), bordered by large reefs and mangroves, with high human and tourist stakes (located in the heart of the Mohéli National Park);

- Ouani, on Anjouan; a mixed rocky/pebbled/river-mouth zone, with strategic and human stakes, exposed chronically.

It should be noted that all the sites except Foumbouni are bordered by quite wide fringing reefs. The Nioumachoua site is located in the heart of Mohéli National Park, created in 1988, and includes important ecosystem (coral reefs, mangroves, vegetation, etc.) to integrate into the adaptation plan to effectively manage the risks of erosion and coastal flooding.

B. *Digital Elevation Model (DEM)*

For the second phase of the project including the construction of coastal flooding models for each site, it was necessary to have accurate and reliable topo-bathymetric data. Several sources were used for this purpose.

The bathymetric data collected are listed below:

- 10m resolution Satellite-Derived Bathymetry (SDB) produced by **EOMAP** in 2022 as part of the project, for the entire coast of the 3 islands.

- 20m resolution DEM, covering the Mohéli National Park area, produced by **CREOCEAN** using SDB and multibeam echosounder (MBES) data from 2019

- MBES data available in some locations, **SHOM**, 2014

- 1000m resolution **SRTM30** DEM

The topographic data collected is listed below:

- Topographic surveys carried out on the 4 selected sites in October/November 2022 as part of the project, using an RTK GPS

- 1m resolution photogrammetric DEM produced in 2018 as part of **AMCC project** (Alliance Mondiale contre le Changement Climatique, *https://comores-europe.km/amcc/*) in Grande Comore and Mohéli

- 30m resolution **SRTM30+** DEM

Topo-bathymetric data was assembled with care in order to produce consistent DEMs on each site. Specific attention was given to the vertical datum of the datasets.

The final concatenation of the topo-bathymetric data and their interpolation on the 4 models grids are illustrated in Figure 2.

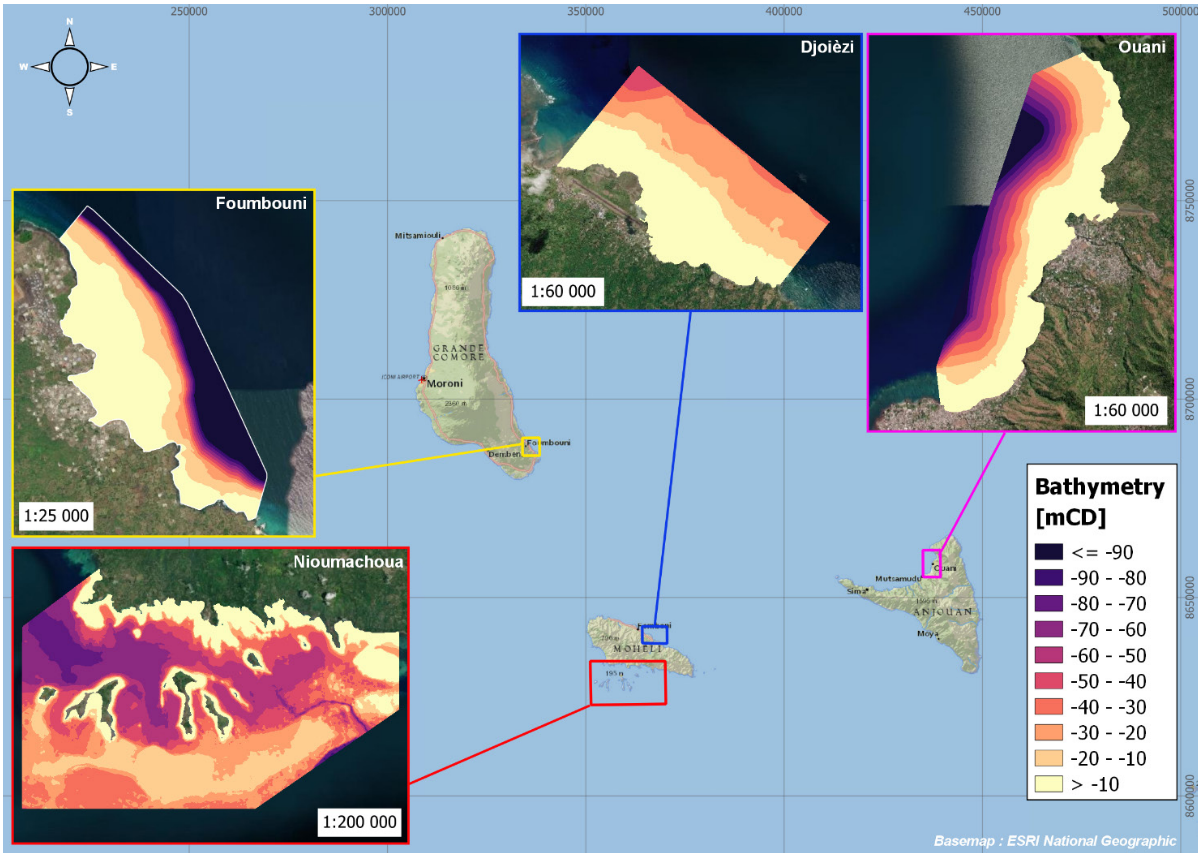

Figure 2. DEMs of the coastal flooding models on the 4 sites in the Comoros Archipelago : Foumbouni, Djoièzi, Nioumachoua and Ouani

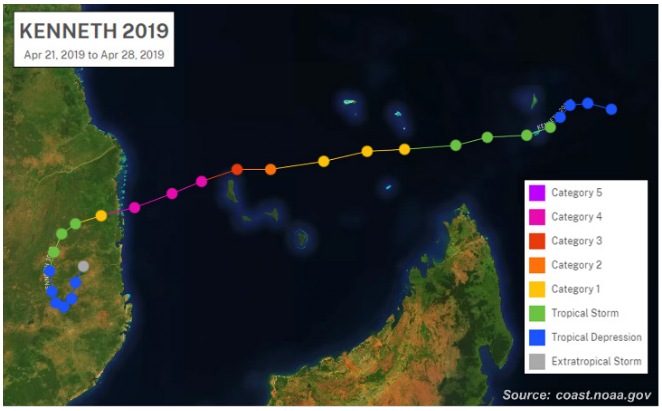

Source: coast.noaa.gov

Figure 3. Path of the cyclone Kenneth path in April 2019, North of the Mozambique channel

C. *Meteocean Conditions*

The Comoros archipelago has a tropical oceanic climate, with a hot and humid season from December to March (austral summer with Kashkasi winds), and a cooler, drier season from June to September (austral winter with Koussi winds). During the rainy season (austral summer), the western part of the islands receive more rainwater with the monsoons arriving from the north-west. It is also during this season that tropical depressions occur, sometimes turning into cyclones. These storms often pass close by the archipelago but do not directly impact it. Cyclone Kenneth's passage over the archipelago in April 2019 is exceptional in this respect. Its path is illustrated in Figure 3.

1) *Wind*

Under normal conditions, the dry season is dominated by East/South-East and South/South-West winds (trade winds), while the wet season is characterised by the North to North-West monsoon, which has a lower amplitude. In cyclonic conditions, winds can blow in any direction and can reach values in excess of 30 m/s (100-year return period; 1-hour average of the wind speed at 10 m elevation).

2) *Water levels*

The Comoros coastline is subject to a semi-diurnal tidal regime with a maximum tidal range of around 3 to 4.5 m and a minimum of around 1 m [1]. The characteristic astronomical tide levels used in this study are those of the port of Moroni, in Grande Comore, and Fomboni in Mohéli, provided by the SHOM.

The analysis of the Coastal Dataset for the Evaluation of Climate Impact [2] carried out in the first phase of this project showed that the meteorological surge could reach around 1.3 m ±0.45 m for a 100-year return period event (including 1.1 m ±0.45 m directly linked to the influence of the wind). These values vary little from one island to another and are consistent with the value of 1.5m reported by the World Bank (2016).

3) *Waves*

The Comoros are protected from the austral swells by Madagascar. In the dry season, there are trade wind swells from the south-west to the south-east. Under normal conditions, the wave climate varies greatly from one side of the islands to the other. In the south of the archipelago, the waves are from the south and higher than in the middle of the archipelago, where waves come from the east. To assess waves in cyclonic conditions, cyclone Kenneth was simulated with SWAN, using the WRF (Weather Research Forecast) atmospheric model as wind input. Extractions were carried out at 2 offshore points (see Figure 4). At the peak of the storm, the significant wave height is estimated to 7m at PL1, located in the middle of the 3 islands, and 5m at PL2, to the south of the archipelago, as the cyclone passed to the north of Grande Comore.

It appears that each site has a very different exposure to the waves. For example, Ouani is fairly well protected from the usual swells due to its orientation (to the north-west of Anjouan). The islets and reefs off Nioumachoua also provide protection from southerly swells. The wave conditions chosen for the modelling are presented in §III-C.

D. *Climate change effect*

Apart from the rise in mean sea level, the Comoros could be impacted by climate change through higher temperatures and increased rainfall, as well as stronger extreme cyclonic conditions. It is difficult to estimate the impact of climate change on the frequency and intensity of future cyclones. However, [3] makes the historical observation of an intensification of storms in the Indian Ocean, which would correspond to a 15% increase in the intensity of cyclonic winds over a 50-year period. This would lead to a 15% increase in wave height and barometric surge, and a 30% increase in wind-induced surge. These assumptions were considered for the modelling, as well as a regional SLR corresponding to the scenario SSP5-8.5 from IPCC AR6.

III. MODELS SET-UP

A. *Domain extents and meshing*

The models extend on the maritime part up to a sea state reanalysis point extracted offshore of each site, and on the terrestrial part up to the elevation +10/+12mCD on the areas of interest, and up to the coastline otherwise. In Nioumachoua, the model was extended in order to include all existing islets off the area of interest, required to adequately represent wave conditions and setup along the area of interest.

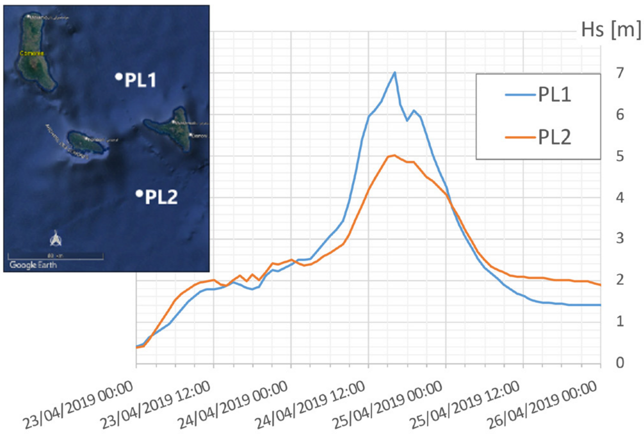

Figure 4. Significant wave height during Kenneth at 2 locations (PL1 and PL2), from WRF cyclonic modelling results

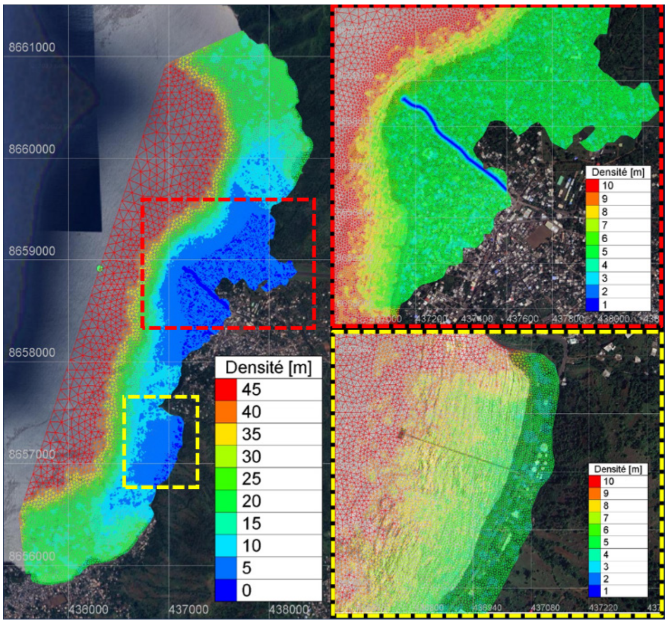

Figure 5. Ouani mesh and density (node size in meters)

The meshes are constructed with triangular elements with variable resolution, ranging from 3-5m on land to 100m or more offshore.

A fine mesh resolution was used in preferential surf zones (corals reefs) in order to correctly estimate the wave setup. In Ouani, a fine mesh is also used to represent the river estuary.

In order to reduce calculation times, the meshes were optimised and coarsened in certain areas (depths <-30m, Djoièzi reef flat, islets off Nioumachoua, etc.).

The correct representation of hydrodynamic phenomena was also checked: swell propagation including shoaling, refraction, breaking at the reefs and on the coast, wave setup, etc.

The total number of nodes for each mesh is around: 28,000 for Foumbouni; 34,000 for Djoièzi; 167,000 for Nioumachoua; and 56,500 for Ouani.

As an example, the Ouani mesh with its density is shown in Figure 5.

B. Bottom friction conditions

Table I - Strickler coefficient assigned according to simplified land use typology

Simplified typology	$K\ [m^{\frac{1}{3}}/s]$
Maritime area	40
Natural area with little or no vegetation / rocky	30
Coral reefs	28
Natural area with dense vegetation (forests), mangroves	15
Relatively dense urban area	10

Because of the specific site conditions, the bottom friction parameter is implemented in the models via a Strickler coefficient K variable in space. The standard values used come from BRGM [4] and Deltares' experience in coral reef areas [5]. The Strickler coefficients used in this study are presented in Table I.

C. Boundary conditions

Three synthetic extreme events have been selected: an annual storm - potentially causing flooding already in the areas of interest - and two cyclonic events (25 and 100-year return period resp.). Each of these events is projected to 2050, taking into account the potential effects of climate change, such as sea level rise (see below).

As no information was available on the joint occurrence of significant wave heights and water levels, a classical conservative approach was adopted. Thus, an event with a return period of N is defined by the conjunction of a swell and a sea level, both with return period N.

1) Water levels

The extreme water level imposed at the boundaries is variable and is a combination of the following phenomena:

- astronomical tides, representative of a mean high water spring (MHWS),
- storm surges based on the Coastal Dataset for the Evaluation of Climate Impact (CoDEC) [6] analysis and potential impact of climate change on extreme cyclonic activity,
- a contribution of +20 cm due to seasonal and/or interannual fluctuations [7],
- a contribution of +27cm as potential SLR due to climate change by 2050, following the SSP5-8.5 pessimistic emission scenario from IPCC AR6 [8],
- an uncertainty of +25cm related to the data used and the methodology adopted (vertical datum, no surfbeat nor seiche modelling, etc.).

In order to accurately represent the dynamics of coastal flooding, two tidal cycles (approximately 24 hours) have been simulated, with the storm surge occurring during the first tidal cycle, at the same time as high tide.

2) Waves

For the annual event, sea state conditions are considered constant over time. For cyclonic events, wave conditions vary in a similar way as the simulation result of the cyclone Kenneth in 2019.

The spectral significant wave height H_s varies with the storm peak occurring at the same time as the water level peak (tide/surge). An increase of 15% is applied to the values of H_s due to the potential future trends in hurricane activity linked to climate change (see §1-D).

The swell direction also varies during the cyclonic simulations, with the critical direction for each site coinciding with the storm peak. The critical swell direction chosen is adapted to the configuration of each site. Most of the time, it is frontal at each site, in accordance with the swell roses. For Nioumachoua - which is sheltered by several reefs and islets, especially to the south and east - three offshore swell directions were tested, and western waves (270°N) have eventually been chosen as the most damaging for the site.

The extreme offshore sea states selected for each site at the storm peak are shown in Table II and Table III.

Table II - Sea states used in modelling non-cyclonic conditions (T1) at the 4 study sites

Site	**Offshore wave direction [°N]**	**T1 – 2050 (non-cyclonic swells)**	
		Hs [m]	***Tp [s]***
Foumbouni	60°	1.81	9.20
Djoièzi	0°	1.67	8.00
Nioumachoua	180°	3.67	12.20
Ouani	330°	1.35	5.20

Table III Sea states used in modelling for cyclonic conditions (T25 and T100) at the 4 study sites

Site	**Offshore wave direction**	**T25 – 2050 (cyclonic swells)**		**T100 – 2050 (cyclonic swells)**	
		Hs [m]	***Tp [s]***	***Hs [m]***	***Tp [s]***
Foumbouni	60°N	5.45	8.60	7.63	9.60
Djoièzi	30°N	5.45	10.10	7.52	11.00
Nioumachoua	270°N	4.80	12.80	6.32	12.90
Ouani	300°N	5.23	13.30	7.09	13.60

It should be noted that the peak enhancement factor γ of the JONSWAP spectrum is set to 2 according to Young's analysis of historical cyclonic data [9]. The directional spread s is set to 25 for cyclonic conditions (T25 / T100), and to 75 for non-cyclonic annual events (T1) according to the sea state classification of Goda (1997) in the Rock Manual.

D. *Specific case: wave overtopping in Foumbouni*

In the Foumbouni area, the calculation of wave overtopping discharges has been included in TELEMAC-2D for both present state and protection scenarios. This application is based on EurOtop formulae for coastal dykes and embankment seawalls (chap. 5) and armoured rubble slopes and mounds (chap. 6) as implemented in [10]. The coastal protection system (or the natural coastline) is discretised into homogeneous sections of length ranging from 15 to 50m having similar geometrical, hydrodynamic and structural characteristics. At each time step and for each section, the calculated overtopping discharge is applied to a 'downstream' node located inland. Water intrusions and related receding processes can therefore be dynamically simulated in a single simulation.

E. *Calibration / validation*

In the absence of calibration data, standard numerical parameters were used for the hydrodynamic modelling (waves, currents, water levels), providing a satisfactory representation of tidal currents and wave breaking, which influence currents and water levels at the coast.

It has also been verified that the flooded zones simulated for the annual return period event are relatively consistent with the testimonies gathered on site during the first phase of the project.

IV. RISK OF FLOODING AND SOLUTIONS

A. *Results of modelling*

For each site and for each return period, maps of maximum water height and velocity were produced. These 2 parameters were combined to produce a graded index for coastal flooding hazard (1: low, 2: medium, 3: high, 4: very high). The index is based on Table IV.

Table IV – Coastal flooding hazard index classification

	Flood dynamics (based on current velocity)		
Water heights	***Slow*** ***$0 < v < 0.2m/s$***	***Medium*** ***$0.2 < v < 0.5m/s$***	***Fast*** ***$v > 0.5m/s$***
$H < 0.5m$	Low	Medium	High
$0.5m < H < 1m$	Medium	Medium	High
$H > 1m$	High	High	Very high

Based on these maps, it was shown that each site was affected differently by coastal flooding.

In Foumbouni, many buildings on the rocky promontory - notably the mosques and the corniche road – are already exposed to waves in the annual event.

In Djoièzi, modelling results highlight the significant exposure of the densely constructed urban centre, already during the annual event (see Figure 6).

In Nioumachoua, contrary to the firsts results of the general assessment at the scale of the archipelago, the site appears to have limited exposure to coastal flooding. Areas at risk are mainly located around watershed outlets, allowing some seawater intrusion due to the lower altimetry of the surroundings.

In Ouani, mainly the first line of houses in the town centre is affected, as well as the western end of the airport runway, which is important to protect. On the other hand, the oil storage depot to the south is not affected by flooding, even in the case of a 100-year cyclone.

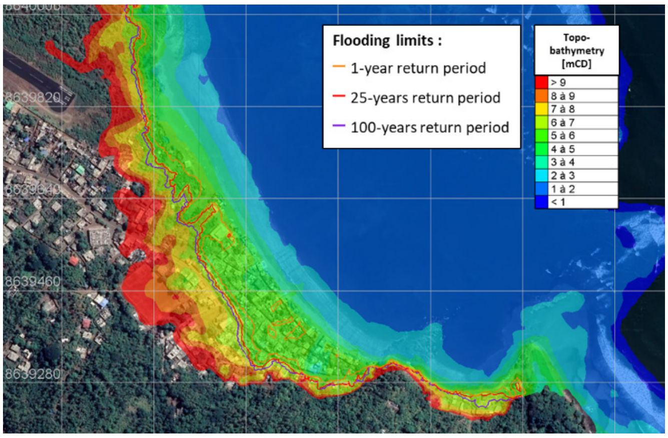

Figure 6. Sea intrusion limits for Djoièzi town centre for the 3 return periods events

B. Proposed solutions

To reduce the coastal flooding hazard, as well as erosion (not addressed in this paper), EGIS proposed 2 different scenarios of mitigation measures for each site. The proposed solutions were integrated into the models and the results were used to feed a Cost-Benefit Analysis.

These scenarios are intended to be hybrid, thus combining hard and soft protection measures whenever possible. The proposed solutions include:

- Seafront structures, such as rubble-mound and vertical seawalls, which are highly effective and long-lasting, although expensive and potentially leading to land-use conflicts;
- Detached breakwaters to reduce waves energy, erosion hazard, and provide a shelter for local fishermen;
- Beach nourishment (nature-based solution), which requires regular maintenance and a certain amount of sand (which may be borrowed elsewhere);
- Restoring the natural habitat (nature-based solution), in particular at upper beaches and dunes, but also at wetlands (mangroves, marshes, coral reefs, seagrass beds), which reduce the impact of coastal flooding thanks to their biological functions. This solution offers significant socio-environmental co-benefits and enables adaptation to climate change, although with no effect in the short term.

It should be noted that in Moheli, the territorial development scheme (a provisional document) promotes a sustainable and inclusive development of the island. It focuses on the island's tourism potential, the development of its agriculture, and the reinforcement of measures to protect the environment and biodiversity. It provides recommendations on planning principles that should be incorporated into planned developments whenever possible. This document places particular emphasis on nature-based solutions.

If possible, the solutions were implemented in the models by constructing new meshes and/or modifying the DEM.

For instance, at Foumbouni, two types of wall have been suggested (curved concrete seawall or a rubble-mound dike made of artificial concrete blocks) to be built along the rocky promontory to protect the road, particularly from wave overtopping.

At Djoièzi (see Figure 7), the first scenario (SC1) consists in detached breakwaters in front of the urban centre, while the second scenario suggests the installation of groynes (SC2). Each scenario should contribute to the stabilization or even an accretion of the beach, thus limiting the impact of waves on the exposed houses.

At Nioumachoua, the linearization of the beach and the creation of a vegetated dune belt is envisaged, involving a sand backpass from one side of the beach to the other.

At Ouani, segmented vertical seawalls are proposed along the Ouani city centre and in front of the airport, with additional detached breakwaters in the city centre for one of the scenarios.

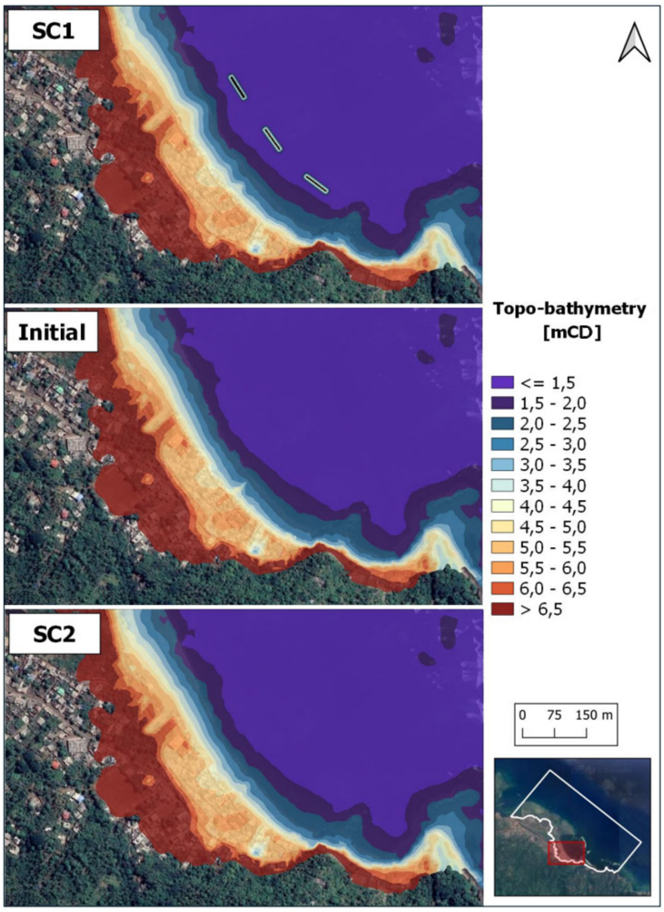

Figure 7. DEM of the initial and modified models at the Djoièzi site

C. Adopted solutions

For each protection scenario, differentials with the initial situation have been made on the maximum water height, velocity, and flood hazard index maps. This enabled a cost-benefit and multicriteria analysis to be carried out to determine the most appropriate solutions for each site. In fact, the scenarios are not assessed on their efficiency only, but also on their cost and non-monetized criteria.

In Foumbouni, the first scenario, with the construction of a curved deflector seawall is preferred. The design of these structures is intended to provide the highest possible level of protection in order to reduce the risk of flooding, while remaining compatible with the uses of the site and the financial constraints. However, this solution will not protect people from the risk of flooding for the major cyclonic events, as significant wave overtopping is expected in some areas due to the low elevation of the area. Relocation will have to be considered for the most vulnerable stakes (houses, buildings, infrastructures…).

In Djoièzi, the second scenario is preferred. In front of the dense urban area, wooden groins and rubble mound embankments will provide transitional protection against erosion and flooding, along with a plan to relocate the most exposed buildings. Access to the beach will be maintained. It is also planned to reinforce the embankment along the strategic coastal road to the East of the city. The risk of flooding will not disappear completely, but will be reduced. The detached breakwaters solution has been discarded because of the expensive costs and the need for a large amount of rocks or concrete material. Moreover, such measure may also create a false security feeling for the population (who might be tempted to go further along the coast).

In Nioumachoua, the first scenario – the relocation of the first line of buildings to the seafront and the creation of a vegetated dune belt - is preferred. SEMS (*Système des Épis Maltais Savard*) type groynes are planned on the beach as well. This is a low cost system of semi-permeable groynes built with wooden stakes (Figure 8). This option aims to re-establish the most natural beach-dune dynamics possible using flexible facilities and mobilising local material and human resources as much as possible.

In Ouani, it was finally decided to opt for an intermediary solution involving a short-term relocation of the first rank of houses along the city centre, as well as the creation of a rubble mound embankment along the coastal road (currently located behind the houses to be relocated). On the airport area, a pebbles nourishment on the beach, maintained by wooden groynes, is considered.

It should be noted that the solutions finally adopted on each site represent a set of diverse, effective and financially reasonable solutions that are intended to serve as an example for the other exposed areas of the Comorian islands.

Figure 8. SEMS (*Système des Épis Maltais Savard*) groynes used in the St. Lawrence Estuary (Canada), using fir stakes (©Photo: N. Roy).

V. CONCLUSION

This coastal flooding hazard characterization study was carried out for 4 priority sites, using coupled wave-current TELEMAC-2D/TOMAWAC hydrodynamic numerical models implemented on continuous land-sea digital terrain models, making it possible to reproduce coastal flooding for annual and extreme cyclonic events in a context of climate change.

The results highlight the high exposure of populations in densely populated areas, as well as certain economic assets (airport), particularly in the case of uncontrolled retreat of the coastline.

Implementing the protection scenarios in the models enabled a cost-benefit and multi-criteria analysis to be carried out in order to determine the most appropriate solutions for each site, based not only on their effectiveness but also on their cost and non-monetised criteria.

ACKNOWLEDGEMENT

The study was financed by the World Bank for the Union of the Comoros' Ministry of Land Management, Urban Planning, Land Affairs and Transport, as part of a Post-Kenneth Recovery and Resilience Project (P171361, Grant No. D549-KM).

REFERENCES

[1] ASCLME, “National Marine Ecosystem Diagnostic Analysis. Comoros. Contribution to the Agulhas and Somali Current Large Marine Ecosystems Project (supported by UNDP with GEF grant financing),” 2012.

[2] S. Muis, M. I. Apecechea, J. Dullaart, J. de Lima Rego, K. Skovgaard Madsen, J. Su, K. Yan et M. Verlaan, “A High-Resolution Global Dataset of Extreme Sea Levels, Tides, and Storm Surges, Including Future Projections,” Frontiers in Marine Science, 2020.

[3] T. Knutson, S. J. Camargo, J. C. L. Chan, K. Emanuel, C.-H. Ho, J. Kossin, M. Mohapatra, M. Satoh, M. Sugi, K. Walsh et L. Wu, “Tropical Cyclones and Climate Change assessment -Part I: Detection and Attribution,” Journal of the American Meteorological Society, pp. 1987-2007, 2019.

[4] Paris F., Pedreros R., Stéphanian A., Bluteau T., et Lecacheux S. (2017) – Modélisation de la submersion marine en Camargue. Rapport final. BRGM/RP-66804-FR, 176 p., 128 fig., 23 tabl., 2 ann.

[5] R Deltares, Wave run-up on atoll reefs, 2015.

[6] S. Muis, M. I. Apecechea, J. Dullaart, J. de Lima Rego, K. Skovgaard Madsen, J. Su, K. Yan et M. Verlaan, “A High-Resolution Global Dataset of Extreme Sea Levels, Tides, and Storm Surges, Including Future Projections,” Frontiers in Marine Science, 2020

[7] M. W. Schouten, W. P. De Ruijter, P. J. Van Leeuwena et H. Ridderinkhof, “Eddies and variabilityin the Mozambique Channel,” Deep-Sea Research II 50 (2003) 1987–2003, 2003.

[8] IPCC, “Sixth assessment report AR6 on climate change,” 2021.

[9] Young, “Parametric hurricane wave prediction model,” Journal of Waterway, Port, Coastal and Ocean Engineering, vol. vol. 114, pp. p. 637-652, 1988.

[10] J.-B. Saulnier, T. Paquereau-Gaboreau and J.-V. Delemasure, “Implementation of Overtopping Discharges in a 2D Coastal Flood Model of the Mont Saint-Michel Bay,” Proc. XXVIIth Telemac User Conference, Antwerp, Belgium, 8pp., 2021.

GIROS: Digital Twins of the Gironde Estuary based on the open TELEMAC-MASCARET suite

Jean-Baptiste Saulnier[1], Vincent Lalire[1], Bénédicte Authié[1], Nicolas Huybrechts[2], Fabrice Klein[3]
[1]: EGIS, Energy & Sustainable Cities
[2]: CEREMA, DTecREM
[3]: Grand Port Maritime de Bordeaux

Abstract – **The GIROS Digital Twins, an online GIS platform dedicated to the analysis and the exploitation of the Gironde estuary in the context of climate change, have been developed. The platform is composed of five modules with specific applications for estuary users, decision-makers, engineers etc. Each module is fed by operational analysis and forecast data produced daily by two core models built with the open TELEMAC-MASCARET suite: a historical 3D hydro-sediment model (Gironde XL 3D), upgraded with the additional coupling to the water quality module WAQTEL and a separate twin wave propagation model (TOMAWAC-TELEMAC-2D). This paper presents the construction of GIROS, its characteristics and the further community actions in view of gaining scientific knowledge, sharing data, prospecting and reducing costs.**

Keywords: GIROS, Digital Twins, Gironde Estuary, TELEMAC-3D, Open-Source.

I. INTRODUCTION

Located in the South-West of France, the Gironde estuary is considered as the largest estuary in Western Europe – 180km along the Gironde, Garonne and Dordogne rivers –, which concentrates many uses (commercial traffic, fishing, nautical activities etc.) and environmental concerns in the climate change context (sea level and temperature rise, reduction of tributaries' flowrates, turbidity maximum zone (TMZ) shift, alteration of water ecosystems etc.).

In the last years, the Grand Port Maritime de Bordeaux (GPMB) has been engaged in various projects involving numerical solutions applied to the Gironde estuary. In 2015, the EU R&D project Gironde XL was launched in partnership with CNRS, EDF, CEREMA, UT Compiègne, University of Bordeaux and Ecole des Ponts ParisTech. The project focused on the development of open-source tools to facilitate the access and the navigability of very large vessels in the Gironde estuary. It ended in 2019 with the release of Gironde XL 3D (denoted as "GXL3D" in the following), a 3D hydro-sediment model built with the open TELEMAC-MASCARET suite (modules TELEMAC-3D and GAIA). In 2020, the Interreg SUDOE project ECCLIPSE was launched, which addresses the impact assessment of climate change on ports in Southwestern Europe including the long-term simulation of the Gironde up to 2100. In the frame of this project, a new version of GXL3D was released by CEREMA [1]. From there on, the GPMB took the opportunity of the national "France Relance" initiative to pursue the development effort on GXL3D and develop digital twins of the Gironde estuary through an innovation partnership involving all estuarine and water stakeholders (Water Agency, GPMB, EPIDOR, SMEAG, SMIDDEST, etc.) The project started in early 2022 with a dedicated Hackathon. This action resulted into the deployment of the webGIS application GIROS (GIRonde Open-Source) by the winning group (EGIS and two IT partners, Oslandia and Fieldbox AI) in early 2023. GIROS is an open-source multi-platform tool, which aims at facilitating estuarine prospection and prevision activities, risk management, decision-making and sustainable development for consultancies, scientists, students, decision-makers, communities, estuary users and citizens. This innovative open-source community tool dedicated to the simulation of a natural heritage – an estuary – is the first one of its kind and may be easily replicated to any other estuary or river.

The GIROS Digital Twins are a complete service hosted on the Cloud, benefiting from high performance computing power at best cost as it is "on demand". The service is accessible to all registered users *via* an internet browser and allow almost unlimited parallelisation of simulations. They are based on the exploitation of the model GXL3D to which the water quality module WAQTEL was added to simulate dissolved oxygen and temperature. A twin spectral wave propagation model, taking tide and wave-current interactions into account (TOMAWAC coupled to TELEMAC-2D), was also set up to provide wave information. Daily and monthly forecast runs are launched to feed the database with near real-time data and trends for the next weeks/months. In addition to model data, the digital twins also will provide users with *in situ* data obtained from mobile sensors, which can be used to check the model accuracy.

Within the GIROS Digital Twin platform five modules are available:

- **Environment:** Observation of near real-time forecast estuarine physico-chemical parameters (water level, currents, salinity, wave, turbidity, temperature, dissolved oxygen etc.);
- **Dredging:** Indicators of sea bottom conditions along the shipping channel and annual dredging strategy;
- **Navigability:** Conditions for navigation, ship mooring and behaviour along the shipping channel;
- **Garonne 2050:** One-year simulation of estuarine conditions in 2050 based on specific climate change assumptions;

- **Study Lab:** Free user simulation run with pre-/post-inspection on GitLab and JupyterLab.

The following sections present the modules of the GIROS platform, the community core models, the operational forecasting and analysis setup, the user access and further actions through the creation of GIROS communities.

II. THE GIROS DIGITAL TWIN PLATFORM

The GIROS digital twin application platform contains five specific modules described below. Each module is fed by the same geospatial database, which stores the Selafin results in a lossy compression way to optimise the volume of data. These modules aim to support decision making related to port and estuarine activities.

A. 'Environment' Module

The 'Environment' module is the core platform of GIROS and dedicated to any estuary/river user. On a webGIS screen, several layers of data – related to geographical and marine indicators and environmental data (significant wave height, wave direction, water level, TMZ, surface/bottom currents, temperature, salinity, dissolved oxygen, SSC etc.) – can be displayed for current time, in the past up to 100 days (with 1 hour time step) and ahead in the future (with 1 day time step). The database is fed on a regular basis by new Telemac results provided by daily and monthly runs. The user can visualise time-series of physical and chemical variables in any location as well as meteorological forecast. The frame of the 'Environment' module is replicated to the other modules so that the user may easily switch from one module to another.

B. 'Dredging' Module

The 'Dredging' module focusses on the channel accessibility for vessels and dredging requirements. One screen allows to check the accessibility of each channel section or ship berth in terms of bottom altimetry (as modified by erosion and sedimentation) or indicate an imminent dredging action. A second screen is aimed at defining annual dredging strategies.

C. 'Navigability' Module

The 'Navigability' module is dedicated to pilots, who can optimise the navigation planning according to the encountered hydrodynamic conditions (currents, suspended sediment concentration, water level etc.).

D. 'Garonne 2050' Module

The 'Garonne 2050' module aims at giving a full prospective view over the estuarine dynamics expected in 2050. In particular, specific evolutions and impacts related to sea level rise and global warming can be specifically studied (for instance, the discharge reduction in the Garonne and Dordogne rivers). Based on deterministic forecasts (IPCC scenario RCP 4.5) and general trends (e.g. temperature rise in air and water), a simulation of the whole year 2050 with the hydro-sediment and water quality model developed in the GIROS project was run. The 'Garonne 2050' module looks much like the 'Environment' module, so that the user can similarly inspect the results on the webGIS interface. The default assumptions (see chapter IV.C.3) and related Telemac files can be updated by the GIROS user community. Indeed, any registered user can access the default Telemac files and run his own prospective simulation on LISOS through the 'Study Lab' module.

E. 'Study Lab' Module

The 'Study Lab' module allows any registered user to create, visualise, modify and launch a run of the 3D hydro-sediment/water quality (incl. Garonne 2050) and wave models over the time period of his choice and finally handle the results files, either by downloading or post-processing them through JupyterLab notebooks. The goal is to facilitate the appropriation of the models to users (communities, consultancies, research laboratories etc.), promote experience sharing and create a community for users and developers.

The 'Study Lab' module looks much like the 'Environment' module. A 'Create Study' button opens a side window, where the user can enter the name of the study, select the model he wants to use and the time period he wants to simulate. Then, the Telemac files corresponding to the requested model and period of time are automatically generated thanks to dedicated API requests to download, process and format raw data from targeted public source (discharges at the tributaries, ocean models, estuarine monitoring network etc.). A 'View Files' button is then enabled to access the files on the NAOS platform (GitLab, see chapter IV.A). The user can modify the files before running. For instance, water treatment releases – with local impact on water temperature, organic and ammoniacal loads etc. – may be added to the simulation by specifying a new source file in TELEMAC-3D. Finally, a 'Launch Run' button allows the user to queue his run on the LISOS platform (dedicated to IT High Performance computing resources on the Cloud). Once completed, the user is notified by an automated e-mail.

III. GIROS "COMMUNITY" CORE MODELS

The hydro-sediment- and water quality models are built upon an existing 3D hydro-sediment model (GIRONDE XL 3D) initially developed by CEREMA [1]. The wave model was developed in the frame of the GIROS project from the 2D version of the model. Both are described in detail below.

A. Gironde XL 3D

The Gironde XL 3D model (see [1]) is the basis on which the main 3D model in GIROS was constructed. Initially based on a coupling of TELEMAC-3D (hydrostatic) and GAIA (version 8.2), it was extended to include WAQTEL for the representation of biochemistry tracers like dissolved oxygen (O_2) and ammoniacal load (NH_4), which are of major interest for the study of the river's ecological health.

The computational domain of GXL3D extends offshore up to 70 km from the mouth and about 200 km alongshore. Inland, the model extends up to 170 km, where the limit of tide of propagation is reached (usually considered in La Réole in the Garonne and Pessac in the Dordogne). The 2D mesh (Figure 1) comprises 58 251 nodes with space varying resolution, as about 4 km offshore, 100 m in the Gironde's navigation channel and about 25 m along the tributaries' riverbanks. The water column is divided in 9 sigma layers, distributed as a geometric progression with finer resolution near the bottom. The whole 3D model therefore comprises 524 259 nodes. The digital elevation model (DEM, Fig. 1) was constructed as a combination of various datasets produced by the French Naval Hydrographic and Oceanographic Service SHOM (ocean) and GPMB (Gironde) in the period 2005-2016 and by Voies Navigables de France (VNF) / Direction Départementale des Territoires et de la Mer (DDTM) in the tributaries (2012-2014 and 1996 for the most upstream part near the boundaries). Bottom level is reported in reference to the general datum of France (denoted as NGF). In GIROS, an automatic bathymetry update was hardcoded so that any recent XYZ data obtained from surveys in the navigation channel may be integrated into the DEM at the beginning of each daily run (see chapter IV.C.1).

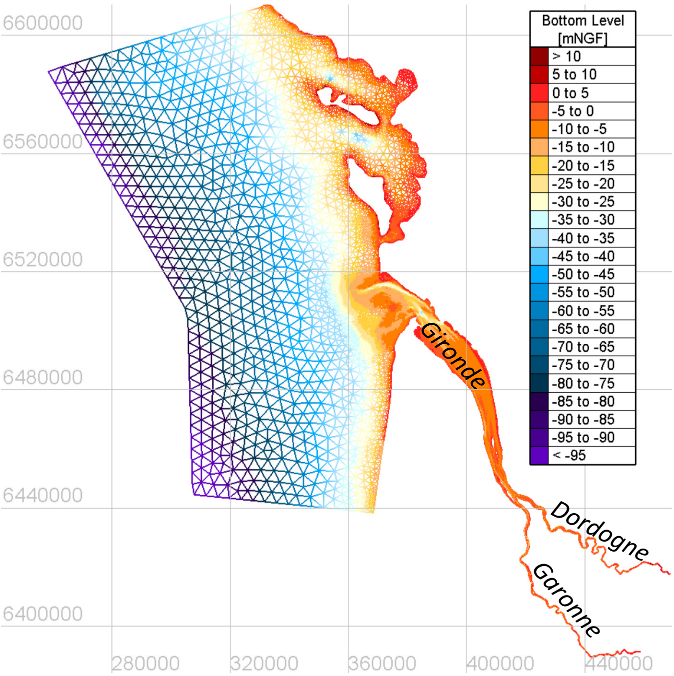

Figure 1. Mesh (2D) colored by topo-bathymetry [m NGF] of GXL3D model (Lambert 93 projection)

Tidal elevations and velocities are prescribed on the offshore boundary using the North East Atlantic (NEA) model of the LEGOS (46 constituents) [2]. Discharges as provided by the Hydroportail (HP, https://hydro.eaufrance.fr) service are prescribed at both tributaries. Bottom friction was initially defined using the Nikuradse law following a regional rugosity (k_s) map, which was adapted in GIROS. As an alternative, as friction is also likely to depend on the instantaneous location of the TMZ, the van Rijn's bed roughness predictor may also be used based on a proper distribution of cohesive (mud) and non-cohesive (sand) sediments on the bed. Horizontal turbulence is represented by constant viscosity ($\nu_{x,y} = 1 m^2.s^{-1}$) while vertical turbulence is based on the Prandtl mixing length model with Munk and Anderson's damping function modified according to [1,3] in order to take density gradients (stratifications) into account. As an alternative, the Tsanis model – adopted in GIROS – may also be used according to previous modelling works on the Gironde estuary [4,5].

The TELEMAC-3D model is coupled with GAIA to model sediment transport and morphodynamics. Four classes of sediments are considered: two classes of sand and two classes of muds, following [4,6]. Bed load for sand may be activated (Meyer-Peter and Müller formula) or not. In GIROS, it is deactivated so that the presence of non-cohesive sediments only influences the properties of mixed sediments. Deposition and erosion of muds follows the classical Krone and Partheniades laws, respectively. For deposition, settling velocity is calculated for each mud class according to the formulae of [7] reported in [4-6], which include flocculation and hindered settling effects as influenced by sediment concentration and salinity. Consolidation process is also included using the multi-layer approach with transfer coefficients calibrated following [8]. For more details on the sediment configuration of GXL3D in GAIA, the reader is referred to [1].

The GXL3D model has been extensively validated against field data in the frame of the Gironde XL project and in [1] for water level, velocity, salinity and suspended sediment concentration (SSC). An example of comparison of water level results (obtained in GIROS) against tide gauge measurements in Bordeaux is shown in Figure 2.

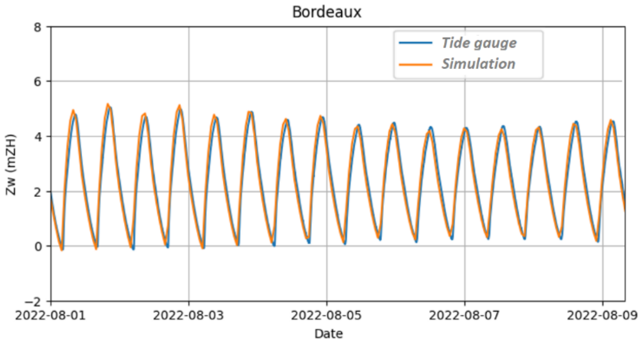

Figure 2. Comparison of water level predicted by GXL3D (orange line) and tide gauge measurements (blue line) in Bordeaux

Beyond the main settings of GXL3D, some features have been added to the TELEMAC-3D module implemented in GIROS. For instance, wind influence on surface currents was activated while air pressure variations have been included to calculate an equivalent set-up/set-down to be applied to the boundary water level to account for storm/anticyclonic situations respectively. Also, as previously mentioned, TELEMAC-3D was also coupled to the water quality WAQTEL "THERMIC+O2" module to include four new tracers: temperature (Sweers' linear formula for water-air exchanges), dissolved oxygen (O_2), ammoniacal load (NH_4) and organic load (L). Finally, the value of sea water density is calculated at each time step based on temperature, salinity and SSC.

The boundary conditions setup for the whole coupled model are shown in Figure 3. Discharges at each tributary (Garonne, Dordogne) are provided by the HP network through the Hub'Eau platform (https://hubeau.eaufrance.fr). Atmospheric data, such as wind velocity/direction, air pressure and temperature are extracted from regional models (ERA5, CERRA, Météo-France etc.) as provided by the Open-Meteo web service (https://open-meteo.com/en) at a central position in the estuary (45.4°N, 0.8°E). Ocean boundary conditions (temperature, salinity, O_2, NH_4) are prescribed using the data produced by operational, regional Copernicus models (Atlantic-Iberian Biscay Irish – IBI – 0.028° to 0.083° analysis & forecast models for ocean physics and biogeochemistry, https://data.marine.copernicus.eu/products). On the tributary side, the same variables are prescribed based on the available measurements provided by the estuarine monitoring network MAGEST (https://magest.oasu.u-bordeaux.fr/) at the stations Cadillac and Branne for the Garonne and Dordogne rivers, respectively. In case these are not available, strategies are applied to overcome the lack of information such as either using the data provided by another MAGEST station located further downstream the river or using those of the other tributary or even prescribing default values. Ammoniacal load is assumed to be zero on the oceanic boundary. At each tributary, pending the installation of sensors, a value of 3 $mg.l^{-1}$ is assumed by default whereas the value 0.054 $mg.l^{-1}$ is prescribed for ammoniacal load, in agreement with [5] and field observations in the Hub'Eau platform. For SSC, zero sediment input is assumed on the oceanic boundary whereas an empirical law is used in each tributary to determine the SSC (in $mg.l^{-1}$) based on the associated discharge. These laws have been chosen based on comparing SSC values as estimated by the national measurement network NAIADES (Water Agency) in close locations against corresponding HP discharges.

Initial conditions are defined by previous run for all variables. It has been observed, that for the salinity gradient to be well reproduced in the estuary, a typical spin-up duration of one month is required whatever the initial state is. For temperature and other water quality variables, this order of magnitude is also valid. For initial sediment state see [1].

B. *Wave Model*

In order to provide wave information into the GIROS interface (for navigability purposes, for instance), a wave model has been developed by coupling the modules TOMAWAC and TELEMAC-2D. The coupling allows to take the effect of water depth variations on wave characteristics (energy and direction, in particular) into account. The 2D current model is based on a previous 2D version of Gironde XL (see [9]), which has been adapted – in version 8.2 – to the same mesh, DEM etc. as the 3D model. To this respect, any bathymetric update performed in the 3D model is *de facto* taken into consideration in the wave model. Refraction, breaking, bottom friction, non-linear wave-wave interactions (quadruplets and triplets), wind input and white-capping are activated in the spectral wave model. Offshore boundary conditions are defined as JONSWAP-$\cos^{2s}$ directional spectra, whose characteristics are provided by the operational, regional (IBI) 0.05° Copernicus wave model, namely significant wave height (H_{m0}), peak period (T_p) and mean direction (θ_m). The model has been developed and validated at an early stage of the GIROS project timeline. Figure 4 and Figure 5 illustrate respectively some calibration tests comparing TOMAWAC-TELEMAC-2D H_{m0} results with the WW3 model results provided on the IFREMER MARC operational forecasting platform (https://marc.ifremer.fr/) or with field data estimated by the CANDHIS buoy '01705' deployed near Royan in 14m depth. The value of wave breaking coefficient (γ_2) was adjusted in order to remain as close to the reference data as possible (with natural expected uncertainties due to bathymetry, model resolution etc.). For Copernicus offshore boundary conditions, an optimal value of γ_2 was found in the range [0.3; 0.5].

Initial conditions are defined by previous run for all variables.

IV. Operational Forecast and Reanalysis

A. *Digital Architecture and Computational Environment*

The architecture of the digital twins is illustrated in Figure 6. The open-source code of GIROS and the digital models of the Gironde estuary are hosted by the regional NAOS (Nouvelle-Aquitaine Open-Source) community repository GitLab. NAOS also hosts the GIROS digital twins website (https://jumeaux-fleuve.naos-cluster.tech/), with the objective of sharing costs and benefiting from the NAOS' community animation and communication. GitLab is the software forge that centralises, in a collaborative way (Version Control System), the development

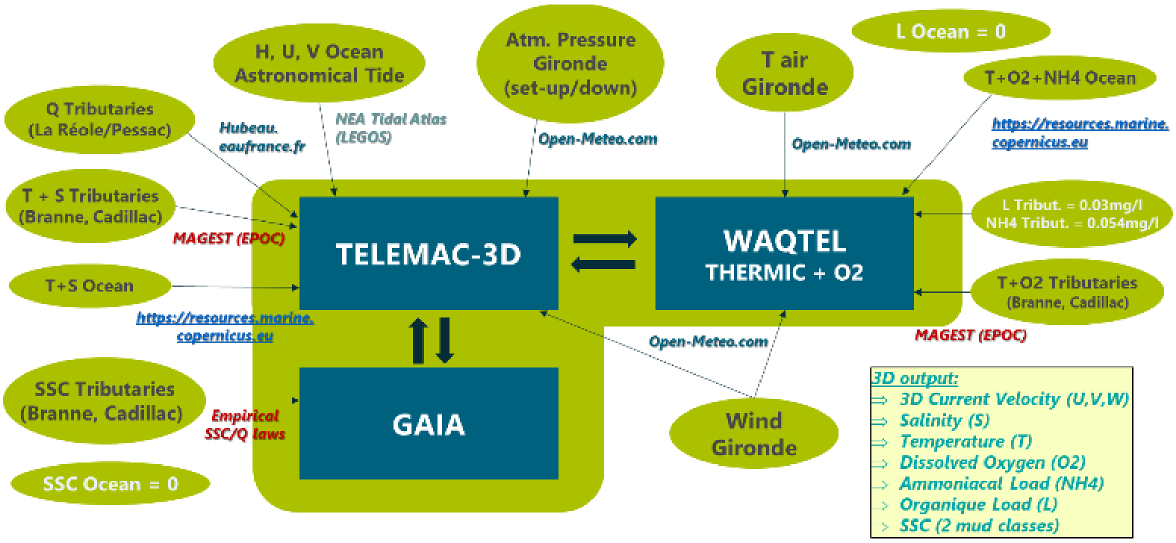

Figure 3. Architecture of the coupled hydro-sediment & water quality model implemented in GIROS along with data sources for boundary conditions

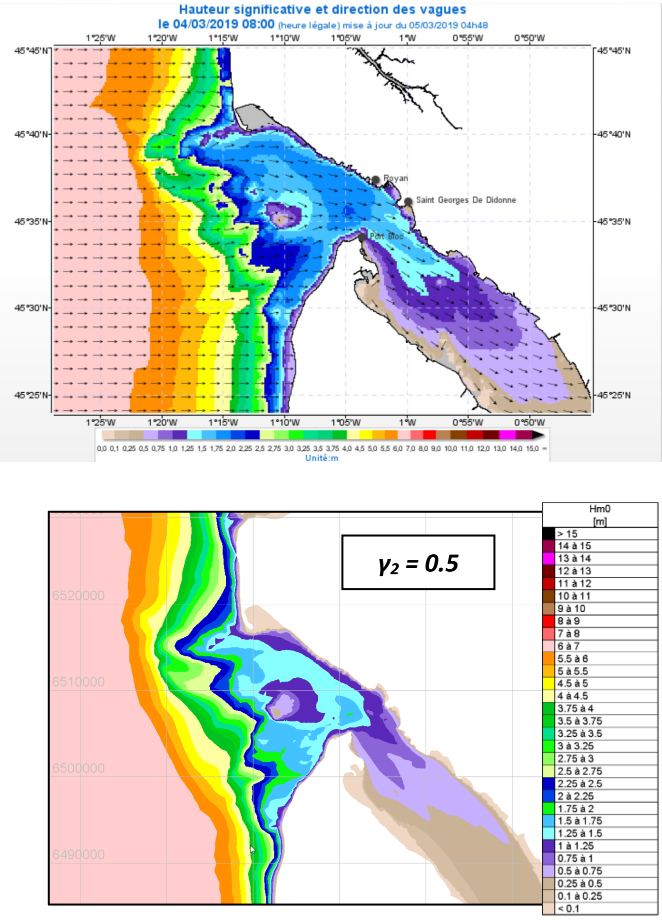

Figure 4. (Top) MARC operational forcast for H_{m0} near the mouth of the Gironde estuary on the 04/03/2019, 8.AM (France time); (Bottom) Corresponding TOMAWAC-TELEMAC-2D result with $\gamma_2 = 0.5$

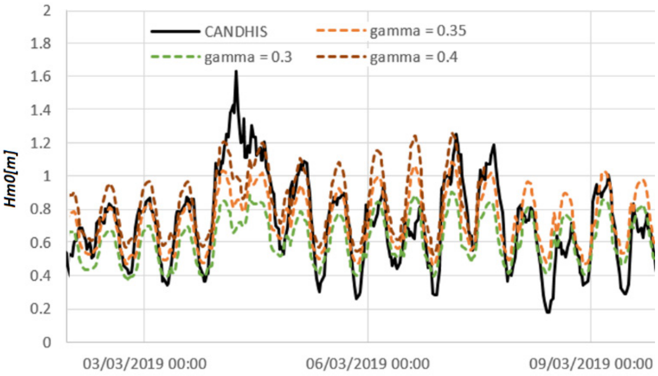

Figure 5. Comparison of TOMAWAC-TELEMAC-2D Hm0 results with CANDHIS estimates in early March 2019 (01705 buoy near Royan)

of the GIROS modules. From the user's side, it can be used to visualise the default core models and the simulation folders. For example, at each new simulation request (either automatically or from user through the 'Study Lab' module), the new calculation folder may be inspected through the GitLab application (see chapter II.E). Results can then be explored by JupyterLab notebook by using numerous example Python scripts in a library.

The simulations are performed on an external platform called LISOS. This platform is built on the cloud computing service of Google, which was specifically designed to execute the many Telemac simulation requests related to GIROS using APIs and many virtual computation cores (parallel computing).

The visual part of GIROS mainly rests on QGIS Server and QGIS web client 2 (QWC2).

B. Lossy Data Compression

Once a simulation is completed on LISOS, the GIROS system is informed: the output Selafin files are retrieved and

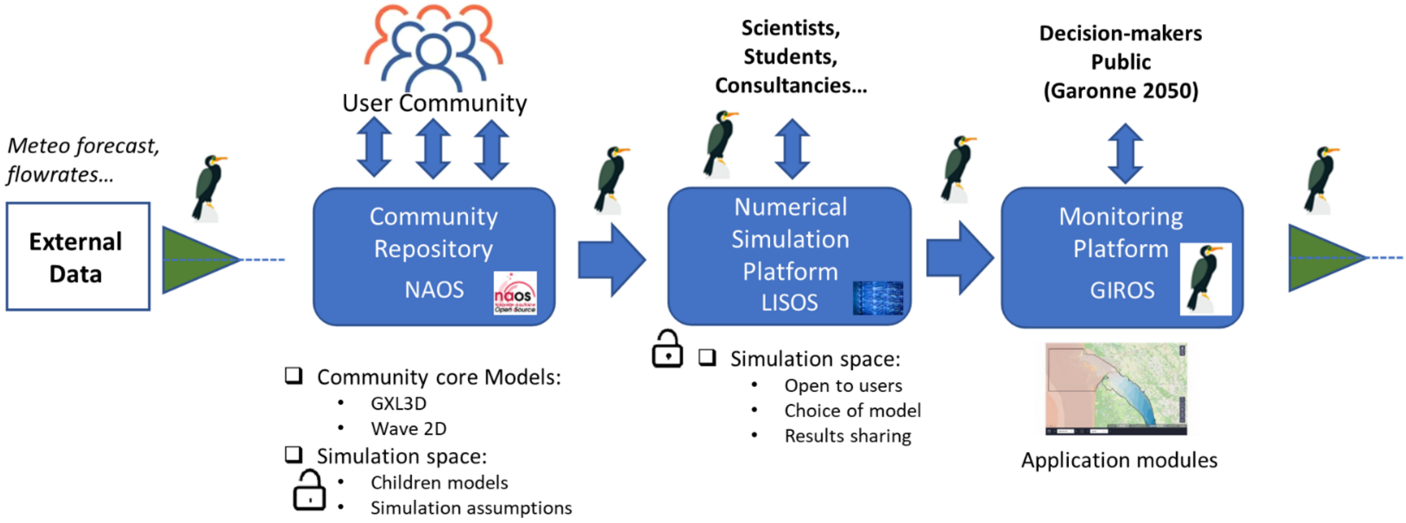

Figure 6. Architecture and platforms of the Digital Twins of the Gironde (the presence of a cormorant means an action supervised by GIROS)

processed to fill the GIROS database with the model results, although not directly. In view of optimizing the volume of data stored in NAOS, indeed, a lossy compression is applied to the raw data, which consists in selecting only a fraction of the 3D nodes (less than 15 000 over about 58 000 in both surface and bottom layers only) and resampling the results according to a specific scale for each variable (range and number of bins) at 1 h time step: at the end of the process, the volume of data is divided by more than 50. Such a procedure is perfectly adapted for result visualization in a webGIS environment (mapped data).

C. Operational Model Running

Simulations are run every day and every 30 days (trends) to feed the GIROS database. Each type of operational run is described below.

1) Daily Forecast Run

Every day D, the two core models are run over the period D-1 to D+10. Coming back one day in the past allows to refresh previous predictions by prescribing boundaries with more reliable data (measurements or assimilated, 'near real-time' model data) and provide better initial conditions for the 10-day forecast. A specific back-end script downloads the available data (discharges from the Hub'Eau platform, MAGEST, Copernicus and atmospheric Open-Meteo data from respective websites etc.) using dedicated API requests, processes (conversions, operations, availability and ranging tests etc.) and formats them in order to produce the boundary and atmospheric files required by TELEMAC-3D, TELEMAC-2D and TOMAWAC. The data sources related to forecast modelling (Open-Meteo, Copernicus) allow at least 5-day ahead predictions while measurement data (Hub'Eau/HP, MAGEST) are extended over 10 days assuming no significant change at short term. As soon as the Telemac files are ready on the GitLab, a running request is sent to the LISOS platform in order to launch the simulation on a large number or virtual cores (parallel run). Each 11-day simulation takes less than 2 hours to complete. With an objective of digital responsibility, IT resources have been voluntarily reduced to daily operations.

At the end of each daily run, the results at day D are stored as an initialisation file for the next day's run. The bottom evolution at D is also taken into account by overwriting the BOTTOM variable in the geometry file. Bathymetric updates – if existing – are included in the model at the beginning of the simulation, as mentioned in chapter III.A.

2) Monthly Forecast Run

As for daily runs, a monthly run is launched every 30 days. In that case, only the 3D hydro-sediment & water quality model is used, which is run over the period D-30 to D+130. The goal of this run is twofold: First, providing "trend results" up to a minimum of 100 days ahead to GIROS users (through the 'Environment' module) and to other GIROS modules (like 'Navigability' and 'Dredging'), and second temporarily providing and storing on LISOS large Selafin files – covering a little more than 5 sliding months – produced by TELEMAC-3D and useful for mid-term model results inspection. Also, this run allows to refresh the GIROS database on a monthly basis by overwriting the 30 past days.

As boundary conditions need to be prescribed over about 4 months ahead, seasonal trends have been analytically defined so that realistic values for river discharges, temperatures, dissolved oxygen etc. may be reproduced whatever the period of the year. Analytical laws based on simple sine formulae have been determined by fitting moving median or trend curves drawn from long-term HP, Copernicus, ERA5 or MAGEST data. An example is shown in Figure 7 and Figure 8 for oceanic and tributary dissolved oxygen respectively. Constant values are assumed for other variables like wind velocity, air pressure, etc. For the past 30 days, global model (Copernicus etc.) and measurements (MAGEST, HP) data are used to prescribe model boundary conditions, just as in the daily run case.

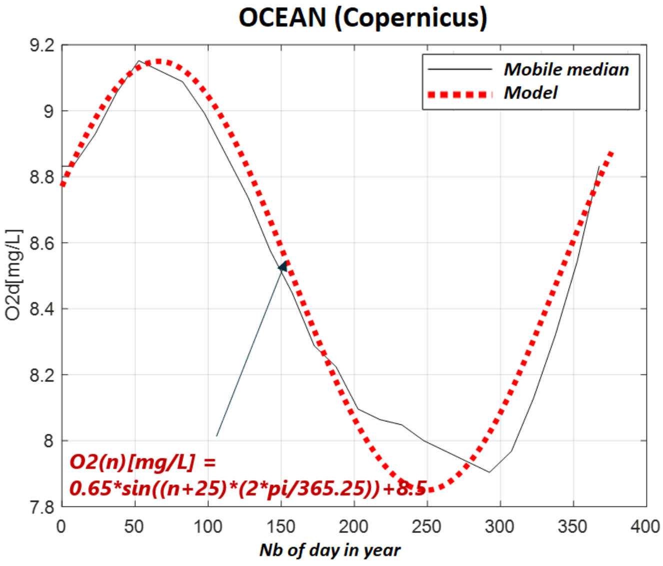

Figure 7. Analytical modelling of seasonal variability (mobile median of Copernicus model data) of oceanic dissolved oxygen

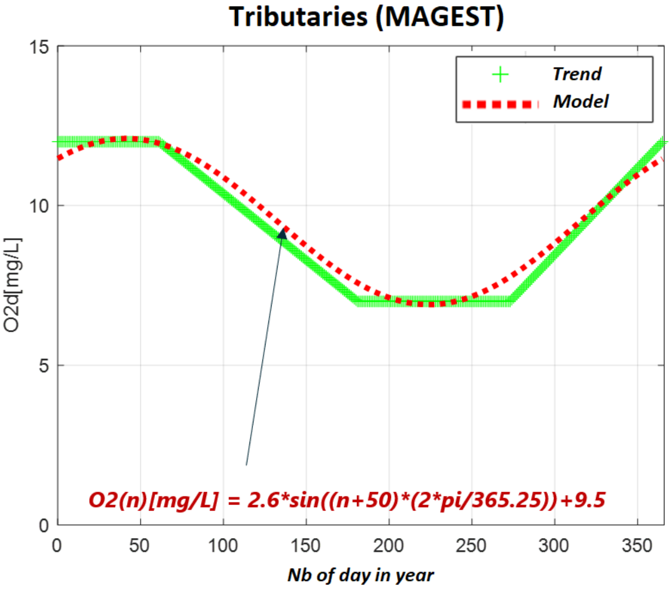

Figure 8. Analytical modelling of seasonal variability (mobile median) of dissolved oxygen in the tributaries (trend based on MAGEST data)

At the end of each monthly run, the results at day D are stored as an initialisation file for the next month's run. The bottom evolution at D is also taken into account by overwriting the BOTTOM variable in the geometry file. Bathymetric updates – if existing – are included in the model at the beginning of the simulation, as mentioned in chapter III.A.

3) *Garonne 2050*

The Garonne 2050 simulation was run only once. As said in chapter II.D, this simulation highly depends on prospective assumptions related to year 2050. For river discharges, CEREMA [10] calculated hydrograms for 2050 in the Garonne and Dordogne rivers following two AR5 IPCC's Representative Concentration Pathways (RCP 4.5 and 8.5, see [11]). Scenario RCP 4.5 was selected for the prescription of river discharge in Garonne 2050. The associated oceanic surge was also included in the offshore water level associated with a seal level rise by 2050 of 0.165 m according to IPCC AR6 (https://sealevel.nasa.gov/ipcc-ar6-sea-level-projection-tool). For the rest of the boundary conditions, a default choice was to consider the moving median value of each parameter (as shown before for seasonal trends) modified by prospective rise or publicly available reduction values (ex: +2°C in tributaries, +0.9°C in air temperature etc.). The other parameters were kept unchanged (namely salinity, ammoniacal and organic loads). The Garonne 2050 simulation starts on the 22/12/2049 to leave a 10-day spin-up time and results are produced on a daily basis.

Let us remind, however, that these assumptions are a first attempt for simulating the behaviour of the Gironde estuary by 2050 and shall be refined in the next steps of the GIROS development.

V. USER ACCESS

The GIROS website – in French – is accessible through the URL https://giros-fleuve.jumeaux-numeriques.fr/. At the time of writing, access to digital twins is restricted to the outcome evaluation community, especially forecasting. Soon, users will be able to contribute to the development of the next version of GIROS. Figure 9 gives a view of the access page and some modules.

VI. FURTHER ACTIONS AND COMMUNITIES

The GIROS Digital Twins have been created in an open-source and collaborative way to respond to the needs of water stakeholders and to accelerate the territorial resilience against climate change. The next developments and actions shall involve relevant public organisations and users as the various specific communities listed below.

A. *Community Creation*

In late 2022, a first workshop was launched with first users, which allowed to start structuring the following communities: Technical experts, IT developments, Users, Decision-maker, Governance. Other workshops are planned to clarify the rules of the governance.

The scientific community and technical experts – gathering all laboratories, consultancies and public institutions related to the Gironde estuary – will be in charge of maintaining and improving the core models – also encouraging the contribution of users – so that the quality and capacity of the models may be regularly enhanced. This collaborative work will also aim at providing a better understanding of the estuarine phenomena by constantly confronting model results to field data (mobile sensors, MAGEST network etc.).

B. *Governance*

A governance is necessary in particular to set the course for future developments, the means of supporting users and the priorities to be given to develop territorial resilience in the face of climate change.

C. *Pool Efforts and Sharing Results*

The replicability to other estuaries of the GIROS platform has already been demonstrated, in particular for a section of the Saint-Laurent River in Quebec, Canada, presented at the "Web à Quebec" event in May 2023.

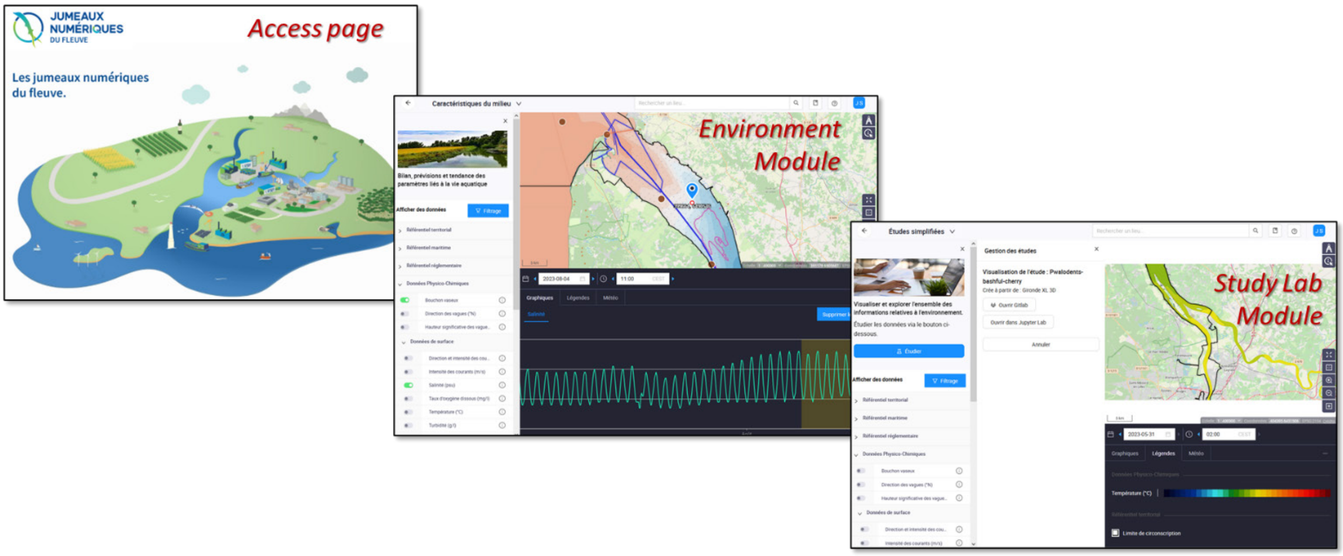

Figure 9. A view on the GIROS website and some modules

The results are already shared, via the regional structure NAOS, which actively participates in the animation of the communities. The choice of open source intellectual property for the tools will ultimately facilitate the creation of a dedicated structure, driven by a governance to be developed, in order to more easily pool efforts and move forward faster.

ACKNOWLEDGEMENT

J.-B. S., V. L., B. A. and F. K. thank Oslandia and Fieldbox AI for their active contribution to the achievement of GIROS. They also thank CEREMA, as the first contributor of the Digital Twins community.

REFERENCES

[1] N. Huybrechts, P. Tassi and F. Klein, “Three-dimensional sediment transport modelling of the Gironde estuary,” SimHydro 2021: Models for complex and global water issues – Practices and expectations, 15pp., Sophia-Antipolis, 2021.

[2] N. Huybrechts, C. Villaret, and F. Lyard, “Optimized predictive 2D hydrodynamic model of the Gironde Estuary (France),” Journal of Waterway, Coast, Port and Ocean engineering, vol. 138 (4), pp. 312-322, 2012.

[3] R. Lehfeldt, S. Bloss, “Algebraic Turbulence Model for Stratified Tidal Flows,” in J. Dronkers, W. van Leussen (eds) Physical Processes in Estuaries. Springer, Berlin, Heidelberg, 1988.

[4] A. Benaouda, “Dynamique saisonnière des sédiments en suspension dans l’estuaire de la Gironde: Modélisation opérationnelle de la réponse aux forçages hydrodynamiques, ” Ph.D report, University of Bordeaux, France, 295 pp, 2008.

[5] K. Lajaunie-Salla, “Modélisation de la dynamique de l’oxygène dissous dans l’estuaire de la Gironde,” Ph.D report, Sciences de la Terre, University of Bordeaux, 244pp., 2016.

[6] A. Sottolichio, P. Le Hir, and P. Castaing, “Modeling mechanisms for the stability of the turbidity maximum in the Gironde estuary, France,” in Proc. Mar. Sci., vol. 3, pp. 373–386, 2000.

[7] P. Le Hir, P. Bassoullet, and H. Jestin, “Application of the continuous modeling concept to simulate high-concentration suspended sediment in a macrotidal estuary,” in: Proceedings in Marine Science, vol. 3, pp. 229–247, 2000.

[8] L. A Van, “Modélisation du transport des sédiments mixtes sable-vase et application à la morphodynamique de l’estuaire de la Gironde,” Ph.D report, University of Paris-Est, 194pp., 2012.

[9] S. Orseau, N. Huybrechts, P. Tassi, D. Pham van Bang and F. Klein, “Two-dimensional modeling of fine sediment transport with mixed sediment and consolidation: Application to the Gironde Estuary, France,” Int. Jour. Sed. Res., vol. 36, pp. 736-746, 2021.

[10] M. Traboulsi, V. Laborie and N. Huybrechts, “Impact of climate change on the hydrodynamic patterns of the Gironde estuary,” Proc. XVIIèmes Journées Nationales Génie Côtier – Génie Civil, Chatou, France, Oct. 2022.

[11] G. Ouzeau, M. Deque, M. Jouini, S. Planton, R. Vautard R. "Le climat de la France au XXIe siècle," Rapport de la Direction générale de l’énergie et du climat, www.developpement-durable.gouv.fr, 62p, 2014.

SCALDIS 2020: An updated 3D hydrodynamic model for the Scheldt estuary

Joris Vanlede[1], Mostafa Nazarali[1,2]
joris.vanlede@mow.vlaanderen.be
[1]: Flanders Hydraulics, Belgium
[2]: HAEDES, Belgium

Abstract – **The SCALDIS model is a reference model for the entire Scheldt estuary, built in TELEMAC-3D. This paper presents the methodology for the (ongoing) calibration of the new version of this model: SCALDIS 2020. The paper discusses methods for gap filling in water level timeseries, the quantification of mesh quality and systematic model skill assessment. The parallelisation performance on the HPC infrastructure of Flanders Hydraulics is also quantified.**

Keywords: Hydrodynamics, Scheldt estuary, Calibration, TELEMAC-3D

I. INTRODUCTION

The SCALDIS model is a reference model for the entire estuary of the Scheldt estuary, built in TELEMAC-3D [1]. The model was initially developed and calibrated for scenario analysis of measures in the Upper Sea Scheldt. Based on the availability of a new spatially covering bathymetry every 6 years, an update cycle with that interval was proposed for a re-calibration of the model [2]. The first SCALDIS model was calibrated for 2013 [3], and a re-calibration was carried out for 2019 [4].

This paper presents a major update of the SCALDIS model with specific attention to the generation of an optimized unstructured mesh and a revision of the type and the location of the open sea boundary condition. The model is optimised for calculation on the High Performance Computing (HPC) cluster of Flanders Hydraulics (FH).

The model is being developed in TELEMAC v8p4r0. The calibration of SCALDIS 2020 is still ongoing; final results are expected in Q3 2023.

II. MODEL DESCRIPTION

A. Model goals

The SCALDIS model is a reference model on which many different applications are based. [1] It provides the hydrodynamic input for sediment transport calculations (sand and mud). [2] The hydrodynamic results are also used to delineate habitats in the subtidal zone of the Sea Scheldt. In particular, the maximum flood current velocity defines robust boundary values for high and low dynamic subtidal zones. [3] The SCALDIS model is also used to evaluate the effect of flood control areas on the hydrodynamics in the Scheldt estuary. [4] Tracer dispersion experiments in the model are used to calibrate an ecosystem model. [5] The flow fields it produces are processed as a flow atlas, and are implemented in the shipping simulator of Flanders Hydraulics (FH).

B. Model domain and grid

SCALDIS 2020 consists of about 1 million elements per layer and 5 vertical interfaces. The length of element edges varies from 3 m at the upstream end of the tributaries to 160 m in the western Scheldt. The model domain covers the tidally influenced part of the Scheldt estuary (see Figure 1).

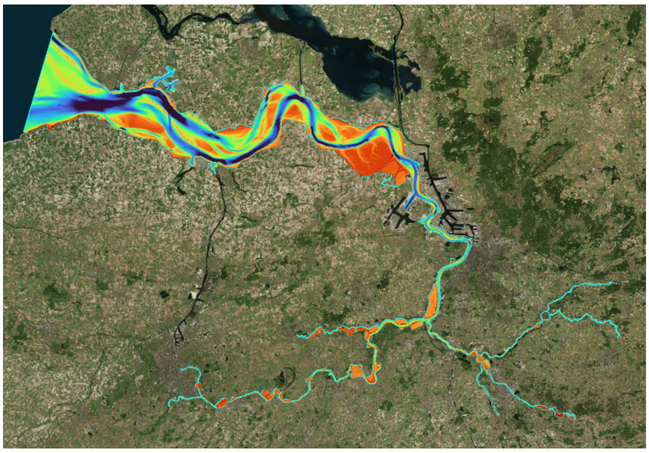

Figure 1. Model domain

Contrary to earlier versions of SCALDIS (2013 and 2019), SCALDIS 2020 does *not* include the Belgian Coastal Zone (part of the Southern North Sea) in its model domain. This is primarily because FH has developed SCALDIS COAST, a sister model that covers the coastal and North Sea domain [5]. Instead of an open boundary in the North Sea, the downstream boundary is now the transect between the (Dutch) measurement stations Cadzand and Westkapelle.

All Flood Control Areas which are currently active or planned are included in the mesh of the SCALDIS 2020 model. During remeshing, the grid quality was monitored with in-house tools, as described in the methodology section IV.B on mesh quality.

C. Boundary conditions

The model is driven by water levels at the downstream boundary (type 5 4 4). The open sea boundary condition is created by linearly interpolating the measured water level data between the two tide gauge stations: Cadzand and Westkapelle.

The measured water level time series are not always perfectly continuous and may contain gaps (no-data values). These gaps need to be filled up before these timeseries can act as boundary conditions (see also the methodology section IV.A on gap filling).

Time series of river discharge are imposed at the eight upstream boundaries of the model.

D. *Initial conditions*

The SCALDIS model is initialised using a hotstart condition. The hotstart condition is the result of a 2-days run. Together with the hotstart, the salinity is initialised from an interpolation of measurements.

III. MEASUREMENT DATA

A. *Bathymetry*

Several topography and bathymetry datasets of the year 2020 are used to update the SCALDIS model. These data have different resolution and reference levels. Some of these data overlap each other in some areas. In those cases, either the most recent dataset or the one with higher resolution is used for model bathymetry interpolation. Overlaps between datasets are checked for continuity in order to avoid vertical datum shifts

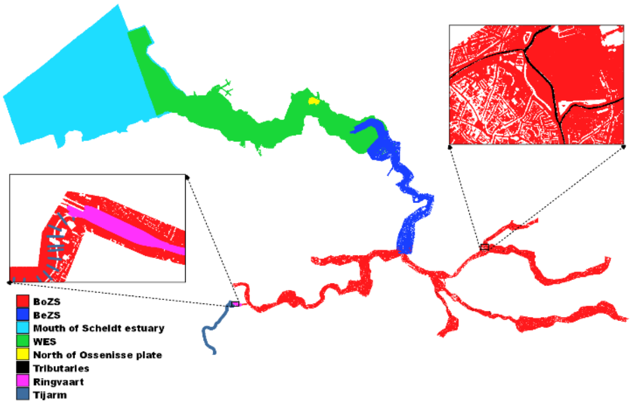

Figure 2. The coverage of topo-bathymetric data used for construction of model bathymetry for the year 2020.

B. *Water level*

In 2020, water level data are available in 55 stations within model domain (Figure 3). These data are measured by either HIC (BE) or HMCZ (NL) every 10 minutes. Stations WestKapelle and Cadzand are used for the downstream boundary condition. Data from the other 53 stations are used for calibration and validation (see sections IV.C to E).

C. *Salinity*

Within the modeling domain, there are 13 salinity measurement stations. Salinity data are used for setting the initial condition, for defining the downstream boundary condition, and for validation of salinity in the domain.

Since there are no measurements available in 2020 at the stations Vlakte van de Raan and Hoofdplaat that are located near the seaward boundary, the boundary condition for salinity at the downstream boundary has to be estimated. The average value of salinity at Vlakte van de Raan (located near the mouth of the estuary) is used as a constant downstream boundary condition for salinity. An average value of 32.5 PSU was calculated from a long timeseries of measurements (2007-2019).

D. *Stationary velocity measurements*

Continuous deep water velocity measurements for the year 2020 are available at two locations: Lillo and Oosterweel. Other measurement data came from shallow water measurement campaigns in the preceding 5 years (2015-2020). The location of these measurements is shown in Figure 3. In total, data at 84 temporary measurement stations are used in calibration or validation. Data at Baalhoek and Knuitershoek (2018) were kindly provided by RWS.

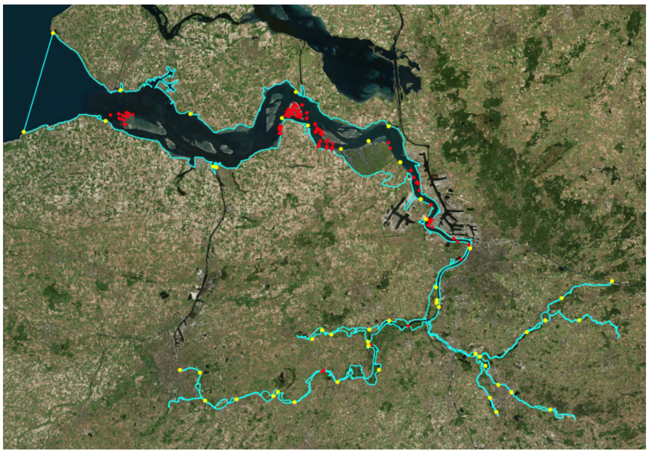

Figure 3. Location of water level (yellow dots) and stationary current velocity measurements (2015-2020) (red dots)

E. *Sailed ADCP measurements*

In total there are 361 sailed ADCP campaigns available in the Scheldt estuary and Belgian Coast. In order to calibrate and validate the SCALDIS 2020 model, a selection was made among those measured in the recent 10 years. This selection was made using two criteria: the measurement transects should be distributed over the model domain and if a transect was measured multiple times, preference is given to the most recent measurement. In total, 44 campaigns are selected for model calibration, and 27 for model validation.

IV. METHODS

A. *Gap filling*

Both previous SCALDIS models (2013 and 2019) were nested in the ZUNO model of the southern North Sea. The downside of nesting a model in another model is that any model error in the mother model (e.g. errors in tidal components or in surge) are imported over the boundary and contribute to the total error in the model domain. The upside is that modelled timeseries are continuous (they contain no gaps in time if no drying/wetting occurs at the boundary of the daughter model), which makes the derivation of boundary conditions more straightforward.

With SCALDIS 2020, this argument is reversed. Since the model uses measured water levels as a downstream boundary condition, any gap in the measured timeseries needs to be resolved. But on the upside, no model error on the water levels is imported at the downstream boundary. In Westkapelle, the gap duration ranges between 1.67 and 42.5 hours for 2020, while in Cadzand the gap durations are between 40 minutes and 42.5 hours.

Three different algorithms are identified that can fill the gaps of a tidal water level signal. They are briefly explained here. The methods (including a decision tree) are implemented in a Gap Filling Toolbox in Matlab at FH.

1) Spline interpolation method

In this method, a spline curve is fitted to the time series of the measured water level. If the gap duration is short, this interpolation method works well. As expected, the interpolation method is ill-suited to fill longer gaps (+4 hours).

2) Comparable Tide (CT) method

In this method, first the water level records over a period of 24 hour before and 24 hour after the gap instance are selected. Then a long historical time series at the same station (or even a nearby station) is scanned to find the most comparable tidal condition. The statistical parameter used to compare these time series is RMSE0 (Bias corrected root mean square error). The gap is filled with the identified comparable tide and any bias at the beginning and end of each gap period is corrected to avoid discontinuity in the time series. This is similar to the comparable tide method that is implemented in the VIMM toolbox [6].

3) Harmonic method

In this method, the amplitude and phase of tidal constituents are calculated by tidal harmonic analysis. These coefficients are then used to predict the time series of water level in the gap period. In order to have a smooth transition between the existing data points and the predicted values during the gap period, a bias correction step is also carried out. The harmonic method can predict the overall shape of the water level time series when the non-tidal signals (like surge) don't vary too much over the duration of the gap.

4) Discussion

The best gap filling method for each specific gap is selected based on the gap duration. In order to determine a suitable decision tree, the performance of each gap filling method is evaluated systematically. Synthetic timeseries are produced by making an artificial gap in a continuous observed time series of water level. The artificial gap duration is varied in steps of 1 hour between 1 and 48 hours. For each gap length, 50 synthetic timeseries are generated by creating a gap of the specific length at a random location in the timeseries. These gaps are then filled using the different methods above.

The performance of the different gap filling methods for varying gap duration is shown in Figure 4. This figure shows the RMSE of the gap-filled timeseries to the original, continuous measurement. The continuous lines are the mean RMSE, the shaded regions show the area between 25th and 75th percentile of the RMSE values, and the scatter points show the individual data points.

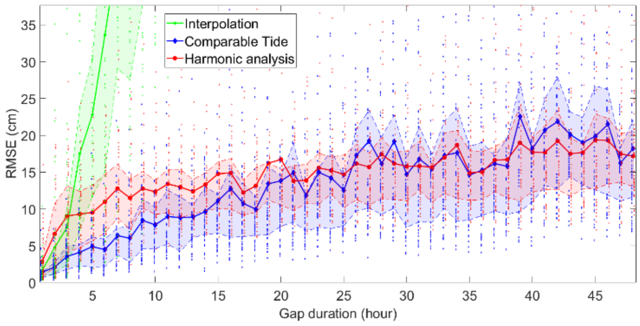

Figure 4. Accuracy of three different gap filling algorithms: Interpolation (green), Comparable tide (blue) and Harmonic analysis (red)

The interpolation method works only for short gap events (<3h). Longer gaps can be better filled by applying either the comparable tide or the harmonic method. For medium-length gaps (3h – 20h), the CT method gives a lower error then the harmonic method. For longer gaps (+20h) the CT method and the harmonic analysis have a similar accuracy. The harmonic analysis method executes much faster though than the CT method. The runtime of the CT method also depends on the length of the long historical timeseries in which the search is performed.

5) Decision tree

The following decision tree is proposed to fill the gaps in both the Westkapelle and Cadzand stations. The thresholds between different algorithms are chosen somewhat arbitrarily based on the results discussed above.

- Gap length less than 1 hour: Spline interpolation method
- Gap length between 1 hour and 24 hours: Comparable tide method
- Gap length between longer than 24 hours: Harmonic method

B. Mesh Quality

The quality of SCALDIS 2020 mesh is checked in MATLAB with the function Telemac_Mesh_Quality, which is part of the WL_Telemac toolbox. The following parameters are used to quantify the mesh quality:

- Skewness: An angular measure of element quality with respect to the 60° angles of an equilateral triangular element (see eq. 1). The skewness of an ideal element is 0 and the value for a bad element is 1. It's preferred to limit the skewness of elements to 0.5.

$$skewness = \max\left[\frac{\theta_{max}-\theta_e}{180-\theta_e}, \frac{\theta_e-\theta_{min}}{\theta_e}\right] \quad (1)$$

θ_{max}: largest angle of the element
θ_{min}: smallest angle of the element
θ_e: angle of the equilateral triangle (equal to 60 degree)

- Edge length ratio: The ratio of the longest edge to the shortest edge of each element. Large aspect ratios increase the inaccuracy of the finite element representation, because they affect the convergence of finite element solutions. The aspect ratio of an ideal element is 1. We aim to maintain it between 1 and 5.

- Aspect ratio: Two times the ratio of the radius of the inscribed circle to the radius of the circumscribed circle, with a reporting threshold of 0.5.
- Smoothness: The maximum ratio of the area of an element to the area of its neighbouring elements. This parameter represents the area change (1<Smoothness<1.5=good, 1.5<Smoothness<2.5=fair, Smoothness>5=poor)
- Overconstrained elements: Triangular elements in which all three nodes are located on boundaries of the model.

For the optimized mesh, 99.95% of elements has a good smoothness; 98% has a skewness lower than 0.5; and 99.99% has a good aspect ratio.

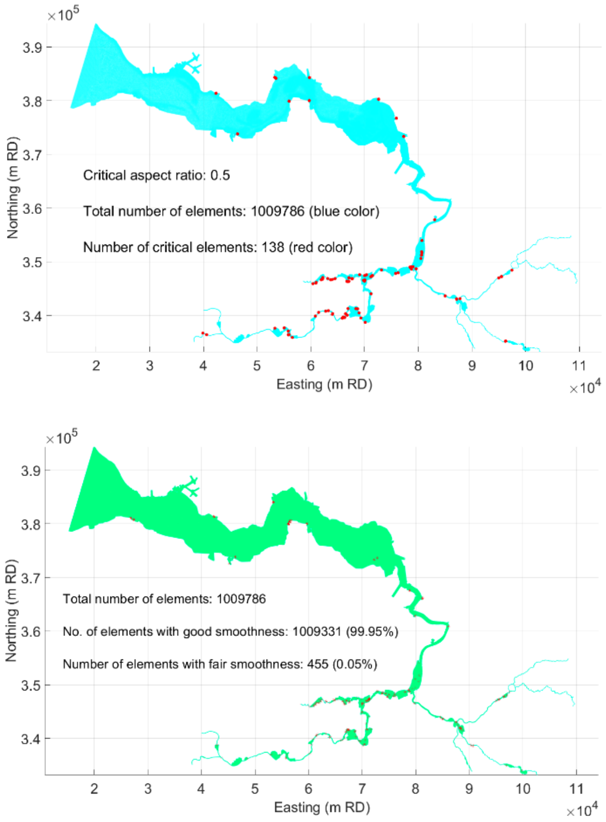

Figure 5. Results of the mesh quality analysis. Top panel: location of elements with a critical aspect ratio; bottom panel: location of elements with fair smoothness

C. *Quantified model skill assessment and Cost function*

For a reference model with a broad possible set of applications, it is important to have a calibration strategy that is sufficiently broad in scope. In order to achieve this goal, the VIMM toolbox is used for the hydraulic model. It is in-house developed at FH and runs in MATLAB [6].

A weighted dimensionless cost function is calculated for each simulation to assess model performance. Each factor is a particular error statistic with the same unit as the measurements on which they are based. The cost function is made dimensionless by normalizing to the factor score in the reference run. The task of calibration is to minimize this objective function.

$$\mathrm{Cost} = \sum_i \frac{\mathrm{Factor_i}}{\mathrm{Factor_{i,ref}}} \mathrm{Weight_i} \qquad (2)$$

Several parameters are selected as factors for the calculation of the cost function. [1] For the vertical tide, the RMSE (Root Mean Square Error) of the complete timeseries, as well as the RMSE of the level of high waters are taken into account. A vector difference is aggregated over 6 harmonic components. [2] For the horizontal tide, the RMAE (Root Mean Absolute Error) of sailed ADCP measurements and the RMSE of stationary velocity measurements are included as factors. Given the broad model goals (see II.A), horizontal and vertical tide are given the same total weight. Given that most model applications for SCALDIS are situated in Belgium, also a greater weight is attributed to the Sea Scheldt (Belgian part) than to the Western Scheldt (Dutch part).

D. *Calibration on roughness*

The Manning law was used to represent the bottom friction in SCALDIS 2013, while the Nikuradse law was applied in SCALDIS 2019. In SCALDIS 2013, the roughness in the Western and Sea Scheldt is between 0.012 and 0.023 s/m$^{1/3}$. In SCALDIS 2019, the range of roughness height is between 3.3327e-5 and 0.1 m. In order to compare the roughness of the SCALDIS 2019 and SCALDIS 2013 models, the Nikuradse roughness height is converted to a corresponding Manning value, using the average water depth along the thalweg.

The previously calibrated values of bed roughness along the thalweg (from the river mouth to upstream Sea Scheldt) are visualized in Figure 5.

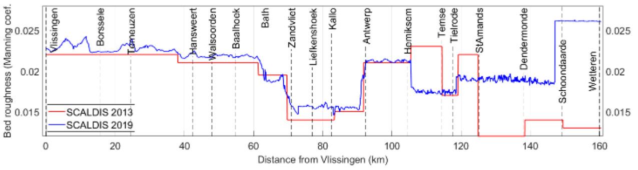

Figure 6. Bed roughness values of SCALDIS 2013 and SCALDIS 2019 models. The roughness of SCALDIS 2019 was converted from Nikuradse roughness height k_s to Manning's n

E. Calibration and Validation periods

The SCALDIS 2020 model is calibrated and validated for different periods in the year 2020. This work is still ongoing. The periods are chosen in a way to cover storm, calm (normal), and high river discharge conditions in the Scheldt estuary.

Calibration and validation data for water level, salinity and continuous velocity measurement stations are separated because the periods do not overlap. The velocity measurements in shallow stations, and the sailed ADCP measurements are distributed between calibration and validation, and over the different conditions.

Table 1. Calibration periods

Condition CALIBRATION	Period in 2020	Duration [days]
Calm	24 Jun to 8 Jul	14 days
Storm	05 Feb to 04 Mar	28 days
High upstream discharge	09 Mar to 16 Mar	7 days

Table 2. Validation periods

Condition VALIDATION	Period in 2020	Duration [days]
Calm	16 Aug to 28 Aug	14 days
Storm	29 Nov to 03 Dec	5 days
High upstream discharge	20 Dec to 31 Dec	11 days
Salinity	01 Jan to 01 Jul	6 months

V. PARALLELISATION PERFORMANCE

The parallel performance of the model was tested on the Bernoulli queue of the HPC cluster at FH. It has 12 nodes with 48 cores/node. Each node has 2 x AMD EPYC 7451 24-Core processors. The model was run for a simulation of 12h on different numbers of cores: 1, 12, 24, 48, 96, 144, 192, and 240 cores. The time step is set to 3 seconds and the culvert function is active in this test. All the benchmark models are started from a hotstart, to avoid the effects of spin up on model speedup.

The total runtime of a TELEMAC model comprises of initialization, partitioning, actual computation time, and I/O time. The runtime of each of the mentioned steps is reported separately. In order extend the output to the logfile with the timing of each step, the homere_telemac3d.f Fortran file is modified. The actual computation time is defined as the time elapsed from the moment that the computation starts to the moment that the last processor finishes execution. This step includes the initialization step (to allocate variables and arrays), solving the equations, and closing computation (deallocating variables), but excludes the time to merge the partitioned output files.

The model performance is measured by three different factors: Speedup factor, Efficiency, and Cost. The speedup factor [-] is defined as the ratio of the simulation period (in our test case = 12 hours) to the actual computation time. It is shown in Figure 6. A speedup factor of 14 is considered to be a minimum for efficient model use (one spring-neap cycle calculated in a day).

$$Speedup\ factor = \frac{simulation\ period}{actual\ computation\ time} \tag{3}$$

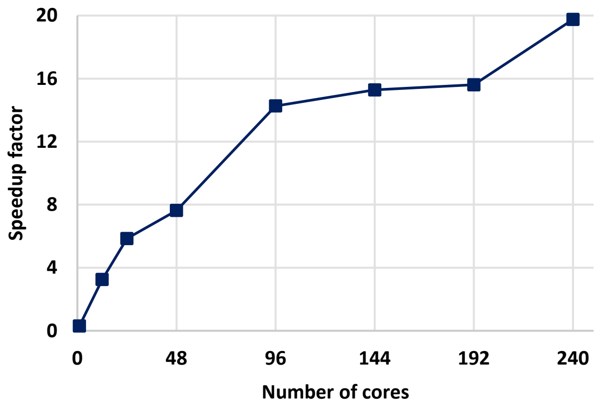

Figure 7. Speedup factor for varying number of cores

The efficiency [-] measures the fraction of time for which a core is usefully utilized. The efficiency of running a model on a single core is 1 by definition. It is calculated as:

$$Efficiency = \frac{serial\ runtime}{parallel\ runtime * number\ of\ cores} \tag{4}$$

The cost [h] scales with the number of credits that are used for a single simulation on a High Performance Cluster (HPC) and is calculated as follows:

$$Cost = runtime * number\ of\ cores \tag{5}$$

Cost and efficiency of the model are shown as function of the number of cores in Figure 7.

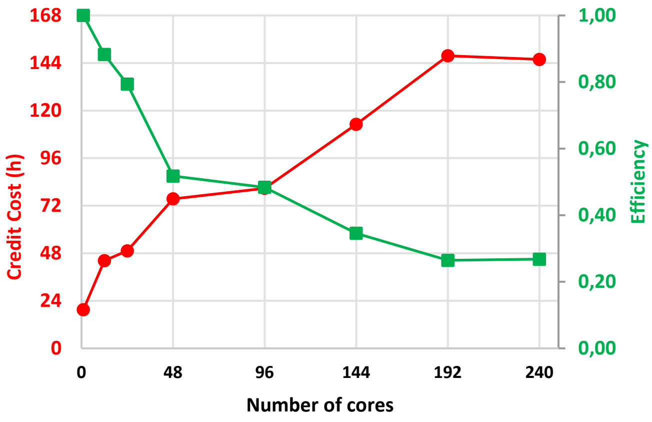

Figure 8. Cost and Efficiency for varying number of cores

CONCLUSIONS

Since the actual calibration and validation of the Scaldis model is still ongoing, this paper focuses on methodological choices that can be of interest to the broader TELEMAC modelling community.

Contrary to earlier versions of SCALDIS (2013 and 2019), SCALDIS 2020 will not include the Belgian Coastal Zone. This gives us the possibility to drive the model at its downstream end with water level measurements. Any gap in the measured timeseries needs to be resolved. This paper presents three possible algorithms for this task, with a validation and a decision tree dependant on the gap length.

A set of parameters is proposed to objectively check the mesh quality: element skewness, edge length ratio, aspect ration, smoothness and the number of overconstrained elements.

Since SCALDIS is a reference model of the Scheldt with a broad possible set of applications, it is being calibrated against a broad dataset of 55 water level stations, 13 salinity stations, 84 temporary stations for velocity and 2 permanent ones, and 71 sailed ADCP transects. The VIMM toolbox is used to perform the task of calculating the error statistics, and a weighted dimensionless cost function is calculated for each simulation to assess model performance.

In order to determine the optimal number of cores to run this model on, the parallel performance of the model is testes and expressed in terms of speedup factor, efficiency and computational cost.

ACKNOWLEDGEMENTS

This work is supported by research contract WL_2021_14, tendered by Flanders Hydraulics.

MDK-aKust, Rijkswaterstaat, Maritime Access Division, and W&Z Sea Scheldt Division are acknowledged for measuring and providing the bathymetric data.

HIC and HMCZ are acknowledged for measuring and providing access to the water level data.

RWS is kindly acknowledged for providing the velocity data at Baalhoek and Knuitershoek for 2018.

The OpenEarth initiative is acknowledged maintaining a version of the t_tide method.

REFERENCES

[1] J. Vanlede, S. Smolders, T. Maximova and M. J. Teles, “The 3D Unstructured SCALDIS Model. A new high resolution model for hydrodynamics and sediment transport in the tidal Scheldt,” in E-proceedings of the 36th IAHR World Congress 28 June – 3 July, 2015, The Hague, the Netherlands, 2015.

[2] J. Vanlede, Y. Plancke, S. Smolders, D. Meire and A. Van Braeckel, “Updatecyclus 2D en 3D Hydraulische modellen,” Flanders Hydraulics, WL2018MPA016_1, 2018.

[3] S. Smolders, T. Maximova, J. Vanlede, Y. Plancke, T. Verwaest and F. Mostaert, “Integraal Plan Bovenzeeschelde: Subreport 1 – SCALDIS: a 3D Hydrodynamic Model for the Scheldt Estuary.,” Flanders Hydraulics Research: Antwerp, Belgium, WL2016R13_131_1, 2016.

[4] J. Vanlede, K. Chu, S. Smolders, B. Decrop and F. Mostaert, “Update SCALDIS 2019: a 3D hydrodynamic model of the,” Flanders Hydraulics Research: Antwerp, WL2020RPA016_1, 2020.

[5] G. Kolokythas, B. De Maerschalck, L. Wang, E. Fonias and A. Breugem, “Scaldis-Coast: An integrated numerical model for the simulation of the Belgian Coast morphodynamics,” in Geophysical Research Abstracts, 2019.

[6] J. Vanlede, K. Chu and E. Fonias, “Introducing the VIMM toolbox for the (re)calibration of the SCALDIS model,” in Online proceedings of the papers submitted to the 2020 TELEMAC-MASCARET User Conference, 2020.

Scaldis Coast: Numerical modelling of 10 years for long-term morphology in the surf zone of the Belgian coast using the TELEMAC-MASCARET system

Bart De Maerschalck[1], W. Alexander Breugem[2], Gerasimos Kolokythas[1,3], Li Wang[1,2]
bart.demaerschalck@mow.vlaanderen.be, Antwerp, Belgium
[1]Flanders Hydraulics
[2]IMDC NV.
[3]ACTAEA Consulting Engineers L.P.

***Abstract* – With the increasing awareness of sea level rise, the Flemish Authorities initiated the *Complex Project Kustvisie* (CPKV) in order to start to define the overall long-term coastal defence strategy for the Belgian Coast together with all involved stakeholders. A flexible coastal model for the Belgian coast and Scheldt mouth area is needed to analyse the impact of sea level rise on the morphology of the coast, and to assess the efficiency of mitigation measures. An integral morphodynamic model for the whole Belgian Coast including the Western Scheldt mouth was built within the TELEMAC- MASCARET models suite.**

Keywords: Coastal modelling, Coastal protection, sediment transport

I. INTRODUCTION

The simulation of the long-term evolution of hydrodynamics and morphodynamics by state-of-the-art numerical modelling tools can give an important contribution to the strategic decision-making for the protection of the Belgian Coast from the climate change hazards. The SCALDIS-COAST model, developed in the present study, aspires to become a valuable tool for the assessment of potential coastal protection measures by predicting the morphological behaviour of the coast driven by the coupled action of currents and waves.

II. SCALDISCOAST

A. Model setup

The model covers the entire Belgian coast and Scheldt mouth area, including the Dunkirk coast, a part of the Dutch coast and the Eastern Scheldt, Figure 1. In order to model the tidal wave propagation correctly, the Western Scheldt is included and the upper part of the Sea Scheldt and its tributary are modelled schematically.

The computational grid is constructed by use of an advanced finite element mesh generator GMSH [4]. The mesh generator does not only allow for an automatic refinement in the vicinity of complex geometries, but also at steep gradients in the bathymetry. This way steep banks, gullies and navigation channels are accurately and efficiently represented in the model, Figure 2. The model resolution reaches from 750 m offshore to 25 m along the Belgian coastline. The resolution in the Western Scheldt estuary varies between 125 to 225 m. In total, the computational mesh consists of 250 000 nodes connecting around 500 000 triangular elements. Along the coastline, the grid is aligned to the crest of the groins which are represented in the bathymetry in combination with a hard layer to prevent the erosion of these structures.

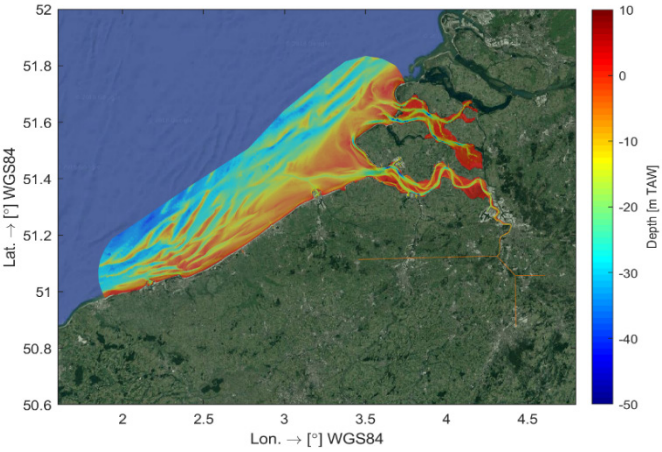

Figure 1. Domain and bathymetry of the Scaldis-Coast model

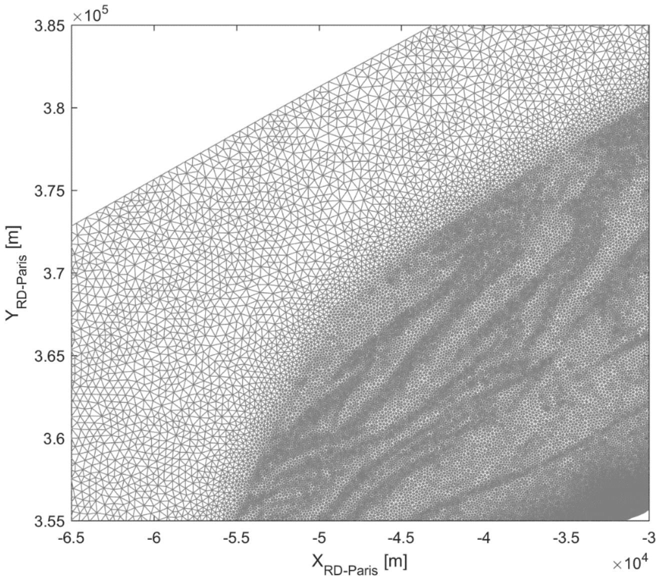

Figure 2. Detail of the mesh: Coarse elements are used offshore and automatic grid refinement is used along the steep bathymetry gradients at the Flemisch banks in the zone of interest

B. Tidal modelling

Water levels and currents are resolved by TELEMAC-2D. Originally the model was built within version v7p2r2, but recently all modules have been updated to v8p4. The offshore boundary conditions of the Scaldis-Coast model come from the regional ZUNOv3 [8] model of the southern North Sea through nesting. Specifically, the nesting procedure consists of numerical simulations conducted at two levels: First a continental shelf model (CSM) is run in order to provide the boundary conditions of the second-level nested model (ZUNO), which includes the southern North Sea and the Channel. The model is forced by 10-minute time series of the water level and velocities calculated by the ZUNOv3 model. The subroutine *bord.f* of TELEMAC was modified properly to allocate water level and velocity values for each boundary node separately. At the upstream boundaries, measured flow discharges at eight tributaries and channels are imposed. For the wind forcing, the measured wind times series at the offshore measurement station *Westhinder* (located at the offshore boundary of the model) was applied uniformly over the model.

The TELEMAC-2D model is validated against 25 tidal gauges along the Belgian coast and Wester Scheldt estuary, eight stationary velocity measurement station, and five sailed ADCP transects: in the vicinity of Zeebrugge port and the fairways, as well as along the Western Scheldt. It was found that the model performs well using a constant bed roughness coefficient (Manning's law) of 0.022 $m^{1/3}/s$. Only in the upper part of the Estuary, the coefficient is gradually reduced to 0.012 $m^{1/3}/s$ and an increased value is applied at the upstream schematized part of the model (0.04 $m^{1/3}/s$).

The RMSE of velocity magnitude is in general around 0.15 m/s. However, the peak flood velocities seem to be underestimated in some of the considered locations.

C. Waves

The wave propagation and transformation from the offshore boundary towards the coast under the influence of tides and wind is modelled using the TOMAWAC module. The waves have a major impact on the coastal morphology of the foreshore and beach. They drive the littoral transport through wave induced currents and steer the sediment up. The wave asymmetry and wave-skewness, Stokes drift, undertow and surface rollers are the main mechanisms for cross-shore sediment transport. In order to include the effect of tide on wave propagation, the TOMAWAC model is coupled to the TELEMAC-2D hydrodynamic model which provides, the water depths and tidal currents. The coupling is a two-way coupling so that TELEMAC-2D on its turn can calculate the wave driven currents.

Computationally, the wave transformation model is by far the most CPU time demanding module, and therefore one of the major limiting factors for long term morphodynamic model runs. Therefore, within the project a module TEL2TOM was developed to couple TOMAWAC with TELEMAC-2D on arbitrary meshes [1]. For the TOMAWAC run, the resolution was reduced by a factor two in the nearshore from 25 m to 50 m, and major parts of the Western and Eastern Scheldt estuaries were omitted. The total number of nodes is reduced from 273 000 to 138 000 nodes and the number of triangular elements from more than 500 000 to nearly 260 000, Figure 3. This way, the computational cost has been reduced by a factor two. For the wave propagation model a time step of 120 seconds and a coupling time with TELEMAC-2D of 30 minutes was used.

The wave boundary conditions are derived from the offshore measurement station Westhinder, which is located on the model boundary. Westhinder is a fixed measurement station part of the monitoring network Flemish Banks (Meetnet Vlaamse Banken, MVB). A JONSWAP spectrum based on the significant wave height, peak wave period and wave direction is applied uniformly on the off-shore boundary. The measured wind speed and direction at Westhinder is applied uniformly over the entire domain.

The wave model was validated against the data obtained within the Broersbank project [7]. In the Broersbank project, wave data was sampled at seven locations during the period between 2013 and 2017, Figure 4. The temporal resolution of the wave data reaches thirty minutes. The other six stations are temporary wave buoys placed for the duration of the Broersbank project. Since they are inside the model at different distances from the coast, they are particularly useful in validating the modelled wave propagation and transformation. For the validation, a seven-day period in November 2015 was selected including two storms, one from the Southwest on November 18, and one from the North on November 21.

The transformation of the significant wave heights and mean wave period from offshore boundary station, Westhinder, to onshore, BRB1GB, are shown in Figure 5 and Figure 6. For comparison both the TEL2TOM coupling and the one-to-one fully coupled version of the model are added to the graph. The wave model predicts the measured wave height and wave period well. The TEL2TOM coupling has hardly any influence on the model quality at the nearshore, even though the resolution is reduced by a factor two.

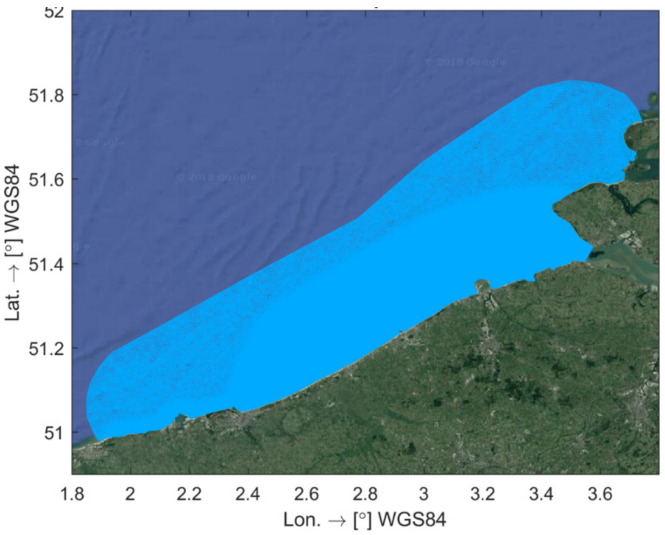

Figure 3. Computational grid of the wave model

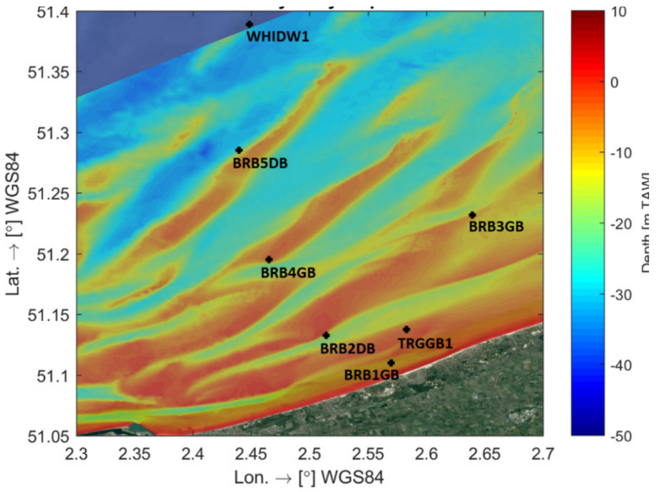

Figure 4. Locations of the Westhinder fixed station (WHIDW1) and the six temporary wave buoys during the Broersbank project.

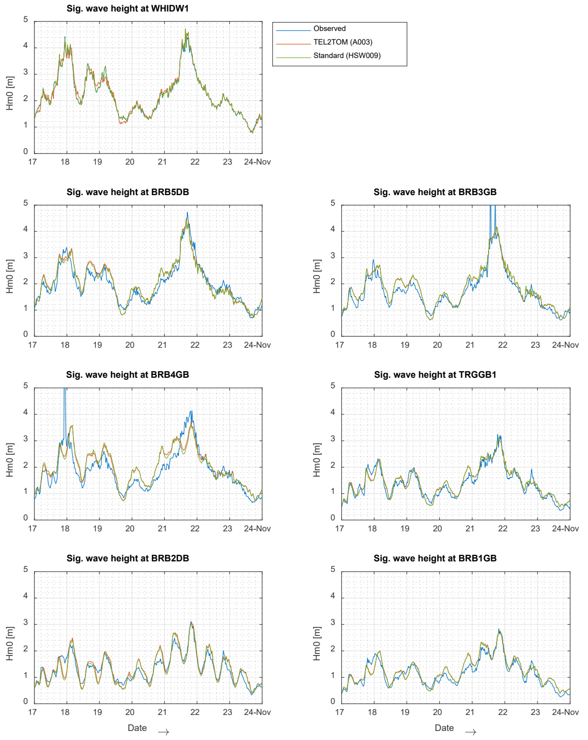

Figure 5. Comparison of significant wave height from offshore to onshore with in blue the observed wave heights, in red the TEL2TOM coupled TELEMAC-2D – TOMAWAC model and in green the standard fully coupled TELEMAC-2D – TOMAWAC model version

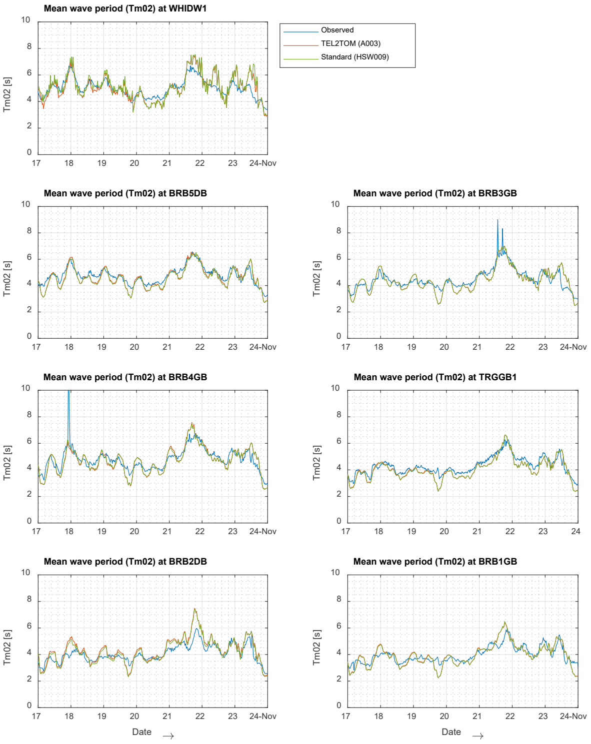

Figure 6. Comparison of mean wave period from offshore to onshore with in blue the observed wave periods, in red the TEL2TOM coupled TELEMAC-2D – TOMAWAC model and in green the standard fully coupled TELEMAC-2D – TOMAWAC model version

D. *Sediment transport and morphodynamic model*

Finally the TELEMAC-2D hydraulic model and the TOMAWAC wave transformation model are coupled to the sediment transport and bed update model. In the first stage of the project this was the SISYPHE model, recently the model has been updated to GAIA.

An input reduction technique named as 'representative tide' is implemented for the generation of simplified tidal forcing suitable for the long-term morphological simulations using a morphological acceleration factor of 10 to 20 (MORFAC). The reduction of hydrodynamic input data of a tide-dominated numerical model aims to reduce the computational cost by finding a satisfactory way to represent a long tidal period by only one (or a small number of) 'representative' tide(s). The concept of input data reduction in long-term morphological simulations under tidal action followed here, was proposed and successfully implemented by Latteux [7]. According to Latteux, this representative tide must lead to the same elementary (flood and ebb) and residual transport as the actual set of natural tides.

The criterion for the selection of the representative tide of the considered year (2014) is the best agreement between the mean sediment transport, resulting from the tested representative tide and the one from the yearly water level time-series. Specifically, the procedure includes to following steps:

- The coupled hydrodynamic and sediment transport model is run for the considered simulation period of one year, imposing a frozen bottom, i.e. no bed updating.
- The two components of the sediment transport rate, Q_x and Q_y (x and y directions) are calculated at every single node of the domain and summed at every time-step of the calculation.
- The two components of the mean sediment transport rate, Q_{xmean} and Q_{ymean}, are calculated by averaging the instantaneous sediment transport rates for each set of two consecutive tidal cycles covering the full year 2014.

Finally, the set of two tides which best represents the magnitude (lowest RMSE) and the patterns (high correlation) of each of the yearly mean Q_x and Q_y components is selected. Note that two consecutive tides were chosen, because of the daily inequality in the tide, which lead to difference in the low water levels between two consecutive tides. This difference is less between the first and last low water in the selected period.

Generally, analogue to the input reduction for the tide, also the wave input is reduced to a limited set of representative wave conditions in morphodynamic modelling. This is to allow a higher morphological acceleration factor necessary to simulate a long term morphodynamic evolution. The waves have a major impact on the shallow near- and on-shore bed evolution. The Belgian coast is characterised by a mean littoral transport from west to east. The annual alongshore transport will be used as validation parameter for the representative wave climate, i.e. the annual longshore transport modelled by a representative wave climate should be in close agreement to the brute force long term mean longshore transport.

At first, a limited set of schematized wave conditions based on equal wave energy was derived from the measured wave data at Westhinder for a one-year period 2014-2015 and applied as boundary condition [6]. It was shown that the limited set of schematized wave conditions gave a similar annual net longshore transport for the selected period 2014-2015 as the full year timeseries of waves. However, when applying the method in the model to a pre-selected representative one-year period for which the derived schematized wave conditions were similar to the schematized ones obtained from a 10-year times series, it turned out the schematized wave conditions did not give the same annual net transport as the one-year timeseries. From this result, it was concluded that the method was not applicable for the Scaldis-Coast model. The main reason for this is that due to the size of the model, the wind generated waves inside the model, especially during western winds, are dominating the littoral transport. When reducing the wave input, a corresponding reduction of the wind input was needed as well.

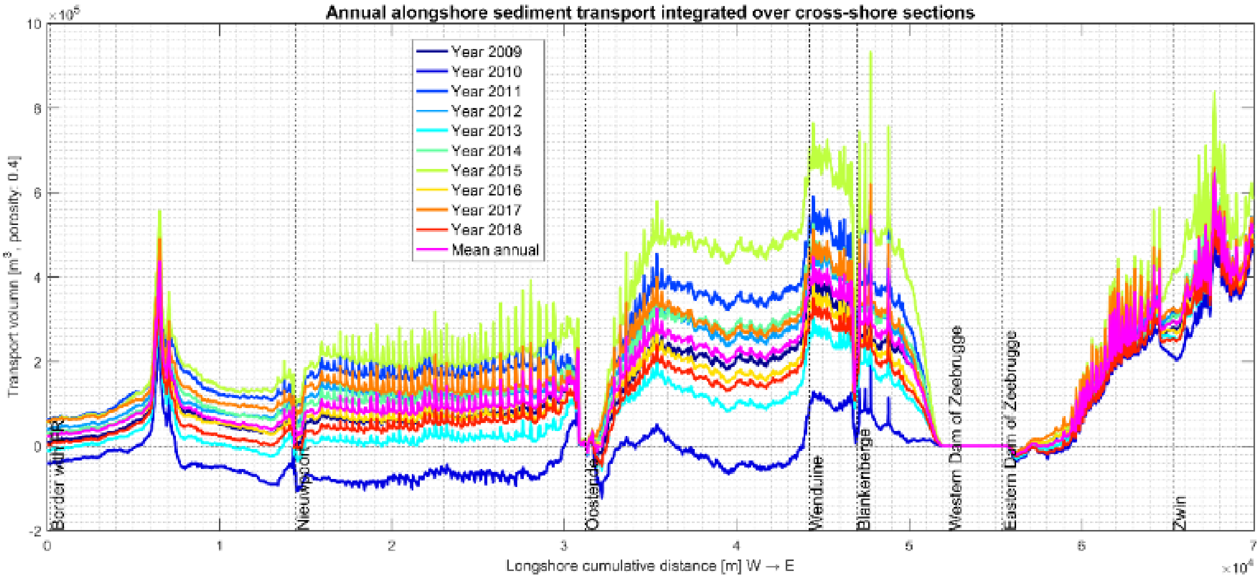

Figure 7. Modelled annual longshore transport rates along the Belgian coastline for ten consecutive years 2009-2018 with in cyan the mean transport rate over the 10-year period

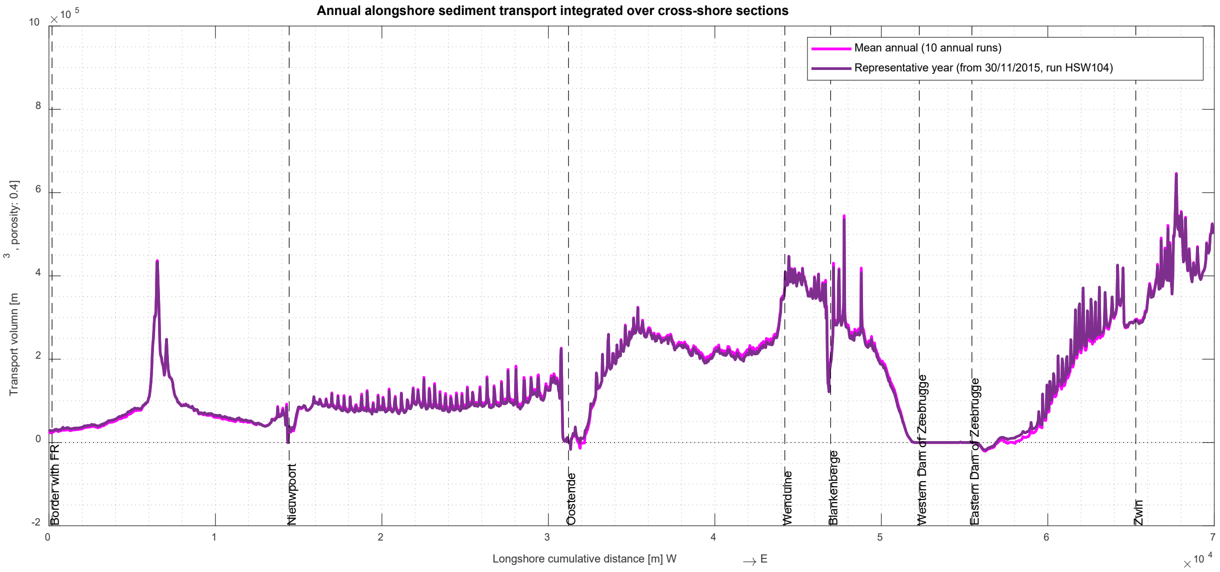

Figure 8. Comparison of the annual mean longshore transport of the brute force 10 year simulation (cyan) and for the representative year (purple)

However, it turned out that is was not appropriate to assume an identical direction for the wave and wind conditions in this study.

Therefore, the model was run for 10-year brute force wind and wave conditions, and the mean annual net alongshore transport was derived, Figure 7. Next, a continuous period of one year observed wave and wind boundary conditions was selected, which represented the long term annual mean longshore transport best, namely November 2015 - November 2016, Figure 8. This period is called the representative year. For the morphodynamic runs, a MORFAC 10 is applied to the one year run in order to model the bed evolution over a 10 year period. In a later phase, the method is repeated to determine a representative half year period, which is applied in combination with MORFAC 20 to simulate a 10 year period.

Different transport formulas and settings have been extensively tested. To evaluate the performance of the model a hindcast of the bed evolution after the extension of the outer port of Zeebrugge in 1986 has been used as testcase. Transport formulas that have been tested were Engelund & Hansen [3], which accounts for steady currents, and formulas that can account for coupled wave- and current-induced transport, i.e. those of Soulsby- Van Rijn [10], Van Rijn 2007, (which was specially implement for the use in this project) [12] and Bijker [2].

The Engeland & Hansen formula tends to perform well at those locations with a tidally driven bed evolution, but does not take the effects of waves on the sediment transport into account, which is crucial in the near-shore area and the shallow areas like *Vlakte van de Raan* in the Scheldt mouth area. The Soulsby-Van Rijn and Van Rijn 2007 formulas tend to overestimate the magnitude of the morphological patterns substantially at deeper areas. Bijker's formula presents many similarities with the formula of Engelund & Hansen, but is also capable of reproducing the morphological patterns close to the coastline when the wave effects are taken into account. Therefore the Bijkers formula was selected as a compromise between the tidally driven off-shore bed evolutions and the nearshore wave driven morphodynamics. The transport formula was further improved by:

- Replacement of the default wave-current bed shear stress, τ_{cw}, formula in Bijker's transport formula with the τ_{cw} formula proposed by Soulsby [10], known as the DATA2 method and based on a fit to laboratory and field measurements:

$$\tau_{cw} = \tau_c \cdot \{1 + 1.2[\tau_w/(\tau_c+\tau_w)]^{3.2}\} \quad (1)$$

  with τ_c the current shear stress and τ_w the maximum wave shear stress.

- Replacement of the default (fixed) breaking wave parameter (b) in the Bijker's transport formula with a spatio-temporal varying expression that depends on the wave height and water depth ratio H_w/h (Bijker, 1971):

$$\begin{aligned} b &= 2 \ , \ H_w/h < 0.05 \\ b &= 2 + 3(H_w/h - 0.05) \ , \ 0.05 \le H_w/h < 0.4 \\ b &= 5 \ , \ 0.4 \le H_w/h \end{aligned} \quad (2)$$

- Minimum depth for bed load equal to 0.1 m (instead of 0.01 m)

The concept of the active bed layer with two sediment classes (200 and 500µm) is applied to mimic a spatially varying grainsize. Briefly, the steps followed for the calculation of bed morphology evolution, in case of sediment mixtures, are:

- Sediment transport rates are computed separately for each class by use of one of the provided bed (or total) load transport formulas
- The Exner equation is solved for each sediment class
- The total bed evolution is calculated by summing the individual bed evolutions of each class

- At the end of each time-step the new bed composition of the active layer is computed, ensuring the mass conservation of each class. The new composition is simply calculated based on the ratio of the evolution of each sediment class over the total evolution within one time-step.

However, in order to achieve a spatially-varying d_{50} transport calculation in the ScaldisCoast model, the concept of equivalent sediment transport is implemented. The number of classes in the active bed layer is limited, in this case to two classes, a fine and a coarse class, even though the Continental Shelf is characterized by a broad range of classes. The initial composition of the active layer is calculated in such a way that the total transport of the two classes togethers is equivalent to the transport rate of the actual in situ d_{50} grain size.

Furthermore, the formula for deviation (correction of sediment transport direction due to slope effect) by Talmon et al. (1995) is used instead of the default one (Koch and Flokstra [5])

$$\tan a = \tan \delta - T(\partial Z_f/\partial n) \tag{3}$$

$$T = 1/(\beta_2 \sqrt{\theta}) \tag{4}$$

with β_2=0.85, a is the direction of bed load transport with respect to the flow direction, δ is the direction of bottom shear stress with respect to the flow direction, Z_f is the bed level, n is the coordinate along the axis perpendicular to the flow and θ the Shields number, i.e. the dimensionless shear stress as a combination of the current shear stress and the maximum wave shear stress:

$$\theta = \theta_c + 0.5\theta_w \tag{5}$$

III. CALIBRATION AND VALIDATION

A. *Calibration test case: Hindcast port of Zeebugge*

For the calibration of the model the 10 years bed evolution after the extension of the outer port of Zeebrugge was used. The extension of the port was finished in 1986. By that time the port was extended about 3 km seaward. In the decades after the extension, severe erosion took place northwest and north of the breakwaters and along the fairway to the port, *Pas van het Zand*. The eroded sediments are mainly deposed at the shallow bank east of the port: *Paardemarkt*, and just east of the eastern dam: *Bay of Heist*. Figure 9 shows the observed sedimentation and erosion patterns between 1986 and 1996.

Figure 10 shows the modelled bed evolution around the port of Zeebrugge between 1986 and 1996. Qualitatively one can notice that the erosion pattern at the entrance of the port (pit) is more or less captured by the model. Strong sedimentation east of the port at *Paardemarkt* (and the surroundings are) is predicted by the model as well. However, the pattern differs from the observed sedimentation and erosion patterns. The strong accumulation of sediments at Bay of Heist, in the axillary between the eastern dam and the beach, is not observed in the model. Instead, the sediment tends to accumulate a bit more off-shore east of the eastern harbor breakwater. This has been observed in other models in the past as well [13]. This discrepancy can be attributed to possible differences in the composition of the transferred material, which in reality contains a large fraction of mud, which is currently missing in the model. In Figure 10 accumulation of sand can be observed in the fairway to the port, Pas van het Zand, and the channel towards the Scheldt estuary. This is because no dredging is included in the hindcast. The maintenance dredging of the channels has been added later on to the model for simulation of the present conditions using the Nestor module. A quantitative comparison between the observed and modelled volume changes in the surrounding of the port is made in Table I. The predicted volumes correspond well to the observed values for the erosion areas, but the volume deposited on the east is captured a bit worse by the model.

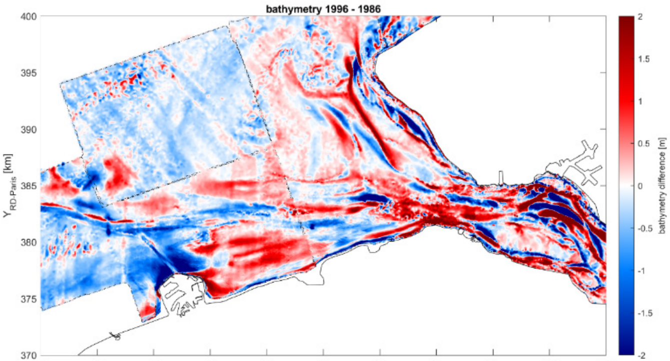

Figure 9. Bathymetric evolution in the first decade after the extension of the outer port in 1986

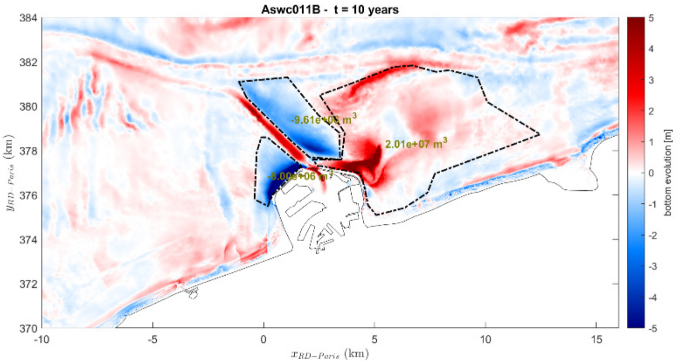

Figure 10. Modelled bed evolution 1986-1996

Table I Observed and modelled volume changes in the polygons of Figure 10

Polygon	**Volume change 1986-1996 (10^6 m³)**	
	Modelled	***Observed***
Erosion area western breakwater	-8.0	-7.4
Erosion area East of the entrance channel	-9.6	-9.0
Sedimentation zone east of the port	+20.1	+14.5

B. *Validation case: Ciara winter storm February 2020*

In February 2020 a single storm event caused an instantaneous sedimentation of the Blankenberge marina access channel. For the preparation of the regular dredging works planned at the end of the winter, the marina entrance and foreshore were surveyed on February 6th, which is only three days before the storm. Shortly after the storm, on February 14th, the survey was repeated, Figure 11. Together with the hydrodynamic and meteorologic measurements of Meetnet Vlaamse Banken, this forms a valuable dataset for model validation.

For this case the model is driven by hydrodynamic boundary conditions from the regional ZUNO model [8]. Wave and wind boundaries are taken from the measurement station Westhinder and applied to the model. No extra model calibration or refinement of the mesh in the vicinity of the marina entrance channel was done, Figure 12.

The pre- and post-storm bathymetric surveys allow to accurately calculate the bed evolution during the storm event. The observed and modelled bed evolution are compared in Figure 13. The sedimentation-erosion patters not only show a good qualitative agreement, but also quantitative there is a good agreement: 44 200 m³ modelled sedimentation versus 43 800 m³ observed. It is understood that the sedimentation of the channel is mainly driven by the littoral alongshore transport. The case shows that the model is capable of representing alongshore littoral transport processes accurately.

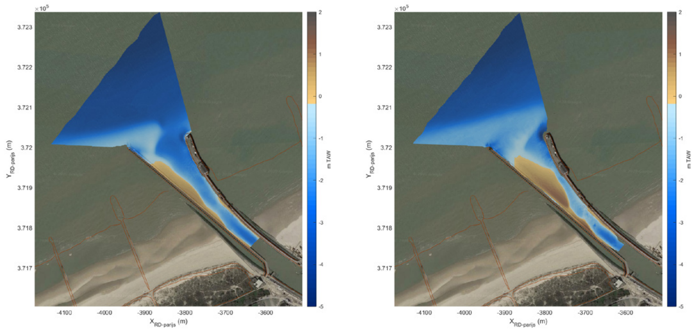

Figure 11. Pre- and post-storm bathymetric surveys

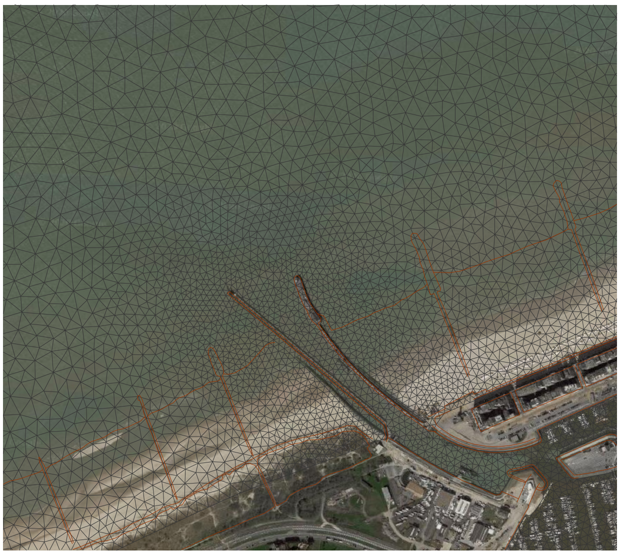

Figure 12. Detail of the ScaldisCoast mesh at the Blankenberge marina entrance channel

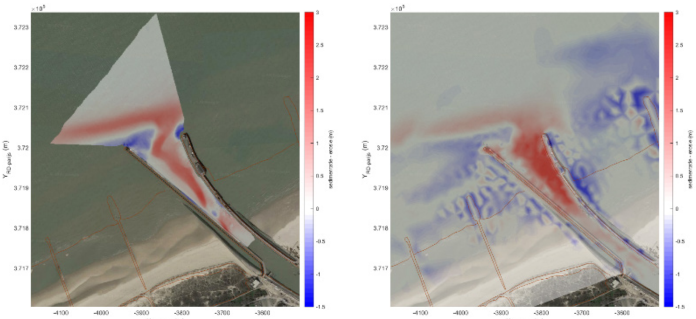

Figure 13. Observed (left) and modelled (right) bed evolution of the Blankenberge marina entrance channel during storm Ciara February 2020

IV. CONCLUSIONS AND FURTHER RESEARCH

An integral morphodynamic model was built for the Belgian coast. The model is capable of modelling long term, decadal scale, bed evolutions, but single storm events are also represented well in the model, at least when the morphological processes are mainly driven by longshore transport processes.

Wave-driven currents are only driven by radiation stresses in the current version of the model. Stokes drift, as well as effects of wave asymmetry and boundary layer streaming are not modelled. This means that the model misses cross-shore processes. The implementation of cross-shore processes is currently under investigation based on the work in [14,15]. The main transport process along the Belgian coast is the longshore transport from west to east. However, cross-shore processes do play a role during storm events and for the long-term natural feeding of the beach during periods of mild wave conditions. Notice however, that the latter are difficult to calibrate because lack of direct and accurate measurements of these processes in situ.

Only sand fractions are modelled. No sand-mud interaction or less erosive clay layers are modelled yet. Mainly in the vicinity of Zeebrugge clay layers are present (Holocene Clay). The extension of the model to sand-mud is another topic of investigation.

REFERENCES

[1] Breugem, W.A.; Fonias, E.; Wang, L.; Bolle, A.; Kolokythas, G.; De Maerschalck, B. "TEL2TOM: coupling TELEMAC-2D and TOMAWAC on arbitrary meshes", XXVIth Telemac-Mascaret User Conference, 15-17 October 2019, Toulouse: proceedings

[2] Bijker, E.W. "Mechanics of sediment transport by the combination of waves and current". Des. Reliab. Coast. Struct. 23rd Int. Conf. Coast. Eng.: 147–174, 1992

[3] Engelund, F.; Hansen, E. "A monograph on sediment transport in alluvial streams". TEKNISKFORLAG Skelbrekgade 4 Copenhagen V, Denmark: Technical University of Denmark 0stervoldgade 10, Copenhagen K., 1967

[4] Geuzaine, C.; Remacle, J.-F.. "Gmsh: a three-dimensional finite element mesh generator with built-in pre-and post-processing facilities." Int. J. Numer. Methods Eng. 79(11), 2009. ISBN 1097-0207 0: 1309–1331. doi:10.1002/nme.2579

[5] Koch, F.G.; Flokstra, C. "Bed level computations for curved alluvial channels", in: XIXth Congress of the International Association for Hydraulic Research: New Delhi, India, 1981.

[6] Kolokythas, G.; Fonias, S.; Wang, L.; De Maerschalck, B.; Vanlede, J.; Mostaert, F. “Modelling Belgian Coastal zone and Scheldt mouth area: Sub report 14: Scaldis-Coast model – Model setup and validation of the morphodynamic model”. Version 0.1. FHR Reports, 15_068_14. Flanders Hydraulics Research: Antwerp. 2023.

[7] Latteux, B. “Techniques for long-term morphological simulation under tidal action”. Mar. Geol. 126(1–4): 129–141. 1995

[8] Maximova, T.; Vanlede, J.; Verwaest, T.; Mostaert, F. “Vervolgonderzoek bevaarbaarheid Bovenzeeschelde: subreport 4 – Modelling Train CSM – ZUNO: validation 2013”. FH Reports, 13_131. Flanders Hydraulics: Antwerp, 2016

[9] Ortega Yamamoto, H.; Monbaliu, J. “Monitoring Broersbank boeidata – Ruwe datarapport periode Sep2015-Dec2015 (Monitoring Broersbank_214339_R08 in opdracht van Afdeling Kust - Agentschap Maritieme Dienstverlening en Kust - Vlaamse Overheid)”. Laboratorium voor Hydraulica, KU Leuven: Leuven. 2016

[10] Soulsby, R. “Dynamics of marine sands”. H.R. Wallingford, 1997

[11] van Rijn, L.; Walstra, D. “Modelling of sand transport in Delft3D”, 2003

[12] van Rijn, L.C.; Ruessink, B.G.; Grasmeijer, B.; van der Werf, J.; Ribberink, J. “Wave-related transport and nearshore morphology”, in: Coastal Sediments ’07. pp.1—14, 2007.

[13] Wang, L.; Zimmermann, N.; Trouw, K.; De Maerschalck, B.; Delgado, R.; Verwaest, T.; Mostaert, F. “Scientific support regarding hydrodynamics and sand transport in the coastal zone: calibration of a Long term morphological model of the Belgian shelf”. Flanders Hydraulics reports, 12_107. Antwerp, 2015

[14] Fonias, E., Breugem, W. A., Wang, L., Bolle, A., Kolokythas, G., & De Maerschalck, B. (2021). Implementation of cross-shore processes in GAIA. 2020 TELEMAC User Conference 138.

[15] Breugem, W. A. (2020). Ongoing developments in TELEMAC and TOMAWAC at IMDC. Online proceedings of the papers submitted to the TUC 2020, 115-121.

Hydro-morphodynamics modelling for the mobilization assessment of UXOs and DMMs

Sebastian Escobar[1], Richard Whitehouse[1], Thomas Benson[1], Michiel Knaapen[1],
s.escobar@hrwallingford.com
[1]: HR Wallingford, Howbery Park, Wallingford OX10 8BA, United Kingdom

Abstract – **A waves, currents and sediment model is implemented in openTELEMAC to simulate morphodynamic changes on the East Coast of Florida, USA. This model produces temporal and spatially varying data for an external software to simulate the exposure and mobilization of UXO and DMM.**

The model retrieves its boundary conditions from global climate (ECMWF ERA-5 reanalysis) and ocean currents (HYCOM GoM regional analysis) models, thus providing a link between mesoscale dynamics and local conditions. Comparison between the model boundary forcings, model results and field measurements during the passage of Hurricane Matthew (October 2016) indicate that the model can simulate the hydrodynamics of the area. Comparisons with available LiDAR data also indicate that the model agrees with erosion and deposition patterns observed along the beach. Lastly, the model was run using conditions for an entire year, which produced a suitably long dataset for undertaking UXO and DMM mobilization studies.

Keywords: morphodynamics, currents, waves, storms.

I. INTRODUCTION

Comprehensive morphodynamics datasets, with high spatial and temporal resolution, are necessary for the assessment of exposure and mobilization of unexploded ordnance (UXO) and discarded military munitions (DMM) in contaminated coastal areas. However, such datasets are expensive and difficult to obtain, especially in the underwater environment, because they require the deployment of specialized measuring equipment to cover extensive areas for prolonged periods of time [1], and for as long as metocean conditions allow safe access.

The work presented here is to provide a modelled morphodynamics dataset valid to perform UXO and DMM exposure and mobilization analysis. It generates space-time-variable hydrodynamics, sediment fluxes and bed elevation changes from a meso-scale numerical model that add to the available localised environmental measurement data of the study area near Fort Pierce in Florida, USA.

Hydrodynamics and morphodynamics of the East Coast of Florida have been simulated for the entire year of 2016. These simulations include the effects of Hurricane Matthew (October 2016), which left major beach and dune erosion and structural damages along the East Coast of the United States [2], [3]. Model results are also presented through monthly averages to describe the overall physics of the study area. The main variables of these monthly assessments are the significant wave height and peak period, the mean current velocities, and the total bed evolution.

II. MATERIALS AND METHODS

A. Model discretizations

TELEMAC (v8p3r2) was used in this work to predict temporal and spatially varying outputs for key parameters including: bed level changes, currents, sea level variations and wave characteristics. The model setup consisted of the TELEMAC-2D, TOMAWAC and GAIA fully-coupled modelling system, where TELEMAC-2D calculates hydrodynamics, TOMAWAC the waves variables, and GAIA the morphodynamics [4].

The spatial discretization enclosed the coast between Port St. Lucie and Cape Canaveral (see Figure 1). It included the Atlantic Ocean waters between the shoreline and approximately 40 km offshore; the Indian River and Banana River lagoons; as well as the tidal inlets of Port St. Lucie, Fort Pierce and Sebastian connecting those lagoons to the shoreface.

The model bathymetry was linearly interpolated from the '2016 USACE NCMP Topobathy Lidar DEM: Florida East Coast' dataset, which is resolved at a pixel size of 0.0315'' x 0.0315'' (approximately 0.87 m x 0.87 m) [5]. The bottom elevation is given in NAVD88.

The spectral discretization (of the waves module) included 30 frequencies and 24 directions. The discretization frequencies were geometrically distributed with a step that follows the distribution: $f_n = f_1 q^{n-1}$. With f_n being the n^{th} discretization frequency, f_1 the first frequency bin (0.04 Hz) and $q = 1.1$ the frequential ratio.

The waves calculations were carried out on a coarser mesh to the morphodynamic model, which did not include the Indian River Estuary (see Figure 2). This was coupled to TELEMAC through the TEL2TOM functionality [6].

B. Model setup

The model setup provided a link between global-scale atmospheric and hydrodynamics processes with county-scale morphodynamics (see Figure 2). Free surface water elevations (NAVD88) and flow velocity components were retrieved from the HYbrid Coordinate Ocean Model (HYCOM) [7], GoM regional analysis (experiment _32.5) [8], and imposed onto the TELEMAC-2D model open boundary nodes.

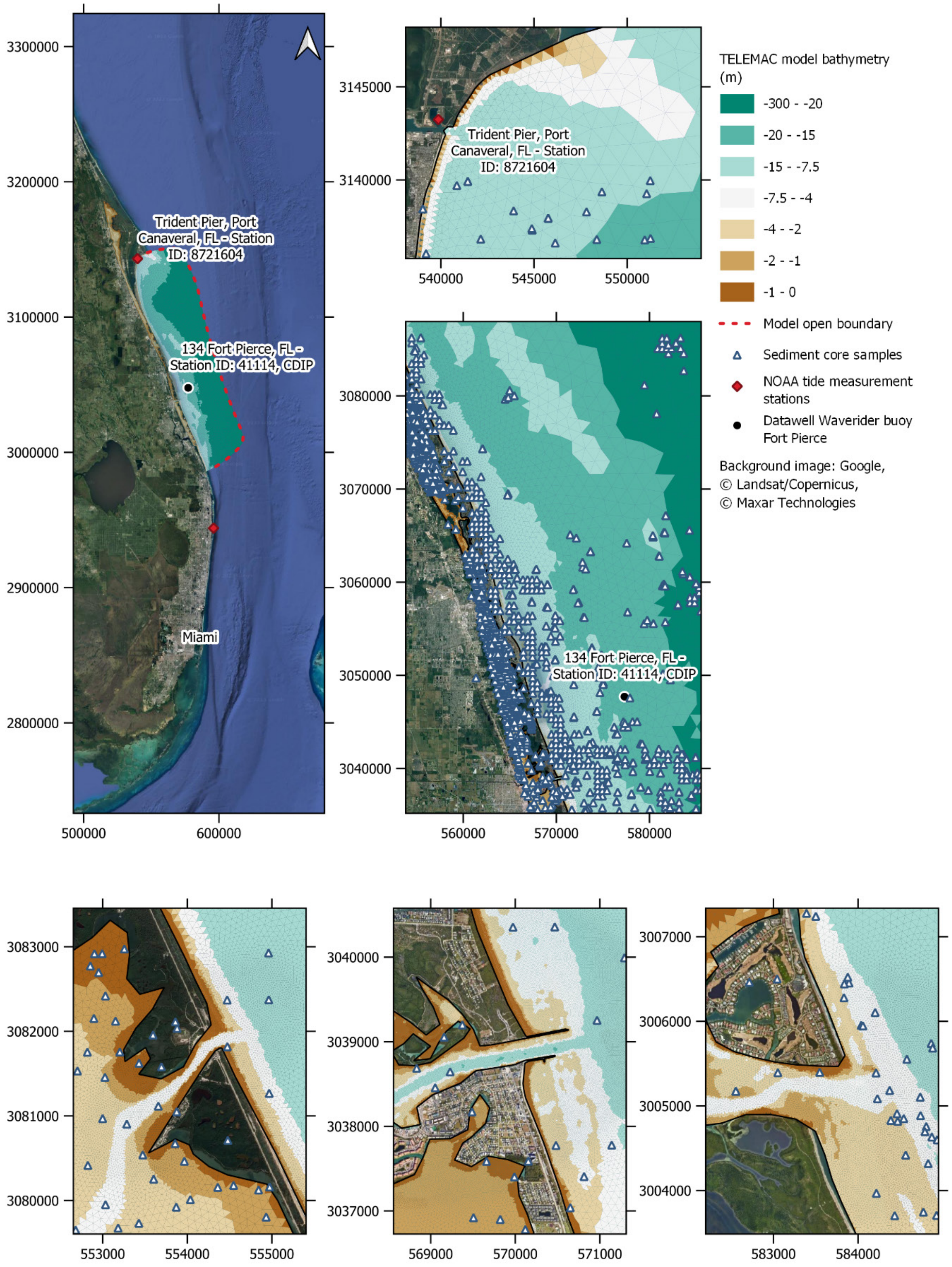

Figure 1. Model spatial discretization (top left). Available tide measurements (top right). Available wave measurements (middle). Sebastian Inlet (bottom left). Fort Pierce Inlet (bottom middle). St. Lucie Inlet (Bottom right).

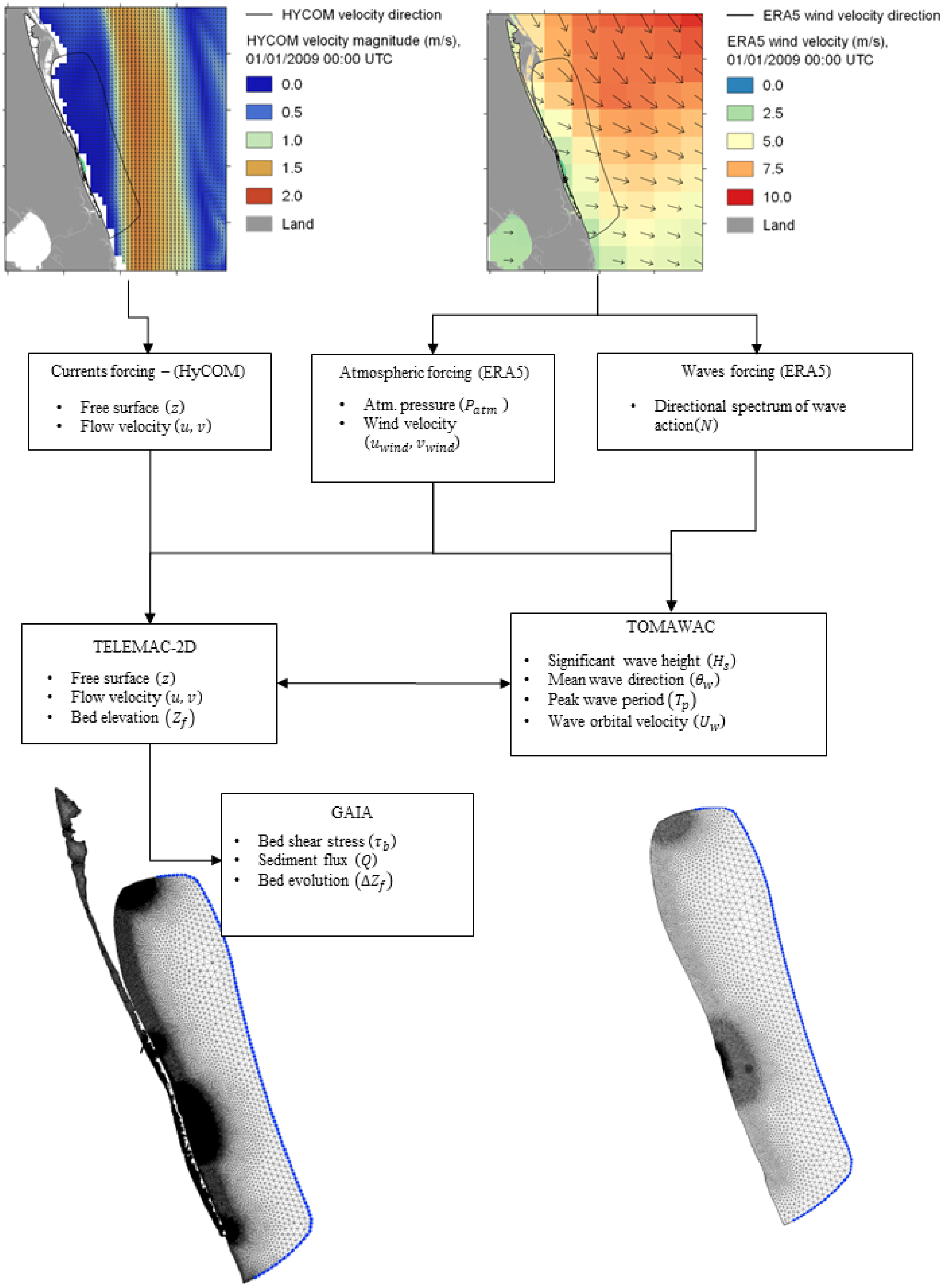

Figure 2. Model layout. Boundary conditions were retrieved from global currents (HYCOM), wind, air pressure and waves (ERA5) models. These were imposed on the open boundaries (blue lines) of the TELEMAC-2D and TOMAWAC models, which modeled local conditions of the East Coast of Florida.

Spatially varying wind velocities and atmospheric pressure from the European Centre for Medium-Range Weather Forecasts (ECMWF) ERA5 dataset were imposed over each mesh node of the TELEMAC-2D and TOMAWAC models.

The offshore wave boundary conditions were also retrieved from the ERA5 dataset. The wave energy was imposed on the boundaries as a two-dimensional wave variance spectrum, variable in time and space, discretised over 30 frequencies and 24 directions.

Because the HYCOM and ERA5 grids were coarser than the TELEMAC model meshes (see Figure 2), new sets of FORTRAN procedures were developed, and others adapted, to interpolate in space and time the free surface levels, flow velocities and wind conditions onto the TELEMAC and TOMAWAC meshes. Figure 3 shows new code that was developed to downscale HYCOM currents onto TELEMAC-2D. The workflow is as follows:

1. Before starting the simulation: The boundary hydrodynamic file from HYCOM (GOMl0.04 -expt_32.5) was downloaded and converted to SELAFIN format.
2. Throughout the simulation:
   a. Subroutine BORD calls the new code, providing the current time and the model mesh.
   b. IMPOSE_BND_TELEMAC retrieves the model geometry and calls INTERP_BND_VALUES.
   c. INTERP_BND_VALUES interpolates, in time and space, the depth values for the simulation's boundary nodes.
   d. The interpolated depth is passed back to BORD, and from there on to the TELEMAC time loop.

The METEO subroutine of TELEMAC-2D, and the VENUTI subroutine of TOMAWAC, were adapted in a similar fashion to what is shown in Figure 3, but with the goal of downscaling wind velocity components.

The initial sediment bed composition was implemented from Florida's Regional Offshore Sand Source Inventory (ROSSI) database [9] and usSEABED [10] (core samples shown on Figure 1). Sediment fluxes and bed evolution were calculated with Soulsby-van Rijn's bedload formula and the Exner equation as defined by Soulsby [11]. The characteristics sizes of the modelled sediment fractions are provided in Table I.

Table I Discrete sediment classes used to simulate morphodynamics of the region

Sediment class number	Grain size (mm)	Classification
1	0.05	Silt (non-cohesive)
2	0.15	Fine sand
3	0.30	Medium sand
4	0.60	Coarse sand

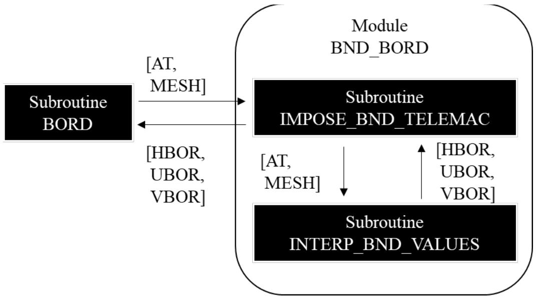

Figure 3. Flow of information between subroutine BORD and the new set of FORTRAN procedures for currents boundary conditions.

Table II Comparison of HYCOM timeseries and measurements at Trident Pier Port Canaveral

Variable	RMSE	WS
Free surface	0.24 m	0.89
Wind speed	2.90 m/s	0.88
Wind direction	42.59 °	

III. RESULTS

The period used for validation was between 01/10/2016 and 10/10/2016, which covers the extreme conditions caused by the passage of Hurricane Matthew through the East Coast of the USA.

A. *Assessment of the boundary forcing data*

The HYCOM and measured timeseries of free surface water elevation, at the Trident Pier station, are in agreement (see Figure 4 and Table II). Underestimation of the surge caused by Matthew are caused by HYCOM's low spatial resolution, and the fact that the measuring device is placed inside of Port Canaveral. Thus HYCOM does not properly represent the processes taking place at a sub-grid scale (e.g. tide transformation and secondary currents). The RMSE (0.24 m) and the Willmott [12] skill score (WS: 0.89) of HYCOM, with respect to the measurements is good.

Regarding the imposed winds, there is a good match between the ERA5 data and the available wind measurements (Figure 4, middle and bottom panels). For the wind speed, the RMSE and the skill score are 2.9 m/s and 0.83 respectively. For the wind direction, the RMSE and the skill score are 42.59° degrees and 0.98 respectively (Table II), and the seemingly large RMSE is explained by oscillation between 0° and 360°, which are nil in reality.

B. *Validation of modelled hydrodynamics*

The model predictions compare well with observations of the free surface level and wave integrated variables (Figure 4 top panel, Figure 5 and Table III).

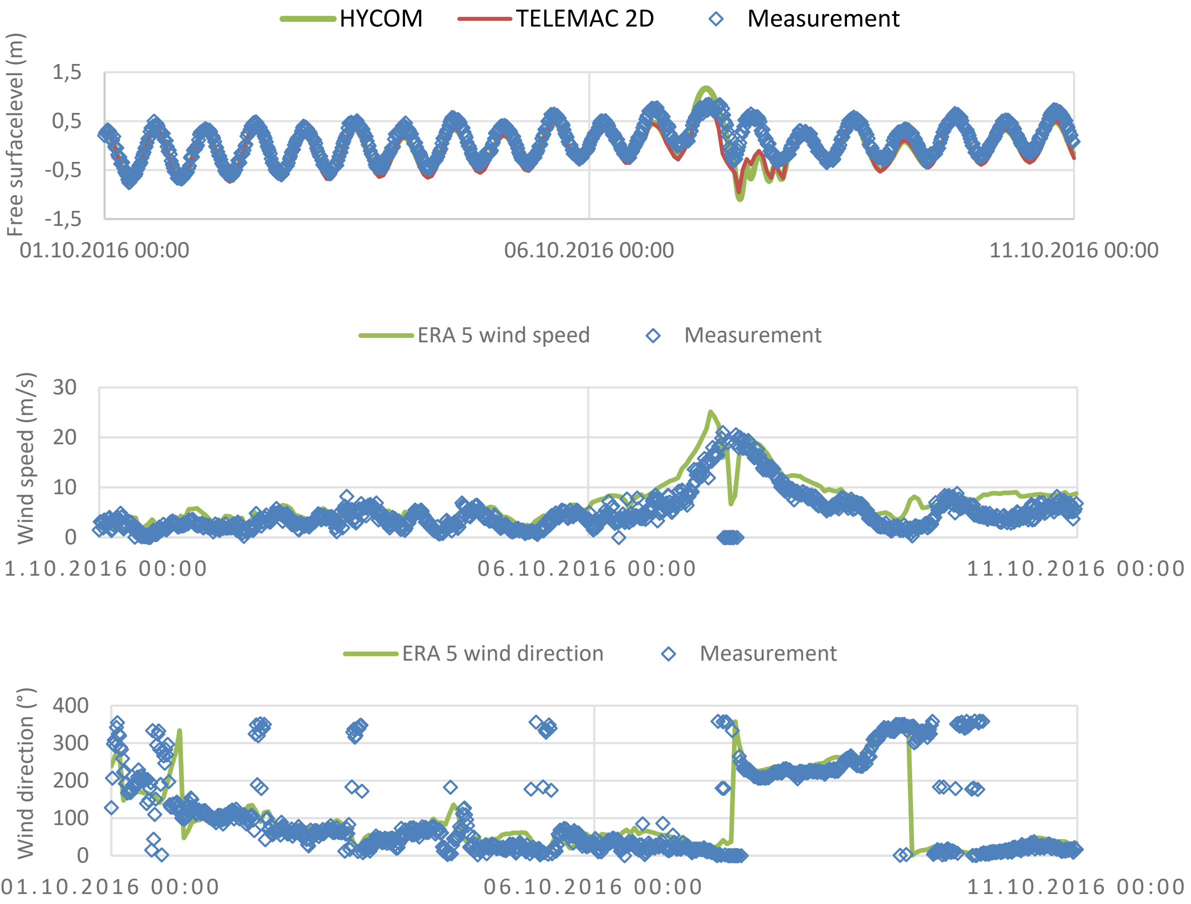

Figure 4. Comparison of imposed, modelled and measured conditions at the Trident Pier station, Port Canaveral, Florida, during Hurricane Matthew. Top: free surface water level (NAVD88). Middle: wind speed. Bottom: wind direction.

The modelled free surface (Figure 4 top panel) closely follows the available measurement. The peak water level is reached during flood tide and both measurements and TELEMAC-2D model results achieve a similar elevation of 0.85 m. However, soon after the end of the ebbing tide (07/10/2016 11:00), the model results suddenly drop, causing underestimation of approximately 0.5 m. After twelve hours from the surge drop, the modelled free surface stabilizes and it starts matching again with the measurements. This discrepancy was also seen in the HYCOM forcing, thus it is an instability inherited from the boundary conditions. Despite this discrepancy, the TELEMAC-2D model has better error statistics than the HYCOM forcing (see Table II and Table III). Its RMSE (0.12 m) is lower than that of HYCOM (0.24 m).

Deviations regarding the wave variables are less acute (see Figure 5). The significant wave height of both the model and the measurements are in phase and their signals overlap during most of the analysed period. The difference is a noticeable underestimation of the peak wave height (07/10/2016 05:00) by the model. The underestimation is as high as 2.3 m, with the modelled peak reaching 4.5 m and the Waverider buoy of Fort Pierce showing a last reading of 6.8 m. We hypothesize that this deviation is caused by the mesh resolution of ERA5, the reduced number of frequencies and directions in TOMAWAC, excessive model energy dissipation by the changing sediment bed and the coupled flow in the form of friction and radiation stresses, as well as by instabilities in the measurements just before the buoy was dragged by the storm.

Table III Error statistics analysis between model prediction and observations

Variable	**Location**	**RMSE**	**WS**
Free surface	Trident Pier Port Canaveral	0.12 m	0.90
Significant wave height	Fort Pierce	0.27 m	0.97
Peak wave period		1.89 s	0.51
Mean wave direction		17.33 °	0.53

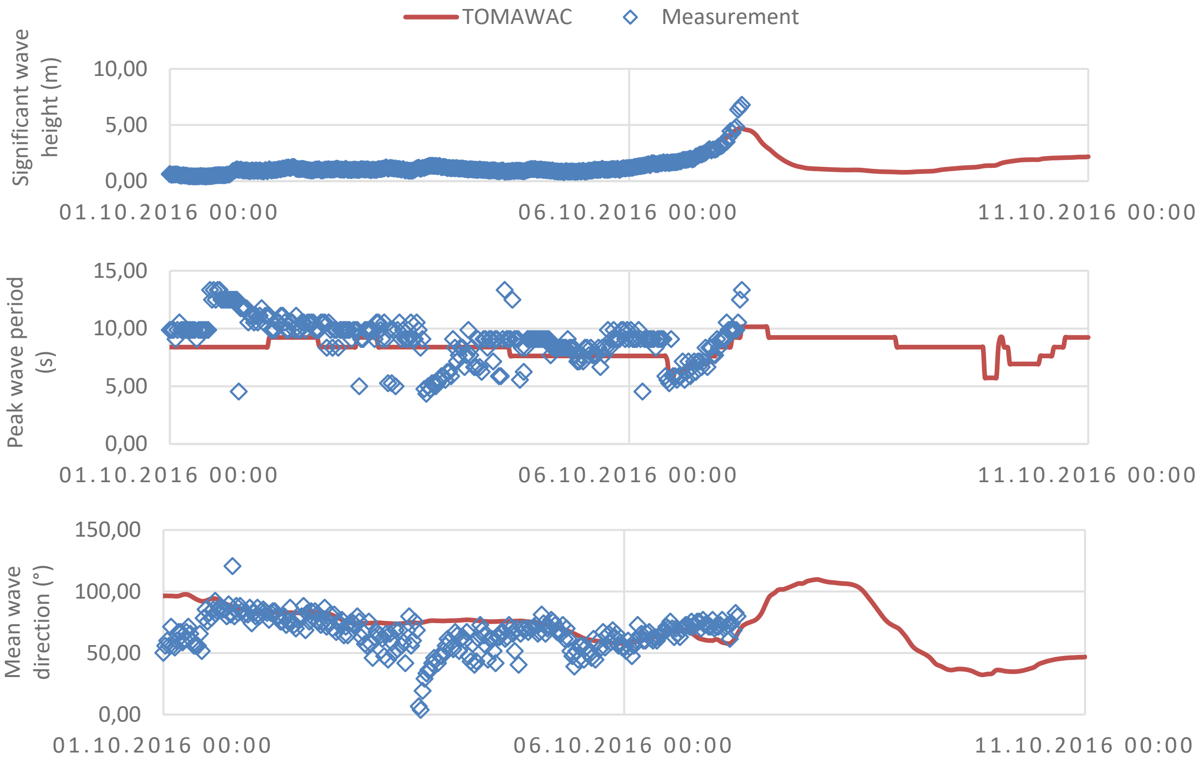

Figure 5. Comparison of modelled and measured wave conditions at the Fort Pierce station, Florida, during Hurricane Matthew. Top: significant wave height. Middle: peak wave period. Bottom: mean wave direction.

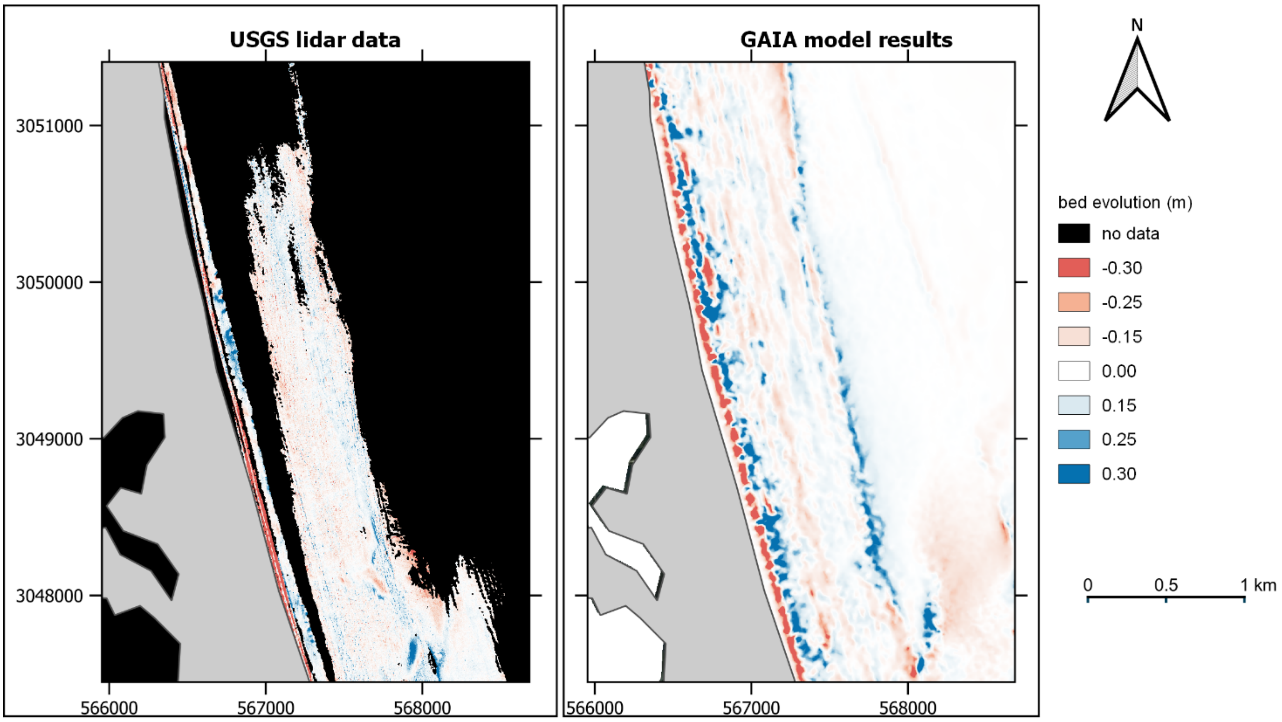

Figure 6. Qualitative comparison of measured bed elevation changes and modelled bed evolution..

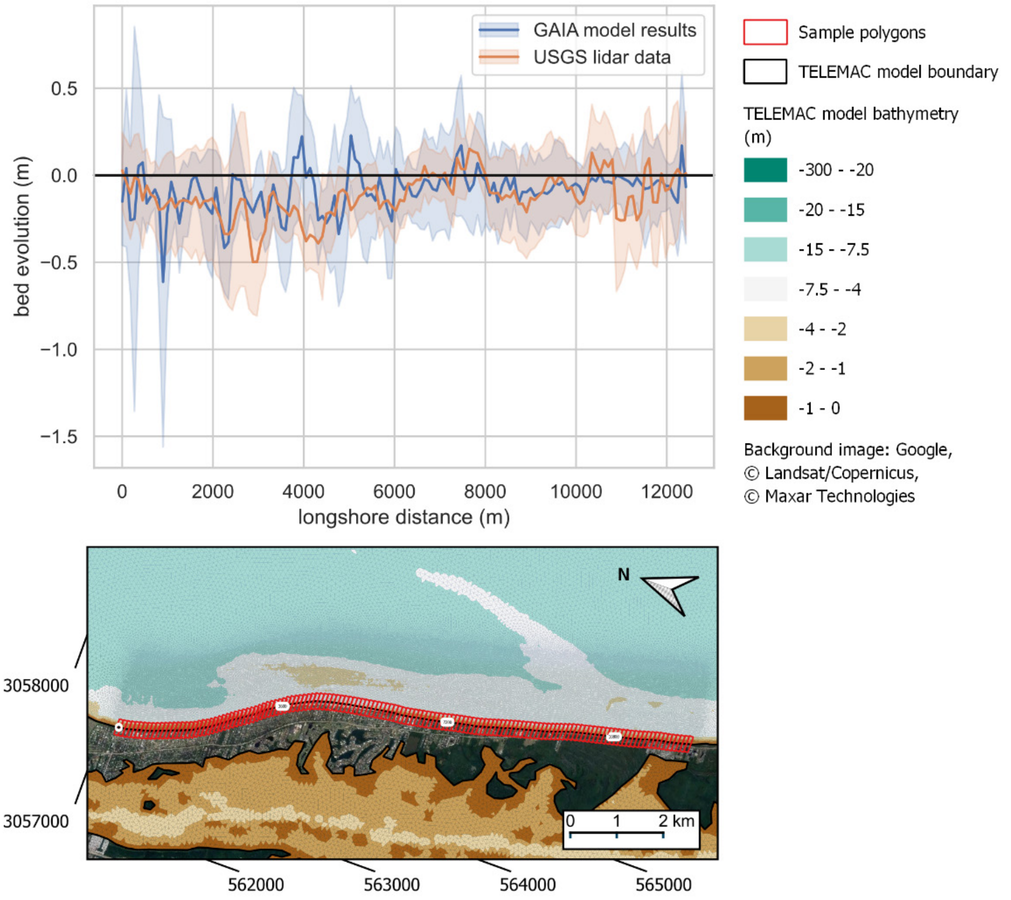

Figure 7. Quantitative comparison of longshore bed evolution from measurements and model results. Top, bed evolution profile, the solid lines are the zonal average and the shaded areas are the standard deviation. Bottom, local coordinates and sample polygons used to calculate the zonal statistics with bathymetry in metres.

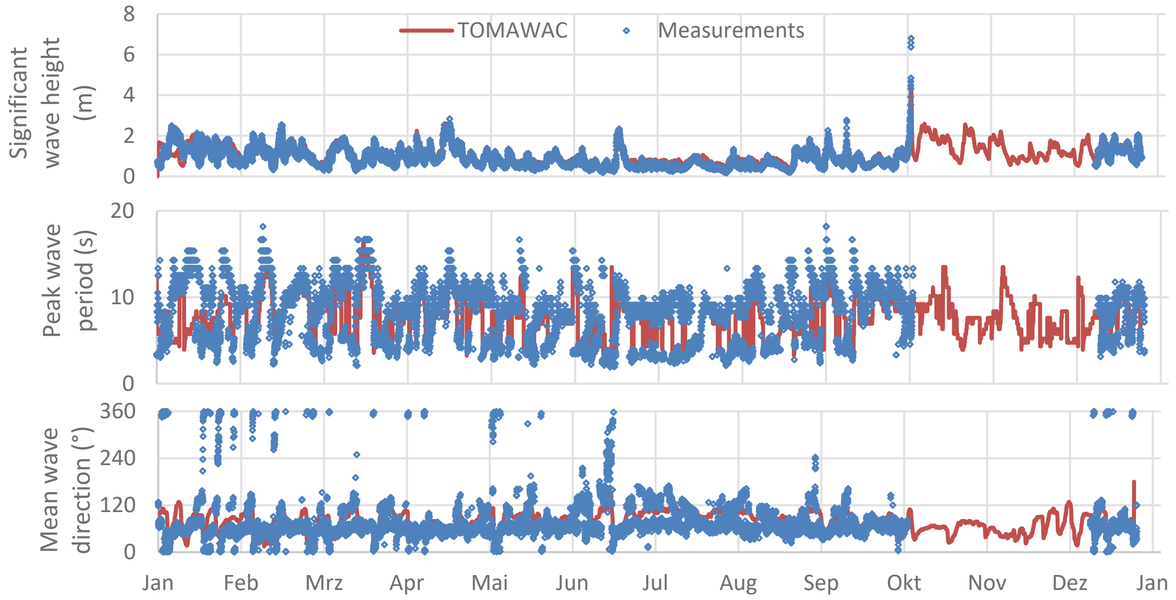

Figure 8. Comparison of modelled and measured wave conditions at the Fort Pierce station, Florida, throughout 2016. Top: significant wave height. Middle: peak wave period. Bottom: mean wave direction.

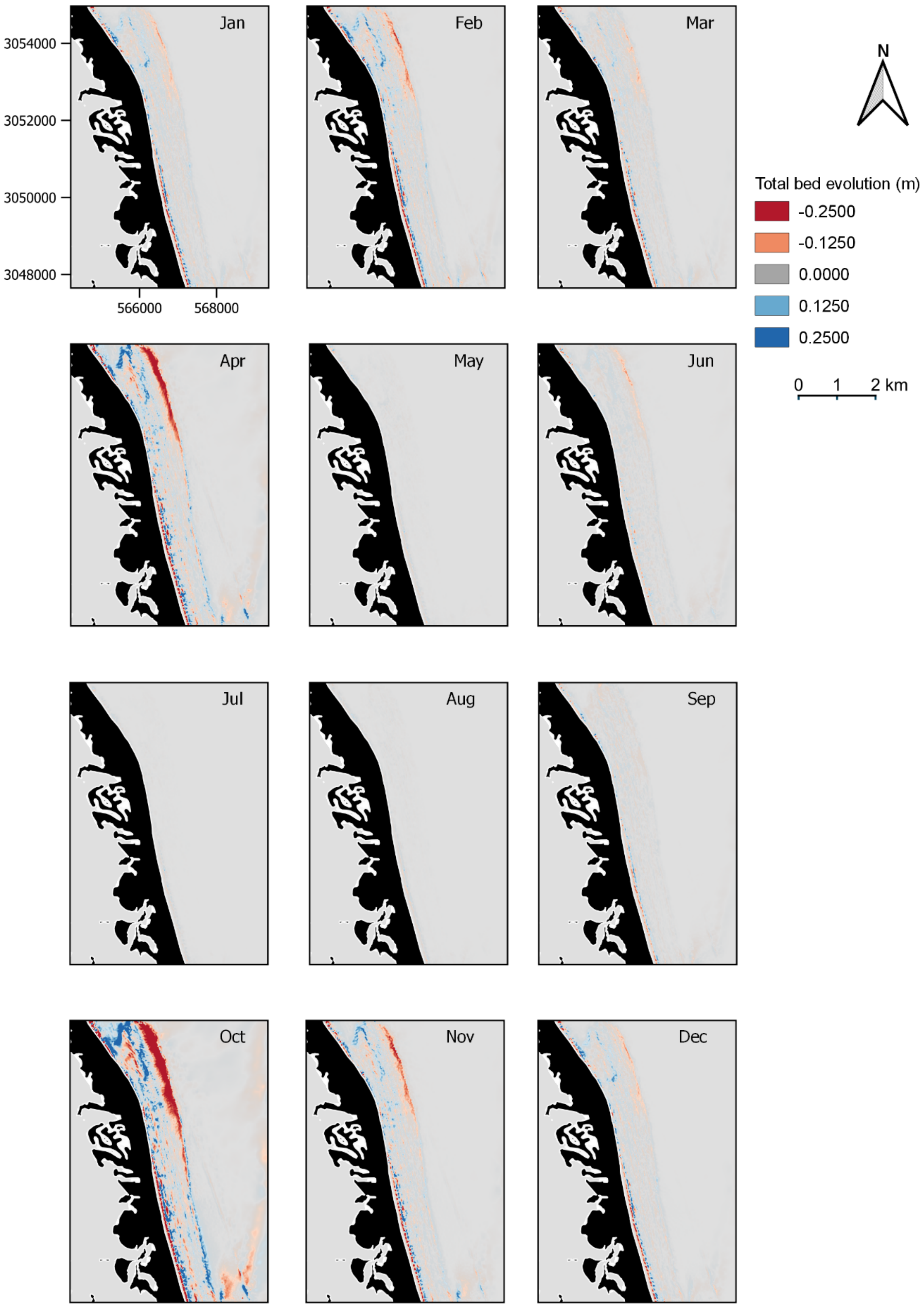

Figure 9. Monthly total bed evolution modelled for 2016

The peak wave period and the mean wave direction are overall within the range of the measurements (see Figure 5, middle and bottom rows). The deviations of these modelled variables are not systematic since overestimation and underestimation take place alternately and over very short periods of time. These seemingly random errors are caused by the lower spectral resolution of the model (30 frequencies, 24 directions), compared to that of the measurements which is much more refined (64 frequencies, and 240 directions with 1.5° per direction bin).

The wave statistics (Table III) indicate a more than sufficient capability of the model to reproduce overall conditions of Hurricane Matthew. The significant wave height has a RMSE of 0.27 m and a skill score of 0.97. The peak wave period and the mean wave direction have RMSE values of 1.89 s and 17.33 ° respectively, and their skill scores are 0.51 and 0.53 respectively.

C. *Qualitative verification of the modelled bed-evolution*

Qualitative comparison with available LiDAR data **[5, 13]**, indicates that the model agrees with erosion and deposition patterns observed along the beach and over offshore sand bars and shoals (Figure 6). The bed evolution patterns, of both the model and the measurements, are characteristic of beach lowering, bedform migration and erosion of shoal areas.

D. *Quantitative verification of the modelled bed-evolution*

Figure 7 (top) presents a quantitative comparison of the post-Matthew measured and modelled bed elevation changes along the shoreline. These profiles have been drawn from the zonal averages (solid lines) and standard deviations (shaded areas) of pixels falling within rectangular sample polygons drawn along the shoreline (see Figure 7, bottom). The sample polygons are spaced at intervals of 90 m and have a cross-shore length of 300 m, their centroids are aligned with the coastline and their longest edges protrude 150 m onshore and 150 m offshore.

From Figure 7, the model results in general are within the range of the variability in the measurements. The mean bed evolution along the shoreline is -0.12 m for the measurements and -0.09 m for the model results. The standard deviations are 0.24 m and 0.27 m for measurements and model results respectively, which is also in agreement with the shoreline changes for the region reported by [14].

E. *Characterization of simulated 2016 monthly morphodynamics*

After setting up and validating the model, it was run for the whole year of 2016 (Figure 8) to generate a space-time varying dataset of hydrodynamics and morphodynamics of the East Coast of Florida.

Waves are the main factor affecting hydrodynamics along East Florida, these are driven by tropical storms (north eastern) and other wind and swell events, which results in a highly dynamic system [15]. Waves vary seasonally, with the strongest event being Hurricane Matthew (October), followed by smaller events taking place during autumn (see Figure 8, top panel). The average significant wave heights are about 0.5 m in summer, increasing to about 1 m in autumn, winter and spring. During storms, the significant wave height can increase to 2 m in summer (e.g., during June 2016); 2.5 m in winter and spring; and 4.5 m during the autumn.

For all the simulated months of 2016 the peak wave period oscillated between wind waves (5 s) and swell (10 s) (Fig. 8, bottom panel). The wave direction is consistent throughout the year, and most of the waves come from the sector between northeast and east (Fig. 8, bottom panel) with an average direction of 76 °.

The largest morphodynamics changes of 2016 occur during Hurricane Matthew (October), followed by significant changes, although of lower magnitude and extension, throughout the rest of the autumn season (November and December), during winter (January, February and December) and during April of 2016. The areas where most elevation changes occur are the beach and shoals ridges located within a distance of approximately 2 km from the beach (see Figure 9).

IV. CONCLUSION

A large scale model of the East Coast of Florida was implemented. It is able to link mesoscale metocean processes with local scale hydrodynamics and morphodynamics.

The model satisfactorily reproduces the free surface elevation and integrated wave variables of the area, despite short-term deviations caused by the rough storm dynamics caused by Hurricane Matthew.

The model is also able to simulate the bed evolution well. Quantitative comparison with available LiDAR data indicates that the modelled bed evolution values are in the same range as measurements along the beach.

Finally, a hydrodynamics and morphodynamics dataset was generated from the model for an entire year. This provides a suitable dataset to perform long term UXO mobilization studies.

ACKNOWLEDGEMENT

This project was supported by the Munitions Response Program of the Strategic Environmental Research and Development Program under project number MR21-1081. The support of the SERDP community is acknowledged. Valuable technical support was also provided by our project partner Corvus Works UG.

REFERENCES

[1] F. Eren, J. Jung, C. E. Parrish, N. Sarkozi-Forfinski, and B. R. Calder, "Total vertical uncertainty (TVU) modeling for topo-bathymetric LIDAR systems," Photogrammetric Engineering and Remote Sensing, vol. 85, no. 8. pp. 585–596, 2019. doi: 10.14358/PERS.85.8.585.

[2] J. T. Backstrom, C. Loureiro, and D. O. Eulie, "Impacts of Hurricane Matthew on adjacent developed and undeveloped barrier islands in southeastern North Carolina," Reg. Stud. Mar. Sci., vol. 53, p. 102391, 2022.

[3] S. D. Miller, W. C. Straka, J. Yue, C. J. Seaman, S. Xu, C. D. Elvidge, L. Hoffmann, and I. Azeem, "The dark side of hurricane matthew: Unique perspectives from the VIIRS day/night band," Bull. Am. Meteorol. Soc., vol. 99, no. 12, pp. 2561–2574, 2018.

[4] P. Tassi, T. Benson, M. Delinares, J. Fontaine, N. Huybrechts, R. Kopmann, S. Pavan, C.-T. Pham, F. Taccone, and R. Walther, "GAIA-a unified framework for sediment transport and bed evolution in rivers, coastal seas and transitional waters in the TELEMAC-MASCARET modelling system," Environ. Model. Softw., vol. 159, p. 105544, 2023.

[5] OCM Partners, “2016 USACE NCMP Topobathy Lidar DEM: Florida East Coast,” 2023. https://www.fisheries.noaa.gov/inport/item/49582 (accessed Mar. 20, 2016).

[6] W. A. Breugem, E. Fonias, L. Wang, A. Bolle, G. Kolokythas, and B. De Maerschalck, “TEL2TOM: coupling TELEMAC2D and TOMAWAC on arbitrary meshes,” in XXVth TELEMAC-MASCARET User Conference, Toulouse, 2019, pp. 15–17.

[7] R. Bleck, “An oceanic general circulation model framed in hybrid isopycnic-Cartesian coordinates,” Ocean Model., vol. 4, no. 1, pp. 55–88, 2002.

[8] E. P. Chassignet, H. E. Hurlburt, O. M. Smedstad, G. R. Halliwell, P. J. Hogan, A. J. Wallcraft, R. Baraille, and R. Bleck, “The HYCOM (hybrid coordinate ocean model) data assimilative system,” J. Mar. Syst., vol. 65, no. 1–4, pp. 60–83, 2007.

[9] J. L. Coor, C. Beauvais, and J. D. Ousley, “ROSS/OSSI (ROSSI): A coastal management tool for offshore sand sources,” in The Proceedings of the Coastal Sediments 2015, World Scientific, 2015.

[10] B. J. Buczkowski, usSEABED: Gulf of Mexico and Caribbean (Puerto Rico and US Virgin Islands) offshore surficial-sediment data release. US Department of the Interior, US Geological Survey Reston, VA, 2006.

[11] R. Soulsby, Dynamics of marine sands. Thomas Telford Publishing, 1997. doi: 10.1680/doms.25844.

[12] C. J. Willmott, “On the validation of models,” Phys. Geogr., vol. 2, no. 2, pp. 184–194, 1981.

[13] OCM Partners, “2016 USACE Post-Matthew Topobathy Lidar DEM: Southeast Coast (VA, NC, SC, GA and FL) from 2010-06-15 to 2010-08-15,” 2017.

[14] J. J. Birchler, K. S. Doran, J. W. Long, and H. F. Stockdon, “Hurricane Matthew: Predictions, observations, and an analysis of coastal change,” US Department of the Interior, US Geological Survey, Reston, VA, 2019. doi: 10.3133/ofr20191095.

[15] T. Ezer, “Analysis of the changing patterns of seasonal flooding along the U.S. East Coast,” Ocean Dyn., vol. 70, no. 2, pp. 241–255, 2020, doi: 10.1007/s10236-019-01326-7.

Application of TOMAWAC for wave energy resource assessment: A North Sea wave database

Qinghui Zhang[1], Sarah Doorme[1], Josselin Figard[1], W. Alexander Breugem[1], Arash Bakhtiari[1]
Qinghui.zhang@imdc.be, Antwerp, Belgium
[1]: IMDC NV

Abstract – **Wave energy resources as a renewable source of energy, has been constantly appraised in the context of the global green/blue energy transition. To ensure a success development of wave energy projects, one of the first steps is to acquire an accurate assessment of wave energy resources using advanced modelling techniques and long-term reliable databases.**

This study focuses on the wave energy resource assessment of the North Sea region where a significant potential of development is detected. To this, an improved version of TOMAWAC model, a 3rd generation wave-model has been used. More detailed attention was given to the Belgian Part of the North Sea (BPNS) to feed a reliable online wave energy database with a proper resolution. A validated inhouse water level database has been implemented into the model, integrating the variation of water level impact on the wave propagation, especially in shallower areas. These improvements speed up the numerical simulations and presents to be computationally more effective, which proves crucial in terms of large-scale metocean conditions evaluation. The model results have been calibrated and validated against in-situ measurements at both nearshore and offshore positions, and the validated model has been applied to generate a 20-year (2001-2020) hourly metocean condition for North Sea, with a geometric resolution of 500-600 meters near the Belgian coast. The model results have been transformed into an online WEC database for the ocean energy at the North Sea.

Keywords: Wave modelling, Metocean conditions, North Sea, Wave Energy Resources.

I. INTRODUCTION

The ocean is host to a variety of human activities, spanning from tourism, coastal infrastructure, navigation to fisheries and more. In recent years, climate change and sea level rise have increased largely the frequency of coastal flooding and coastal erosion, posing a continuous threat for economic and human life. As such, amongst the efforts to restore the balanced earth environment and seeking a durable development, scientists have been searching for renewable clean energy, such as solar energy, wave energy and ocean energy. New devices and technologies are being developed to generate electricity from waves, tides, as well as offshore wind farms. With an identified resource in the range of 1000 TWh of wave energy and around 150 TWh of tidal energy annually, ocean energy is the largest unknown untapped renewable energy in Europe, and it is expected to provide 10% of the EU's power demand by 2050 [1].

In terms of wave energy exploitation, the North Sea had been long overlooked due to its perceived 'lower' energy resource; however, it has been pointed out in [2] that the wave conditions for North Sea are moderate to high and more importantly, they are more easily accessible thanks to the low distance to coasts. An essential step towards a reliable estimation of the ocean energy is an accurate assessment of the metocean conditions. Three main ways are exploited, include: in-situ measurements, satellite data as well as numerical models. The in-situ measurements are usually for data collection at limited number of locations and cannot be extrapolated to cover a larger domain, moreover, gaps in data are observed, especially during severe weather conditions; the satellite data become more promising in recent years, although they are still limited for the moment by data quality, especially in the near shore region [3]. Large scale numerical models have been widely used: they provide metocean data with high temporal- and spatial-resolution, with the precondition that the model performance has been tested, validated with existing measurements.

In [2], SWAN has been used for generating a 38-year wave database of North Sea, focusing mainly on the Dutch coast. In building up the model, a better parameterization, especially in terms of wind generation and whitecapping, was sought for.

In the current study, a highly-efficient 3rd generation spectral wave model (updated TOMAWAC) has been exploited for simulating the wave conditions on North Sea, with a focus on the Belgian coast. A modelling improvement has been performed, that the water level variations have been incorporated into the wave propagation simulation. Consequently, the influence of tidal variation, the storm surge has been accounted for. This is very relevant for the North sea since the water level remains shallow for a large part near the coast. The tidal level for the North Sea reaches up to more than 4 meters, leading to a non-negligible effect of water level modulation on the wave propagation. This effect is even more pronounced closer to the Belgian coast, where tidal banks with water depth of 15-20 meters are present. As a matter of fact, it has been pointed out in [4] that the wave-current interaction can lead to a variation of wave energy by up to 30%, especially in the shallower zone.

To fully take the wave-current interaction into account, a more comprehensive approach would be exploitation of a full TELEMAC-TOMAWAC coupling, nevertheless, it is too time consuming. In this study, we have incorporated the influence of water level to the wave propagation thanks to a pre-computed reliable database for hydrodynamics in the North Sea. A 20-year metocean conditions for the North sea have been generated. This database can also serve as a useful tool for other offshore and nearshore ocean applications, for example, the extracted wave characteristics can be used to compute the working availability in terms of weather conditions for a certain area. The metocean data has been also translated to an online wave energy database.

II. STUDY AREA

The Belgian Part of the North Sea covers approximately 3,500 km^2 and extends up to 87 km offshore from the coast (Figure 1). There are currently several renewable energy projects active in a series of concession areas of in total 225 km^2 along the Dutch-Belgian maritime border, primarily consisting of offshore wind parks. However, the concessions also contain various pilot projects, notably a planned 5MW wave energy project to be developed by Otary, a major stakeholder in offshore renewables in Belgium. Further concessions are planned for a total additional area of 281 km^2 to be made available between 2020 and 2026[1]. The further expansion of offshore wind concessions falls into the framework of a planned increase in capacity from approximately 2.3 GW to 4 GW by 2030.

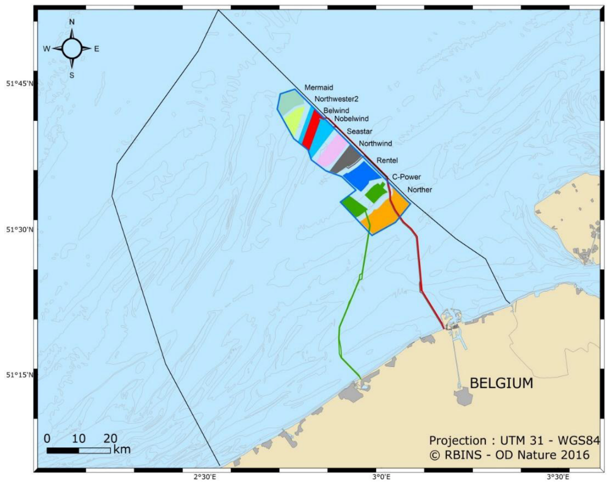

Figure 1 Map of BPNS and current offshore wind concessions.

The possibility of integrating offshore wind and wave power in a combined format allows for maximized power output from the available energy resources. Given the large area currently dedicated to offshore wind which will more than double by 2026 it is key to identify the most suitable technologies available for potential application in new and existing concessions.

III. METHODOLOGY

A. Model description

TOMAWAC (TELEMAC-based Operational Model Addressing Wave Action Computation) is a scientific software which models the changes, both in the time and in the spatial domain, of the power spectrum of wind-driven waves and wave agitation for applications in the oceanic domain, in the intracontinental seas as well as in the coastal zone. The model uses the finite elements formalism for discretizing the sea domain; it is based on the computational subroutines of the TELEMAC system.

TOMAWAC is a 3rd generation spectral wave model, which solves the wave action balance equation:

$$\frac{\partial N(\theta,\sigma)}{\partial t}+\frac{\partial c_j N(\theta,\sigma)}{\partial x_j}=S$$

Where N is the wave action, it is defined as: $N=E/\sigma$, with σ the wave frequency; θ is the wave propagation direction; c_j is the propagation velocity of the wave energy along the four dimensions (x, y, θ, and σ); S represents all the source and sink terms that parametrize different physical processes accounting for wave energy production and dissipation; in TOMAWAC, the following aspects have been taken into account:

$$S=S_{in}+S_{ds}+S_{nl}+S_{bf}+S_{br}+S_{tr}+S_{ds,cur}+S_{veg}$$

Where: S_{in} is the wind-driven wave generation; S_{ds} is the whitecapping-induced energy dissipation; S_{nl} is the non-linear quadruplet interactions; S_{bf} and S_{br} are the bottom friction-induced and breaking-induced wave energy dissipation, they are more important for shallower near-coastal regions; S_{tr} is the non-linear triad interaction; $S_{ds,cur}$ is the enhanced wave breaking dissipation by currents and S_{veg} is the dissipation due to vegetation. These source and sink terms have been numerically parameterised and integrated in the model (the dissipation due to vegetation has been left out).

In TOMAWAC, unstructured grid has been exploited, it can be used as a stand-alone wave prediction tool; meanwhile, it offers the possibility to be coupled to TELEMAC for a full wave-current simulation: this method, accounts for more comprehensive physical processes, demonstrates to be computationally expensive. In this study, pre-stored water levels [5], [6] have been read at each time step, integrating the influence of the water levels without largely increasing the computational cost of the wave model.

---

[1] *https://economie.fgov.be/en/themes/energy/belgian-offshore-wind-energy-4*

B. *Numerical scheme*

TOMAWAC exploits a fractional time step; for the advection, the method of characteristics is used, which presents to be fast and unconditionally stable, yet it poses issues in forms of the numerical diffusion and loss of energy conservation; for the source terms, a sub-time step has been applied for rapidly varying processes (depth-induced breaking and triad interactions). The method leads to a time-step restriction for accuracy reasons, which substantially increases the computational cost.

To overcome these limitations, a new architecture of TOMAWAC has been introduced [7]. The current numerical scheme has been optimised in the following aspects: (1) A second order spatial advection scheme has been implemented; it decreases the numerical diffusion and presents to be energy-conservative. (2) For the source terms, a separation has been made between the slow and fast physical processes, where different time steps have been applied. As such, the computation time has been reduced substantially. One is referred to [7] for a more comprehensive discussion of the methods and results. In this study, this updated version of TOMAWAC had been applied.

C. *Model inputs*

1) *Geometry and grid*

In this study, the computation domain covers largely the North Sea. In the West, it reaches to the intersection point of English Channel and Celtic Sea, comprising of the whole English channel, extending further to the whole east coastline of UK; in the South, it comprises of the Northern coastline of France, Belgium, Netherlands and Germany; the east side covers the West Coastline of Norway and Sweden until Gothenburg and then it extends to the coastline of Denmark.

The whole domain covers roughly 500,000 km^2 area. The bathymetric data come from the EMODNET database, combined with a more refined Belgian coast coming from the Bathymetry of the Belgian Continental Shelf (Flemish Authorities, Agency of Maritime & Coastal Services, Coastal division, Gridding Ghent University, Renard Centre of Marine Geology). The simulated domain and final bathymetry are shown in Figure 2.

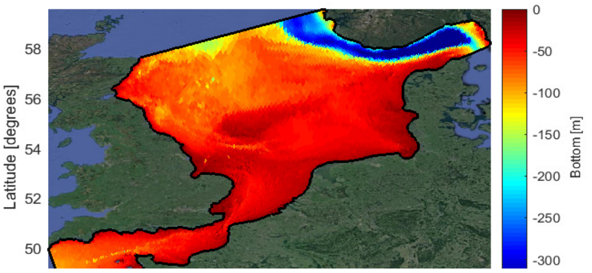

Figure 2 Geometry and coverage of the simulation domain. The mesh is created in latitude and longitude to account for the Earth's curvature.

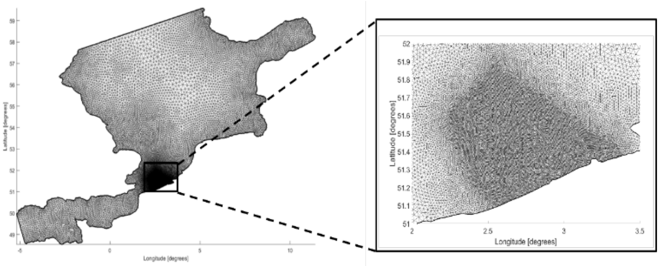

Figure 3 Computational grid for the wave model. The unstructured grid has been refined closer to the Belgian coast.

For the computational grid, a non-homogeneous unstructured triangular grid has been applied: the mesh size presents to be coarser to the northern side open sea, with a rough size of 20km, it is refined for the Belgian coast and the mesh size reduces to 400m. There are in total 30395 nodes and 60615 elements (Figure 3).

2) *Wind*

Wind is a main driver behind the energy source of locally generated ocean waves. A well-chosen wind source is an essential segment of a highly performant ocean wave models. Wind data are usually provided by institutional or governmental bodies, in which different re-analysis techniques and various atmospheric models have been exploited. In this study, two wind sources, ERA5 and CFSR, have been considered and their performances have been compared.

CFSR wind data exhibiting higher spatial resolution, and it captures well the peak of waves. However, for wider domain, the use of re-analysis CFSR data may lead to higher scatter [2]. Given the primary goal of this study is to yield reliable wave energy estimation, especially for the Belgian coast, both wind source performances were compared with a focus closer to the coast.

3) *Spectral wave boundary condition*

The boundary condition for waves has been extracted from the ECMWF data (ERA5), which had been reconstructed by the WAve Model (WAM). It had been imposed mainly at the North and West side of the domain boundary. At each boundary node, significant wave height, peak period and wave main propagation direction were used to construct the synthetic JONSWAP spectrum. The spectral wave boundary condition is essential for introducing the swell waves into the wave estimation, which was mainly generated and propagated from the North Atlantic Ocean and the Norwegian sea. This part of the boundary condition has been validated by comparing the modelled 1D spectrum to the measurements.

4) *Tide and water level variation*

In this study, the influence of hydrodynamics environments has been integrated. Instead of a fully coupled wave-hydrodynamics model, which requires heavy computational cost, results of a pre-constructed hydrodynamics database (North Sea Metocean Database for hydrodynamics: [5]) have been read at each time step of the wave model. The North Sea metocean Database for hydrodynamics has been constructed based on a long-term simulation of in-house iCSM model for 26 years from 1995 to 2020. The iCSM is a tidal surge model developed in TELEMAC-2D, focusing on the continental shelf of the North Sea. The model has been systematically calibrated and validated on water level and velocities for both ordinary and extreme events [5]. The model shows reliable ability to precisely reproduce the hydrodynamics in the North Sea. As such, this pre-stored database has provided valuable hydrodynamical information for this wave model.

IV. MODEL RESULTS

A. *Calibrations and verification of the model*

The model calibration involved two different periods: December 2013 (including Sinterklaas storm event) and in winter 2017. Both periods were marked by significant wave heights that exceeded 3.0 m height. To compare the wave height and wave period between the model results and available measurement over the North Sea, several points were selected, ranging from Belgian nearshore positions (Bol Van Heist) to North Sea offshore positions (Ekofisk) illustrated in Figure 4 and Table I. This approach facilitated a comprehensive evaluation of the model performance across varying distances from the coast.

Table I Points where the measurements and the numerical results have been compared.

	A12	**Bol Van Heist**	**Euro-plat-form**	**K13**	**WestH inder**	**Ekofisk**
Lat.	55.38	51.40	51.98	53.22	51.38	56.54
Lon.	3.80	3.22	3.42	3.22	2.43	3.22

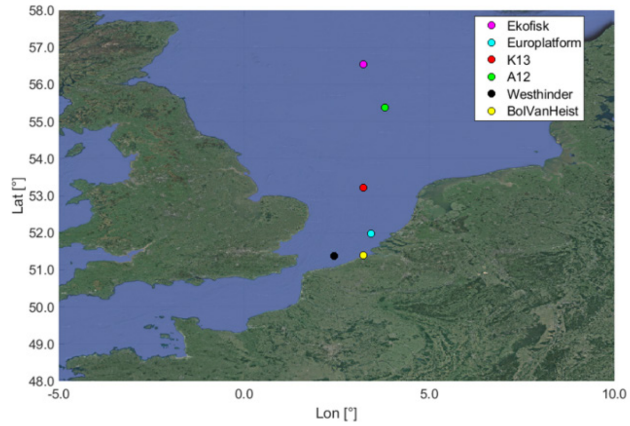

Figure 4 Geographical representation of points where the measurements and the modelling results have been compared.

Bathymetric treatment, wind sources, mesh resolution, wave propagation method, and water level impact were tested and evaluated during the calibration procedure. A summary of model setting has been listed in Table II. Note that the optimal whitecapping dissipation coefficient for CFSR is concluded to be 4.5, while for ERA5, it is found to be a lower value of 3.0.

The model performance was assessed using several statistical indicators, including bias, Root Mean Square Error (RMSE), Scatter Index (SI), and the correlation coefficient (R). In the context of wave simulation, a low SI of $\leq 25-30\%$ indicating that the general trends have been captured; R is the Pearson correlation coefficient. It is computed as the ratio between the covariance of two variables and the product of their standard deviations; it measures the linear correlation between two sets of data. Therefore, a correlation coefficient of 1 corresponds to data points lying exactly on a line. For wave energy, for a model to be reliable a correlation coefficient higher than 0.9 is required. In Table III, Table IV, Table V and Table VI, model and measurement comparisons for both the December 2013 and the winter 2017 period are summarized.

Our final objective for constructing a wave database is to evaluate the potential of WEC near the Belgian coast, therefore, more weights have been put at points closer to the Belgian coast. Different sources of measurements data have been exploited and they are listed below:

(1) Wave data at BolVanHeist, WestHinder:
Monitoring Network Flemish Banks (Meetnet Vlaamse Banken)

(2) Wave data at EuroPlatform, A12, K13:
Rijkswaterstaat waterinfo (wave characteristics) Rijkswaterstaat Waterinfo (rws.nl)

(3) Wave data at Ekofisk:
FROST : https://frost.met.no/index.html

(4) Wave spectrum at EuroPlatForm: Dutch Rijkswaterstaat.

Table II Final parameters used in setting up the model.

Parameters name	**Value**
Time step [s]	600
Minimal frequency [Hz]	0.03
Number of frequencies	36
Number of directions	36
Implicitation coefficient for source terms	0.55
Limiter for refraction velocity [7]	Only for directions
Numbers of iterations for small scale processes	10
Number of iterations for advection	1
Linear wave growth	1, Cavaleri & Malanotte-Rizzoli formulation
White capping dissipation	Yes
White capping dissipation coefficient	4.5 for CFSR, 3.0 for ERA5
Depth-induced breaking dissipation	10, see [7]
Number of iterations for the source terms	1
Number of breaking time steps	10

Table III Statistical assessments for significant wave height for December 2013.

	Bol van Heist		**Westhinder**		**Europlatform**		**A12**		**Ekofisk**	
	ERA5	CFSR	ERA5	CFSR	ERA5	CFSR	ERA5	CFSR	ERA5	CFSR
Bias [m]	-0.13	-0.08	-0.09	0.11	-0.09	0.08	-	-	-0.02	0.12
RMSE [m]	0.25	0.25	0.29	0.35	0.49	0.41	-	-	0.44	0.90
SI [%]	35%	30%	22%	23%	22%	22%	-	-	13%	24%
R [-]	0.93	0.93	0.92	0.93	0.96	0.95	-	-	0.96	0.89

Table IV Statistical assessments for Tm02 for December 2013.

	Bol van Heist		**Westhinder**		**Europlatform**		**A12**		**Ekofisk**	
	ERA5	CFSR	ERA5	CFSR	ERA5	CFSR	ERA5	CFSR	ERA5	CFSR
Bias [m]	0.57	0.47	-0.15	0.06	-0.31	-0.05	-0.05	0.34	-	-
RMSE [m]	0.98	0.76	0.55	0.57	0.61	0.68	0.59	1.19	-	-
SI [%]	20%	23%	14%	13%	14%	14%	12%	18%	-	-
R [-]	0.71	0.78	0.79	0.79	0.74	0.78	0.92	0.79	-	-

Table V Statistical assessments of the significant wave height for winter 2017.

	Bol van Heist		**Westhinder**		**Europlatform**		**K13**		**A12**	
	ERA5	CFSR	ERA5	CFSR	ERA5	CFSR	ERA5	CFSR	ERA5	CFSR
Bias [m]	-0.17	-0.12	-0.04	0.04	-0.04	0.06	0.06	0.07	0.32	0.30
RMSE [m]	0.27	0.25	0.23	0.25	0.29	0.33	0.32	0.43	0.67	0.66
SI [%]	32%	28%	17%	17%	15%	18%	16%	21%	24%	24%
R [-]	0.91	0.92	0.94	0.94	0.95	0.92	0.93	0.88	0.84	0.84

Table VI Statistical assessments of Tm02 for winter 2017.

	Bol van Heist		**Westhinder**		**Europlatform**		**K13**		**A12**	
	ERA5	CFSR	ERA5	CFSR	ERA5	CFSR	ERA5	CFSR	ERA5	CFSR
Bias [m]	0.17	0.15	-0.03	0.09	-0.15	0.10	-0.16	0.09	-0.09	0.20
RMSE [m]	0.77	0.75	0.44	0.45	0.47	0.48	0.56	0.52	1.0	1.0
SI [%]	17%	17%	10%	10%	11%	10%	12%	12%	16%	16%
R [-]	0.71	0.72	0.83	0.84	0.80	0.85	0.72	0.80	0.65	0.77

From the model performance shown in these tables, it is seen that overall, the performance of two wind sources is very similar. At offshore points, the CFSR model over-estimate the wave energy (positive bias) while with ERA5 wind, a general underestimation for storm conditions has been observed. At nearshore stations, both wind sources generate a wave energy that slightly underestimate the measured wave height.

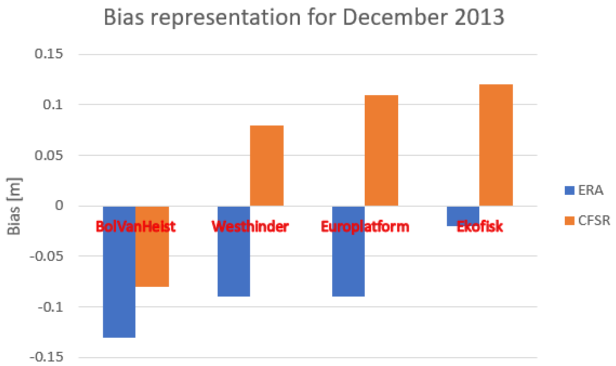

Figure 5 Bias plot for significant wave height for December 2013: from left to right the distance to the shore increases.

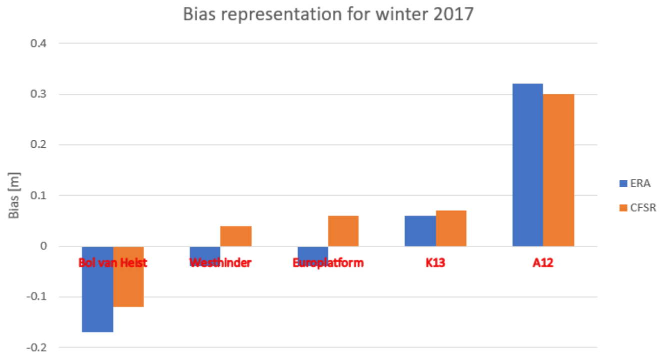

Figure 6 Bias plot for significant wave height for winter 2017: from left to right the distance to the shore increases.

In general, a better performance of ERA5 wind at offshore positions was observed. For instance, at A12 location, for the Sinterklaas storm event, the Tm_{02} has been better captured by ERA5 than the CFSR. At location Ekofisk, a better capture of wave energy has also been represented by ERA5. However, at nearshore point (Bol Van Heist), CFSR outperforms ERA5 wind. The tendency becomes obvious in Figure 5 and Figure 6. In both figures, the bias for significant wave height has been plotted, the distance to shore increases from left to right. It is seen that ERA5 generally performs better at offshore whilst opposite can be concluded for CFSR. For buoy position A12 which is situated the farthest from the coast, each wind generates a bias that reaches roughly 30 cm for winter 2017. Given the main attention of this project focusing more on the nearshore positions, that most of the WEC will be placed near the coastline, thus the quality of nearshore wave energy computation is important. Moreover, CFSR wind performs better for extreme values. For the WEC, it is important to have well-captured extreme values to determine the workability of the device. As such, CFSR wind has been chosen for further construction of the model, bearing in mind that for offshore positions, the results await to be improved.

Apart from the wind sources and the spectral results, other parameters, including time step, wave breaking and whitecapping parameters have also been well calibrated and the highest performance parameters have been chosen. The performance of the final model has been verified not only in terms of the bulk statistical parameters (for an example of wave height and period plot over time at WestHinder, see Figure 8), but also in terms of the spectral results. In Figure 7, measured and simulated 1D spectrum (with CFSR model) has been compared at a nearshore position: Europlatform. Two time instants have been chosen, including the peak of the storm, where wind generated waves are dominant (on top); nearly equally partitioned wind waves and swell for relatively strong wave (below). From these comparisons, it is seen that not only the locally generated wind waves have been well captured, but the sea swell, which are propagated from offshore boundary are also well reproduced, especially its energy partition and distribution over the frequency.

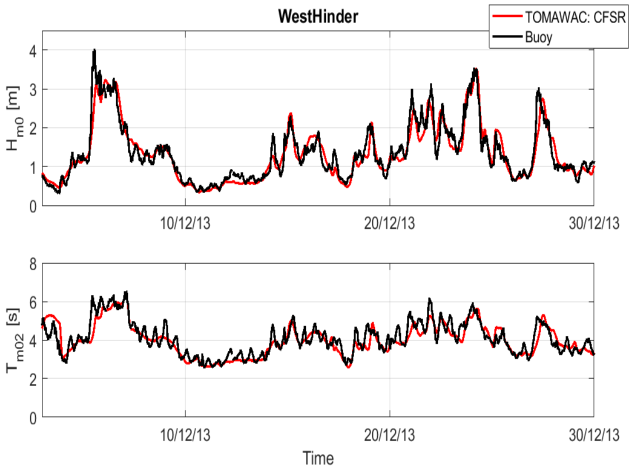

Figure 7 Significant wave height and Tm02 comparison between measurements and modelled results for Sinterklaas storm.

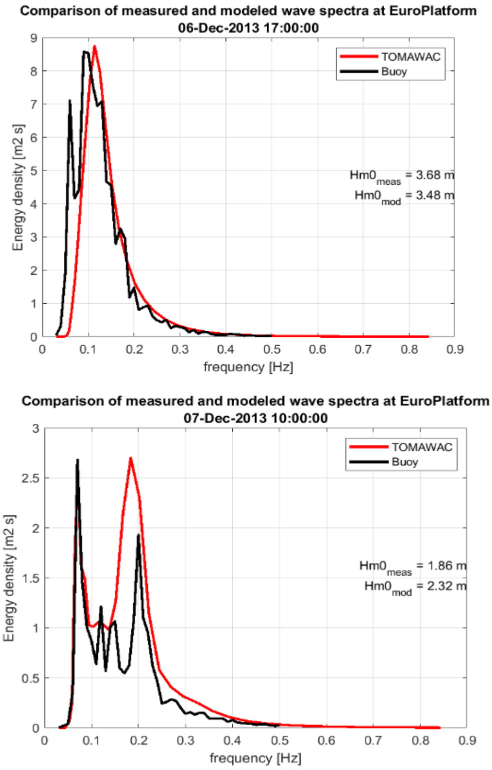

Figure 8 1D spectrum comparison between the Tomawac model and measurements at EuroPlatform.

B. *Validation and production runs*

With the final parameters being determined, we had used the model for hindcasting another independent period from April to August 2018 for the validation of the model. This period has been chosen for its calmer sea state, with a highest wave reaches at nearshore less than 2 meters. Results at the various locations have been listed in Table VII and Table VIII. It is seen that the bias and RMSE are well bounded, and a lower index of SI has been produced, especially for Tm_{02}. The correlation numbers for R for significant wave height are found to be more than 0.9, it is lower for the wave period. The observation is consistent with beforehand, that using CFSR wind over-estimates the wave energy at offshore points, at its performance improves when approaching the coast.

A general satisfying performance of the model can be concluded. This well-calibrated model has been used to generate a North Sea metocean database for 20 years (2001-2020). A general performance of the models has been evaluated by computing the statistics at nearshore points (WestHinder) for the data availability. The detailed errors for significant wave height have been listed in Table IX. An average bias of -1cm is found, marking the high performance of TOMAWAC model in reproducing the wave energy over a long period of time. It is also noted that the average RMSE is around 20cm, with a high correlation number of > 0.95. These statistical indicators prove the reliability of the constructed database in terms of the wave energy estimation and its potential for offering a first insight into the use of clean ocean energy. This database not only offers a first impression of the local wave and wind conditions for a specific period, but also can provide a general wave condition at specific points for a long period of time. For example, in Figure 9, the wave rose at Bol Van Heist for 20 years has been reproduced. During most of the period, wave energy presents to be in calmer state. The highest waves travel most to East or Southeast direction. Based on this database, it is also possible to extract a seasonal or monthly wave energy and direction fluctuation, providing valuable benchmark for the workability of ocean platforms for the North Sea.

Table VII Statistical assessments for model performance for April to August 2018: significant wave height.

	BVH	Westhinder	Europlatform	K13	A12	Ekofisk
Bias [m]	-0.09	0.04	0.06	0.09	0.25	0.15
RMSE [m]	0.19	0.21	0.22	0.30	0.39	0.71
SI [-]	28%	24%	24%	28%	35%	22%
R [-]	0.91	0.93	0.96	0.91	0.93	0.91

Table VIII Statistical assessments for model performance for April to August 2018: Tm02.

	BVH	Westhinder	Europlatform	K13	A12	Ekofisk
Bias [s]	0.41	0.04	-0.23	-0.12	-0.15	0.19
RMSE [s]	0.81	0.51	0.59	0.63	0.78	0.91
SI [-]	20%	13%	14%	14%	16%	31%
R [-]	0.72	0.81	0.77	0.77	0.72	0.75

Table IX Errors calculated for 20 years (2001-2020) for significant wave height at WestHinder.

	2001	2002	2003	2004	2005
Bias [m]	-0.05	-0.07	-0.05	-0.08	0.02
RMSE [m]	0.22	0.22	0.20	0.21	0.21
SI [-]	20%	22%	25%	21%	21%
R [-]	0.97	0.97	0.96	0.97	0.97
	2006	**2007**	**2008**	**2009**	**2010**
Bias [m]	-0.03	-0.06	-0.11	-0.12	-0.04
RMSE [m]	0.22	0.20	0.25	0.22	0.21
SI [-]	20%	22%	22%	23%	22%
R [-]	0.97	0.95	0.96	0.95	0.96
	2011	**2012**	**2013**	**2014**	**2015**
Bias [m]	0.01	0.04	0.02	0.03	0.02
RMSE [m]	0.22	0.23	0.25	0.23	0.22
SI [-]	20%	22%	21%	22%	19%
R [-]	0.97	0.97	0.97	0.97	0.95
	2016	**2017**	**2018**	**2019**	**2020**
Bias [m]	0.09	0.03	0.02	0.03	0.03
RMSE [m]	0.28	0.22	0.21	0.21	0.25
SI [-]	18%	21%	22%	20%	22%
R [-]	0.97	0.97	0.95	0.97	0.97

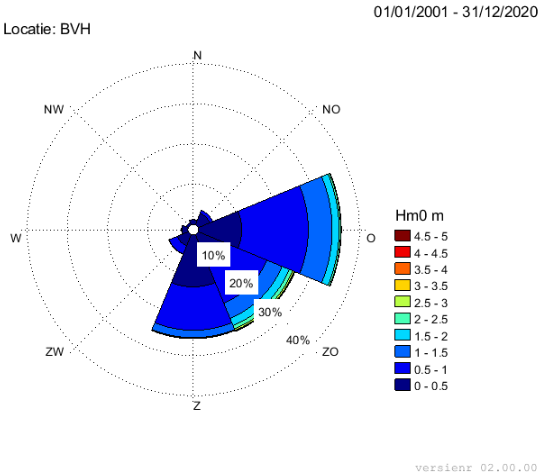

Figure 9 wave rose at BVH for 20 years.

V. CONCLUSIONS

In the current study, we have constructed a semi-coupled (hydrodynamics and waves) model for the North Sea, focusing on Belgian coast. The performance of the model has been evaluated using several reliable statistical parameters. Two wind sources have been compared: ERA5 wind and CFSR wind. The performances of two wind sources are very similar; in general, ERA5 wind has been found to yield a better result regarding wave energy and period at offshore whilst at nearshore, CFSR wind outer-performs ERA. Both winds have been found to underestimate the wave energy at nearshore points, especially at the peak of the storm. Due to the higher performances of CFSR close to the coast, we have constructed the model using this wind source.

The model has been run for 20 years (2001-2020: each year individually for storage and data accessibility reasons). This database offers large potential. It can serve as a basic database for projects that are relevant to the areas and providing a first and fast evaluation of wave energy in terms of seasonal/monthly and yearly changes. It brings valuable insights into the feasibility of WEC at nearshore coastlines, where the wave energy potential has been currently largely overlooked. As a matter of fact, the results of these runs have been converted onto WEC database and presents to be available online (https://sinapps.imdcapps.be/).

VI. ACKNOWLEDGEMENTS

This project is executed in the framework of the Bluecluster research into blue energy the financial support from Bluecluster is highly appreciated.

VII. REFERENCES

[1] "Oean energy forum. Ocean Energy Strategic Roadmap," building ocean energy for Europe, 2016.

[2] G. Lavidas and H. Polinder, "North Sea Wave Database (NSWD) and the need for reliable resource data: a 38 year database for metocean and wave energy assessments," Atmosphere, vol. 10, p. 551, 2019.

[3] L. Cavaleri, L. Bertotti and P. Pezzutto, "Accuracy of altimeter data in inner and coastal seas," Ocean Science, vol. 15, pp. 227-233, 2019.

[4] L. Romero, L. Lenain and W. K. Melville, "Observations of surface wave-current interation," Journal of Physical Oceanography, vol. 47, no. 3, pp. 615-632, 2017.

[5] K. Chu, A. W. Breugem, T. Wolf and B. Decrop, "Improvement of a continental shelf model of the North Sea," in TUC, 2020.

[6] K. Chu, A. W. Breugem, L. Wang and B. Decrop, "Automatic calibration of a continental shelf model of the North sea using data assimilation algorithm," in IAHR, Granada, Spain, 2022.

[7] A. W. Breugem, S. Doorme, A. Bakhtiari, J. Figard and E. Di Lauro, "Speeding up TOMAWAC by means of improved numerical methods," in TUC, 2021.

[8] "History of the Study of Marine Biology," https://www.marinebio.org/creatures/marine-biology/history-of-marine-biology/, 25 01 2013. [Online].

3D numerical modelling of the sediment transport in a tropical estuary influenced by Amazonian mud banks

Nicolas Huybrechts, Thi Kim-Anh Do[1], Noelia Abascal Zorrilla[2], Antoine Gardel[3], Aldo Sottolichio[4]
nicolas.huybrechts@cerema.fr
[1]: Cerema REM RHITME Research Team, Margny Lès Compiègne, France
[2]: ARGANS Ltd, Chamberlain House, 1 Research Way, Plymouth PL6 8BU, United Kingdom
[3]: CNRS LEEISA URS 3456, 5 Centre de Recherche de Montabo, 97334 Cayenne, French Guiana,France
[4] : Université Bordeaux CNRS UMR Epoc 5805, Pessac

***Abstract* – A TELEMAC-3D model coupled with Gaia has been developed for the Maroni estuary located in French Guiana. One of the unusual characteristics of the Guaina estuaries is the episodic presence of huge coastal mud banks near their mouth. These mud banks constitute a source of fine sediment and the fluid mud is able to damp the wave propagation. The wave action is included in the model in both an uncoupled and a coupled way. Sensitivity studies have been performed on the vertical turbulence models and on the wave damping term. Finally the model is applied to explore seasonal variations in the saline intrusion and turbidity maximum.**

Keywords: cohesive sediment, Gaia, wave-mud interactions, estuary

I. INTRODUCTION

Estuaries located along the Guiana coastline are under the influence of the Amazon estuary. A part of the Amazonian turbid plume is transported alongshore towards French Guiana [1]. Between the Approurague and Ayapoque estuaries, the turbid plume is transformed into huge coastal mud banks 10 km in width, 30 km in length, 5 to 10 m in depth and migrating about 1-2 km/year [2]. Such a volume of fluid mud is able to completely damp wave propagation whereas waves can still reach the shoreline located between mud banks where the mud is more consolidated [3,4]. Once a mud bank approaches an estuarine mouth, it constitutes a source of fine sediment potentially transported by the combined action of wave and tidal current into the central part of the neighbouring estuary. The attenuation of the wave due to the mud bank has been integrated into spectral wave models [5,6] via the implementation of an additional source term into WavewatchIII or Swan. Abascal Zorrilla [7] has developed a 2D numerical model of the Mahury estuary. The model is based on a coupling between TELEMAC-2D, TOMAWAC and SISYPHE. TOMAWAC has been modified to integrate the Ng (2000) formulation [8] to apply the wave damping effect as proposed by [5]. Do et al [9] have built a 3D model of the Maroni estuary based using TELEMAC-3D. The model was used to analyse the seasonal variation in the hydrodynamic pattern of stratification and residual currents.

In the present study, the TELEMAC-3D model of the Maroni is coupled with GAIA. Wave influence is considered in both an uncoupled way and a coupled way. The hydro-sedimentary model is used to determine the main characteristic of the turbidity maximum and the sediment exchanges between the coastal area and the downstream part of the estuary.

Some characteristics of the Maroni estuary are first presented in section 2 and the set-up of the numerical model is detailed in section 3. A sensitivity analysis is then performed on the turbulence models and different sediment parameters. The model is finally exploited to explore the sediment dynamics and the wave coupling strategy.

II. CASE STUDY

The Maroni river is 677 km long with a catchment area of 60,930 km². In the estuarine area, its width is 700-900 m near Apatou (100 km upstream from the mouth Fig.1a) and up to 4,000-5,000 m between kilometric point (KP) 10 and 23 (Fig. 1b). Small tributaries, mostly on the right bank, flow into the estuary and some islands built from alluvial deposits are present upstream of Crique Vache (Fig.1b).

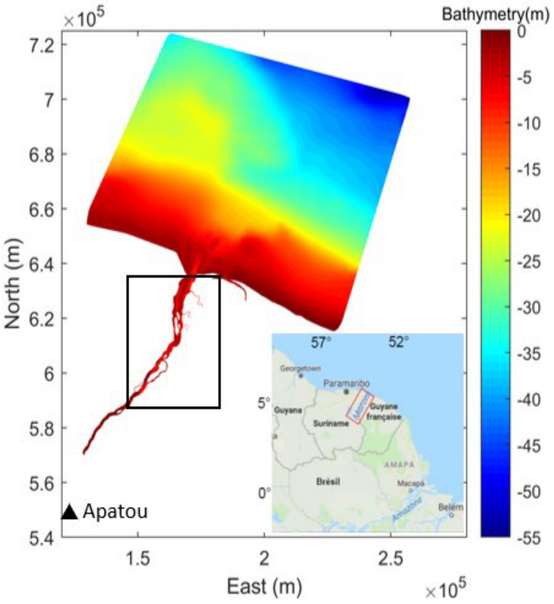

Figure 1a The Maroni estuary

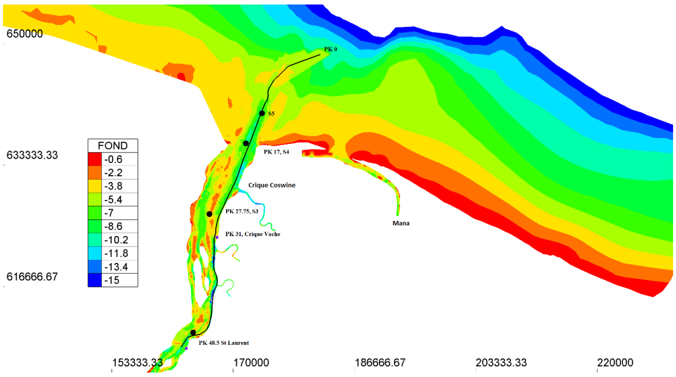

Figure 1b The Maroni estuary, showing kilometre points and key locations

The climate is equatorial and within the intertropical convergence zone. Well contrasted seasonal variations are characterised by a high river discharge from the end of December to July and a low river discharge from August to December. Trade-winds are weak and characterised by a quasi-constant direction of about 10°–15° (direction from the north) throughout the year [3]. River discharge is estimated by Direction de l'Equipement, de l'Aménagement et du logement (DEAL) at Apatou via a rating curve. The mean annual discharge reaches 1700 m^3/s with lower values down to 100 m^3/s during the low flow periods and higher values up to 5000 m^3/s during the high flow periods.

Bed material samples have been collected by Jouanneau and Pujos [10] during the low river discharge (November 1984) and high river discharge periods (May 1985). From their analysis, it appears that the upstream part of the estuary (upstream of St Laurent) is composed of coarse sand whereas fine materials are found near the mouth.

The tide propagates up to 100 km upstream inland until a natural weir at Apatou. No continuous tidal gauge is installed inside the Maroni estuary, although water levels are recorded at three locations by the Port Authorities during two months each year.

III. MODEL SET UP

A. *Hydrodynamic Module – TELEMAC-3D*

The computational domain extends over 90 km in width and 97 km in length for the maritime part. Inland, the domain extends until the limit of tide propagation where observed river discharge is available. The distance between nodes of the horizontal mesh resolution decreases from 2.5 km in the coastal zone to 120 m inside the central part of the estuary, to 50 m in the navigation channel or in the tributaries and down to about 10 m around islands.

The horizontal mesh contains about 48000 nodes. For the vertical mesh, 8 vertical planes are used with a finer resolution near the bottom. The distribution of vertical mesh layers from bottom to water surface have been defined as a percentage of the water depth as follows: 0, 0.075, 0.15, 0.3, 0.5, 0.7, 0.85 and 1.0.

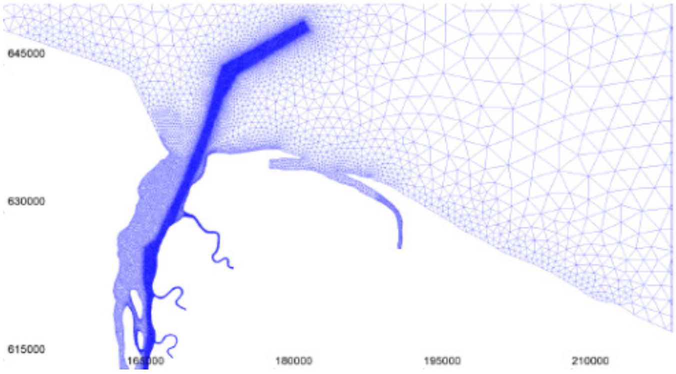

Figure 2 The model mesh

The computational domain contains six open boundaries. Upstream, daily fresh river discharges are forced for Maroni and Mana rivers whereas constant discharges are imposed for Crique Rouge, Crique Vache and Crique Coswine. Offshore, tidal levels and currents are imposed using atlases of the Amazon shelf from Oregon State University. The offshore imposed salinity is 35 PSU. A time step of 20 s is used for each case investigated.

The bathymetry interpolated onto the model mesh combines a number of different datasets: DTM of the French Guiana shelf from the Shom, bathymetries collected by CNRS and DEAL in the downstream estuary in October 2017.

For the vertical turbulence, two approaches are tested: (1) Prandtl mixing length model combined with Lehfeldt and Bloss [11] damping functions and (2) the multilayer mixing length model (MML) developed by Walter et al [12] on the Loire estuary.

B. *Sediment Module – GAIA*

During a bathymetric survey in October 2017, bed samples were collected to determine the sediment composition. The bed samples have been interpolated onto the mesh (Fig. 3) using a working variable (SEDMIX17).

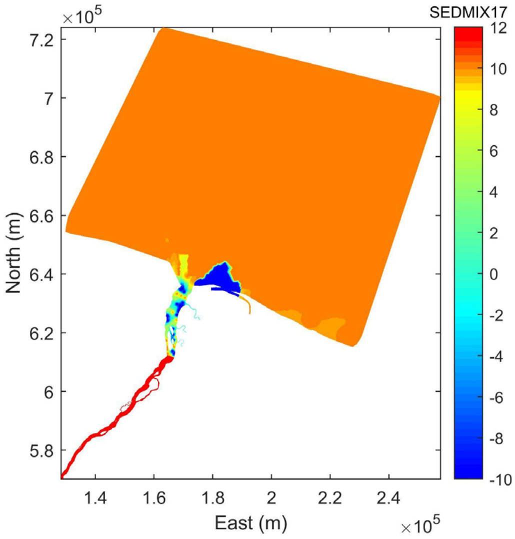

Figure 3 The sediment composition

Offshore the bed material is composed of fine marine sand (SEDMIX17=10). Upstream the sand is coarser (SEDMIX17>12.5). In the central part, the sediment is composed of sand-mud mixture (SEDMIX17 ranging from 0 to 7.5) or fluid mud (SEDMIX17<0). For the initial condition of the sediment concentration, a satellite image from Abascal Zorrilla et al [13] has been used (Figure 4). This image is also used to determine the location of the coastal mud bank.

In GAIA, the bed composition is divided into 4 classes: one coarse sand, one fine sand and two mud classes (one from upstream and one for the coastal mud) The initial percentage of the different classes is defined according the SEDMIX17 variable. Sand is transported by total transport equation (Soulbsy van Rijn). Consolidation and flocculation are considered for the cohesive material. The van Leussen formulation is used for flocculation. Mud sliding is also considered. Three zones of constant bed friction are defined: coastal area, central part and upstream with Nikuradse bed roughness (ks) ranging from 0.1 to 0.5 m. Locally when the thickness of the fluid mud is larger than 0.2 m, a reduced friction is applied (ks=10^{-5} m).

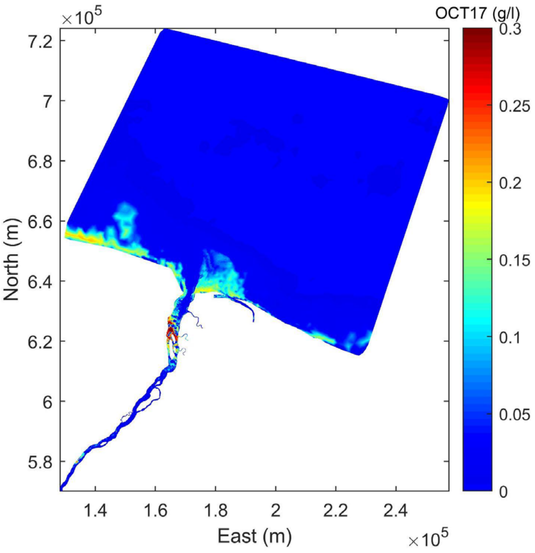

Figure 4 Initial condition of the suspended sediment

C. *Wave Module – TOMAWAC*

TOMAWAC is applied in both an uncoupled and a coupled way. For the uncoupled implementation, first a simulation is launched with TELEMAC-2D coupled with TOMAWAC (using 25 frequencies and 36 directions). The offshore boundary is extracted from a large-scale Wavewatch III model. The results of the wave module are then read by TELEMAC-3D as an external forcing. The wave module serves here to mainly integrate the influence of the waves on the bed shear stress and associated sedimentation rate. To mimic the damping effect due to fluid mud, the shear stress due to the wave action is added to the current shear stress only when the fluid mud thickness is lower than 0.2 m.

For the coupled implementation, the same discretization in frequency and direction is used. The wave action influences the shear stress and the current pattern. Two simulations are performed with the triple way coupling: with or without the source term of the wave damping due to the muddy bed. The Ng [8] formulation has been implemented in TOMAWAC. GAIA provides TOMAWAC with information related to the thickness of the fluid mud and the mean concentration (density) of the deposit.

IV. RESULTS

A. *Influence of the vertical turbulence model*

The hydrological year from October 2017 to October 2018 has been simulated. Water level measurements are available at two stations Saint Laurent (KP 49) and Crique Vache (KP 31) in October-November 2017.

The comparison between measured and computed tidal range estimated for each tide is shown in Figure 5.

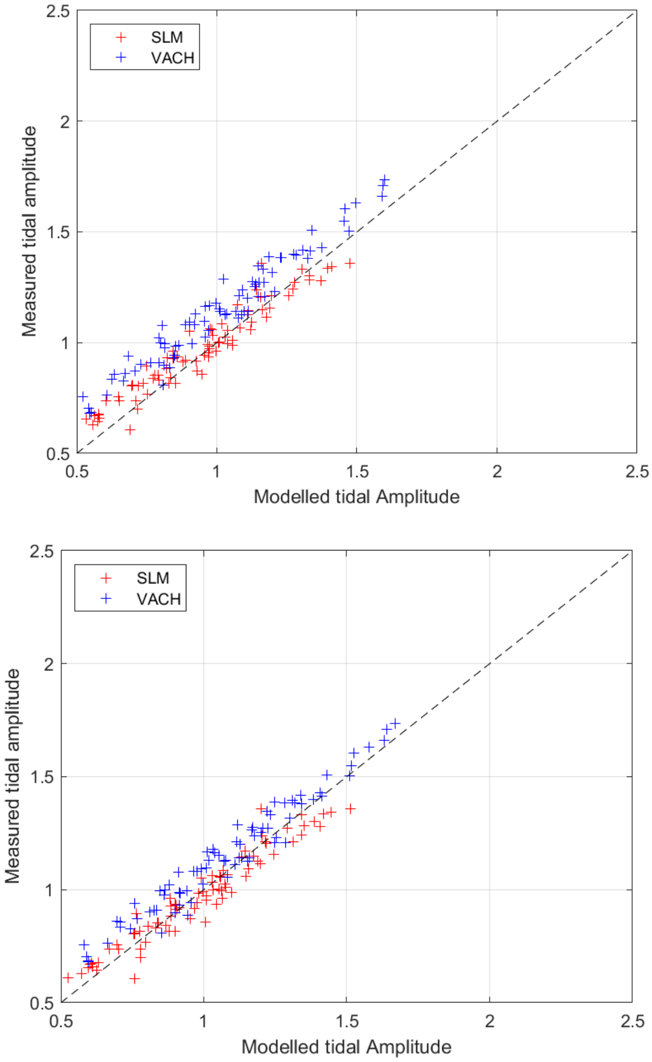

Figure 5 Tide propagation comparison at Saint Laurant (SLM) and Crique Vache (VACH) for the Prandtl mixing length with damping function (top) and MML (bottom).

The differences between modelled and measured tides are below 12 cm. For the configuration using Prandt mixing length model with damping functions, tidal water levels are less correctly predicted at Crique Vache than at Saint Laurent. The tide propagation at the two stations is slightly better predicted with the configuration based on the MML model.

For an along-channel profile (Fig 1b), the residual currents have been predicted during the dry and wet season. For the wet season, the residual currents are mostly directed downstream with the two turbulence models. More differences in residual flow direction are noticed for the dry season (Fig. 6).

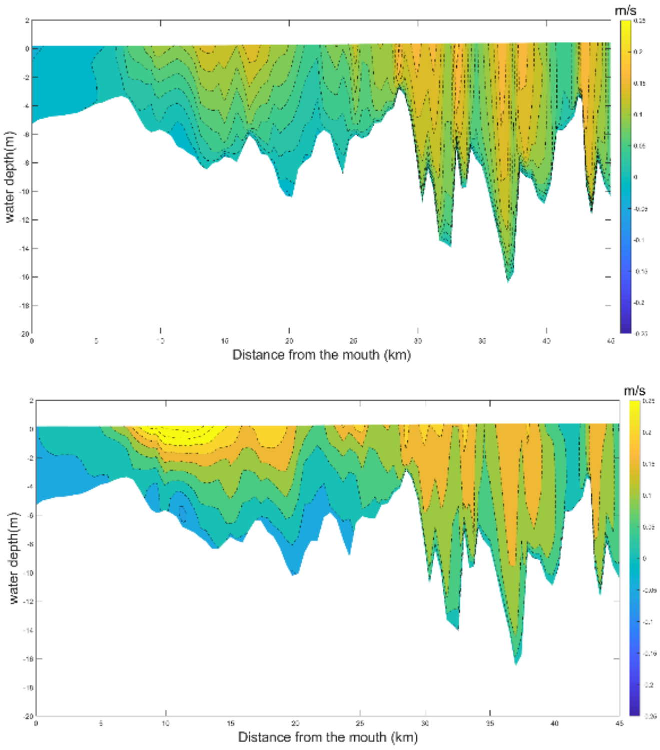

Figure 6 Residual currents during the dry season for Prandtl mixing length with damping (top) and MML (bottom). Positive velocities are oriented downstream and negative velocities are oriented upstream.

With the configuration based on Prandtl mixing length model with damping, some residual currents oriented upstream are detected between KP 10 and 20. Such conditions are favourable for transport of mud from the mud bank to the central part of the estuary. With the MML, upstream oriented residual currents extend over a larger area KP 7.5 to 25 and affect a larger part of the water column. The presence of a two layers behaviour (Do et al. [9]) is better captured. In the wet season, the MML also captures an upstream residual current in the first 5 kilometres (not shown here).

B. Seasonal variations of the turbidity maximum and of the residual fluxes

The model parameterized with the MML is used to simulate three different hydrological years from October 2016 to November 2018 (a year for each simulation). Time variations of the residual sediment fluxes, salinity and suspended sediment for the hydrologic year 2017-2018 are shown in Figures 7 and 8. The variations are extracted at KP 10, 16, 22 and 28.

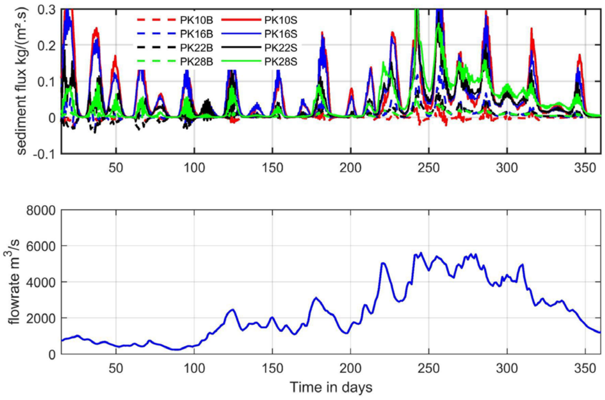

Figure 7 Time variation of residual fluxes along a hydrological year

At the surface, residual sediment fluxes are oriented downstream for the whole year. Until day 100, upstream residual sediment fluxes are observed at the bottom between PK 10 and 22 for river discharge (Q) lower than 1000 m^3/s. Between day 100 and 200 (1000<Q<3000 m^3/s), the fluxes are oriented mainly downstream. Input of sediment is then observed but only at KP 10 during the peak of the dry season (Q> 4000 m^3/s)

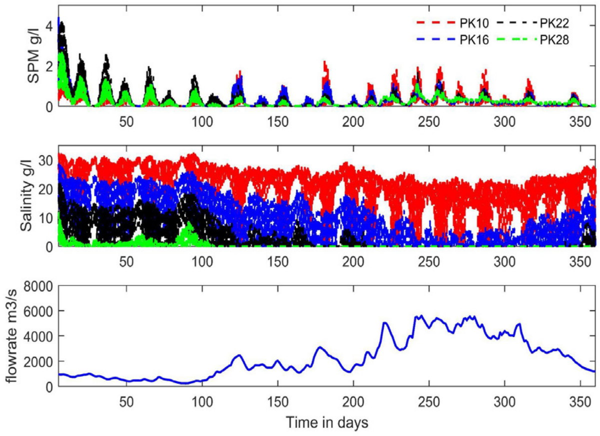

Figure 8 Time variation of the concentration, salinity and flow rate

Similarly, SPM is high from KP 16 to 28 for discharges lower than 1000 m^3/s. Salinity at KP 28 still reaches levels higher than 1. Between days 100 and 200, salinity at KP 22 progressively decreases and the turbidity maximum migrates between KP 16 to 10. After day 200, the turbidity maximum is located at around KP 5. At the upstream stations, the sediment load is mainly advected with small tidal variability.

The migration of the turbidity maximum is illustrated for the 2016-2017 hydrological year in Figure 9. This hydrological year is characterised by a low discharge (300 m^3/s) during the dry season.

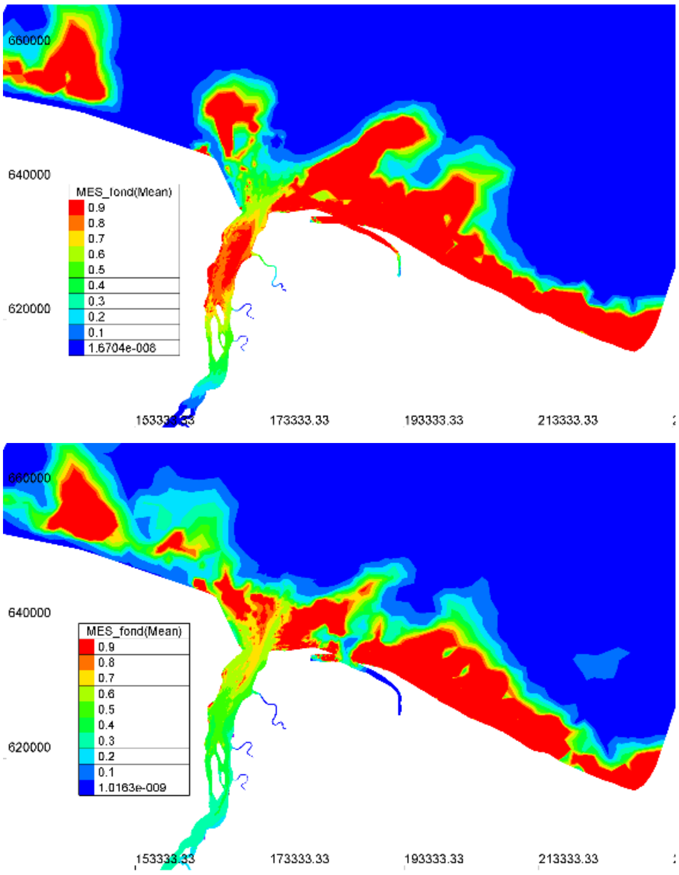

Figure 9 Migration of the turbidity maximum: residual SPM (MES in French) for modelled discharges of 300 m^3/s (top) and 4000 m^3/s (bottom)

For the pronounced dry season, the residual SPM reaches maximum values between Crique Coswine and Crique Vache. High values are however also reached in the upstream part near Saint Laurent. Conversely during the wet season, the turbid plume has shifted downstream of Crique Coswine, up to the mouth.

A. Coupled versus uncoupled implementations

In terms of computational time, the simulation of a hydrological year takes one CPU day on the Cerema cluster (48 nodes) for the uncoupled method. However, neglecting the influence of the bed change on the wave propagation is a crude assumption for such a dynamic area. Despite this, it sounds reasonable to perform, with the uncoupled methodology, preliminary sensitivity studies mainly on some upstream processes. To investigate the influence of the uncoupled approximation, two further simulations have been performed using the triple way coupling. The computational time increases up to 15 CPU days to simulate 40 days. The time steps of TELEMAC-3D and TOMAWAC have been reduced to ensure stability. The high computational time comes from slow convergence of TOMAWAC probably due to significant bathymetric changes near the navigation channel.

The mean suspended concentration near the bottom (over 40 days) is plotted in Figure 10 for uncoupled waves and for coupled waves with and without the damping term. It should be kept in mind that the analysed period corresponds to the dry season with lower wave activities.

Figure10a shows the turbid plume with the uncoupled methodology for the waves. With the wave coupling (Fig 10b), the coastal plume is more elongated just in front of the Mana and concentration levels are higher in the deeper coastal zone.

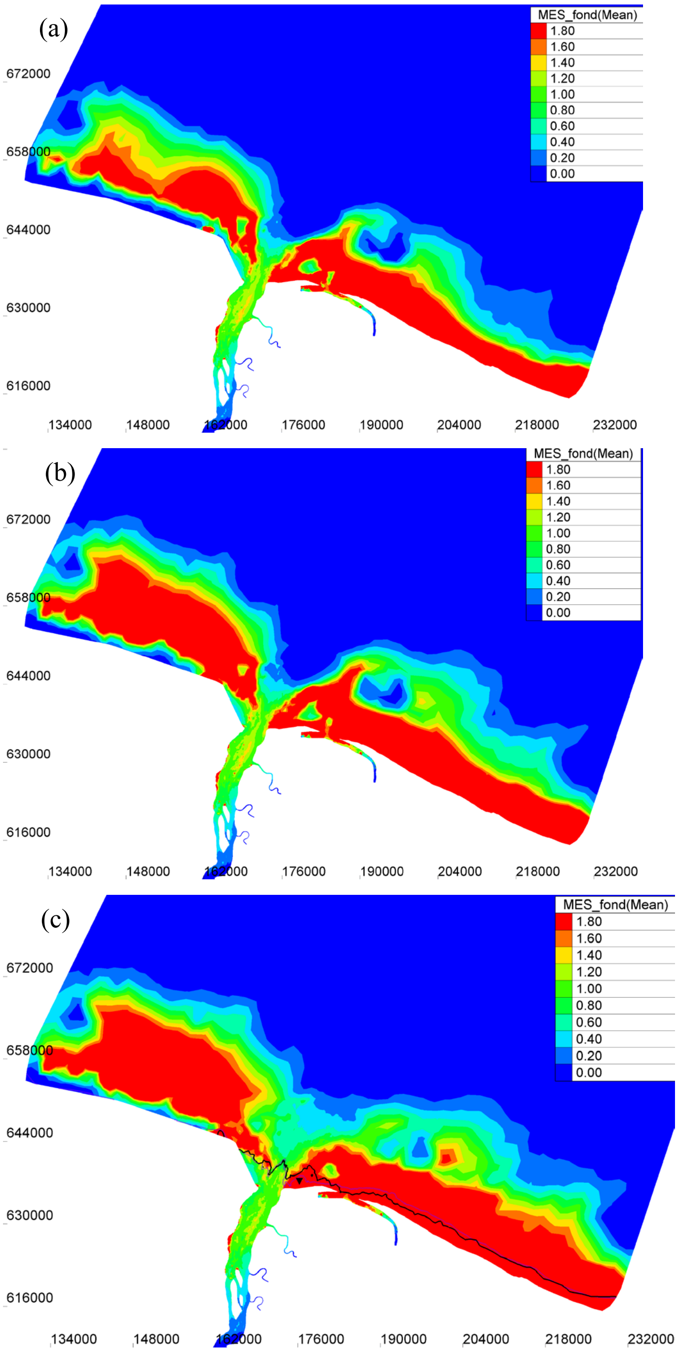

Figure 10 Influence of the damping term on the turbid plume for (a) uncoupled waves, (b) coupled waves without damping term, and (c) coupled waves with damping term. The isovalue of Hs=0.3m is plotted for the damping term model result (black line), and without the damping term (purple dashed line). Wave time series are extracted at the point marked by a triangle.

The addition of the damping term (Fig 10c) leads to higher concentrations in the estuary mouth. In Figure 10c, the isoline for significant wave height (Hs) of 0.3m is plotted separately for the two coupled simulations. This isoline is 3 km away from the shore with the damping term. Without the damping term, the isoline moves nearer to the estuarine beach. The effect of the damping term appears to act quite locally but on the key area where the sediment exchange between the coastal mud bank and the navigation channel happens. Time series of the wave height, with and without the damping term, are illustrated on Figure 11.

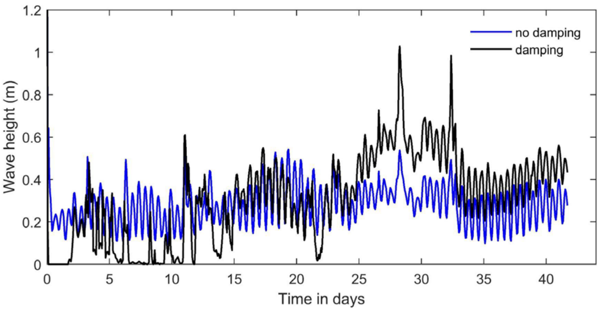

Figure 11 Time series of the wave heights with the coupled waves method

For the first 25 days, the modelled wave height is completely damped by the fluid mud presence. Once the fluid mud has been eroded (or consolidated), the wave propagates as without the damping term until the next significant fluid mud deposition event. After day 25, the behaviour is reversed since the wave height is higher than without the damping term. This is probably due to a bed modification. In the developed approach described here, one important process is missing: the fluidization of the mud by wave action. Wave action can deconsolidated older bed deposits and the way to integrate this process needs to be investigated.

V. CONCLUSIONS AND PERSPECTIVES

A 3D numerical model of the Maroni estuary has been built to investigate the development of the estuarine turbidity maximum and its connection with the coastal sediment plume. Using TELEMAC-3D coupled with GAIA, wave influence has been integrated as an external forging (uncoupled) using a previously calculated wave field from TOMAWAC. Consolidation, flocculation and sliding processes are integrated for the cohesive sediment whereas total transport is selected for sandy material.

The model predicts residual currents in the upstream direction during dry season conditions which are likely to be the key mechanism by which mud is transported from the coastal mudbanks up the estuary. A sensitivity study on the vertical turbulence model has pointed out that the MML model displays a more pronounced two layer flow with more intense residual currents and associated saline and mud transport fluxes near the bottom. The model has then been applied to determine the seasonal variation of the saline intrusion and the migration of the turbidity maximum.

Preliminary results using triple-way coupling (TELEMAC-3D, GAIA and TOMAWAC) highlight the importance of the damping term on the wave propagation and the development of the turbid plume. Some efforts are however needed to optimise the coupling with TOMAWAC in order to reduce the computational time and thus be able to simulate the whole hydrological year. In the near future, the model will be used to test the different recent coupling approaches for TOMAWAC (i.e. the tel2tom and tomawac3d options). Research efforts are still needed to integrate the full interaction between the wave and the mud dynamics, such as including the potential for fluidisation of the mud layer by wave action.

ACKNOWLEDGEMENT

This work is part of the MAroni Estuary Sediment TRansport mOdeling (MAESTRO) project funded by the Communauté de Communes de l'Ouest Guyanais and led by CNRS Guyane (LEEISA URS 3456). The authors thank the Shom for the DEM of the Guiana shelf, the DEAL Guyane for the flowrate and bathymetry dataset.

REFERENCES

[1] M.A Allison, M.T. Lee, A.S. Ogston, R.C Aller, "Origin of Amazon mudbanks along the northeastern coast of South America". Mar. Geol. 163, 200 241–256. https://doi.org/10.1016/S0025-3227(99)00120-6

[2] A. Gardel, N. Gratiot,"A Satellite Image–Based Method for Estimating Rates of Mud Bank Migration, French Guiana, South America". J. Coast. Res. 2005, 214, 720–728. https://doi.org/10.2112/03-0100.1

[3] N. Gratiot, A. Gardel, EJ Anthony, "Trade-wind waves and mud dynamics on the French Guiana coast, South America: Input from ERA-40 wave data and field investigations". Mar. Geol. 2007 236, 15–26. https://doi.org/10.1016/j.margeo.2006.09.013

[4] J.C. Winterwerp, R.F Graaff, J.de Groeneweg, A.P Luijendijk,, "Modelling of wave damping at Guyana mud coast". Coast. Eng. 2007 54, 249–261. https://doi.org/10.1016/j.coastaleng.2006.08.012

[5] W.E. Rogers K.T Holland. "A study of dissipation of wind-waves by mud at Cassino Beach, Brazil: Prediction and inversion". Cont. Shelf Res. 2009,29, 676–690. https://doi.org/10.1016/j.csr.2008.09.013

[6] W.M Kranenburg, J.C Winterwerp, G.J de Boer, J.M Cornelisse, M Zijlema, "SWAN-Mud, an engineering model for mud-induced wave-damping". J. Hydraul. Eng. 2011 137, 959–975. https://doi.org/10.1061/(ASCE)HY.1943-7900.0000370.

[7] N. Abascal Zorrilla. Dynamics of the Amazon mud bank system through spatial observation and hydro-sedimentary modeling: application to the coastal domain of French Guiana, Phd thesis, 2019 Univ de Guyane. 660p

[8] C.O "Water waves over a muddy bed: A two layer Stokes' boundary layer model". Coast. Eng. 2000 40, 221–242. https://doi.org/10.1016/S0378-3839(00)00012-0

[9] K.A. Do, A. Sottolichio, N. Huybrechts, and A. Gardel,. Circulation patterns and implication for fine sediment transport in a preserved tropical estuary: The case of the Maroni (French Guiana). Regional Studies in Marine Science, 2021, 40, 101493

[10] J.M Jounneau, and M. Pujos. Suspended matter and bottom deposits in the Maroni estuarine system (French Guiana). Netherlands Journal of Sea Research, 1988 22(2), 99-108.

[11] R. Lehfeldt, S. Bloss, Algebraic Turbulence Model for Stratified Tidal Flows. In: Dronkers J., van Leussen W. (eds) Physical Processes in Estuaries. Springer, Berlin, Heidelberg. 1988

[12] R. Walther, L. Hamm, E. David, "Coupled 3D Modeling of Turbidity Maximum Dynamics in the Loire Estuary , France". Coastal Engineering 2012.

[13] N. Abascal Zorrilla, V. Vantrepotte, N. Huybrechts, N.D Ngoc, E.J Anthony, A. Gardel, Dynamics of the estuarine turbidity maximum zone from Landsat-8 data: The case of the Maroni River estuary, French Guiana. Remote Sensing,2020, 12, 2173. doi:10.3390/rs12132173.

Offshore windfarm scour prediction under storm surge using the open TELEMAC system

Zijun Mai [1], Yue Zhang[1], Hanyu Zhan[1], Lu Zhou[2], Jiesheng Min[2]
edward.mai@yuansuan.com, Hangzhou, China
[1]: Zhejiang Yuansuan Technology Co., Ltd., Hangzhou, China
[2]: EDF China, R&D Centre, Beijing, China

***Abstract* – In offshore wind farms, storm surge and waves caused by typhoons can have a strong influence on the morphology of the seabed. These tropical cyclones can severely affect wind power foundations, leading to scour processes around piles, which, in turn, may affect the instability of structures. In this study, a three-way coupled model (hydrodynamic, wave, and sediment transport processes) was implemented to study sediment transport and the evolution of the bed around the piles under the influence of typhoons and storm surge. Numerical simulations were conducted using the modules TELEMAC-2D, TELEMAC-3D, TOMAWAC and GAIA in the open TELEMAC system. Based on the data obtained from the analysis of existing databases, a historical typhoon was reconstructed using Fujita-Takahashi air pressure model and Jelesnianski wind velocity model. The numerical model was established by considering several different time and space scales. At the oceanic-scale, a hydrodynamic model was built to consider tide, wind effect, white capping and non-linear transfer effects. Within the scope of the wind farm, a middle-scale model has been established to focus on the seabed evolution under the influence of tides and waves using the simulation results of the oceanic-scale model as forcing input at the model boundaries. Finally, a local-scale model was established for each pile foundation to simulate the evolution of scour pits. Simulation results of the multi-scale model with and without storm surge are also compared. The numerical results showed that sediment transport is generally enhanced by the storm surge, and the evolutions of the seabed and local scour are strongly influenced by the effect of the typhoon.**

Keywords: hydrodynamic-wave-sediment coupled model, storm surge, multi-scale model, TELEMAC

I. INTRODUCTION

As a clean and renewable energy source, offshore wind power is an important approach to the generation of electricity in bodies of water. During the passage of a typhoon, with the change of air pressure and extreme wind velocity, it is prone to generate a storm surge that influences the water level and brings significant strong waves. The hydrodynamic and wave conditions will change drastically under such extreme weather, and will have a direct impact on the morphodynamics of the seabed around pile foundations, cause erosion and pose a serious threat to the safety and stability of the pile foundations.

Various studies have investigated the characteristics of storm surges and strong waves caused by typhoon, confirming their patterns and the extreme impacts on the state of the sea (e.g., [1], [2]). The sediment transport under the influence of tropical cyclones has been discussed by numerous researchers, that the effect of a typhoon usually triggers significant changes in solid discharge, sediment distribution and seabed of coastal area (e.g., [3], [4]).

The main objective of this work is to investigate the sediment transport around an offshore wind farm under storm surge caused by a typhoon. This numerical study was carried out by implementing a multi-scale coupled model approach in both 2D and 3D. The modules TELEMAC-2D and TELEMAC-3D were used to compute the hydrodynamic conditions under storm surge. The waves under atmospheric effect were calculated by TOMAWAC. The module GAIA was used to simulate the evolution of seabed and scour pits. In the following sections, the study methodology is described, followed with model construction and validation. Finally, the simulation results are discussed.

II. METHODOLOGY

A. Typhoon Model

Tropical cyclones or typhoons feature a strong, circular wind field and a minimum pressure at the centre of the storm. Low pressure and extreme wind speed are the main reasons of violent changes in hydrodynamic and wave conditions. The typhoon model is used to reconstruct the wind field of typhoon, characterised by the key elements such as pressure, wind velocity and direction. The pressure of typhoon is given by the Fujita-Takahashi[6] model:

$$P(r) = P_\infty - \frac{P_\infty - P_0}{\sqrt{1+\left(\frac{r}{R_0}\right)^2}}, 0 \le r < 2R_0 \qquad (1)$$

$$P(r) = P_\infty - \frac{P_\infty - P_0}{1+\frac{r}{R_0}}, 2R_0 \le r < \infty \qquad (2)$$

where r is the radius, P_∞ is the pressure at infinite, P_0 is the central pressure and R_0 is the radius of maximum wind speed which is given by the following semi-empirical formula:

$$R_0 = 28.52th[0.00873(\varphi - 28)] + 12.22\exp\left(\frac{P_0 - P_\infty}{33.86}\right) + 0.2V_s + M \qquad (3)$$

where φ is latitude, V_s denotes typhoon movement velocity and M is a constant.

The gradient wind field V_g is calculated as follows:

$$V_g(r) = -0.5fr + \sqrt{(0.5fr)^2 + \frac{r}{\rho_a}\frac{\partial P}{\partial r}} \qquad (4)$$

where f denotes the constant of Coriolis and ρ_a is the density of air.

The movement wind field is given by Jelesnianski's model[7]:

$$V_d(r) = V_s\left(\frac{r}{R_0+r}\right), 0 \leq r < R_0 \qquad (5)$$

$$V_d(r) = V_s\left(\frac{R_0}{R_0+r}\right), R_0 \leq r < \infty \qquad (6)$$

The wind field generated by the typhoon model can only reflect the atmospheric conditions within a certain region and period. A background wind field covers the entire domain and for the period of interest. However, it could underestimate the intensity of typhoon. Therefore, a superposition of wind fields is necessary, where the typhoon wind field is considered inside the impact area of the typhoon, and the region outside this area is controlled by the background wind field. The superposition with the background wind filed by Climate Forecast System Reanalysis (CFSR)[8] allows for considering the complete atmospheric conditions in TELEMAC and TOMAWAC.

B. Hydrodynamics

The hydrodynamic conditions are computed by the modules TELEMAC-2D and TELEMAC-3D. The calculation of storm surge takes into account astronomical tides and meteorological effects in real time, namely the wind field and the pressure field under the effect of typhoon. The hydrodynamic conditions, such as water level and flow velocity, are obtained by solving the Reynolds-Averaged Navier-Stokes equations (3D) and the shallow-water equations (2D).

C. Wave Propagation

Using the TOMAWAC module, the calculation of wave transformation and propagation is based on the third-generation wave spectrum variance analysis method[9]. It considers the effect of wind, bottom friction, white capping, wave breaking, and non-linear transfers, and eventually calculates the wave elements such as the wave field and the wave action force caused by the typhoon.

D. Sediment Transport

The GAIA module allows the study of coastal sediment transport and morphological changes in the seabed. The van Rijn sediment transport formula[13] is used to compute the solid discharge. The slope effect formulation by Koch and Flokstra[14] is considered to compute the magnitude of sediment transport. Based on the hydrodynamic conditions and wave conditions generated by the modules briefly described above, the sediment transport process and seabed evolution are simulated[10].

III. MODEL CONSTRUCTION

A. Study Area

The study area is located in the east coast of China as shown in Figure 1, covering the China Yellow Sea and the East China Sea. The offshore wind farm is in the east of Jiangsu province and was built on the radial sand ridge in the South Yellow Sea. This radial sand is characterised by its complex morphology and tide conditions[5]. Thought abundant in wind power resources and favourable of a number of offshore wind farms, the area is constantly impacted by the presence of typhoon, especially during summer and autumn, which puts the wind farms into a risky situation. Strong variations of the seabed and scour could occur around the wind farm under storm surge caused by a typhoon. Thus, both the region around the wind farm and the areas around each pile foundation are to be studied.

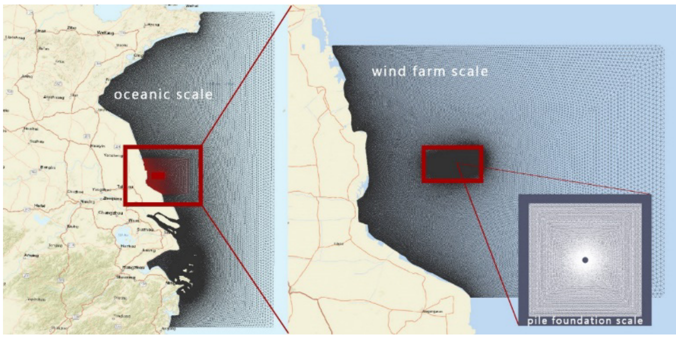

Figure 1. Study area of the multi-scale coupled model

B. Grid Generation

In this multi-scale coupled model, different meshes were used.

The oceanic scale model is shown in Figure 1. It covers an area of approximately 960 km from north to south, 500 km from offshore to the coast. The model has 189257 elements, with the resolution ranges from 250 m to 10 km. This mesh is applied in simulations both in hydrodynamics and wave propagation.

In the wind farm scale model, with a computational domain of about 120 × 100 km^2, two sets of grids are used. The mesh used for the hydrodynamics and morphodynamics simulation has 740669 elements, with typical edge length ranging from 500 m to 2 km and refined to 5 m over an area of 100 × 100 m^2 around each pile. The mesh used for wave propagation simulations contains 36162 elements, with typical edge length varying from 500 m to 2 km.

Finally, a refined mesh has been built at pile scale, consisting of a computational domain covering a squared-shape area of 100 × 100 m^2 around the pile, with resolution of 0.25 m at the wall of pile and 1 m on the boundary of mesh. The number of elements is between 30647 and 31175 as the diameter of piles changes. Additionally, a double precision format is adopted for each mesh.

C. Model Setup

1) General

The bathymetry of the domain consists two types of sources: the GEneral Bathymetric Chart of the Oceans (GEBCO)[11] and the bathymetric field survey data around the piles. The tidal conditions forced on the boundaries are provided by the Oregon State University Tidal Prediction Model (TPXO9-atlas)[12]. The database Climate Forecast System Reanalysis (CFSR)[8] is used for the background wind field and the tropical cyclone track from National Meteorological Centre of China (NMC) is used for the typhoon model. The complete atmospheric conditions are read in TELEMAC-2D and shared with TOMAWAC to generate waves. The reference cases in which the effect of typhoon is not taken into account are in the absence of atmospheric conditions. Given by in-situ measurements, the sediment is mainly composed of silt with a particle size of about 0.25 mm, a porosity of 0.7, and a density of 1960 kg/m^3. On each scale, the simulation period is the same 5 days when the typhoon passes over the study area.

2) *Oceanic scale model*

In the oceanic scale model, hydrodynamics and wave propagation are simulated by the coupling between TELEMAC-2D and TOMAWAC. The TPXO tidal conditions are applied on boundaries. Wind and air pressure are considered in the simulations. In wave propagation simulation, various source and sink terms are considered, including wind, strong current, bottom friction, white capping, breaking and non-linear transfers between frequencies. The BAJ configuration is used to improve the performance of wave generation and dissipation. A set of coordinates within this oceanic scale and at the same time located on the offshore boundaries of the wind farm scale model are given to write the spectra which describe the wave states, the spectra will be imposed into the wave propagation simulation in wind farm scale.

3) *Wind farm scale model*

The wind farm scale model is used to compute the hydrodynamics, wave propagation and morphodynamics by a three-way modelling approach. Tidal and atmospheric conditions are applied by the same way as on the oceanic scale. The wave spectra obtained from the simulation in oceanic scale then are imposed at the offshore boundaries before the simulation of wave propagation. The same source and sink terms as those on the oceanic scale are considered. In the GAIA module, the van Rijn sediment transport formula is adopted. The evolution of seabed under storm surge in wind farm scale obtained is to be analysed. The hydrodynamic conditions that contain the flow velocity and water level for each pile foundation under the effect of a typhoon obtained in the wind farm scale model are transferred to the pile foundation scale model.

4) *Pile foundation scale model*

Hydrodynamics and morphodynamics coupled simulations are conducted for pile foundation in the local scale. The hydrodynamic conditions calculated in the previous wind farm scale model are extracted based on the pile foundation model, and the hydrodynamic conditions are imposed in TELEMAC-3D. The bathymetry of each pile foundation model is projected from the survey data of each scour pit. 20 layers are considered along the vertical direction. The k-epsilon model is adopted as the turbulence model for both the horizontal and vertical directions. The results of the evolution of scour pit obtained in pile foundation scale model is to be analysed. In this study, we focus on the results of foundation 1 and foundation 2 shown in Figure 8.

D. Model validation

The hydrodynamic state formed by tides and the influence of waves have a direct driving effect on the transport of sediment, and considering that typhoons can bring storm surges, quantitative analyse of the calculation error of the tide calculation is necessary. Therefore, two error parameters, mean error and root mean square error, are introduced to analyse the accuracy and rationality of the model calculation results. The two error parameters are calculated formulas:

$$Mean\ error = BIAS = \frac{1}{n}\sum(x_{mi} - x_{oi}) \tag{7}$$

$$Root\ mean\ square\ error = RMSE = \sqrt{\frac{1}{n}\sum(x_{mi} - x_{oi})^2} \tag{8}$$

where, n represents the quantity of data points, x_{mi} represents the modelled values, x_{oi} represent the observed values at the stations.

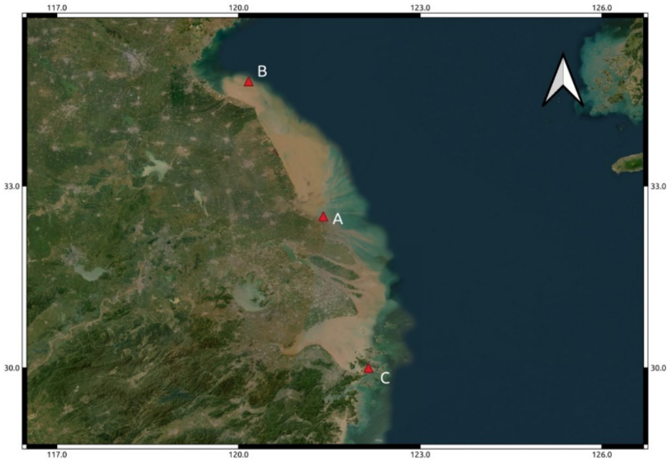

Figure 2. Locations of stations A, B and C, unit in degree

The tidal verification is based on the comparison between simulated and observed water level at station A, which is close to the study area, shown in Figure 2 in March 2021, which are compared and verified with the publicly available tidal data of this station. The model uses the TPXO Pacific Tidal Database as the input of tide. The calculated tidal water levels in Figure 3 show a consistent period with the tidal data of station A. The tidal range and the high and low tide level correspond with the tidal data of station A, with mean errors of 0.184 m and root-mean-square errors of 0.443 m. The model is capable of effectively reflecting the tidal dynamics of the marine area.

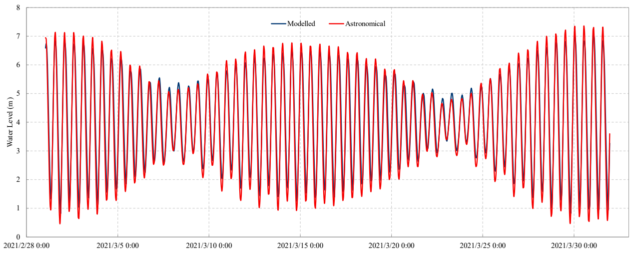

Figure 3. Water level validation, station A, March 2021

Figure 4 shows the comparison between simulated and measured significative wave height and mean period at the station B shown in Figure 2, in Jiangsu Province, in January 2012. The values of the significant wave height match well, and the time series tendency of the significant wave height is consistent, with mean errors and root-mean-square errors being equal to -0.036 m and 0.158 m, respectively. The mean period of wave is consistent with observation data with mean and root-mean-square errors being equal to -0.390 s and 1.695 s, respectively.

In summary, the comparison between the simulated and observed values confirms that this model is able to provide a relatively reasonable description of tidal and wave propagation of this area.

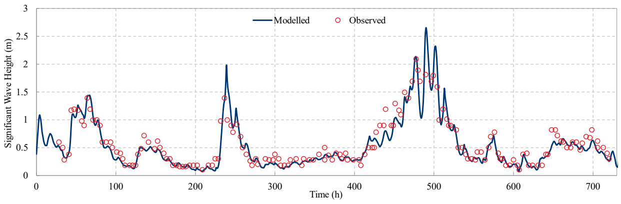

(a) Significant wave height

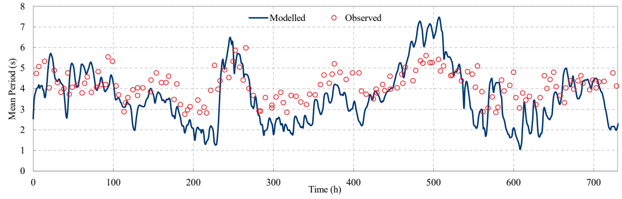

(b) Mean period

Figure 4. Wave validation, station B, January 2012: (a) Significant wave height; (b) Mean period

Verification of typhoon, storm surge and wave processes are based on the typhoon In-fa (No. 2106). The maximum wind velocity calculated by the typhoon model is close to 35 m/s, which is consistent with the meteorological data recorded. As shown in Figure 5, a comparison of the simulated and observed tide level of storm surge processes before and after the passage of typhoon In-fa at station C. Figure 5 shows a significant increase in water level when the typhoon made landfall on July 25, 2021 and the simulated tide level is in good agreement with the measured tidal level. From the Figure 6, it is observed that both the wave field calculated by the model and the significant wave height are consistent with the changes in wind field intensity (vector arrows) and the movement path of the typhoon. The comparison and verification of the above data indicate that the model has the ability to describe satisfactorily the physical processes of hydrodynamics and wave propagation in the sea area affected by typhoons, and thus these factors can be considered in the sediment transport simulations.

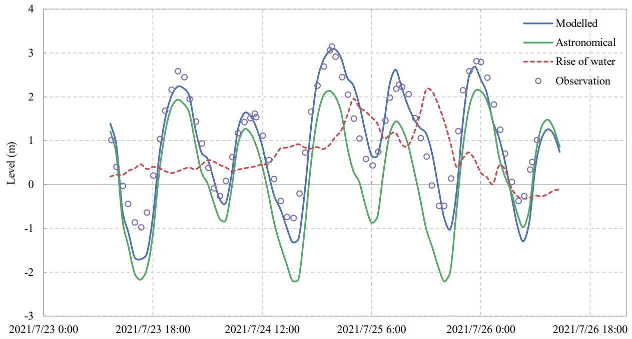

Figure 5. Storm surge validation, station C, during the passage of the typhoon In-fa

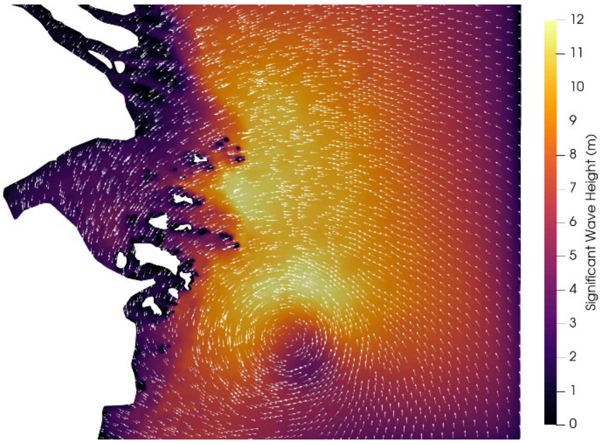

Figure 6. Wave field during typhoon In-fa

IV. TYPHOON SCENARIO

In this study, the multi-scale coupled simulations were conducted with the scenario of typhoon Muifa (No. 2212). The National Meteorological Centre of China identified Typhoon Muifa as having formed in the northwest Pacific Ocean on the morning of September 8th 2022, gradually gaining strength. It was later identified as having made landfall on Zhoushan, Zhejiang (East coast of China) on the evening of September 14th, as a strong typhoon, then headed northwest and it gradually degraded into a tropical storm. On the evening of September 16th, typhoon Muifa stopped being numbered by the National Meteorological Centre of China. Muifa became the first typhoon to land in East China in 2022 as well as the strongest one. The maximum wind velocity near the centre of typhoon Muifa reached level 14 (42 m/s), and the lowest central pressure was 960 hectopascals. It brought significant strong winds and rains to East China and Northeast China. Figure 7 shows the track of typhoon Muifa. A set of reference cases without typhoon were simulated in the absence of meteorological conditions at the same period. The locations to be focused on in the study are shown in Figure 8.

Figure 7. Track of the passage of the typhoon Muifa

V. RESULTS AND DISCUSSION

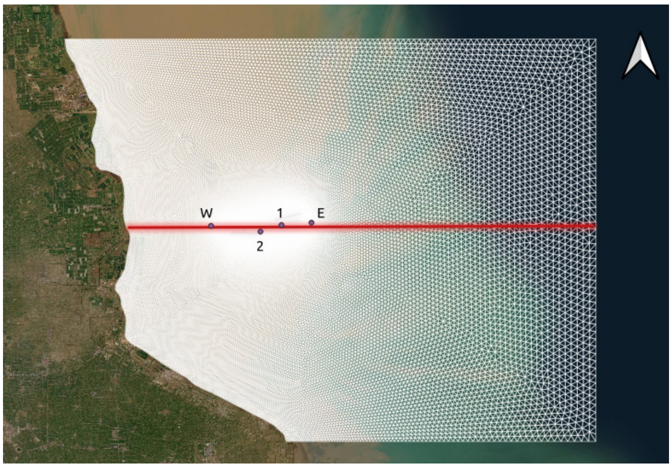

Figure 8. Locations and references of the study area, E: East side of wind farm, W: West side of wind farm, 1: Foundation 1, 2: Foundation 2, Red line: study profile.

A. *Storm Surge under Typhoon*

Simulations were conducted from 11th to 16th September 2022, and the typhoon Muifa passed over the study area at the 90th to 110th hour of the simulation. The water level was extracted at two locations situate respectively at east and west of the wind farm and denoted as E and W in Figure 8. The rise of water level was obtained by differencing the water level under storm surge by the reference water level in the absence of atmospheric conditions. the curves in Figure 9 show the rise of water level under storm surge at east and west of the wind farm. The rises of water level at the two locations increases as the typhoon gets closer and reaches the maximum value over 1 meter at around 95 h, then with the departure of typhoon, the rise of water level drops below zero with the minimum value of -0.41 m at 103 h at the west side of the wind farm.

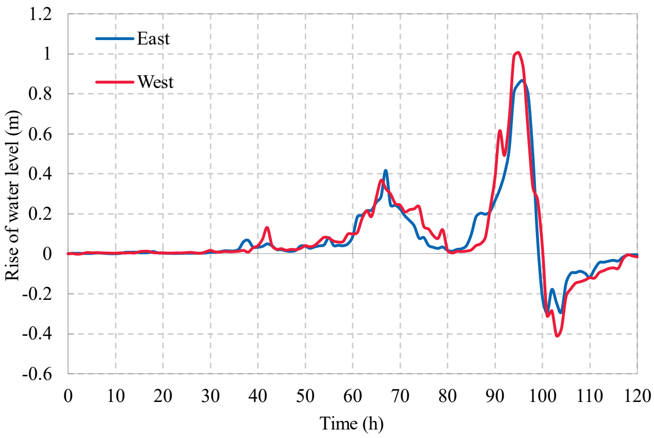

Figure 9. Rise of water level under storm surge during the passage of the typhoon Muifa

B. *Wave Conditions under Typhoon*

Figure 10 shows the effect of typhoon Muifa on the wave propagation (wave height, mean period and mean direction). The maximum wave height can reach 2.6 m at the east side of the wind farm, while at the west side the maximum wave height is around 1.5 m as the water is shallower. The evolution of mean period increases from approximately 3 s in normal state to 6-7 s when the typhoon approaches. Before the storm approaches, the wave direction is close to 250 deg, and it turns out to be around the direction of 50 deg under the effect of cyclone track and wind direction. The higher wave height infers the higher energy of water, where greater forces and more violent hydrodynamic and wave conditions present.

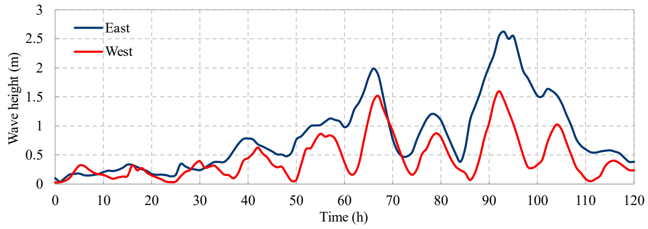

(a) Significant wave height

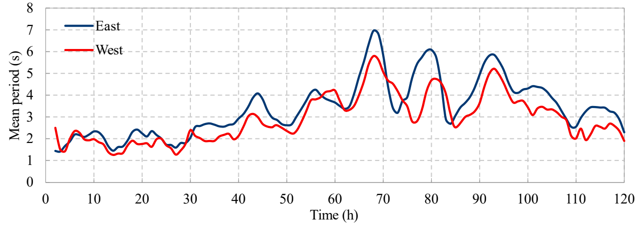

(b) Mean period

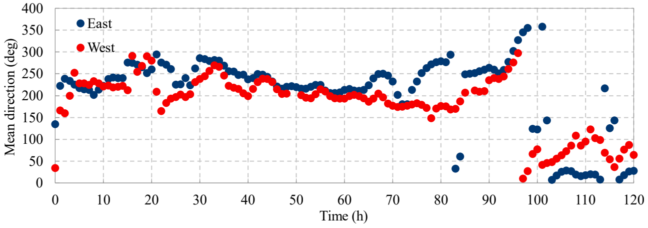

(c) Mean direction

Figure 10. Effect of typhoon Muifa on wave propagation: (a) significant wave height; (b) mean period; (c) mean direction.

C. *Effect of Typhoon on Seabed Evolution*

The evolution of seabed is computed by internal coupling of hydrodynamics-wave-sediment computations with TELEMAC-2D, TOMAWAC and GAIA. The results with/without the effect of typhoon are compared.

Figure 11(a) shows the bed evolution under the effect of a typhoon at 120 h, where the colour red refers to the increase of seabed and the colour blue refers to decrease of seabed. Some differences are observed between the cases with typhoon and without typhoon (Figure 11(b)), where the increase and decrease took place at similar locations. The layer of seabed evolution with typhoon differenced by the layer without typhoon at 120 h is shown in Figure 12. The presence of the typhoon influences both the sediment erosion and deposition of the seabed in the study area. The difference in bed evolution is generally limited within ±0.5 m comparing with the case without the effect of a typhoon. Table I indicates that 99.98% of the domain has the difference of bed evolution between -1 and 1 meter with/without typhoon, and the difference of bed evolution within ±0.5 m covers 99.77% of the area.

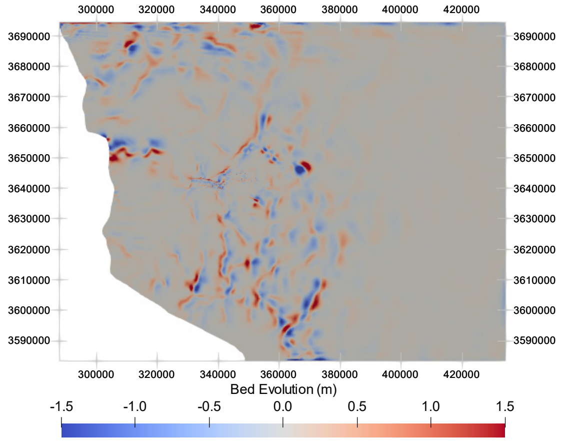

(a) With typhoon

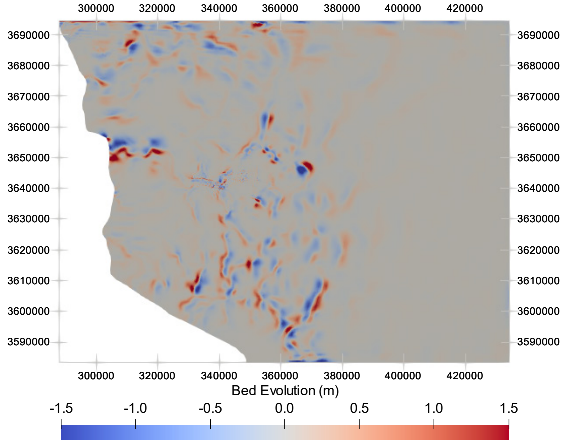

(b) Without typhoon

Figure 11. Bed evolution at 120 h

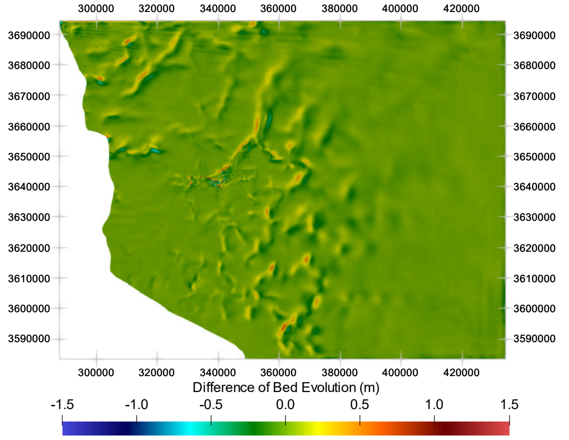

Figure 12. Difference of bed evolution with/without the passage of the typhoon at 120 h

Table I Area ratio within range of the difference of bed evolution

Difference of Evolution (m)	±1	±0.5	±0.25
Ratio of area (%)	99.98	99.77	97.92

To better understand the impact of typhoon on sediment transport, the solid discharge is studied along the slice crossing the wind farm as shown in Figure 8. At 95 h, the position of cyclone is the closest to the study domain and Figure 13 shows that the effect of typhoon facilitates greatly the transport of solid. The solid discharge increases up to 21 kg/s under the effect of typhoon while it is lower than 6 kg/s at the absence of typhoon. As mentioned above, the higher energy of water, the greater forces and more violent hydrodynamic and wave conditions present, enhancing the transport of sediment and the migration of the seabed.

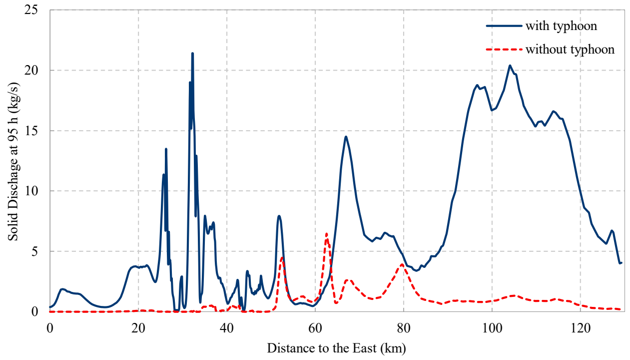

Figure 13. Solid discharge along the profile indicated in Figure 8 at 95 h

D. *Effect of Typhoon on Local Scour*

The initial bathymetry and the evolution of local scour around the pile foundation are considered from a field survey performed in the study area, with resolution of 2.5 m. In this study, the results of two pile foundations are discussed.

Figure 14(a) and (b) show the difference of bed evolution of foundation 1 and 2 with/without typhoon with time, respectively. It is found that both the increase and decrease of morphology were enhanced under the effect of typhoon, especially the area close to the pile.

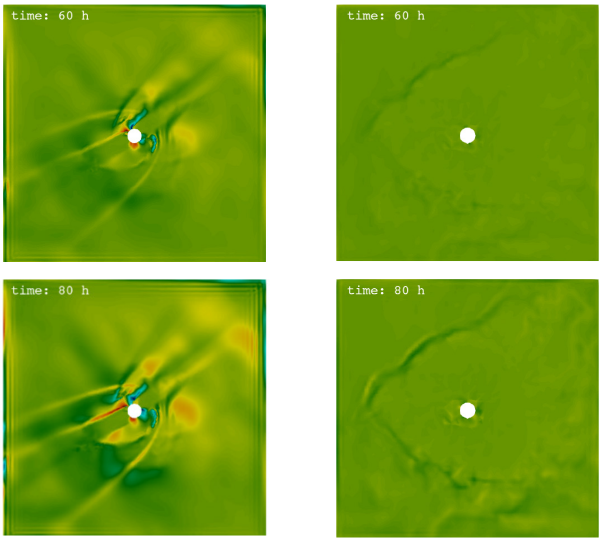

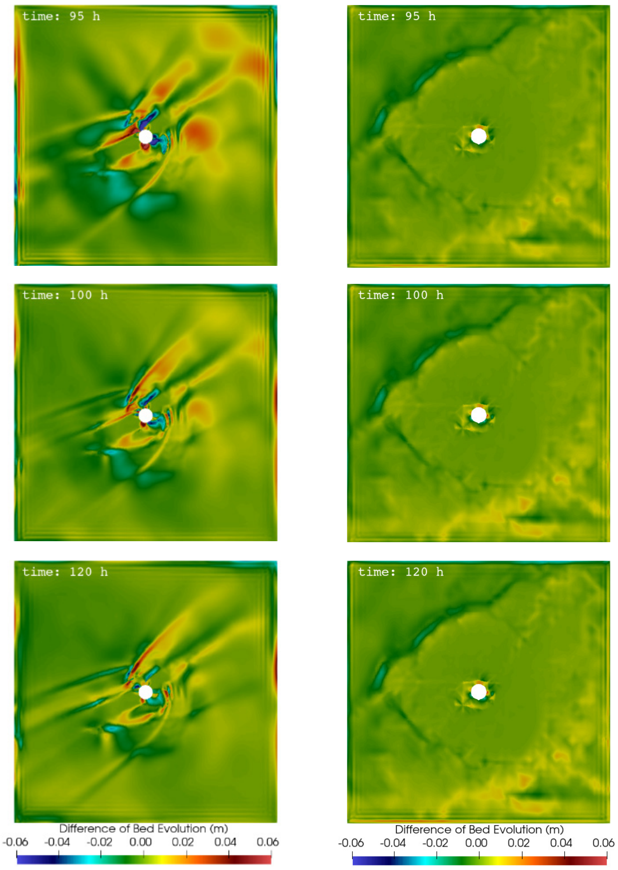

(a) Foundation 1 (b) Foundation 2

Figure 14. Difference of foundation bed evolution with/without typhoon at different times

Figure 15 shows the comparison of the scour maximum depth evolution with or without typhoon. Before 60 h, as the tropical cyclone is far from the piles, the evolutions of scour are basically the same for the 2 scenarios. During 60 h and 100 h, the typhoon approaches and its impact starts to take effect. The depth of scour pit has increased up to 0.47% for foundation 1 and 0.06% for foundation 2. At around 95 h, when the typhoon is passing through the site, the depth of scour pit with typhoon experiences a rapid swich of state, which agrees with the difference of bed evolution shown in Figure 14. After the passage of typhoon at 95 h, the difference of bed evolution is less significant.

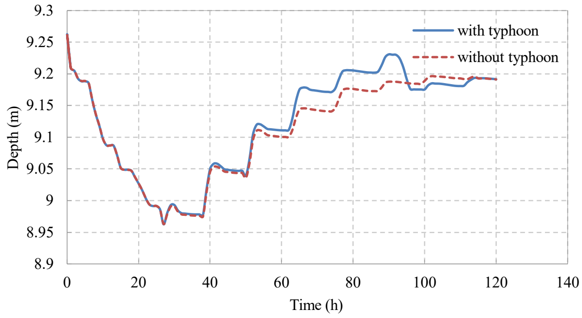

(a) Foundation 1

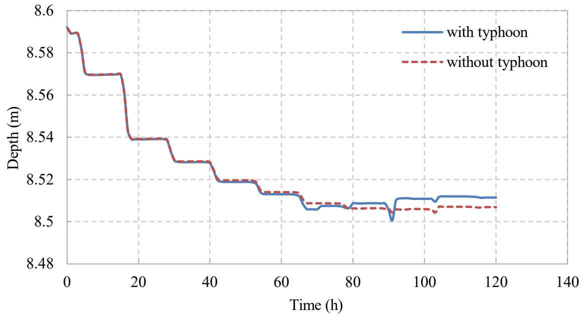

(b) Foundation 2

Figure 15. Evolution of scour pits depth and radius with/without typhoon, see profile location in Figure 8

VI. CONCLUSION

The investigation on the sediment transport under storm surge is numerically carried out for seabed of wind farm and the scour of pile foundations, based on the multi-scale coupled simulations using the modules TELEMAC-2D, TELEMAC-3D, TOMAWAC and GAIA. Numerical results were compared with a set of typhoon-free reference cases. During the passage of typhoon Muifa, meteorological conditions have led to an increase in water in the study area. Changes in the wave conditions were caused by the typhoon. Both the increase (sediment deposition) and the decrease (sediment erosion) of the seabed are facilitated by the effect of typhoon-induced storm surge, while they are generally limited within 0.5 m due to the short duration of action. Hydrodynamic and wave conditions have strengthened solid transport during the typhoon period. The influence of storm surge on the evolution of the scour is mainly concentrated on the zone close to the pile, affecting the depth of the local scour. Although the difference is slight compared to cases without a typhoon, the rapid impact could be risky for the long-term safety of the wind farm. Therefore, the long-term trends in sediment transport for offshore wind farms need to be studied in further research.

ACKNOWLEDGEMENT

The authors are grateful to Drs Pablo TASSI, Thierry FOUQUET, Sebastien BOURBAN from EDF R&D for their support.

REFERENCES

[1] Needham, H.F., B.D. Keim, and D. Sathiaraj, "*A review of tropical cyclone ‐ generated storm surges: Global data sources, observations, and impacts".* Reviews of Geophysics, 2015. 53(2): p. 545-591.

[2] Meng, F., et al., "*Forecasting tropical cyclones wave height using bidirectional gated recurrent unit".* Ocean Engineering, 2021. 234: p. 108795.

[3] Galewsky, J., et al., "*Tropical cyclone triggering of sediment discharge in Taiwan".* Journal of Geophysical Research: Earth Surface, 2006. 111(F3).

[4] Li, M., et al., "*The impact of energetic tropical cyclones (typhoons) on the modern sediment magnetism along the South China coast".* Continental Shelf Research, 2021. 224: p. 104447.

[5] Xing, F., Y.P. Wang, and H.V. Wang, "*Tidal hydrodynamics and fine-grained sediment transport on the radial sand ridge system in the southern Yellow Sea".* Marine geology, 2012. 291: p. 192-210.

[6] Fujita, T., "*Pressure distribution within typhoon".* Geophysical Magazine, 1952. 23(4): p. 437-451.

[7] Jelesnianski, C.P., "*Numerical computations of storm surges without bottom stress".* Monthly Weather Review, 1966. 94(6): p. 379-394.

[8] Saha, S., et al., "*The NCEP climate forecast system reanalysis".* Bulletin of the American Meteorological Society, 2010. 91(8): p. 1015-1058.

[9] Benoit, M., F. Marcos, and F. Becq, *Development of a third generation shallow-water wave model with unstructured spatial meshing*, in *Coastal Engineering 1996*. 1996. p. 465-478.

[10] Prodanovic, P. *Wave library: A strategy for reducing computation times in coastal sediment transport studies*. in *Proceedings of the XXIIIrd TELEMAC-MASCARET User Conference 2016, 11 to 13 October 2016, Paris, France*. 2016.

[11] Kapoor, D., "*General bathymetric chart of the oceans (GEBCO)".* Marine Geodesy, 1981. 5(1): p. 73-80.

[12] Egbert, G.D., A.F. Bennett, and M.G. Foreman, "*TOPEX/POSEIDON tides estimated using a global inverse model".* Journal of Geophysical Research: Oceans, 1994. 99(C12): p. 24821-24852.

[13] van Rijn L.C. Sediment transport - Part II : suspended load. J. of Hydraulic Division, HY11:1631–1641, 1984.

[14] Koch F.G. and Flokstra C. Bed level computations for curved alluvial channels. In Proceedings of the XIXth Congress of the Int. Ass. for Hydr. Res., New Delhi, India, 1980

Investigating the contribution of waves on the sediment dynamics of the Southwest Atlantic Continental Shelf, off Río de La Plata and Patos Lagoon estuaries

Juliana Costi[1,3], Nicolas Huybrechts[2], Elisa Helena Leão Fernandes[3], Aldo Sottolichio[1]
juliana.costi@u-bordeaux.fr, Bordeaux, France
[1]: Univ. Bordeaux, CNRS, Bordeaux INP, EPOC, UMR 5805 - France
[2]: Cerema REM, RHITME Research Team - France
[3]: Universidade Federal do Rio Grande, Instituto de Oceanografia - Brazil

Abstract – **The wide continental shelf of the Southwest Atlantic Ocean receives substantial continental freshwater discharge and suspended sediment from Rio de La Plata and Patos Lagoon estuaries, which define its sedimentary behavior. Although the overall distribution has predominantly sandy deposits, the mudbelt connecting Brazil and Uruguay is an important bottom feature still poorly understood. Our work investigates the contribution of suspended sediment from each basin to the deposition and erosion patterns observed in the area, as well as the impact of extreme events in the observed patterns. We employ the GAIA morphodynamic model coupled to the hydrodynamic module TELEMAC-3D and the wave module TOMAWAC, of the open TELEMAC-MASCARET system. The models are forced by river discharge and sediment in suspension in the continental liquid boundaries, wind data at the air-water interface, currents, tides, and wave spectra at the offshore liquid boundary, and have been fully calibrated and validated. Preliminary results of a 75-days long simulation in winter conditions indicate that suspended sediments from Rio de La Plata can spread over the southern coast of Brazil during intense storms, but the wave action limits this spreading by constricting the plume closer to the estuarine area. The spreading of the Patos Lagoon plume was also constricted by the wave action, with lower peaks of sediment in suspension associated with wave heights higher than 2 m. Further long-term simulations will contribute to the identification of the role of each different forcing and will improve the understanding of present deposition patterns and provide resources for adaptation to future climate changes.**

Keywords: Suspended sediment transport, hydrodynamic, inner shelf, wave-induced current.

I. INTRODUCTION

Coastal and transitional waters connect continental and oceanic systems in the river-estuary-ocean continuum. The flows exhibit complex responses to anthropogenic pressures and climate changes, which overlap with the natural variability of the systems. Globally, human activities related to land use and dam construction, as well as climate changes, have rapidly altered the flow of freshwater and sediment from rivers to the ocean [1,2,3].

The Southwest Atlantic Ocean Continental Shelf (SWACS) (figure 1) is strongly influenced by river discharge, particularly from the plumes of the Rio de La Plata and Patos Lagoon. In the drainage basins of these systems, there have been predominantly increasing trends in both discharge and suspended sediment concentration [4] for the period that measurements are available (~1940 – present), and a shift towards a wetter hydrological regime [5]. The increased suspended sediment concentration in rivers of the Southern Hemisphere is linked to expansion of the agricultural activities and to increasing precipitation rates, which enhances soil erosion in the river basins. Besides changes in freshwater and sediment input, other significant forcing factors for sediment dynamics, such as increased wind velocity [6,7] and wave energy [8], have also occurred. Wave action is an important factor in sediment dynamics, especially during storm conditions, at depths of up to -120 m [9,10].

In this context, where most of the forcings that influence the sediment dynamics are changing, it is expected that the sediment dynamics are also being impacted by anthropogenic activities and climate changes. Therefore, it is essential to apply modeling systems that simulate hydrodynamic, morphodynamic, and wave processes in a coupled manner to represent the effects of these changes on sediment dynamics. In this article, we present the first insights on how the wave action changes the currents near the coast, and the dynamics of cohesive sediment in suspension in the study region.

II. METHODS

The numerical domain comprises the SWACS, between 28°S and 40°S, and the Rio de La Plata and Patos Lagoon estuaries. It has a total of 46043 nodes for each horizontal plane, and 11 vertical levels equally spaced in sigma coordinates. The horizontal resolution is of 250 m by the coast and increases progressively to 5000 m, at the continental shelf break. Near the jetties the spatial resolution is set to 50 m, and 150 m in the estuarine zones.

Bathymetry data was obtained from nautical charts, GEBCO and previous surveys conducted by the Laboratorio de Oceanografia Costeira e Estuarina and the Laboratorio de Oceanografia Geologica of the Universidade Federal do Rio Grande. The location and composition of the bottom deposits were obtained from [11].

Both suspension and bedload transport are simulated in this study. Two classes of cohesive sediment (COH1 and COH2) and two classes of fine sand (NCOH1 and NCOH2) are taken in consideration for suspension. COH1 and NCOH1 classes are imposed at the Río de La Plata tributary, whereas COH2 and NCOH2 are imposed at the Patos Lagoon tributaries. For the bottom deposits, 2 states of consolidation of mud on the bottom are considered for modern and relict mud deposits, with 3 mud layers with τe = 0,015 Pa, 0,15 Pa and 1,5 Pa.

Current velocity, salinity and temperature were imposed in the oceanic northern and southern boundaries of the mesh. uTidak harmonics were obtained from the TPXO model (version 7.2) to force current velocities, whereas salinity and temperature fields were obtaied from HYCOM. Wave average period, significant height and average direction were obtained from ERA-5 and imposed at the oceanic boundaries. The wind action was imposed using ERA-5 hourly data. Freshwater discharge time series from Rio de La Plata and the main tributaries of Patos Lagoon were used to force the continental liquid boundaries.

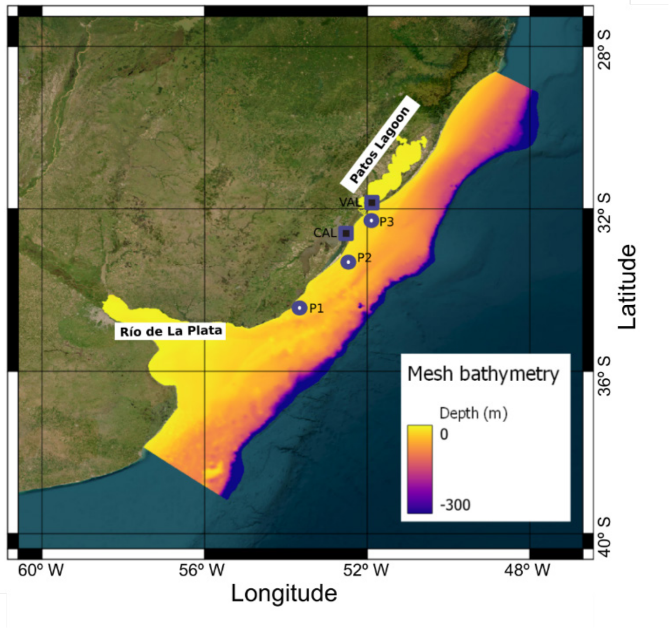

Figure 1. Map of the study site, showing the numerical domain and bathymetry and the location of Río de La Plata and Patos Lagoon. The circles P1, P2 and P3 indicate the sites where time series were extracted, and the squares indicate the calibration and validation sites.

The open TELEMAC-MASCARET software has been previously employed in the study area and extensively calibrated and validated for the Patos Lagoon and Rio de La Plata estuary and the adjacent continental shelf. We adopted a parameterization similar to that used by [12,13] and [9]. A further calibration exercise was conducted for the coefficient of wind influence, by comparing simulated and observational times series of the current velocity components u and v, in the site indicated as CAL in Fig. 1. Current velocity obtained in the site indicated as VAL were used to validate the model results.

The hydrodynamics, waves and morphodynamics were simulated first by coupling the TELEMAC-3D and GAIA modules (simulation HM). Subsequently a new simulation was performed with TELEMAC-3D, GAIA and TOMAWAC fully coupled (simulation WHM). Both simulations were carried out considering the same boundary conditions, covering the period 01 July 2006 to 15 September 2006.

III. RESULTS

A. Calibration and validation of the model

The coefficient of wind influence was tuned by comparing modeled time series of the u and v components of currents at surface (-3 m) and bottom (-10 m) with current data measured in the site indicated as CAL (see fig 1). Nine simulations were carried out using different coefficients, and the best combination of RMSE, R and Bias was achieved by the one using the coefficient varying with velocity (according to the Institute of Oceanographic Sciences - United Kingdom formula). The values of RMSE = 0.1, R = 0.74 and Bias = 0.01 obtained are comparable to those obtained by [12,13] for the SWACS. The validation was performed at the site indicated as VAL (Fig. 1), by comparing current velocity measured data with modeling results, resulting in RMSE = 0.3, R = 0.73 and Bias = 0.04.

B. Spatial patterns of currents and SSC

Figures 2 and 3 show the temporal average of the fields of currents, and cohesive suspended sediment concentration in the study area respectively, obtained by the HM simulation. Figures 4 and 5 present the temporal average of the fields of currents, and cohesive suspended sediment concentration obtained by the WHM.

Results indicate that waves influence the vertically-averaged currents, especially near the mouth of the Patos Lagoon estuary. There, the average velocities are reduced and the direction is slightly modified. Directly beside the jetties, the current directions are turned toward the coast, whereas the waves turn the directions more toward north far from the coast. Regarding the average distribution of cohesive sediments, the WHM results show that the wave action limits the spreading of the sediment plumes. The concentration of suspended cohesive sediments is reduced along the coastline in the WHM simulation, compared with the HM simulation results, whereas the concentration is increased in both estuarine zones.

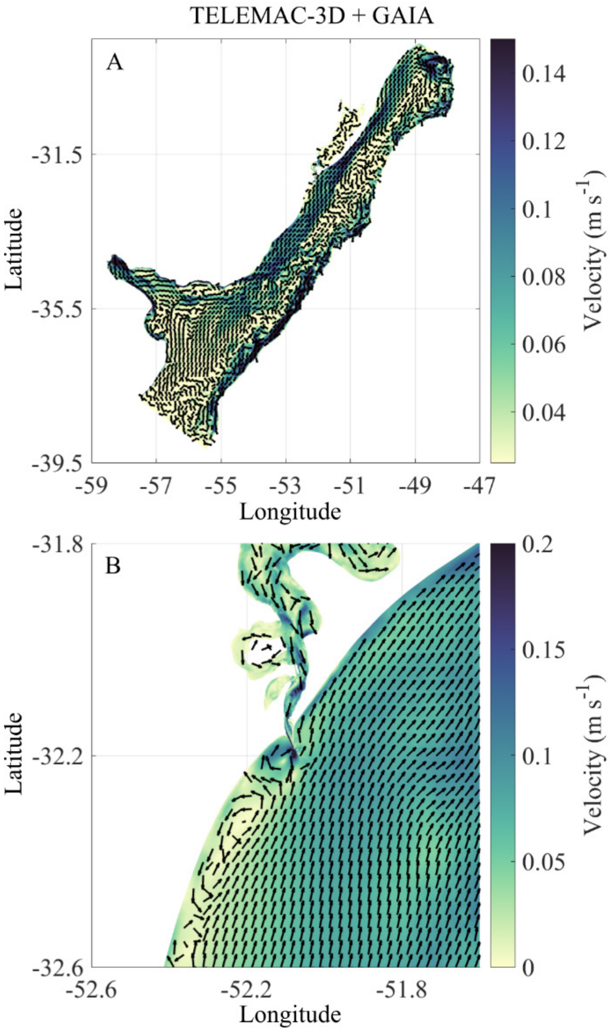

Figure 2. Average fields of velocity for the entire study area (upper pannel) and for the vicinity of the Patos Lagoon estuary mouth (lower pannel), obtained by the simulation HM.

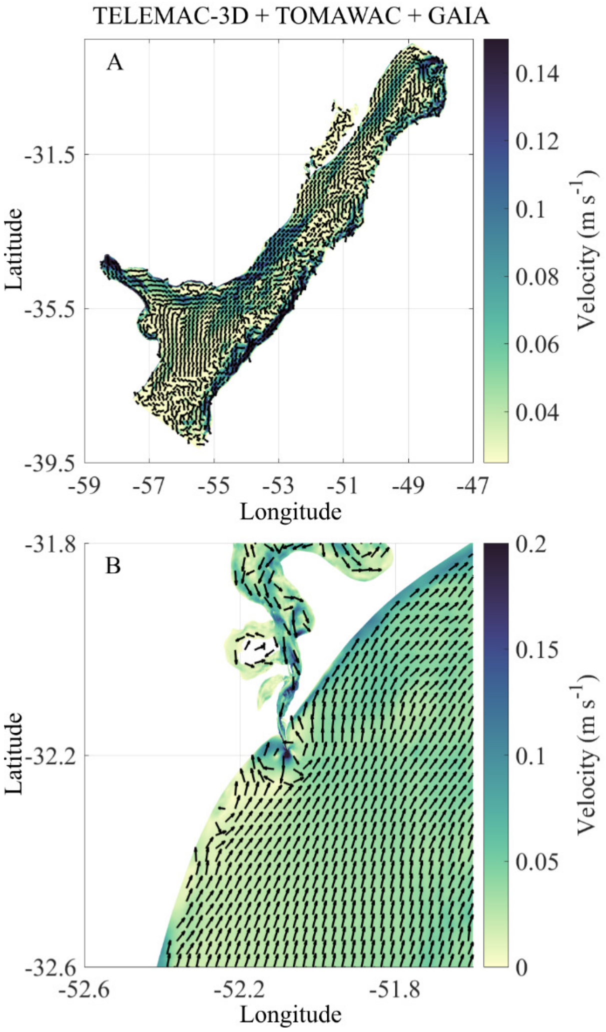

Figure 4. Average fields of velocity for the entire study area (upper pannel) and for the vicinity of the Patos Lagoon estuary mouth (lower pannel), obtained by the simulation WHM.

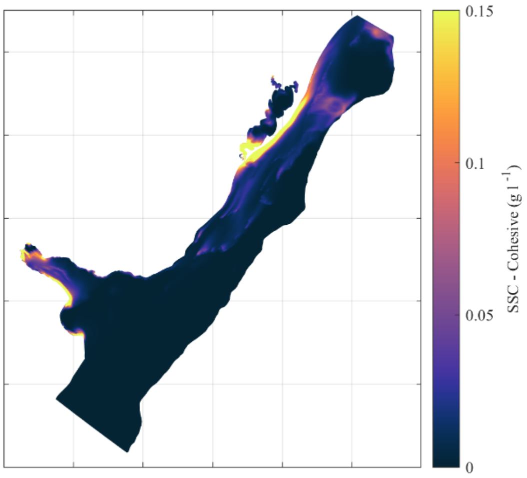

Figure 3. Average field of cohesive suspended sediment concentration (SSC) obtained by the simulation HM.

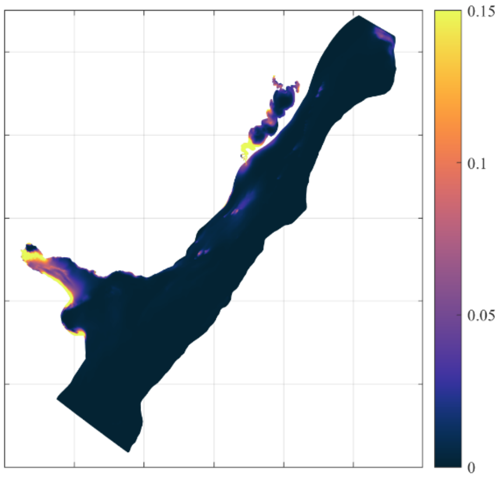

Figure 5. Average field of cohesive suspended sediment concentration (SSC) obtained by the simulation WHM.

C. Temporal behaviour of currents, SSC and bottom shear stress associated with the wave action

Time series of the current velocities, SSC, bottom shear stress and bottom evolution were extracted at the locations P1, P2 and P3 (see Fig. 1), to investigate their temporal behaviour. P1, P2 and P3 are located on the -20 m isobath, and equally spaced between the Rio de La Plata and Patos Lagoon estuaries mouths. Considering that the Rio de La Plata plume spreads predominantly to the north, and that the Patos Lagoon plume spreads predominantly to the south, this is expected to be the region with highest SSC.

P1 presented a net evolution of -0.15 m, whereas P2 -0.125 m and P3 0.025 m. Figures 4, 5 and 6 present the time series of bottom shear stress, total suspended sediment concentration, u component of current velocity and v component of current velocity, in P1, P2 and P3 respectively. Bottom shear stress increases in all locations in the WHM simulation, and more pronouncedly at P2.

Figure 9 presents the wave height (WSH), period (WPP) and direction (WMD), and the radiation forces in x and y directions (X-RF and Y-RF), extracted for each location (P1, P2 and P3). The wave results indicate that events with higher waves were more frequent after the end of July, and implied in higher radiation force peaks in both directions. During most of the time, the wave directions are similar in P2 and P3. However, the long jetties in the Patos Lagoon mouth causes wave diffraction, which causes modifications in the wave direction in P3.

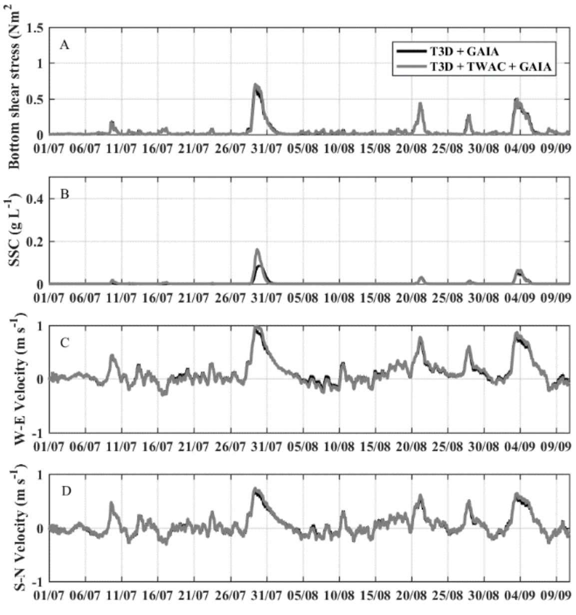

Figure 6. Time series of bottom shear stress (A), SSC (B), W-E current velocity (C) and S-N current velocity (D) extracted at P1, from the HM (black) and WHM (grey) simulations

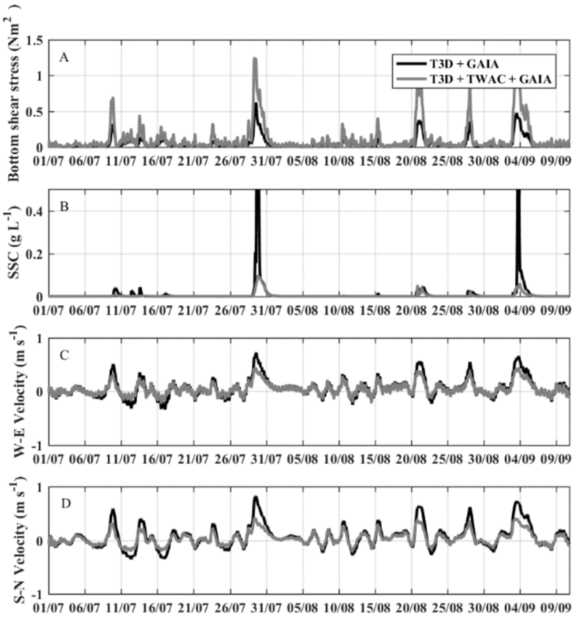

Figure 7. Time series of bottom shear stress (A), SSC (B), W-E current velocity (C) and S-N current velocity (D) extracted at P2, from the HM (black) and WHM (grey) simulations

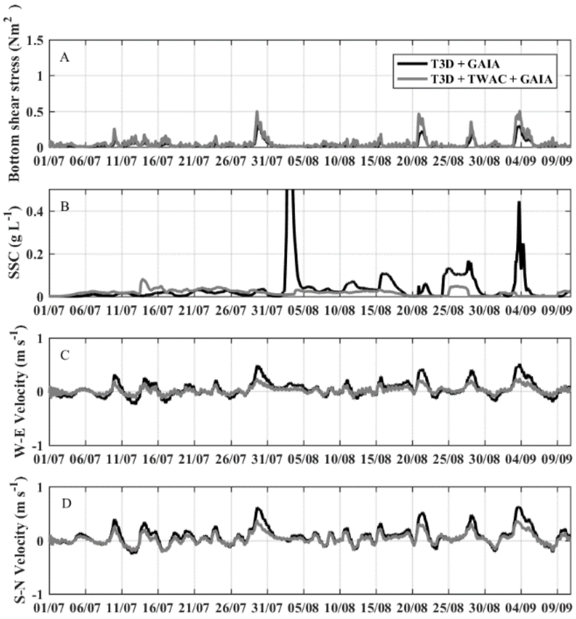

Figure 8. Time series of bottom shear stress (A), SSC (B), W-E current velocity (C) and S-N current velocity (D) extracted at P3, from the HM (black) and WHM (grey) simulations

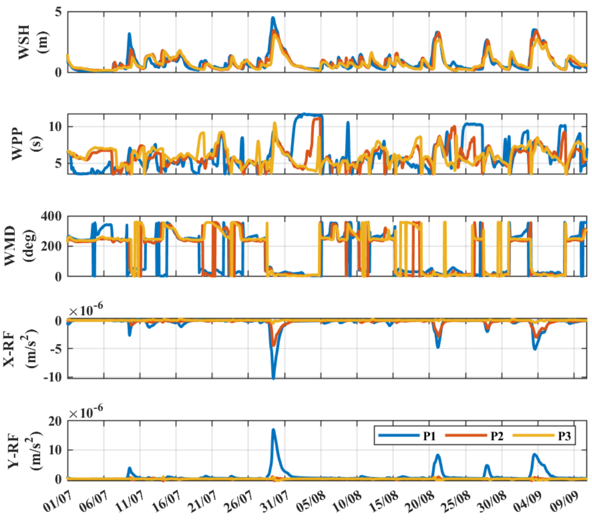

Figure 9. Time series of wave height (WSH), period (WPP) and direction (WMD), and the radiation forces in x and y directions (X-RF and Y-RF), extracted in P1, P2 and P3.

The temporal behaviour of SSC suggests that the wave-induced currents counteracts the currents generated by wind, tide and river discharge. P1 is closer to the Rio de La Plata estuary, and presents higher SSC in the WHM simulation, despite that the velocities are not reduced. However, current velocities are lower in the WHM simulation in P2, and SSC are higher when compared to the HM simulation. This behaviour indicates that the Rio de La Plata plume is constricted by the wave action.

In P3, the lower SSC peaks in the WHM simulation is associated with wave heights larger than 2 m, occurring after the end of July (late winter), whereas lower SSC are observed during July (early winter). This temporal behaviour indicates that the SSC plumes are constricted towards the coast with higher waves.

IV. DISCUSSION AND CONCLUSIONS

The results of these 75-days simulations showed that the wave action limits the spreading of the suspended sediment coastal plumes in the SWACS. The smaller current velocities and the slight deflection of their directions towards the coast in the WHM simulation resulted in lower SSC along the inner continental shelf, and higher SSC in the estuarine zones. The wave-induced current dams the continental discharge towards the coast, preventing the export of larger loads of fine suspended sediments.

Few studies have approached the effects of gravity waves on the behaviour of coastal plumes. [14] similarly observed that small scale freshwater plumes are constricted near the shoreline by the wave action, keeping the coastal plume within the surf zone, in Southern California. For the Columbia River plume, [15] showed that the wave action displaced the coastal plume in the wave propagation direction.

Apart from the direct effect that the radiation force implied by the wave action causes in the purely hydrodynamic-driven currents, it is important to note that lateral density gradients in the plume front are also disturbed by the waves. Such gradients are one of the forcings that cause plume expansion [16], and the extra mixing provided by wave action may reduce the lateral gradients too. However, further analyses are required to better address this effect.

The mesh horizontal resolution adopted in this study allows for the general representation of the wave-induced currents and wave-currents interactions in a regional spatial scale. However, finer spatial resolution is required to investigate the formation and evolution of bed forms, deposits and processes that occur at smaller spatial scales. Moreover, longer simulation periods are required to address the role of waves on the morphodynamic processes.

The first evaluation of the coupled TELEMAC-3D, TOMAWAC and GAIA showed that waves impact the current fields in the study area, resulting in a slight shift in the current directions towards the coast and regions with reduced velocities. Such changes impacted the behaviour of the Rio de La Plata and Patos Lagoon suspended sediment coastal plumes, causing reduced spreading of both plumes over the continental shelf during winter conditions. These preliminary results contribute to the implementation of a modelling framework that will allow simulating long-term patterns and trends of sediment transport, including erosion and deposition rates in the study area, taking into consideration the role of currents driven by wind, density, tides and waves.

ACKNOWLEDGEMENT

This study is funded by the SUNSET Project - South Brazilian Shelf sediment transport: sources and consequences (CAPES/COFECUB, Process 88887.192855/2018-00), and by the LOAD Project - Long-term analysis of suspended particulate matter concentrations affecting port areas in developing countries (Office of Naval Research (ONR), Grant Number N62909-19-1-2145). The authors are grateful to CAPES (Coordination for Personal Improvement of Personnel) for granting the post doctoral scholarship of the first author. Computer time for this study was provided by the computing facilities of the MCIA (Mésocentre de Calcul Intensif Aquitain).

REFERENCES

[1] Dethier, Evan N., Carl E. Renshaw, and Francis J. Magilligan. 2022. “Rapid Changes to Global River Suspended Sediment Flux by Humans.” Science 376 (6600): 1447–52. https://doi.org/10.1126/science.abn7980.

[2] Zarfl, Christiane, and Frances E. Dunn. 2022. “The Delicate Balance of River Sediments.” Science 376 (6600): 1385–86. https://doi.org/10.1126/science.abq6986.

[3] Gardner, John, Tamlin Pavelsky, Simon Topp, Xiao Yang, Matthew R V Ross, and Sagy Cohen. 2023. “Human Activities Change Suspended Sediment Concentration along Rivers.” Environmental Research Letters 18 (6): 064032. https://doi.org/10.1088/1748-9326/acd8d8.

[4] Li, Li, Jinren Ni, Fang Chang, Yao Yue, Natalia Frolova, Dmitry Magritsky, Alistair G.L. Borthwick, et al. 2020. "Global Trends in Water and Sediment Fluxes of the World's Large Rivers." Science Bulletin 65 (1): 62–69. https://doi.org/10.1016/j.scib.2019.09.012.

[5] Zaninelli, Pablo G., Claudio G. Menéndez, Magdalena Falco, Noelia López-Franca, and Andrea F. Carril. 2019. "Future Hydroclimatological Changes in South America Based on an Ensemble of Regional Climate Models." Climate Dynamics 52 (1–2): 819–30. https://doi.org/10.1007/s00382-018-4225-0.

[6] Jong, Pieter de, Tarssio B. Barreto, Clemente A.S. Tanajura, Daniel Kouloukoui, Karla P. Oliveira-Esquerre, Asher Kiperstok, and Ednildo Andrade Torres. 2019. "Estimating the Impact of Climate Change on Wind and Solar Energy in Brazil Using a South American Regional Climate Model." Renewable Energy 141: 390–401. https://doi.org/10.1016/j.renene.2019.03.086.

[7] Pryor, Sara C., Rebecca J. Barthelmie, Melissa S. Bukovsky, L. Ruby Leung, and Koichi Sakaguchi. 2020. "Climate Change Impacts on Wind Power Generation." Nature Reviews Earth and Environment 1 (12): 627–43. https://doi.org/10.1038/s43017-020-0101-7.

[8] Maia, Natan Zambroni, Luis Pedro Almeida, Leonardo Emmendorfer, João Luiz Nicolodi, and Lauro Calliari. 2022. "Wave Climate Trends and Breakpoints during the Atlantic Multidecadal Oscillation (AMO) in Southern Brazil." Ocean and Coastal Research 70 (2018): 1–22. https://doi.org/10.1590/2675-2824070.21086nzm.

[9] Santoro, Pablo, Mónica Fossati, Pablo Tassi, Nicolas Huybrechts, Damien Pham Van Bang, and J. C.Ismael Piedra-Cueva. 2017. "A Coupled Wave–Current–Sediment Transport Model for an Estuarine System: Application to the Río de La Plata and Montevideo Bay." Applied Mathematical Modelling 52: 107–30. https://doi.org/10.1016/j.apm.2017.07.004.

[10] King, E. V., D. C. Conley, G. Masselink, N. Leonardi, R. J. McCarroll, and T. Scott. 2019. "The Impact of Waves and Tides on Residual Sand Transport on a Sediment-Poor, Energetic, and Macrotidal Continental Shelf." Journal of Geophysical Research: Oceans 124 (7): 4974–5002. https://doi.org/10.1029/2018JC014861.

[11] Martins, L.R., Martins, I.R., Urien, C.M., 2003. Aspectos sedimentares da plataforma ontinental na área de influencia de Río de la Plata . Gravel 1, 68-80.

[12] Lisboa, Paulo Victor, Elisa H Fernandes, Aldo Sottolichio, Nicolas Huybrecht, and Raylton Bendô. 2022. "Coastal Plumes Contribution to the Suspended Sediment Transport in the Southwest Atlantic Inner Continental Shelf." Journal of Marine Systems, 103796. https://doi.org/https://doi.org/10.1016/j.jmarsys.2022.103796.

[13] Lisboa, Paulo Victor, Elisa H. Fernandes, Aldo Sottolichio, Nicolas Huybrecht, Antonio Raylton Rodrigues Bendô, and Juliana Costi. 2023. "Bottom Evolution Patterns Driven by Hydrodynamic Forcing in the Southwest Atlantic Inner Continental Shelf, off Río de La Plata and Patos Lagoon." Continental Shelf Research, January, 104934. https://doi.org/10.1016/J.CSR.2023.104934.

[14] Rodriguez, A. R., Giddings, S. N., & Kumar, N. (2018). Impacts of nearshore wave-current interaction on transport and mixing of small-scale buoyant plumes. Geophysical Research Letters, 45, 8379–8389. https://doi.org/10.1029/2018GL078328

[15] Akan, Ç., Moghimi, S., Özkan-Haller, H. T., Osborne, J., and Kurapov, A. (2017), On the dynamics of the Mouth of the Columbia River: Results from a three-dimensional fully coupled wave-current interaction model, J. Geophys. Res. Oceans, 122, 5218–5236, doi:10.1002/2016JC012307

[16] McCabe RM, MacCready P, Hickey BM. 2009. Ebb tide dynamics and spreading of a large river plume. J. Phys. Oceanogr. 39:2839–56

A new semi-unsteady sand transport formula in GAIA

Davide Boscia[1], Thomas Benson[1], Michiel Knaapen[1], Jeremy Spearman[1]
[1]: HR Wallingford, Coasts & Oceans

***Abstract* – The numerical morphodynamic model GAIA predicts bed changes due to hydrodynamics by means of empirical sand transport formulae. The physical transport processes in the near shore, particularly the wave related processes, which are important during storms, are still poorly represented by the majority of the available transport formulae. Wave related processes become important in shallow waters, where currents are relatively small and waves undergo shape changes. As a consequence of the lack of wave related processes in the sand transport formulae, sand bar formation and migration cannot be modelled yet in TELEMAC. To address this, wave related transport processes were implemented in GAIA using the semi-unsteady sand transport formula of [11], known as the SANTOSS formula. The novelty of this formula, compared to other existing sand transport formulae in GAIA, is that SANTOSS calculates the sand transport rate accounting for wave non-linearity without the need of a phase-resolving wave model. The formula, implemented in a fully coupled 2D model (TELEMAC2D-TOMAWAC-GAIA), was tested against in situ measurements, showing good agreement with the measurements.**

Keywords: Near-shore processes, Wave-induced transport rate, Wave skewness.

I. INTRODUCTION

Understanding and prediction of sand transport driven by waves and currents is fundamental to predict changes in the coastline, or seabed, in response to the impact of human activity or meteorological events such as storms. Coastal practitioners use large-scale morphodynamic models such as GAIA [10] to predict bed changes due to hydrodynamics by means of empirical sand transport formulae. However, the nearshore physical transport processes, particularly the wave related processes, are still poorly represented by the majority of the available transport formulae. Wave induced transport processes become important during storm events, particularly in shallow waters where currents are relatively weak and wave skewness generates a net transport rate. As a consequence of the lack of wave related processes in the sand transport formulae, sand bar formation and migration cannot at present be accurately captured using GAIA.

Semi-unsteady practical formulae improve the capability of numerical models to include wave-related transport processes. These are based on the “half-cycle” concept of [1] which considers separately the processes of entrainment, transport, and settling of the sand particles during each half-cycle. By doing so, the formulae calculate the amount of sand transported during each half-cycle, accounting for the sand carried over from one half-cycle to the next because of phase-lag effects, resulting in net transport either with or against the wave direction depending on the size and asymmetry of the waves.

Here, the semi-unsteady sand transport formula of [11], known as the SANTOSS formula, is implemented in the coupled GAIA morphological module of the TELEMAC system. The performance of the implementation was assessed against in-situ transport rate measurements using a real world test case.

II. WAVE DRIVEN SAND TRANSPORT

A. *Definition of wave skewness and asymmetry.*

Waves propagating toward shores change shape. In deep waters, waves are generally symmetrical and sinusoidally shaped. Travelling towards the shore, wave celerity and wavelength decrease while wave height increases. This process, called wave shoaling, leads to steeper wave crests of short duration and longer duration flatter wave troughs. These changes in wave shape are mirrored in the orbital velocities beneath the water surface (Figure 1).

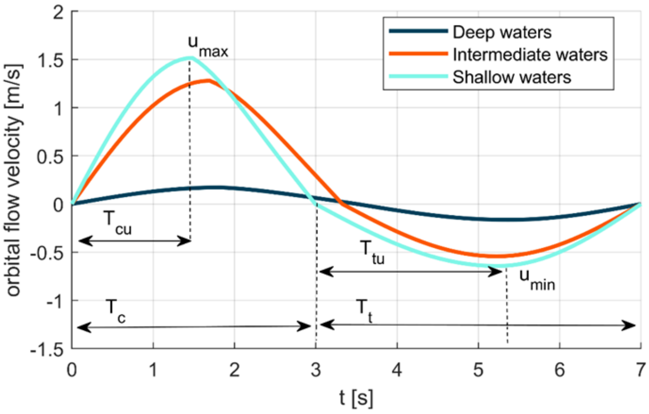

Figure 1. Change in orbital flow for waves in different water depths.

Figure 1 shows hypothetical near-bed orbital flow velocities over the wave period, for a wave travelling towards shore. In deep water the orbital flow is very small with the flow-crest period very similar the flow-trough period. As the wave propagates into shallower water the shoaling effect causes the two half-cycles to differ. The flow crest has a shorter duration with a large crest velocity (u_{max}), while the trough half cycle has a longer duration but smaller (negative) velocities (u_{min}). This effect is more evident for a wave in shallow waters. This difference in maximum half-cycle velocities is often referred to as velocity skewness (S_k), which can be calculated as follows:

$$S_k = \frac{u_{max}}{u_{max}+u_{min}} \tag{1}$$

In addition, as the wave height increases during shoaling, waves become progressively more forward leaning until they become too steep and break. This forward leaning of the wave during the wave crest leads to a shorter "acceleration" time between flow reversal and maximum velocity (T_{cu}) compared to the "deceleration" time between u_{max} and subsequent flow reversal (T_c -T_{cu}). The opposite happens under the wave trough where it now takes longer to reach maximum (negative) velocity. This difference in acceleration duration between the two half-cycles is referred to velocity asymmetry.

B. Sand bed response to orbital flow

Sand particles on the seabed start moving and generate transport when the mobilising force on a particle due to the bed shear stress exceeds the stabilising force due to gravity, often parameterised using the Shields formula [8] written as:

$$\theta = \frac{\tau_b}{(s-1)\rho g d_{50}} \tag{2}$$

where τ_b is the bottom shear stress, s is the ratio of sand and water density, ρ is the water density, and d_{50} is the median sand size. According to [6], rolling grain ripples grow in size until equilibrium is reached with the flow, generating vortex ripples for $0.05<\theta<0.8$. Sand transport over rippled beds occurs mainly through vortex-ejection, which for sinusoidally reversing flow conditions can be briefly described as follows. As the flow accelerates over the rippled bed, a small vortex begins to form and grow on the lee side entraining sand from the ripple trough and lee side (Figure 2); at the time of flow reversal (B) the sand laden vortex moves over the ripple lee side and gets ejected into the flow. When the flow changes direction, the vortex moves over the ripple and dissipates in the flow. As a consequence, water flows between the ripple crest and the departing vortex causing erosion of the ripple side (C). As the flow accelerates in the negative direction the vortex dissipates in the flow while the suspended sand particles are transported and another vortex forms on the stoss side of the ripple (D). For sinusoidal orbital flows the vortex generation and ejection process are identical for the two half-cycles, hence the wave-averaged or "net" sediment transport is zero. For velocity skewed flows, however, the hydrodynamics are different in magnitude and duration during the two half-cycles which generates an asymmetry in vortex processes between the two sides of the ripple resulting in a non-zero net transport rate.

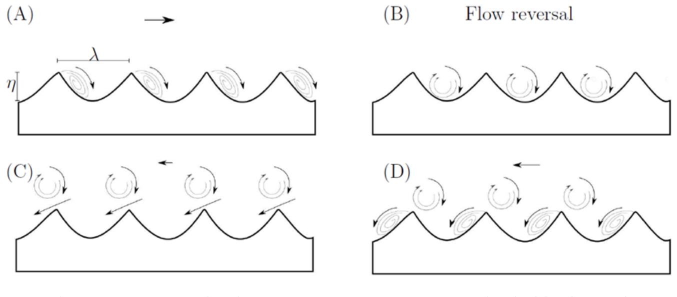

Figure 2. Vortex-ejection transport process over a rippled bed. Sand particles are not drawn to simplify the sketch. λ is the ripple length defined as the distance between two successive crests and η is the ripple height defined as the distance between the crest and the trough. The horizontal arrows represent the orbital flow direction and magnitude

For energetic orbital flows, $\theta> 0.8$, the ripples are washed away and the sand is transported in a thin, high concentration, layer near the bed, called sheet-flow. Coarse sand in sheet-flow layers show a positive (in the direction of the flow crest) net transport rate, because their concentration is in phase with the orbital flow. Fine sands (d_{50}<0.2 mm) are usually entrained high into suspension during the first high velocity half-cycle and, owing to their small settling velocity, they remain in suspension to be transported in the opposite direction to the crest during the second half-cycle. The changes in suspended concentrations of fine sands typically `lag' behind the maximum orbital velocity. This so-called phase-lag effect is responsible for reducing the net transport rate of finer sands, or even reversing the net transport against the direction of the wave crest [2].

III. A NEW SEMI-UNSTEADY FORMULA IN GAIA

A. The SANTOSS formula

The semi-unsteady sand transport formula of [11], known as the SANTOSS formula, is implemented in GAIA. The SANTOSS formula reads as follows:

$$\Phi = \frac{\sqrt{\theta_c} T_c\left(\Omega_{cc}+\frac{T_c}{2T_{cu}}\Omega_{ct}\right)\frac{\theta_c}{|\theta_c|}+\sqrt{\theta_t} T_t(\Omega_{tt}+\frac{T_t}{2T_{tu}}\Omega_{tc})\frac{\theta_t}{|\theta_t|}}{T} \tag{3}$$

where $\Phi = q_s/\sqrt{(s-1)gd_{50}^3}$ is the non-dimensional transport rate, θ_i (with i=c for the flow crest and i=t for the flow trough) is the wave half-cycle Shields parameter generated by the combined waves and current hydrodynamics; Ω_{ii} represents the sand load entrained and transported during the i half-flow cycle; and the terms Ω_{ij} represent the sand load entrained during the i half-flow cycle, and transported during the following j half-flow cycle. The sand loads are calculated as follows:

$$\Omega_i = \begin{cases} 11(|\theta_i| - \theta_{cr})^{1.2} & \text{if } \theta_i > \theta_{cr} \\ 0 & \text{if } \theta_i \leq \theta_{cr} \end{cases} \tag{4}$$

where θ_{cr} is the critical Shields parameter. While the sand load Ω_{ii} and Ω_{ij} are calculated as follows:

$$\Omega_{ii} = \begin{cases} \Omega_i & \text{if } P_i \leq 1 \\ \frac{1}{P_i}\Omega_i & \text{if } P_i > 1 \end{cases} \tag{5}$$

$$\Omega_{ij} = \begin{cases} 0 & \text{if } P_i \leq 1 \\ \left(1-\frac{1}{P_i}\right)\Omega_i & \text{if } P_i > 1 \end{cases} \tag{6}$$

With P_i the phase lag parameter:

$$P_i = 8.2\left(\frac{1-1.7\,\hat{u}_i}{c_w}\right)\frac{r_i}{2(T_i-T_{iu})w_s} \quad (7)$$

Where c_w is the wave celerity, $(1 - 1.7\,\hat{u}_i)/c_w$ accounts for the influence of horizontal sand advection by progressive wave, and $r_i/2(T_i - T_{iu})w_s$ represents the ratio between the half-cycle sand stirring height, r_i, and the settling distance within the half-cycle. The sand stirring height is the ripple height or the sheet-flow layer thickness depending on the regime of transport.

The novelty of this formula and its implementation, compared to all other existing sand transport formulae currently in GAIA, is that it calculates the sand transport rate in the direction of the combined wave and current velocity, taking into account the maximum velocities of both wave crest and trough. Moreover, the formula accounts for the estimated wave skewness in orbital flow without the need of a phase-resolving wave model. The formula accounts for wave induced sand transport processes such as: (i) phase-lag between the sand concentration and the flow velocity, which is important for rippled beds and fine sands in sheet-flow conditions, (ii) wave non-linearity effects such as wave skewness and asymmetry, (iii) the effects of boundary layer streaming and (iv) sand advection effects (i.e. transport in the wave direction for symmetric waves).

B. Implementation in GAIA

Morphodynamic changes can be predicted with the TELEMAC-MASCARET morphodynamic suite, so-called GAIA [10]. In GAIA numerical simulations of sediment transport processes in rivers, coastal seas and transitional waters can be performed by integrating several modules accounting for different physical mechanisms, acting according their characteristic time response. In GAIA the influence of the waves on sediment transport is accounted for in the transport formulae using the wave orbital velocity U_w [10]. The transport formulae currently implemented in GAIA are mostly “quasi-steady” transport formulae which assume that the suspended sand concentration is in phase with the flow, and hence ignore any phase-lag effects. This approach performs well for coarse sediments and tidal current dominated hydrodynamics. However, these formulae do not perform well for fine sands and wave dominated hydrodynamics.

Using a semi-unsteady formulae would be an improvement in such situations because the amount of sand transported during each wave half-cycle is accounted for (as explained in the previous section). As well as dealing with fine sands and wave-dominated hydrodynamics, semi-unsteady formulae also perform well for coarse sand in tidal dominated hydrodynamics. It should be noted that GAIA does include an implementation of the Dibajnia & Watanabe formula [1], which is semi-unsteady, but the direction of the transport is presently forced in the direction of the currents. Furthermore, the formula of Dibajnia & Watanabe does not account for flow acceleration nor for horizontal sand advection by progressive wave (i.e., symmetrical waves do not produce a net transport rate according to the formula of Dibajnia & Watanabe).

Because the only functioning sand transport formulae available in GAIA are quasi-steady, the accuracy of morphodynamic simulations is presently limited in coastal situations where the hydrodynamics are wave dominated, especially during storms.

To improve GAIA’s capability to predict morphodynamic changes in coastal areas, the formula of [3] was implemented to calculate the orbital flow timeseries. A key advantage of how this formula has been implemented is that it uses common wave spectral parameters to determine the orbital flow skewness and hydrodynamics. An example of near bed orbital flow generated with the formula of [3] can be seen in Figure 1. This removes the requirement to couple GAIA with a phase-resolving wave model and hence could potentially allow the formula to be applied to very large scale morphological models with minimal computational overhead. The current authors could find no other 2DH model in the literature which applies this methodology.

SANTOSS uses this information on wave orbital flow hydrodynamics, together with the depth-averaged current velocities calculated by TELEMAC2D, to calculate the transport rates.

IV. SANTOSS PERFORMANCE

A. Application to Poole and Christchurch bays

To test the capability of the SANTOSS formula, HR Wallingford’s model of Poole and Christchurch bays, described in [4], was adopted. The main differences with the original model are the followings:

- Smaller computational mesh
- TEL2TOM, instead of direct coupling with TOMAWAC
- Use of GAIA instead of SISYPHE
- Constant sediment size with d_{50}=0.15 mm, instead of a sediment size map

The new model was forced with the original model hydrodynamic result, the same atmospheric boundary conditions, and same wave spectra of the original model (see [4]). The computational model mesh of the edited model is presented in Figure 3(a), while its bathymetry is shown in Figure 3(b) together with nine locations were AWAC measurements were taken during the period of December 2017.

Transport rate measurements were obtained at these AWAC locations as the product of the suspended concentration profile of the fine sand and the wave averaged velocity profile. As discussed in [4], the seabed is characterised by different sediment sizes, whereas the present model only uses a fine sand with d_{50}=0.15 mm. However, this simplification of the characteristic seabed is considered sufficient since measurements are representative of the fine sand in the bed. It may however lead to some over-estimation of the transport rates as more fine sand is available in the model than in reality.

B. Results

Figure 4(a) and Figure 4(b) show the instantaneous sediment transport during the first and second storm of December 2017, respectively. The figures also show the current speed vectors in black, the near bed orbital velocity U_w along the wave direction in blue, and in orange the transport rate resulting from the combined wave and current hydrodynamic.

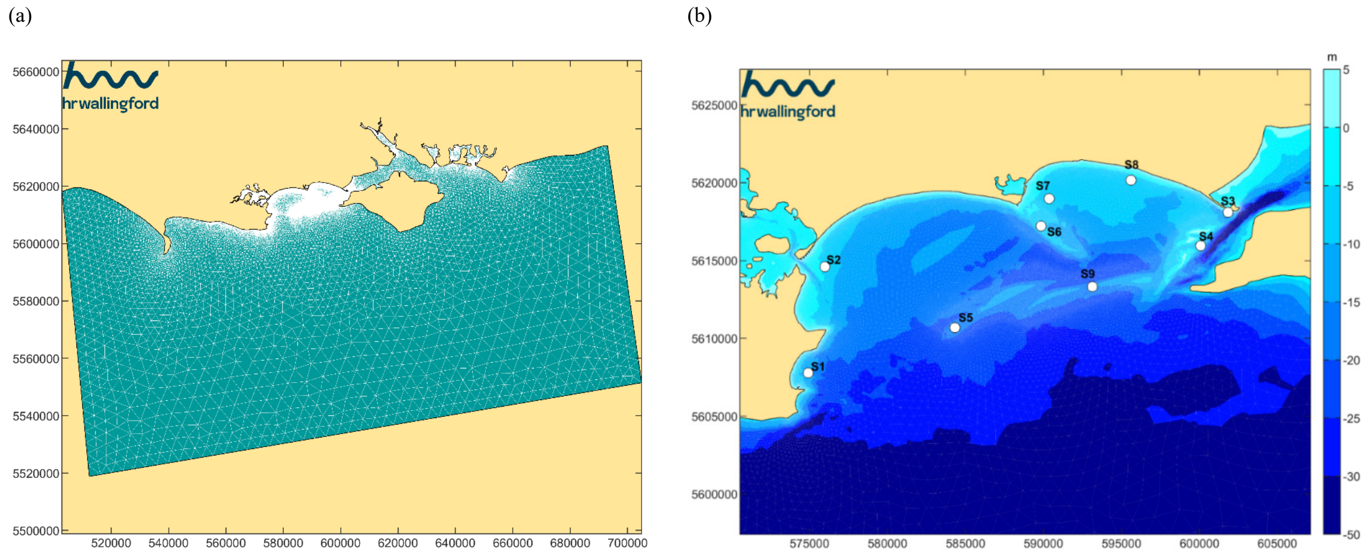

Figure 3. (a) Computational mesh; (b) Model bathymetry and location of the measurement points S1 to S9

In Figure 4(a), the current speed and orbital velocity U_w have similar magnitude but current and waves are almost in opposite direction. Therefore, the resultant sediment transport rate is generally small (q_s<50 mm^2/s), despite the relatively large wave height. The transport rate increases along the coastline (i.e., for bathymetry smaller than -5 m) because the current speed decreases while U_w increases due to wave shoaling. During the second storm (Figure 4(b)), the current and waves are almost in the same direction. As a consequence, the resultant transport rate in the bay is higher than during the first storm (q_s>50 mm2/s), despite H_s being similar, and q_s is neither in the direction of the current nor in the direction of the waves.

Figure 5 shows, as an example, the comparison between measurements and model results at point S6. The model correctly predicts both the hydrodynamics and the waves (i.e. H_s and T_p), as expected. The predicted transport rates are also in similar good agreement. The transport increases as the wave height increases, matching the magnitude of the measurements. The third plot in Figure 5 shows the modelled wave skewness on the right-hand axes (dashed black line). Wave skewness increases for large wave heights reaching values of 0.65 during the storms, meaning that waves are strongly non-linear, thus wave induced transport processes are important in the calculation of the transport rates.

Figure 6 shows the comparison between the measured and predicted transport rates at all measurement locations. Measurements were not available at S8 for the modelled period. The agreement is generally within a factor of two for the majority of the points except S2, S4 and S7. At points S4 and S7 the predicted transport rate is larger than the measured one. However, at these locations the seabed is characterised by coarse sediments (d_{50}>1.0mm), reducing the availability of fine sand whereas the model assumes a bed of fine sand. Therefore, the overprediction at S4 and S7 can be explained by the reduced sand availability.

At point S2 the waves, currents and transport rates are generally small (q_s<50 mm^2/s) and the measured transport rates are probably related to fine silt and clay particles originating from Poole Harbour to the west of the measurement point.

V. FUTURE WORK

The sediment transport model GAIA is now capable of accounting for wave induced transport rates and therefore has an improved capability for predicting near shore sand transport. To further investigate its new capability, the next step will be to use GAIA to model the sand bar migration during both storms and "calm" wave conditions. Validation of a fully-coupled model (TELEMAC2D, TOMAWAC, GAIA) will be carried out using measurements taken at Duck, North Caroline (U.S.A), in 1994 (Figure 7(e)). The model results will be compared against measurements of water elevation, wave height, undertow current, and sand bar morphology.

VI. CONCLUSIONS

The semi-unsteady sand transport formula, SANTOSS, has been implemented in GAIA, the sediment transport module of openTELEMAC. The novelty of this formula and its implementation, compared to other existing sand transport formulae currently functioning in GAIA, is that it accounts for the estimated skewness in the orbital flow without needing a coupled phase-resolving wave module and can therefore be applied in 2DH simulations with low computational overhead. This improves the capability of GAIA to predict sand transport rates in the near shore region, where waves become asymmetric due to shoaling and produce net transport rates that are not necessarily aligned with the flow direction.

The newly implemented SANTOSS formula was tested against in-situ transport rate measurements taken in Poole-Christchurch bay (see [4]). The modelled transport rates showed good agreement with the measurements and clearly showed the influence of the waves in the transport rate magnitude and direction, especially in the near shore region. Further validation will follow in the near future with another real test case study applied to the measurements of Duck 1994, North Caroline, (U.S.A.).

(a)

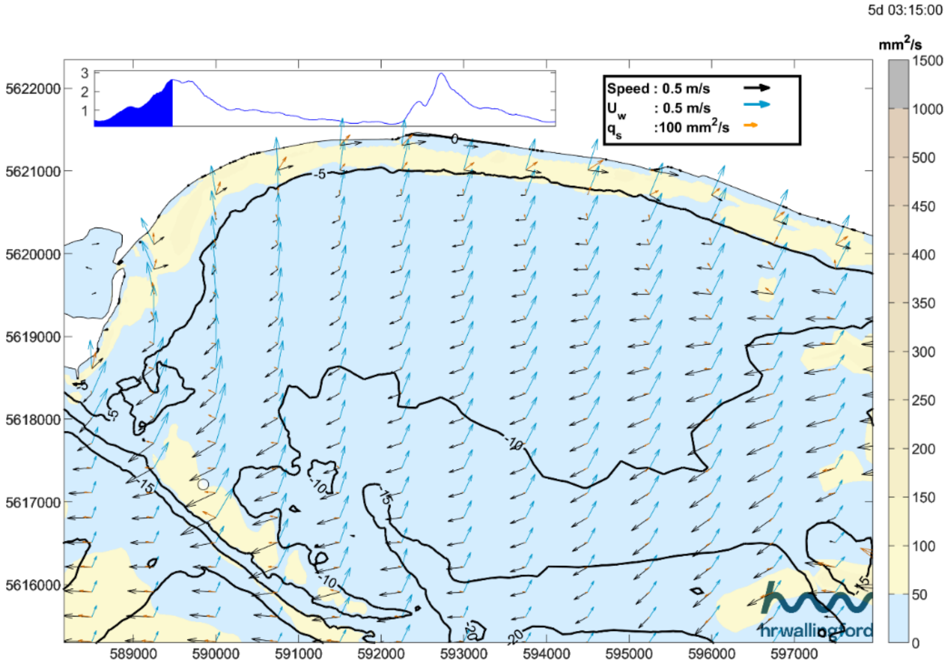

(b)

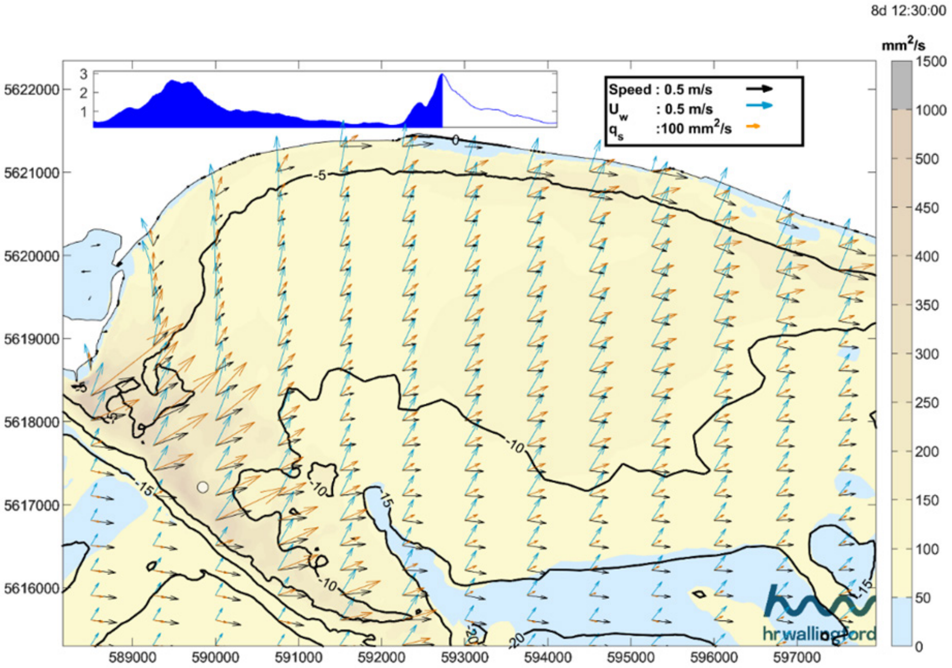

Figure 4. – Instantaneous sediment transport during the first storm. Black arrows represent the current speed; blue arrows represent the orbital velocity U_w and the orange arrows the transport rate. Significant wave height at S6 represented in the top left plot (units in metres). (a) first storm, (b) second storm.

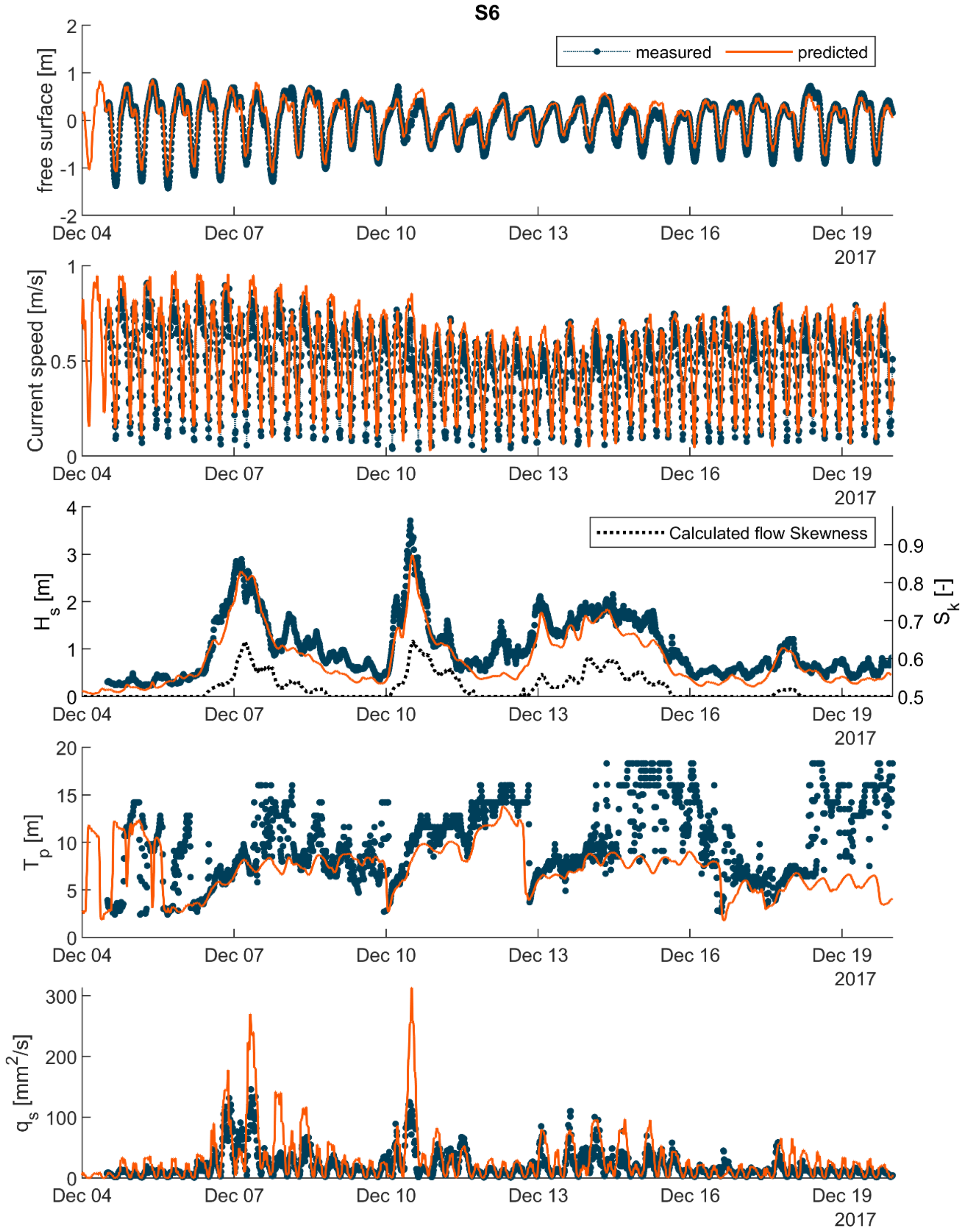

Figure 5. – Comparison between measurements and model results. T_p is the peak wave period. Location S6.

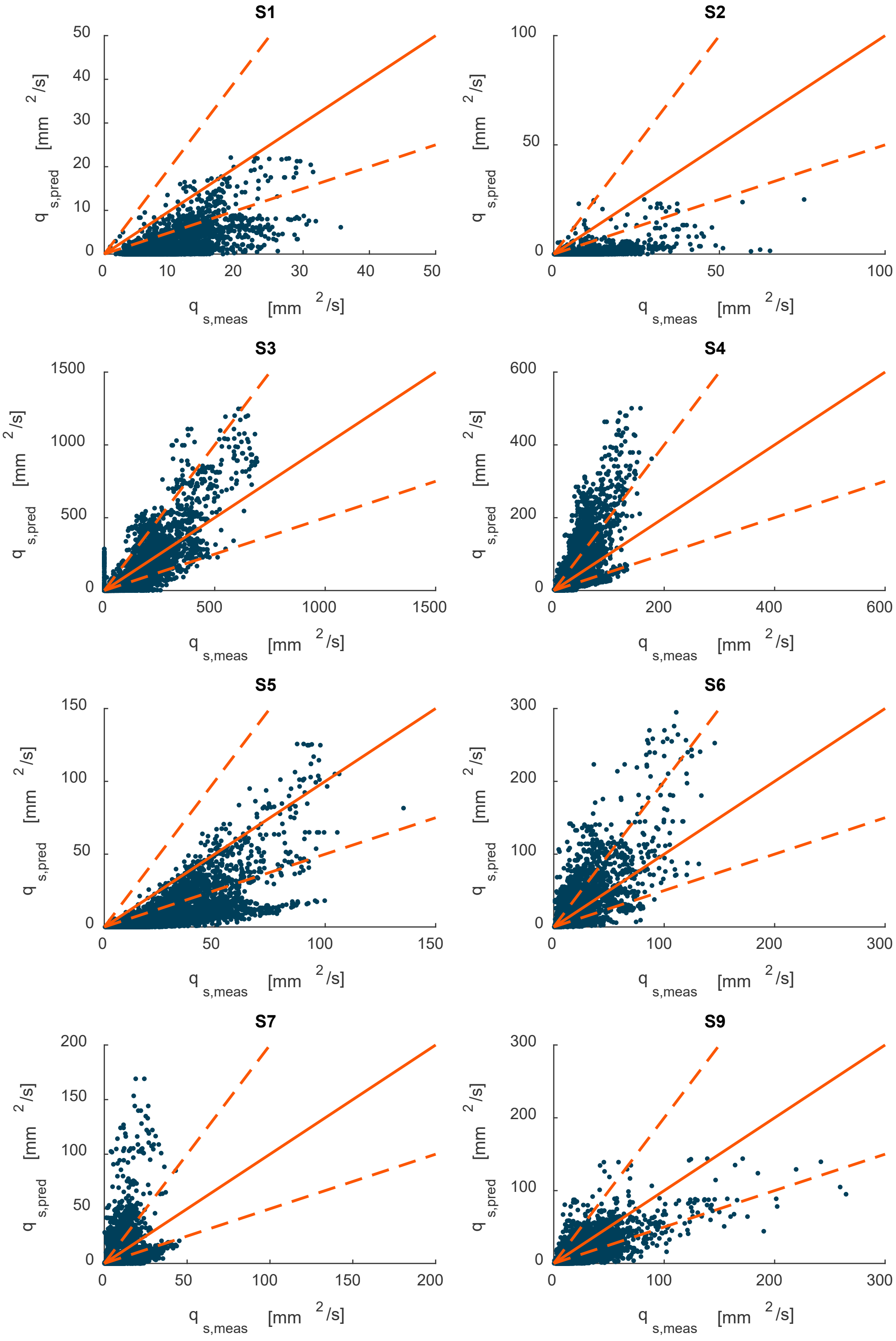

Figure 6. – Comparison between measured and predicted transport rates at the measurement locations. The solid line represents the 1:1 relationship, while the dashed lines represent 1:2 and 2:1. Measurements are not available at S8 for the modelled period..

.

ACKNOWLEDGEMENT

The research presented in this paper are funded from the Internal Research Program of HR Wallingford.

REFERENCES

[1] Dibajnia, M., & Watanabe, A. "Sheet flow under nonlinear waves and currents". *Proceedings of the Coastal Engineering Conference*, vol. *2*, pp. 2015–2028, 1992. https://doi.org/10.1061/9780872629332.154

[2] Dohmen-Janssen, C. M., & Hanes, D. M. "Sheet flow dynamics under monochromatic nonbreaking waves". *Journal of Geophysical Research: Oceans*, vol. *107, issue* 10 2002. https://doi.org/10.1029/2001jc001045.

[3] Elfrink, B., Hanes, D. M., & Ruessink, B. G. "Parameterization and simulation of near bed orbital velocities under irregular waves in shallow water". *Coastal Engineering*, vol. *53, issue* 11, pp 915–927, 2006. https://doi.org/10.1016/j.coastaleng.2006.06.002

[4] Knaapen M A. F, "Sediment modelling for Poole and Christchurch Bays", TELEMAC User Conference, 2019

[5] Meyer-Peter, E. and Muller, R. "Formulas for bed-load transport". In Proceedings of the 2nd Meeting of the International Association of Hydraulic Research, pages 39-64, 1948.

[6] Nielsen, P. "Coastal bottom boundary layers and sediment transport". Advanced series on ocean engineering, volume 4 of Advanced Series on Ocean Engineering. WORLD SCIENTIFIC, 1992.

[7] Rafati, Y., Hsu, T. J., Elgar, S., Raubenheimer, B., Quataert, E., & van Dongeren, A. "Modeling the hydrodynamics and morphodynamics of sandbar migration events". *Coastal Engineering*, vol. *166,* March 2021, pp 103885. https://doi.org/10.1016/j.coastaleng.2021.103885

[8] Shields, A. "Application of similarity principles and turbulence research to bed-load movement","Anwendung der Aehnlichkeitsmechanik und der Turbulenzforschungauf die Geschebebewegung. Mitteilungen der Preussischen Versuchsanstalt fur Wasser-bau und Schibau", No. 26, 1936.

[9] Soulsby, R. L. "Dynamics of marine sands: a manual for practical applications. Telford", 1997.

[10] Tassi P., Benson T., Delineares M., Fontaine J, Huybrechts N, Kopmann R, Pavan S, Pham C, Taccone F, Walther R, "GAIA - a unified framework for sediment transport and bed evolution in rivers, coastal seas and transitional waters in the TELEMAC-MASCARET modelling system", Environmental modelling and software vol. 159, pp 105544, 2023

[11] van der A, D. A., Ribberink, J. S., van der Werf, J. J., O'Donoghue, T., Buijsrogge, R. H.,.and Kranenburg, W. M. "Practical sand transport formula for non-breaking waves and currents". Coastal Engineering, vol. 76, pp 26-42, 2013

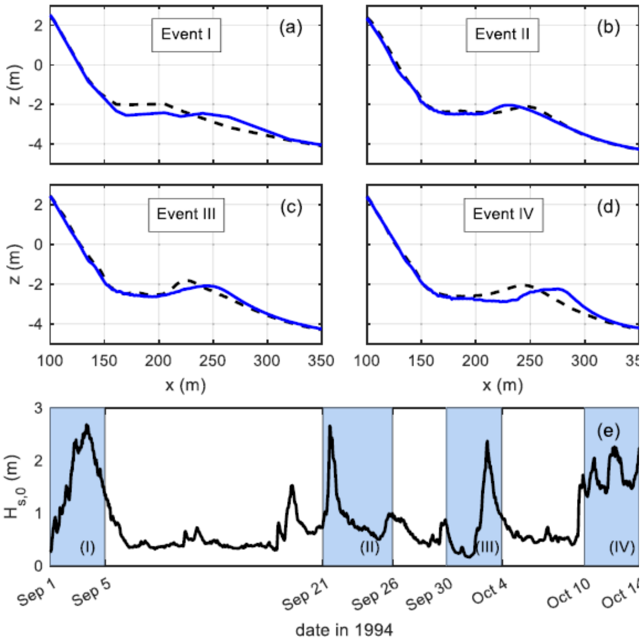

Figure 7. – (a) to (d) measured morphology before and after storm events. (e) measured significant wave height. Taken from [7].

Transmission of waves through structures in ARTEMIS, and long-term time series of wave data in harbours

W. Alexander Breugem[1], Sarah Doorme[1], Arash Bakhtiari[1], Gijsbert van Holland[1], Boudewijn Decrop[1]
abr@imdc.be, Antwerp, Belgium
[1]: IMDC NV

***Abstract* – ARTEMIS is a tool that is often used to calculate the wave field in a harbour based on the mild slope equation. Special boundary conditions exist in ARTEMIS to include the (partial) reflections of wave on structures like breakwaters or groynes. However, ARTEMIS currently has two limitations that are addressed in this paper:**

1. **ARTEMIS cannot take account of the transmission of wave energy through porous structures,**
2. **ARTEMIS cannot be used to generate long time series of wave conditions for calibration or extreme value analysis.**

Therefore, in this paper, first an adaptation to ARTEMIS is presented, which allows the transmission of wave energy through permeable structures. This is implemented as an extra functionality on the model boundaries that determines which fraction of the incoming wave potential is to be transmitted to another nearby node on the boundary (depending on the user-defined transmission coefficients). This feature is compatible with reflection of the incoming wave energy. Schematic test cases are shown that demonstrate the correct function of this module.

Then a method is presented, which allows the generation of long time series of wave conditions inside harbours. It uses the time series of wave spectra at the boundary of the ARTEMIS model (for example obtained from a wave transformation model like TOMAWAC) and the results of a large set (order 10000) of monochromatic ARTEMIS wave runs. The applicability of this method is demonstrated with the calibration of an ARTEMIS wave model against wave data measured in a marina.

***Keywords*: ARTEMIS, Wave, Harbour agitation, Transmission, Wave time series**

I. INTRODUCTION

ARTEMIS is a numerical model that is often used to calculate the wave field in a harbour based on the mild slope equation. Using this equation, the effects of refraction, diffraction and propagation of waves can be taken into account. Special boundary conditions exist in ARTEMIS to include the (partial) reflections of wave on structures like breakwaters or groynes. However, ARTEMIS cannot yet account for the transmission of wave energy through porous structures. The implementation of transmission would allow many new applications of ARTEMIS, including the simulation of floating breakwater and porous structures.

The mild slope equation is does not have any time dependency. Therefore ARTEMIS is typically used to calculate the wave conditions given a single set of wave boundary conditions.. While it is in principle possible to perform independent ARTEMIS simulations for each moment in time, the computational costs of doing so would be prohibitively expensive. This makes it difficult to obtain time series of wave conditions, for example for calibration purposes.

Therefore, the objectives of this paper are twofold:

1. To implement a new functionality to allow wave transmission through structures to be simulated in ARTEMIS,
2. To develop a methodology for obtaining time series of wave data from ARTEMIS, with reasonable calculation times.

The first part of this paper deals with the implementation of wave transmission. The section starts with a theoretical explanation of the physics involved and is followed by details of the implementation in ARTEMIS. Verification tests are presented to show that the correct behaviour is obtained. In a second part, a methodology is presented to generate time series of wave conditions using ARTEMIS and wave spectra at the boundary of the ARTEMIS model. This methodology is applied for the calibration and validation against wave data inside a marina. The paper ends with some brief conclusions.

II. IMPLEMENTATION OF WAVE TRANSMISSION

A. Theoretical background

In ARTEMIS, the mild slope equation [1] is solved for the wave potential Φ. The potential is a complex variable, such that the amplitude and phase of the wave are both considered. The transmitted potential is Φ_t is obtained from the incoming wave potential Φ_i by:

$$\Phi_t = T\Phi_i. \qquad (1)$$

Here T is the transmission coefficient. The current implementation assumes that there is no phase shift of the waves (this might be added relatively straightforwardly in a future update), and that the direction of the transmitted wave is equal to the direction of the incoming wave. The magnitude of the reflected wave potential Φ_r is given:

$$|\Phi_r| = R|\Phi_\mathrm{i}|. \tag{2}$$

Here R is the reflection coefficient. The reflected waves have a different direction to that of the incoming waves. Note that in ARTEMIS, a phase shift can also be applied to the reflected wave potential.

In order to have energy conservation, the reflection and transmission coefficients need to be chosen such that:

$$T^2 + R^2 \leq 1. \tag{3}$$

B. *Implementation in ARTEMIS*

The transmission is always applied between two nodes, that are on a transmissive boundary (defined by the code 2 1 1 in the .cli file see section II.D). We will call the node with the incident wave the **source node**; and the node where the transmitted wave is released the **receiver node.** The method is designed for infinitely thin structures in the first instance. Source and receiver nodes may be located at a distance of 0 m from each other . So there are two nodes at the same place, but they are separated topologically, because there is no mesh edge connecting them. The limiting assumption in the current implementation is that the source and receiver nodes need to be closer than a threshold distance. In order to implement the transmission of waves in ARTEMIS, the following algorithm is used:

1. During the initialization step, a corresponding source node is searched for each receiver node on a transmission boundary. This source node is taken to be the first node within a distance to the receiver node that is smaller than the threshold distance specified in the .cas file (Figure 1).
2. At each iteration in the loop for automatic calculation of TETAP, the incoming potential at a source node is multiplied with the transmission coefficient (1), and this is added to the potential at the receiver node.

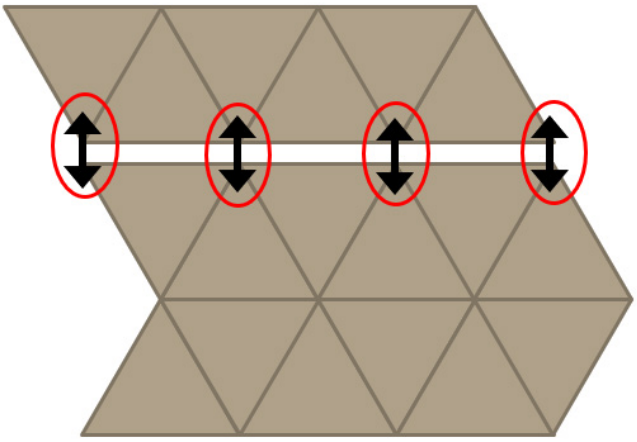

Figure 1 Connections in the mesh, through which waves are transmitted.

The current implementation only works on a single processor. The parallelisation of this algorithm will be implemented in the future.

C. *Validation tests*

In order to verify the correct implementation of the wave transmission feature, a schematic test case was made. It consists of two basins with a width of 400 m and a length of 100 m each, and a depth of 5 m. The mesh resolution is 4 m (Figure 2). The two basins are separated by a 2-m thick wall. There are two very small opening connecting the two basins; an initial test showed that the wave energy penetrating through this opening is limited. Monochromatic waves are prescribed on the left boundary, with a wave height of 1 m and a wave period of 5 s. These waves have a wavelength of 30 m. With a mesh resolution of 4 m, 7.5 nodes define a wavelength, which is sufficient. The direct solver is used. Wave dissipation is neglected.

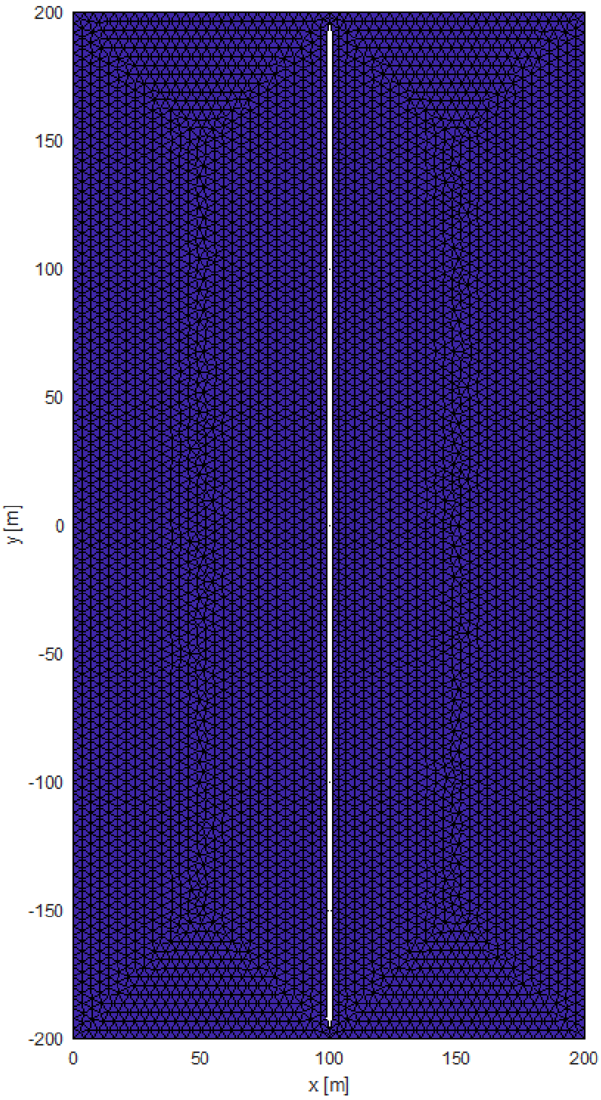

Figure 2 Mesh used in the schematic test case.

Different cases were studied, changing transmission coefficients, reflection coefficients and the incoming wave direction. In Figure 3, the wave height is plotted along the centre line (y=0) for a case with R = 0.5 (on the left side of the wall) and T = 0.5 (on the right side of the wall) with a wave angle of 0 degrees at the boundary (cartesian convention), i.e.

waves propagating from left to right, parallel to the centre line of the basins. The waves in the left basin (partially) reflect against the wall. In the right basin, the wave height is 0.5 m, which corresponds to the expected value (incoming waves of 1.0 m multiplied by a transmission coefficient T of 0.5).

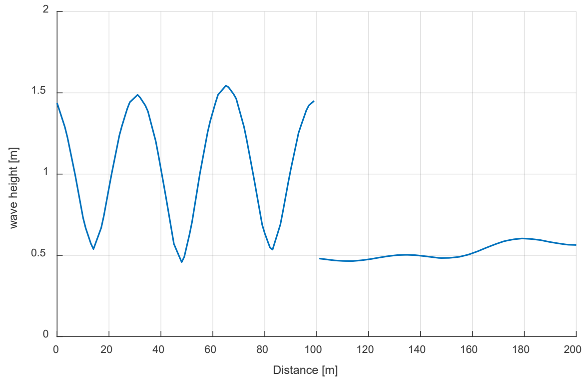

Figure 3 Wave height along the centre line of the basins for waves of 0 degrees, R = 0.5 (left side of the wall), and T= 0.5 (right side of the wall).

A second case was tested, also with a wave angle of 0 degrees at the open boundary, with a transmission coefficient T of 1.0 (fully transmissive), hence R = 0 at the structure (on both sides). At the right boundary, a reflection coefficient of R=0.5 is applied. The wave height at the centre line is shown in Figure 4. This figure shows a standing wave in both basins, caused by reflections off the right boundary. The full transmission lets the waves propagate from either side. This is needed to get the correct standing wave patterns. There is a small discontinuity in wave height at the location of the wall. This might be related to the thickness of the structure separating the two basins (2 m), to neglecting the phase difference between both sides of the structure, or a combination of the two. Changing the mesh, such that the wall becomes thinner, might reduce this discontinuity.

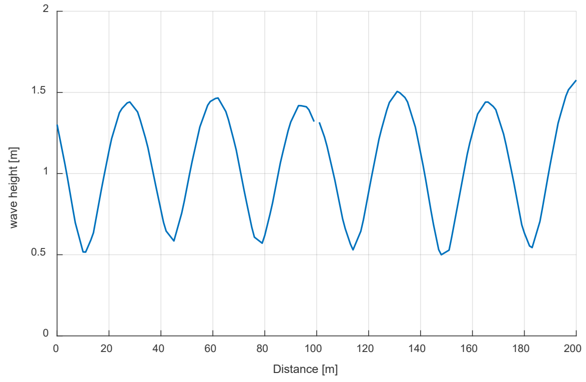

Figure 4 Wave height along the centre line of the basins for waves of 0 degrees, T= 1.0 (both sides of the wall), and R = 0.5 (right boundary).

The results of a case with waves at 30 degrees, a transmission coefficient of T = 1.0 (fully transmissive), and a reflection coefficient of R= 0 (no reflection) is shown in Figure 5. In this case, we see that the waves pass through the structure without change in wave direction and wave height (as if the structure were not there). This is the expected behaviour.

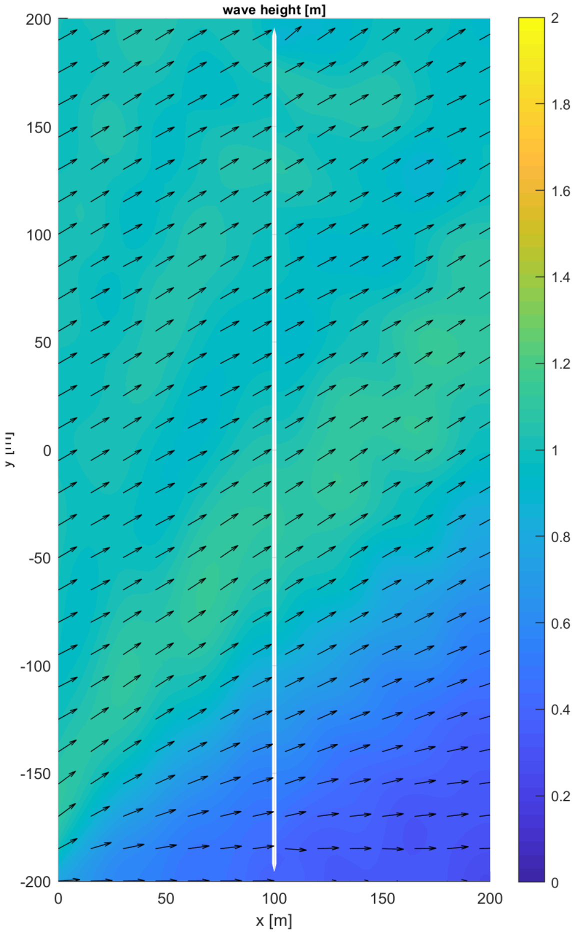

Figure 5 Wave height and wave direction for a case with waves at an angle of 30 degrees, T = 1.0 and R = 0.0.

Results from the three examples presented here are in line with the expected behaviour of the wave transmission through a structure. Therefore, it can be concluded that the wave transmission is correctly implemented in ARTEMIS.

D. *User procedure*

In order to use the wave transmission feature, the following steps need to be taken:

1. Adapt the mesh in such way that at the boundary, in which one want to apply wave transmission there are two nodes at a short distance from each other (Figure 1). The wave energy will transferred between these two nodes. This distance between these nodes needs to be smaller than the distance between the node and the closest node on the boundary. This requirement is similar to that when using weirs and culverts in TELEMAC-2D and TELEMAC-3D.
2. Set the maximum distance between pairs of nodes to be connected, using the keyword in the .cas file:

```
THRESHOLD DISTANCE FOR TRANSMISSION
```

3. Use `AUTOMATIC TETAP CALCULATION : YES` in the .cas file (with a minimum of two iterations), to make sure that sub-iterations are used.
4. Adapt the .cli file. For a boundary with transmission, a new code (2 1 1) is needed on both sides of the transmitting boundary in the first three columns of the .cli file (Figure 6).
5. Add the transmission coefficient in column 9 of the .cli file. Note that this is consistent with the definition of the reflection coefficient (RP) and reflection phase shift (ALFAP) in columns 7 and 6. Therefore, it is possible to define different reflection and transmission coefficients on each side of the structure, thus allowing to model a complex structure. Thus in this implementation, reflection works on boundaries with code (2 2 2) as well as with (2 1 1), but only the latter always transmission of wave energy.

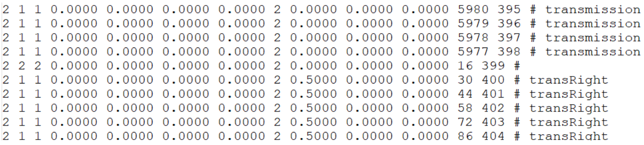

```
2 1 1 0.0000 0.0000 0.0000 0.0000 2 0.0000 0.0000 0.0000 5980 395 # transmission
2 1 1 0.0000 0.0000 0.0000 0.0000 2 0.0000 0.0000 0.0000 5979 396 # transmission
2 1 1 0.0000 0.0000 0.0000 0.0000 2 0.0000 0.0000 0.0000 5978 397 # transmission
2 1 1 0.0000 0.0000 0.0000 0.0000 2 0.0000 0.0000 0.0000 5977 398 # transmission
2 2 2 0.0000 0.0000 0.0000 0.0000 2 0.0000 0.0000 0.0000 16 399 #
2 1 1 0.0000 0.0000 0.0000 0.0000 2 0.5000 0.0000 0.0000 30 400 # transRight
2 1 1 0.0000 0.0000 0.0000 0.0000 2 0.5000 0.0000 0.0000 44 401 # transRight
2 1 1 0.0000 0.0000 0.0000 0.0000 2 0.5000 0.0000 0.0000 58 402 # transRight
2 1 1 0.0000 0.0000 0.0000 0.0000 2 0.5000 0.0000 0.0000 72 403 # transRight
2 1 1 0.0000 0.0000 0.0000 0.0000 2 0.5000 0.0000 0.0000 86 404 # transRight
```

Figure 6 Extract of a .cli file, which contains a transmissive boundary.

III. GENERATION OF LONG TIME SERIES OF WAVE CONDITIONS IN ARTEMIS

A. Methodology

In many practical applications, one is interested in obtaining long time series of wave conditions including the effects of refraction, reflection, transmission and diffraction. Possible applications include statistical analysis of extreme values, which is often required for design purposes. In principle, it is possible to do so in ARTEMIS, by calculating the wave field for every set of conditions (water depth, wave height, wave period and wave direction at the boundary of the ARTEMIS model). However, in practice, this is too computationally expensive to do in real cases. Therefore, a new methodology is presented in this paper, which is faster. It has the additional benefit that the output spectral resolution can be much higher than in a standalone ARTEMIS simulation where resolution is typically reduced in favour of computational efficiency.

In the absence of dissipation terms (depth induced wave breaking and bottom friction), the processes modelled in ARTEMIS are linear. Therefore, the superposition principle applies. Whether or not the dissipation of wave energy can be neglected is case dependent. However, in many practical applications, which deal with the wave field inside ports and harbours, the water depth is relatively deep and neglecting the wave dissipation is justified.

The new methodology uses the linearity of ARTEMIS to reconstruct spectra in the ARTEMIS model domain from spectral input of data (Figure 7). Thereto the following steps are performed:

1. A time series of wave data (ideally in the form of wave spectra) is obtained from wave buoys or a large-scale wave model (such as ERA5) in the region of interest.
2. Depending on the location of the available time series with respect to the boundary of the ARTEMIS model, a wave transformation model (e.g. SWAN or TOMAWAC) is used to obtain time series of wave spectra at the boundary of the ARTEMIS model [2].
3. Water level data are obtained at the boundary from measurements or an appropriate numerical model such as iCSM [3].
4. The ARTEMIS model is run to generate a database of wave transformation in the area of interest This is done by performing multiple runs with monochromatic waves, without any wave dissipation, for a wave height at the boundary of 1 m with the wave directions and wave frequencies that correspond exactly to the spectral bins in the time series of wave spectra at the boundary (e.g. the spectral mesh of the wave model used in the wave transformation in step 2). Iterations to estimate the incoming wave direction on reflecting boundaries are applied, as these iterations are not related to any non-linearity, and hence the superposition principle can still be used. These runs are performed for a range of water levels covering the data obtained in step 3. Typically, this results in thousands of simulations, but these simulations are very fast (order of seconds to minutes on a single processor) and can easily be executed simultaneously. Typically, we use the Linux *xarchs* command to make sure that these ARTEMIS runs are executed simultaneously in order to save on the total time needed to obtain all simulation results.
5. A MATLAB script is used to reconstruct the wave spectra inside the ARTEMIS model domain from 1) the ARTEMIS wave transformation database and 2) the time series of wave spectra at the ARTEMIS boundary and water levels, which are assumed to be continuous in the full model domain. This script determines at each moment in time the nearest water level in the ARTEMIS database to the observed water level and selects the wave results for this water level. These wave spectra are then used to determine the spectral wave parameters (significant wave height, peak and mean wave period and mean wave direction). These results are stored in a Selafin file.
6. A separate postprocessing can be performed on the Selafin file generated in step 5 to determine extreme value distributions or to compare to measurements.

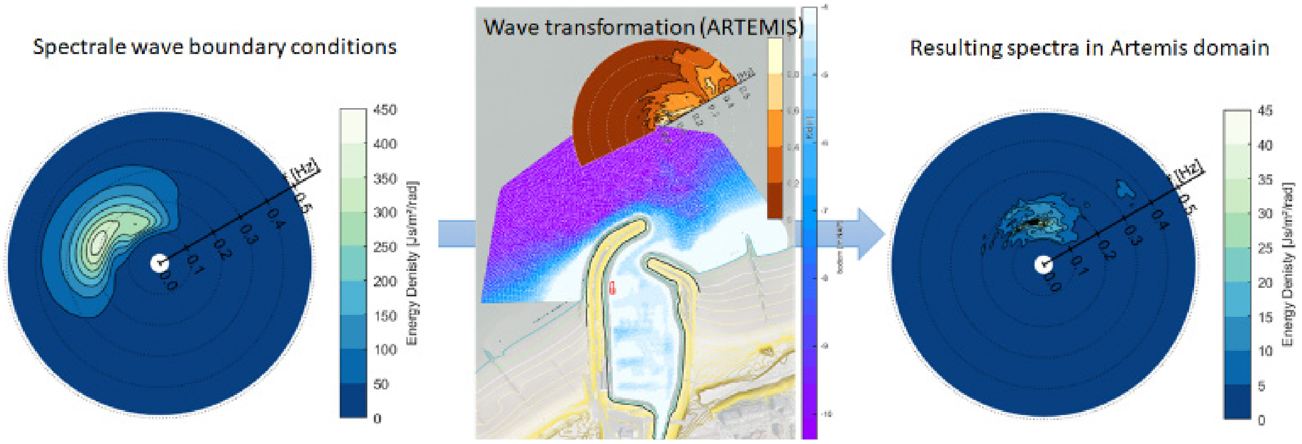

Figure 7 Schematic image of the wave transformation methodology.

B. *Application for the calibration of an* ARTEMIS *model of a marina*

The methodology presented in section III A is used to calibrate an ARTEMIS model of the marina of Cadzand in the Netherlands (Figure 8).

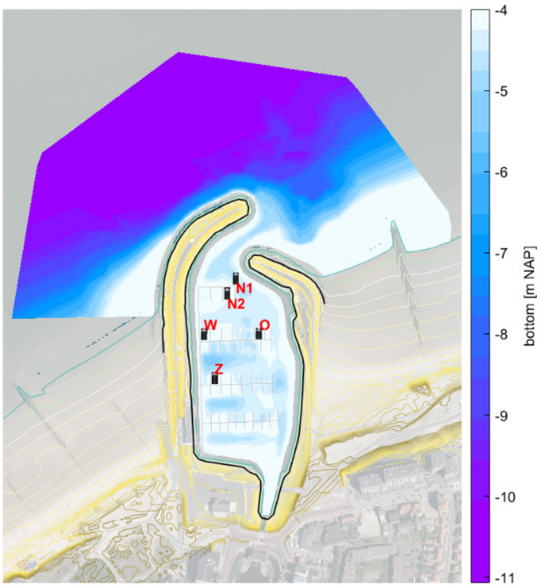

Figure 8 Bathymetry of the marina of Cadzand and location of the observations

A database was made of 25380 ARTEMIS simulations, using the discretisation in Table 1. Time series of wave data were generated from observed wave spectra in the vicinity of the model domain, such that no wave transformation modelling was necessary in this case. The observed wave spectra data consisted of one-dimensional wave spectra with the mean wave direction and directional spreading for each frequency bin. These data were converted to two-dimensional wave spectra using the $\cos^{2s}$ directional spreading distribution.

Table 1 Classes used for the wave transformation database in ARTEMIS

Variable	Nr of classes	Range	Resolution
Water level	12	-2.5 m to +3.0 m	0.5 m
Frequency	47	0.03 Hz to 0.49 Hz	0.01 Hz
Direction	45	116 deg to 60 deg	4 deg

The model was calibrated by changing the reflection coefficients at the breakwaters inside the marina. For the calibration, measurements were performed inside the marina using Aquadopp and OBS sensors at different locations inside the marina.

The results are presented in Figure 9 and Figure 10. The presented methodology has made it possible to obtain time series of significant wave height and peak period from the ARTEMIS model, which can be compared directly to the observed measurement data. From the presented data, it appears further that ARTEMIS can represent the wave height and wave period in the marina rather well using the presented methodology.

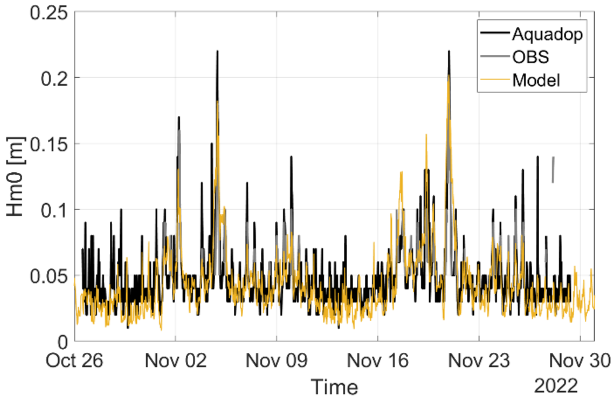

Figure 9 Comparison of measured wave height and modelled wave height inside the marina.

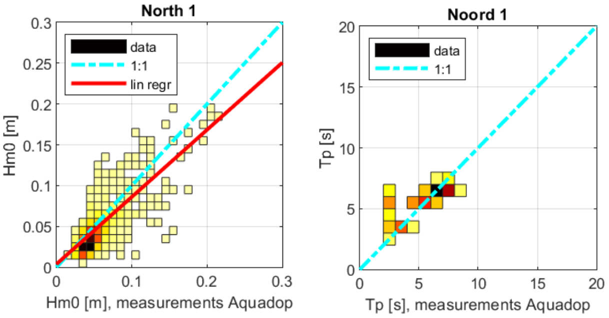

Figure 10 Summary of the calibration results at one of the observation points

IV. SUMMARY AND CONCLUSIONS

In this paper, first a new implementation is presented, that allows to use wave transmission through porous structures in ARTEMIS. This is done by copying the imaginary wave potential from one point at the boundary representing the structure to a point on the opposite side of that boundary after applying a transmission coefficient. Any phase shift in the potential is currently neglected. At present, the method only works on a single processor, but parallelisation of the code is foreseen for the near future. This approach can be combined with reflection at the boundary. Theoretical tests are performed in order to verify the correct implementation of the feature.

Then, a methodology is presented to determine time series of wave conditions in the ARTEMIS domain. In this methodology, a large set (ten thousands) of monochromatic ARTEMIS simulations is performed to obtain a database of wave results for each component in the two-dimensional wave spectrum inside the ARTEMIS domain. Together with timeseries of wave spectra at the boundary and water levels in the domain, this database can be used to reconstruct the wave conditions in the model domain, provided that wave dissipation can be neglected. This method was applied to perform a calibration of a wave model of a marina. The time series obtained using this procedure are directly compared to the time series measured inside the marina and show a good agreement.

REFERENCES

[1] Berkhoff, J. C. (1973). Computation of combined refraction—diffraction. In Coastal Engineering 1972 (pp. 471-490).

[2] Q. Zhang, S. Doorme, J. Figard1, E. Di Lauro, W.A.Breugem , A. Bakhtiari1 (2023) Application of TOMAWAC wave model for wave energy resource assessment: a North Sea wave database, in preparation for TUC 2023

[3] Chu, K., Breugem A., Wolf, T., & Decrop, B. (2020). Improvement of a Continental Shelf Model of the North Sea. 2020 TELEMAC-MASCARET, 146.

Coarse sediment transport with GAIA: Case study on the Drac River

Matthieu de Linares[1], Florian Ronzani[1], Eric Tiriau[1], Téa Piednoir[1], Thomas Laurent[1], Damien Kuss[2]
matthieu.delinares@arteliagroup.com, Echirolles, France
[1]: ARTELIA
[2]: SYMBHI

Abstract – **The study presented here apply recently validated formulations for sediment transport to a large gravel-bed river case. This modelling work was done in order to study intended restoration and flood protection works on the Drac river near the city of Grenoble.**

In this article we focus on the calibration of two TELEMAC-2D / GAIA models and the lessons learned in terms of methodology (role of graded sediment, methodology for long-term simulations, impact of mobile-bed modelling on the maximum simulated water levels during flood…).

Keywords: gravel, sediment, bedload, morphology, GAIA.

I. INTRODUCTION

GAIA has been validated recently on a well-controlled case (physical model of a debris basin) involving deposition of coarse sediment [1]. A set of formulations and parameters was proposed, and the role of the coupling between hydraulics (TELEMAC-2D) and sediment transport (GAIA) was highlighted.

The new study presented here undertakes to apply the recently validated formulations to a larger and more general gravel-bed river case (involving sequences of both erosion and deposition). This modelling work was done in order to study intended restoration and flood protection works on the Drac river near the city of Grenoble. These works will involve broadening of the bed upstream of Grenoble (for regulation of sediment transport fluxes) and lowering of vegetated bars in the embanked stretch of river in Grenoble.

Every site where a work is planned was studied in a separate TELEMAC-2D / GAIA model, to investigate its effects, while a 1D mobile bed model was used to study the full project and the interactions between the different works. The presentation will focus on the calibration of the TELEMAC-2D / GAIA models and the lessons learned in terms of methodology (role of graded sediment, methodology for long-term simulations, impact of mobile-bed modelling on the maximum simulated water levels during flood…).

II. PRESENTATION OF THE SITE AND THE OBJECTIVES OF THE STUDY

A. The Drac river near Grenoble

The Drac river is located in the French Alps and is one of the main tributaries of the Isère River with the confluence downstream Grenoble. It has a watershed area of 3 600 km^2, and an average mean flow of around 100 m^3/s. The dominant sediment class in its bed is coarse pebbles.

Near Grenoble, the morphology of the Drac river has been severely impacted by different measures of development, and in particular hydropower, embankments, and gravel extraction. Since the end of gravel extraction, the riverbed along Grenoble has steadily risen, thus increasing the flood risks.

B. The flood protection and restoration project

SYMBHI, the local river basin agency, is in charge of the "Programme d'Actions et de Prévention des Inondations" (scheme for flood prevention) on a 27 kilometers stretch of river upstream and along Grenoble.

Flooding from the Drac river indeed poses a risk to the urban area. Previous studies have shown that a potential risk of dike failure is anticipated in urban areas for the 30-years flood and higher. Protective structures (dykes) must therefore be reinforced in order to prevent any risk of failure (or breach).

At the same time, flood water levels must be lowered through works within the main channel (by lowering of transverse sills, lowering of gravel deposits in the bed) to reduce the risk of overloading protective structures. Sediment management is thus an underlying key issue in this flood protection scheme.

C. How numerical modelling helps design the project

Despite past developments (dikes, extraction, hydroelectric development, embankments…), the Drac river remains able to transport gravel and pebbles during floods. This can increase the impact of floods (lateral erosion, raising of water levels during floods), as well as constrain certain uses (water intakes, hydroelectricity). Sediment transport must therefore be regulated. The main levers that are envisioned for this are large-scale broadening of the riverbed in some sectors upstream of the urban area, and managing excess sediment at specific locations with sediment traps (local broadening of the bed).

Modelling of hydrodynamics and sediment transport as presented in this paper is used to check the effectiveness and refine (dimensions, need of maintenance, timing of the works…) the developments envisioned in the flood prevention scheme for sediment management.

Note that a "reference" hydrodynamic TELEMAC-2D model of the whole study site, built during a previous study, is used to estimate the impact of the scheme in terms of water levels at the scale of the whole river reach. In addition, a 1D sediment transport model (CAVALCADE) of the whole reach has been set-up, and is used for the preliminary investigation of the sediment management levers, and study their interaction.

III. 2D SEDIMENT TRANSPORT MODELLING – GENERAL DESCRIPTION

A. The models

In order to be able to focus on different sites with adequately sized meshes, three distinct reaches of the 27-kilometers long study area where modelled (while the 1D model was able to simulate bed evolution for the whole study area).

One model, 5.3 kilometers long, represents the embanked Drac river inside Grenoble (see Figure 1). In a first step, it is used for calibration because this is the reach for which some reliable estimates of solid fluxes are available.

The other model, 4 kilometers long, represents a more natural stretch of river upstream the urban areas (see Figure 2below). The main objectives of this model are to check the impact of sediment transport on water levels during flood, and to assess the influence of the broadening of the bed in terms of sediment regulation.

The representative mesh size for these models is 3 meters. It is a compromise between computer resources demand on one hand, and result "quality" on the other hand. With the 3 meters mesh, for some locations and some hydrological situations, the infamous wiggles associated to the resolution of the Exner equation become significant. These wiggles are strongly reduced with a 1.5 meters mesh, but the computing time then becomes too long to perform the needed amount of test runs.

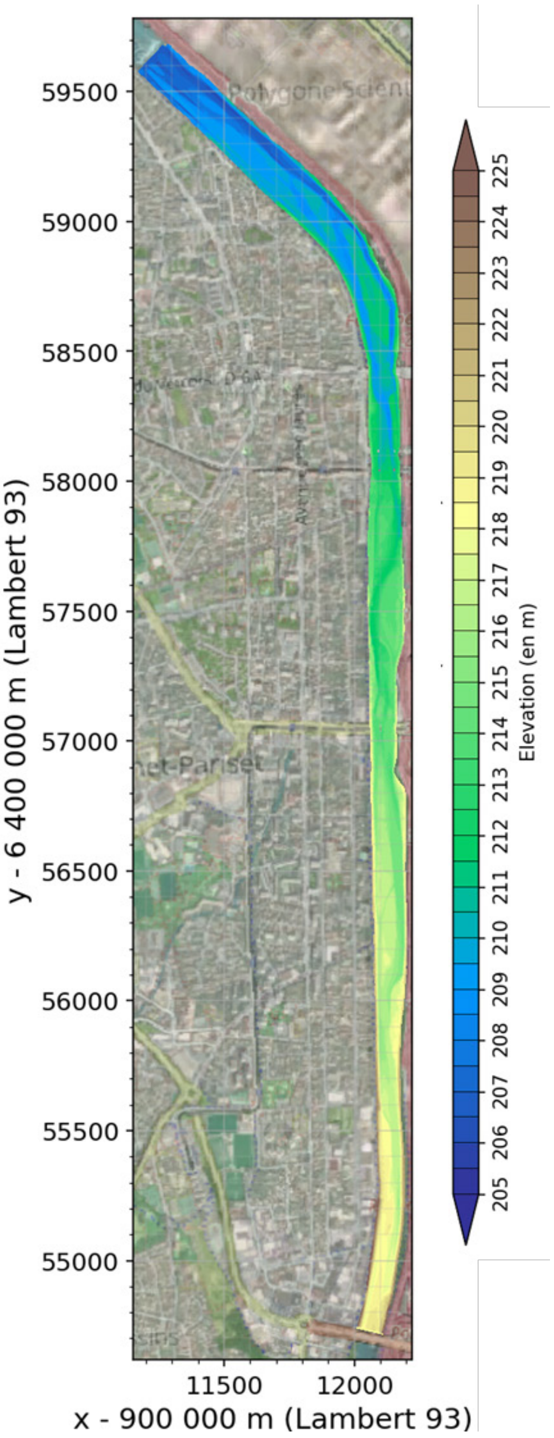

Figure 1. Bathymetry of the Drac model along Grenoble

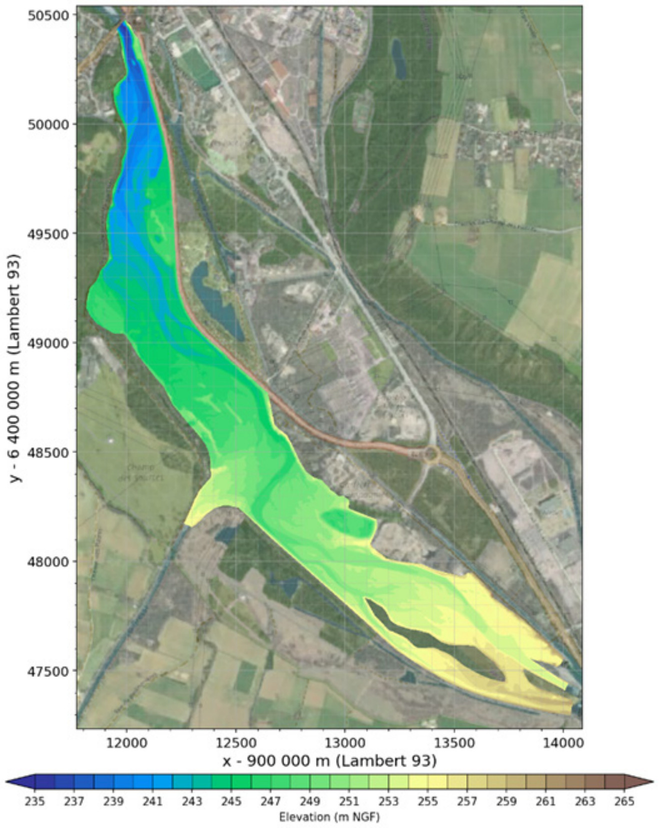

Figure 2. Bathymetry of the upstream Drac model

B. *The physics*

The formulations and parameters used for the calculations , are very similar to the ones used in SISYPHE by the first author, dating back from 2007 ([2]), on rivers such as the Rhône and the Arc, whose bed presents a similar pebble-size as the Drac. The formulation for bedload flux estimation is based on Meyer-Peter Müller equation without the notion of grain shear stress, and can be used considering uniform (single size-class) or graded (multiclass: 8 classes) sediment. In the case of graded sediment, the impact of the grain-size distribution on the erosion threshold of size-classes (so called "hiding-exposure" processes) is simulated using a simple hiding function of Parker and Klingeman with an exponent of -0.8 (an exponent of -1 corresponding to equal mobility). In both cases (graded or uniform sediment), friction law in TELEMAC-2D is linked (through a roughness length formulation) with the representative grain size of the bed.

Recent work ([1]) has enabled to further validate these formulations, and to improve significantly the link between grain size and bed friction. The "variable power equation" of Ferguson [3] was used as friction law in TELEMAC-2D. This equation uses the D_{84} as a "friction coefficient". The D_{84} of the active layer in GAIA is used directly as input of the friction law in TELEMAC 2D, thus having a friction which is taking the local surface grain size distribution and its variation over time into account. The significant role (and improvement) of this coupling of friction and grain size in the computation of morphodynamics has been demonstrated in [1], at least for the case simulated at the time. Note that an implementation of Ferguson formula in TELEMAC-2D system had already been proposed, validated and presented by [4].

IV. CALIBRATION

A. *Water elevation*

The alibration of a hydraulic model with a mobile bed poses a very serious challenge because of the interaction between hydrodynamics and sediment transport. Indeed, one must be certain that the bathymetry in the model during the flood is well represented in order to properly calibrate the hydrodynamic model on known water levels. And of course, the sediment transport model (and thus the bathymetry simulated by the model) is strongly dependant on the hydrodynamics. Hydrodynamics and sediment transport must thus be calibrated simultaneously, meaning a very large number of parameters. The only hope of solving this conundrum lies in improving strongly the physics captured by the formulations, and thus strongly reducing the variability of the parameters (the ultimate goal being to be able to set these parameters a priori).

In our case, no data of morphological evolution during flood is available because no significant flood happened on the Drac river in recent times, which is making a proper calibration even less possible. A large-scale hydrodynamic model (TELEMAC-2D) had previously been calibrated based on "historic" flood and on recent water lines surveyed during moderate flows. This previous model has been used here as a reference to be compared to the hydrodynamic results of our new model.

B. *Bedload fluxes*

The embanked reach along Grenoble is the place for which different estimates of solid fluxes have been produced, both by diachronic analysis of the bathymetry (and the fact that all coarse sediment transport is trapped in an hydropower reservoir downstream of this reach) and by direct measurement through sampling and hydrophone surveys [5].

On the corresponding model, a methodology for long term modelling has been developed in order to be able to compare the yearly estimates of bedload fluxes from surveys to the yearly model results. This methodology consists in basing the time series of liquid inflows on the flow duration curve (separated in a rising limb and a decreasing limb), along with a morphological factor (consisting in an "acceleration" of the hydrograph, which is compensated from a morphological point of view by an amplification of the bedload fluxes during the solving of Exner equation). An optimisation of the use of the morphological factor (through a variation of this factor along the discharge time-series) is proposed later in a specific paragraph.

The only parameter used for the calibration of the morphological model on yearly sediment fluxes is the critical Shields parameter. A value of 0.045 is retained, which enables to obtain a yearly sediment flux of 15 000 to 40 000 m^3 (depending on the location in the reach), which is roughly in line with the aforementioned estimations reported in [5], which range from 17 000 to 27 000 m^3.

In our case (a gravel bed river with hydrodynamics influenced by dams), the most significant flows contributing to the transported sediment volume are rather low, corresponding to a rather low transport stage. For this kind of transport stage, the sensitivity of the model results to the value of the critical Shields parameter is huge: a value of 0.04 for the critical Shields parameter generated a yearly sediment flux 2-3 times higher than the calibrated value of 0.045. This very strong variability of the results with the main parameter renders totally unrealistic the dream of dispensing of a model calibration.

V. VARIABLE MORPHOLOGICAL FACTOR

The use of a morphological factor is a well-known methodology for dramatically reducing the computational demands of morphological long-term simulations.

It consists in imposing an amplification (by a so-called morphological factor, or "MOFAC") of the bedload fluxes during the solving of Exner equation, so that the simulated morphological evolution corresponds to a timeframe which duration equals the duration of the simulation hydrograph multiplied by the morphological factor. The available flow duration curve (limited to discharges above 80 m^3/s as below this value solid discharge is negligible according to hydrophone surveys presented in [5]) is used to build an average yearly hydrograph with a rising limb a decreasing limb. This hydrograph is then "compressed" or "accelerated" by the MOFAC so that the TELEMAC-2D/GAIA run based on this hydrograph is representative of one year.

If this methodology is applied with a constant MOFAC (see for instance the black curve in Figure 3, with a MOFAC of 200), numerous difficulties arise, linked with the steepness of the hydrograph for the highest discharges. First, spurious hydrodynamic effects might appear because of the steepness of the flood, which can increase the water slope. Secondly, the fact that solid discharge during high flows is amplified means that the hypothesis of non-coupling between hydrodynamics and morphodynamics at the time-step scale might not be so well fulfilled. Finally, the constant output period in GAIA must be very fine (thus generating very large results file) so that the results during the high flows can be captured adequately.

In order to circumvent these problems, a methodology involving a variable MOFAC has been developed. The idea behind it consists in making MOFAC vary depending on the rate of variation of the hydrograph: the higher the rate of variation (during the peak of the hydrograph), the lowest the MOFAC (with a minimum value of 1). The different steps of the methodology are the following:

1) Generation (through a spreadsheet) of a time series of MOFAC and the corresponding input hydrograph (presented in blue in Figure 3)

2) Modification of GAIA source code to make MOFAC variable according to a text file containing the time series of MOFAC

3) Use of a script to convert to real time TELEMAC-2D and GAIA result file (which use a "variably compressed time" similarly as the input hydrograph).

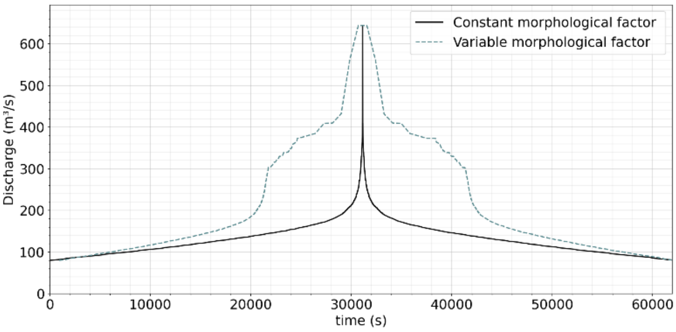

Figure 3. Input hydrograph for constant morphological factor and for variable morphological factor

VI. IMPACT OF SEDIMENT TRANSPORT ON FLOOD LEVELS

We endeavour here to determine if, as previously thought, sediment transport during flood might have a significant effect on water levels during flood. Indeed, since a rocky gorge at the downstream end of the upstream model creates a strong backwater effect during floods, it was expected that the area upstream of the gorge could undergo significant deposition, which would in turn raise the water levels.

To check this, the results on the bicentennial flood of the TELEMAC-2D/GAIA sediment transport model as described above (with graded sediment, and Ferguson friction law coupled with the grain size of the active layer) are compared (see Figure below) to the results of the same model with no bathymetric evolution. Longitudinal profiles of maximum water levels are presented in the figure below.

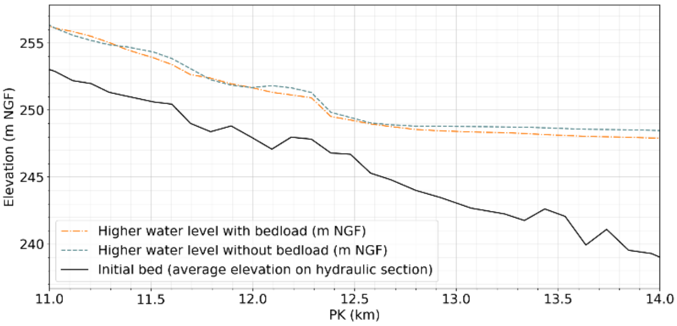

Figure 4. Comparison of maximum water levels computed on the upstream Drac model during 200-years flood.

Contrary to previously thought, it appears that sediment transport tends to decrease the maximum water levels reached during the flood.In our opinion, this stems first from the fact that during floods there is no large influx of sediment to be expected at the upstream boundary of the model because of the presence of hydropower plants upstream. In addition, simulated morphodynamic evolution during the rising limb of the flood tends to have a smoothing effect on bed bathymetry. This can be seen by comparing Figure 5, which shows the bathymetry of the upstream model at the 200-years flood peak, to Figure 2, which shows the initial bathymetry of the same model. During the flood peak, the main channel tends to fill while some banks tend to lower, and the whole bed width, which is smoothened and therefore generates lesser form drag, conveys the flow. This pattern is also shown in Figure 6 which shows bed evolution at the flood peak.

Contrary to what happens during the rising limb of the flood hydrograph, morphological patterns tend to reappear during the decreasing limb of the flood hydrograph (see bathymetry at the end of the 200-years flood in Figure 7), in particular with some channel incision compared to the flood peak bathymetry (although not enough to reach a similar morphology as what can be observed in the initial bathymetry).

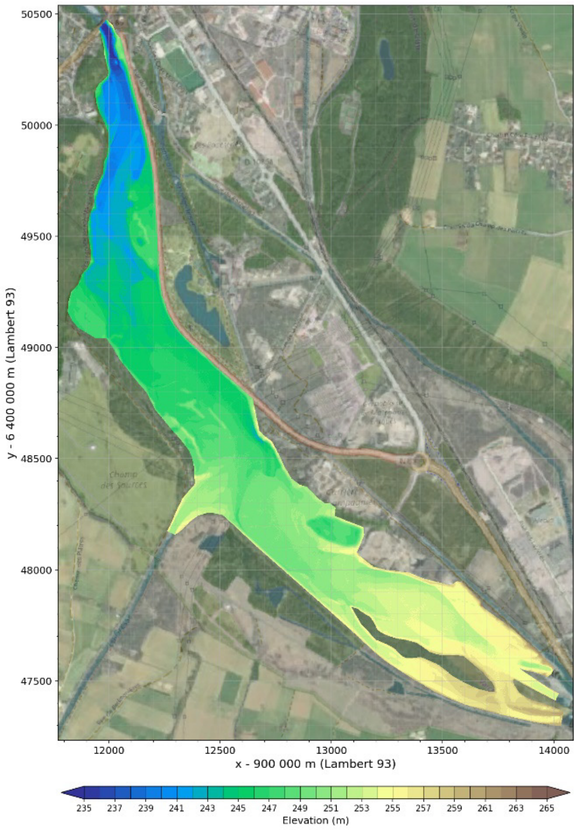

Figure 5. Simulated bathymetry of the upstream Drac - 200-years flood peak

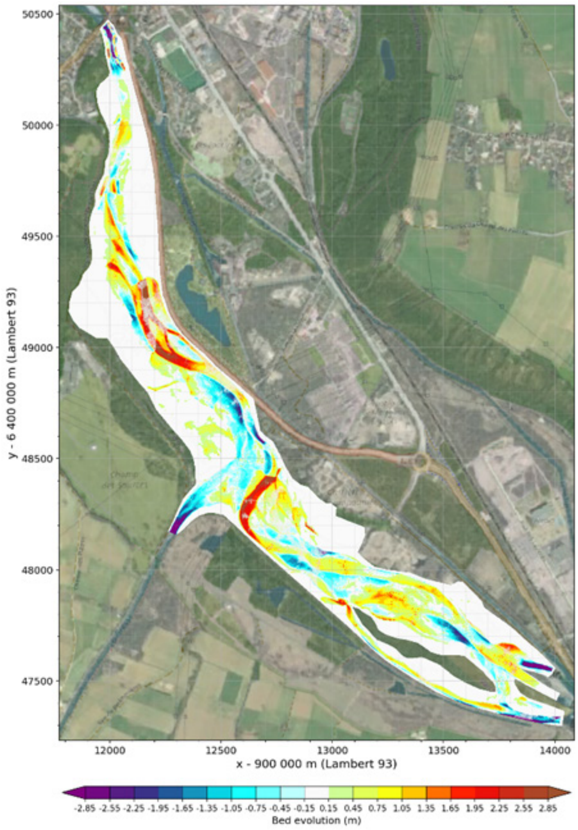

Figure 6. Bed evolution of the upstream Drac – 200-years flood peak

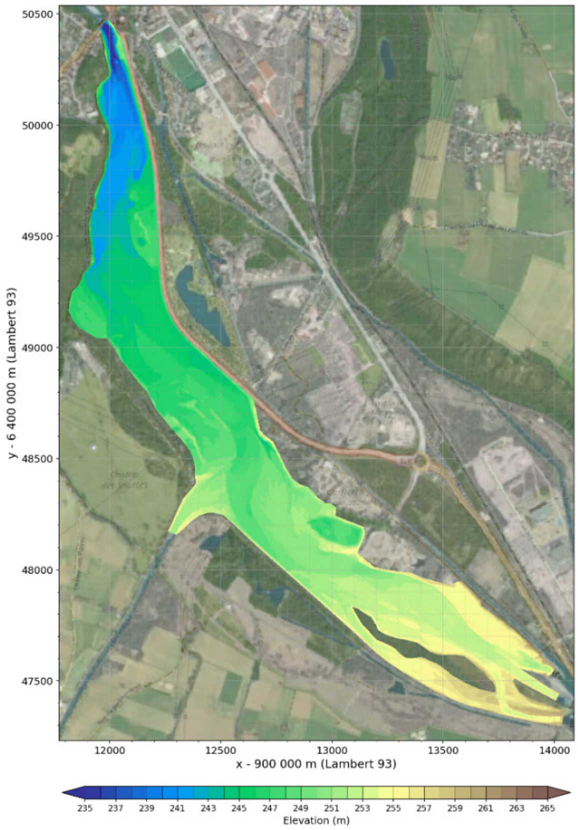

Figure 7. Bathymetry of the upstream Drac – end of the 200-years flood

VII. ROLE OF GRADED SEDIMENT ON MORPHODYNAMICS RESULTS

Previous work ([1]) had shown that, at least for the specific case simulated at the time (which involved massive deposition of coarse sediment), modelling of the coupling between (variable in space and time) grain-size distribution and bed friction was necessary to simulate correct morphodynamics patterns (in particular channel meandering and avulsion).

Sediment transport on the Drac river at our study sites is quite different, in particular because of the sediment depletion generated by upstream hydropower plants. We test here if the impact of the modelling of graded sediment and its interaction with hydraulic friction is as important as in [1]. To do this, the results in terms of bathymetric evolution for the 200-years flood with graded sediment (result presented previously) are compared with results for the same run considering a single grain size (corresponding to de D_{50} of the initial sediment gradation of the multiclass model). For Friction, Ferguson law is also applied, with a D_{84} constant in space and time.

Results in terms of bathymetric evolution for the single grain size model are presented in Figure 8 below.

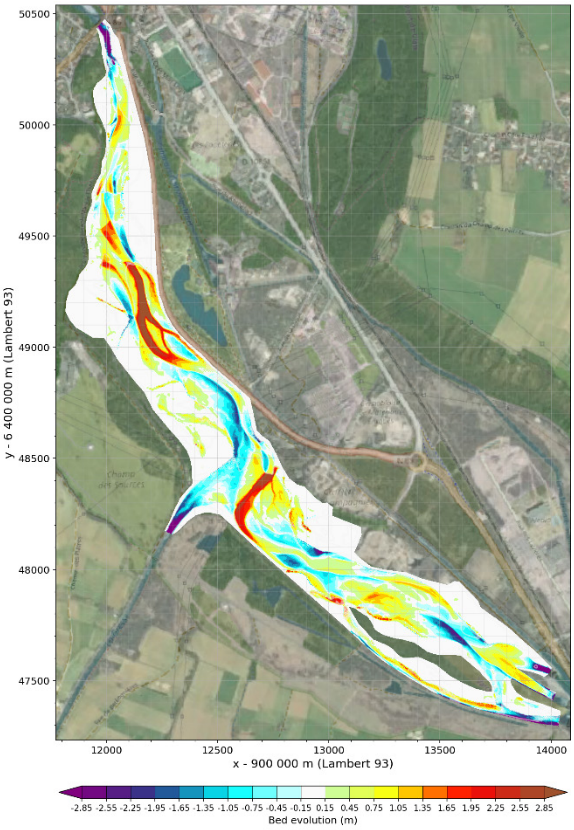

Figure 8. Bed evolution of the upstream Drac – 200-years flood peak - single-grain size model

The comparison of Figure 6 (bathymetric evolution with graded sediment) with Figure 8 (bathymetric evolution with single grain size sediment) indicates that bed evolutions are very similar in both cases. The results with the single grain size model tend to show deeper incision, which show the direct impact of paving generation with the graded-sediment model.

The results of this test thus show that, contrary to the results of [1], using graded sediment (and its interaction with friction) has no effect here on simulated morphodynamic patterns. This probably stems from the fact that because of the low sediment input, braiding (which was the main pattern observed in [1]) cannot happen in the model of the Drac river.

VIII. CONCLUSION

The different results presented here highlight some of the challenges posed by morphodynamic modelling in gravel-bed rivers.

Mesh size is a very important factor in obtaining results relatively free of numerical instabilities. Therefore, the duration of computation can become problematic. A methodology based on a variable morphological factor is proposed to enable long term simulations.

In our case, due to the influence of hydropower on hydrology, no definitive data for hydraulic or morphodynamic calibration could be found. The formulations and parameters used had been calibrated on a previous (and rather different case). Here, they provided (nearly) "out of the box" results that seem realistic when compared to the limited available data. More work (and in particular more experience feedback) remains necessary to improve the confidence in the formulations used.

For the specific study for which the presented models were built, a global 1D model (with CAVALCADE) has also been built to compute longitudinal bed evolution of the whole river reach studied. It gives similar general trends of deposition and erosion than the 2D models presented here (in the common river reaches), but it is much less dynamic (with smaller sediment fluxes) for the largest flood simulated, which indicate the inherent uncertainty of this kind of modelling.

ACKNOWLEDGEMENT

The work presented in this paper is part of the design studies for the "PAPI Drac" works and is funded by SYMBHI.

REFERENCES

[1] de Linares, M., Ronzani, F., Recking, A., Mano, V., Piton, G. 2022. Coupling Surface Grain-Size and Friction for Realistic 2D Modelling of Channel Dynamics on Massive Bedload Deposition. In: Gourbesville, P., Caignaert, G. (eds) Advances in Hydroinformatics. Springer Water.

[2] de Linares, M. "Modélisation numérique bidimensionnelle du transport solide et de la dynamique fluviale. Validation sur deux sites en Loire et sur l'Arc". Université Joseph Fourier – Grenoble, 2007

[3] Ferguson, R. 2007. Flow resistance equations for gravel-and boulder-bed streams. Water Resources Research. 43.

[4] Gegenleithner, S., Dorfmann, C. and Schneider, J. 2021 New friction law for TELEMAC-2D (Ferguson, 2007). Presentation at TELEMAC Scientific Committee

[5] Nasr, M. "Development of an acoustic method for bedload transport measurement in rivers". Université Grenoble Alpes, 2023

TELEMAC hydrodynamic models over time: A case study with the Danube

Stanko Stankov, W. Alexander Breugem, Mariana Damova, Theofano Koutrouveli, Boudewijn Decrop
mariana.damova@mozajka.co, Sofia, Bulgaria
stanko.stankov@mozajka.co, Sofia, Bulgaria
alexander.breugem@imdc.be, Antwerp, Belgium
theofano.koutrouveli@imdc.be, Antwerp, Belgium
boudewijn.decrop@imdc.be, Antwerp, Belgium
Mozaika, Ltd.
http://www.mozajka.co
IMDC
https://imdc.be/

***Abstract* – The Danube River, an essential waterway in Europe, poses complex hydrodynamic challenges due to its varying flow conditions. In this study, we focus on the Bulgarian segment of the Danube River to compare the TELEMAC simulations with different mesh configurations and assess the differences when used with real and with forecasted water level and discharge data. We study the riverbed in two points in time – 2010 and 2017 to investigate the accuracy of the TELEMAC simulations. The study area encompasses one hydrodynamic environment along the Bulgarian stretch of the Danube River. To evaluate the performance of the TELEMAC simulations, we compare the model results from forecasts obtained from in-situ measurements, referred to as real data and from forecasts obtained from high-resolution earth observation data of meteorological features like precipitations, soil moisture, vegetation index, combined with in-situ measurements. The analysis focuses on key hydrodynamic variables, such as water velocities, free surface elevation and riverbed. In addition, we explore the discrepancies between real and forecasted data when incorporating GAIA sediment transport data into the TELEMAC simulations. We assess the impact of this data source on model performance, identify potential areas for improvement in sediment transport modelling and data assimilation techniques. This paper contributes to the advancement of river engineering practices and the development of more accurate and reliable hydrodynamic models for decision-making and flood risk management in the Danube River Basin and beyond.**

Keywords: TELEMAC, GAIA, Danube, River, Forecast, AI.

I. INTRODUCTION

The TELEMAC software is recognized for its ability to perform 2D and 3D modelling of various hydrodynamic phenomena, including the movement and behaviour of water bodies, sediment transport, and water quality assessments. TELEMAC employs the finite element method to the shallow water equations , allowing it to simulate and predict a wide range of scenarios [10].

The Danube River, with its diverse geographical and hydrological features, is a perfect example for this study. As one of Europe's longest and most important rivers, traversing multiple countries, it presents a myriad of hydrodynamic phenomena. The complexity and diversity of the Danube make it a suitable site for demonstrating the robustness and versatility of the TELEMAC system.

The TELEMAC system has been instrumental in predicting and understanding the hydrodynamic behaviour of the Danube [13,2]. Researchers have leveraged this tool to anticipate a range of scenarios, encompassing potential flood incidents, patterns of sediment transport, and water quality parameters [6].

This case study takes a closer look at a specific segment of the Danube River - the area around Svishtov in Bulgaria. Svishtov is located in the middle part of the Bulgarian segment of the Danube.

Our study examines how the hydrodynamic models outputs have evolved when used with data from two time periods with 10 years difference. This article provides a detailed exploration of comparing hydrodynamic models derived with real and with forecasted data using TELEMAC. It is important to note that this comparison involves two distinct meshes, and the resulting data is displayed through charts and tables for a more visual analysis. Two types of data for the hydrological features – discharge and water level were used for the experiment – real data gathered from in-situ measurements and forecasted data generated by a trained neural network. The comparison reveals a significant similarity between real and forecasted data due to the high accuracy of the forecasting model.

II. PREPARATION

Mesh comparisons provide insight into geographical changes, environmental dynamics, and various anthropogenic effects.

This examination is centred around comparing two distinct meshes, one from 2010 and the other from 2017, both depicting the Danube region around Svishtov, an area of significant economic and ecological importance. The differences and similarities between these meshes will help us understand the changes that occurred in the river morphology over these seven years.

Such analyses can lead to conservation strategies and environmental impact predictions for future development.

For the Bulgarian segment of the Danube River around Svishtov, two unique Selafin objects were developed using BlueKenue, each with a mesh resolution of 50 meters. The 2010 mesh represents a river segment of 45.5 km in length and width of 0,67 km at the west end edge and around 1,2 km at the east end edge.

The first Selafin object is based on bathymetric data, the riverbed, from 2010 (see Figure 1). This object was tailored to encapsulate the unique topographical and hydrological features of the critical area of Danube river around Svishtov.

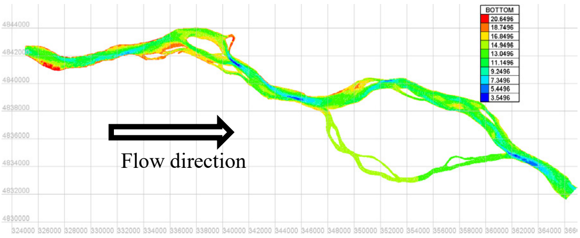

Figure 1. Mesh of the area around Svishtov with data from 2010

The second Selafin object with bathymetric data, the riverbed, was developed using data from 2017 (see Figure 2). This object was designed to model the critical area of the Danube River around Svishtov, focusing on a different set of hydraulic conditions and characteristics. It has a length of 57.2 km and features river width of around 0,7 km meters at the west end edge and 0,9 km meters at the east end edge of the mesh.

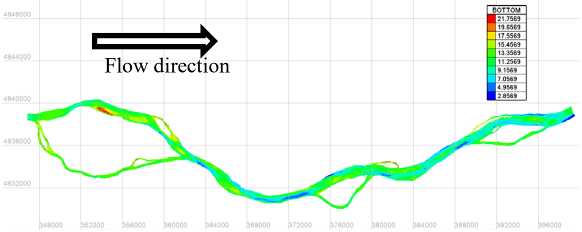

Figure 2. Mesh of the area around Svishtov with data from 2017

To provide fair comparison the common parts of the two meshes were extracted and studies. Figure 3 below shows the riverbed in years 2010 to the left and 2017 to the right in this common parts of the mesh of approx. 20 km river length with width of ~0,7 km in the west end edge and ~1,2 km at the east end edge. The differences in the riverbed in 2010 and 2017 can be clearly seen through the different colours of the two images.

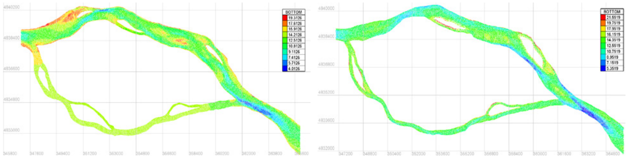

Figure 3. Common area between the meshes from year 2010 and 2017

It can be seen with bare eye that the colors of the two mesh images differ, indicating the difference in the riverbed in the two years 2010 and 2017 with deeper stretches in 2010 and shallower stretches in 2017.

Upon the generation of these meshes, boundary conditions were established. At the upstream boundary discharge is prescribed, whereas water level is used at the downstream boundary.

In conjunction with the creation of these Selafin objects, a comparative analysis was performed to highlight the differences between the two datasets using the common area and a thalweg. These differences are illustrated in Figure 4, which explicitly displays the changes in the bathymetry between 2010 and 2017, the curve in red for 2010 and the curve in green for 2017. The x axis shows the mesh stretch in consecutive points and the y axis shows the coresponding depth in meters. It shows similarities and discrepancies in the curves that correspond to the two images on Figure 3. Some of the discrepancies might be due to the seasonal effects of the different time of the year the two bathymetry measures have been performed, though.

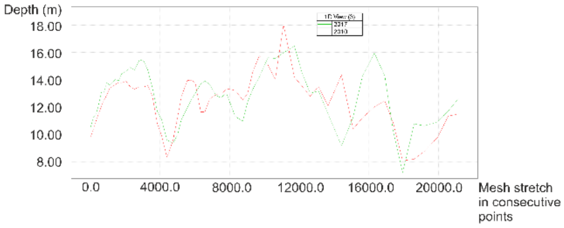

Figure 4. Difference in the Riverbed of the common area between the two bathymetries for years 2010 (red) and 2017 (green).

The development of two unique Selafin objects for the Bulgarian segment of the Danube River around Svishtov has provided important insight about the river's hydraulic and topographical changes over the years. Through the use of high-resolution meshes and the careful application of boundary conditions, it has been possible to accurately model the specific features and conditions of this segment of the river in 2010 and 2017. Not only does this provide a detailed snapshot of the past, but it also lays a robust foundation for predicting future conditions.

III. FORECASTING METHOD

Building on the constructed meshes, we insert timeseries of forecasted values for discharge and water levels in order to obtain TELEMAC simulations and output of forecasted values for a series of hydrodynamic features [7], supporting informed decision-making for the region's future.

For the forecasts of discharge and water level we adopt an EO4AI[1] method, where we use earth observation data describing meteorological features, such as precipitations, soil moisture, vegetation index, snow cover, solar irradiance, each offering a unique viewpoint on the environmental and hydrological conditions impacting the Danube River, mixed with timeseries with daily in-situ measurements for discharge and water level and apply them to a pipeline of neural network architectures using the TensorFlow framework [11]. These include Convolutional Neural Networks (CNNs), known for their pattern recognition prowess; Long Short-Term Memory networks (LSTMs), which effectively handle long-term dependencies in time series data; Recurrent Neural Networks (RNNs), ideal for short-term forecasting due to their proficiency in recognizing temporal patterns and Convolutional Long Short-Term Memory networks (ConvLSTMs), combining the spatial pattern recognition of CNNs with the temporal dependency capturing of LSTMs.

Given its proficiency with sequential data, the ConvLSTM is a fitting choice for the task of generating forecasts. It processes timeseries data, learns from historical patterns, and forecasts future water levels and discharge rates.

The method generates forecasts for 30 days into the future, a critical aspect of this study. It enables us to project the potential changes in the Danube River's conditions over a month, providing useful insights that could inform river management decision-making and planning processes.

The satellite data come from ADAM (adamplatform.eu), through ESA NoR service. They provide the data from different satellites depending on the meteorological feature required, including for example SMOS, MODIS, SENTINEL, IMERG. This allows us to provide with a unique set of data allowing for a comprehensive environmental and hydrological assessment of the Danube River region. The combination of these satellite data ensures a multifaceted understanding of the environmental and hydrological conditions impacting the Danube River region. They not only help in understanding the current conditions but also aid in making accurate forecasts for future developments.

IV. EXPERIMENTS WITH TELEMAC SIMULATIONS

Experiments with TELEMAC simulations were made using two different meshes from the years 2010 and 2017. Each of these meshes were paired with measured Liquid Boundary File (LBF) containing real data and forecasted data. For the simulation we have adopted the following hydrological features: VELOCITY U, VELOCITY V, FREE SURFACE, BOTTOM and FRICTION.

A visual representation of one of these variables – velocity U, faciliating a comprehensive spatial understanding is shown (see Figure 5).

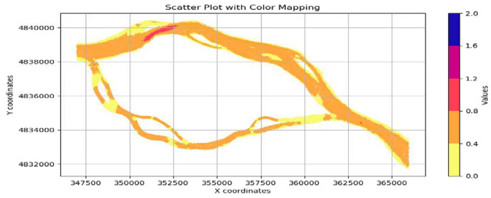

Figure 5. Velocity U output from Telemac on a maps plot

The use of two meshes in the experiment allows to explore and analyse the outputs of the simulations with data of two different time periods.

We used timeseries of daily data for discharge and water level from year 2015 to year 2019 to generate simulations with the two meshes, the 2010 and the 2017 one, their resolution being of 50 meters.

The visual representations, such as the one shown on Figure 5, of the experiment output facilitate a clear comparison between real and forecasted data. The differences between the results of the TELEMAC simulation are detailed in the comparison section, underscoring its reliability in forecasting future hydrodynamic conditions.

V. COMPARISON PROCESS

The comparison process involves extracting data from the four Selafin objects generated from both real and forecasted data simulations for the 2010 and 2017 meshes. This data is then cross-examined, and provide insight into the performance and reliability of the forecasting model used.

In studying river dynamics, it is crucial to focus on the most informative features. In this context, the 'FREE SURFACE' and 'VELOCITY MAGNITUDE' were selected. The ‘FREE SURFACE’ offers crucial information about the elevation of the water level, which is essential in predicting flood events and understanding water flow patterns. On the other hand the 'VELOCITY MAGNITUDE' delivers a comprehensive perspective on both the speed and direction of water flow in the river. This is a key aspect for interpreting erosion rates, sediment transport, and overall river hydrodynamics. Importantly by having a clear understanding of the velocity components (along the X and Y axis), we can calculate the 'VELOCITY MAGNITUDE', which provides a more complete picture of the river flow dynamics and speed. Examining these variables at the upstream, middle stream and downstream points of the river provides a more holistic understanding of the behaviour of the Danube River.

We examined thoroughly how the river's state varied over time by analysing it for the two time periods covered. Thus, we have been able to observe the intricate transformation patterns of the river. This has enabled us to highlight the various states the river can transition through and to predict future scenarios based on our observations.

The extraction of these parameters was performed on all four Selafin objects. Once extracted the values of the processed features can be visualized and studied using various toolsets. For visualization of the ‘FREE SURFACE’ variable in the upstream

---

[1] EO4AI – Earth observation for AI

see Figure 6, where the date is on the x axis and the depth is on y axis in measurement unit of meters (M). It shows a comparison between the 'FREE SURFACE' feature and the calculated magnitude from the hydrodynamic model, built with the 2010 data for the mesh and that of hydrodynamic model, built with data 2017 data for the mesh, utilizing both real and predicted values. Figures 6 – 8 below show these comparisons for three points - upstream, middle stream and downstream one.

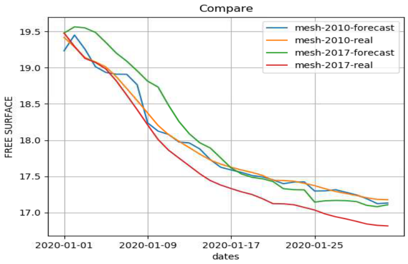

Figure 6. Free surface comparison for upstream

A comparison for the middle stream has been made for the free surface variable (see Figure 7).

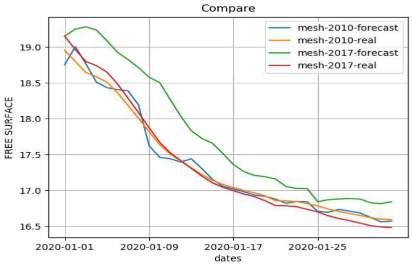

Figure 7. Free surface comparison for middle stream

A comparison for the downstream has been made for the free surface variable (see Figure 8).

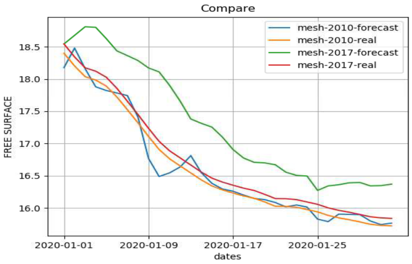

Figure 8. Free surface comparison for downstream

Same comparison has been made for the VELOCITY MAGNITUDE. The result for a upstream point is shown below (see Figure 9).

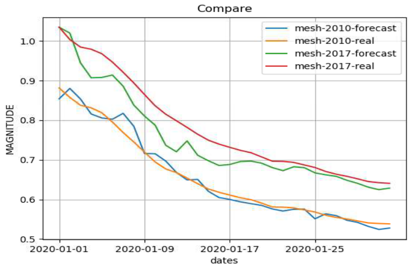

Figure 9. Magnitude comparison for upstream

A comparison for the middle stream has been made for the velocity magnitude (see Figure 10).

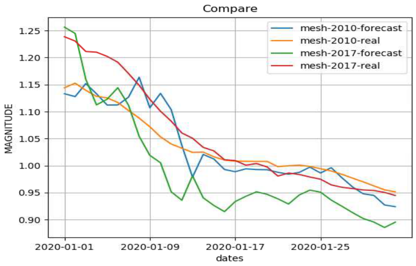

Figure 10. Magnitude showing middle stream

A comparison for the downstream has been made for the velocity magnitude (see Figure 11).

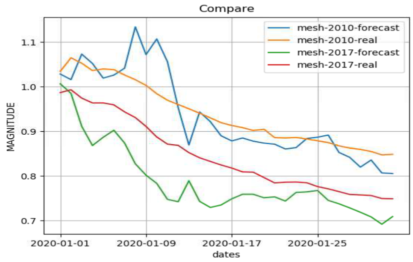

Figure 11. Magnitude showing a downstream

For further clarity, the comparison of the FREE SURFACE is shown in numerical values measured in meters (M) (see Table 1).

Table I Free surface bathymetries 2010 / 2017 with Real (R) and Forecasted (F) upstream / middle stream and downstream

Up stream / Date	**2010 bathymetry F (M)**	**2010 bathymetry R (M)**	**2017 bathymetry F (M)**	**2017 bathymetry R (M)**
1/1/2020	19.48	19.48	19.23	19.42
1/2/2020	19.56	19.29	19.45	19.28
1/3/2020	19.55	19.13	19.25	19.14
1/4/2020	19.49	19.07	19.01	19.08
Middle stream / Date	**2010 bathymetry F (M)**	**2010 bathymetry R (M)**	**2017 bathymetry F (M)**	**2017 bathymetry R (M)**
1/1/2020	19.15	19.15	18.75	18.95

1/2/2020	19.25	18.96	19	18.8
1/3/2020	19.28	18.8	18.77	18.65
1/4/2020	19.24	18.74	18.51	18.59
Down stream / Date	**2010 bathymetry F (M)**	**2010 bathymetry R (M)**	**2017 bathymetry F (M)**	**2017 bathymetry R (M)**
1/1/2020	18.54	18.54	18.18	18.4
1/2/2020	18.68	18.34	18.48	18.2
1/3/2020	18.81	18.17	18.16	18.04
1/4/2020	18.8	18.12	17.88	17.98

In Table II, we present the calculated VELOCITY MAGNITUDE in meters per second (M/S) values derived from Figures 9,10 and 11.

Table II Magnitude between bathimetries 2010 / 2017 with real and forecasted data for up stream middle stream and down stream

Up stream / Date	**2010 bathymetry F (M)**	**2010 bathymetry R (M)**	**2017 bathymetry F (M)**	**2017 bathymetry R (M)**
1/1/2020	19.48	19.48	19.23	19.42
1/2/2020	19.56	19.29	19.45	19.28
1/3/2020	19.55	19.13	19.25	19.14
1/4/2020	19.49	19.07	19.01	19.08
Middle stream / Date	**2010 bathymetry F (M)**	**2010 bathymetry R (M)**	**2017 bathymetry F (M)**	**2017 bathymetry R (M)**
1/1/2020	19.15	19.15	18.75	18.95
1/2/2020	19.25	18.96	19	18.8
1/3/2020	19.28	18.8	18.77	18.65
1/4/2020	19.24	18.74	18.51	18.59
Down stream / Date	**2010 bathymetry F (M)**	**2010 bathymetry R (M)**	**2017 bathymetry F (M)**	**2017 bathymetry R (M)**
1/1/2020	18.54	18.54	18.18	18.4
1/2/2020	18.68	18.34	18.48	18.2
1/3/2020	18.81	18.17	18.16	18.04
1/4/2020	18.8	18.12	17.88	17.98

The detailed comparison of the 'FREE SURFACE' and the 'VELOCITY MAGNITUDE' yielded significant insights into the performance of the two models. As evidenced by the tables and charts, the forecasted data from both models aligns closely with the real-world observations. Whether considering FREE SURFACE levels or VELOCITY measurements, the predicted values exhibit a strong similarity to the actual ones, which speaks volumes about the models' accuracy and reliability.

Tables I and II clearly demonstrate the close alignment of forecasted and real-world observations for both 'FREE SURFACE' and the 'VELOCITY MAGNITUDE'. This similarity underscores the effectiveness of our forecasting models, bolstering our assurance in their ability to predict the hydrodynamic behaviour of the Danube River with considerable accuracy.

VI. GAIA COMPONENT

To further expand our analysis on the Danube area around Svishtov, we turned to GAIA - another powerful modelling tool designed for the study and prediction of sediment transport phenomena. GAIA is specifically known for its ability to model sedimentary processes and their interaction with hydrodynamics [4]. In the GAIA configuration we have selected type of sediment to be NCO and we have set CLASSES SEDIMENT DIAMETERS with the value of 323D-6.

For the sediment transport equation we have used Engelund-Hansen sediment transport equation. It is an explicit function of stream power (V2τ3/2) and the d50 of the material [3]. It is not an "excess" stream power equation, so it does not control for competence and often can, therefore, compute low transports for large grain classes. Engelund-Hansen should usually be restricted to sand systems.

Within the context of this study, we utilized GAIA to extract two important hydrodynamic variable: the 'BED SHEAR STRESS' and 'CUMUL BED EVOL'. Measured in Newtons per square meter (N/m^2), this variable quantifies the force exerted by flowing water on the river bed. It provides crucial insights into sediment transport and erosion patterns, which are integral to understanding and forecasting the overall behaviour and evolution of the Danube River. Using the same approach as with the variables free surface and magnitude we have plotted the BED SHEAR STRESS (see Figures 12,13 and 14) showing on the x axis the dates and on y the calculated value.

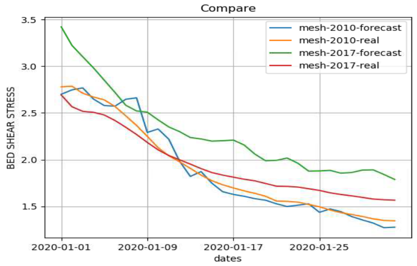

Figure 12. Bed shear stress showing a upstream

A comparison for the middle stream has been made for the bed shear stress (see Figure 13).

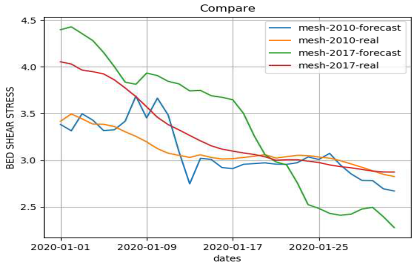

Figure 13. Bed shear stress showing a middle stream

A comparison for the downstream has been made for the BED SHEAR STRESS (see Figure 14).

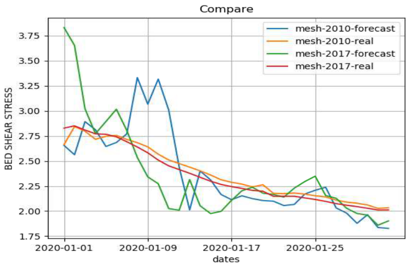

Figure 14. Bed shear stress showing a downstream

For a table view of the BED SHEER STRESS see table III.

Table III Bed shear stress bathimetries 2010 / 2017 with real and forecasted data for up stream, middle stream and down stream

Up stream Date	2010 bathymetry F (N/m2)	2010 bathymetry R (N/m2)	2017 bathymetry F (N/m2)	2017 bathymetry R (N/m2)
1/1/2020	3.42	2.69	2.7	2.78
1/2/2020	3.22	2.57	2.75	2.79
1/3/2020	3.1	2.52	2.77	2.71
1/4/2020	2.98	2.51	2.65	2.67
Middle stream Date	**2010 bathymetry F (N/m2)**	**2010 bathymetry R (N/m2)**	**2017 bathymetry F (N/m2)**	**2017 bathymetry R (N/m2)**
1/1/2020	4.4	4.05	3.38	3.42
1/2/2020	4.43	4.03	3.31	3.5
1/3/2020	4.35	3.96	3.5	3.44
1/4/2020	4.28	3.95	3.43	3.39
Down stream Date	**2010 bathymetry F (N/m2)**	**2010 bathymetry R (N/m2)**	**2017 bathymetry F (N/m2)**	**2017 bathymetry R (N/m2)**
1/1/2020	3.83	2.83	2.65	2.66
1/2/2020	3.65	2.85	2.56	2.84
1/3/2020	3.02	2.81	2.89	2.8
1/4/2020	2.77	2.77	2.81	2.72

From Figures 12, 13, 14 and Table III, we can see that the predicted 'BED SHEAR STRESS' values from the two models align differently at various points with the observed data due to Danube River's hydrodynamic conditions. This shows the effect of the application of the different data about the river's flow for the two models, that lead to different predictions of the BED SHEAR STRESS.

CUMULATIVE BED EVOLUTION (CUMUL BED EVOL) is the other parameter through which we measured the difference in the simulations with data from the two time periods 2010 and 2017. It is a process by which the bed of a river or stream changes over time due to the deposition and erosion of sediment. This process is driven by a number of factors, including the flow of water, the composition of the sediment, and the slope of the riverbed.

On Figure 15 is shown the chart of CUMUL BED EVOL upstream displaying the date on the x axis and the corresponding value on y in meters.

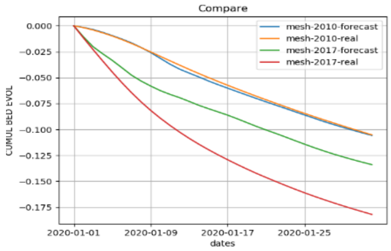

Figure 15. Cumul bed evol showing a upstream

A comparison for the middle stream has been made for the CUMUL BED EVOL (see Figure 16).

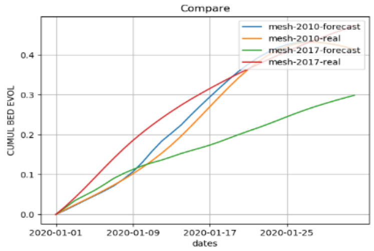

Figure 16. Cumul bed evol showing a middle stream

Same comparison has been made with a point on the downstream (see Figure 17).

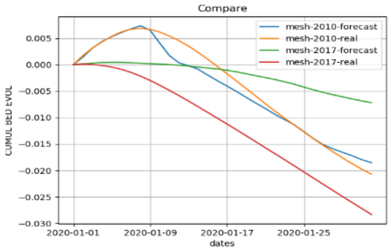

Figure 17. Cumul bed evol showing a downstream

In Table IV, we present the cumulative bed elevation from figures 15,16 and 17.

Table IV Cumul bed evol bathimetries 2010 / 2017 with real and forecasted data for upstream, middle stream and downstream

Up stream Date	2010 bathymetry F (M)	2010 bathymetry R (M)	2017 bathymetry F (M)	2017 bathymetry R (M)
1/1/2020	0	0	0	0
1/2/2020	-0.01	-0.01	0	0
1/3/2020	-0.02	-0.02	0	0
1/4/2020	-0.03	-0.03	-0.01	-0.01
Middle stream Date	**2010 bathymetry F (M)**	**2010 bathymetry R (M)**	**2017 bathymetry F (M)**	**2017 bathymetry R (M)**
1/1/2020	0	0	0	0
1/2/2020	0.02	0.02	0.01	0.01
1/3/2020	0.04	0.04	0.02	0.02

1/4/2020	0.05	0.07	0.03	0.04

Down stream Date	2010 bathymetry F (M)	2010 bathymetry R (M)	2017 bathymetry F (M)	2017 bathymetry R (M)
1/1/2020	0	0	0	0
1/2/2020	0	0	0	0
1/3/2020	0	0	0	0
1/4/2020	0	0	0	0

Figures 18, 19 show the difference between the 'CUMULATIVE BED EVOLUTION' in the two meshes on the 18th day and their calculated difference on Figure 20.

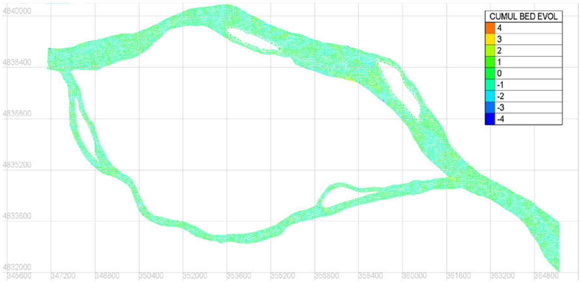

Figure 18. CUMUL BED EVOL variable using the 2017 mesh with real values on the 18th day

Figure 19 shows the GAIA result for the 18 day with the forecasted values.

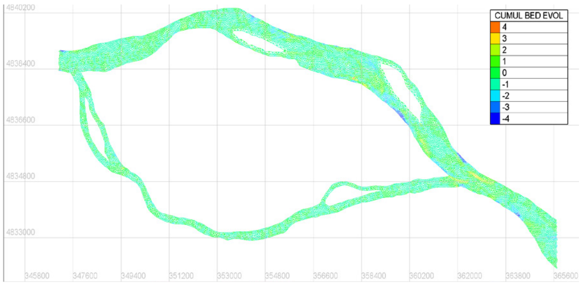

Figure 19. CUMUL BED EVOL variable using the 2017 mesh with forecasted values

Knowing the real and the forecasted values we were able to calculate the difference between them and the result is shown below. The calculated mesh is showing the absolute difference of each point between the cumulative bed evolution variable for the year of 2017 (see Figure 20).

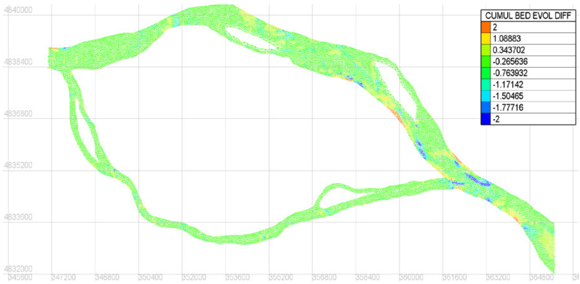

Figure 20. Calculated difference for CUMUL BED EVOL between real and forecasted values

The cumulative bed elevation with forecasted data for year 2020 is shown on Figure 21.

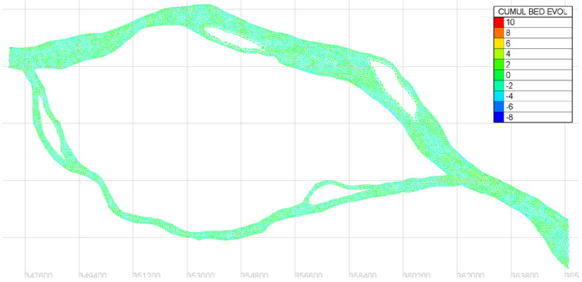

Figure 21. CUMUL BED EVOL values using forecasted data for year 2020

Lastly we have calculated the difference between the forecasted data for different years. For the calculation we have used the TELEMAC output for the cumulative bed evolution for year 2017 and year 2020 and plotted the absolute difference (see Figure 22).

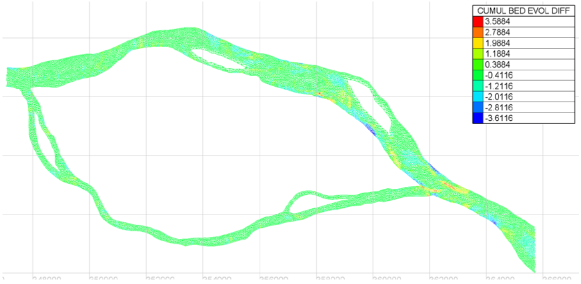

Figure 22. Calculated difference for CUMUL BED EVOL between forecasted data for year 2017 and 2020

Figure 22 shows that the maximum difference is 2.57 M which indicates that in certain areas the simulated 'CUMULATIVE BED EVOLUTION' was slightly higher than the forecasted values. These differences, while important to note, are relatively small, suggesting that our simulation is capturing the key dynamics of the terrain evolution quite well.

Despite using the same resolution for generating the Selafin objects, a slight distinction was noted between the meshes based on their geographical location. The difference is not in the level of detail or granularity provided by the meshes but rather the specific areas of the Danube River they represent. These variations led to subtly different calculated values for the featured variables free surface, velocity magnitude, 'BED SHEAR STRESS' using the LBF file for the year 2020 and the 'CUMULATIVE BED EVOLUTION' with Liquid Boundary File (LBF) for years 2017 and 2020. However, despite these minor differences, the overall trends and patterns remain consistent across both models, underlining their effectiveness and reliability in forecasting the river's hydrodynamic behaviour.

VII. RELATED WORK

Hydrodynamic modelling [8] serves as the basis for numerous studies, prominently in domains like sediment transport and water quality. This type of modelling aids in understanding riverine phenomena, with a specific focus on currents. The development of diverse river models underscores the maturity of these modelling methods [1].

River dynamics have been monitored and predicted using a variety of mathematical models [12,14] which are gaining popularity in solving a range of natural fluid mechanical problems. Tools commonly employed for studying free-flow currents and sediment transport processes in open channels are one-dimensional (1D) and two-dimensional (2D) digital models. A recently developed approach combines hydraulic input forecasts, derived from historical satellite meteorological data and in-situ measurements from designated hydrometric stations, with the TELEMAC system, representing a novel advancement in the field of hydrodynamic modelling [7].

Several studies have delved into various aspects of river behaviour, analysing features such as daily flow, responses to extreme weather conditions, and the speed of water movement under different circumstances [9]. Data required for these detailed studies were compiled from multiple databases, including those providing daily river flow information, precipitation radar data, and specific flow data.

It is important to highlight that there are multiple neural network architectures capable of working with river dynamics.

One approach involves the use Deep Neural Networks (DNN). These neural networks, fundamental in their architecture, connect each neuron in one layer to all neurons in the subsequent layer. This extensive interconnectivity equips the network to uncover complex patterns and relationships inherent in hydrodynamic data. Although DNNs may not be specialized for dealing with temporal or spatial data, with appropriate data preprocessing and correct network tuning, they can effectively be used to predict river dynamics [16].

An alternate approach utilizes the Gated Recurrent Unit (GRU) networks. GRU networks are a type of Recurrent Neural Network (RNN) with an architecture that's simpler yet parallel in functionality to LSTM. Specifically designed to remember past information, GRUs are particularly adept at handling time-series data, such as river dynamics. Similar to LSTMs, GRUs can learn to recognize patterns over time, but with the advantage of being computationally more efficient. This efficiency can be beneficial in applications where computational resources or processing time are limiting factors [15].

For our specific study we have chosen to adopt ConvLSTM networks to forecast hydrological features for their ability to process spatial data from satellite imagery alongside their proficiency in handling temporal sequences from in situ measurements making them an exceptionally suitable tool for our hydrodynamic forecasting tasks. The results we obtained confirm the effectiveness of our chosen approach and the potential of ConvLSTM networks in the realm of hydrodynamic modelling.

VIII. CONCLUSION AND FUTURE WORK

Comparison of the simulations reveals a high degree of similarity between the real and forecasted data, indicating the forecasting model's high accuracy. The data points from the forecasted simulation align closely with those from the real-world observations, suggesting that the model has been successful in predicting fluid behaviour in this scenario. These findings highlight that our approach not only captures the current state of the river effectively but is also robust in its ability to anticipate future conditions.

Through our research, we focused on comprehending the river's different states using key hydrodynamic parameters: 'FREE SURFACE', MAGNITUDE, 'BED SHEAR STRESS' and ‘CUMUL BED EVOL’. Even when considering minor geographical variances, the models consistently portrayed the river's dynamic transformations. This reveals a solid potential for understanding and predicting the evolving hydrodynamic behaviour of rivers in future investigations.

We aim to extend our efforts to further areas, exploring different segments of the Danube River and other river basins. The high degree of alignment between our forecasted and actual observations provides a solid foundation for future research, underscoring the potential of these approaches to drive better river management and conservation strategies.

The proposed method and its outcomes has been integrated into ISME-HYDRO the integrated e-Infrastructure for water resources management of Mozaika [5].

ACKNOWLEDGEMENT

This work has been carried out within ESA Contract No 4000133836/21/NL/SC of Mozaika and with the support of ESA NoR Service.

REFERENCES

[1] Chau, KW Modelling for coastal hydraulics and engineering, Taylor and Francis Ltd., 231 pp., 2010

[2] Daniela E. Nistoran Gogoase, Iuliana Armaş, Cristina S. Ionescu, Inundation Maps for Extreme Flood Events at the Mouth of the Danube River

[3] Engelund-Hansen https://www.hec.usace.army.mil/confluence/rasdocs/rassed1d/1d-sediment-transport-technical-reference-manual/computing-transport-capacity/sediment-transport-potential/engelund-hansen

[4] GAIA Reference Manual

[5] ISME-HYDRO. http://www.isme-hydro.com

[6] Keivan Kaveh, Minh Duc Bui, Peter Rutschmann, Integration of artificial neural networks into TELEMAC-MASCARET system, new concepts for hydromorphodynamic modeling, June 2019

[7] Mariana Damova, Stanko Stankov. River Dynamics Forecasting using Telemac, Earth Observation and AI. In Proceedings of Telemac User Conference 2022 (TUC 2022), Paris-Saclay, France, October 2022, pp. 281-289

[8] Modelling coastal hydrodynamics http://www.coastalwiki.org/wiki/Modelling_coastal_hydrodynamics

[9] Peifeng Li, Jin Zhang, Prediction of Flow Based on a CNN-LSTM Combined Deep Learning Approach

[10] TELEMAC MODELLING SYSTEM, User Manual

[11] TensorFlow https://www. .tensorflow.org/api_docs

[12] Tomasz Kolerski, Mathematical Modeling of Ice Dynamics as a Decision Support Tool in River Engineering

[13] Valentine Audrey, Baron Manuela, Sensitivity analysis of secondary currents in Telemac-2D: a study case at the Danube River

[14] Vijay P. Singh, MATHEMATICAL MODELING OF FLOW IN WATERSHEDS AND RIVERS

[15] Yuanyuan Man, Qinli Yang, Enhanced LSTM Model for Daily Runoff Prediction in the Upper Huai River Basin, China

[16] Yuki Wakatsuki,Hideaki Nakane,Tempei Hashino, River Stage Modeling with a Deep Neural Network Using Long-Term Rainfall Time Series as Input Data: Application to the Shimanto-River Watershed

Modelling a turbidity maximum in a schematized estuary coupling TELEMAC-3D with GAIA

Sven Smolders[1]; Diem Nguyen[2]
sven.smolders@mow.vlaanderen.be
[1] Flanders Hydraulics, dept. of Mobility and Public Works, Flemish Government, Antwerp, Belgium
[2] Antea Group, Roderveldlaan 1, 2600 Berchem, Belgium

***Abstract* – An existing cohesive sediment TELEMAC-3D model for the Scheldt estuary (i.e. SCALDIS MUD) is able to simulate an estuarine turbidity maximum (ETM). However, this ETM is not stable over time. Simulating longer time periods will result in the disappearing of the ETM. This model uses the SEDI3D sediment module (incorporated in the TELEMAC-3D module) to perform the cohesive sediment modelling. The SCALDIS model covers a large domain and its computation times are long. This makes model improvement using multiple test simulations very time consuming. In addition, in this complex model it is more difficult to understand the different processes that play a role in the functioning of a good cohesive sediment model. Therefore, in a next step to improve our understanding of the transport mechanisms of cohesive sediments a schematized estuary model is used first. The schematized estuary uses some geometry measurements from the Scheldt estuary to have some overlap, but does not claim to be a schematized Scheldt estuary. It is merely used as a test case to gain more experience in cohesive sediment modelling and to show that a stable ETM can be reached in a cohesive sediment model. This is the subject of this paper. In a future stage the lessons learnt will be applied back on a Scheldt estuary model like SCALDIS.**

Keywords: schematized estuary, cohesive sediment, GAIA, TELEMAC-3D.

I. INTRODUCTION

Cohesive sediments play an important role in the Scheldt estuary. They form the majority of the suspended sediments in the Scheldt estuary and are important for the dynamics of tidal flats and marshes. With an increasing tidal amplitude and with sea level rise, abundant sediment is important for tidal flats and marshes to grow and follow the high water levels in the estuary. Cohesive sediments settle typically in locations with low flow, like sluice inlets, docks, depoldered areas or branches with no upstream discharge. For navigation purposes its important to keep the fairway open, docks and sluices accessible. Dredging is in this case inevitable. For an optimal dredging and disposal strategy a good understanding of sediment behavior in the estuary is necessary. As a last example, cohesive sediments tend to form flocks and suspended in the water column their concentration determines the light climate in the estuary. For good plant, algae and fauna growth abundant light penetration in the water column is necessary. A very turbid system is not desirable. Understanding the sediment budget of an estuary, understanding the flow from sediment input to output is of the utmost importance for good estuarine morphological management.

A few years ago, Flanders Hydraulics invested in a new detailed 3D hydrodynamic model of the Scheldt estuary, called SCALDIS [1]. This was done within the framework of an integrated management plan for the upper Scheldt estuary. Based on the hydrodynamic model a sand transport and a separate cohesive sediment model [2] were built. The latter however struggled keeping sediment in the water column. Almost immediately an ETM appeared in the model and at the right location, but it was not stable. Very high sedimentation rates were noticed in the shallow areas. This included the tidal flats and the shallower parts of the navigation channel. It was thus not only a wetting and drying problem. The same problem occurred at the upstream discharge boundaries of the model where the sediment that entered the model domain immediately settled, not transporting new sediment downstream. Sedimentation rates were in the order of 1 m in two weeks, which is far from physically correct. The cohesive sediment modelling was done using the module SEDI3D, which was part of the TELEMAC-3D module. Trying all kinds of parameter settings did not improve the model results. Improvement at that time were made by using some hard coding tricks not based on any physical evidence at all. Examples are amongst other decreasing the settling velocity to almost zero at the upstream boundaries or using a wind induced bottom shear stress over the entire model domain (as was done by [3]). The latter solved the problem with the very high sedimentation rates, but then the sediment in the water column was flushed out of the estuary in the matter of days. So, it was clear this was not the good way to go for model improvement.

It was clear that when building a numerical model, staying close to the physical reality with as many parameters as possible will result in better model results and less unphysical problems to solve: for example, when using the bottom roughness coefficient as a calibration parameter, can result in very unphysical values in your model, which in turn can lead to lower or higher flow velocities, as demonstrated in [4]. A flow aligned mesh was used to minimize numerical diffusion and by doing this a higher value of the bottom roughness parameter could be used, one that was much closer to physical reality and not just a value to compensate for the loss of tidal energy in the model by numerical diffusion. This automatically leads to better representation of the flow velocities. A more uniform value of the bottom roughness parameter over the entire model domain is also closer to the physical reality and will respond better when using it in a sediment transport model.

Present day a new module for sediment transport modelling was introduced in the open TELEMAC-MASCARET modelling package and its called GAIA. It was an incentive to also have a new look at cohesive sediment modelling in the Scheldt estuary. However, experiences from the previous effort showed that testing with a computation intensive and complex model domain, results often in long waiting times and difficult to interpret results. Starting with a smaller model with a more schematized model domain would decrease the complexity a little and computation effort a lot. Setting up this model, learning how to use GAIA and trying to reach a stable ETM are the goals for this paper and are a starting point for a new cohesive sediment model for the Scheldt estuary. Lessons learnt from the schematized estuary model will later be applied to a new cohesive sediment model for the Scheldt estuary.

This paper describes the setup of three schematized estuaries, closely related to the Scheldt estuary. It will give the results of the first computations with cohesive sediments in terms of ETM formation and stability.

II. SCHEMATIZED ESTUARY MODEL

Because the lessons learnt from the schematized estuary model will be applied to a Scheldt estuary model, geometric values of the Scheldt estuary were used to make the schematized estuary. The schematized estuary is 16 km wide at the mouth and only 50 m wide 160 km at the upstream boundary. It has no side branches. For the mesh, which consists of 38228 nodes and 69705 triangular elements in the 2D plane, the upstream part (km 100-160) was made using the Blue Kenue channel mesher. The downstream part was created with the regular mesh generator in Blue Kenue. The resolution ranges from 500 m on the downstream boundary to 6 m on the upstream boundary perpendicular to the flow and 25 m along the main flow line. The width B of the estuary exponentially declines from mouth to upstream according to equation (1), copied from [5].

$$B(x) = \exp\left(\frac{-0.027*10^{-3}x+1.9}{5.0*10^{-11}x^2-9.2*10^{-6}x+1}\right) \tag{1}$$

For the bottom level three variants were used, resulting in three variants of the schematized estuary. First a linear declining bottom depth H, constant over the estuary width, was implemented. This linear relationship is given in equation (2):

$$H(x) = -0.000075x - 15 \tag{2}$$

The values of this linear relationship were calculated based on the average depth at the cross section at the mouth and at the upstream boundary of the estuary (based on 2013 bathymetry) This schematized variant will be referred to in this paper as the linear schematized estuary. It is shown in top view in Figure 1 and the bottom profile is shown in Figure 2.

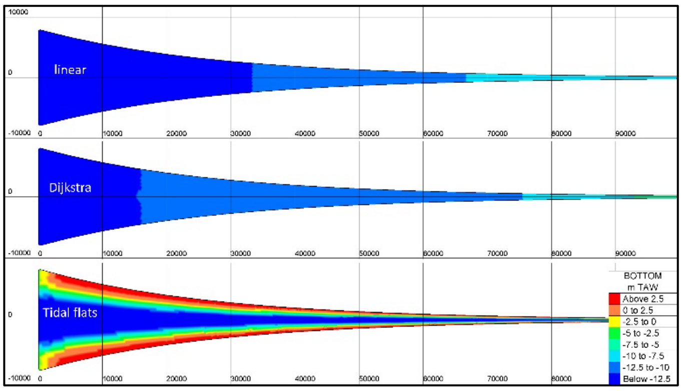

Figure 1. Shape and bottom representation of the three scheamtized estuaries: linear, Dijkstra and tidal flats.

For the second variant the bottom profile follows a fifth polynomial given in equation (3) and this was copied from [5]. This polynomial was fitted by [5] to Scheldt estuary data.

$$H(x) = -2.9*10^{-24}x^5 + 1.4*10^{-18}x^4 - 2.4*10^{-13}x^3 + 1.7*10^{-8}x^2 - 5.2*10^{-4}x + 17.3 \tag{3}$$

This bottom profile is also shown in Figure 1 and Figure 2. It is referred to in this paper as the Dijkstra schematized estuary, after the name of the first author in [5]. This variant is however still very different from the version made in the iFlow model software by [5] and it is not the intention of this paper to compare both models.

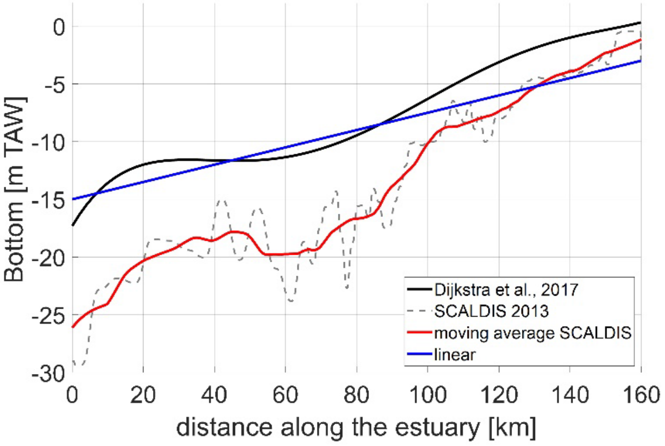

Figure 2. Bottom profiles along the estuary for the three schematized estuaries. Eleveations are expreseed in m TAW, where TAW is the Belgian reference level, with 0 m TAW corresponding to average low water level at sea.

For the third and last variant the bottom of the thalweg of the SCALDIS model was taken and smoothed using a moving average, clearly shown in Figure 2. However, unlike the two previous variants, this variant does not have a constant bottom over the estuary width. Tidal flats are introduced and their height varies along the length of the estuary. Intertidal measurements from the Scheldt estuary were used to determine the height of the deepest and highest point of the intertidal area in this schematized model. On average every 20 km a cross section was made with different heights, linearly interpolating in between the cross sections. The width of the tidal flats however was always kept at 15% of the total width. Therefore, 30% of the total width of this schematized estuary is intertidal area (like some parts of the Scheldt estuary). A cross section is shown in Figure 3.

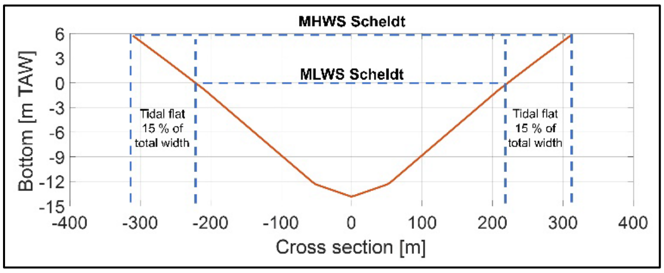

Figure 3. Schematic cross section of variant three of the schematized estuaries introducing tidal flats. Cross section at 90 km from mouth is shown with water levels of mean high water spring tide (MHWS) and mean low water spring tide (MLWS).

Although the heights vary along the estuary and coincide with the heights in the Scheldt estuary, the water level in this schematized estuary does not necessarily follow the high and low water levels of the Scheldt estuary and so the 30% intertidal area provided in the model might not be used entirely, depending on the water levels reached in the model.

Although the schematized estuaries use some or more geometric values of the Scheldt estuary, they are still very different and so it is not the intention to calibrate water levels to the water levels of the Scheldt estuary. They are considered as different estuaries with similar characteristics.

The bottom roughness is described by the Nikuradse bottom roughness value of 0,02 m for the entire model domain.

All three model variants use 15 horizontal plains evenly distributed over the depth. This brings the total node count for these models to 573420.

The downstream boundary is a water level boundary where the tides enter the model domain. Subroutine SL3 is used to describe the downstream water level at the boundary using three important tidal constituents: M2, S2 and M4 (see Table 1). Including the S2 constituent introduces the spring neap variation in the tides. Using tidal constituents to describe the boundary condition has the advantage that they can be analysed also inside the model domain and they can be changed in the future for analysing the effect of tidal asymmetry on sediment transport in the model domain. For this first exercise in this paper the boundary water level, SL3, is described by equation (4). The values for the tidal constituents are taken again from the Scheldt estuary, station Vlissingen, which lies near the mouth of the estuary. These values are kept the same for all simulations presented in this paper and values for amplitude and phase are given in Table 1.

$$\mathrm{SL3} = Z_0 + A_{M2}\sin(F_{M2} * t + \varphi_{M2}) + A_{M4}\sin(F_{M4} * t + \varphi_{M4}) + A_{S2}\sin(F_{S2} * t + \varphi_{S2}) \tag{4}$$

For the upstream boundary a constant discharge Q is imposed. The discharge varies between simulations from 5 m³/s to 50 m³/s and 200 m/³s. The latter two are introduced in the model by starting with a lower value and increasing this value over the course of a few hours in the simulation for stability reasons.

Table 1. Values for de tidal forcing at the downstream boundary. Values correspond with similar values from the Scheldt estuary near Vlissingen (=mouth).

Z_0	2,31 m TAW	Reference level
A_{M2}	1,71 m	Amplitude M2
A_{M4}	0,13 m	Amplitude M4
A_{S2}	0,57 m	Amplitude S2
φ_{M2}	66*π/180	Phase M2
φ_{M4}	133* π/180	Phase M4
φ_{S2}	114* π/180	Phase S2
F_{M2}	2* π/(3600*12,42)	Frequency M2
F_{M4}	2*F_{M2}	Frequency M4
F_{S2}	2* π/(3600*12)	Frequency S2

Salinity is an active tracer in the models. In the Scheldt estuary the salinity is well mixed and so for these schematized models the initial values are described by a horizontal salinity profile which ranges from salinity 30 at the mouth and decrease linearly to salinity 0 towards km 88.

The time step for the linear and Dijkstra schematized estuaries is 15 s, for the variant with tidal flats the time step is 10 s. 100 days were simulated each time and graphic output was given every 10 minutes.

For the turbulence modelling a mixing length model of Nezu and Nakagawa is used for the vertical and a constant turbulence model is used for the horizontal.

The cohesive sediment model in GAIA starts with one fraction of sediments. Initially 0,3 g/L of sediment is present in the water column. Water that enters at the downstream boundary has a sediment load of 0,02 g/L. 0,098 g/L is used for the upstream boundary. The bed is initially empty. Settling velocity is set at 0,1 mm/s. This is a good value for individual clay particles, but is an order of magnitude too low for flocks. But flocculation is not yet considered in this exercise. The critical shear stress for erosion is 0,05 N/m². The Partheniades constant or erosion constant is set at 1,5E-4. The value of the parameter for the critical shear stress for deposition is not used in these simulations, but is calculated by the code. Settling lag is turned on. The minimal value for the water depth is set to 0,1 m. These values are kept the same for all simulations shown in this paper.

In this paper only the results of five simulations are shown and discussed. All parameters are kept the same except for the upstream discharge:

- Linear schematized estuary with Q = 50 m³/s
- Dijkstra schematized estuary with Q = 5, 50 and 200 m³/s
- Tidal flats schematized estuary with Q = 50 m³/s

III. ETM IN THE SCHELDT ESTUARY

Four times per year a vessel sails along the Scheldt estuary following the ebb tide to measure, amongst others, the suspended sediment concentration (SSC) near the bottom and near the surface. Figure 4 shows the measurements from 2021. An ETM shows around km 110-120. With high freshwater discharges this ETM migrates downstream or is sometimes flushed entirely. In very dry conditions with very low freshwater discharge (yellow line, September 2021 in Figure 4) an additional ETM shows upstream around km 140-150. Further an ETM is seen around km 60-70. This is just downstream of Antwerp. A lot of dredging and disposal activities are carried out in this region and this ETM might be fed by he disposed dredged material. With higher winter discharges this is the first ETM to be flushed out of the estuary.

These measurements give a view on the SSC along the Scheldt estuary on four single time steps. Further 6 permanent measuring stations monitor the SSC in the estuary at fixed locations. These measurements give an idea of the fluctuation over longer periods of time and sometimes the migration of an ETM can be noticed in one of these stations.

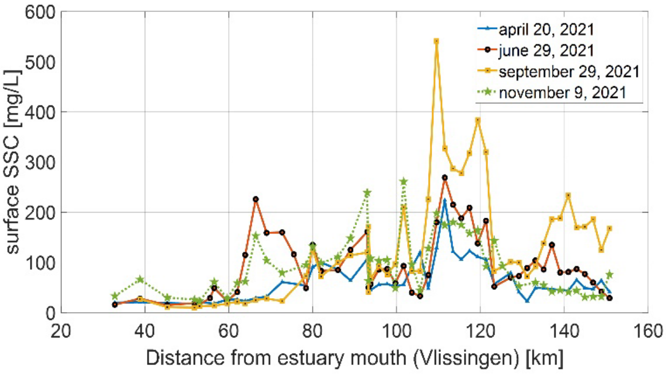

Figure 4. Measured surface suspended sediment concentrations along the Scheldt estuary for the four seasons in 2021.

From previous modelling experience the ETM furthest downstream occurs easily when dredging and disposal activities are incorporated into the model. The ETM around km 110-120 showed in the old cohesive sediment model when sufficient sediment was present. Due to high sedimentation rates upstream and the unphysical measures taken in the old model to prevent this, the most upstream ETM during low discharge periods was not yet found in the model. The exercise in this paper is however to show a stable ETM can be formed in an estuary model in TELEMAC-3D coupled with GAIA.

The different physical processes that form a turbidity maximum in estuaries, like gravitational circulation, tidal pumping, Stokes drift, scour lag and spatial settling lag are not discussed here and will not be discussed in the model results sections as this paper shows only preliminary results. Further research will need to follow.

IV. MODEL RESULTS

A. Tidal constituents

The tidal constituents imposed on the downstream boundary are known. How they evolve traveling along the estuary can be deducted from water level time series extracting the constituents using t_tide from [6]. Figure 5 shows the M2, S2 and M4 amplitudes of the three schematized estuary variants for a simulation with constant upstream discharge equal to 50 m³/s. For comparison the values for the Scheldt estuary are added to the figure. For all estuaries the values diverge the more upstream the location. The Dijkstra and tidal flats variant show an increase in M2 amplitude followed by a decrease near the upstream end, like in the Scheldt estuary. For all three constituents it is clear that the Dijkstra and tidal flats variant follow the trend of the Scheldt estuary the best. The difference upstream are quite large, and this is seen in the low water level behaviour much more than in the high water levels as will be shown in the next section.

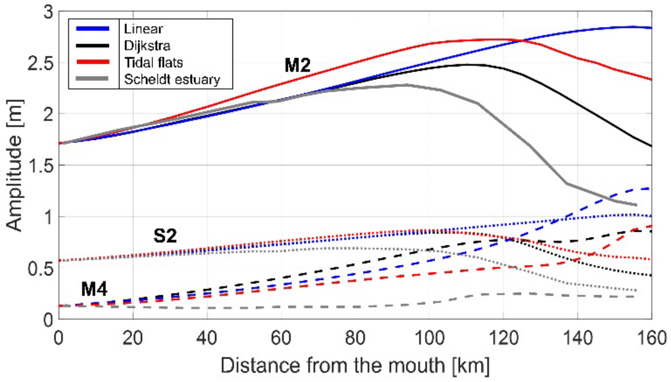

Figure 5. Comparison of the M2, S2 and M4 amplitudes of the three different modelled schematized estuaries and measured values from the Scheldt estuary. The modelled results are taken from simulations with upstream discharge Q = 50 m ³/s.

B. Water levels

The maximum high water level and the minimum low water level during spring tide for the three schematized estuary variants is given in Figure 6. For the Dijkstra variant three different water levels are given for three different upstream discharges, i.e. for 5, 50 and 200 m³/s. The higher the discharge the higher the water level (low and high) upstream. The influence of the discharge on the water levels reaches approximately 45 km downstream. The linear variant has the highest tidal range upstream the estuary, followed by the tidal flats variant.

Despite the differences in bottom level being quite high between the schematized estuary variants, the high and low water levels remain close to each other in the downstream part of the estuaries. At least it seems that way in Figure 6 because of the large scale on the y-axis. The differences reach up to 20 cm with the tidal flats variant having the highest high water levels downstream and the linear variant the lowest high water levels. For the low water levels the tidal flats variant has the lowest water levels and the linear variant the highest, giving the tidal flats variant the highest tidal range in the downstream part of the estuary.

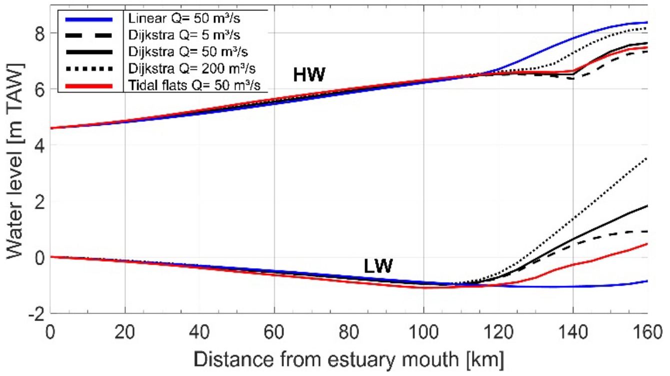

Figure 6. High (HW) and Low (LW) water levels during spring tide in the different schematized estuaries for different upstream discharges Q.

C. *Cohesive sediment*

After 100 simulated days the suspended sediment concentration in the water column along the central axis x of the estuary is plotted to see if an ETM occurs and to see the differences between the variants and the difference within one variant with different upstream discharges. The results are plotted in Figure 7. Compared to the linear and Dijkstra variant the tidal flats variant shows still a distinct area with increased suspended sediment concentration, but the values are much lower. All found ETM's are found relatively stable as they did not change much in the last 20 days of the simulation. For the Dijkstra variant the differences in upstream discharge show that with higher discharges the ETM is narrower and situated more downstream.

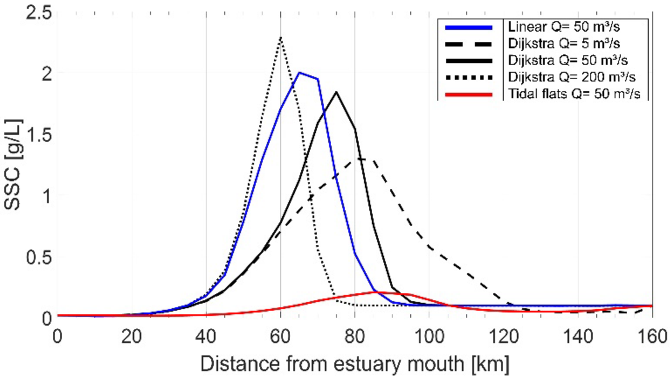

Figure 7. SSC values [g/L] for the three schematized estuaries after 100 simulated days. The results show maximum SSC values during spring tide, during flood.

The SSC values for the linear and Dijkstra variant are however far above the measured values of ETM of just SSC values in the Scheldt estuary (see Figure 4). Looking in detail to only the results of the tidal flats variant in Figure 8 it shows that SSC values are in the same order of magnitude as the measured values in the Scheldt estuary. With the y-axis scale in Figure 8 a clear ETM is visible around km 60-110. The range of this ETM along the central estuary axis is quite large. The sediment transport over several transects (0, 20, 40, 60, 80, 100, 120, 140 km) was calculated for each time step of the last full spring neap tidal cycle and averaged. This is called the averaged sediment flux and is expressed in kg/s. negative values indicate a net downstream transport and positive values a net upstream transport. They are represented by red and green arrows respectively in Figure 8. This shows that there is a large input on the downstream boundary. The sediment load in the water column there is small but the volume of water is large, resulting in a large sediment input. In the region of the ETM there is a net upstream transport of sediment. Further downstream and upstream there is a net downstream transport. The flux of sediment entering the estuary upstream is 5 kg/s. However, in the first cross section downstream this value drops significantly, showing that most of the sediment entering the estuary upstream remains in the upstream section. This is a point of attention for further improvement as this is caused by the boundary itself (low flow velocities entering the estuary).

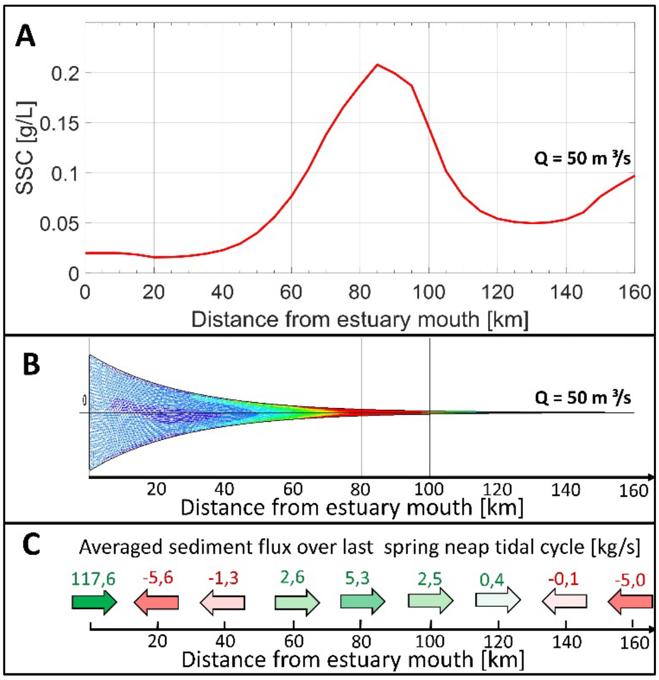

Figure 8. A. SSC values along the tidal flats schematized estuary variant after 100 simulated days; B. SSC values shown in top view of the model; C. the sediment fluxes averaged over the last spring neap tidal cycle are given in green (upstream transport) and red (downstream transport) arrows for transects every 20 km.

The he same evaluations are made for the different discharges of the Dijkstra variant. The averaged fluxes and representing arrows are shown in Figure 9. For the Q = 50 m³/s scenario only one section in the middle of the estuary is showing an upstream sediment transport flux (compared to four sections in the tidal flats variant above). When the upstream discharge is very low, from km 80 and upstream the sediment transport is directed in the upstream direction. The higher values of fluxes entering at the downstream boundary, compared to the tidal flats variant are due to the fact that the model water volume of the Dijkstra variant is almost double of that from the tidal flats variant and this causes the entrance of a much larger sediment volume at the downstream entrance for the Dijkstra variant. Increasing the upstream discharge to 200 m³/s will point all fluxes at all transects in the downstream direction. This means that eventually the ETM will disappear and the sediment will settle in the mouth region. The upstream discharge did not affect the flux direction in the downstream part (under 60 km) of the estuary. There the arrows remained pointed in the downstream direction. The tidal volume in this variant is much higher than that of the tidal flats variant or the Scheldt estuary, which makes that higher discharge values are needed to influence it. However, usually a higher discharge points the net sediment transport in downstream direction and in the Dijkstra variant it already pointed in the downstream direction. It is worth investigating how different discharge values influence the sediment transport direction in the tidal flats variant.

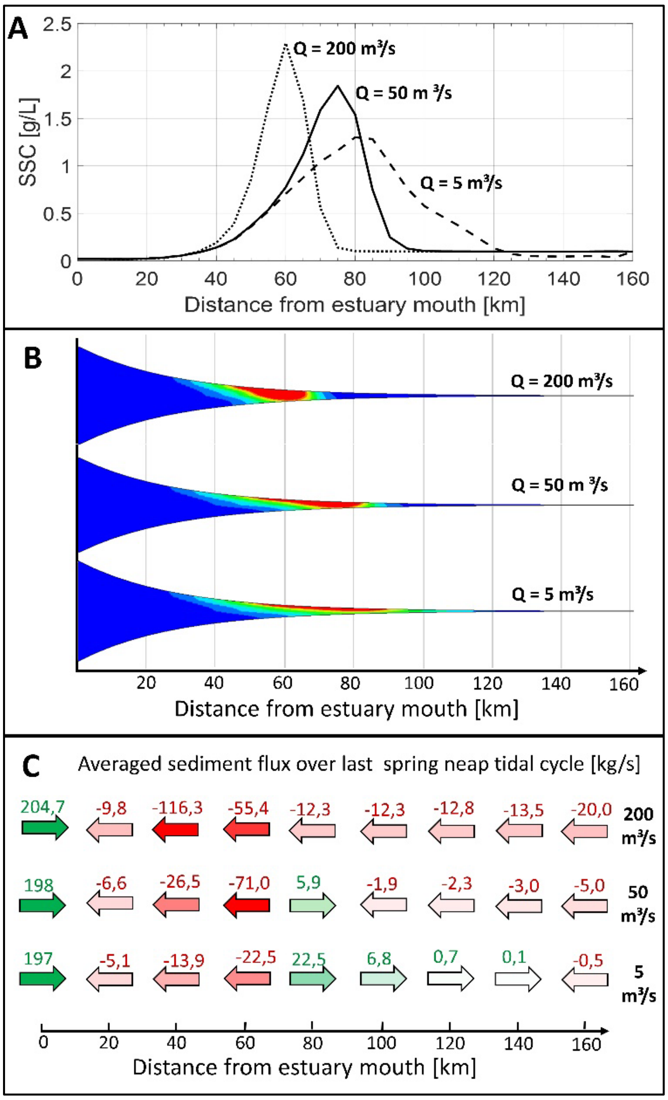

Figure 9. A. SSC values along the Dijkstra schematized estuary variant after 100 simulated days for three different upstream discharges: 200, 50 and 5 m^3/s.; B. SSC values shown in top view of the model for the different upstream discharges; C. the sediment fluxes averaged over the last spring neap tidal cycle are given in green (upstream transport) and red (downstream transport) arrows for transects every 20 km for three different upstream discharges.

With the given fluxes some parts of the models, where more sediment is flushed downstream compared to the amount of sediment that enters from upstream, or part where there is a downstream flux on the downstream side and an upstream flux on the upstream side, will run out of sediment. In these simulations this process appears to evolve slowly, making the formed ETM's seem stable over a shorter period of time. This might be due to the constant parameter values and the low settling velocity. A higher settling velocity will have a larger effect on some of the ETM forming processes and dynamics. Despite this, ETM showing quite stable values after 100 simulated days is already a good step forward compared to the old SCALDIS mud model, where sediment settled or was flushed in a 30 day period.

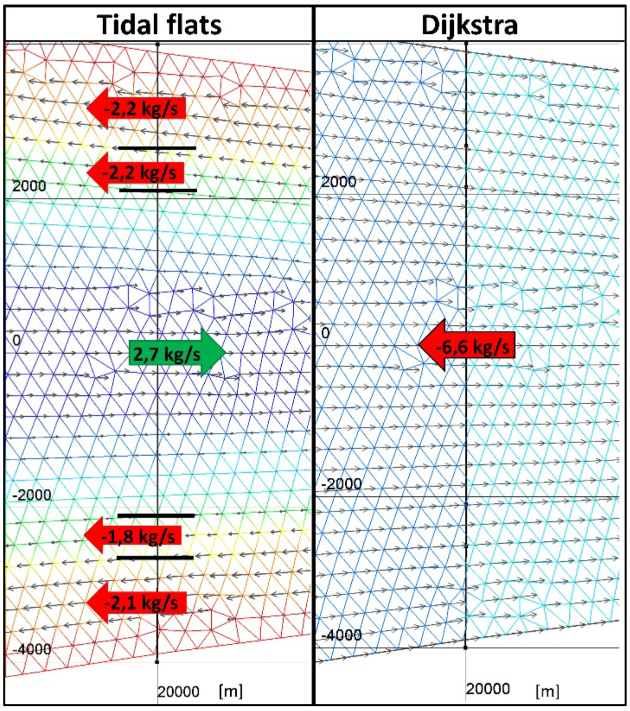

Figure 10. Comparing flow velocity direction at the end of flood for the tidal flats and Dijkstra schematized estuary variants. For the tidal flats variant the averaged fluxes over the last spring neap tidal cycle are given for parts of the 20 km transect.

The three variants of the schematized estuary model are quite different. Sometimes they give a comparable result, suggesting the act similar, but further analysis reveals big differences in processes. One example is the downstream sediment flux at the transect of km 20. The Dijkstra and tidal flats variant both give a negative flux of around 5 to 6 kg/s. Figure 10 shows the flow velocity direction at the end of flood tide. In the tidal flats variant a strong current starts to form on the tidal flats and shallower areas in the downstream direction, while the flow velocity in the deep main channel still points towards upstream. Analysing averaged sediment fluxes over parts of the transect reveals that in the deep main channel the net sediment transport is pointed upstream and the parts above -5 m TAW have a net sediment transport pointed downstream. The downstream transport over the shallow areas is bigger than the upstream transport in the main channel, resulting in a net downstream sediment transport over the entire transect. As the bottom depth is equal over the entire width in the Dijkstra variant, this phenomenon does not occur. Flow velocities are divided differently over ebb and flood resulting in a net downstream transport over all parts of the transect.

V. CONCLUSION

The first results of modelling cohesive sediments in schematized estuaries shows promising results in ETM formation. All modelled schematized estuary variants, linear, Dijkstra and tidal flats, show the formation of an ETM that is stable over time. This was the goal of this first exercise.

More analysis and longer simulation periods will be needed to see how the ETM behaves in different situations, like sediment starvation or particles with different parameter setting (especially settling velocity). The schematized estuaries forced by tidal constituent offer the possibility to also investigate how different settings for these constituents affect sediment behaviour (through tidal asymmetry).

When the different parameter settings and their impact on the global modelling result are better understood in the schematized estuary, in a next step the lessons learnt can be translated back to a full scale Scheldt estuary model, which is the final goal of this exercise.

Finally this exercise shows that TELEMAC-3D coupled with GAIA offers possibilities to model cohesive sediments and ETM formation in estuaries.

REFERENCES

[1] Smolders, S.; Maximova, T.; Vanlede, J.; Plancke, Y.; Verwaest, T.; Mostaert, F. (2016). Integraal plan Bovenzeeschelde: Subreport 1. SCALDIS: a 3D Hydrodynamic model for the Scheldt Estuary. WL Rapporten, 13_131. Flanders Hydraulics Research: Antwerp

[2] Smolders, S.; Bi, Q.; Vanlede, J.; De Maerschalck, B.; Plancke, Y.; Mostaert, F. (2020). Integraal plan Boven-Zeeschelde: Sub report 6 – Scaldis Mud: a Mud Transport model for the Scheldt Estuary. Version 4.0. FHR Reports, 13_131_6. Flanders Hydraulics Research: Antwerp.

[3] van Kessel, T.; Vanlede, J.; Bruens, A. (2006). Development of a mud transport model for the Scheldt estuary in the framework of LTV: phases 1 and 2. Versie 1.0. Delft Hydraulics/Flanders Hydraulics Research: Delft. 79 + appendices pp.

[4] Smolders, Sven (2022): How a Flow Aligned Mesh Improves TELEMAC Model Results. In: Bourban, Sébastien E.; Pham, Chi Tuân; Tassi, Pablo; Argaud, Jean-Philippe; Fouquet, Thierry; El Kadi Abderrezzak, Kamal; Gonzales de Linares, Matthieu; Kopmann, Rebekka; Vidal Hurtado, Javier (Hg.): Proceedings of the XXVIIIth TELEMAC User Conference 18-19 October 2022. Paris-Saclay: EDF Direction Recherche et Développement. S. 45-49.

[5] Dijkstra, Y. M., Brouwer, R. L., Schuttelaars, H. M., & Schramkowski, G. P. (2017). The iFlow modelling framework v2. 4: A modular idealized process-based model for flow and transport in estuaries. Geoscientific Model Development, 10(7), 2691-2713.

[6] Pawlowicz, R., B. Beardsley, and S. Lentz, (2002). "Classical Tidal Harmonic Analysis Including Error Estimates in MATLAB using T_TIDE", Computers and Geosciences, 2002.

GAIA can model large marine dunes: Results from a sensitivity study in the southern North Sea

Noémie Durand[1,3], Pablo Tassi[2,3], Olivier Blanpain[1] and Alice Lefebvre[4]
noemie.durand@france-energies-marines.org
[1]: France Energies Marines, Brest, France
[2]: EDF Recherche & Développement, Chatou, France
[3]: Laboratoire d'Hydraulique Saint-Venant, Chatou, France
[4]: MARUM, Bremen, Germany

***Abstract* – Tides, winds, and waves shape the seabed of shallow shelf seas. In sandy energetic environments, marine dunes can develop. These sedimentary bedforms are present worldwide, in a variety of environments. They abound in the North Sea. Our interest is in an area offshore Dunkirk (northern coast of France) where migration rates as high as 30 m/yr have been observed. A coupled TELEMAC-3D+GAIA model has been set up for a simplified configuration, to assess the contributions of the hydro-meteorological parameters, and how their variability influences the evolution of the dune field over time. Several sediment transport formulae (based on both energetic and shear-stress considerations) are investigated. Their suitability to reproduce the seabed evolution observed over a period of four months is discussed.**

Keywords: Marine environment, Marine dunes, Morphodynamics, TELEMAC-3D, GAIA.

I. INTRODUCTION

Large, dynamic sedimentary bedforms are common occurrences on the bed of shallow shelf seas worldwide. They are present in the Irish Sea, the English Channel and in the North Sea, where most of the proposed European offshore wind farms will be located. Constantly remodelled by the combined action of tidal currents and waves, they pose a challenge to the design, implementation, safety, and maintenance of marine renewable energy systems. Therefore, it is essential to be able to predict the evolution and migration of large marine dunes.

Marine dunes of 2 to 3 m in height are present offshore Dunkirk, in the Southern Bight of the North Sea. The region is characterised by a macro-tidal regime, with a spring tidal range = 5.5 m. The tide is asymmetric: it rises faster than it falls, and the flood currents are generally stronger than those during the ebb, resulting in a net current trending North-East. The offshore wave climate consists of waves that originate from the Atlantic Ocean as well as from the North Sea. The 1-year condition (all directions) is estimated at significant wave height H_s = 4.4 m and mean period T_z = 6.5 s.

Recurrent bathymetric surveys have been conducted between 2019 and 2021 in three predefined tiles: 1) in the approach channel, 2) immediately north of the Breedt sand bank, and 3) on top of the Binnen Ratel bank (Figure 1). The surveys document the evolution of the dune field offshore Dunkirk over successive periods ranging from 1 to 4.5 months. There are times when the morphology of the dune changes, resulting in an apparent migration of the crest, and others when the body of the dune moves as a whole. Overall, the dunes have been observed to migrate at a net rate of the order of 30 m/yr towards the North-East.

The purpose of this work is to gain insight into large dune modelling in open marine environments, a research area that is still poorly understood. For this, tile#1 is of particular interest. The currents there are mostly bidirectional, restricted by the orientation of the navigation channel (approximately trending 80°N during the flood; 260°N during the ebb). This allows a

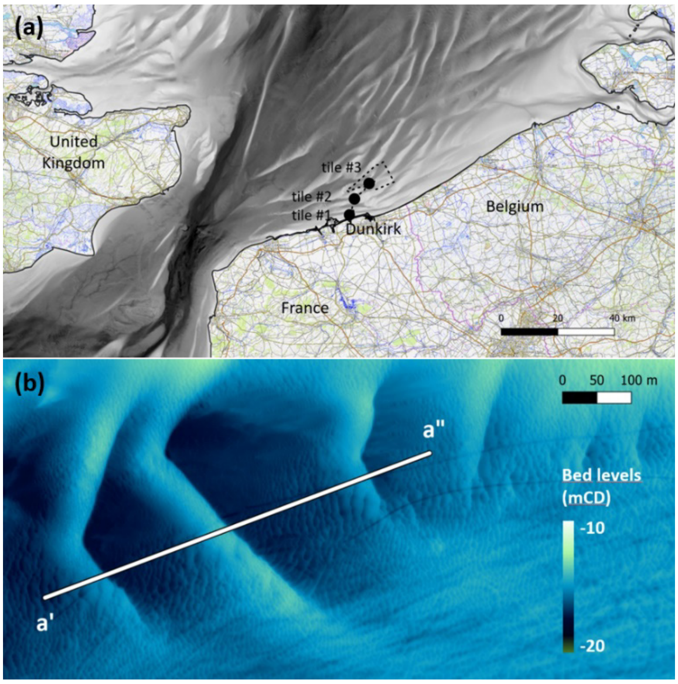

Figure 1. (a) Location map showing the bathymetric survey tiles as filled circles. (Source of the background data: Shom 2015 and https://opentopomap.org/) (b) Close-up view of tile#1 in the navigation channel showing bed levels in November 19. Dune profiles are extracted along section a'-a". (Source of the data: France Energies Marines).

simplified (flume-like) configuration to be developed that captures the main sediment transport processes in and around tile#1 area at reduced computational time.

A 4-month period (November 2019 to March 2020) is modelled. During this time, the morphology of the dunes has not changed significantly, but they have migrated approximately 15 m to the North-East. If it can be shown that the model performs well under high hydrodynamic stresses, then it gives confidence in the predictions for other periods.

II. MATERIAL AND METHODS

A. Local numerical model

A coastal area model based on the open source TELEMAC system is being developed. This model will consider the interactions between tidal flows, winds, waves, sediment transport processes, and bed evolution. The same computational domain and spatial discretisation are used throughout. References [1] and [2] detail the procedure for the calibration and validation of this regional hydrodynamic and wave model against in situ data. Updated results have been presented by [3]. Good performance was achieved under a range of tidal currents and offshore wave and wind conditions.

Subsequently, a simpler configuration was developed to gain insight into dune modelling, with a focus on the choice of a suitable transport formula that would reproduce the bed evolutions observed in situ, as well as the parameters to which it might be sensitive. This model is described herein.

It consists of a flume-like representation of tile#1. The mesh is based on the *bosse* test case provided in the GAIA examples folder [4], where dimensions have been scaled so that the mesh resolution is approximately 10 m in both x- and y-directions (consistent with the regional model). This gives an 800-m-long by 110-m-wide computational domain comprising 891 nodes and 1600 elements. The digital elevation model of the seabed has been constructed from a dune profile extracted from the November 2019 bathymetric survey data and taken in the predominant direction of the flow, approximately perpendicular to the dune crests (Figure 1). This profile is duplicated across the domain so that the elevation of the bed does not vary laterally. This representation is deemed appropriate as a first instance, given the strong bidirectionality of currents in the navigation channel.

Time-varying water discharges and free surface elevations are applied at both ends of the flume. For that purpose, time histories of velocities and levels have been extracted from a long-term simulation of the regional model in the middle of section a'-a''. Water fluxes are calculated as the product of the instantaneous magnitude of the current by the instantaneous water depth, integrated across the width of the flume (Figure 2). Larger peak fluxes are predicted during the flood cycle (positive values) than during the ebb cycle (negative values). The resulting easterly residual (obtained from a rolling average of the instantaneous water flux values) is shown in black in Figure 2; the dark red circles indicate times when the net water flux was directed opposite the dominant easterly direction. Negative net water fluxes are associated with sustained wind events from the North-West; strong positive net water fluxes (in excess of 500 m^3/s) with energetic events from the South-West. In light of these results, it is anticipated that the preferred direction of sediment transport is towards the East. This is supported by the morphology of the dunes, which exhibits a gentler side facing west and a steeper side facing east (Figure 1b), typical of bedforms subjected to prevailing flow direction.

Several authors have identified the waves dampening effect on the dune height (e.g. [5], [6], [7], [8]). In the Southern Bight of the North Sea, [9] has observed that it is controlled in some instances by the frequency of occurrence of strong events and the elapsed time between these energetic periods. Although the southern North Sea is open to waves from the Atlantic Ocean and the North Sea, they are relatively short. Due to the large water depth in the navigation channel compared to wavelength ($kh > 0.5$, k the wave number and h the water depth), wave activity is a second-order process for sediment transport [3]. Therefore, wave processes are not included in this exploratory work, and numerical simulations are performed by internally coupling the 3D Reynolds-averaged Navier-Stokes module TELEMAC-3D with the sediment transport and bed evolution module GAIA [10].

B. TELEMAC-3D settings

Bed friction is expressed in the form of a Nikuradse roughness. A value of 862.5 µm is adopted that is based on a representative grain size for the area.

Turbulent diffusion is defined by a constant eddy viscosity (taken as 10^{-6} m^2/s) in the horizontal direction, and by the Tsanis mixing length model along the vertical direction.

Good performance of the regional hydrodynamic model was achieved with these settings, compared to observed in situ level and velocity data [3].

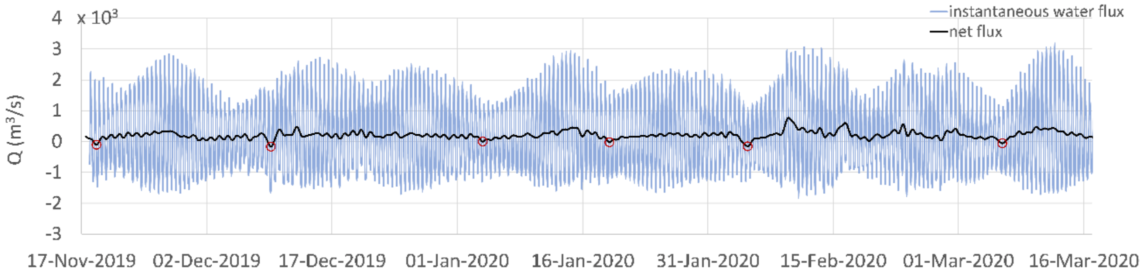

Figure 2. Instantaneous water flow predicted by the regional model. Positive values correspond to the flood cycle, trending eastward.

C. GAIA settings

Bed sample data have been collected offshore of Dunkirk. Grain size distributions were derived from the most recent samples (October 2019 and May 2020, France Energies Marines) that suggest little spatial or seasonal variability in the area. Sediments are generally reasonably well-sorted medium sands with grain sizes of d_{50} between 230 µm and 450 µm, and little fine content (typically less than 1% passes through the N°200 sieve). The grain size d_{10} is estimated at 210 µm on average. Therefore, sediments are not expected to exhibit cohesive properties [11]. These values are generally in agreement with those collated by the Service hydrographique et océanographique de la marine (Shom) at different times in recent years.

For the purpose of the modelling, a unimodal distribution is adopted with a median grain diameter of d_{50} = 345 µm, and d_{90} = 1 mm.

D. Sediment transport formulae

The Rouse number, *P*, is a non-dimensional parameter that defines the shape of the suspended sediment concentration profile. By extension, it is often used to determine the prevailing mechanism of sediment transport [12]. Reference [3] has concluded that the region offshore Dunkirk was predominantly bedload, in accordance with findings that marine dunes could only form on the Dutch continental shelf when the Rouse number was in excess of 2.0 [13]. Therefore, in this work we limit ourselves to bedload transport.

Various bedload transport rate formulae have been proposed. Owing to the location of the site, only the transport formulae applicable to coastal areas are considered. These formulae are largely based on parameterisation of physical processes and have been calibrated by their authors with experimental or field data.

Two formalisms emerge and are explored in this work:

- methods based on current velocities (of all nature, tidal or not). In GAIA, they are Soulsby and van Rijn (1997) (hereafter SvR97) [11], Bailard (1981) [14], and Dibajnia and Watanabe (1992) [15] (revisited by [16]); and
- those based on bed shear-stresses. In GAIA, this is Bijker (1968) [17]. The excess shear formula proposed by Soulsby and Damgaard (2005) (hereafter SD05) [18] was implemented in GAIA as part of this work.

Bailard formula is said to perform best in wave-dominated environments [19]. Because of its formulation, the question arises whether the Dibajnia and Watanabe formula is suitable without waves. Soulsby and Damgaard formula is preferred over Bijker's as it incorporates the notion of threshold of motion. Therefore, in this paper, we will focus on the SvR97 and SD05 sediment transport formulae.

1) Soulsby and van Rijn (1997): The SvR97 formula provides an estimate of the total transport rate (bedload + suspended load) by currents and waves. It was adapted from van Rijn (1984) sand transport formula by currents only, following the methodology introduced by [20] to add the wave contribution. It does not include complex wave processes such as velocity asymmetry, acceleration asymmetry, or boundary layer streaming. It is only valid for non-breaking waves. The coefficients A_{sb} and A_{ss} in the formula had originally been derived for river settings based on a combination of physical and empirical considerations. They are valid for depths in the range 1 to 20 m, depth-averaged velocities in the range 0.5 to 5 m/s and sediment grains between 0.1 and 2 mm.

In this work, wave processes are considered to be of second order and discarded as a first approximation. In this case, the SvR97 formula reduces to:

$$q_t = (A_{sb} + A_{ss}) \left\|\overrightarrow{U_{2D}}\right\| \left[\left\|\overrightarrow{U_{2D}}\right\| - U_{cr}\right]^{2.4} \qquad (1)$$

where q_t is the volumetric total transport rate per unit width and $\left\|\overrightarrow{U_{2D}}\right\|$ the depth-averaged current velocity. $A_{sb} = f(h^{-0.2})$ denotes the bedload coefficient (*h* the water depth), $A_{ss} = f(d_{50}^{-0.8})$ the suspended load coefficient, and $U_{cr} = f(d_{50}, h/d_{90})$ the threshold velocity defined by van Rijn (1984).

Some limitations have been identified with this formula. Above all, it is based on a depth-averaged current speed when, intuitively, bedload transport is closely related to near-bed processes. Furthermore, the ratio of suspended load to bedload contributions (given by A_{sb}/A_{ss} in (1)) is only determined by grain size in relation to water depth (d_{50}/h) and by dimensionless grain size (D_*). In our configuration, it is overwhelmingly biased towards suspended load, which is not in line with current knowledge of marine dune settings (bedload dominated).

2) Soulsby and Damgaard (2005): The SD05 formula provides an estimate of bedload transport rate by currents and sinusoidal or asymmetric waves. Therefore, velocity asymmetry can be considered as waves shoal and become increasingly skewed. The contribution of currents alone is derived from sheet flow theory. Sediment concentration and velocity profiles are defined in the sheet flow layer, whose thickness is determined by Coulomb friction. Integration of sediment flux through the sheet flow layer gives the non-dimensional transport rate. It is interesting to note that the same formula was independently obtained by fitting a curve to bedload transport data [21].

The SD05 formula is an excess shear-stress formula. In that sense, it is consistent with the physical intuition that sediment grains can only be mobilised when the shear-induced forces exceed the resisting forces (e.g. friction).

In the absence of waves, the SD05 transport formula simplifies to:

$$q_b = 12\, d_{50} \sqrt{\frac{\tau}{\rho}} \left(\frac{\tau - \tau_{cr}}{g\,(\rho_s - \rho)\, d_{50}}\right) \qquad (2)$$

where q_b is the volumetric bedload transport rate per unit width, τ the bed shear-stress, and τ_{cr} the threshold bed shear-stress for onset of motion. ρ denotes the water density, ρ_s the sediment density, and g the acceleration due to gravity.

E. Migration speed estimate

Digital Elevation Models (DEMs) had been constructed from the local survey data (0.5 m resolution, 0.05 m vertical accuracy) collected at 8 survey times: S1 to S8 (Figure 3). The seabed profile was extracted from these DEMs along section a'-a". The evolution of the dunes is not constant in time (Figure 3) and is rather dependent on external factors. Dunes are very mobile during period S1-S2 (compared to S3-S4 and S6-S7 with similar duration). In that period, the dunes migrate ca. 15 m to the East while retaining a mostly unchanged morphology. Interestingly, the steep slopes of the dunes become gentler during periods S2-S3 and S7-S8, resulting in an apparent migration of the crest towards the west.

The dune crests and troughs had separately been digitised off the DEMs of the surveys to characterise the morphology of the dunes and assess the migration speed of their crests [22]. Over the course of 21 months, from S1 to S8, the average migration speed for Dune2, the central dune of our transect, was estimated to be 37.2 m/yr (standard deviation = 11.7 m/yr). This should be considered an average (over the dune length) net migration speed because the crest position fluctuates with the tidal state and does not always move in one direction.

Many authors have quantified the speed of dune migration from the ratio of crest displacement to time. We adopt the same approach in this work, in part to allow comparison with the above estimates, and because the crest is an easy feature to identify. However, it may be more appropriate to consider the position of the steep face of the dune rather than the crest, as a marker for dune migration. Indeed, as noted previously, changes in crest position may result from changes in dune morphology alone, without dune migration.

We have focused our analysis on the central and larger dune of the transect. A spline is fitted to the bed levels predicted by the model to add the resolution lacking from the local model mesh (from 10 m to 1 cm resolution). The crest is taken to be the highest bed level, and its displacement is divided by the model output time step to give an hourly migration speed expressed in cm/day. The average over the 4-month period (S1-S2) can be compared to the estimates obtained by [22] for S1-S8.

III. RESULTS AND DISCUSSION

A. Behaviour of sediment transport formulae

An extensive range of simulations was performed to identify the sensitivities of the sediment transport formulae to parameters such as temporal and spatial resolution, vertical discretisation, friction, sediment grain size, slope effect, and consideration of dynamic pressure. Some conclusions from these simulations are presented in the following sections.

1) Influence of vertical plane distribution: SvR97: Five irregularly spaced sigma planes were used in the vertical for the SvR97 model runs. These were defined at approximately $1/6^{th}$, $1/3^{rd}$ and $2/3^{rd}$ of the water column, the first plane representing the seabed and the last the free surface. No sensitivity to the distribution of the vertical planes was performed on the grounds that the SvR97 sediment transport formula is based on depth-averaged velocities.

SD05: This formula is expressed in terms of bed shear-stresses. In TELEMAC-3D, the shear-velocity, hence shear-stress, is computed from the second plane velocity under the assumption that the vertical profile close to the seabed is logarithmic. If that assumption held true, then the distribution of the vertical planes in a 3D model would not be an issue: the velocity at any position in the water column would give the (same) near-bed shear-velocity. Reference [23] has shown that this was not the case over dunes. Therefore, some attention was paid to the computation of the grain bed shear-stress, and to the vertical discretisation.

Alternative methods were explored to compute the shear-velocity: based on a Chézy coefficient, assuming different profiles, or calculated from the velocity at a reference level (akin to van Rijn's approach [24]). None of these alternatives proved entirely satisfactory, so the original shear-velocity formulation was retained. Several tests with different vertical distributions were then carried out: (i) a limited number of 5 planes carefully selected at 0%, 0.3%, 2.3% 15% and 100% of the water column (this meant a near-bed resolution of about 5 cm); (ii) 5 planes; (iii) 11 planes; and (iv) 16 planes distributed logarithmically with a growth ratio of 1.3 (as was done for SvR97).

As expected, the bed shear-stresses predicted by the model, and the resulting bed evolution, are found to be quite sensitive to the vertical plane distribution. The more planes in the vertical from (ii) to (iv) (hence the finer the near-bed resolution, from approximately 3 m to 40 cm to 11 cm), the more the dunes move as a whole. With 5 planes (ii), only the lower section of the dunes moves. A drawback of finer near-bed resolution, however, is that the crests tend to be exaggerated and the troughs eroded. This is illustrated in

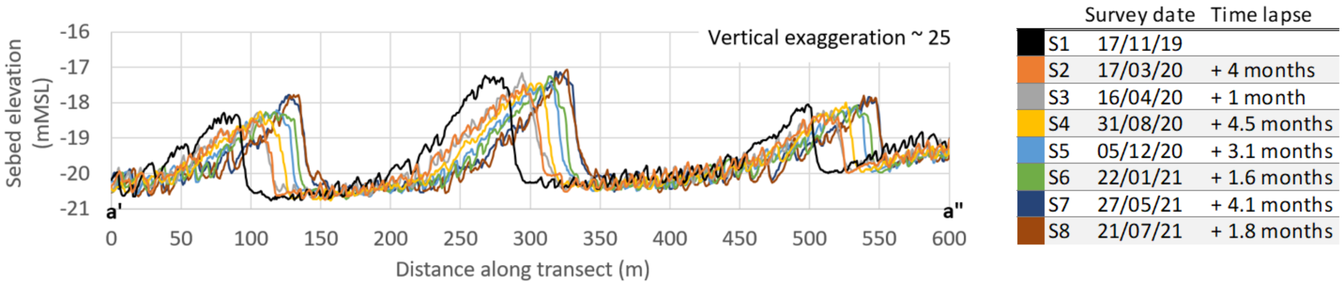

	Survey date	Time lapse
■ S1	17/11/19	
🟧 S2	17/03/20	+ 4 months
▨ S3	16/04/20	+ 1 month
🟨 S4	31/08/20	+ 4.5 months
🟦 S5	05/12/20	+ 3.1 months
🟩 S6	22/01/21	+ 1.6 months
■ S7	27/05/21	+ 4.1 months
🟫 S8	21/07/21	+ 1.8 months

Figure 3. Dune profiles along section a'-a", in tile#1, showing the evolution from Nov19 to July21. The predominant flow direction is from left to right.

Figure 4, where the envelop of the bed evolutions predicted using log-distributed planes (ii), (iii) or (iv) is represented as a shaded area. The refined 5-plane distribution (i) seems like a good compromise (solid line in Figure 4): it captures the bed evolution as well as (iv) (arguably closer to observations near the crest, albeit further eroding the troughs). Importantly, the run time is approximately halved (1 day and 2 hours with (i) versus 2 days and 8 hours with (iv) to model 121 days).

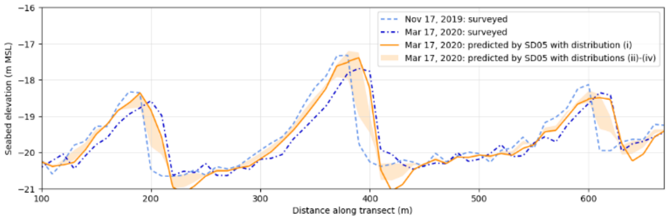

Figure 4. Influence of vertical plane distribution on bed evolution with the SD05 formula.

2) Influence of friction: Simulations were performed in which secondary bedforms (0.1 to 0.2 m high) were filtered from the bed profile and a higher roughness length of 0.1 m, and then 0.2 m, was used as a proxy to account for form drag.

SvR97: A very limited effect was observed with this configuration compared to the original (raw) bed profile. This is attributed to the fact that only hydrodynamics are directly affected by smoother bed and higher friction (SKIN FRICTION CORRECTION = 1 in GAIA), and only a marginal reduction of the depth-averaged velocity is predicted.

SD05: The simulation did not complete and so no conclusions can be drawn as to the influence of friction in this sediment transport formula.

3) Influence of grain size: A single sand fraction is used. Sensitivity to sediment grain size was investigated by varying the median grain diameter within the range observed during recent sediment grab samples in 2019-20 (see Section C), or ± 30% about the average value of 345 μm used throughout.

SvR97: Changes in d_{50} affect not only U_{cr} but also the suspended load coefficient A_{ss} in (1). Finer sediments are slightly easier to mobilise (indicated by a 4% reduction in U_{cr} for $d_{50} = 230$ μm compared to 345 μm), while coarser sediments are slightly harder to mobilise (3% increase for $d_{50} = 450$ μm compared to 345 μm). At the same time, the transport rate associated with suspended load is 34% higher with $d_{50} = 230$ μm and 19% lower with $d_{50} = 450$ μm. This means that, although the morphology of the dunes is not significantly modified, they move at a noticeably faster rate with finer sediments (ca. +50% for $d_{50} = 230$ μm compared to 345 μm). With coarser sediments, the crests are levelled, and the migration rate is reduced (ca. -25% for $d_{50} = 450$ μm compared to 345 μm). The range in predicted bed evolution about that obtained with $d_{50} = 345$ μm (solid line) is represented by a shaded area in Figure 5.

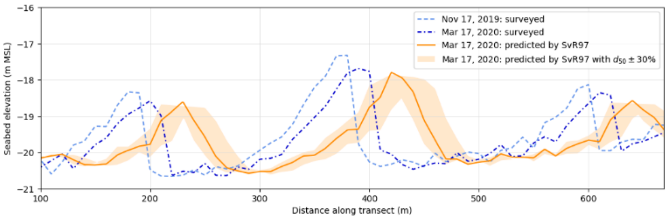

Figure 5. Influence of sediment grain size on bed evolution with the SvR97 formula.

SD05: Bed evolution is shown to be relatively insensitive to grain size with this sediment transport formula. Varying the median grain diameter d_{50} in the range ± 30% leads to a ± 10% difference in the transport rate, but the dune migration rate does not change in the same proportions and the effect is hardly noticeable.

4) Influence of slope effect correction: SvR97: The correction proposed by [25] (FORMULA FOR SLOPE EFFECT = 1) modifies the bedload transport rate to account for the streamwise bed slope effect. By its form, it acts as a diffusion term in the bed evolution equation. Unlike other corrections, it does not modify the critical Shields stress, and so is the only slope effect parameterisation in GAIA that is consistent with the use of the SvR97 sediment transport formula. A simulation run with this correction, and the default β value of 1.3, was not very satisfactory: the dunes slump and decay with time.

SD05: Without slope effect, the formula tends to be unstable: the crests accrete, the troughs erode, and the dunes eventually become too high to be sustainable. Adding the slope effect to the model proved useful for controlling dune growth.

Koch and Flokstra's correction [25] (FORMULA FOR SLOPE EFFECT = 1) was used in the first instance, with default coefficient β = 1.3. The results are encouraging in terms of migration rate, dune height, and slopes (Figure 6), but the lee face migrates faster than the stoss face, meaning that the dunes become wider over time. Soulsby's equation 80a [11] (FORMULA FOR SLOPE EFFECT = 2 and FRICTION ANGLE OF THE SEDIMENT = 32°) was subsequently tested. This formulation adjusts the value of the threshold shear-stress τ_{cr} according to the angle between the flow and the slope direction, the angle of the bed slope, and the angle of repose. The lee slope being steeper than the stoss slope, this is where deviations from τ_{cr} are the largest (± 14-21% compared to 6-7% on the stoss slope; $\tau_{cr} \sim 0.22$ N/m^2). The steep slopes are better conserved with Soulsby's correction, now close to those observed (Figure 6). On the other hand, the dune heights being less dampened than with Koch and Flokstra's correction are high compared to observations. Apsley and Stansby formulation [26] (FORMULA FOR SLOPE EFFECT = 3 and SEDIMENT SLIDE = 2), recently available from the main, was also tested. The agreement is certainly improved for the last dune in the transect, which now follows quite closely the observed steep face. By and large, the dunes are more forward inclined than they were with Soulsby's correction, where the crests were held back; the erosion of the trough is accentuated (Figure 6).

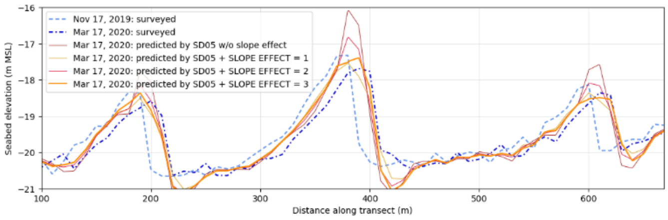

Figure 6. Influence of slope effect correction on bed evolution with the SD05 formula.

5) *Influence of dynamic pressure:* SvR97: Including or not including the dynamic pressure in the simulation does have a noticeable but slight effect. It is noteworthy that the run time is halved when only the hydrostatic pressure is considered.

SD05: On the contrary, dynamic pressure is critical to the good performance of the SD05 formula, as illustrated in Figure 7. Without it, the dunes hardly move; the crests remain at the same location while the troughs fill in to some extent, resulting in a shallower steep slope than initially or observed at the end of the period. This result is not unrelated to the findings of several authors (for example [27]) that vertical flow structures are an important process to support dune development.

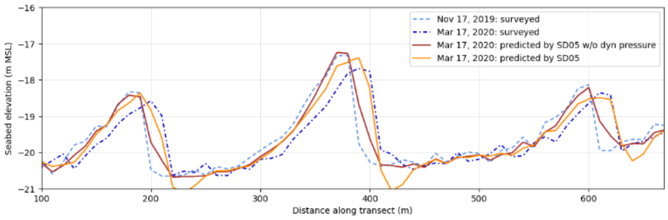

Figure 7. Influence of dynamic pressure on bed evolution with the SD05 formula.

B. Bed evolution and crest migration

1) *With SvR97 total sediment transport formula:* With the current model configuration ((ii) vertical discretisation, $dt = 5\text{s}$) and the use of the SvR97 formula, it takes just over 8 hours to simulate one complete year (without using the morphological factor to accelerate the simulation) on 10 cores of an Intel® Xeon® Platinum 8260 processor.

The threshold velocity, U_{cr}, is in the range 0.41 - 0.43 m/s (for the water depth and sediment conditions at the site) and is exceeded between 60% and 69% of the time over the 4-month period.

Early runs with SvR97 revealed an overprediction of the dune migration rate. This is consistent with the general experience that the formula tends to overestimate the sediment transport rate. The steep slopes become too shallow. After an initial phase of migration, the dunes flatten. If we consider only the bedload component in (1), the transport rate becomes much lower. This is in line with the observation that suspended load transport accounts for approximately 85% of the total transport in (1). There is an indication, over a period of one year, that the dunes are not migrating as much as changing shape (to become more symmetrical).

It is generally accepted that estimates of sediment transport rates are valid within a factor of 2 to 5, particularly in coastal environments. Reference [11] suggests that calibration of formula parameters is possible to improve its performance should site-specific data be available. In our application, a factor of 1/3 was applied to the original total load formula (dark red line in Figure 8), which agreed surprisingly well with the dune profile observed at the end of 4 months.

There is, of course, room for improvement. Lee slopes are not as steep as observed, and the crests tend to hang back compared to the steep face (Figure 8). Over time, a tendency was noted for crest heights to lower and for dunes to become more symmetrical in shape (not shown). This could be attributed to the form of the SvR97 formula, expressed in terms of depth-averaged velocity.

The speed of migration of the central dune crest is plotted in Figure 10 as a function of excess velocity $U - U_{cr}$. A trend seems to emerge of a quadratic relationship between crest migration and excess velocity. Overall, the crest migrates towards the East (the positive values associated with the flood cycle trending East are higher than the negative values associated with the ebb cycle trending West). The net migration speed is equal to 6.8 cm/day or 25 m/yr over the 4-month period between S1 and S2. This is in line with Le Bot's estimate of 37.2 m/yr [22] considering that the crest tends to hold back (i.e., does not move as fast as the body of the dune) with the SvR97 formula.

2) *With SD05 bedload sediment transport formula:* With the current model configuration ((i) vertical discretisation, $dt = 1\text{s}$, slope effect correction) and the use of the SD05 formula, one year does not run to completion on 10 cores of an Intel® Xeon® Platinum 8260 processor with a 3-day wall-time restriction (without morphological factor). The simulation is stopped after 338 days.

The threshold shear-stress τ_{cr} is about 0.22 N/m^2 at the site (uniform in space and time since it depends only on D_*, hence d_{50}). It is exceeded between 42% and 79% of the time over the 4-month period (the lower values are associated with the troughs, and the higher values with the more active crests). Good agreement is obtained with this sediment transport formula at the end of the period (Figure 9). In particular, the slopes of the dunes are correctly predicted. However, it should be noted that the simulation shows signs of divergence (exacerbation of crests and troughs) and that, over a longer period (November 2019 to August 2020, not shown), the agreement with observations is not as satisfactory as that depicted in Figure 9.

The speed of migration of the central dune crest is plotted in Figure 11 as a function of excess shear-stress. The correlation is less clear than it was for the SvR97 formula: there is quite some spread in the data. The net migration speed is 8.7 cm/day or 32 m/yr over the 4-month period. This is comparable to Le Bot's estimate of 37.2 m/yr [22] and ties in with the observations that the SD05 formula is able to closely predict the dune morphology (in particular the slopes).

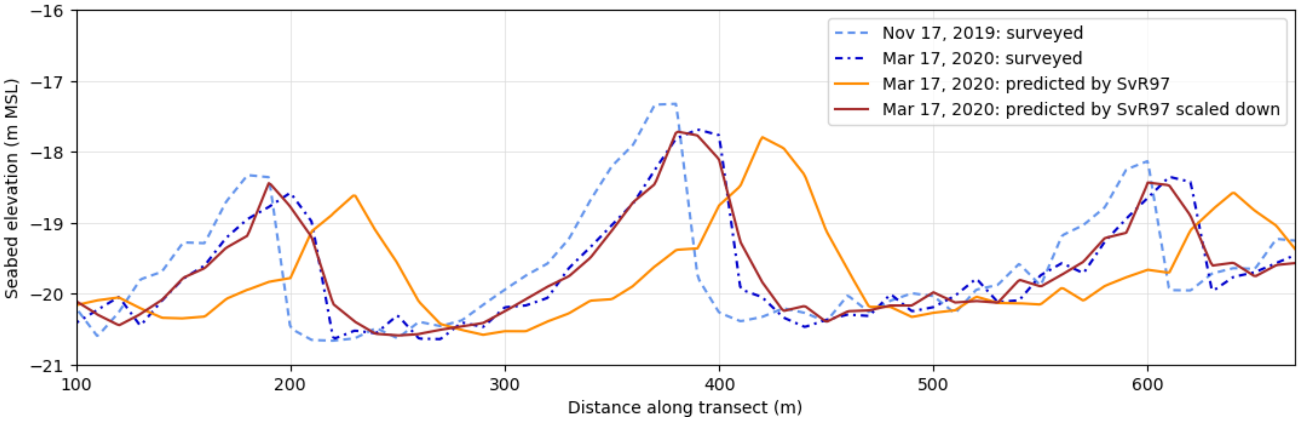

Figure 8. Comparison of SvR97 model predictions against observed dune migration for the period S1-S2, including results from scaled down transport rates.

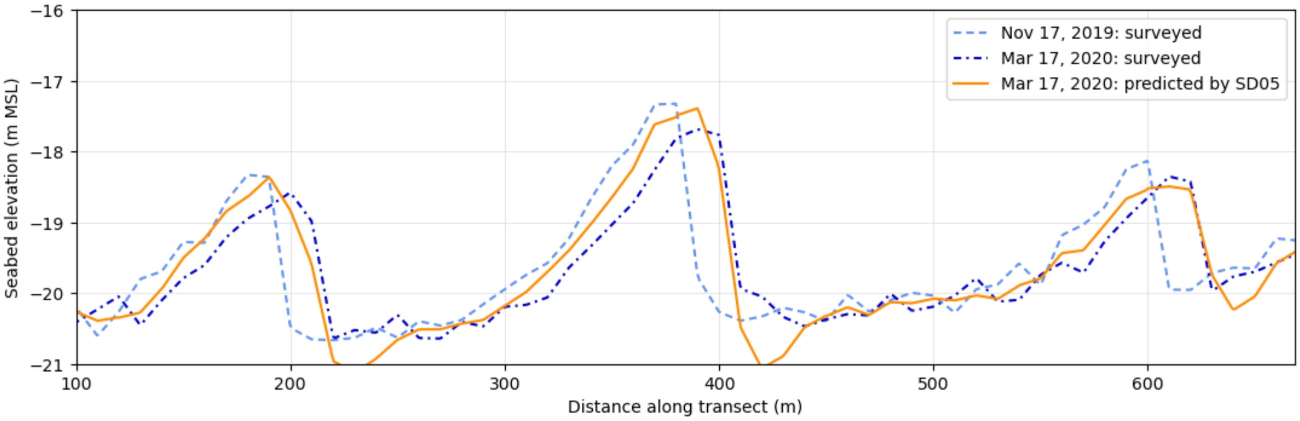

Figure 9. Comparison of SD05 model predictions against observed dune migration for the period S1-S2.

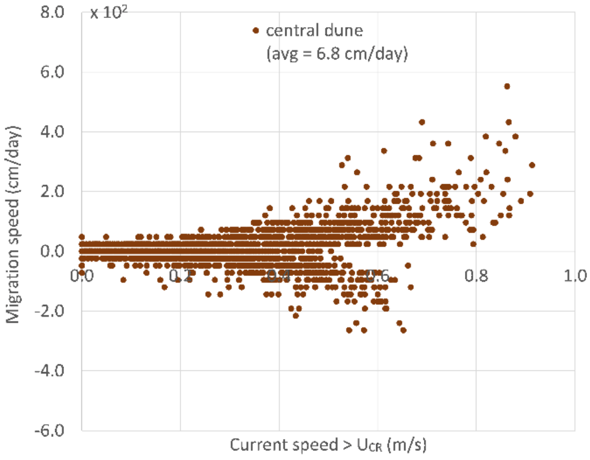

Figure 10. Relationship between crest migration speed and excess velocity predicted with the SvR97 (scaled down) formula.

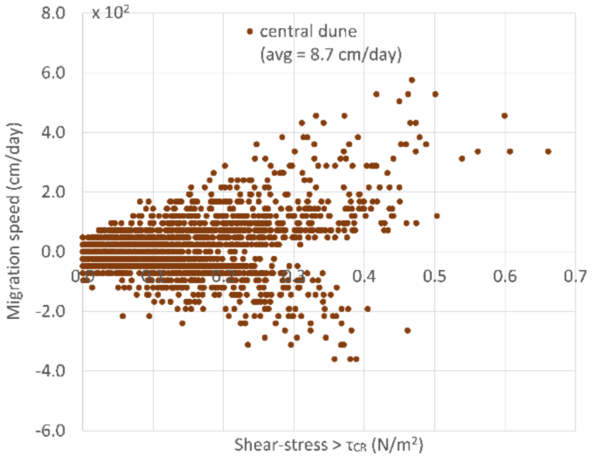

Figure 11. Relationship between crest migration speed and excess shear-stress predicted with the SD05 formula.

IV. CONCLUDING REMARKS

A simplified flume-like configuration has been developed to model the evolution of a marine dune train over a period of 4 months. This made it possible to study the behaviour of two sediment transport formulae that are relevant to coastal settings, one based on velocities and the other on bed shear-stresses; and to identify the sensitivities and optimal parameters to reproduce in situ data. In keeping with earlier findings that the area is current-dominated and bedload is the main mechanism of sediment transport, suspension and wave processes have been omitted in this work.

The Soulsby and van Rijn (SvR97) formula is a simple, robust, and efficient formula. The analysis performed here showed that this formula is sensitive to grain size. Corrections to integrate the slope effect have been found to lead to dune decay and are, therefore, not desirable. Some limitations are identified in the form of the SvR97 formula, but overall, we found that it is able to model the seabed evolution quite satisfactorily once a scaling factor was applied.

The Soulsby and Damgaard (SD05) formula is a promising formula that predicts the morphology of the dune quite closely once an adequate vertical plane distribution is adopted. It tends to exaggerate the crest and trough elevations. This makes the model liable to instabilities over long periods of time, although the slope effect correction does help. We found that dynamic pressure is crucial to the good performance of the formula.

The next step will be to transfer these findings to the regional TELEMAC-3D+GAIA model (computational domain ca. 55 x 75 km^2) to consider 3D effects on large-scale morphological processes and how they could affect the evolution of the dune field. Another area of interest is the inclusion of wave processes to model a period with intense wave activity.

ACKNOWLEDGEMENTS

This work was initiated by France Energies Marines, with financial support from the French National Research Agency ANR (Grant no ANR-10-IEED-0006-34) and EDF R&D POWERX project. The authors thank the partners of the MODULLES project for providing site-specific data and giving permission to publish this work. N.D. thanks Ecole Doctorale SIE for awarding a grant to attend and present this work at the TELEMAC User conference.

REFERENCES

[1] N. Durand, P. Tassi, O. Blanpain, and A. Lefebvre. Towards numerical modelling of marine dunes in a shallow shelf sea. In Actes des XVII^{èmes} Journées Nationales Génie Côtier - Génie Civil, 2022.

[2] N. Durand, P. Tassi, O. Blanpain, and A. Lefebvre. Hydrodynamic modelling as a first step to assess marine dune dynamics: influence of waves. In XXVIIIth Telemac-Mascaret User conference, 2022.

[3] N. Durand, P. Tassi, O. Blanpain, and A. Lefebvre. Understanding marine dune dynamics in a shallow shelf sea using sediment mobility indices. In Marine and River Dune Dynamics VII Book of Proceedings, pages 109–116, 2023.

[4] GAIA Validation Manual, v8p4, December 2022.

[5] P.K. Tonnon, L.C. van Rijn, and D.J.R. Walstra. The morphodynamic modelling of tidal sand waves on the shoreface. Coastal Engineering, 54(4):279–296, 2007.

[6] G.H.P. Campmans, P.C. Roos, H.J. de Vriend, and S.J.M.H. Hulscher. The influence of storms on sand wave evolution: A nonlinear idealized modeling approach. Journal of Geophysical Research: Earth Surface, 123(9):2070–2086, 2018.

[7] G.H.P. Campmans, P.C. Roos, and S.J.M.H. Hulscher. Storm influences on sand wave dynamics: an idealized modelling approach. In Marine and River Dune Dynamics VI Book of Proceedings, pages 33–39, 2019.

[8] C. Auguste, P. Marsh, J.-R. Nader, I. Penesis, and R. Cossu. Modelling morphological changes and migration of large sand waves in a very energetic tidal environment: Banks Strait, Australia. Energies, 14(13), 2021.

[9] J.H.J. Terwindt. Sand waves in the southern bight of the North Sea. Marine Geology, 10(1):51–67, 1971.

[10] P. Tassi, T. Benson, M. Delinares, J. Fontaine, N. Huybrechts, R. Kopmann, S. Pavan, C.-T. Pham, F. Taccone, and R. Walther. GAIA - a unified framework for sediment transport and bed evolution in rivers, coastal seas and transitional waters in the TELEMAC MASCARET-modelling system. Environmental Modelling Software, 159:105544, 2023.

[11] R.L. Soulsby. Dynamics of marine sands. Thomas Telford Publishing, 1997.

[12] J. Fredsøe and R. Deigaard. Mechanics of Coastal Sediment Transport. World Scientific, 1992.

[13] B.W. Borsje, W.M. Kranenburg, P.C. Roos, J. Matthieu, and S.J.M.H. Hulscher. The role of suspended load transport in the occurrence of tidal sand waves. Journal of geophysical research. Earth surface, 119(4):701–716, 2014.

[14] J.A. Bailard. An energetics total load sediment transport model for a plane sloping beach. Journal of Geophysical Research: Oceans, 86(C11):10938–10954, 1981.

[15] M. Dibajnia and A. Watanabe. Sheet flow under non-linear waves and currents. In Coastal Engineering 1992, number 23, page 2015–2029. ASCE, 1992.

[16] P.A. da Silva, A. Temperville, and F. Seabra Santos. Parameterized sand transport model for combined currents and waves in rippled and flat bed regimes. SEDMOC Sediment Transport Modelling in Marine Coastal Environments, chapter C, pages CE1–CE10. Aqua Publications, 2001.

[17] E.W. Bijker. Littoral drift as function of waves and current. In Coastal Engineering 1968, number 11. ASCE, 1968.

[18] R.L. Soulsby and J.S. Damgaard. Bedload sediment transport in coastal waters. Coastal Engineering, 52(8):673–689, 2005.

[19] R.L. Soulsby. The “bailard” sediment transport formula: comparison with data and models. Advances in Coastal Morphodynamics, pages 2.48–2.53. Delft Hydraulics, 1995.

[20] A.J. Grass. Sediment transport by waves and currents. Technical Report FL29, SERC London Cent. Mar. Technol., 1981.

[21] P. Nielsen. Coastal Bottom Boundary Layers and Sediment Transport. World Scientific Publishing, 1992.

[22] S. Le Bot, M. Bary, M. Fournier, A. Husté, N. Michelet, O. Blanpain, M. Nexer, and T. Garlan. Marine dune morphodynamics and sediment fluxes (off dunkirk, france). spatio-temporal variability and relations with hydrodynamic forcings. In Marine and River Dune Dynamics VII Book of Proceedings, pages 155–162, 2023.

[23] A. Goll, R. Kopmann, and T. Brudy-Zippelius. Numerical modelling of bed formes (dunes) with TELEMAC-3D and SISYPHE. In XVIIIth Telemac-Mascaret User conference, pages 16–21, 2011.

[24] L.C. van Rijn. Unified view of sediment transport by currents and waves. I: Initiation of motion, bed roughness, and bed-load transport. Journal of Hydraulic Engineering, 133(6):649–667, 2007.

[25] F.G. Koch and C. Flokstra. Bed level computations for curved alluvial channels. In Proceedings of the XIXth Congress of the Int. Ass. for Hydr. Res., 1980.

[26] D.D. Apsley and P.K. Stansby. Bed-load sediment transport on large slopes: Model formulation and implementation within a RANS solver. Journal of Hydraulic Engineering, 134(10), 2008.

[27] S.J.M.H. Hulscher. Tidal-induced large-scale regular bed form patterns in a three-dimensional shallow water model. Journal of geophysical research : Oceans, 101(C9):20727–20744, 1996.

Application of the Lower Sea Scheldt model in TELEMAC-2D: Studying the impact of bridge piers

Jeroen Stark[1], Bart De Maerschalck[1]
jeroen.stark@mow.vlaanderen.be, Antwerp, Belgium
[1]Flanders Hydraulics

Abstract **– The potential impact of the construction of a new cyclist bridge south of Antwerp is studied using a TELEMAC-2D model of the Lower Sea Scheldt. The hydro-morphological impact of the bridge piers is assessed by changes in flow patterns and changes in bottom shear stresses as a result of the pier construction. Exceedance frequencies of a relevant critical shear stress are calculated as well to illustrate potential changes in high- or low-dynamic zones in the study area. Various configurations of bridge piers and support buttresses are tested in a scenario analysis. In addition, several horizontal turbulence model settings are tested in a sensitivity analysis to optimize the representation of the flow patterns and turbulent wakes around the bridge piers.**

Keywords: TELEMAC-2D; bridge piers; Scheldt estuary; horizontal turbulence model.

I. INTRODUCTION

To increase the accessibility of the city of Antwerp for cyclists and to support a modal shift in passenger traffic, the *“OVER THE RING”* project provides for the construction of a new Scheldt bridge for cyclists near the existing Kennedy tunnel just south of Antwerp (Figure 1). This study concerns the hydro-morphological impact of the construction of bridge piers for this new bridge over the Scheldt river in Antwerp, Belgium. A TELEMAC-2D model of the Lower Sea Scheldt, developed by Flanders Hydraulics [1], is applied to study the impact of the bridge piers and quay wall buttresses on the tidal flow patterns in the navigation channel and at the surrounding intertidal flats at the left bank side.

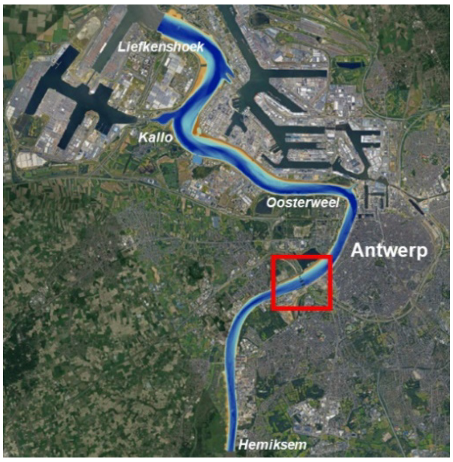

Figure 1. Study area and model domain.

A. Study area

Figure 2 shows the study area just upstream from Antwerp. Along the left bank, the river is surrounded by intertidal mud flats and salt marshes, whereas a vertical quay wall is present along the right bank. The bridge piers are located just upstream of the Kennedy tunnel, recognizable by the protruding levees at the left bank and hence local narrowing of the river width. The most southern main pier is located close to the quay along the right bank, while the other main pier is located centrally in the present fairway. After construction, the main shipping channel will be located between the two main piers, while inland navigation can also move between the left bank and the central pier. The piers are all surrounded by guiding fenders. In addition to the design options with two main bridge piers (i.e., the central and southern pier in Figure 2), several configurations with additional smaller piers closer to the left bank are tested as well. Some of the proposed designs also provide for the construction of an underwater buttress along the existing quay walls at the right bank. These buttresses must stabilize the relatively old quay walls. One of the design options tested in this modelling study also includes an excavation of part of the existing quay to 0 m TAW (i.e., around low water level) along with the construction of a new embankment with a gentle slope of 1:5.

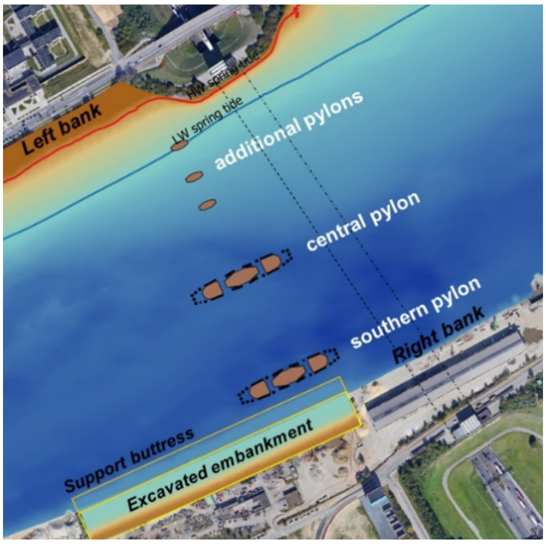

Figure 2. Overview of design scenarios including bridge piers, support buttress and quay wall excavation.

II. MODEL DESCRIPTION

The Lower Sea Scheldt model (here referred to as BZS model) was originally set up by Flanders Hydraulics [1] in TELEMAC-2D (v7p2r2). It covers a 25-km estuary stretch around Antwerp and is forced by observed water level series at both the upstream and downstream boundary. The BZS model has been applied for several hydro-morphological impact studies, including the impact of quay walls, jetties and piers on local flow patterns. This study concerns the potential impact of new bridge piers on flow patterns and tidal flat stability.

The computational mesh of the BZS model was constructed with the advanced triangular mesh generator GMSH [2]. A channel-mesh (structured triangular grid) is applied along the fairway, while adaptive refinement of an unstructured mesh was applied to achieve more accurate predictions at areas of interest or with a complex geometry, such as along the river banks. The total number of elements of the computational grid of the BZS model is approximately 330000 to 350000, depending on the scenario, while the node number varies between 168000 and 180000. The average node distance varies between 10 m and 20 m in the original BZS model without implementation of the bridge piers. However, the resolution is refined up to about 1.5 m in the scenario analysis to adequately implement the piers (Figure 4).

Some numerical settings and physical parameters of the BZS model are included in Table I. For the present analysis, a reduced time-step of 0.5 s was selected after initial testing, ensuring computational stability and accuracy. In particular, longer time-steps induce instabilities at specific dry-wet zones of high spatial resolution (i.e., after mesh refinement at the bridge piers for this scenario analysis). As initial condition, a constant water level equal to 1.57 m TAW is implemented over the entire computational domain. Hence, a hydrodynamic spin-up period of one day is necessary before the model produces relevant output. The relevant simulation period covers one spring-neap tidal cycle (02/04/2018 - 18/04/2018) after this spin-up period. Figure 3 shows modelled water levels at Antwerp for the entire simulation period. The red part of the curve illustrates the spring tide that is selected for the analysis of maximum flood and ebb currents, which provided input for further assessments of the nautical safety [3]. This spring-tide has a tidal range of over 6.5 m at Antwerp, which is considerably higher than the average spring tidal range of 6.0 m. The hydro-morphological impact of the bridge piers is analysed using the full time series (i.e., full spring-neap cycle). This impact is assessed based on maximum velocities, maximum bed shear stresses as well as exceedance probabilities of a critical bed shear stress.

Table I General model settings

Parameter	***Value***
Time step	0.5 s
Initial conditions	constant elevation: 1.57 m
Coriolis force	No
Salinity transport	Off
Law of bottom friction	Manning (n = 0.018 $m^{1/3}/s$)
Option for treatment of tidal flats	1
Treatment of negative depths	1: smoothing
Free surface gradient compatibility	0.9
Turbulence model	5: Mixing length model
Scheme for advection of velocities	1: method of characteristics
Scheme for advection of water depth	5: conservative scheme
Implication for depth	0.6
implication for velocities	1.0
Solver	7: GMRES method

A. *Calibration and validation*

The BZS model was calibrated by tuning bottom friction and varying the turbulence model. The impact of various settings of the turbulence model is discussed in more detail in Section IV. Sensitivity tests indicated that a uniform Manning roughness coefficient of $n = 0.018\ m^{1/3}/s$ could be applied for bottom friction over the entire model domain.

Moreover, the influence of wall friction was assessed by varying the ROUGHNESS COEFFICIENT OF BOUNDARIES between $k_s = 0\ m$ (i.e., smooth wall), $k_s = 0.05\ m$ and $k_s = 1.0\ m$ using the Nikuradse formula. However, no significant differences were noticed between those configurations.

The model was validated for the representation of water levels at the permanent tidal measurement stations at Kallo and Antwerp and for velocity measurements at Oosterweel (see Figure 1 for these locations). Validation shows that the model represents tidal water level variations with a ME and RMSE of

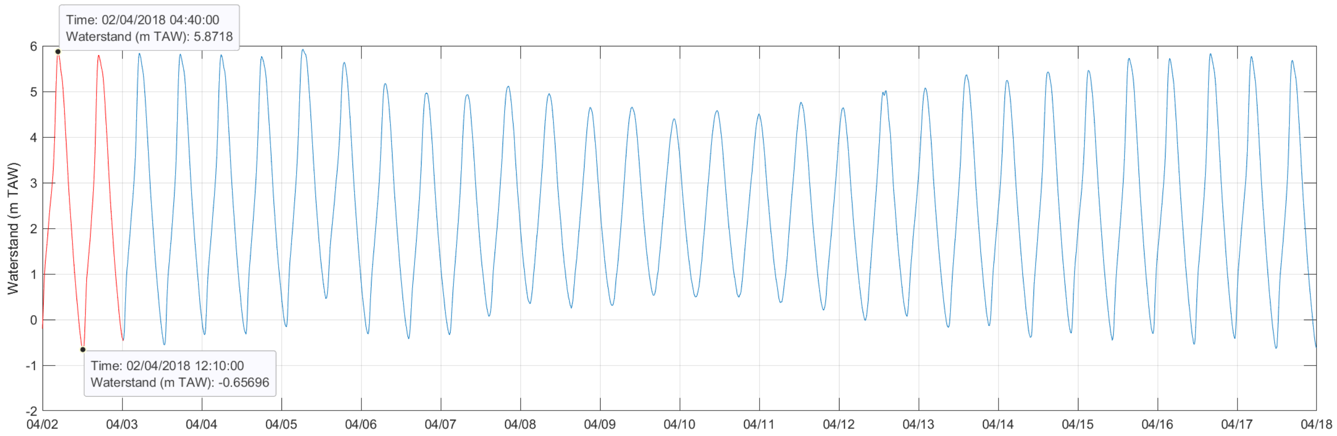

Figure 3. Modelled water level time series at Antwerp.

less than 0.05 m throughout the model domain (Table II). Flow velocities along a sailed ADCP measurement transect and at single-point measurement stations are also represented well. However, ebb velocities at the measurement transect are underestimated near the river banks when the default settings of the mixing length model are applied (Figure 5).

Table II Model validation: water levels

Station	***BIAS [m]***	***RMSE [m]***	***RMSE$_0$ [m]***
Kallo	0.01	0.02	0.02
Antwerpen	-0.03	0.05	0.03

B. Implementation of model scenarios

Table III gives an overview of the various configurations that were tested. Figure 2 shows the locations of the bridge piers as well as the surface area of the excavated right bank that are implemented in these scenarios. For each of the investigated scenarios the computational grid had to be properly adapted and refined in the vicinity of the interventions in order to be aligned with the outline of the proposed constructions (i.e., bridge piers and support buttresses). The refined mesh thus follows the detailed geometry of the piers (Figure 4). For some scenarios, planned excavations of the existing river bank are included by locally expanding the mesh.

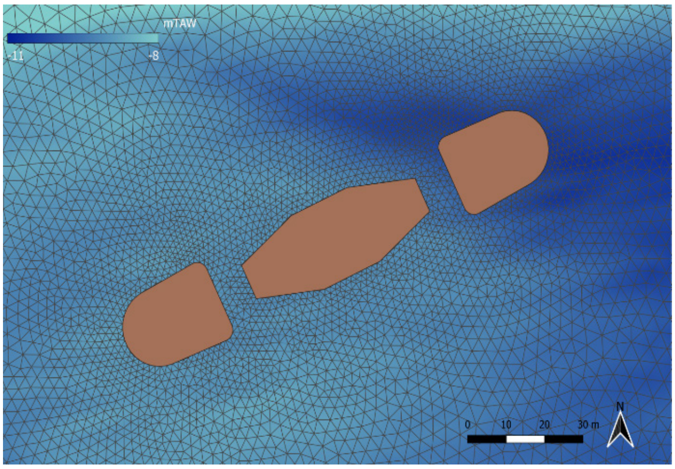

Figure 4. detail of the mesh at one of the bridge piers.

Table III Overview of model scenarios

id	***Description***
ref005	*Reference run "present" situation (2018 bathymetry)*
scen012	*two main pylons*
scen023	*two main pylons + excavation and support buttress at right bank*
scen024	*two main pylons + small pylon 1 + excavation and support buttress at right bank*
scen025	*two main pylons + small pylon 2 + excavation and support buttress at right bank*
scen026	*two main pylons + small pylon 3 + excavation and support buttress at right bank*
scen027	*central pylon + excavation and support buttress at right bank*
scen028	*central pylon + small pylon 2 + excavation and support buttress at right bank*

III. RESULTS

The potential impact of the new bridge was assessed by changes in flow patterns (e.g. during maximum ebb and maximum flood) and changes in bottom shear stresses due to the pier construction. As current velocities in very shallow zones and areas that dry up are not very adequately represented in TELEMAC-2D, only model output is used in the analysis for which the water depth in the grid point is at least 1 cm.

In this section, the results of the reference scenario (without bridge piers) and scen023 (i.e., base scenario with two main piers, a support buttress and quay wall excavation along the right bank) are discussed in more detail. The results of all other scenarios with various bridge pier configurations (i.e., combinations of main piers and additional pylons) and different geometries of the support buttresses are available in two Flanders Hydraulics reports [4] and [5].

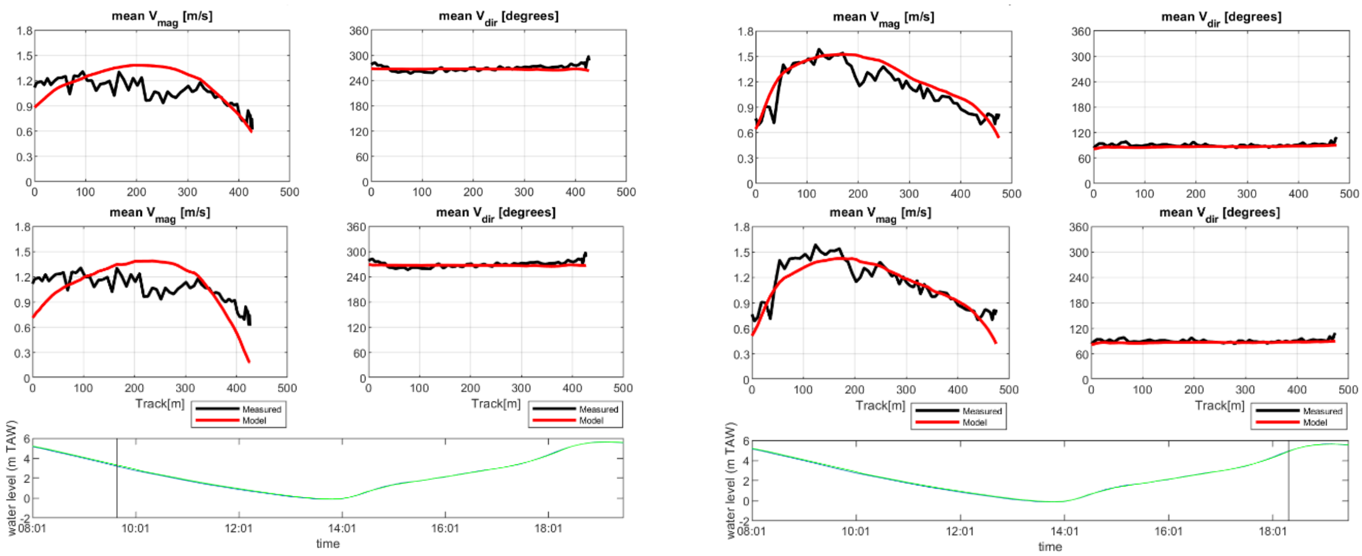

Figure 5. Validation of current velocities at Oosterweel during maximum ebb (left) and maximum flood (right) for two configurations of the horizontal turbulence model: mixing length model with $C_L = 0.26$ (upper panels) and a time- and water level dependent C_L (mid panels).

A. Hydrodynamic impact

Figure 6 shows the modelled maximum velocities. The maximum flood current in the study area is significantly higher than the maximum ebb current. In the reference run without bridge piers, peak flow velocities are up to 2.1 m/s during high tide and up to 1.7 m/s during ebb tide. The highest current velocities occur centrally in the river during both high tide and low tide, approximately at the location where the central pier will be constructed.

As a result of the construction of the two bridge piers and the support buttress in scen023, which reduce the cross-sectional area by approximately 10-20% depending on the water level, peak flow velocities in the study area increase to more than 2.4 m/s during maximum flood and more than 1.9 m/s during maximum ebb, with the highest velocities in the middle of the main fairway. In between and around the two main bridge piers, both the ebb current and the flood current increase by +0.2 to +0.3 m/s compared to the current situation.

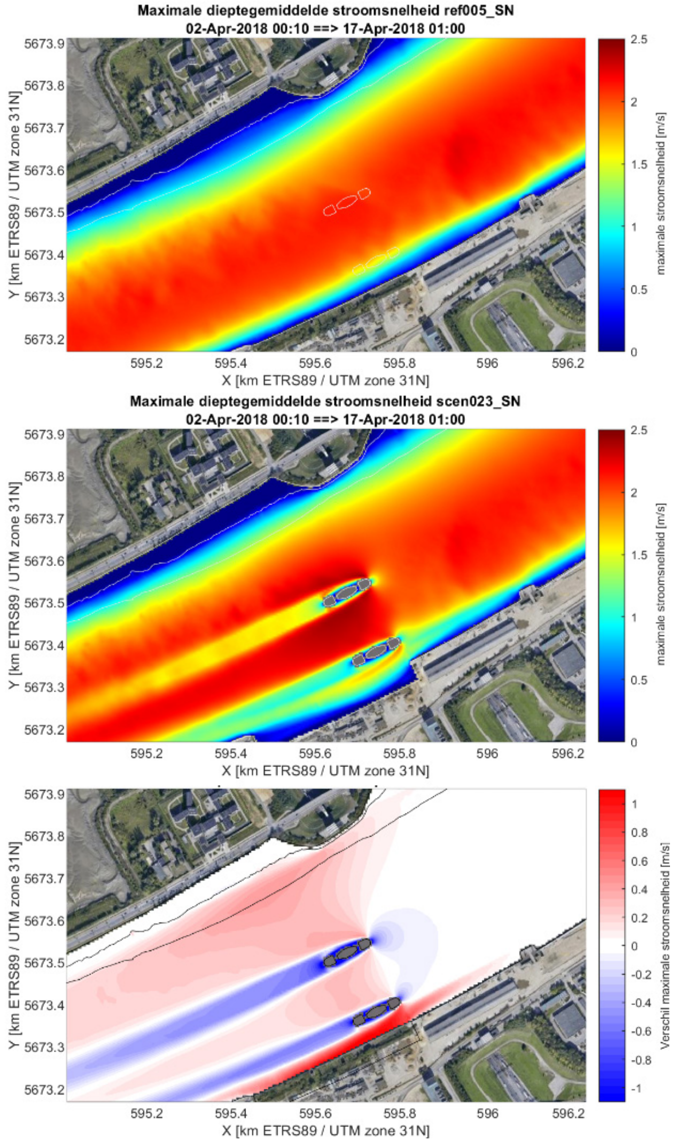

Figure 6. Maximum modelled velocities over a full spring-neap cycle in reference scenario ref005 (top), in scen023 (mid) and the difference (bottom).

There is also a significant increase in maximum flow velocities along the left bank, potentially affecting the intertidal mudflats which are situated there. Just upstream of the Kennedy tunnel, peak flood velocities increase by up to +0.5 m/s during high tide. Ebb flow increases slightly less severe in this area (up to +0.2 m/s). The downstream situated mudflats are less affected as the ebb currents are weaker and due to the sheltering effect of the protruding dike at the Kennedy-tunnel.

Figure 7 illustrates the influence of the support buttress and shallow excavation of the right bank on the maximum speed based on scen023 (i.e., with bridge piers, support buttress and right bank excavation) and scen012 (without support buttress and quay wall excavation). The excavation on the right bank enlarges the tidal flow between the right bank and the southern pier and slightly reduces the tidal flow and hence maximum currents near the left bank. However, the impact of the support buttress and excavation is much less than the impact of the bridge piers themselves.

B. Morphodynamic impact

Figure 8 shows the maximum bed shear stresses, as well as the exceedance frequency of a relevant critical shear stress, both based on the full spring-neap simulation period. The exceedance frequencies are calculated to illustrate potential changes in high- or low-dynamic zones in the study area. In particular, a low exceedance probability of <10% for $\tau_b \geq 1.0\ N/m^2$ approximately coincides with the low-water mark on the left bank (i.e., black contour line in Figure 2) in the reference run (Figure 8). Higher elevated intertidal zones have a lower exceedance frequency, while the subtidal in and the trench are characterized by a higher exceedance frequency. Therefore, an exceedance probability of $\tau_b \geq 1.0\ N/m^2$ will be considered as a proxy for the boundary between intertidal and subtidal areas along the left bank in the scenario analysis.

In scen023, the bed shear stresses and the exceedance probability of $\tau_b \geq 1.0\ N/m^2$ increase in a zone along the left bank, affecting a stretch of approximately 500 m of intertidal flats. There is also an increase in bed shear stresses in the subtidal zone along the left bank, which may imply that protective measures against erosion are necessary in this area. The impacted zone is mainly situated upstream of the bridge, with the strongest effects parallel to the piers and around the

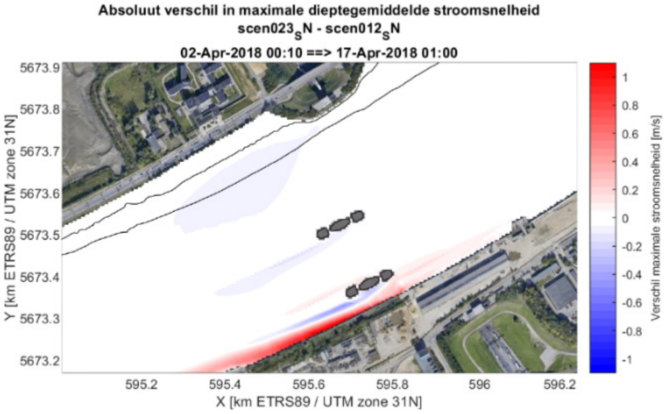

Figure 7. Difference in maximum flow velocities over a full spring-neap cycle between scen023 and scen012.

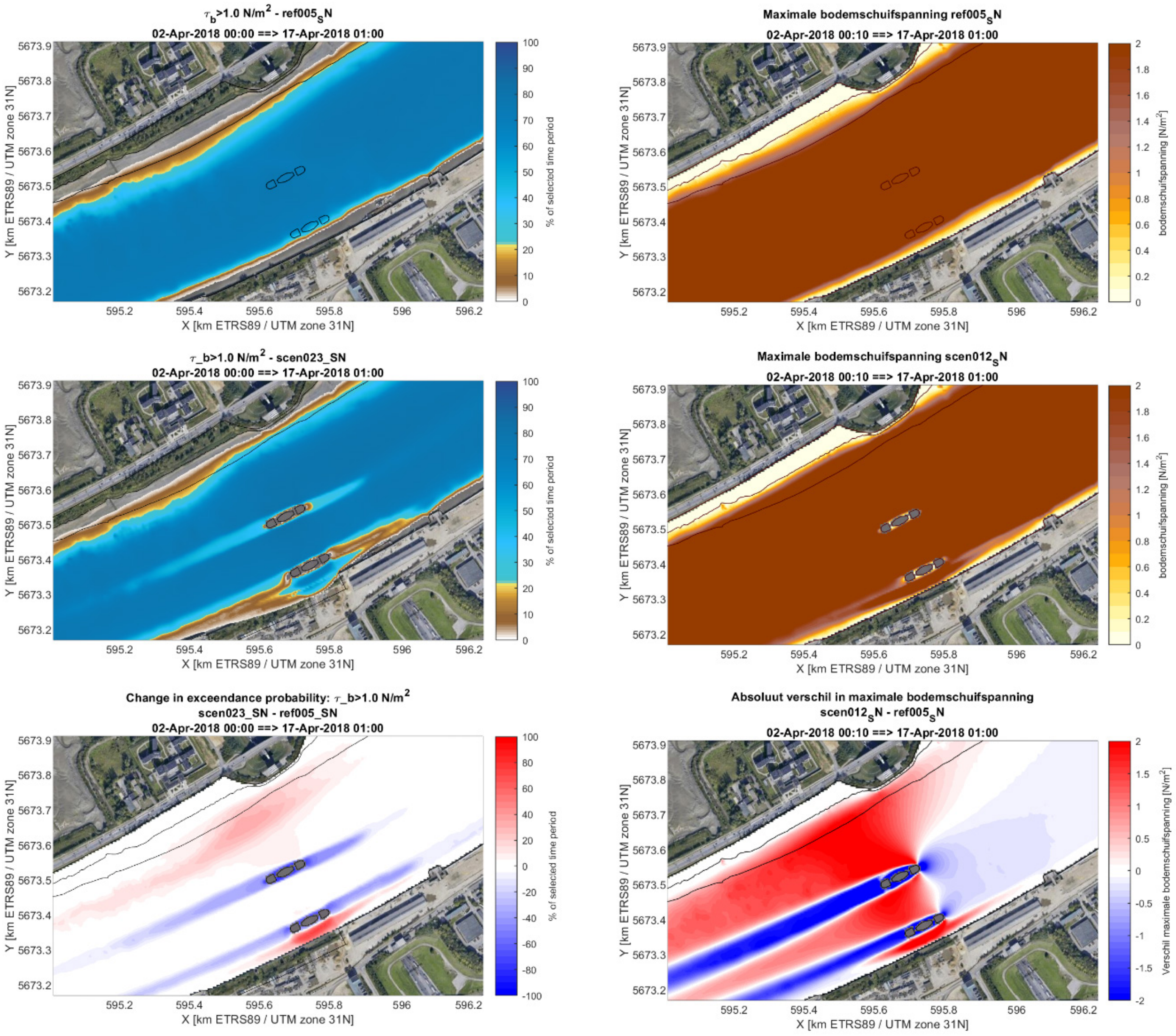

Figure 8. Maximum modelled bed shear stresses (right panels) and exceedance probabilities (left panels) of a critical bed shear stress of $\tau_b \geq 1{,}0\ N/m^2$ over a full spring-neap cycle in reference scenario ref005 (top panels), in scen023 (mid panels) and the difference (bottom panels).

low water line.

Between the two bridge piers, the exceedance frequency of $\tau_b \geq 1.0\ N/m^2$ barely increases, as this zone in the middle of the existing fairway is already characterized by a very high exceedance frequency in the reference situation. However, there is an increase in the maximum bed shear stress, related to higher peak velocities, but further deepening of the main fairway will probably be rather limited due to the presence of less erodible clay layers.

As for the flow velocities, the implementation of the bridge piers causes a strong decrease in the maximum bed shear stresses and the exceedance frequency of $\tau_b \geq 1.0\ N/m^2$ in the wake behind the bridge piers. This wake is present in both upward and downward direction. It should be noted that turbulent flows caused by the fender piers and guiding constructions are not calculated by the current TELEMAC-2D model as they are too small to implement correctly with the applied model resolution and that the structure of the wake could not be validated either. Three-dimensional effects at the foot of the bridge piers, which are typically responsible for erosion pits that are formed around such cylindrical structures, are not simulated either. Finally, the feedback from morphological developments on the hydrodynamics as a result of changed flow patterns is neither calculated. For example, erosive behaviour at the shoal near the left bank can be expected where shear stresses increase. Similarly, zones with decreasing bed shear stresses could accrete. Such morphological changes may in turn influence current velocities.

IV. SENSITIVITY ANALYSIS: THE HORIZONTAL TURBULENCE MODEL

While calibrating the BZS model, various turbulence models and settings were tested to optimize the model performance and in particular to enhance ebb velocities over the shallow river banks as these were underestimated in the original model validation runs with Prandtl's mixing length model and a constant mixing length coefficient of $C_L = 0.27$ (Figure 5). The mixing length L_m itself is calculated as $L_m = C_L \cdot \kappa \cdot h$, in which C_L is a calibration coefficient with $C_L = 4/15 \approx 0.27$ as default value, κ is the Von Kármán constant and h is the water depth. The model was further calibrated by applying a variable mixing length coefficient C_L in order to enhance the ebb velocities along the banks. In particular, C_L is configured to remain constant and equal to its default value during flood, and gradually increases up to 10 times its default value, i.e. from $C_L = 0.27$ to $C_L = 2.67$ for free surface elevations lower than 4 m TAW during the ebb phase. The above criterion is regulated by a free surface gradient condition, i.e., based on water depth and water level gradients. It is noted that the high-end values of the time-varying C_L are outside the range of what is considered common in literature (i.e., $0.27 < C_L < 1.25$) [6].

Increasing the mixing length coefficient C_L on shallow areas during ebb leads to higher ebb velocities along the banks and hence improves the representation of the observed tidal flow velocities along the shallow banks at the Oosterweel transect (Figure 4). However, these settings also induced strongly asymmetric flow patterns between flood and ebb at the study site (Figure 9), which were deemed unrealistic. Therefore, several turbulence models and settings are tested in a sensitivity analysis to optimize the model settings for the representation of tidal flow around the bridge piers. Table IV shows some of the configurations that are used to assess the impact of applying various turbulence models to the maximum flood and ebb flow around the bridge piers in the scenario with two large piers and without excavation of the right river bank. These configurations include the mixing length model with various settings for C_L and a simulation with the K-ϵ turbulence model as the mixing length turbulence model does not take into account turbulent kinetic energy transport and dissipation. Finally, a model simulation with a low constant velocity diffusivity is carried out as well.

These sensitivity tests show that the mixing length model with default settings and the K-ϵ model lead to very similar results. Despite the fact that C_L is only increased in the shallow parts during ebb, Figure 9 shows that applying the time-varying C_L has a significant impact on the flow around the piers during ebb current. In this configuration, the flow around the piers becomes strongly asymmetric between ebb and flood (i.e., for similar ebb and flood velocities), while there is no physical explanation for this asymmetry. On the other hand, when applying a constant C_L or the K-ϵ model, the flow pattern around the piers is more comparable between ebb and flood. As scen012 with the default settings of the mixing length model leads to more reliable results than scen009 with variable C_L and also gives the more stable results than scen015 with the K-ϵ model, this configuration is eventually applied in the present scenario analysis.

Table IV Overview of sensitvity tests.

id	***Description***
scen009	Mixing length model (C_L time/depth-dependent)
scen012	Mixing length model (C_L = 0.27; TELEMAC-2D default)
scen013	Mixing length model (C_L = 2.67)
scen014	Mixing length model (C_L = 1.25; maximum according to [6])
scen015	K-ϵ turbulence model
scen016	CONSTANT VELOCITY DIFFUSIVITY = 0.005

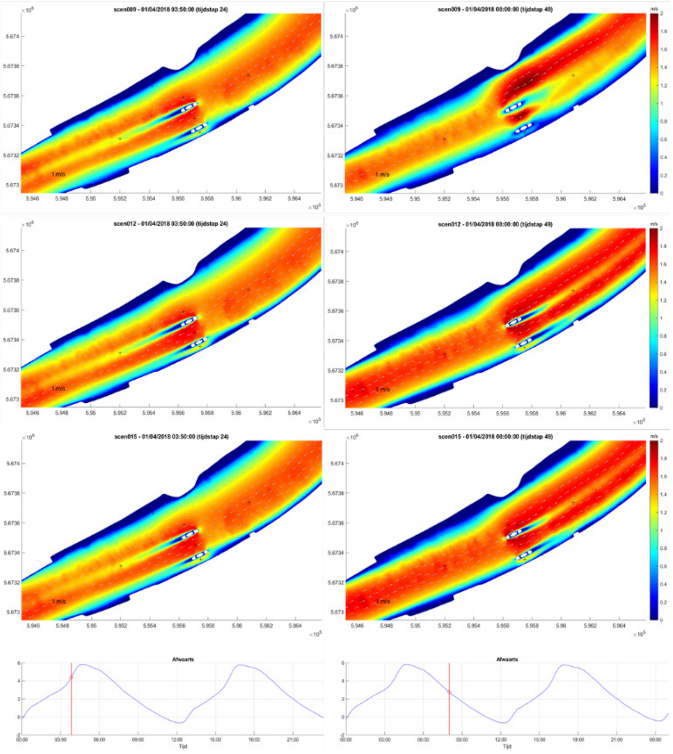

Figure 9. Modelled typical flow patterns at the bridge piers during flood (left) and ebb (right) for scen009 (top), scen012 (mid) and scen015 (bottom).

A. *Oscillating vortex streets*

In the above simulations, no oscillating Von Kármán vortices are noticeable in the wake behind the bridge piers. It is known that shallow water solvers based on finite element methods, such as TELEMAC-2D, induce numerical diffusion which tends to smooth out any vortices in the wake due to additional diffusion in the momentum equation [7]. Nevertheless, additional sensitivity tests with a CONSTANT VELOCITY DIFFUSIVITY = 0.005 in scen016 allow for the reproduction of oscillating Von Kármán vortices behind the bridge piers (Figure 10) as the additional diffusivity induced by the turbulence model is now limited to a relatively low value. The size and frequency of these vortices could not be validated due to a lack of measurements at similar sites along the Scheldt river. From literature, it is known that the formation of oscillatory vortices behind piers or pylons is highly dependent on the shape of these piers as well as on the Reynolds number ($RE = V \cdot d \cdot v^{-1}$, with V the undisturbed upward velocity, d the characteristic length related to the diameter of the pier and v

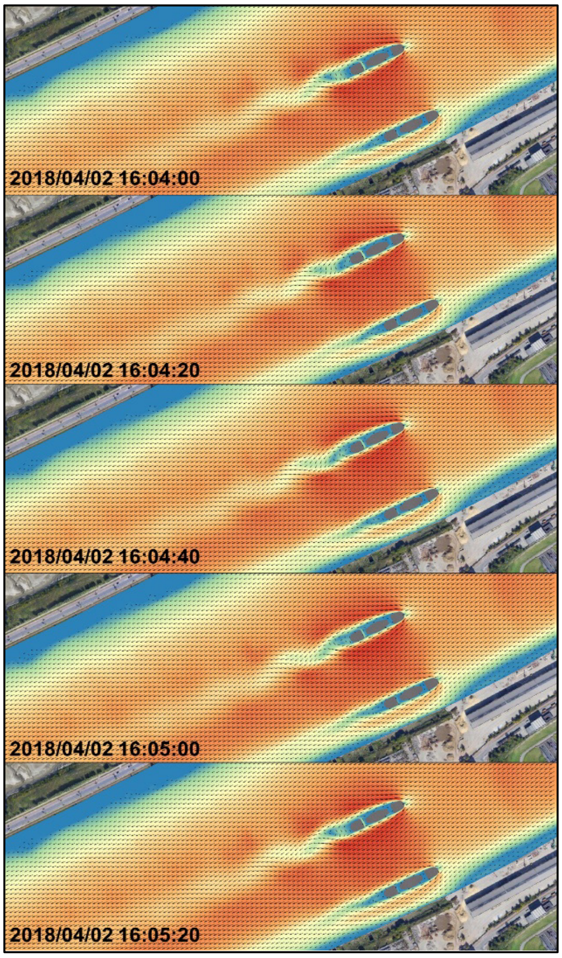

Figure 10. Oscillating Von Kármán vortices in scen016 with CONSTANT VELOCITY DIFFUSIVITY = 0.005.

the kinematic viscosity). For comparison, for a cylindrical pier with a diameter of 20 m and a flow velocity of 1.0 m/s, the Reynolds number is approximately $15{\cdot}10^6$, which should induce a turbulent flow with or without an oscillating character.

V. CONCLUSIONS

The potential impact of the construction of bridge pylons for a new cyclist bridge south of Antwerp was studied using a TELEMAC-2D model of the Lower Sea Scheldt (BZS model). The hydro-morphological impact was assessed by changes in flow patterns and changes in bottom shear stresses due to the pylon construction. Exceedance frequencies of a relevant critical shear stress were calculated as well to illustrate potential changes in high- or low-dynamic zones in the study area.

The implementation of the bridge pylons induces an increase in current velocities in the fairway during both ebb and flood. Contrastingly, flow velocities actually decrease in the wake behind the pylons, causing more cross-sectional variation in current velocities. The reduction of the cross-sectional area as a result of the construction of the bridge pylons also enlarges the maximum flow over the intertidal flats along the left bank. The construction of an underwater buttress to protect the quay wall along the right bank has a much more limited influence than the bridge pylons themselves.

A sensitivity analysis for the influence of the horizontal turbulence model indicates that the (turbulent) structure and length of the wake behind the pylons is very sensitive to the applied settings of the horizontal turbulence model. Typical Von Kármán vortices could only be represented using a low constant diffusivity coefficient. It should be noted that the 2D character of the model would only allow for an accurate representation of the wake if vortex shedding is present according to [8]. Moreover, the BZS model resolution does not include all details of the pylons, such as the support fenders along the piers, individual piles in front of the bridge piers, or the pile construction under the collision protection. All these structural elements determine the turbulence induced by the bridge piers and thus the structure of the wake. Ultimately, the computed flow patterns are also used as input for the Flanders Hydraulics ship manoeuvring simulator [3]. Depending on the results of the nautical simulation study, it may be appropriate to model the length of the wake and the possible turbulent vortices in the wake behind the piers in more detail using a CFD (Computational Fluid Dynamics) simulation or a physical scale model.

REFERENCES

[1] G. Kolokythas, S. Smolders, B. De Maerschalck, F. Mostaert, “Accessibility INEOS Oxide jetty: sub report 3. Development of a high-resolution 2D hydrodynamic model for the Lower Sea Scheldt,” FHR reports, 19_075_3. Flanders Hydraulics Research: Antwerp, 2020.

[2] C. Geuzaine, J.-F. Remacle, “Gmsh: a three-dimensional finite element mesh generator with built-in pre-and post-processing facilities,” Int. J. Numer. Methods Eng. 79(11), 2009, pp. 1309–1331.

[3] K. Eloot, J. Verwilligen, “Antwerpen Oeververbinding tussen linker- en rechteroever: Deelrapport 3 – Simulatiestudie invloed brugpijlers en onderwatertalud rechteroever,” FHR reports, 21_113_3. Flanders Hydraulics Research: Antwerp, 2022.

[4] J. Stark, B. De Maerschalck, “Antwerpen Oeververbinding tussen linker- en rechteroever: Deelrapport 2 – Hydrodynamische modellering brugpijlers,” FHR reports, 21_113_2. Flanders Hydraulics Research: Antwerp, 2023.

[5] B. De Maerschalck, J. Stark, K. Eloot, “Antwerpen Oeververbinding tussen linker- en rechteroever: Deelrapport 4 – Hydrodynamische beoordeling ontwerpvarianten,” FHR reports, 21_113_4. Flanders Hydraulics Research: Antwerp, 2023.

[6] C. Dorfmann, G. Zenz, “The depth-averaged Mixing Length turbulence model for Telemac-2D,” In: Proceedings of the XXIIIrd TELEMAC-MASCARET User Conference 2016, 11 to 13 October 2016, Paris, France., 2016, pp. 163-168..

[7] C. Kessler, U. Merkel, “Vortex streets behind bridge piers, studies with TELEMAC 2D/3D & TELEMAC AD”, In: Proceedings 23rd TELEMAC & Mascaret User Club, Paris, 2017.

[8] P.K. Stansby, “Limitations of Depth-Averaged Modeling for Shallow Wakes,” Journal of Hydraulic Engineering (ASCE), 132, 2006, pp. 737-740.

Advanced representation of near-natural vegetation in hydrodynamic modelling

Antonia Dallmeier[1], Frederik Folke[2], Nils Rüther[1]
antonia.dallmeier@tum.de, Munich, Germany
[1]: Technical University of Munich (TUM), Chair of Hydraulic Engineering
[2]: Federal Waterways Engineering and Research Institute (BAW), Dept. of Hydraulic Engineering

Abstract – **The correct representation of the hydraulic resistance of flexible floodplain vegetation in two-dimensional hydrodynamic models is still a challenging task. In previous studies [1, 2], different vegetation resistance approaches have been implemented in TELEMAC-2D, and their performance has been tested. However, the vegetation resistance approaches implemented so far work well for emerged flexible vegetation, and both emerged and submerged rigid vegetation. The existing two-layer approaches have been shown to work well for submerged conditions but do not account for plant flexibility.**

Box et al. [3, 4] conducted laboratory experiments to investigate the flow resistance of flexible vegetation at relative submergence levels of 1 to 3.4. To model submerged flexible vegetation, Box et al. [4] extended the existing one-layer approaches of Järvelä [5] by assuming a logarithmic velocity profile in the free surface layer above the vegetation. A similar approach was presented in parallel by Folke et al. [6].

In this study, we describe the implementation of the developed two-layer approach by [4] in TELEMAC-2D. Subsequently, the laboratory tests according to Box et al. [3] are simulated in TELEMAC-2D using the existing two-layer approach of Baptist et al. [7] and the newly implemented two-layer approach. To model the mixture of understory grass and flexible woody vegetation, the resulting individual vegetation resistances were superimposed. The results demonstrate the applicability of this method in the present case. In addition, several parameters influencing the approaches are varied. The Darcy-Weisbach friction values of the simulations are compared with the experimentally obtained ones. The results show good agreement between the measured and simulated friction factors. Using these insights, users are encouraged to apply vegetation approaches for modelling the hydraulic resistance in vegetated areas.

Keywords: flow resistance, submerged vegetated flow, numerical hydraulic modelling.

I. CHALLENGES OF MODELLING SUBMERGED FLEXIBLE VEGETATION AND MIXTURES OF VEGETATION

In numerical modelling, the representation of the hydraulic resistance of floodplain vegetation remains a challenging task. With its diverse and complex forms, vegetation plays a crucial role in altering flow patterns, affecting water levels, and influencing sediment transport in riverine environments [3, 4]. Over the years, several approaches have been developed to simulate the interaction between hydrodynamics and vegetation. These approaches share the common feature of considering the underlying fundamental physical mechanisms – even though the assumptions may differ significantly. Especially the influence of flexibility is often not adequately considered.

Early studies focused on emerged rigid vegetation. Typically, in these studies, vegetation was simplified as rigid cylinders. Despite the known shortcomings of such approaches in capturing crucial vegetation properties, valuable insights into the effects of vegetation on flow patterns and turbulence were provided. To account for the impact of submergence, subsequent multi-layer approaches were developed, e.g. [7]. However, these approaches generally rely on the simplified assumption of rigid cylinders, limiting their transferability to natural vegetation. Parallel to these developments, Järvelä [5] has presented an approach for flexible foliated vegetation. While this approach considers the flexibility of plants, allowing for a more realistic representation of natural vegetation, it is limited to emerged vegetation. Accurately representing submerged flexible vegetation in hydrodynamic modelling is crucial for comprehensively representing flow dynamics on floodplains. Therefore, approaches for submerged flexible vegetation have recently been developed by extending the formulation of [5] to submerged conditions, as presented by [4,6].

Within this study the two-layer approach of [4] was implemented into TELEMAC-2D. The performance of the new approach is tested using data from the laboratory experiments of [3], and compared with the results of the already available two-layer approach of [7]. The mixture of the understory grass and the flexible woody vegetation used in the laboratory experiments are each represented by a vegetation approach. The resulting vegetation roughness is determined using the superposition principle. In addition, the influence of the sensitivity of various input parameters is investigated. The aim of this contribution is to draw attention to the new vegetation approaches and their potential within 2D hydrodynamic modelling. Users are encouraged to take advantage of the use of vegetation approaches in TELEMAC-2D and critically question the use of conventional roughness laws to model vegetation induced resistance.

II. ROUGHNESS MODELLING OF VEGETATION

A. Principle of superposition

The total resistance can be determined according to the principle of superposition of the individual resistances. For flow influenced by vegetation, the total Darcy-Weisbach friction coefficient λ is the sum of the bottom friction λ' and the vegetation form roughness per unit surface λ''

$$\lambda = \lambda' + \lambda''. \tag{1}$$

Based on this principle, different vegetation modelling approaches are implemented in TELEMAC-2D [2]. The vegetation approaches can be coupled with all available laws of bottom friction. In this study, the Nikuradse roughness law is used to model the bottom friction. The vegetative drag is modelled using the vegetation approaches of Baptist et al. [7] (referred to as BAPT) and the new extended hybrid approach of [4,6] (referred to as HYBR). Both vegetation approaches are briefly described below.

B. Two-layer approach for rigid vegetation (BAPT)

The BAPT two-layer approach assumes constant velocity within the vegetation layer and a logarithmic velocity profile within the free surface layer. The resistance of vegetation λ'' is calculated as:

$$\lambda'' = \begin{cases} 4 \cdot \left(\frac{1}{\sqrt{C_D \cdot mD \cdot h_p}} + \frac{1}{\kappa\sqrt{2}} ln\left(\frac{h}{h_p}\right) \right)^{-2} & for\ h_p \leq h \\ 4 \cdot C_D \cdot mD \cdot h & for\ h_p > h \end{cases}, \tag{2}$$

with the drag coefficient C_D [-], the hydrodynamic density mD [m^{-1}], the plant height h_p [m], the flow depth h [m], and the von Kármán constant $\kappa = 0.41$ [-]. The hydrodynamic density is defined as the sum of the projected plant area per unit volume.

The BAPT two-layer approach was initially developed for rigid vegetation only, simplifying vegetation as rigid cylinders. To account for flexible leafy vegetation, [2] suggests to estimate the hydrodynamic density based on the leaf area index (LAI), which is defined as the one-sided green leaf area per unit ground area, and the vegetation height h_p. Both in [4] and [8], a direct proportionality of the hydrodynamic density to the ratio of the leaf area index to the plant height is assumed:

$$mD = k \cdot LAI/h_p, \tag{3}$$

with the constant of proportionality k. In [8], a value of 0.5 for k is proposed, while [4] suggests a value of 1 since they assume the LAI to be evenly distributed over the plants canopy. It should be noted that the parameters cannot be directly converted to the respective other format. These two formulas only provide rough estimates of the relationship between the vegetation density parameters.

C. Two-layer approach for flexible vegetation (HYBR)

To account for flexible emerged and submerged vegetation, [4] and [6] have developed a two-layer approach in parallel. This new approach represents an advancement of the one-layer approach of [5], which was developed to model the hydraulic resistance of emerged flexible woody vegetation.

As described above, the BAPT vegetation approach has the advantage of being suitable to calculate the hydraulic resistance of emerged as well as submerged vegetation due to the two-layer concept that describes the velocity profile in and above the vegetation. However, the approach was only developed for rigid vegetation. Järvelä's [5] approach quantifies the flexible foliated plant characteristics but is only suitable for emerged and just-submerged flow conditions due to the one-layer approach. [4] and [6] have combined the benefits of both approaches, resulting in a two-layer approach for flexible woody vegetation. In this way, the flexible plant properties and the velocity profile within the free surface layer, and thus different relative submergences depths, can be considered.

In addition to merging the equations, [4] introduced the scaling factor α for the von Kármán constant to account for the dependence on the velocity profile, the roughness of the plant canopy, and the relative submergence. They proposed a value of $\alpha = 1.5$, while [7] assumed a value of 1.0 for α in the original equation. Finally, the following formulas were obtained

$$\lambda'' = \begin{cases} 4 \cdot \left(\frac{1}{\sqrt{C_{D,\chi} \cdot LAI \cdot \left(\frac{u}{u_\chi}\right)^\chi}} + \frac{1}{\alpha\kappa\sqrt{2}} ln\left(\frac{h}{h_p}\right) \right)^{-2} & \text{for } h_p \leq h \\ 4 \cdot C_{D,\chi} \cdot LAI \cdot \left(\frac{u}{u_\chi}\right)^\chi \cdot \frac{h}{h_p} & \text{for } h_p > h \end{cases}, \tag{4}$$

with the species-specific drag coefficient $C_{D,\chi}$ [-], the species-specific Vogel exponent χ [-], the species-specific reference velocity u_χ [m/s], and the flow velocity u [m/s]. The species-specific reference velocity u_χ is the lowest flow velocity in the experimental determination of the species-specific vegetation parameters.

During the implementation of the approaches of [4] and [5] into TELEMAC-2D, the equations were slightly modified. In both approaches, the ratio u/u_χ is limited so that it cannot become smaller than 1. Otherwise, a too high vegetative Darcy-Weisbach friction factor would occur for flow velocities much smaller than the reference velocity. The treatment of lower velocities needs further research.

III. METHODOLOGY

A. Laboratory datasets

This study uses the dataset of the flume experiments of [3] to investigate the performance of the newly implemented hybrid vegetation friction approach in TELEMAC-2D. The original experiments were conducted to determine the hydraulic resistance of a mixture of vegetation using understory grass and flexible woody foliated plants at different relative submergences. The dataset of the laboratory experiments of [3] were conducted using the Aalto Environmental Hydraulics Flow Channel. In a 16 m long and 0.6 m wide working section, fully developed flow conditions were produced. Since the flume bottom is horizontal for the experimental runs, non-uniform flow conditions were achieved. The nature-like flexible woody plants used to model the vegetation elements had an undeflected height of 0.22 m, and the understory grass was 0.03 m tall. Three different densities of flexible woody foliated plants (LAI of 1.4, 3.8, and 5.2) combined with understory grass at different relative submergences H/h_p (1, 1.5, and 2) were used. Water levels were measured at two positions, X_{up} and X_{down}, within the vegetated section using high-accuracy pressure sensors. The location of these pressure sensors is shown in Figure 1 (P_{up} and P_{down}). The longitudinal distance dx between the two sensors is 3.45 m in the case of sparse vegetation ($LAI = 1.4$), while the sensors are located at a distance of 1.25 m at higher vegetation densities ($LAI = 3.8 \div 5.2$). In addition, eight more pressure sensors were installed (P1-P8), which have been used to check the water level slope but have not recorded any data for post-processing. Using the measurements at the locations X_{up} and X_{down}, the bulk friction factors are obtained using the water surface slope and the Darcy-Weisbach equation. More information can be found in [3].

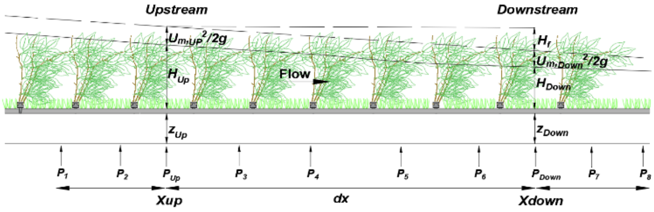

Figure 1. Longitudinal representation of measurement setup [3]

B. *Numerical Hydrodynamic Model*

A simplified two-dimensional numerical model of the laboratory flume described above was set up (TELEMAC-2D v8p3r1). Installations, such as weirs of rectifiers, are not represented in the numerical model. The numerical model has a length of 32.5 m to ensure fully developed flow conditions and a width of 0.60 m. At the model outlet, the average flow depth determined from the experiments is uniformly applied across the cross-section, while the corresponding discharge is imposed at the inlet. Much like the experimental setup, the numerical model features a horizontal bed. The side walls are assumed to be smooth.

The computational grid has an average edge length of 0.05 m and comprises 9613 nodes and 17920 unstructured triangular elements. The time step Δt was chosen between 0.1 s and 0.5 s based on the mean velocity in the experiments to ensure acceptable Courant numbers for all scenarios. A semi-implicit finite element scheme and the mixing-length turbulence model were chosen for this application.

The total friction of the numerical model was obtained by superposing the bottom roughness obtained through Nikuradse's law and the friction due to understory grass obtained using the vegetation approach of BAPT. The woody vegetation elements are modelled using the above presented vegetation approaches. It is assumed that the vegetation is uniformly distributed throughout the entire channel.

IV. RESULTS AND DISCUSSION

A. *Modelling understory grass*

Since [3] investigated mixed vegetation in laboratory experiments comprising understory grass and flexible woody plants, the hydraulic resistance of the understory grass is also modelled using a vegetation approach in this study. For this purpose, the vegetation approach BAPT is used in combination with the Nikuradse roughness law. The vegetation approach calculates the hydraulic roughness of the grass cover, while a small value of 0.001 m was chosen for the equivalent sand roughness k_s to map the bottom friction of the flume. The values of the BAPT friction approach used to model the understory grass are $mD = 74\,m^{-1}$ and $h_p = 0.03\,m$, accordingly to the experiments of [3].

Figure 2 shows the results of the simulation of the understory grass using the BAPT approach. Since [3] determined the Darcy-Weisbach friction factors λ using formula (5), λ_{bulk} of the simulation results is also determined here using this formula.

$$\lambda_{bulk} = \frac{8gH}{u_m^2} \cdot \frac{H_f}{dx}\,, \qquad (5)$$

with the mean water depth H of the water depth H_{up} at X_{up} and the water depth H_{down} at X_{down}, the mean velocity u_m calculated using the continuity equation, and the friction loss H_f calculated using Bernoulli's equation.

Figure 2 shows the comparison of the Darcy-Weisbach friction factors λ obtained from the measurements (exp) and the simulations (sim). Here, a good agreement between the measured and simulated values is achieved using the vegetation parameters above and without any further adaption. Consequently, using the BAPT approach can be assumed to be suitable for modelling the hydraulic resistance of the understory grass.

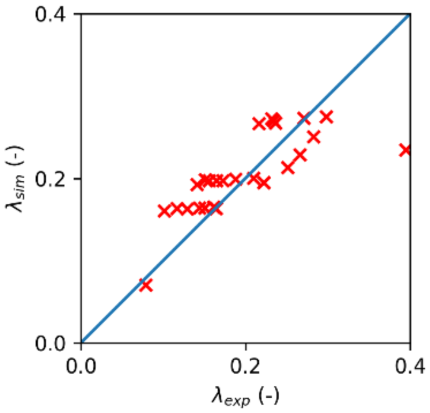

Figure 2. Comparison of measured (exp) and simulated (sim) Darcy-Weisbach friction factors for the calibration of the understory grass

B. *Emerged and submerged flexible woody vegetation*

The laboratory experiments, including the flexible woody vegetation and the understory grass, are simulated using the BAPT and HYBR approaches and subsequently compared. The parameters used for the vegetation approaches according to [3] are listed in Table 1. [3] conducted drag force measurements at velocities ranging from 0.2 to 0.8 m/s to determine these plant-specific parameters. The drag forces were measured using a force sensor, with one specimen on the flume bottom covered with a grass mat. In addition to the functionality of the newly implemented vegetation approach HYBR, the influence of the parameters α, mD, and the used plant height $h_{p,0}$ (undeflected plant height) or $h_{p,defl}$ (deflected plant height) on the simulation results are investigated. In order to compare the BAPT approach with the HYBR approach, the Darcy-Weisbach friction factors are calculated for each simulation. For this purpose, equation (5) is applied.

Table I Vegetation parameters used for the simulations [3]

Parameter	**Box et al. (2021)**
$C_{D,\chi}$ [-]	0.51
χ [-]	-0.95
u_{χ} [m/s]	0.20
C_D [-]	1.0
α [-]	1.0 / 1.5
$h_{p,0}$ [m]	0.22
$h_{p,defl}$ [m]	0.13 – 0.22

In TELEMAC-2D, the HYBR approach is implemented using a limit for the ratio u_m/u_{χ} of 1, which means that for $u_m < u_{\chi}$ the ratio is limited to 1. Otherwise, the friction coefficient would approach infinity for very low flow velocities. For the data of [3], u_m is lower than u_{χ} in 28 of 116 experimental runs. This leaves the question of how to deal with flow velocities smaller than u_{χ}. Consequently, they behave more or less rigid up to this flow velocity. Therefore, only the experimental runs with $u_m > 0.2\ m/s$ were selected for the simulations.

The simulated and experimentally obtained Darcy-Weisbach friction factors of the dataset of [3] are shown and compared in Figure 3. The simulations have been conducted using the undeflected plant height $h_{p,0}$, since in nature often only this parameter is available and the deflected plant height is difficult to determine in the field. For the simulations where the HYBR approach has been used, α was varied by using once the proposed value of 1.5 [4] and once the value of 1.0 [7]. For applying the BAPT approach, the influence of the method used to estimate the hydrodynamic density was investigated (see formula (3)). $k = 0.5$ describes the method of [8], while $k = 1$ defines the approach of [4]. The blue line defines the values of the optimal agreement of the measured and simulated Darcy-Weisbach friction factors. The red crosses show the actual correspondences for each experimental run.

When using the HYBR approach, the simulated and measured Darcy-Weisbach friction factors λ fit slightly better for $\alpha = 1.5$ (see Figure 3a) than for $\alpha = 1.0$ (see Figure 3b). For $\alpha = 1.0$, the friction factors are slightly underestimated by the HYBR approach. However, the differences in the results are minor compared to the change in the value of α. Therefore, the influence of the used value for α can be assumed to be small as both configurations give good agreement of the results. When the BAPT approach is used, the simulated Darcy-Weisbach friction factors are significantly overestimated when the hydrodynamic density is determined with $k = 1.0$ (see Figure 3d). In comparison, the simulated and measured values show a better agreement when using the approach according to [8] with the factor $k = 0.5$ (see Figure 3c). If the results of the two approaches, HYBR and BAPT, are compared, a larger scatter of the results is visible when using the BAPT approach. The best fit of simulated and measured friction factors is achieved using the HYBR approach with $\alpha = 1.5$ (see Figure 3a).

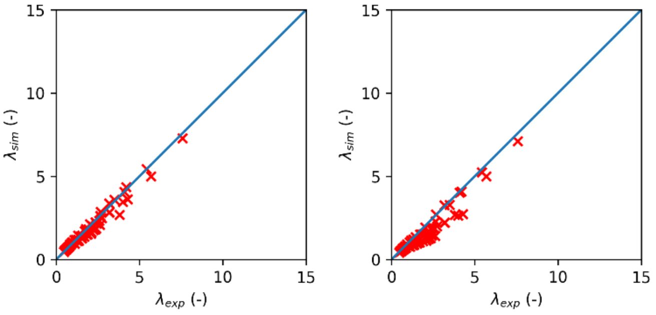

(a) HYBR, α=1.5, $h_{p,0}$ (b) HYBR, α=1.0, $h_{p,0}$

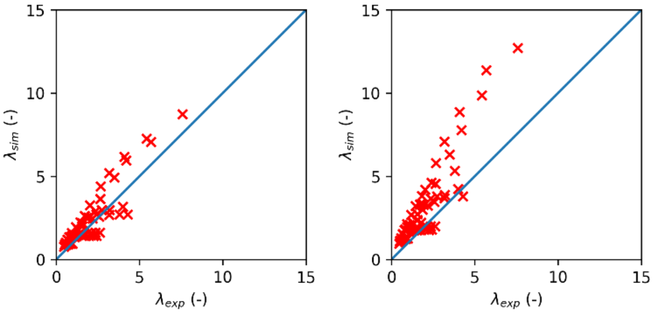

(c) BAPT, k=0.5, $h_{p,0}$ (d) BAPT, k=1.0, $h_{p,0}$

Figure 3. Comparison of measured (exp) and simulated (sim) friction values for different combinations of vegetation approaches and parameters, using the undeflected plant height $h_{p,0}$ evaluated for the data of [3]

In order to investigate the influence of the used plant height, further simulations were carried out using the deflected plant height $h_{p,defl}$. Here, α was again varied for the HYBR approach and k for the BAPT approach. The results are shown in Figure 4. When using the HYBR approach, the Darcy-Weisbach friction factors λ are underestimated for both $\alpha = 1.5$ and $\alpha = 1.0$ when applying $h_{p,defl}$ (see Figure 4a and b). Here, the results show also a better agreement of measured and simulated λ for $\alpha = 1.5$ than $\alpha = 1.0$. This trend confirms the results of the simulations with $h_{p,0}$. In general, however, the HYBR approach performs better when using $h_{p,0}$. When using the BAPT approach with $h_{p,defl}$, the same trends are visible when using $h_{p,0}$. The results also show a significantly larger scatter at $k = 1$ than at $k = 0.5$. In general, using $h_{p,defl}$ in the BAPT approach provides a better agreement of the results. However, it must be noted that $h_{p,defl}$ must be calculated using an additional model, since is difficult to determine in the field. Furthermore, it varies for different hydraulic conditions, so it needs to be implemented dynamically for each setting.

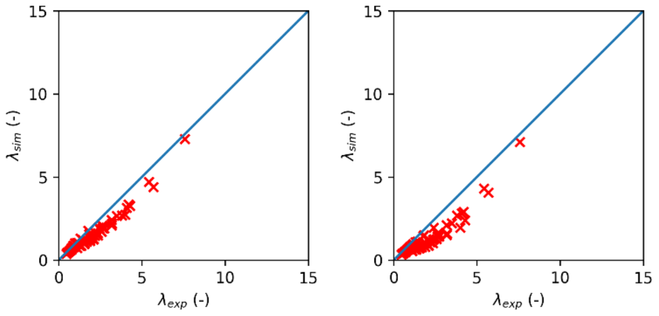

(a) HYBR, α=1.5, $h_{p,defl}$ (b) HYBR, α=1.0, $h_{p,defl}$

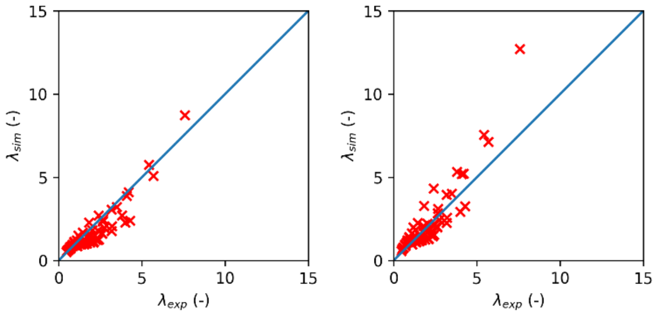

(c) BAPT, k=0.5, $h_{p,defl}$ (d) BAPT, k=1.0, $h_{p,defl}$

Figure 4. Comparison of measured (exp) and simulated (sim) friction values for different combinations of vegetation approaches and parameters, using the deflected plant height $h_{p,defl}$ evaluated for the data of [3]

Figure 5 shows the deviations of the simulated and measured Darcy-Weisbach friction factors λ for each combination of vegetation approach and used parameters. Here, the observations described above are clearly presented and the conclusions supported. The HYBR approach with $\alpha = 1.5$ and $h_{p,0}$ shows the best agreement between the measured and simulated roughness values. The largest scatter, on the other hand, can be seen with the BAPT approach with $k = 1$ and $h_{p,0}$. For the use of the BAPT approach, the deflected plant height $h_{p,defl}$ seems to give better results, whereas, for the use of the HYBR approach, a slightly better fit for the undeflected plant height $h_{p,0}$ can be seen. However, it must also be considered how easily the input values can be determined since $h_{p,0}$ can be obtained from field measurements or remote sensing while $h_{p,defl}$ needs to be determined in a more complex way. Hence, the error that is made when simulating with input values from e.g. literature or field measurements may be small compared to the accuracy of the simulation results.

V. CONCLUSION

In this study, a new two-layer approach for calculating the hydraulic resistance of flexible woody plants in TELEMAC-2D was implemented. The functionality of the approach was tested using the laboratory experiments of [3] and compared with the existing BAPT two-layer approach. Since the experiments investigated the hydraulic resistance of mixed vegetation consisting of understory grass and flexible woody plants, the understory grass was also modelled using the BAPT vegetation approach. In the simulations, the influence of the input parameters, the von Kármán scaling factor α, the method for the estimation of mD, and the used plant height, were investigated. The simulation results show a good agreement of the measured and simulated values for both the existing BAPT and the newly implemented HYBR approach. The best fit was achieved using the HYBR approach with $\alpha = 1.5$ and $h_{p,0}$.

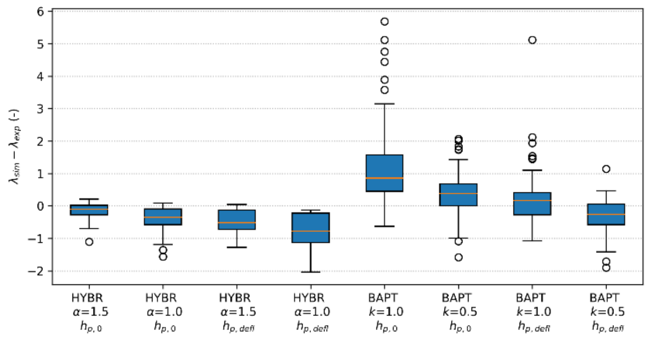

Figure 5. Deviations of the simulated (sim) and measured (exp) friction factors for each combination of vegetation approach and used parameters

Applying both vegetation approaches, BAPT and HYBR, generally works well. The simulations provide satisfactory results with a good agreement of the measured and simulated friction factors. The von Kármán scaling factor α shows minimal effect on the quality of the results with relatively large variation. The same applies to the use of undeflected or deflected plant height. Furthermore, it has to be investigated how to deal with flow velocities smaller than the species-specific reference velocity u_χ, since the HYBR has been implemented with a limit, so that in the case of $u_m < u_\chi$ the ratio is limited to 1. The influence of this limit on the quality of the results has to be further investigated.

The study shows that a new two-layer approach has been successfully implemented in TELEMAC-2D. The simulations using this and an existing approach show that applying the vegetation approaches provides satisfactory results with relatively few input parameters. Regarding the quality of the results, this makes the vegetation approaches superior to conventional roughness approaches, especially in vegetated floodplains. Although the vegetation approaches require more input parameters than conventional roughness approaches, these parameters can easily be taken from the literature or collected by remote sensing or field measurements. Although some questions remain unsolved, e.g. predicting the deflection height of plants under different flow conditions and accurately describing the vertical velocity profile in the free surface layer, the vegetation approaches implemented in TELEMAC-2D offer a promising and easy-to-use alternative to conventional roughness approaches.

ACKNOWLEDGEMENT

The authors would like to thank Juha Järvelä, Aalto University, Helsinki, for providing the data for the numerical investigations and his answers to questions.

REFERENCES

[1] Folke, Frederik; Attieh, Mohamad; Kopmann, Rebekka (2019): In search of friction laws for vegetated flow within 2D large-scale applications. In: Calvo, Lucas (Hg.): 38th IAHR World Congress: Water: Connecting the

World; September 1-6, 2019, Panama City, Panama (E-Proceedings). Madrid: IAHR. S. 5527-5536.

[2] Folke, Frederik; Kopmann, Rebekka; Dalledonne, Guilherme; Attieh, Mohamad (2019): Comparison of different vegetation models using TELEMAC-2D. In: XXVIth TELEMAC-MASCARET User Conference, 15th to 17th October 2019, Toulouse. https://doi.org/10.5281/zenodo.3611486.

[3] Box, Walter; Järvelä, Juha; Västilä, Kaisa (2021): Flow resistance of floodplain vegetation mixtures for modelling river flows. In: Journal of Hydrology 601, S. 126593. DOI: 10.1016/j.jhydrol.2021.126593.

[4] Box, Walter; Järvelä, Juha; Västilä, Kaisa (2022): New formulas addressing flow resistance of floodplain vegetation from emergent to submerged conditions. In: International Journal of River Basin Management. DOI: 10.1080/15715124.2022.2143512.

[5] Järvelä, J. (2004): Determination of flow resistance caused by non–submerged woody vegetation. In: International Journal of River Basin Management 2.1, 61–70. doi: 10.1080/15715124. 2004.9635222.

[6] Folke, Frederik; Niewerth, Stephan; Aberle, Jochen (2021): Modelling of just-submerged and submerged flexible vegetation. In: Kalinowska, Monika (Hg.): Abstract Book, 6th IAHR Europe Congress Warsaw Poland 2020. Warschau: IAHR. S. 263-264.

[7] Baptist, M. J., Babovic, V., Rodríguez Uthurburu, J., Keijzer, M., Uittenbogaard, R. E., Mynett, A. & Verwey, A. (2007): On inducing equations for vegetation resistance. In: Journal of Hydraulic Research 45.4, 435–450. doi: 10.1080/00221686.2007.9521778.

[8] Finnigan, J. (2000): Turbulence in Plant Canopies. In: Annual Review of Fluid Mechanics. 32, 519-571. Doi: https://doi.org/10.1146/annurev.fluid.32.1.519.

A head loss based bridge module for TELEMAC-2D

Sebastian Gegenleithner[1], Clemens Dorfmann[2], Gabriele Harb[3], Josef Schneider[1]
s.gegenleithner@gmail.com, Graz, Austria
[1]: Institute of Hydraulic Engineering and Water Resources Management, Graz University of Technology
[2]: flow engineering, Graz, Austria
[3]: VERBUND Hydro Power GmbH, Vienna, Austria

***Abstract* – Capturing the backwater effects introduced by bridge structures is crucial for environmental flow studies. Hydrodynamic processes at these structures are inherently three-dimensional, particularly during high-flow stages when the bridge deck becomes submerged and pressurized flow occurs. Incorporating these effects into 2D depth-averaged models is not a straightforward task. One possible approach to approximate the three-dimensional effects is by computing the head losses exerted by the bridge on the flow and incorporating them as a source term in the momentum equation. In this contribution, we present a new head loss based bridge module for TELEMAC-2D that is based on Borda-Carnot expansion and contraction losses. The losses are computed in 1D, by utilizing the bridge's geometry and location as well as cross-sectional averages of velocities and free surface elevations. The resulting head losses are then directly applied as additional momentum sources, opposing the main flow direction at the vicinity of the bridge. The presented bridge module was validated with a comprehensive set of 176 experimental test cases. The results from the validation examples support the applicability and effectiveness of the presented approach.**

Keywords: Borda-Carnot, head loss, bridge modelling

I. INTRODUCTION

Bridge structures have a large influence on the overall runoff regime in free surface flows. Considering their effect is essential, especially in high flow conditions when the bridge deck gets submerged and pressurized flow occurs. In principle, the runoff at such structures can be divided into a total of three cases [1], which are schematically shown in Figure 1. The first case, Case 1 (blue line), occurs when the water level is far below the deck of the bridge and the runoff can be considered as free surface flow. For the second case, Case 2 (red lines), the upstream side of the bridge gets in contact with the water surface (section BU). Depending on the flow conditions, the downstream edge of the bridge (section BD) can be in contact with water (Case 2b, red solid line) or not (Case 2a, red dashed line). While in Case 2a a sluice gate type flow occurs, the flow for Case 2b is fully pressurized along the entire width of the bridge. For the third case (Case 3), the water level is above the upper edge of the bridge deck. For this case, the runoff is partly occurring as pressurized flow below the bridge deck and partly as free surface flow on the deck itself.

Modelling Case 1 in 2D depth-averaged models, such as TELEMAC-2D, can be easily done by considering the abutments and bridge piers geometrically in the mesh. This method allows for fully resolving the hydraulics of the bridge structure, e.g. the flow phenomena around the bridge piers. However, it falls short in capturing the additional increase in upstream water level when the bridge deck gets submerged.

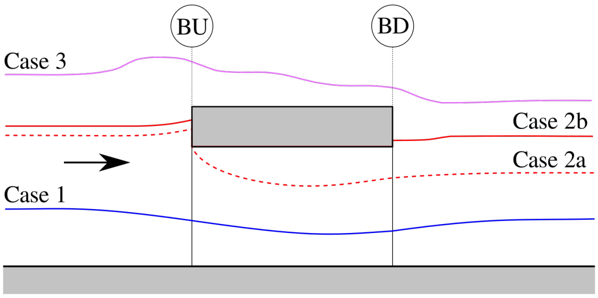

Figure 1. Schematic representation of water levels for different flow conditions at bridge structures. From [1] modified

For modelling the high flow conditions shown in Figure 1 (Case 2 and Case 3), several approaches can be found in literature. *HEC-RAS 2D* [2] computes the bridge flow by either solving the energy equation in 1D under consideration of contraction, expansion and friction losses or by computing the discharge through the structure by means of separate hydraulic equations for sluice gate flow (Case 2a), orifice flow (Case 2b) or a combination of weir flow and orifice flow (Case 3). The resulting difference in upstream and downstream water level is equated to a force, which is then applied in the momentum equation. *RiverFlow2D* [3] uses a modified Borda-Carnot approach to derive 1D contraction and expansion losses, which are applied as a head loss gradient in the momentum equation. In *Hydro_AS-2D,* bridges are modelled by means of the pressurized Saint Venant equations in combination with the weir flow equation for the overflow [4].

Approaches that are based on 1D hydraulic formulas, like weir flow, sluice gate type flow and orifice flow, are usually highly parameterized and thus the quality of the results strongly depends on the selected parameters for the application. In order to minimize the required user input, we settled for a similar method as it is used in *RiverFlow2D*, where the head loss formulation does not require any user defined parameters. Instead, the new bridge module solely requires a set of polylines, defining the locations and cross sections of the bridge structures.

II. METHODOLOGY

A. *Modified subroutines and Keywords*

The bridge module was implemented for TELEMAC version v8p4r0. Compiling the bridge module requires replacing and adding the files and subroutines listed in Table I. The subroutines can be obtained from the following GitHub repository: https://github.com/tuggegese/T2D_BridgeModule.

Table I Modified and added files required for compiling the bridge module

TELEMAC file	**Changes/Implementations**
bief_def.f	Added new vector structures
declarations_telemac_2d.f	Added bridge relevant variables and allocatable containers
interface_telemac2d.f	Added new interface of the bridge module
lecdon_telemac2d.f	Added I/O operations for bridge keywords
telemac2d_init.f	Added call to the bridge routine “*bbuilder.f*”
deall_telemac2d.f	Added deallocation of bridge related variables
bbuilder.f	New subroutine that computes bridge parameters that do not change in time
prosou.f	Added the possibility to apply bridge head losses in each time step
telemac2d.dico	Added new variables
telemac2d.cmdf	Added new subroutine “bbuilder.f”
api.cmdf	Added new subroutine “bbuilder.f”

In order to model bridges in the study area, three additional keywords were added, namely:

- “NUMBER OF BRIDGES”: Defines the total number of bridges in the study domain
- “BRIDGE LOCATION FILE”: Links a file in .i2s format that contains all polylines defining the location of the bridges in the domain
- “BRIDGE SECTION FILE”: Links a file in .i2s format containing closed polygons of all bridge cross sections

B. *1D Head loss formulation*

Figure 2 presents a simplified sketch of a bridge with two abutments and a deck. The visualized flow conditions correspond to Case 2 in Figure 1. However, the hereafter presented methodology is thought to be valid for all cases. For the example case given in Figure 2, the head losses exerted by the bridge on the flow can be represented by summing the contraction losses between sections 1 and 2, the expansion losses between sections 3 and 4 and the friction losses between sections 1 and 4.

According to [5] and [6], the well-known Borda-Carnot expansion and contraction losses, that are commonly used to estimate energy losses due to sudden contractions and expansions in pipe flows, can be employed for free surface flows as well.

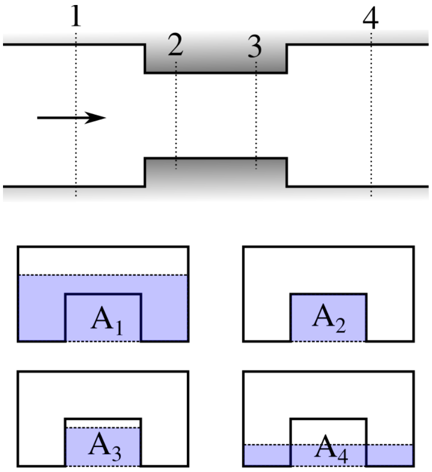

Figure 2. Schematic view of individual head loss components for cross sections 1 to 4

For the example bridge case, visualized in Figure 2, the Borda-Carnot expansion and contraction losses can be written as follows:

$$\Delta H_E = \frac{v_3^2}{2g}\left(1 - \frac{A_3}{A_4}\right)^2 \qquad (1)$$

and

$$\Delta H_C = \frac{v_1^2}{2g}\left(\frac{1}{\mu} - 1\right)^2 \left(\frac{A_1}{A_2}\right) \qquad (2)$$

where v_1 and v_3 are cross-sectional averages of the velocities upstream and below of the bridge. A_1 to A_4 are the cross-sectional areas covered by the flow and μ is the contraction coefficient, with typical values around 0.62 (see for example [5]). However, studies have shown (see for example [7]) that the contraction coefficient is not constant and is in fact dependent on several factors, such as the ratio of the downstream and upstream areas. For computing the contraction coefficient, we thus opted for the simplified approach of Weisbach, which can be written as follows:

$$\mu = c_1 + c_2 \left(\frac{A_2}{A_1}\right)^3 \qquad (3)$$

with the coefficients c_1 and $c_2 = 1 - c_1$ being 0.63 and 0.37 [8], respectively. For the here presented implementation, we adjusted the parameters c_1 and c_2 trying to account for effects that influence the complex real-world energy losses, such as accelerations of the flow, deflections [7], the angle of the contraction or other 3D effects. By calibrating the later presented validation case, we have determined the coefficients to be $c_1 = 0.3$ and $c_2 = 0.7$. However, it has to be mentioned that the calibrated coefficients might not be optimal for all real-world examples and should be carefully assessed for each individual case.

The total losses of the bridge structure can be obtained by summing the individual components from contraction, expansion and friction, which can be expressed as:

$$\Delta H = \Delta H_C + \Delta H_E + \Delta H_F \qquad (4)$$

In the current implementation, we have chosen to neglect the additional friction losses from the walls of the bridge. Consequently, the friction between sections 1 and 4 is solely determined by the bottom friction, potentially leading to slightly lower computed head losses compared to those occurring in nature.

C. *Implementing the head loss to the momentum equation*

The head loss exerted by the bridge structure on the flow can be added to the momentum equation as follows:

$$\frac{\partial u}{\partial t} = other\ terms - g\frac{\partial H}{\partial x} \tag{5}$$

$$\frac{\partial v}{\partial t} = other\ terms - g\frac{\partial H}{\partial y} \tag{6}$$

Where $\partial u/dt$ and $\partial v/dt$ are the local acceleration terms in x and y direction, $other\ terms$ include all not explicitly written terms, such as the gravitational acceleration, friction, diffusion, etc. and $\partial H/dx$ and $\partial H/dy$ are the derivatives of the local head loss.

For applying the head loss of a given bridge structure, we first have to define its location in the computational grid. The here presented implementation assumes that the entire head loss attributed to the bridge structure is acting on a number of cell edges, forming the cross section of the bridge (see Figure 3, purple line). At those edges, the total energy losses can be obtained by summing the head loss components from contraction, expansion and friction (Formula 4). The losses are constant for all element edges and are visualized in Figure 3 (Detail).

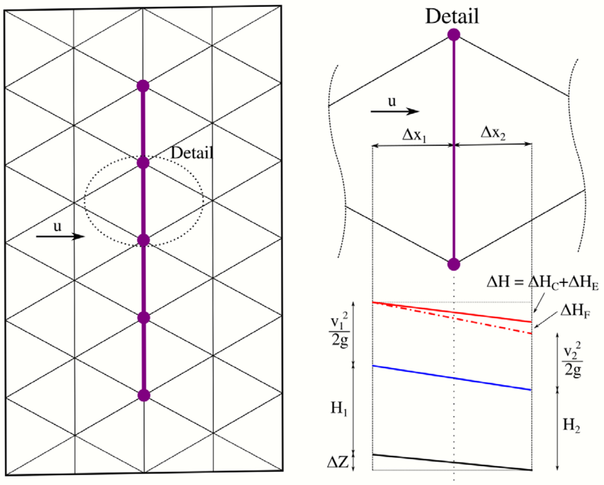

Figure 3. Scheme for computing head loss derivatives

Assuming that the head losses due to friction are solely introduced by bottom friction, which are already included in Equations 5 and 6, the additional head loss derivatives are composed of contraction and expansion only. Considering this as well as the fact that the head loss is always acting against the main direction of the flow, allows for computing the head loss derivatives with a cell centered finite difference scheme (shown for x direction only) as follows:

$$\frac{\partial H}{\partial x}_{CC} \approx \frac{\Delta H}{\Delta x_1 + \Delta x_2}\frac{u}{|u|} \tag{7}$$

where $\partial H/dx_{cc}$ is the head loss derivative computed by the cell centered scheme in x direction, ΔH is the head loss from contraction and expansion, $\Delta x_1 + \Delta x_2$ is the distances between the cell centers and $\partial u/|u|$ defines the directions of the head loss by taking a value of either -1 or 1 if the velocity is not zero. The compatibility with the node based formulation of TELEMAC-2D is reached by mapping the derivatives to the relevant nodes, effectively obtaining $\partial H/dx$.

D. *Detailed description of the algorithm*

The bridge module commences by initializing all static variables required for the analysis. Specifically, the two sets of polylines, given in the steering file are read. One file defines the bridge locations in the computational grid, and the other describes their respective cross sections (see Figure 4 dark blue lines). Assuming constant cross sections for both the bathymetry and the bridge structure along the entire width of the bridge, i.e. upstream geometry is equal to downstream geometry, enables the derivation of two functional relationships. The first links the free surface elevation to the unobstructed cross-sectional area just outside of the bridge, i.e. $A_{out} = f(FS)$. The second relationship connects the free surface elevation to the effective flow area of the bridge, considering the obstruction of the bridge structure, i.e. $A_{in} = f(FS)$.

Next, the algorithm identifies the set of nodes, referred to as nodestring, which closely matches the bridges specified location (Figure 4, blue line). Subsequently, the elements belonging to the nodestring are identified and the neighbouring nodes on both sides of the nodestring are extracted. Up to this point, the algorithm has no information which of the neighbouring nodes lie upstream and which lie downstream of the bridge. Since in environmental flow studies the flow might reverse, the choice which nodes lie upstream and which lie downstream is done in each time step in a later stage. Figure 4 gives an example for the upstream (red) and downstream (green) nodes for a given flow direction (black arrow). Additionally, the algorithm retrieves distances to the element centers (black line) required for computing the head loss derivatives (Formula 7)

After the initialisation step, head losses are computed and applied in each time step. The algorithm begins by calculating the average flux through the nodestring. Based on the present flow conditions, it determines which nodes lie upstream and downstream of the bridge. These nodes are then used to compute average free surface elevations, H_{US} and H_{DS}, respectively. Utilizing the previously derived functional relationships between free surface elevations and the areas below and outside, the algorithm determines the unobstructed and obstructed flow areas upstream and downstream of the bridge (see Figure 4). From the computed fluxes, cross sectional averages of flow velocities are obtained by applying the continuity equation. These velocities, along with the extracted flow areas, are used to derive the Borda-Carnot expansion (Formula 1) and contraction (Formula 2) losses, respectively. From those 1D losses, we are able to derive the head loss derivatives in x and y direction by using Formula 7 and apply them as additional terms in the momentum equation (Formula 5 and 6).

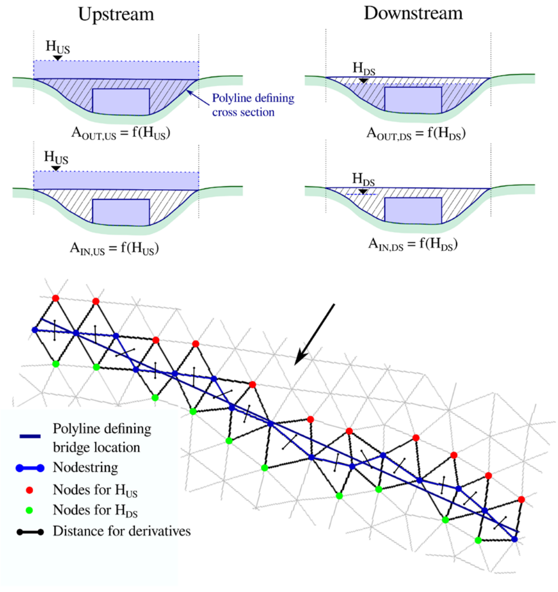

Figure 4. Implementation detail for a real case

III. VALIDATION CASE

The bridge module was validated through an experimental study conducted by [5]. The study was carried out in a 0.24 m wide and 6.0 m long laboratory flume. The bottom roughness in the flume was reported to be $n = 0.011\ s/m^{1/3}$. The experimental study encompassed a wide range of different bridge geometries, orientations to the flow and hydraulic boundary conditions, resulting in a total of 207 measurement points. The head losses exerted by the bridge structures were quantified by measuring the water levels upstream and downstream of the bridges. Upstream measurements were performed at a distance of 1.0 m from the bridge, while downstream measurements were taken at a distance of 3.0 m.

To validate the bridge module, we replicated the measurements numerically. Due to data availability, we considered 176 of the 207 experimental cases for validation. In the numerical model, the channel was expanded upstream to minimize the influence of the upstream boundary condition. For each case, the measured discharge was imposed at the upstream boundary and the measured water depth was prescribed at the downstream boundary. The bridge geometries were implemented as described in the prior sections of this paper. The simulations were run until steady state conditions were reached and the simulated upstream water level was compared to the measured one. The numerical model setup is illustrated in Figure 5.

Prior to validating all 176 experimental cases, we tested if the implementation is mesh independent. To do this, we compared the results obtained from simulations using the original mesh to simulations with a much finer computational grid. The original spatial resolution in longitudinal direction was about 0.1 m, whereas the resolution of the finer grid was around 0.025 m. The observed differences between the modelling results showed to be dependent on the specific case. However, the maximum observed difference in the water levels was merely around 1.5 %.

Figure 6 presents a comparison between the measured and simulated water depths for all 176 investigated cases (indicated by blue crosses). Overall, the head losses could be replicated well by the numerical model, yielding a coefficient of determination of $R^2 = 0.962$. This value is comparable to the results of [5], who reported statistics of 0.934 for their Borda-Carnot approach, 0.991 for their Borda-Carnot approach including a calibration coefficient and 0.953 for simulations performed with HEC-RAS. In Figure 6, several data points exhibit higher measured water levels compared to the simulated values. This phenomenon was also observed in the Borda-Carnot implementation of [5]. Contrary to that, the HEC-RAS simulations demonstrated less systematic underprediction of the head losses. We found that the Borda-Carnot based formulations tended to underestimate the energy losses for partly and fully submerged bridges, particularly when lower water levels were present downstream of the bridge (see Figure 1, Case 2a)

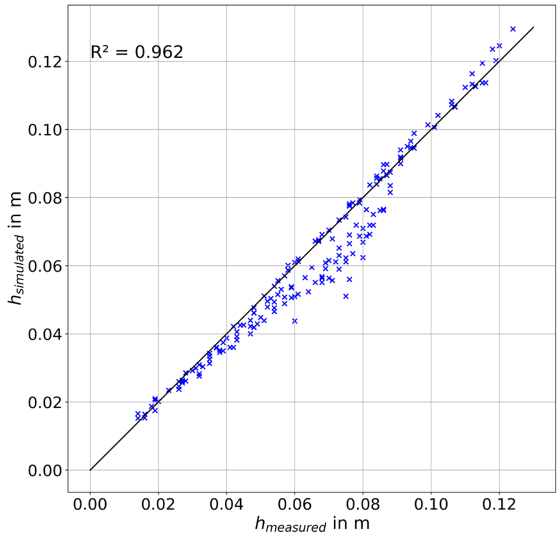

Figure 6. Comparison between simulated and observed upstream water depths for all 176 test cases (indicated by blue crosses)

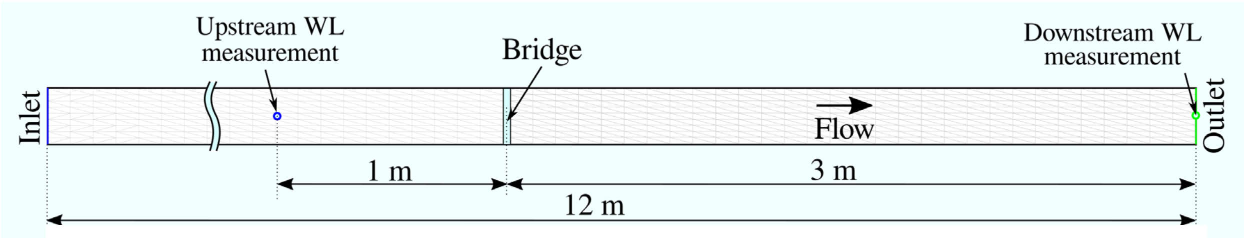

Figure 5. Setup of the numerical experiment, plan view

IV. USER EXAMPLE

A. Setup of the user example

This section demonstrates the implementation of multiple bridges for a generic test case. The test case was set up with one inlet and two outlet boundaries. The computational grid consisted of a total of 86,420 unstructured triangular elements with a mean edge length of about 1 m. The bottom elevations ranged from 0 to 16.2 m and the area of the study domain was about 60,000 m². The simulation was driven with a constant discharge of 30 m³/s until steady state conditions were reached. The study included three bridges with different cross sections. The elevations of the computational grid, the inlet and outlet boundary conditions and the locations of the three bridges are illustrated in Figure 7. This test case is meant to demonstrate the usage of the bridge module and is available on GitHub: https://github.com/tuggegese/T2D_BridgeModule

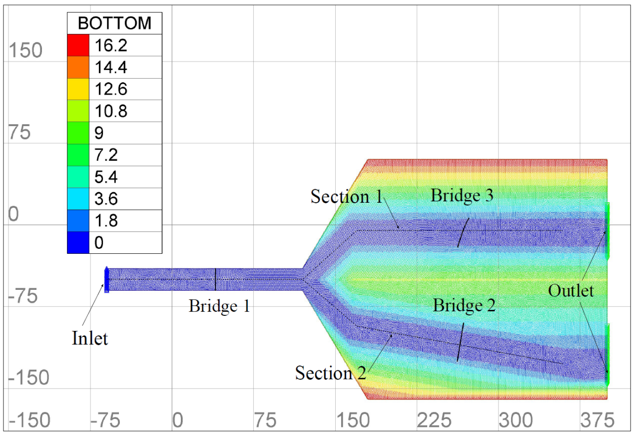

Figure 7. Overview of the example case, its bottom elevations and the locations of the bridges and longitudinal sections

For implementing the bridges, we first created two BlueKenue line sets. The first polyline was of the type “Open Line” and defined the location of the bridges in the computational grid (see Figure 7). This set of polylines was called “bridges.i2s” and was defined in the steering file by adding the following keyword: BRIDGE LOCATION FILE = ‘bridges.i2s’.

The next step was to resample the polylines defining the locations of the bridges. Afterwards, the bottom elevations were mapped to the lines and the resulting cross sections were saved in the ‘.xy’ data format. Converting the ‘.xy’ data sets to ‘.i2s’ allowed for loading the bottom cross sections of the bridges into the 2D canvas of BlueKenue. Subsequently, the cross sections of the bridges were drawn with polylines of the type “Closed Line”. The resulting cross sections of the bridges (dark blue polyline) and the extracted cross sections of the bottom elevations (red line) are shown in Figure 8. All three bridges were added to a single ‘.i2s’ line set, which was added to the steering file by setting the following keyword: BRIDGE SECTION FILE = 'bridgesCS.i2s'.

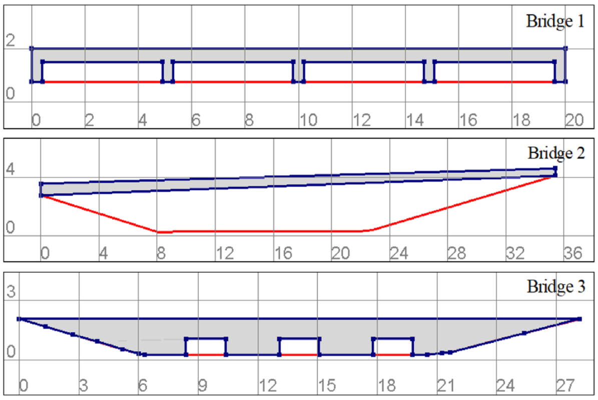

Figure 8. Cross sections of the three bridges (dark blue line) and bottom elevations (red line) in the study domain. The polylines are visualized in the 2D canvas of Blue Kenue

Besides the location and section files, the bridge module requires defining the number of implemented bridges, which was done in the steering file by adding the following keyword: NUMBER OF BRIDGES = 3.

B. Results of the test case

Figure 9 displays the simulated free surface elevations for the presented test case. Specifically, upstream water levels at the three bridge cross sections (B1, B2 and B3) and the free surface elevations along two longitudinal sections (S1 and S2, see also Figure 7) are visualized. The figure includes simulated water levels with and without considering the added head losses of the bridge structures, shown with blue and red lines, respectively.

Upon considering the effects of the bridges, we observed increases in the upstream water levels as follows: 0.11 m for Bridge 1, 0.02 m for Bridge 2, and 0.16 m for Bridge 3, respectively. Notably, the water level difference for Bridge 2, which did not come in contact with water, resulted from the backwater effects of Bridge 3. For the here presented case, the model computed contraction coefficients of 0.58 for Bridge 1, 1.0 for Bridge 2 and 0.34 for Bridge 3, by utilizing Equation 3 with the calibrated coefficients. For Bridge 1, the contraction coefficient was found to be in close agreement with the constant value of 0.62 suggested by [5]. As for Bridge 2, the presence of equal areas below and outside of the bridge led to a contraction coefficient of 1.0, effectively resulting in the contraction losses becoming zero, as evident from Equation 2. For the third bridge, Bridge 3, the contraction coefficient became quite small, allowing the consideration of additional energy losses due to the very small unobstructed flow area.

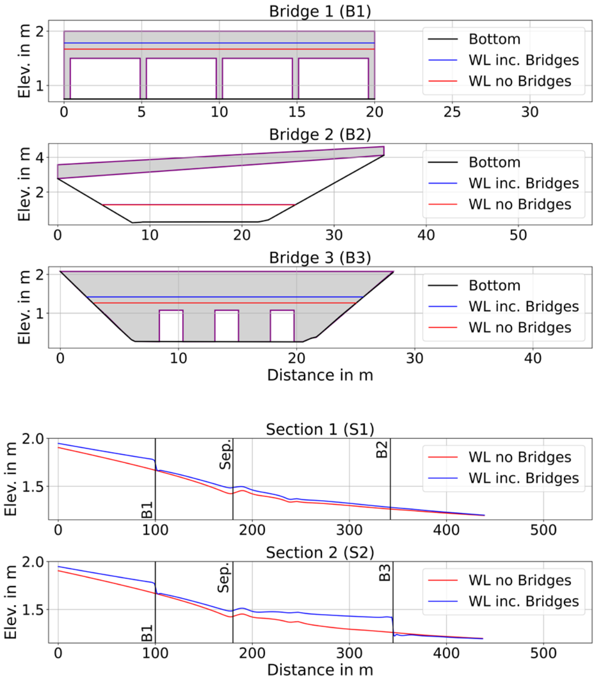

Figure 9. Results of the generic test case. Shown are the water levels (WL) with and without considering the backwater effects of the bridges upstream (US) of three bridge sections (B1, B2 and B3) and along two longitudinal sections (S1 and S2).

V. DISCUSSION AND CONLUSION

The bridge module presented here was developed with the objective of providing a user-friendly method to consider backwater effects of both unsubmerged and submerged bridges with minimal user-defined parameters. To achieve this, we adopted a head loss based approach that relies solely on geometrical relationships and hydrodynamic flow properties at the bridge structure.

Our investigations and also the study conducted by [5] showed that the traditional Borda-Carnot approach, commonly used for pipe flows, underestimates the total energy losses imposed by the bridge structure on the flow, particularly when the bridge deck became submerged, leading to pressurized flow conditions. This underestimation could be attributed to the more irregular geometries of real bridges compared to pipes, as well as additional 3D hydrodynamic effects that cannot be accurately captured by contraction and expansion losses alone.

In an attempt to account for these additional losses, [7] proposed a constant multiplication factor of 1.31 for the contraction losses. On the other hand, [5] used a dynamic calibration factor, dependent on the Froude numbers upstream and downstream of the bridge, the ratio of the occluded area, and a constant describing the bridge regime (unsubmerged, partially submerged, or fully submerged). We observed that a constant calibration factor, as suggested by [7], failed to accurately represent the additional losses for all test cases. Similar to [5], we thus opted for a dynamic calibration parameter that increased the computed energy loss in proportion to the blocked area. Consequently, a more occluded cross section would result in significantly higher head losses compared to a barely submerged bridge.

To address this, we calibrated the head losses using the contraction coefficient and employed Formula 3 as a starting point. This formulation offered the advantage of yielding higher losses as the flow area became more obstructed and also resulted in a head loss of zero when the bridge did not come in contact with water (see Formula 2). This adapted approach for computing the contraction coefficient produced satisfactory results for the validation case. In the user example, this led to contraction coefficients of 0.58 for Bridge 1, 1.0 for Bridge 2, and 0.34 for Bridge 3, respectively. For reference, [5] used a constant contraction coefficient of 0.62.

To conclude, we can give the following remarks and suggestions, when applying this approach for modelling unsubmerged and submerged bridges:

- The algorithm works well for a wide range of flow conditions, however, during high flow conditions the standard Borda-Carnot equation tends to underestimate the energy losses exerted by the bridge structure. Although we introduced a dynamic calibration coefficient, it may be necessary to perform additional calibration for each individual case.
- Our investigation reveals that the proposed module remains largely stable when the underlying hydrodynamics are stable. This emphasizes the importance of considering the overall hydrodynamic conditions to ensure the model's reliability and robustness.
- During our simulations, we observed minimal slowdown when incorporating the bridge structures (at least with three bridges). This demonstrates the computational efficiency of the proposed approach, making it a practical choice for large-scale applications.

ACKNOWLEDGEMENT

We like to thank our colleagues from “Niederer and Pozzi” (www.nipo.ch) for testing the here presented bridge module. We also express our gratitude to the independent reviewer.

REFERENCES

[1] T. Picel, A. Havlik, D. Mattas and K. Mares, “Hydraulic calculations of bridges at high water stages” in Journal of Hydraulic Research, vol. 45, Taylor & Francis, pp. 400-406, 2007.

[2] Hydrologic Engineering Center, “HEC-RAS 2D user’s manual”, U.S. Army Corps of Engineers, Davis CA., 2023.

[3] Hydronia LLC, “RiverFlow2D Reference Manual”, March 2023

[4] Hydrotec Ingenieurgesellschaft für Wasser und Umwelt mbH, “Hydro-AS-2D Benutzerhandbuch“, Aachen, Germany, version 5.1.5, september 2019

[5] H. Ratia, J. Murillo and P. García-Navarro, “Numerical modelling of bridges in 2D shallow water flow simulations”, in International Journal for Numerical Methods in Fluids, Wiley, 75:250-272, 2014

[6] VT. Chow “Open Channel Flow” MacGraw-Hill Book Co. Inc, New York, 1959

[7] D. Aigner and G. Bollrich, “Handbuch der Hydraulik für Wasserbau und Wasserwirtschaft“, 2nd Edition, Beuth Verlag GmbH, Berlin Germany, 2021

[8] H. Oertel, L. Prandtl, M. Böhle, K. Mayes, “Prandtl’s Essentials of Fluid Mechanics“, Springer, 2004

A simplified approach to modelling all types of obstacles in TELEMAC-2D and 3D

Sébastien E. Bourban[1], Michael S. Turnbull[2]
sebastien.bourban@edf.fr
[1] EDF R&D LNHE / LHSV, 6, Quai Watier, 78400 CHATOU, France
[2] HR Wallingford, Howbery Park, Wallingford Oxfordshire OX10 8BA, UK

Abstract – **A simplified approach has been implemented in the openTELEMAC system to represent most types of obstacles, or hydraulic structures, including weirs, culverts, bridges, turbines, pumps, sluices, porous or solid barriers, storage ponds, etc., each including several variations of their defining hydraulic characteristics taken from empirical formulations. For instance, weirs can now either be sharp- or broad-crested, v-shaped or tilted, submerged or not, reversable or linked to a storage pond.**

The objective of the work was to simplify user inputs and completely generalise hydraulics structures based on an abstraction of "obstacle". For instance, the user should not have to enter node numbers or duplicate information while providing georeferenced definition of geometries.

To achieve this, the geometry of the obstacle is defined through a set of georeferenced lines, within a single file for all geometries, whether open polylines or closed polygons. The defining parameters are keyword-based similar to those of the steering files of the openTELEMAC system, again, stored in a single file for all obstacles. Other files can then be used to control the operation of the obstacle, whether driven by time sequences or water level variations. Finally, as it is customary with the openTELEMAC system, user subroutines can also help manually control gates, sluices, pumps, turbines, etc.

Keywords: Hydraulic Structure, Obstacle, Weir, Turbine, Pumps, Barrier, Sluice, Bridge, Culvert, Storage Pond.

I. INTRODUCTION

A very few hydraulics structures had been implemented within TELEMAC-2D and 3D so far, to represent either a weir, a dyke, or a culvert. Unfortunately, their usage required the setup of complex input files defining their geometrical characteristics and parameterisations, including having to maintain lists or mesh-dependant node numbers and manually pairing nodes across or along obstacles.

This article presents the initial implementation of a novel approach to modelling obstacles in the open**TELEMAC** system, which defines an abstraction of "obstacle" capable of holding the characteristics of most types of hydraulics structures, if not all. The approach also includes a complete automatization of the search for mesh information given geometrical inputs, automatically connecting nodes, control locations and ponds where necessary. This approach is inspired from the work of the authors together with N. Durand and co-authors on the modelling of the Northern European waters to inform tidal power industry decisions (see [1]).

This initial work has been carried out in a branch on the open git repository of the open**TELEMAC** system, the so-called searobin branch, and is due to be merged to the main trunk of the system later in 2023. It includes examples of applications of five of its concepts: (a) a weir for which the flow goes over the length of the obstacle; (b) a storage pond which can be connected to one or more obstacles; (c) a control location which can be used to automate the operation of an obstacle; (d) a culvert, for which the flow tunnels through the length of the obstacle; and (e) both a porous and solid barrier blocking or controlling the flow through the obstacle.

Section II introduces the simplification of user inputs defining obstacles in open**TELEMAC**. Section III details the automation procedure linking properties of the mesh to the user inputs, including its parallelisation. Section IV follows with a detailed explanation of the simplified implementation of all hydraulic laws representing all obstacles. Section V shows results from examples of test cases and Section VI concludes with anticipated developments.

II. SIMPLIFIED USER INPUTS TO OBSTACLE DEFINITION

A. Obstacles' defining characteristics

The physical and operational characteristics of obstacles are now defined within a single file added to a simulation via the keyword: FILE OF SETTINGS FOR THE OBSTACLES. The content of the file is defined as a series of sections and subsections, one for each obstacle and obstacle type.

Figure 1 below shows an example defining two types of obstacles (weirs and storage ponds, defined as sections), within which four weirs are named from WEIR 0 to WEIR 3 in the first section and one storage pond is named POND 1 in the second section (all obstacle names in green). Colours on Figure 1 are set only for illustrative purposes.

Within each section (or for each type of obstacle), a number of obstacles of that type defines how many of those will be read. The physical characteristics of each obstacle are specific to that type of obstacle (defining subsections, dark highlight). While the order defining each type of obstacles in the file does not matter, it is important that all obstacles of the same type are defined within the same section. In Figure 1, the four NAME OF THE WEIR subsections are under the keyword NUMBER OF OBSTACLES DEFINED AS WEIRS = 4. Similarly, the one NAME OF THE POND subsection is under the keywork NUMBER OF STORAGE PONDS = 1.

As it is the case for the steering file, indentations and spaces between values and keywords do not matter. A pair of keyword and values are separated by either “:” or “=” indifferently. Multiple values provided for one keyword are separated by “;”. The decimal point follows the English convention of a “.”. Within a section, the order of the obstacles does not matter. For each obstacle, the order of the keywords defining its physical and operational characteristics does not matter either. Commented lines start with “#”.

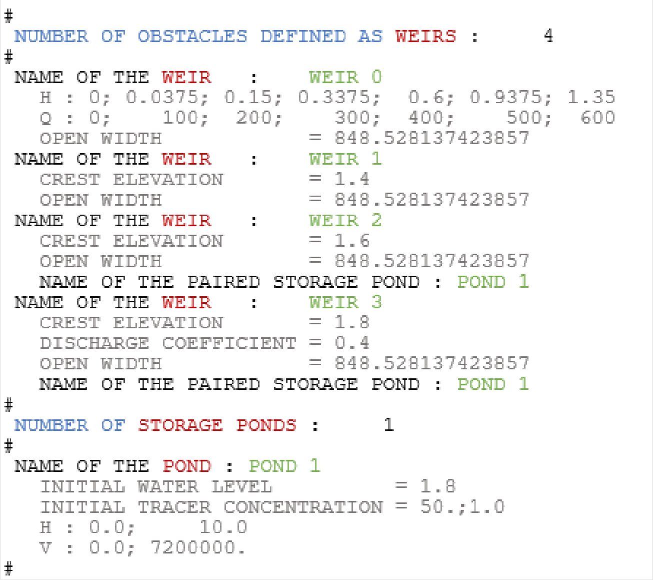

```
#
 NUMBER OF OBSTACLES DEFINED AS WEIRS :     4
#
 NAME OF THE WEIR    :     WEIR 0
   H : 0; 0.0375; 0.15; 0.3375;  0.6; 0.9375; 1.35
   Q : 0;    100;  200;    300;  400;    500;  600
   OPEN WIDTH                = 848.528137423857
 NAME OF THE WEIR    :     WEIR 1
   CREST ELEVATION           = 1.4
   OPEN WIDTH                = 848.528137423857
 NAME OF THE WEIR    :     WEIR 2
   CREST ELEVATION           = 1.6
   OPEN WIDTH                = 848.528137423857
   NAME OF THE PAIRED STORAGE POND : POND 1
 NAME OF THE WEIR    :     WEIR 3
   CREST ELEVATION           = 1.8
   DISCHARGE COEFFICIENT = 0.4
   OPEN WIDTH                = 848.528137423857
   NAME OF THE PAIRED STORAGE POND : POND 1
#
 NUMBER OF STORAGE PONDS :     1
#
 NAME OF THE POND : POND 1
   INITIAL WATER LEVEL              = 1.8
   INITIAL TRACER CONCENTRATION = 50.;1.0
   H : 0.0;     10.0
   V : 0.0; 7200000.
#
```

Figure 1. Example of file content setting characteristics for the obstacles

Finally, it is important to highlight that the names of the obstacles (highlighted in green in Figure 1) have to match those in their associated geometric definitions to enable open**TELEMAC** to make the connection.

B. *Obstacles' defining geometries*

Similar to the obstacles' physical characteristics detailed previously, the geographical characteristics of obstacles are defined within a single file added to a simulation via the keyword: FILE OF GEOMETRIES FOR THE OBSTACLES. For now, the content of the file follows the Blue Kenue i2s file format (see [2]). Extension of that format to i3s or to shape file is planned for future developments.

Figure 2 below shows an example of i2s defining the five geometries associated to those obstacles shown on Figure 1, four open lines (although these could be polylines) each associated to the name of a weir (highlighted in green) and one closed polygon associated to the storage pond. Colours on Figure 2 are here only for illustrative purposes.

Similar to those examples of weirs, geometrical lines can also be used to represent culverts, tunnels, turbines, pumps, etc, connecting ponds and areas on either ends of the lines, with their mesh connectivity and processing being handled automatically by open**TELEMAC**.

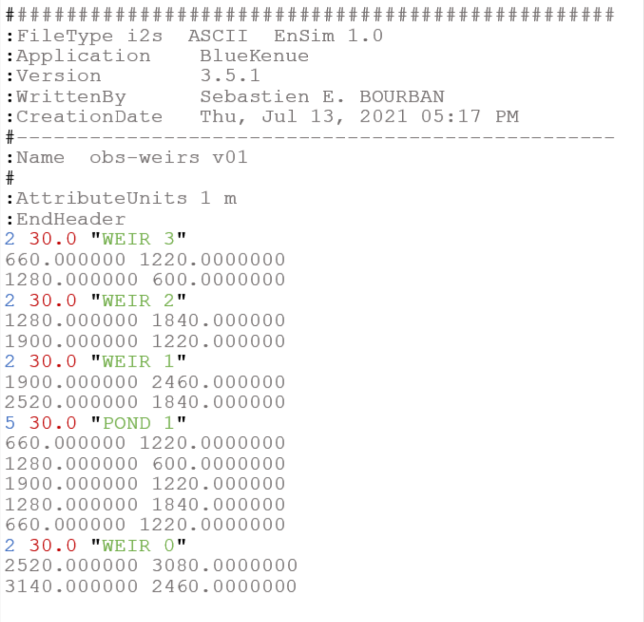

```
##################################################
:FileType i2s  ASCII  EnSim 1.0
:Application    BlueKenue
:Version        3.5.1
:WrittenBy      Sebastien E. BOURBAN
:CreationDate   Thu, Jul 13, 2021 05:17 PM
#-------------------------------------------------
:Name  obs-weirs v01
#
:AttributeUnits 1 m
:EndHeader
2 30.0 "WEIR 3"
660.000000 1220.0000000
1280.000000 600.0000000
2 30.0 "WEIR 2"
1280.000000 1840.000000
1900.000000 1220.000000
2 30.0 "WEIR 1"
1900.000000 2460.000000
2520.000000 1840.000000
5 30.0 "POND 1"
660.000000 1220.0000000
1280.000000 600.0000000
1900.000000 1220.000000
1280.000000 1840.000000
660.000000 1220.0000000
2 30.0 "WEIR 0"
2520.000000 3080.0000000
3140.000000 2460.0000000
```

Figure 2. Example of file content setting geometries for the obstacles

Finally, it is noted that the polygon associated to the obstacle named POND 1 is closed, following the Blue Kenue convention that duplicates the first and last point. Should a storage pond be defined by an open polyline, open**TELEMAC** would automatically close it.

C. *Conclusions on user inputs*

From a user viewpoint, obstacles can now be defined simply given only two files as detailed above, regrouping all obstacles for a given simulation. Physical characteristics are defined by keywords and values, just as the steering file, and geometric characteristics are defined through a georeferenced file. Besides, there is no requirement to tie obstacles to given node numbers on the mesh allowing the user to modify the mesh without having to regenerate the obstacles' definition files. A simplified approach to modelling obstacles has been implemented in open**TELEMAC**.

III. AUTOMATED APPROACH TO USER AND MESH INPUTS

Once the geometrical definitions of the obstacles are read in and matched to their associated type of hydraulic structure, open**TELEMAC** will automatically set up the necessary structure to link those geometries to the nodes and elements of the domain mesh. Linking approaches vary depending on the type of hydraulic structures. Here below are details for each type of obstacle programmed so far.

A. *Barriers*

The simplest obstacle type is the barrier (also called a closure) as it does not require a connection nor a computed transfer of water across. It can be used to either define an embankment, a causeway, a reclamation, or an area separated from the rest of the model. A distinction is made between a porous or a closed barrier through the keyword TYPE OF IMPLEMENTATION, for which 1 is closed and 2 is porous, providing a porosity value for the latter between 0 and 1.

Figure 3 below show an example of two such obstacles, the second one being provided a porosity of 0.1.

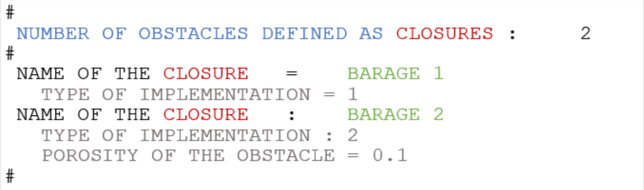

```
#
 NUMBER OF OBSTACLES DEFINED AS CLOSURES :     2
#
 NAME OF THE CLOSURE    =     BARAGE 1
   TYPE OF IMPLEMENTATION = 1
 NAME OF THE CLOSURE    :     BARAGE 2
   TYPE OF IMPLEMENTATION : 2
   POROSITY OF THE OBSTACLE = 0.1
#
```

Figure 3. Example of file content setting characteristics of closures

The automated approach of incorporating these types of barriers into a simulation consists of identifying all segments of the mesh (edges of the triangular elements) that cross the georeferenced polyline defining the obstacle and tagging left and right nodes for every intersection found. For illustration purposes, Figure 4 below shows part of the domain of the TELEMAC-2D test case of the Mersey Estuary, with two arbitrary user-defined barriers (in black) and their intersections (in light green) with the mesh (in light grey). Once all tagged nodes are known, a first row of elements (triangles) is identified for which all three nodes must be tagged. That row of triangles is subsequently widened (lighter white areas), if necessary, according to the user-defined thickness of the barrier, a value found in the georeferenced file (value in red in Figure 2).

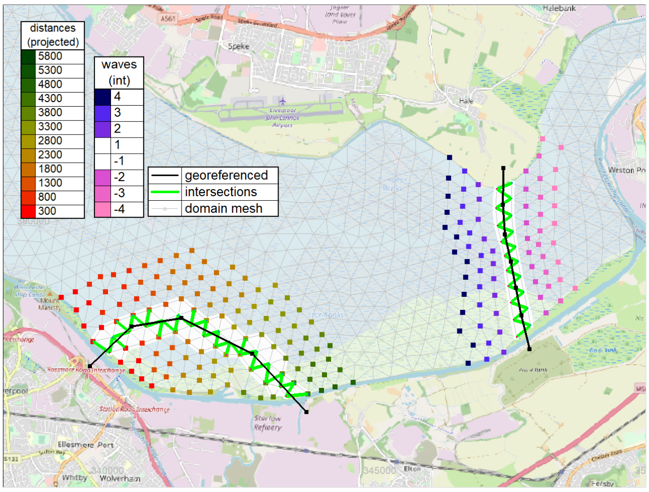

Figure 4. Example of computed intersections leading to proximity waves

It is important to note that if the polyline does not intersect the domain mesh, then there would be no possible masking of any area, nor a possible way of defining a porous barrier. Additionally, although it is the case in the illustration above, the barriers do not necessarily have to join edges of the model domain.

During the simulation, the area around the barrier (lighter white areas) is either masked out or defined as a porous region, depending on its type. Operational control files or user subroutines could be used to compute or define possible variations in the porosity value over time for each obstacle.

B. Flow passing over or through obstacles

The second type of obstacles regroups all structures for which water (and tracers) will be carried over from one side of the obstacle to the other side. It can be used to either define weirs, bridges, tidal barrages, or breaches over a dyke.

The approach of incorporating these types of obstacles into a simulation is identical to that of barriers (or closures), which consists of identifying all segments of the mesh that cross the georeferenced polyline defining the obstacle and tagging left and right nodes for every intersection. Rows of triangular elements are then identified (for which all three nodes have been tagged) and are masked during the simulation effectively blocking the processes along that area.

Once the first row of triangles (within the thickness of the obstacle) has been established, a cloud of nodes is added to the geometrical definition of each obstacle depending on the keyword DISTANCE OF INFLUENCE as set in the FILE OF SETTINGS FOR THE OBSTACLES for a given obstacle. This cloud is built iteratively in waves of connectivity away from the first row of triangles intersecting the obstacle. For illustration purpose, Figure 4 highlights in colours, the clouds of nodes around each obstacle. These are used as a physical support to a variety of local information and purposes. For instance:

- Each node within the cloud is associated to one integer in particular, called “WAVE”, with positive values on one side and negative equivalent on the other. The WAVE integer values of 1 and -1 are used to establish a connections or pairs of nodes across the obstacle. They are part of the first row of masked triangles. Higher positive and negative values (called “MATES”) are used as support to compute spatial average of the free surface level over a wide area of influence. Figure 4 shows in variations of pink and blue the WAVE tags associated to the cloud of the obstacle on the right.
- Each node within the cloud is associated to a distance projected along the obstacle, used to pair nodes (amongst those tagged with a WAVE of ±1) on either side of the obstacle. The projection is perpendicular to the segments of the polyline defining the obstacle. Figure 4 shows, in colour variations from red to green, the projected distances of the nodes in the cloud along the obstacle on the bottom left.
- Each node within the cloud is also associated to a vector, the direction of which is computed perpendicularly to the segments of the polyline defining the obstacle, the magnitude of which is set according to the distance to the polyline.

For illustration purposes, Figure 5 below shows part of the domain of the TELEMAC-2D test case of the flume (blue background), with one arbitrary user-defined angled weir (in black) and its intersection (in light green) with the mesh (in light grey). Given the thickness of the weir, seven rows of triangles are to be masked in that example (lighter white areas). As the weir is defined as a 90-degree angle, the arrows are fanning out from the corner on the right of the obstacle, while arrows combine on the longitudinal symmetry line on the left.

Figure 5 also shows the pairing of nodes (pink segments) on either side of the masked area (lighter white area). As said previously, the pairing is based on the projected distance along the segments of the polyline. For every node on the right and on the left of the masked area (WAVE = ±1), the closest (projected) node is chosen, and a pair is set. This approach guaranties that every node has at least one opposite, although some nodes could end up being connected to more than one opposite.

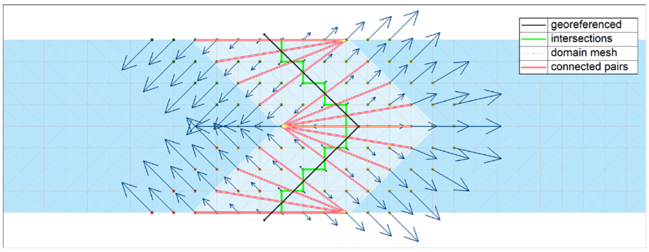

Figure 5. Example of directionality of flow and pairing across an obstacle

It is important to note that if the polyline does not cross the domain mesh, a cloud will still be built but according to the proximity of the nodes with the georeferenced polyline defining the obstacle, the proximity being defined through the same keyword DISTANCE OF INFLUENCE as set in the FILE OF SETTINGS FOR THE OBSTACLES for a given obstacle.

To illustrate this last point, Figure 6 shows the domain of a modified version the TELEMAC-2D test case of the "weir" (blue background). The mesh is also displayed (in light grey). In the original test case, 4 ponds were separated by 3 gaps. In this case, one pond has been removed from the mesh and replaced by a virtual storage pond (see definition of storage pond below). Georeferenced polylines (in black) defining the 3 weirs go through the original gaps. One could note that the domain has here been tilted by 45 degrees clockwise compared to the original TELEMAC-2D test case, to limit the size taken by the capture of the geometry within the figures of this article.

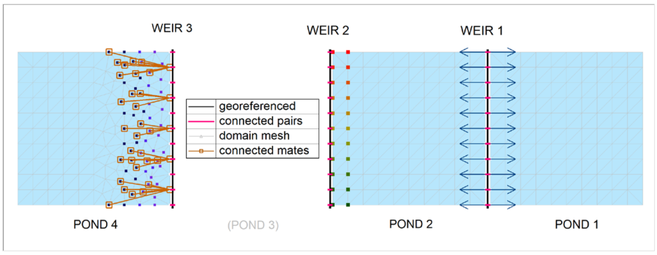

Figure 6. Example of pairing across a gap and of mates' connectivity

Even though there are no intersecting segments between the obstacles and the mesh, the novel approach is able to automatically connect nodes between ponds (pink segments across the gaps) and to build clouds of nodes depending on the DISTANCE OF INFLUENCE. In this example, WEIR 1 is on the right and has been set with a minimum distance of influence sufficient to just bridge the gap: there are no MATES. In contrary, WEIR 3 is on the left and has been set with a large distance of influence, going up to WAVE=5 (in colour variations between pink and blue).

As previously mentioned, the cloud of nodes is built iteratively in waves of connectivity away from the first row of triangles intersecting the obstacle (or not) and are used as a physical support to a variety of local information and purposes. Based on that support, MATES are selected within a certain vision angle away from the obstacle, and a connection is made for every node making up the pairing across the obstacle (WAVE = ±1). The vision angle for this type of obstacle is by default about 14 degrees ($= arcsin(1/4)$) defined around the direction associated to each node, perpendicularly to the segments of the polyline defining the obstacle. Figure 6 above shows the connections of the MATES (brown lines) with some the nodes of the pairs crossing the obstacle on the left. Using a narrow vision angle allows for the spatial averaging of variables elevation to remain directional away from the obstacle.

C. Flow tunneling under or within an obstacles

This third type of obstacle groups all hydraulic structures where water (and tracers) will be tunnelled under, from one opening of the obstacle to the other opening. It can be used to either define a culvert, a siphon, or a tunnel equipped with a pump, a valve and / or a turbine.

The approach of incorporating these types of obstacles into a simulation is much simpler than the previous type of obstacles, as it considers only one pair of connected areas (together with their associated MATES). Besides, there is no crossing of polylines nor masking of elements nor building up WAVE tags in this case.

To illustrate this type of obstacle, Figure 7 shows the domain of the TELEMAC-2D test case of the "siphon" (blue background, made of two ponds separated by a gap. The culvert is defined by a georeferenced line (in black) linking nodes from either pond (pink squares). The mesh is also displayed (in light grey).

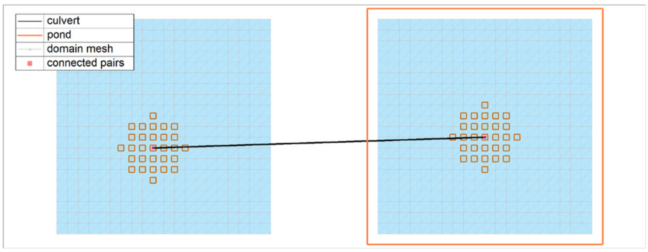

Figure 7. Example of pairing across two ponds and of mates' connectivity

Similar to other obstacles, clouds of nodes (brown squares) are built depending on the DISTANCE OF INFLUENCE centred on the nearest node on either end of the obstacle. These clouds will be used to maintain information around the connected nodes (in pink), such as to spatially average water level on either side of the culvert.

Figure 8 shows the associated keyword settings for the example shown in Figure 7 above (accessed from FILE OF SETTINGS FOR THE OBSTACLES) defining two types of obstacles (a culvert and a storage pond, blue / red highlights, defined as sections), within which one culvert named SIPHON 1 in the first section and one storage pond is named POND 1 in the second section (all obstacle names in green). One should note that some of the keywords have two values, for instance ELEVATION OF EACH OPENING, OPENING HEIGHTS, or HEAD LOSS COEFFICIENT AS ENTRY. Each value corresponds to one end of the obstacle, the order being the same as in the order of the first and last locations found in the georeferenced file.

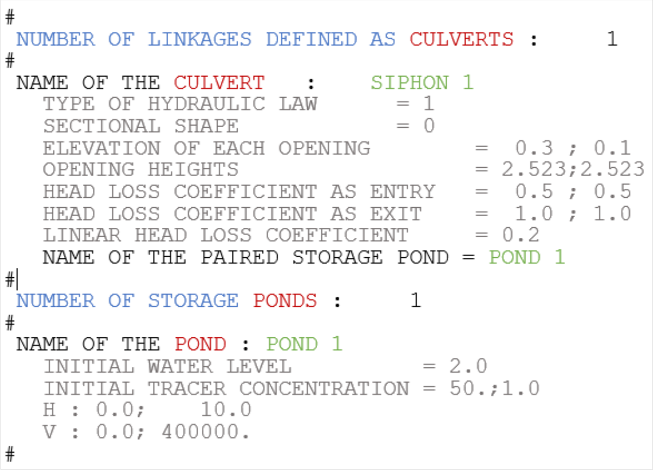

```
#
 NUMBER OF LINKAGES DEFINED AS CULVERTS :     1
#
 NAME OF THE CULVERT    :    SIPHON 1
   TYPE OF HYDRAULIC LAW       = 1
   SECTIONAL SHAPE             = 0
   ELEVATION OF EACH OPENING         =  0.3 ; 0.1
   OPENING HEIGHTS                   = 2.523;2.523
   HEAD LOSS COEFFICIENT AS ENTRY    =  0.5 ; 0.5
   HEAD LOSS COEFFICIENT AS EXIT     =  1.0 ; 1.0
   LINEAR HEAD LOSS COEFFICIENT      = 0.2
   NAME OF THE PAIRED STORAGE POND = POND 1
#|
 NUMBER OF STORAGE PONDS :     1
#
 NAME OF THE POND : POND 1
   INITIAL WATER LEVEL          = 2.0
   INITIAL TRACER CONCENTRATION = 50.;1.0
   H : 0.0;    10.0
   V : 0.0; 400000.
#
```

Figure 8. Example of file content linking a culvert to a storage pond

Figure 9 shows an example of i2s defining the two geometries associated to those obstacles shown in Figure 7, one open line associated to the culvert and one closed polygon associated to the storage pond.

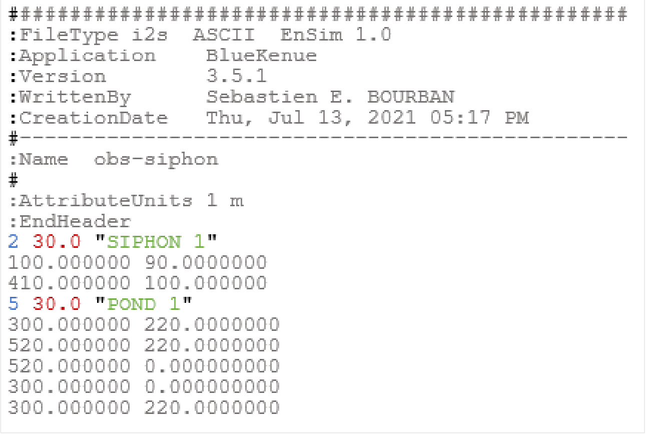

```
#################################################
:FileType i2s  ASCII  EnSim 1.0
:Application    BlueKenue
:Version        3.5.1
:WrittenBy      Sebastien E. BOURBAN
:CreationDate   Thu, Jul 13, 2021 05:17 PM
#------------------------------------------------
:Name  obs-siphon
#
:AttributeUnits 1 m
:EndHeader
2 30.0 "SIPHON 1"
100.000000 90.0000000
410.000000 100.000000
5 30.0 "POND 1"
300.000000 220.0000000
520.000000 220.0000000
520.000000 0.000000000
300.000000 0.000000000
300.000000 220.0000000
```

Figure 9. Example of file for setting geometries of a culvert and a pond

Similar to the examples of weirs, the processing of these geometrical lines is done automatically by open**TELEMAC**.

D. Storage ponds

The fourth object programmed as an obstacle has been called a storage pond to represent just that. This type of obstacle groups all areas where water (and tracers) will be stored and connected to the simulation through obstacles. It can be used to either define a reservoir, a retention pond, a tidal barrage, or a flood plain, for which the geometry does not require to be meshed but could be defined as a function of the water elevation to its volume of water (or tracer quantities).

A storage pond is assumed to be connected to the simulation through at least one discharge law (provided by the pairing with one or more weirs, culverts, etc.). The discharge through the paired obstacle is computed from the difference in water levels between that of the storage pond on one side and that of the simulation domain (MATES) on the other side of the paired obstacle. The volume of water (and the tracer concentrations) in the storage pond varies according to the discharge computed (positive or negative).

There are two approaches of incorporating these types of obstacles into a simulation:

- The first approach consists in defining a virtual location. The virtual pond exists through the keyword NAME OF THE PAIRED STORAGE POND within the subsection of one or more paired obstacle definitions. For instance, Figure 8 above shows that the CULVERT named SIPHON 1 is connected to the POND named POND 1 (names highlighted in green) through that keyword. In addition, multiple obstacles can be connected to the same pond as is the case for WEIR 2 and 3 shown Figure 1, both connected to POND 1. Finally, a virtual pond does not have to be associated to a georeferenced polygon but can be.
- The second approach consists in defining a georeferenced polygon encapsulating an actual area of the domain mesh. Together with Figure 8, Figure 9 shows the five nodes defining the contour of POND 1, which is also shown as a georeferenced feature on Figure 7 (orange line). In that case, the simulation will mask the elements found in the delineated area and replace graphical output variables in that area by computed spatially averaged variables (such as water level or tracer concentrations).

One should note that the function level-volume defined by the keywords H and V, should have the same number of ";"-separated values, and that linear interpolation is used in between pairs. Additional keywords are used to define the initial water level and tracer concentrations in the pond (for illustration see Figure 1 and Figure 8).

E. Control locations

The last object programmed refers to user defined locations, anywhere in the domain, from which information will be gathered (and averaged spatially and temporally) so it can be accessible to all other obstacles for operation purpose. Having already programmed MATES around given nodes, a control location can be defined with the same structure.

Within the cloud of MATES, computed variables such as water level, velocities or tracer concentrations can be spatially averaged around the control location and / or temporarily relaxed to finally be used to operate another defined control structure. In addition to computed variables, time dependent controls can also be read from a file given through the keyword TEMPORAL CONTROL FILE FOR THE OBSTACLES, which has the format of an open**TELEMAC** liquid boundary file. This operation procedure or hydraulic structure control can be programmed through user subroutines available for each type of obstacle.

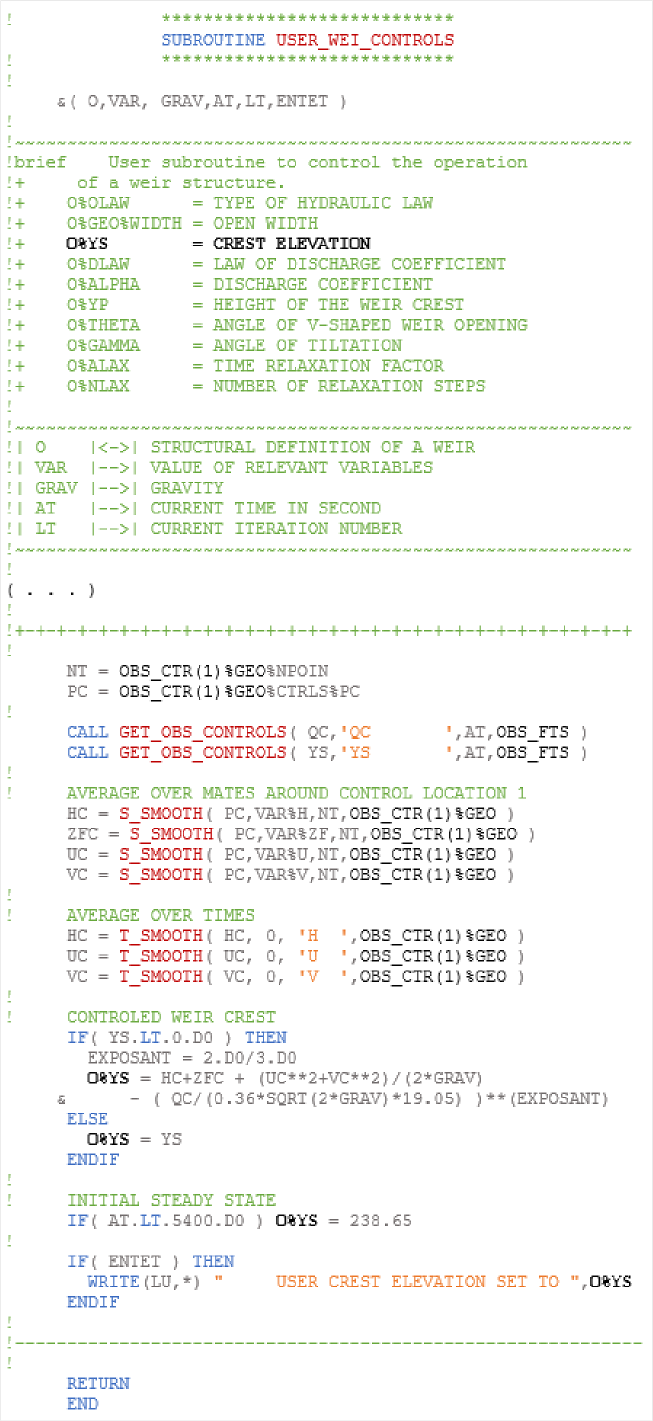

```
!              ****************************
               SUBROUTINE USER_WEI_CONTROLS
!              ****************************
!
     &( O,VAR, GRAV,AT,LT,ENTET )
!
!~~~~~~~~~~~~~~~~~~~~~~~~~~~~~~~~~~~~~~~~~~~~~~~~~~~~~~~~~~~~~
!brief    User subroutine to control the operation
!+      of a weir structure.
!+     O%OLAW      = TYPE OF HYDRAULIC LAW
!+     O%GEO%WIDTH = OPEN WIDTH
!+     O%YS        = CREST ELEVATION
!+     O%DLAW      = LAW OF DISCHARGE COEFFICIENT
!+     O%ALPHA     = DISCHARGE COEFFICIENT
!+     O%YP        = HEIGHT OF THE WEIR CREST
!+     O%THETA     = ANGLE OF V-SHAPED WEIR OPENING
!+     O%GAMMA     = ANGLE OF TILTATION
!+     O%ALAX      = TIME RELAXATION FACTOR
!+     O%NLAX      = NUMBER OF RELAXATION STEPS
!
!~~~~~~~~~~~~~~~~~~~~~~~~~~~~~~~~~~~~~~~~~~~~~~~~~~~~~~~~~~~~~
!| O    |<->| STRUCTURAL DEFINITION OF A WEIR
!| VAR  |-->| VALUE OF RELEVANT VARIABLES
!| GRAV |-->| GRAVITY
!| AT   |-->| CURRENT TIME IN SECOND
!| LT   |-->| CURRENT ITERATION NUMBER
!~~~~~~~~~~~~~~~~~~~~~~~~~~~~~~~~~~~~~~~~~~~~~~~~~~~~~~~~~~~~~
!
( . . . )
!
!+-+-+-+-+-+-+-+-+-+-+-+-+-+-+-+-+-+-+-+-+-+-+-+-+-+-+-+-+-+-+
!
      NT = OBS_CTR(1)%GEO%NPOIN
      PC = OBS_CTR(1)%GEO%CTRLS%PC
!
      CALL GET_OBS_CONTROLS( QC,'QC       ',AT,OBS_FTS )
      CALL GET_OBS_CONTROLS( YS,'YS       ',AT,OBS_FTS )
!
!     AVERAGE OVER MATES AROUND CONTROL LOCATION 1
      HC = S_SMOOTH( PC,VAR%H,NT,OBS_CTR(1)%GEO )
      ZFC = S_SMOOTH( PC,VAR%ZF,NT,OBS_CTR(1)%GEO )
      UC = S_SMOOTH( PC,VAR%U,NT,OBS_CTR(1)%GEO )
      VC = S_SMOOTH( PC,VAR%V,NT,OBS_CTR(1)%GEO )
!
!     AVERAGE OVER TIMES
      HC = T_SMOOTH( HC, 0, 'H  ',OBS_CTR(1)%GEO )
      UC = T_SMOOTH( UC, 0, 'U  ',OBS_CTR(1)%GEO )
      VC = T_SMOOTH( VC, 0, 'V  ',OBS_CTR(1)%GEO )
!
!     CONTROLED WEIR CREST
      IF( YS.LT.0.D0 ) THEN
        EXPOSANT = 2.D0/3.D0
        O%YS = HC+ZFC + (UC**2+VC**2)/(2*GRAV)
     &      - ( QC/(0.36*SQRT(2*GRAV)*19.05) )**(EXPOSANT)
      ELSE
        O%YS = YS
      ENDIF
!
!     INITIAL STEADY STATE
      IF( AT.LT.5400.D0 ) O%YS = 238.65
!
      IF( ENTET ) THEN
        WRITE(LU,*) "     USER CREST ELEVATION SET TO ",O%YS
      ENDIF
!
!-------------------------------------------------------------
!
      RETURN
      END
```

Figure 10. Example of operation of a weir crest based on a control location

For illustration purpose, Figure 10 above shows the core of the user subroutine USER_WEI_CONTROLS, that controls parameters of a weir at every time step, before the discharge is computed.

In this case, the parameter O%YS (crest elevation, in bold) is lowered or raised according to both a time control variable read from a file and the total load computed at a control location (case of a disappearing barrage).

The Fortran subroutine reads as follows:

- The subroutine GET_OBS_CONTROLS is called twice to read the interpolated values of both QC and YS at the time AT from the file unit OBS_FTS corresponding to the file TEMPORAL CONTROL FILE FOR THE OBSTACLES.
- The subroutine S_SMOOTH is called four times to average spatially over the MATES, the water depth (HC), the bathymetry level (ZFC) and the u- and v-components of the velocity (UC and VC), around the first control location OBS_CTR(1)%GEO.
- The subroutine T_SMOOTH is called thrice to relax the dynamic variables HC, UC, and VC, over time. These are associated to the first control location OBS_CTR(1)%GEO.
- Finally, at time when YS is negative, the weir's crest (O%YS) is set according to a function of the total load less a function of a control flow QC or otherwise set to the provided value read from the file YS.

Defining one or more control locations for a simulation provides, in parallel and scalar modes, a method to gather and spatially average model data around that location and use it to control the operation of any other hydraulic structure or obstacle. Given the specificity of the possible controls and operational procedures of an obstacle, these controls must be implemented with a user defined subroutine.

F. Parallelisation of obstacles

Given the relatively small footprint of an obstacle and its clouds of MATES, it was decided that all processors would share the information as well as the computation of discharges given their associated hydraulics laws. A dynamic array of pointers for every obstacle, the so called IPID array, is used to sort the global list of nodes linking a given processor to the local node number on the processor's mesh. Having said that, information is shared as follows:

- Each processor contributes its computed variables (such as water depth, velocities, tracer concentrations) at every time step to a referred place within common arrays of variables based on the order provided by the IPID array of pointers. The values of these common arrays are then shared through the standard parallelisation interface to all processors.
- Each processor has all the information on all nodes to compute the flow and tracer concentrations through all the obstacles within the simulation.
- Each processor computes source and sink values on all nodes of the clouds for every obstacle that is within its local mesh, again using the IPID array of pointers.

In scalar mode, the IPID array of pointers simply becomes the list of nodes on the mesh. Test cases developed so far for the implementation of obstacles show that the comparison of results between parallel and scalar modes is identical.

IV. SIMPLIFIED APPROACH TO ALL HYDRAULIC LAWS

In addition to providing a simplified approach to user inputs, this work on obstacles has also looked into a simplified approach to the implementation of hydraulic laws, for each of the types of obstacles.

The pairing of nodes on either side of the obstacle allows for the computation of the total discharge across or through the obstacle to be divided into one or more 1D segments. These 1D segments act as the support to empirical hydraulic discharge laws, depending on the type of obstacle and of the type of law chosen.

To sort out these numerous empirical laws, each obstacle has been built as a separate Fortran module within which characteristics specific to that obstacle are stored, including the hydraulic discharge laws for that obstacle. For instance, the module OBS_WEIR contains a function called GET_WEI_HYDRAULICS, returning the discharge given the upstream and downstream water level. An extract of that function is shown in Figure 11 below.

As can be observed:

- The discharge Q (character in bold black) is computed as a function of the upstream and downstream water level (SLUP and SLDW respectively) and from a weir coefficient CD, itself set according to the hydraulic laws chosen (here 5 laws have been implemented so far).
- A correction to the CD coefficient is made to go from a sharp-crested weir to a broad-crested weir, or to a tilted weir.
- A correction to the discharge Q is also made to go from an unsubmerged weir to a completely submerged weir.
- Other hydraulics laws can be added for v-shaped weirs or trapezoidal weirs, for instance, or as user defined.

Similarly, the module OBS_BRIDGE has a function called GET_BDG_HYDRAULICS, that includes all hydraulics laws, the module OBS_CULVERT has GET_CVT_HYDRAULICS, (formerly known as BUSE in the open**TELEMAC** system) etc.

It is the view of the authors that the implementation of all discharge laws characterising a type of obstacle within a single function simplifies the approach of having to code or modify existing user defined laws. Additionally, all other structural aspects of the obstacle and its interaction with the mesh, its nodes, and the parallelisation of it all has been abstracted in this implementation leaving the user just the important part: the definition of the hydraulic laws.

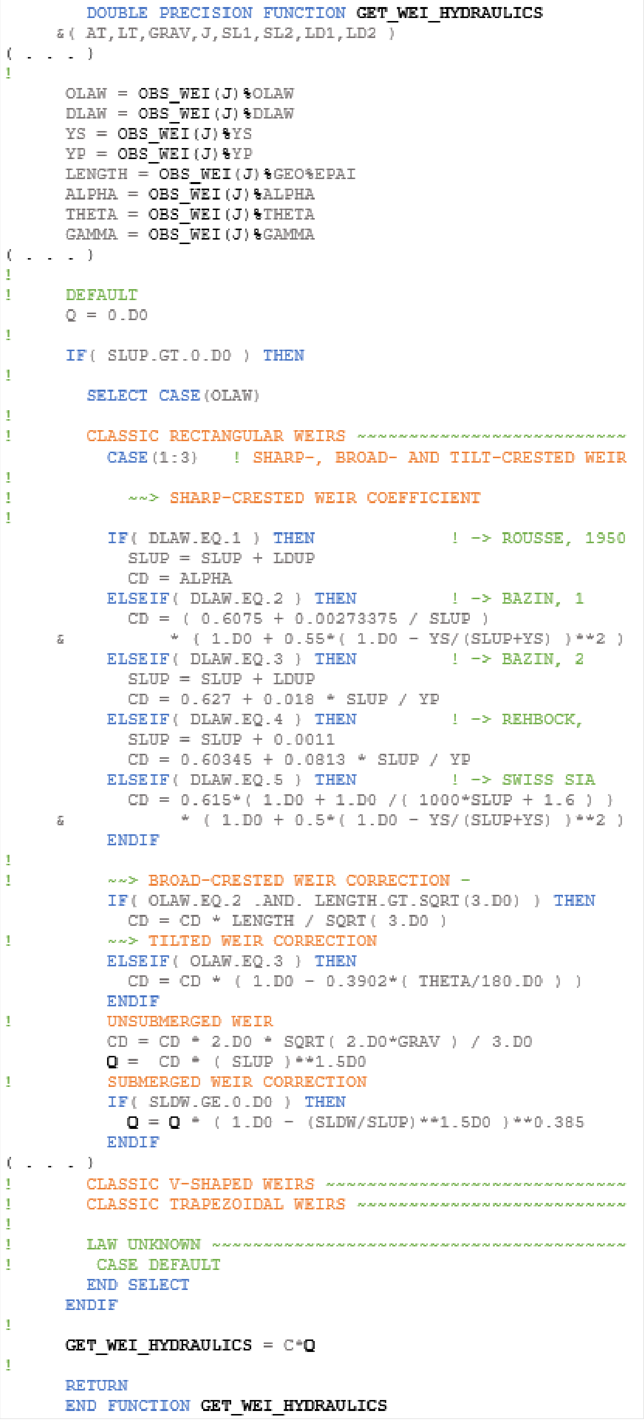

```
        DOUBLE PRECISION FUNCTION GET_WEI_HYDRAULICS
     &( AT,LT,GRAV,J,SL1,SL2,LD1,LD2 )
( . . . )
!
      OLAW = OBS_WEI(J)%OLAW
      DLAW = OBS_WEI(J)%DLAW
      YS = OBS_WEI(J)%YS
      YP = OBS_WEI(J)%YP
      LENGTH = OBS_WEI(J)%GEO%EPAI
      ALPHA = OBS_WEI(J)%ALPHA
      THETA = OBS_WEI(J)%THETA
      GAMMA = OBS_WEI(J)%GAMMA
( . . . )
!
!     DEFAULT
      Q = 0.D0
!
      IF( SLUP.GT.0.D0 ) THEN
!
        SELECT CASE(OLAW)
!
!       CLASSIC RECTANGULAR WEIRS ~~~~~~~~~~~~~~~~~~~~~~~~~~~~
          CASE(1:3)   ! SHARP-, BROAD- AND TILT-CRESTED WEIR
!
!           ~~> SHARP-CRESTED WEIR COEFFICIENT
!
          IF( DLAW.EQ.1 ) THEN              ! -> ROUSSE, 1950
            SLUP = SLUP + LDUP
            CD = ALPHA
          ELSEIF( DLAW.EQ.2 ) THEN          ! -> BAZIN, 1
            CD = ( 0.6075 + 0.00273375 / SLUP )
     &          * ( 1.D0 + 0.55*( 1.D0 - YS/(SLUP+YS) )**2 )
          ELSEIF( DLAW.EQ.3 ) THEN          ! -> BAZIN, 2
            SLUP = SLUP + LDUP
            CD = 0.627 + 0.018 * SLUP / YP
          ELSEIF( DLAW.EQ.4 ) THEN          ! -> REHBOCK,
            SLUP = SLUP + 0.0011
            CD = 0.60345 + 0.0813 * SLUP / YP
          ELSEIF( DLAW.EQ.5 ) THEN          ! -> SWISS SIA
            CD = 0.615*( 1.D0 + 1.D0 /( 1000*SLUP + 1.6 ) )
     &           * ( 1.D0 + 0.5*( 1.D0 - YS/(SLUP+YS) )**2 )
          ENDIF
!
!         ~~> BROAD-CRESTED WEIR CORRECTION -
          IF( OLAW.EQ.2 .AND. LENGTH.GT.SQRT(3.D0) ) THEN
            CD = CD * LENGTH / SQRT( 3.D0 )
!         ~~> TILTED WEIR CORRECTION
          ELSEIF( OLAW.EQ.3 ) THEN
            CD = CD * ( 1.D0 - 0.3902*( THETA/180.D0 ) )
          ENDIF
!         UNSUBMERGED WEIR
          CD = CD * 2.D0 * SQRT( 2.D0*GRAV ) / 3.D0
          Q =  CD * ( SLUP )**1.5D0
!         SUBMERGED WEIR CORRECTION
          IF( SLDW.GE.0.D0 ) THEN
            Q = Q * ( 1.D0 - (SLDW/SLUP)**1.5D0 )**0.385
          ENDIF
( . . . )
!       CLASSIC V-SHAPED WEIRS ~~~~~~~~~~~~~~~~~~~~~~~~~~~~~~~
!       CLASSIC TRAPEZOIDAL WEIRS ~~~~~~~~~~~~~~~~~~~~~~~~~~~~
!
!       LAW UNKNOWN ~~~~~~~~~~~~~~~~~~~~~~~~~~~~~~~~~~~~~~~~~~
!        CASE DEFAULT
        END SELECT
      ENDIF
!
      GET_WEI_HYDRAULICS = C*Q
!
      RETURN
      END FUNCTION GET_WEI_HYDRAULICS
```

Figure 11. Example of the weir's implementation of discharge laws

Similar functions exist for each obstacle (culverts, bridges, turbines, pumps, etc.), many of which remain to be implemented and documented with references.

Finally, one could note that the pairing of nodes across obstacles, represented by one or more 1D segments also allows for the implementation of actual 1D models along these pairs, depending on the obstacle properties. This could be a future extension of the work on obstacles.

V. EXAMPLES OF APPLICATIONS

To support this simplified approach to obstacles in the open**TELEMAC** system, several test cases have been created, some to reproduce existing test cases (for instance "weir" and "siphon"). In fact, the illustrations shown so far in this article have been extracted from these test cases, the results of two of which will be presented here. Detailed descriptions of the other test cases will be part of the open**TELEMAC** system.

A. Test case for weirs and storage ponds: "obs_weirs_v1"

The test case "obs_weirs_v1" in fact includes three test case configurations, each referred to by a different steering file and their associated obstacle files.

1) The clone: The first steering file is a clone of the existing "weir" test case ("t2d_obstacle-weirs_v01.cas").
Figure 12 below shows the domain (blue background) and the mesh (in light grey). The test case includes 4 ponds separated by 3 gaps, with georeferenced polylines (in black) representing the 3 weirs going through the gaps. One could note that the domain has here been tilted by 45 degrees clockwise compared to the original TELEMAC-2D test case, to limit the size taken by the capture of the geometry within the figures of this article.

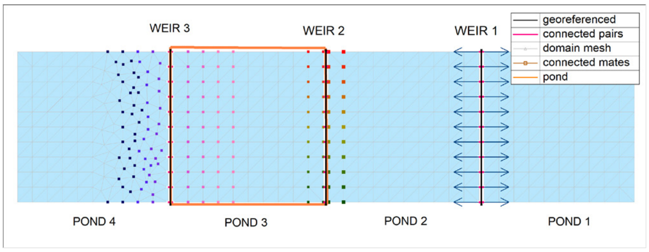

Figure 12. Example of test cases playing with weirs and storage ponds

The initial condition is at still water, with a free surface elevation of 1.8 m (bottom elevation is at 0 m). A constant discharge of 600 m3/s is imposed on the upstream boundary (on the left) and a water level of 1.35 m is imposed on the downstream boundary (on the right). The simulation is run until a steady state is reached. Figure 1 and Figure 2 describe the characteristics and the geometry of the 3 weirs, the 3 weirs having different crest level making the case of a stepping ponds, the highest crest elevation being at 1.8 m.

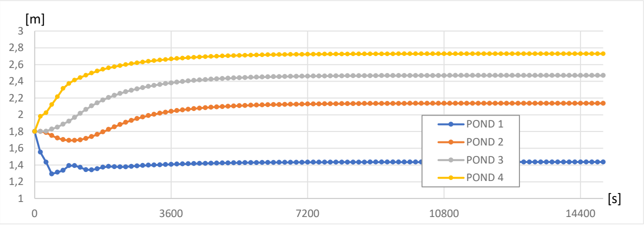

Figure 13. Example of test cases playing with weirs

Resulting time series of water elevation extracted from the middle of each pond are shown on Figure 13. While the level in POND 1 (blue curve) is essentially driven by the downstream boundary conditions, the water levels in the 3 other ponds are the result of a balance between their upstream and downstream pond level, given the constant discharge through the model and the weir characteristics.

2) The virtual pond: The second steering file is a modified version of the first ("t2d_obstacle-weirs_v02.cas"), in which POND 3 has been removed from the mesh and replaced by a virtual storage pond.
Figure 6 illustrates the domain (blue background) and the mesh (in light grey) with only 3 ponds and georeferenced polylines (in black) representing the 3 weirs as before.

Initial and boundary conditions are unchanged. Figure 1 and Figure 2 describe the characteristics and the geometry of the 3 weirs respectively, together with the virtual pond.

One should note that, having removed POND 3 from the domain, results within that pond are not available anymore, but instead results within the virtual storage pond are written within the on-screen listing printout. Because time series are identical to the next configuration, these are not shown here.

3) The masked pond: The third steering file is a yet another modified version of the first test case ("t2d_obstacle-weirs_v03.cas"), in which a georeferenced polyline encircling POND 3 has been added to the definition of the obstacles in the simulation.
Figure 12 shows the closed polyline in orange.

Again, initial and boundary conditions are unchanged. Figure 1 and Figure 2 describe the characteristics and the geometry of the 3 weirs and of the pond.

As shown previously, resulting time series of water elevation extracted from the middle of each pond are shown in Figure 14. While part of the mesh has been masked of (or entirely removed from) the computation, the results using virtual or masked storage ponds are almost identical to those of the original test case. The only slight difference is in that pond 3 now has a uniform water level, while the original test case had a slight slope in the direction of the flow, changing slightly the balance over the WEIR 3 and 2.

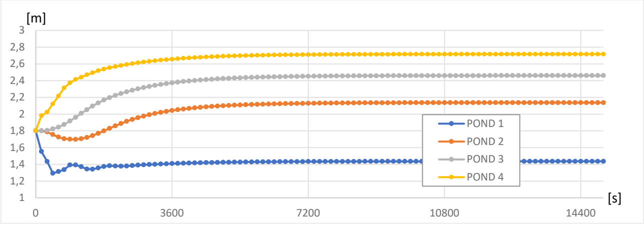

Figure 14. Example of test cases playing with storage ponds

Should the hydrodynamic of the storage pond or the flood plains not be critical for a simulation, then this new feature has the potential to save on computational time.

B. Test case for culverts: "obs_siphon"

The test case "obs_siphon" also includes three test case configurations, each referred to by a different steering file and their associated obstacle files. The first steering file ("t2d_siphon-v01.cas") is a clone of the existing "siphon" test case. The two others see the replacement of one of the two ponds by a virtual and a masked storage pond respectively. Having illustrated the use of storage ponds previously, only the clone siphon is presented here.

Figure 7 shows the domain (blue background) and the mesh (in light grey). Figure 8 and Figure 9 describe the characteristics and the geometry of the culvert linking the two ponds (called SIPHON 1).

Initial conditions are set as a level difference between the two ponds, instantly triggering a discharge through the culvert. The initial water level is set at 4 m in the pond on the left and at 2 m in the other pond.

Resulting time series of water elevation extracted from the middle of each pond are shown in Figure 15. Given that the two ponds have the same surface area, the decrease of water level in one pond corresponds exactly to the increase in the other pond. The use of a temporal relaxation and of a spatial averaging renders the results stable with no oscillatory behaviour. As anticipated, both levels eventually converge to a water level of 3 m.

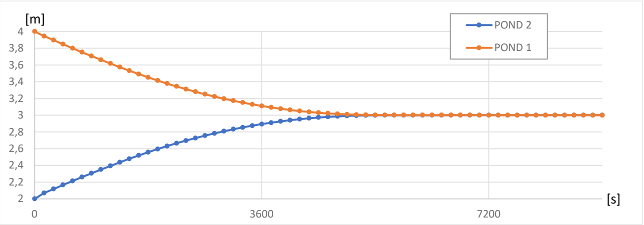

Figure 15. Example of test cases playing with a siphon between ponds

VI. CONCLUSION AND PERSPECTIVES

A simplified and generic approach has been implemented in the open**TELEMAC** system to enable the representation of most type of obstacles, or hydraulic structures, including weirs, culverts, porous or solid barriers, storage ponds, etc. In doing so, additional structures can now be included within the same framework, such as bridges, sluices, tidal barrages, bypasses, pumps, etc., together with their empirical variations. For instance, weirs can now either be sharp- or broad-crested, v-shaped or tilted, submerged or not, reversable or linked to a storage pond or not, etc.

The novel approach is believed to have simplified both user inputs (through the combination of a keyword based steering file and a georeferenced geometry file of polylines and polygons) and the implementation of empirical hydraulic laws (grouped by types of obstacles as a single discharge function of upstream and downstream information). The objective of the work was indeed to completely generalise hydraulics structures based on an abstraction of "obstacle". Besides, although it is recommended, the geometry and density of the modelled mesh does not have to be aligned with the presence of the obstacle.

Other files can also be used to control the operation of the obstacle, whether driven by time sequences or water level variations or by information computed at a control location within the domain. User subroutines have also been introduced to help manually control gates, sluices, pumps, turbines, etc.

Still, a lot of work remains before the branch "searobin" can be merged with the main version of the open**TELEMAC** system. Remaining work includes:

- The implementation of other empirical hydraulic laws for all obstacles, in particular for bridges, pumps and tidal barrages. Should you have references to empirical laws, EDF R&D would be pleased to add these with the code for you.
- The documentation of the work remains to be written, also; this article will be used as a reference for the time being and a starting point for the future user manual. Contributions are evidently welcomed.
- The validation remains to be augmented with many more test cases, both in 2D and 3D, at least one for every type of obstacle and their associated empirical laws.
- A new output file format could be developed to track the structure of the obstacles once linked to the mesh as well as time varying variables passed through obstacles or stored within ponds.
- Use of 3D shape file format as input geometries for a better integration with open source graphical applications such as QGIS, and e.g. the use of additional elevation data for possible variation of the crest of the weir.

Finally, it is anticipated that ongoing work on other types of advanced hydraulic structures will benefit from this work. For instance, a dynamic coupling of the open**TELEMAC** with the rainfall underground pipe network code SWMM (see [3]), will use similar linking features. Further, a detailed representation of dynamic breaching mechanisms inspired by the code EMBREA (see [4]) will be built through the 1D segmentation of obstacles.

REFERENCES

[1] S.E. Bourban, N. Durand, M.S. Turnbull et al, "Coastal Shelf Model of Northern European waters to inform tidal power industry decisions," TELEMAC User Conference, Oxford, UK, 2013

[2] Canadian Hydraulics Centre, NRC-CNRC, "Blue Kenue Reference Manual," Sept 2011

[3] USEPA, USA, "Stormwater Management Model, v5p2, Software and Documentation", Jan 2022

[4] HR Wallingford, UK, "EMBREA, a full featured breach model, the successor of the HR BREACH model", 2020

Two-way-coupling near-field and far-field models for the simulation of plumes

Thom Wolf[1], W. Alexander Breugem[1], Bart Verheyen[1], Boudewijn Decrop[1]
abr@imdc.be, Antwerp, Belgium
[1]: IMDC NV

Abstract – **In this paper, two different coupling methodologies between near-field and far-field models are presented. In the first coupling methodology, the near-field model of Lee and Cheung [3] is coupled directly (online coupled) to TELEMAC-3D, in order to calculate the vertical displacement of the near-field plume, taking into account the flow velocity and density in the far field model to calculate the near-field model. In the second methodology, an offline methodology is presented, in which the results of an separate calculation with CORMIX are used to generate input in a far-field TELEMAC-3D model. Three applications are presented. In the first application, the online coupling is used to generate the spreading of a plume generated during deep-sea mining activities. In the second example, the modelling of faecal bacteria due to the release of waste water in the Adriatic sea are presented. Finally, the use of online coupling of near-field and far-field models to model the impact of dredging on the turbidity are shown.**

Keywords: plumes, TELEMAC-3D, Near-field model; Far-field model; Model coupling

I. INTRODUCTION

Plumes play an important role in environmental problems. Examples consist of sediment plumes generated by dredging works, thermal plumes or waste water releases.

The physical processes concerning plumes differ between the near field and the far field. In the near field, plumes move due to inertia and buoyancy, while strong entrainment of ambient fluids occur. In the far field on the other hand, these processes are not significant and the plume behaves as a passive plume, which moves due to advection and turbulent diffusion. Because of the different physical processes in the near-field and far-field, different numerical models are typically used for each of these, where TELEMAC-3D is often used to model the far-field dispersion of plumes.

Different near-field models exist. An often used model is CORMIX [1]. CORMIX consist of a decision support system, in combination with different modelling approaches for the simulation of the near-field plume, which are chosen based on the conditions (based on the release, the ambient flow and the ambient stratification). For each of these cases, the appropriate near-field model is based on integral models for the conservation of mass, momentum, buoyancy and scalar quantities [4,5,6]. In this way point sources as well as line sources can be simulated. CORMIX is a closed source model, which makes it difficult to couple it to directly to TELEMAC.

A different modelling approach was taken by Lee & Cheung [3]. They model the near-field plume using a Lagrangian (particle tracking) approach. The flow velocity of the plume is determined based on the conservation of mass and momentum of the plume, using a simplified expression to determine the entrainment of fluid from the ambient flow into the plume. This approach is used for example in the model VISJET.

The objective of this paper is to present the coupling between near-field models and TELEMAC-3D. Two different methodologies are discussed for the coupling:

- An online approach. In this approach the Lagrangian plume is used directly coupled with TELEMAC-3D, where the vertical flow and stratification profiles in TELEMAC-3D are used in the near-field calculations. The resulting data of the near-field model is then applied every time step in TELEMAC-3D as a Dirac source.
- An offline approach. In this approach, near-field calculations are performed beforehand for different typical conditions using CORMIX. Based on the results of these calculation, and the expected results of the simulation (put into TELEMAC-3D as a text file), a source term, is generated and applied every time step in TELEMAC-3D.

In this paper, first the coupling approaches are discussed in section II. Then, the use of the coupled models is illustrated using three different cases. In the first case, plumes generated during deep sea mining are simulated using an online coupled model. The modelling of faecal bacteria is illustrated as a second case. In this case, the offline modelling approach is used. As a third example, the online coupling approach is used to model dredging plumes due to dredging works. Finally, an outlook is given on future developments to improve the coupling methodology, and the paper is finished with comes conclusions.

II. COUPLING TELEMAC-3D TO NEAR FIELD MODELS

A. Requierements for coupling near-field and far-field models

When coupling, a near field model to a far field model, there are different considerations that need to be taken into account:

- **Coupling dynamics:** there are different coupling methods. A coupling can be offline or online and dynamic or static [2]. In an online coupling, the near-field model uses data from the far-field model and/or the far field model uses data from the near field model.

In case only one of these couplings, we speak of one-way coupling, whereas when both area present, we speak of two-way coupling. In a dynamic coupling [2], the transfer of data from or to the near-field and far-field model occurs on time scale that is small compared to the variation of the ambient conditions.

- **Tracer mass conservation**: this is the most important requirement in the coupling. The mass of the released material must be the same in the near-field and far-field model, in other to have meaningful balances of the released material in the far field model.
- **Water mass conservation**: In many cases, also mass conservation is applied to the released water by adding the same amount of water in the far field model. The objective of doing so, is to have some effect of the release on the large scale flow structure in the far field model. Care must be taken when doing so, because the near field model considers entrainment of the ambient fluid into the jet. Therefore, sources as well as sinks of fluid might be considered in the far field model. Different methods were considered in [7]:
    - Use undiluted source in the far field model
    - Use the diluted source in the far field model.
    - Use the diluted source in the far field model in combination with sink terms to represent the entrainment.

  It was found that the third method works best.

  Note that the water mass balance in many cases has a limited influence on the results, especially when the released volume is small compared to the volume in the far field model. In those cases, the addition of water can be ignored altogether.
- **Separation of scales**: there should a clear difference between the length and time scales in the near field and in the far field. If not, coupling between these two models is not needed and either a far field or a near field model can be used stand alone.
- **Dynamic coupling**: [2]

B. *Online coupling for the Lee and Cheung model*

In order to couple TELEMAC-3D to a near field model, a new Fortran module was developed called `moving_source.f`, in which the equations from Lee and Cheung [3] are solved in a one-dimensional vertical profile model. The velocity and tracer concentration from TELEMAC at the location of the release are applied as input data to this near -field calculation. From this, the concentration distribution in the near-field is calculated with different methods for specific methods. In order to release the tracers, the existing Dirac source terms in TELEMAC-3D are used. When using Dirac source terms, the flowrate and concentration need to be prescribed. In the present implementation, the flow is homogeneously divided over the vertical profile, in order to limit disturbance to the flow as much as possible. Using these flow rates, the concentrations are calculated, taking into account the vertical profile calculated by the near field model, and correcting the data, in such way that the released tracer mass correspond exactly to the amount specified by the user. The fluid flux in the far field model is equal to the amount of fluid released in the near field model, i.e. the influence of the entrainment was not taken into account.

In developing the current approach, several simplifying assumptions were made. First it is assumed that the time for the tracer transport in the near-field is negligible compared to the time scales at which the plume and flow adopts in the far field, and to the time scale at which the releases vary in time. Hence the delay between the release of tracer in the near field model and the time the tracer enters the far field model is not taken into account. Second, it is assumed that the horizontal distance travelled in the near-field model is small compared to the dimensions of the far-field plume. Hence the release of tracers and waste water is applied at the location of the release, rather than at the calculated distance downstream of the release. Third, it is assumed that the horizontal size of the plume (at the moment it enters into the far field model) is small compared to the mesh resolution. Hence the release is applied at one node in the mesh.

C. *Offline coupling of Cormix*

Because the CORMIX software is not open source, a fully coupled approach is not possible. Instead an offline approach was developed. In this approach, CORMIX simulations are performed first for a set of flow and stratification conditions that occur in the model domain. For each of these conditions, the elevation, height and width of the resulting plume are determined. These conditions are then given to TELEMAC-3D in the form of an Ascii input file, together with the released amount of tracer. In the offline coupling, the water release is not taken into account. Therefore, the total amount of tracer released during a time step is added to the existing tracer in TELEMAC-3D using a shape function, that is based on the gaussian profile of the plume that is assumed in CORMIX:

$$\Delta C = F\Delta T \frac{\exp\left(\frac{-\vec{x} - \overrightarrow{x_0}}{\vec{\sigma}}\right)^2}{\int \exp\left(\frac{-\vec{x} - \overrightarrow{x_0}}{\vec{\sigma}}\right)^2 d\vec{x}}$$

Here, F is the tracer flux, ΔT the time step, $\vec{x}$ the (3d) coordinates of the mesh, $\overrightarrow{x_0}$ the coordinate of the location of the release and, $\vec{\sigma}$ the width and height of the plume coming from CORMIX.

In this approach, the same limiting assumptions are applied as in the online approach (section II.B), with one exception. The third assumption, that the dimensions of the plume are small compared to the mesh size in the far field model, is lifted here.

III. APPLICATIONS

A. *Deep sea mining*

During deep sea mining, nodules are collected from the sea bed and pumped towards the surface. The water sediment mixture that is pumped can form plumes when released in midwater. The online coupling between TELEMAC-3D and the Lee- and Cheung [3, section II.B] model was used to study these plumes (see section). The TELEMAC-model was setup for an area in the deep ocean (with a depth of 4-5 km), using a combination of 66 z and sigma layers. Here, the z layers are used in the top 1500 m of the water column, in order to limit artificial mixing of the temperature and salinity, whereas the sigma coordinates are used below. The KPP turbulence from the General Ocean Turbulence Model (GOTM) was used to parametrize the turbulence [9]. The model was driven by meteorological data, in combination with data from OSU/TPXO for the tide [10] and HYCOM [11] for the large-scale flow [more details can be found in 8].

In order to couple the near field and far field, the near field model was run every time step of the far field model. From the result of the near-field model, the release height in the far field model was determined, as the vertical location, where the vertical velocity in the near field had decreased to a sufficiently low value. At this location, the near field material was released into the far field model. A gaussian distribution for the concentration profile was used, for which the thickness depends on the cross section of the plume calculation in the Lagrangian plume model. In the far field model, the sediment was modelled as a tracer with a constant settling velocity.

A typical result of the calculation is shown in Figure 1. A comparison between experimental data and a similar near field model [8] shows that these near field models work well to simulate the near field behaviour of this kind of plumes. Unfortunately, no measurements are available to validate the far field approach.

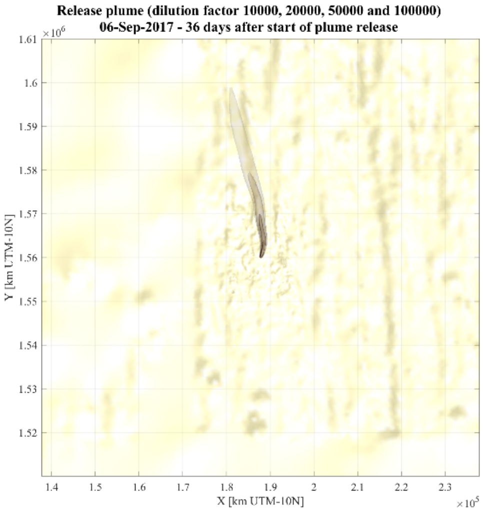

Figure 1. Example (top view of the plume of a midwater release)

B. *Faecal bacteria modelling*

Bathing water in coastal areas is unfortunately not always meeting the water quality required standards for faecal bacteria. To guarantee a good quality of bathing water, or to asses potential risks causing poorer quality, (local) governments have measurements being carried out to base assessments on. However, these often lack the temporal and spatial extent to make a sound assessment of the water quality of a coastal area. Numerical water quality models can provide these insights by simulating both the dispersion and fate of introduced faecal bacteria.

An example of this, is a recently developed numerical model train which has been used to study of the dispersion of sewage effluent (faecal bacteria) along the Istrian coast. Here, a large-scale TELEMAC-3D model of the Istrian coast was constructed to study the dispersion and fate (decay) of faecal bacteria released through an opening at the end of a number of sewage outfall pipes at the sea bed. The initial dispersion and mixing processes of the waste water discharge from the outfall pipes cannot be captured well using the coastal model. Therefore, a near-field CORMIX model is applied to analyse the near field behaviour of the waste water discharge and results are used to provide boundary conditions for the far-field model. For each outfall. A CORMIX model was set up consisting of a diffusor or single pipe outlet. As input, it furthermore uses the local water depth, ambient flow velocity from the far-field model and a schematized density profile. The latter is in this area different for summer (stratified) and winter (mixed) conditions (Figure 2) and hence investigated as distinct scenarios.

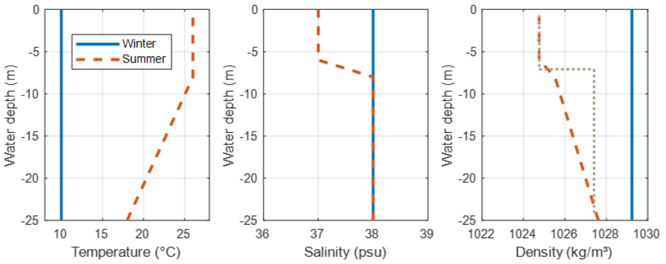

Figure 2. Variation in sea water conditions over the vertical for winter and summer. Left: variation in temperature, middle: variation in salinity, right: variation in water density (blue: well mixed winter conditions, red: stratified summer conditions that are represented by the grey dashed line in CORMIX).

The calculated result of CORMIX indicates the dimensions (vertical position in the water column and width) of the waste water plume at the edge of the near field mixing area. At this point, the dispersion of the waste water plume is dominated by the local flow conditions, which are calculated using the far-field coastal model. Because the density of the waste water effluent (having zero salinity) is lower than the sea water, a positively buoyant jet is generated, which has the tendency to move towards the water surface. Depending on the water depth and the exit velocity from the pipe, the waste water plume will be fully mixed or spread towards the higher parts of the water column. Examples of the plume dimensions calculated using CORMIX are shown in Figure 3 and Figure 4 for respectively a winter case (well mixed sea water conditions) and a summer case (stratified sea water conditions). The comparison of the cross section shows that the waste water plume during summer is trapped beneath the thermocline in summer.

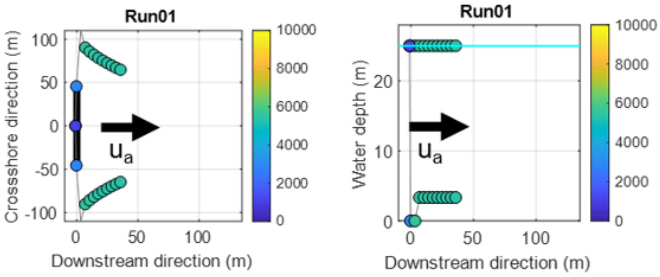

Figure 3. Illustration of CORMIX results for the winter case with indication of the direction of ambient flow (U_a). Left: top view of the waste water plume (black is the diffusor), right: cross section through the waste water plume indicating that the plume spreads from 3 meters above the bed towards the water surface.

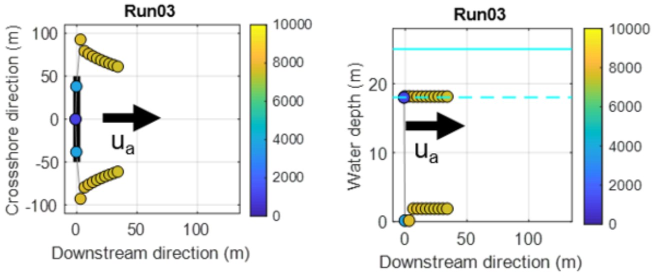

Figure 4. Illustration of the CORMIX results for the summer stratified case with indication of the direction of ambient flow (U_a). Left: top view on the waste water plume (black is the diffusor), right: cross section through the waste water plume spreading from one meter above the bed towards the location of the pycnocline.

The shape of the waste water plume at the edge of the near field mixing area is given by CORMIX as the parameters (width and height) of a top-hat profile to TELEMAC, and applied using the method described in section II.C.

In this study, a model mesh was constructed with 97,000 nodes and a mesh resolution ranging between 50 m in the area of interest to 4 km near the offshore model boundary. The model domain is divided into 15 double sigma vertical layers. Because a good turbulence model is essential in order to correctly model the vertical stratification and mixing in the Adriatic Sea, GOTM was coupled to TELEMAC-3D [9] using a k-epsilon model with a second-order algebraic closure model for the stratification fluxes. To capture the fate of faecal bacteria, a decay rate was used in TELEMAC.

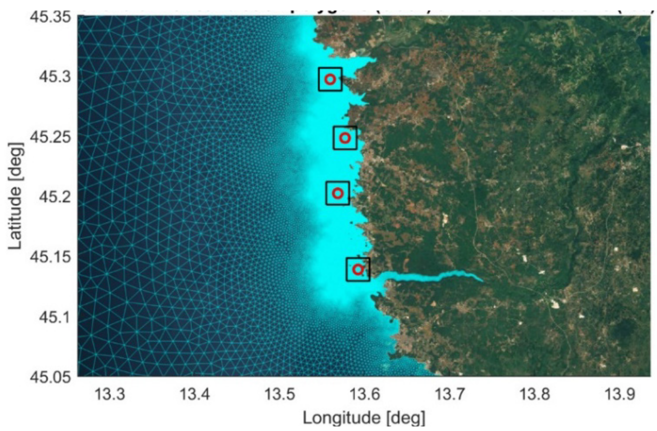

Figure 5. Model grid (zoom) of the Istrian coast TELEMAC model. Red dots indicate the approximate locations of sewage outfall pipe ends.

Time averaged ECOLI concentrations for a ten day simulation period are shown for the summer and winter case in Figure 6 and Figure 7, respectively. Both cases show that there is a main north south transport orientation of the concentration patterns of the faecal bacteria around the outfalls.

Similar to the near field model, it is found that during stratified conditions (which often occur in summer), the waste water discharge is trapped deeper in the water column and cannot reach the surface easily, even though it consists of fresh water with a density smaller than the sea water. Therefore, the highest faecal bacteria concentrations are found near the middle of the water column, where the density gradient is strongest (Figure 6), whereas significantly less ECOLI bacteria are found near the surface. Conversely, for the mixed winter case (Figure 7), results show that the highest concentrations are found at the water surface. This is due to the fresh water effluent being strongly positive buoyant, by which faecal bacteria quickly disperse to the water surface after which the bacteria further disperse with the local currents.

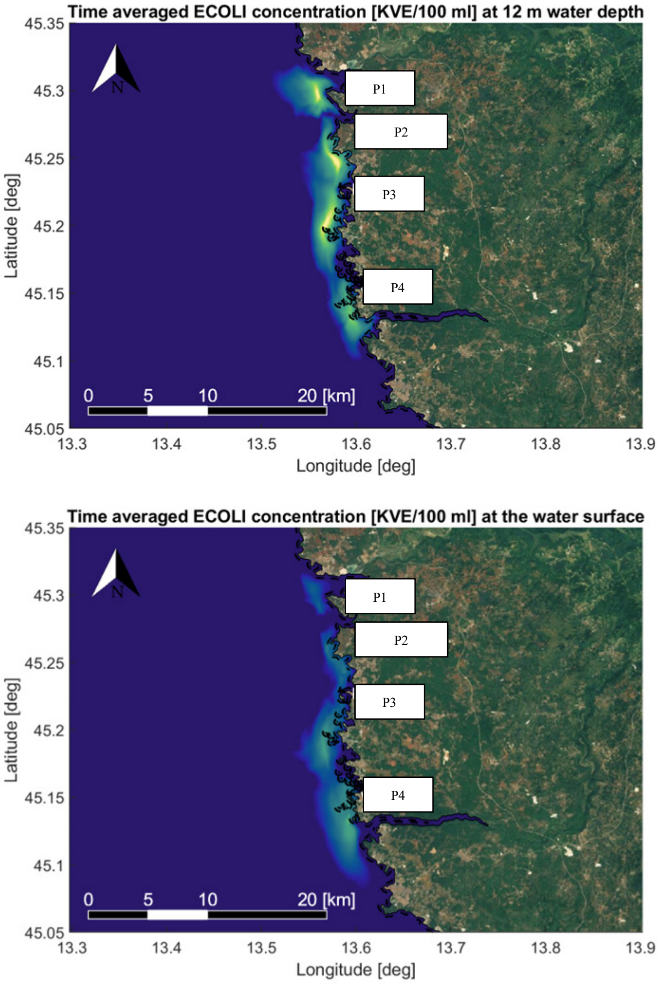

Figure 6. Summer scenario results of time averaged ECOLI concentrations at a level of 12 m water depth (top figure) and at the water surface (bottom figure).

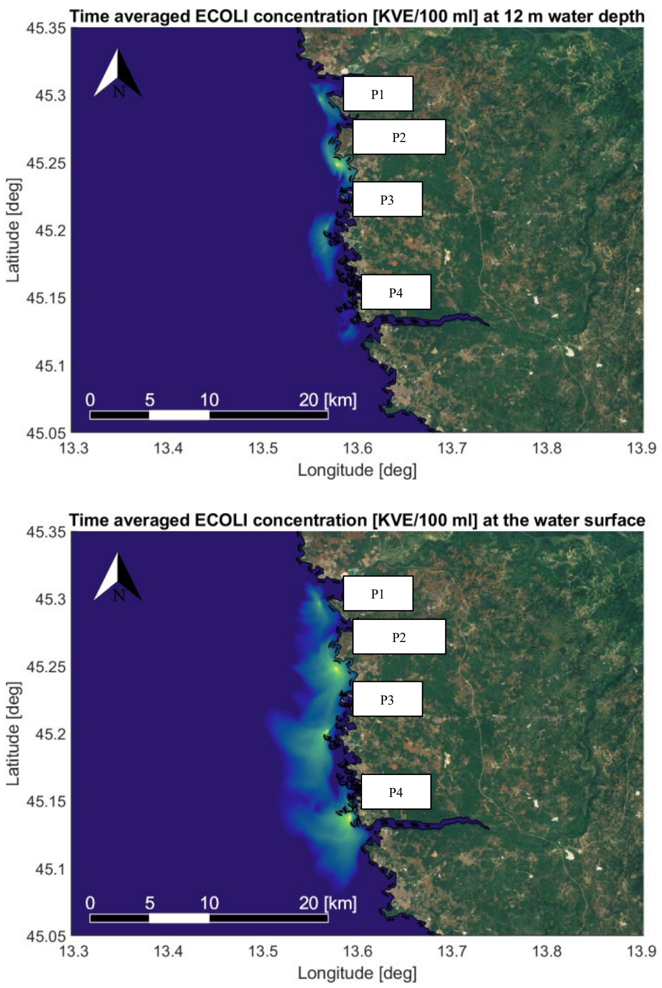

Figure 7. Winter scenario results of time averaged ECOLI concentrations at a level of 12 m water depth (top figure) and at the water surface (bottom figure).

With this kind of water quality modelling, model results can be used to identify beaches with a likelihood of being exposed to high concentrations of faecal bacteria or for instance to investigate the effectiveness of potential measures such as filtering systems of waste water treatment plants.

C. Dredging plume simulations

Dredging works are often executed, for example to maintain a sufficient draft for shipping traffic. Different equipment is used to dredge. An often used vessel is the trailing suction hopper dredger (TSHD). These vessels dredge sediment, and store it in a barge. In order to store as much sediment as possible, an overflow is used to release water and fine sediment from the barge while the coarser sediment settles in the barge. This generates plumes of sediment, whose behaviour is important to know for to environmental reasons.

For the simulation of dredging plumes, the online model of Lee and Cheung [3] is used, which uses the local flow velocity in a profile in TELEMAC-3D to calculate the sediment concentration profile. The results of the Lee and Cheung model were then used in the parametric model develop by [12], that was based on CFD simulations of the dredging plume around a TSHD (Figure 2). In the far-field model, a standard advection diffusion approach is used to simulate the transport of suspended sediment.

In the coupling code, a functionality was made, such that the location of the dredging vessel can change each time step, based on prescribed positions in a text file, in order to simulate the motion of the dredging vessel. Additionally, the release of sediment at the dredge head was simulated using a simple parametric profile, and the resuspension of sediment by the propeller of the dredging vessels was simulated using an additional parametrisation based on a parametrised model of the propellor jet, in combination with the Partheniades equation to calculate the resuspension of sediment from the bed from the jet velocity.

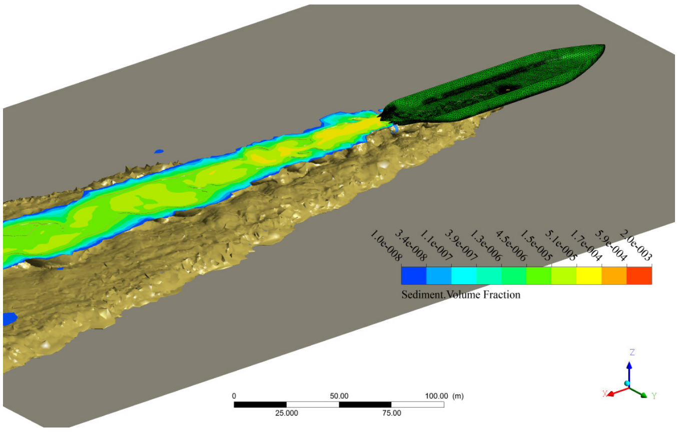

Figure 8. Example result of the CFD calculations of the dredging plume of TSHD from [11]

The characteristic result of an application is shown in Figure 9. In this figure different dredging plumes are visible, calculated using the coupled TELEMAC-3D near field model.

Figure 9. Instantaneous snapshot sediment concentrations due to dredging activities simulated using the coupled near-field far-field model.

IV. OUTLOOK

The current methodologies work well in practise, despite some limiting approximations. The online-approach is the preferred method for future tracer dispersion modelling. However, the offline approach uses a slightly more advanced approach for applying the near-field data in the far field model (using a plume that is not restricted to a single node). Therefore, the idea is to merge these two approaches, in order to have the advantages of each of these two approaches.

There are multiple limitations in the online model. First, the calculation of the plume in a 1DV vertical profile model, instead of in the full model, which leads to the neglect of horizontal displacements of the near-field plume. Further, no time lag is applied between material entering the near-field model and leaving the near-field model, which is not fully realistic (particularly for large near-field plumes and low vertical velocities). In order to overcome these two assumptions, the idea is to use the particle tracking module (*streamline.f*) in TELEMAC to calculate the Lagrangian model of Lee and Cheung [3]. For this, the flow field needs be modified such that the particle tracking module uses the velocity of the near-field jet, which depends on its buoyancy and momentum as well as on the entrainment of the ambient fluid. A methodology to use particle velocities that differ from the ambient fluid velocity has previously been applied in the simulation of macro-plastic objects in TELEMAC-3D [13], and seems applicable here as well.

V. SUMMARY AND CONCLUSIONS

In this paper, two different approaches were presented for coupling near-field models to TELEMAC-3D for the simulations of plumes:

- An online approach, based on the Lagrangian model of Lee and Cheung [3]. Successful applications of this model for simulation of dredging plumes as well as plumes due to return flow of deep sea mining activities were shown.
- An offline approach, in which results from separate CORMIX calculations were applied into TELEMAC-3D. A successful application is shown for the calculation of plumes of faecal bacteria in the Adriatic Sea, where it is shown that the seasonal differences in the spreading of the bacteria are well captured by the model.

REFERENCES

[1] Doneker R. & Jirka G.. Cormix User Manual. A hydrodynamic mixing zone model and decision support system for pollutant discharges into surface waters. EPA-823-K-07-001 (2017).

[2] Morelissen, R., Kaaij, T. V. D., & Bleninger, T.. Waste water discharge modelling with dynamically coupled near field and far field models. In International Symposium on Outfall Systems (2011, May).

[3] . Lee, J. H. & Cheung, V.. Generalized Lagrangian model for buoyant jets in current. Journal of Environmental Engineering, 116(6), 1085-1106 (1990).

[4] Jirka, G. H.. Integral model for turbulent buoyant jets in unbounded stratified flows. Part I: Single round jet. Environmental fluid mechanics, 4(1), 1-56 (2004).

[5] Jirka, G. H.. Buoyant surface discharges into water bodies. II: Jet integral model. Journal of Hydraulic Engineering, 133(9), 1021-1036 (2007).

[6] Jirka, G. H.. Integral model for turbulent buoyant jets in unbounded stratified flows Part 2: Plane jet dynamics resulting from multiport diffuser jets. Environmental Fluid Mechanics, 6, 43-100 (2006).

[7] Choi, K. W. & Lee, J. H.. A new approach to effluent plume modelling in the intermediate field. In XXXI IAHR congress, Seoul, Korea 11-16 (2005, September) .

[8] Muñoz-Royo, C., Peacock, T., Alford, M. H., Smith, J. A., Le Boyer, A., Kulkarni, C. S., Lermusiaux P.F.J., Haley Jr P.J., Mirabito C., Wang D., Adams E.E., Ouillon R. , Breugem A. , Decrop B. , Lanckriet T., Supekar R.B. , Rzeznik A.J., Gartman A. & Ju, S. J.. Extent of impact of deep-sea nodule mining midwater plumes is influenced by sediment loading, turbulence and thresholds. Communications Earth & Environment, 2(1), 148. https://www.nature.com/articles/s43247-021-00213-8 (2021)

[9] Lanckriet, T., Breugem, A., & Decrop, B. . CouplingTELEMAC-3D with the General Ocean Turbulence Model (GOTM). In Proceedings of the XXVth TELEMAC-MASCARET User Conference, 9th to 11th October 2018, Norwich (pp. 137-144).

[10] Egbert, G. D., Bennett, A. F., & Foreman, M. G.. TOPEX/POSEIDON tides estimated using a global inverse model. Journal of Geophysical Research: Oceans, 99(C12), 24821-24852 (1994).

[11] Chassignet, E. P., Hurlburt, H. E., Smedstad, O. M., Halliwell, G. R., Hogan, P. J., Wallcraft, A. J., & Bleck, R.. Ocean prediction with the hybrid coordinate ocean model (HYCOM). Ocean weather forecasting: an integrated view of oceanography, 413-426 (2006).

[12] Decrop, B.. Numerical and experimental modelling of near-field overflow dredging plumes. Doctoral dissertation, Ghent University (2015).

[13] Breugem W., Chu K., Koutrouveli T., Wang L. & Decrop B.. Numerical modelling of plastic dispersion: a case study of the river Scheldt. 39th IAHR World Congress, Granada, Spain (2022).

A local Lax-Friedrichs flux applied to the finite volume method of GAIA

Leopold Stadler, Martin Utz
leopold.stadler@baw, Karlsruhe, Germany
BAW

Abstract **– In this work we apply a local Lax-Friedrichs flux (LLF) as numerical flux to the finite volume method of GAIA. The numerical flux is applied to compute the bedload flow between the local elements/nodes of a finite volume/finite element method. We present two different methods to estimate the bed celerity, which is used as dissipation parameter of the local Lax-Friedrichs flux. The first method applies a scaling between the shallow water flow and the bedload flow (SLLF). The second method uses the assumption the water depth is considerable higher than the bed evolution and the bedload formula of Grass to estimate the bed celerity (GLLF). In order to validate both methods, we study 1D test cases with moving dunes under different flow conditions. The results of GLLF and SLLF are compared with the standard finite volume method and the standard finite element method of GAIA. It is shown that the finite element method of GAIA and the GLLF create unphysical oscillations when the characteristics of the underlying equation intersects. We also present the results from a 1D finite volume model for the same test cases. It is shown that both estimations of the bed celerity for the local Lax-Friedrichs flux (GLLF and SLLF) lead to stable results without oscillation. A further test shows that the 1D model can also reproduce the pattern of an antidune.**

Keywords: bedload transport, stability, numerical flux, TELEMAC.

I. INTRODUCTION

Bedload transport is usually modelled by solving the shallow water equations (SWEs) and the Exner equation [1] in a coupled system of equations (SWE-Exner system). In this system, the SWEs describe the relation between water flow and water depth. The Exner equation describes the relation between bed elevation and bedload. Different methods exist to solve the coupled SWE-Exner system. GAIA applies a splitting approach and solves first the shallow water equations and afterwards the Exner equation for each time step. Applying a splitting approach to the SWE-Exner system can lead to instabilities [2]. Therefore, it can be beneficial to solve the coupled SWE-Exner system with a coupled method, as it has been done by several researchers. Stadler [3] developed a 2D prototype with a fully implicit time discretization, solving the coupled nonlinear equations with a Newton method. Bilanceri et al. [4] avoided the need of a nonlinear solver by creating a linearized implicit scheme. Audusse et al. [5] applied a relaxation scheme to solve the 1D and 2D SWE-Exner system.

Instabilities in the solution process of the SWE-Exner system are often triggered by the numerical flux which is applied to compute bedload flow between elements/nodes. A more diffusive numerical flux is often able to damp numerical instabilities [2]. Therefore, the computation of bedload fluxes between elements/nodes becomes a critical part of bedload modelling. Usually, the bedload discharge q_{sed} is computed with a bedload transport formula for each element/node. Later a numerical flux is applied to compute the resulting bedload flux f_{sed} between elements/nodes. The use of empirical formulas for bedload transport, bed roughness and shear stress make it hard to define a general numerical flux which can be applied to all bedload formulas. Several numerical fluxes and schemes have been developed, some of them combine the hydrodynamic and bedload fluxes in a coupled system (e.g. by a Riemann Solver) to increase the stability and accuracy (e.g. [6] and [7]).

Numerical fluxes with a high complexity in their computation may have some drawbacks for real-world applications. Especially when the velocities from the hydrodynamic system are adapted for the bedload flux computation to account for effects like secondary currents and gravitational transport. It is unclear how these changes can be incorporated into the coupled flux. If different sediment fractions are considered (multigrain model), the bedload discharge is often computed for each sediment fraction individually. Some of the more complex numerical fluxes can only be applied to a SWE-Exner system with a single sediment fraction.

The aim of this work is to study if the local Lax-Friedrichs flux can be applied to the finite volume method of GAIA as a general monotone and stable numerical flux. For this purpose, we investigate two different methods to compute the diffusion parameter of the local Lax-Friedrichs flux. Both methods can be applied to multigrain models. First, we introduce a simple scaling method to estimate the bed celerity for the local Lax-Friedrichs flux (SLLF). The SLLF was successfully applied in a 2D prototype for the SWE-Exner system [4]. Second, we introduce the Grass local Lax-Friedrichs flux (GLLF) which uses the bedload transport formula of Grass to estimate the bed celerity [8]. It should be noted that this approach assumes that the water depth is considerable higher than the bed evolution. The GLLF can also be applied for other bedload formulas. Therefore, the wave speed can be estimated by transforming these bedload formulas into the general Grass formulation [8]. The bedload discharge itself can be calculated by the original bedload formula, since the bed celerity is only applied to estimate the diffusion parameter of the local Lax-Friedrichs flux.

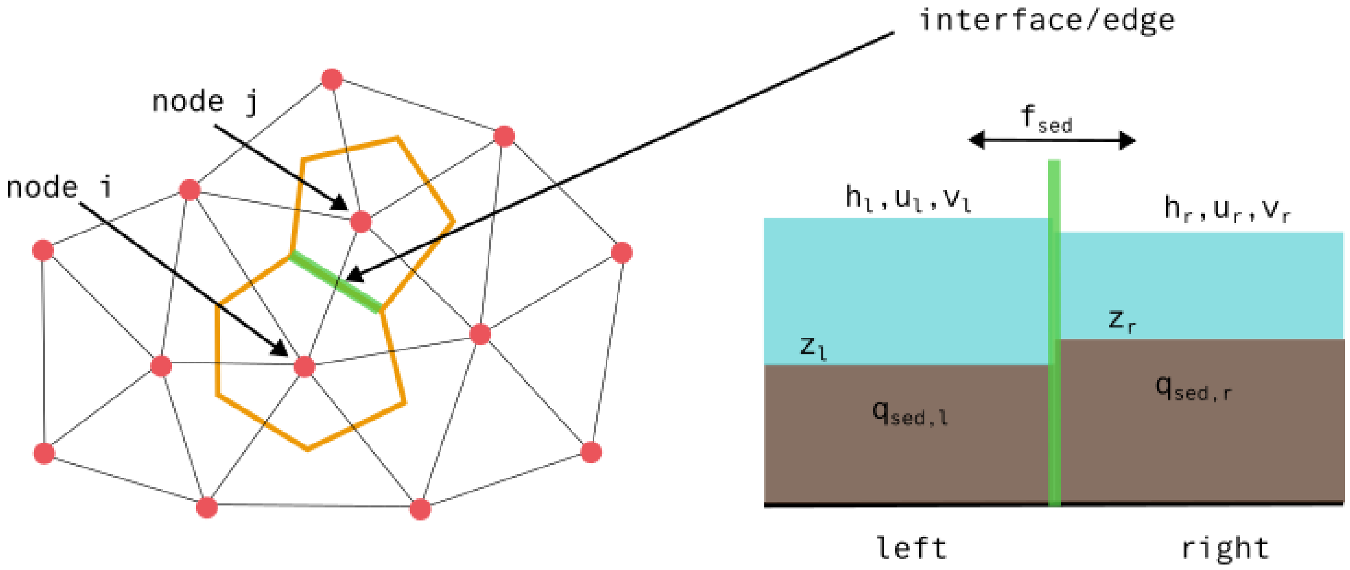

Figure 1. Computation of the sediment flux f_{sed} over an interface/edge.

We present three 1D test cases with moving dunes under various flow conditions to study the different numerical fluxes. We compare the results of the local Lax-Friedrichs fluxes (GLLF, SLLF) with the upwind scheme of the finite volume method of GAIA (UPWIND) and the finite element scheme of GAIA (FEM). In addition to GAIA, we created a 1D finite volume model in Python to study the GLLF and SLLF in detail. The 1D model combines the HLL solver [9] for the 1D shallow water equations with the GLLF/SLLF flux to solve the Exner equation. The 1D model allows to solve the problem with an explicit or a fully implicit time integration (fully coupled system).

II. THE LOCAL LAX-FRIEDRICHS FLUX

Figure 1 shows the interface/edge between two nodes in GAIA. There are two different states on the left side (node *i*) and the right side (node *j*) of the interface. The state variables are used to compute the numerical fluxes of the SWE-Exner system. The given state variables on both sides are the water depth h, the velocities u and v, the bed elevation z and the bedload discharge q_{sed}. The bedload discharge can be computed with one of the available bedload formulas of GAIA. For simplicity's sake, in the test cases herein the Grass formula is applied. The numerical properties of the underlying Exner equations makes it impossible to apply a simple average between the discharge of the left ($q_{sed,l}$) and right side ($q_{sed,r}$) of the interface to compute the bedload flux f_{sed} over the interface. The following formula with the bedload fluxes normal to the interface

$$f_{sed} = 0.5\left(q_{sed,l} + q_{sed,r}\right) \tag{1}$$

will lead to an unstable scheme. The finite volume method of GAIA applies an upwind scheme to overcome this problem. Upwind schemes can be written in a general notation,

$$f_{sed} = \alpha\, q_{sed,l} + (1 - \alpha) q_{sed,r}\ , \tag{2}$$

where α is the upwind parameter. Typically, α is computed depending on the flow direction or the Froude number [10]. A fully upwind scheme will set α as 0 or 1, depending of the propagation direction. Therefore, the bedload discharge is taken from the left/right side (fully upwind). Setting α equal to 0.5 will lead to the unstable centered scheme (1). Fully upwind schemes tend to be very diffusive, since all information is always taken from just one side.

The local Lax-Friedrichs method can be seen as a combination of a centered flux (1), with an additional diffusive term to guarantee stability

$$f_{sed} = 0.5\left(q_{sed,l} + q_{sed,r}\right) - 0.5\,\lambda\,(z_r - z_l), \tag{3}$$

where the dissipation parameter λ is the parameter controlling the diffusive part of the equation and $(z_r - z_l)$ is the difference in the bed elevation between the right and the left side. For the Exner equation, λ can be set to the bed celerity. The computation of the bed celerity is not trivial, since the bedload formulas compute only the bedload discharge q_{sed} and not the bed celerity.

Stadler (2021) estimated λ from the wave speed of the hydrodynamic model and the discharge relation between bedload and the water flux. For the SLLF λ is defined as:

$$\lambda_l = abs\left(\frac{\lambda_{w,l}\, q_{sed,l}}{u_l h_l}\right) \tag{4}$$

$$\lambda_r = abs\left(\frac{\lambda_{w,r}\, q_{sed,r}}{u_r h_r}\right) \tag{5}$$

$$\lambda = \max(\lambda_l, \lambda_r), \tag{6}$$

where $\lambda_{w,l}$ and $\lambda_{w,r}$ are the eigenvalues of the hydrodynamic problem. For details for computing the eigenvalues with a Riemann solver see [9]. We applied a hydrostatic reconstruction [11] to modify the Riemann problem in the case of a varying topography.

A more sophisticated approach to estimate λ is to calculate the bed celerity (λ_l and λ_r) with the general Grass formula as presented in [8]

$$\lambda_l = \zeta \frac{Ag\ m}{h_l} u_l^m \tag{7}$$

$$\lambda_r = \zeta \frac{Ag\ m}{h_r} u_r^m. \tag{8}$$

With ζ as the porosity and $m = 3$. As mentioned before, this approach can also be applied to many other bedload formulas by transforming them into the general Grass formulation [8].

III. NUMERICAL BENCHMARK - GAIA

Three test cases are presented to compare the local Lax-Friedrichs fluxes GLLF and SLLF with the upwind scheme of the finite volume method of GAIA (UPWIND) and the finite element scheme of GAIA (FEM). All test cases use the bedload formula of Grass with one grain class. We implemented both local Lax-Friedrichs schemes in GAIA by adding local FORTRAN files in the user directory for the files ‘bedload_solvs_vf_gaia.f and ‘user_bedload_qb.f’.

A. Dune evolution low and high interaction

The test cases for low and high interaction between the hydrodynamic and morphodynamic system are taken from Cordier et al. [2]. The initial bed topography for both test cases is defined as

$$z = 0.1 + 0.1e^{-(x-5)^2}. \tag{9}$$

A discharge boundary condition is applied as inflow on the left side of the domain. The specific discharge is set to q = 0.5 m^2/ s and is constant over time. On the right side, a fixed water depth of 0.5 m is applied as outflow boundary condition. The domain is 10 m long times 1 m wide, and a mesh with 4000 elements and a distance of 0.1 m between the nodes is used for the studies.

A simulation with a fixed bed was carried out to compute the initial conditions for the shallow water equations. Bedload transport is simulated with the Grass formula. Reference [2] applied two different Grass parameters to generate a system with low interaction (*Ag = 0.005*) and a system of high interaction (*Ag = 0.07*) between bedload transport and shallow water equations. The parameter for the high interaction was chosen to show that most splitting schemes will fail to predict the bed evolution.

Figure 2 shows the bed development for the all four schemes for the case with low interaction. The FEM and GLLF show good results until the formation of a discontinuity. This discontinuity occurs when the characteristics of the bedload system intersect. Afterwards numerical instabilities (oscillations) are visible near the top of the dune. UPWIND and SLLF show no oscillations.

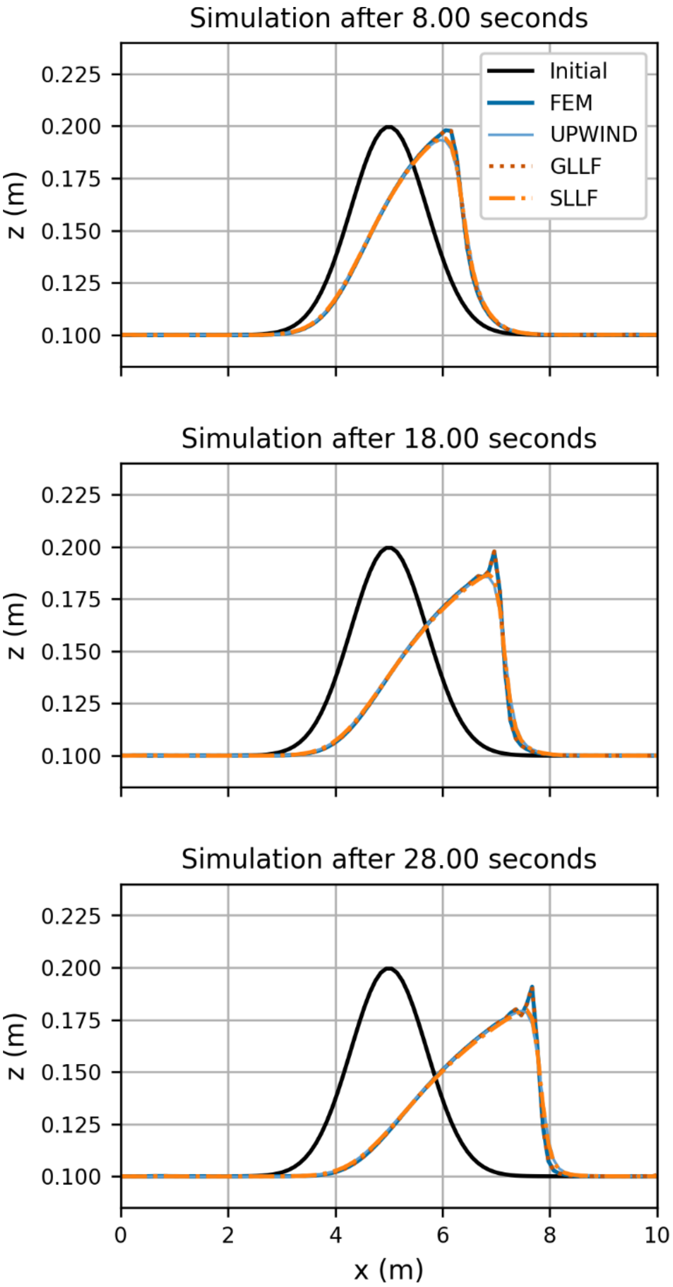

Figure 2. Dune evolution with low interaction [2].

For the system with the higher interaction (Figure 3), UPWIND shows strong oscillations over the whole domain. FEM and GLLF show again oscillations after the characteristics intersect. The SLLF is the only scheme which produces a monotone solution. However, the results of the SLLF are much more diffusive compared to the FEM and GLLF after 2.6 seconds. The oscillations are maybe caused by the free surface boundary condition at the outflow boundary. We observed an upstream moving variation in the flow velocity which may trigger the first oscillation, later the oscillations are maybe amplified. As mentioned by Cordier et al. [2], a more diffusive numerical bedload flux can damp such small oscillations.

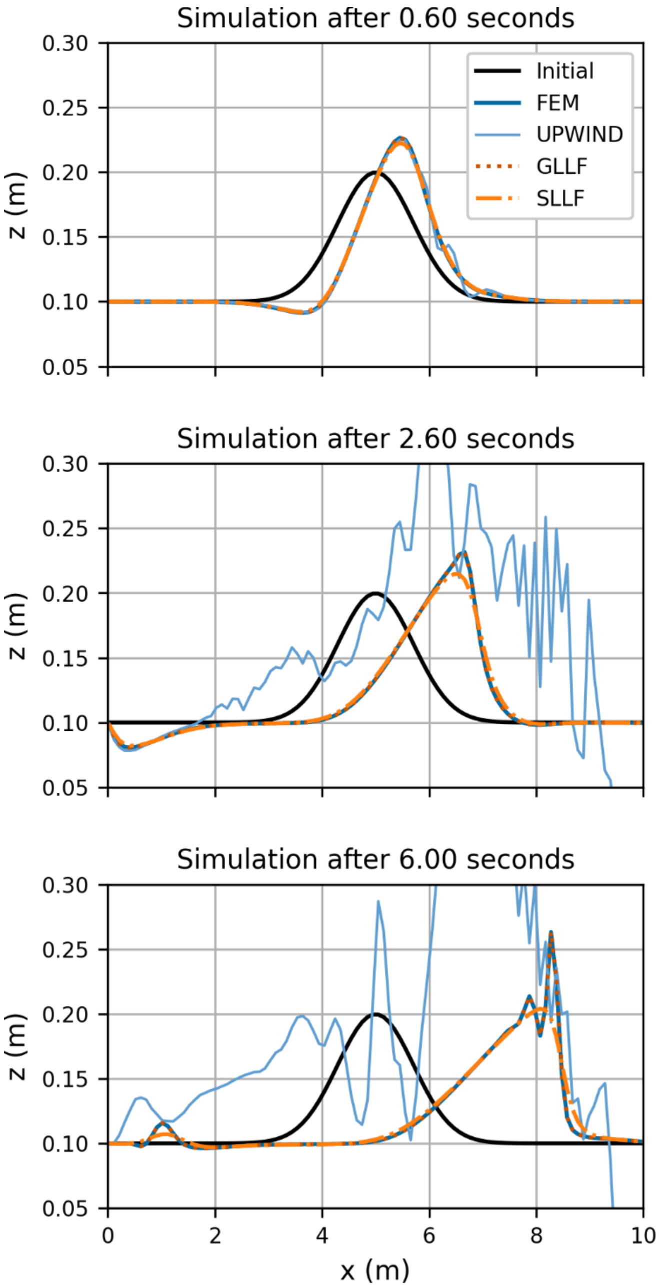

Figure 3. Dune evolution with high interaction [2].

B. Dune evolution -Hudson bump

The test case of Hudson [12] is a common benchmark for bedload transport modelling since an analytical solution for the bed evolution exists. The solution is valid until the characteristics off the bedload problem intersects. The initial bed of the 1000 m long and 10 m wide channel between $300 \leq x \leq 500$ m is given by:

$$z = 0.1 + sin(\frac{(x-300)\pi}{200})^2 \qquad (10)$$

and a constant bed elevation ($z = 0.1\ m$) elsewhere. A constant specific discharge with q = 10 m^2/s is set at the left side (inflow) and free surface of 10 m is set at the right side (outflow). The computational domain is discretized using 10000 elements and a distance between 2 m between element nodes.

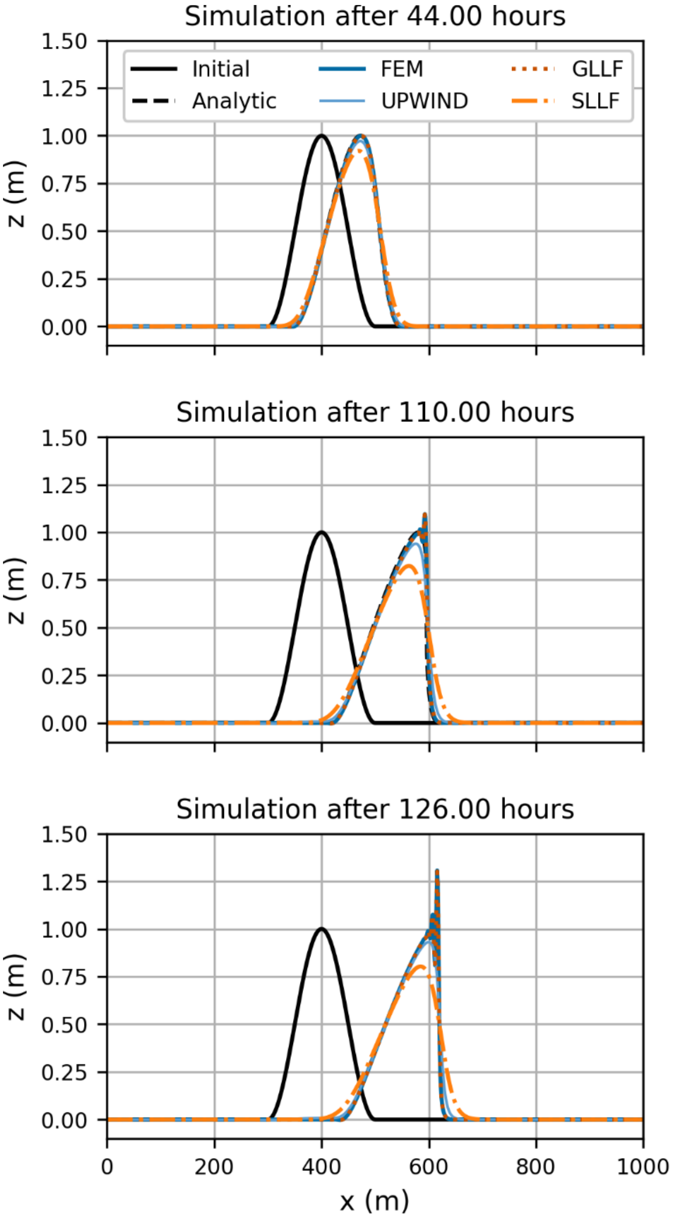

Figure 4. Dune evolution Hudson bump test case [12].

In Figure 4, FEM and GLLF show again good results at the beginning of the simulation, later the solution gets unstable with large oscillations. UPWIND and SLLF are both more diffusive, but stable over the whole simulation time. It seems like the numerical diffusion of the SLLF and UPWIND scheme prevents both schemes from oscillations. We observed some small wiggles at the inflow boundary condition which travel downstream during simulation. However, it is not clear if the wiggles are caused by the instabilities for FEM and GLLF.

IV. NUMERICAL BENCHMARK – 1D FINITE VOLUME MODEL

In the following, the previous test cases are simulated with a 1D finite volume model, which we created in Python to study the behavior of the GLLF and the SLLF. A further test case of the evolution of an antidune has been added to study the GLLF and SLLF under supercritical flow conditions.

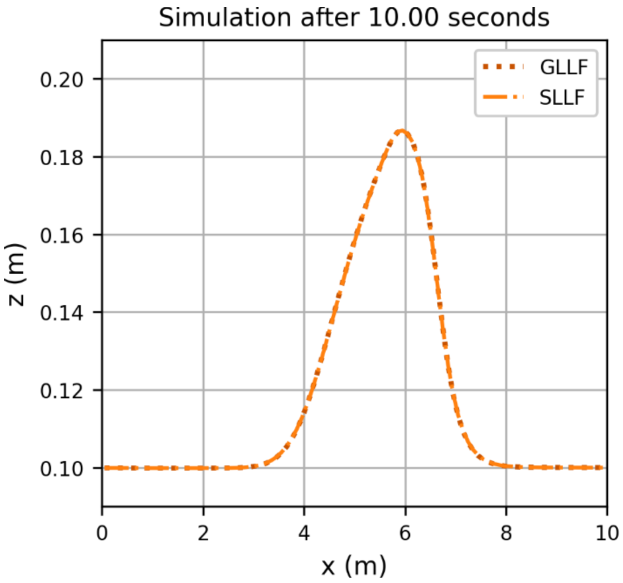

Figure 5. 1D results: Cordier et al. [2] example with low interaction.

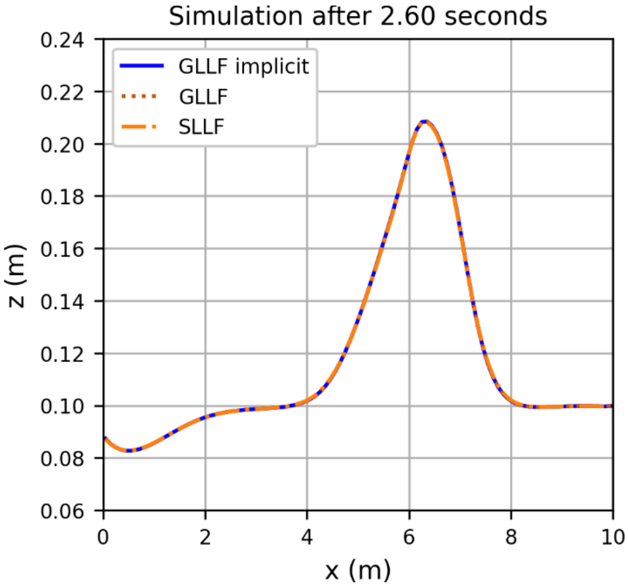

Figure 6. 1D results: Cordier et al. [2] example with high interaction.

A. Dune evolution low and high interaction

Figure 5 and 6 show the results of the GLLF and SLLF for the dune test case of Cordier et al. [2] with high interaction and low interaction respectively. The domain is discretized using 100 cells with a constant length of 0.1 m. The differences between SLLF and GLLF are negligible for both test cases. There are also no visible differences between the explicit approach and the fully coupled implicit solution (Figure 6).

B. Dune evolution – Hudson bump

Figure 7 shows the results of the 1D model for the Hudson bump test case. Here we can see that the SLLF is much more diffusive and the GLLF would be the better choice (Figure. 7)

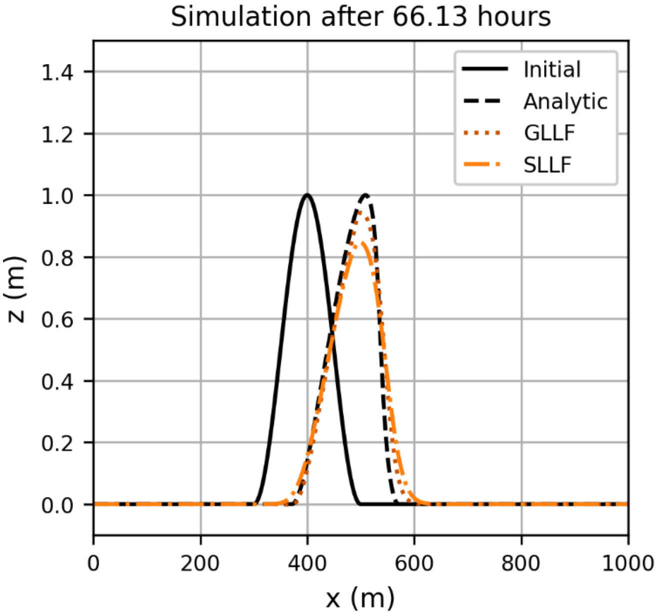

Figure 7. 1D results: Hudson bump test case [12].

C. Evolution of an antidune

Audusse et al. [5] presented a test case for simulating the evolution of an antidune under supercritical flow conditions. The domain is 24 m long and includes a parabolic bump in the center of the domain given by:

$$z = 0.2 - 0.05 + sin(x - 10)^2 \tag{11}$$

Between $8 \leq x \leq 12$ m and z = 0.2 m elsewhere. A constant uniform specific discharge q = 1.7 m^2/s is applied on the left side of the supercritical system. A water height of 0.5 m and a fixed flow velocity v = 0.85 m/s are set as boundary condition on both sides. A free outflow boundary condition might be better choice at the outflow boundary. Nevertheless, Figure 8 shows that the 1D method is able to reproduce the upstream propagation of the sediment bump (antidune). The differences between SLLF and GLLF are negligible, both fluxes can reproduce qualitatively the antidune pattern presented in [5].

V. DISCUSSION AND CONCLUSION

The results show how hard it is to create a general-purpose numerical scheme for bedload transport modelling. The FEM of GAIA and the implemented GLLF scheme are only stable as long as the characteristics of the sediment problem do not intersect. The UPWIND scheme of GAIA is more stable, but fails for the Cordier example with a high interaction. The SLLF scheme was the only scheme that was able to simulate all three test cases with GAIA without oscillations. However, the SLLF scheme can be more diffusive compared to the other schemes, especially if the bed celerity is small. Nevertheless, the SLLF scheme in combination with a higher mesh resolution can be a good choice if the UPWIND scheme cannot be used. Reference [10] discussed the situations where the UPWIND scheme of Gaia should not be applied in detail.

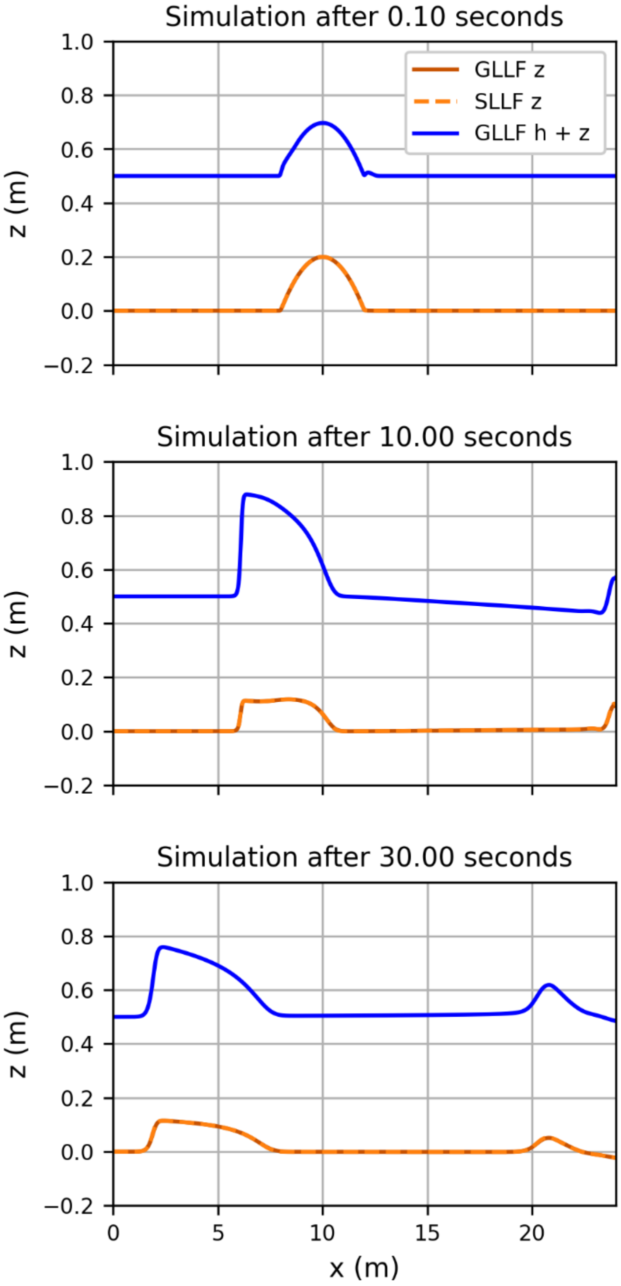

Figure 8. 1D results: antidune evolution [5].

The results of the benchmark with the 1D finite volume model, which we implemented in Python to investigate the behavior of the GLLF and the SLLF show that the both schemes can produce monotone and stable solutions for all investigated problems. Both schemes are also able to simulate the evolution of an antidune under supercritical flow conditions. The differences between GLLF and SLLF are negligible for the test cases with a high interaction and high bed celerity. However, the GLLF shows better results for the test case with a low interaction. The only disadvantage of the GLLF is that the applied bedload formulas must be transferred to the general Grass formula to estimate the bed celerity. We know from other simulations with the 2D finite volume model of DuMu^x (https://dumux.org) that the GLLF scheme can also be applied in 2D on triangular grids. The DuMu^x results of the GLLF are much less diffusive compared to the SLLF. Therefore, future work in Gaia should focus on finding a way to implement a stable version of the GLLF scheme into Gaia. It looks like our implementation in Gaia underestimates the bed celerity λ, leading to the unstable centered flux (1). However, it is also possible that the instabilities are caused by an error in the hydrodynamic solution.

References

[1] F. M. Exner, “Über die Wechselwirkung zwischen Wasser und Geschiebe in Flüssen“, Sitzungsberichte. Abt. 2a, Mathematik, Astronomie, Physik und Meteorologie, 1925.

[2] S. Cordier, M.H. Le and T. Morales de Luna, “Bedload transport in shallow water models: Why splitting (may) fail, how hyperbolicity (can) help”, Advances in Water Resources, 34(8), 2011.

[3] L. Stadler, “Entwicklung eines voll impliziten Verfahrens zur Simulation der langfristigen und großräumigen Sohlentwicklung in Fließgewässern“, 2021.

[4] M. Bilanceri, F. Beux, I. Elmahi, H. Guillard and M.V. Salvetti, “Implicit time advancing combined with two finite-volume methods in the simulation of morphodynamic flows”, Mathematics and Computers in Simulation, 99, 2014.

[5] E. Audusse, O. Delestre, M.H. Le, M. Masson-Fauchier, P. Navaro and R. Serra, “Parallelization of a relaxation scheme modelling the bedload transport of sediments in shallow water flow”, ESIAM Proceedings, 43, 2013.

[6] L. Goutière, S. Soares-Frazão, C. Savary, T. Laraichi, Y. Zech, “One-Dimensional Model for Transient Flows Involving Bed-Load Sediment Transport and Changes in Flow Regimes”, Journal of Hydraulic Engineering, 134(6), 2008.

[7] S. Soares-Frazão, Y. Zech, “HLLC scheme with novel wave-speed estimators appropriate for two-dimensional shallow-water flow on erodible bed”, International Journal for Numerical Methods in Fluids, 66(8), 2011.

[8] D. F. Bautista-Parada, A. Chaves-Guerrero; D. A. Fuentes-Díaz, “Decoupled solution of the sediment transport and 2D shallow water equations using the finite volume method”, Results in Engineering, 15, 2022.

[9] E.F. Toro, “Shock-capturing methods for free-surface shallow flows”, 2001.

[10] S. Revillon, F. Taccone, F. Souillé, ”A newly implemented upwind scheme and numerical benchmark for the resolution of the Exner equation in GAIA”. Online proceedings of the 2020 TELEMAC-MASCARET User Conference, 2020.

[11] E. Audusse, F. Bouchut, M. Bristeau, R. Klein, B. Perthame, “ A Fast and Stable Well-Balanced Scheme with Hydrostatic Reconstruction for Shallow Water Flows”, SIAM Journal on Scientific Computing, 25 (6), 2004.

[12] J. Hudson, “Numerical Techniques for Morphodynamic Modelling”, 2001.

BAW
Federal Waterways Engineering
and Research Institute

Kussmaulstrasse 17 · 76187 Karlsruhe
Tel.: +49 (0) 721 9726-0 · Fax: +49 (0) 721 9726-4540

Wedeler Landstrasse 157 · 22559 Hamburg
Tel.: +49 (0) 40 81908-0 · Fax: +49 (0) 40 81908-373

www.baw.de